Present day sea level: global and regional variations

Hindumathi K. Palanisamy

THÈSE

En vue de l'obtention du

DOCTORAT DE L'UNIVERSITÉ DE TOULOUSE

Délivré par l'Université Toulouse III - Paul Sabatier
Discipline ou spécialité : Océanographie Spatiale

Présentée et soutenue par Hindumathi Kulaiappan Palanisamy
Le 06 janvier 2016

Titre: Le niveau de la mer actuel: variations globale et régionales

Title: Present day sea level: global and regional variations

JURY

Nicholas Hall (Président du Jury)
Jérôme Vialard (Rapporteur)
Johnny A. Johannessen (Rapporteur)
Joshua Willis (Examinateur)
Anny Cazenave (Directrice de Thèse)
Thierry Delcroix (Directeur de Thèse)

Ecole doctorale: SDUEE
Unité de recherche: LEGOS UMR 5566
Directeurs de Thèse: *Anny Cazenave et Thierry Delcroix*
Rapporteurs: voir le Jury

Acknowledgements

I would first like to thank Anny for her marvelous support all through the duration of this thesis. Her vast knowledge is highly impressive and her curiosity to learn new things has always been a motivating factor to me. Through her, I learnt that neither age nor intellectual status is a barrier when it comes to constant quest for knowledge. I am also impressed with the importance she has given and still continues to give her students irrespective of her schedule. I am deeply honored to be one of her students.

I would also like to thank Thierry for his patience, pedagogic skills and his vast knowledge in the field of oceanography. His astonishing ability to explain concepts in a very simple manner has been of great help for someone like me having no prior education in the domain of oceanography. Our Thursday discussions have also helped me uncover his humorous and easy-going attitude!

I would also to acknowledge the financial support from CNES and CLS and thank Michaël, Gilles for their support in obtaining the financement.

My sincere thanks to Philippe; without his help I would not have been able to start my career in this field of research. I would also like to thank Benoit and Mélanie who have both been my first mentors. It's still a great pleasure to discuss and learn a lot from you both.

My special thanks to Martine, Nadine, Catherine and Agathe for their help with the paper works irrespective of their workloads. I still remember the days when I hardly spoke French and would go to them for help. If not for them, I would have had a tough time getting adapted at LEGOS.

Thanks to Olivier with whom I shared my office for more than two years. It was fun working with him, discuss science and have various other non-scientific debates. I would also like to thank Brigitte for the coffee break sessions. It has always been a pleasure and a great relief to take a break and just walk into her office to discuss everything but science. My special thanks also go to Wojtek, Vanessa, Ivonne, Sylvain, Laurence, Angélique, Elodie, Téodolina, William, Akhil, Alejandro, Caroline and every other colleague who has made this journey pleasurable.

I would also like to take this opportunity to thanks my friends Thomas, Olivier, Pascal, Eric, Sangeeth and Florian for their moral support and my family members Brigitte, François, Charlotte, Alix, Hubert and Brinda for having stood by me through rough times.

I am deeply grateful to my parents for who I am today…

I dedicate this thesis to Thibaud…

Le niveau de la mer actuel: variations globale et régionales

Auteur: Hindumathi K. Palanisamy
Directrice/Directeur de thèse: Anny Cazenave & Thierry Delcroix
Discipline: Océanographie Spatiale
Lieu et date de soutenance: Observatoire Midi-Pyrénées, 6 Janvier, 2016
Laboratoire: LEGOS, UMR5566 CNRS/CNES/IRD/UPS, Toulouse, France.

Résumé: Le niveau de la mer est une des variables climatiques essentielles dont la variabilité résulte de nombreuses interactions complexes entre toutes les composantes du système climatique sur une large gamme d'échelles spatiales et temporelles. Au cours du XXème siècle, les mesures marégraphiques ont permis d'estimer la hausse du niveau de la mer global entre 1,6 mm/an et 1,8 mm/an. Depuis 1993, les observations faites par les satellites altimétriques indiquent une hausse du niveau de la mer plus rapide de 3,3 mm/an. Grâce à leur couverture quasi-globale, elles révèlent aussi une forte variabilité du niveau de la mer à l'échelle régionale, parfois plusieurs fois supérieure à la moyenne globale du niveau de la mer. Compte tenu de l'impact très négatif de l'augmentation du niveau de la mer pour la société, sa surveillance, la compréhension de ses causes ainsi que sa prévision sont désormais considérées comme des priorités scientifiques et sociétales majeures.

Dans cette thèse, nous validons d'abord les variations du niveau de la mer mesurées par la nouvelle mission d'altimétrie satellitaire, SARAL-AltiKa, en comparant les mesures avec celles de Jason-2 et des marégraphes. Un autre volet de cette première partie de thèse a consisté à estimer les parts respectives des facteurs responsables des variations du niveau de la mer depuis 2003 en utilisant des observations issues de l'altimétrie satellitaire (missions altimétrique Jason-1, Jason-2 et Envisat), de la mission GRACE, et des profils de température et salinité de l'océan par les flotteurs Argo. Une attention particulière est portée à la contribution de l'océan profond non 'vue' par Argo. Nous montrons que les incertitudes dues aux approches du traitement des données et aux erreurs systématiques des différents systèmes d'observation nous empêchent encore d'obtenir des résultats précis sur cette contribution.

Dans la deuxième partie de la thèse, en utilisant les données de reconstruction du niveau de la mer dans le passé, nous étudions la variabilité régionale du niveau de la mer et estimons sa hausse totale (composante régionale plus moyenne globale) de 1950 à 2009 dans trois régions vulnérables: l'océan Indien, la mer de Chine méridionale et la mer des Caraïbes. Pour les sites où l'on dispose de mesures du mouvement de la croûte terrestre par GPS, nous évaluons la hausse locale du niveau de la mer relatif (hausse du niveau de la mer totale plus mouvement de la croûte locale) depuis 1950. En comparant les résultats de ces trois régions avec une étude précédente sur le Pacifique tropical, nous constatons que le Pacifique tropical présente la plus forte amplitude des variations du niveau de la mer sur la période d'étude.

Dans la dernière partie de la thèse, nous nous concentrons par conséquent sur le Pacifique tropical. Nous analysons les rôles respectifs de la dynamique océanique, des modes de variabilité interne du climat et du forçage anthropique sur les structures de la variabilité régionale du niveau de la mer du Pacifique tropical depuis 1993. Nous montrons qu'une partie importante de la variabilité régionale du niveau de la mer du Pacifique tropical peut être expliquée par le mouvement vertical de la thermocline en réponse à l'action du vent. En tentant de séparer le signal correspondant au mode de variabilité interne du climat de celui de la hausse régionale du niveau de la mer dans le Pacifique tropical, nous montrons également que le signal résiduel restant (c'est-à-dire le signal total moins le signal de variabilité interne) ne correspond probablement pas à l'empreinte externe du forçage anthropique.

Mots-clés: Hausse du niveau de la mer, SARAL-AltiKa, bilan du niveau de la mer, contribution l'océan profond, Pacifique tropical, thermocline, mode de la variabilité interne, impacts anthropiques.

Present day sea level: global and regional variations

Author: Hindumathi K. Palanisamy
Ph.D. directors: Anny Cazenave & Thierry Delcroix
Discipline: Space Oceanography
Place and Date of defense: Observatoire Midi-Pyrénees, 6th January, 2016
Laboratory: LEGOS, UMR5566 CNRS/CNES/IRD/UPS, OMP, 14 Avenue Edouard Belin, 31400, Toulouse, France.

Summary: Sea level is an integrated climate parameter that involves interactions of all components of the climate system (oceans, ice sheets, glaciers, atmosphere, and land water reservoirs) on a wide range of spatial and temporal scales. Over the 20th century, tide gauge records indicate a rise in global sea level between 1.6mm/yr and 1.8 mm/yr. Since 1993, sea level variations have been measured precisely by satellite altimetry. They indicate a faster sea level rise of 3.3 mm/yr over 1993-2015. Owing to their global coverage, they also reveal a strong regional sea level variability that sometimes is several times greater than the global mean sea level rise. Considering the highly negative impact of sea level rise for society, monitoring sea level change and understanding its causes are henceforth high priorities.

In this thesis, we first validate the sea level variations measured by the new satellite altimetry mission, SARAL-AltiKa by comparing the measurements with Jason-2 and tide gauge records. We then attempt to close the global mean sea level budget since 2003 and estimate the deep ocean contribution by making use of observational data from satellite altimetry, Argo profiles and GRACE mission. We show that uncertainties due to data processing approaches and systematic errors of different observing systems still prevent us from obtaining accurate results.

In the second part of the thesis, by making use of past sea level reconstruction, we study the patterns of the regional sea level variability and estimate climate related (global mean plus regional component) sea level change over 1950-2009 at three vulnerable regions: Indian Ocean, South China and Caribbean Sea. For the sites where vertical crustal motion monitoring is available, we compute the total relative sea level (i.e. total sea level rise plus the local vertical crustal motion) since 1950. On comparing the results from these three regions with already existing results in tropical Pacific, we find that tropical Pacific displays the highest magnitude of sea level variations.

In the last part of the thesis, we therefore focus on the tropical Pacific and analyze the respective roles of ocean dynamic processes, internal climate modes and external anthropogenic forcing on tropical Pacific sea level spatial trend patterns since 1993. Building up on the relationship between thermocline and sea level in the tropical region, we show that most of the observed sea level spatial trend pattern in the tropical Pacific can be explained by the wind driven vertical thermocline movement. By performing detection and attribution study on sea level spatial trend patterns in the tropical Pacific and attempting to eliminate signal corresponding to the main internal climate mode, we further show that the remaining residual sea level trend pattern does not correspond to externally forced anthropogenic sea level signal. In addition, we also suggest that satellite altimetry measurement may not still be accurate enough to detect the anthropogenic signal in the 20 year tropical Pacific sea level trends.

Keywords: Sea level rise, SARAL-AltiKa, Global mean sea level budget, deep ocean contribution, regional sea level variability, total relative sea level change, tropical Pacific, thermocline, internal climate mode, anthropogenic sea level fingerprint.

Table of Contents

Introduction générale (en français)

L'élévation du niveau de la mer est considérée comme une menace majeure pour les zones côtières de basse altitude de la planète en raison du réchauffement climatique actuel d'origine humaine (*Nicholls et al.,* 2008). Terres riches fertiles, transports maritimes, accès aux ressources halieutiques ont toujours attiré les populations humaines le long de la frange côtière des terres émergées. Au cours des dernières décennies, de nombreuses mégalopoles du monde peuplées de plusieurs dizaines de millions d'habitants se sont développées le long des côtes. On estime qu'au moins 650 millions de personnes vivent à moins de 10m du niveau actuel de la mer (*McGranahan et al.,* 2007), et ce nombre est en croissance constante. Il devrait atteindre 800 millions d'ici 2080 (*Nicholls et al*. , 2010).

L'élévation du niveau de la mer et ses impacts côtiers sont l'une des principales conséquences du changement climatique. Elle affecte non seulement les côtes continentales mais aussi de nombreuses îles basses des océans tropicaux (*Mimura et al.,* 2007, *Nicholls et al.,* 2011). L'élévation du niveau de la mer en réponse aux concentrations croissantes de gaz à effet de serre est un défi majeur auquel l'humanité doit faire face au 21e siècle. Des enregistrements marégraphiques indiquent que le niveau moyen de la mer s'est élevé d'environ 20 cm au cours du 20ème siècle. Les modèles de climat montrent aussi que cette hausse va se poursuivre au 21ème siècle et même au-delà. Bien que les estimations de l'élévation future du niveau de la mer soient encore incertaines en raison des incertitudes des émissions futures de gaz à effet de serre et de la réponse associée du système climatique, on estime que le niveau de la mer va continuer à monter de plusieurs dizaines de cm, voire plus d'1 m dans les prochaines décennies (*IPCC,* 2013). En effet, même si les émissions de gaz à effet de serre se stabilisaient rapidement, la durée de vie du dioxyde de carbone dans l'atmosphère, l'inertie thermique de l'océan et le lent temps de réponse de certaines composantes du système climatique, la hausse du niveau de la mer se poursuivra pendant plusieurs siècles (*Dutton et al.,* 2015, *GIEC,* 2013, *Levermann et al .,* 2013, *Meehl et al*.,

2012, *Meehl et al.*, 2005, *Wigley*, 2005). Par conséquent, il est impératif d'identifier et de quantifier les causes qui contribuent aux variations actuelles du niveau de la mer, non seulement pour la compréhension des phénomènes en jeu, mais aussi afin que d'améliorer les performances des modèles climatiques développés pour simuler les évolutions futures.

Ma thèse contribue à une meilleure estimation et à la compréhension des variations du niveau de la mer au cours des dernières décennies, non seulement à l'échelle mondiale mais aussi régionale. En effet, nous savons aujourd'hui que régionalement, la hausse du niveau de la mer peut très sensiblement dévier de la moyenne mondiale sur une large gamme d'échelles spatiales et temporelles. Les principaux objectifs et l'organisation de la thèse sont décrits ci-dessous.

- Le premier chapitre est une introduction dans laquelle nous résumons l'état des connaissances sur les variations actuelles et passées du niveau de la mer, depuis le dernière maximum glaciaire il y a 20000 ans jusqu'à l'ère instrumentale. Nous décrivons aussi les principales contributions à la variation moyenne globale du niveau de la mer du 20ème siècle. Ce chapitre fournit ainsi le cadre général dans lequel s'inscrivent les sujets abordés au cours de ce travail de thèse.
- Dans le deuxième chapitre, nous fournissons une description détaillée des différentes missions altimétriques utilisées pour mesurer de façon précise et globale le niveau de la mer depuis le début des années 1990s. Nous décrivons aussi le principe de mesure de la hauteur de la surface de la mer par altimétrie satellitaire et les différentes corrections géophysiques et instrumentales appliquées à la mesure de la hauteur de la surface de la mer. Dans ce chapitre, nous présentons un premier travail dédié à la validation des mesures du niveau de la mer réalisées par la nouvelle mission d'altimétrie spatiale, SARAL-AltiKa, lancée en février 2013. Cette validation est basée sur la comparaison avec les mesures du satellite Jason-2 et des données marégraphiques. Un autre volet de cette première partie de thèse a consisté à estimer les parts respectives des facteurs responsables des variations du niveau de la mer depuis 2003 en utilisant des observations issues de l'altimétrie satellitaire (missions altimétriques Jason-1, Jason-2 et Envisat), de la mission de gravimétrie spatiale GRACE, et des profils de température et salinité de l'océan par les flotteurs Argo. Une attention particulière est portée à la contribution de l'océan profond non 'vue' par Argo.

- Le chapitre 3 porte sur la variabilité régionale du niveau de la mer et ses causes. Il décrit les études que nous avons réalisées sur l'estimation de la variation totale du niveau relatif de la mer depuis 1950 dans diverses régions vulnérables du monde: en utilisant les données de reconstruction du niveau de la mer dans le passé, nous étudions la variabilité régionale du niveau de la mer et estimons sa hausse totale (composante régionale plus moyenne globale) de 1950 à 2009 dans trois régions, l'océan Indien, la mer de Chine méridionale et la mer des Caraïbes. Pour les sites où l'on dispose de mesures du mouvement de la croûte terrestre par GPS, nous évaluons la hausse locale du niveau de la mer relatif (hausse du niveau de la mer totale plus mouvement de la croûte locale) depuis 1950.
- Dans le chapitre 4 nous analysons les rôles respectifs de la dynamique océanique, des modes de variabilité interne du climat et du forçage anthropique sur les structures de la variabilité régionale du niveau de la mer du Pacifique tropical au cours des 20 dernières années. On observe en effet sur cette période que la hausse de la mer dans cette région a été 3 à 4 fois plus importante qu'en moyenne globale. Au cours de cette thèse, nous expliquons les mécanismes physiques causant cette hausse plus rapide. Enfin dans une dernière partie, nous cherchons à déterminer les parts respectives du forçage anthropique et de la variabilité naturelle interne du climat, pour expliquer l'origine de cette importante variabilité régionale observée dans la hausse de la mer.

Chapter 1

Introduction

Sea level rise has been seen as a major threat to low-lying coastal areas around the globe since the issue of human-induced global warming emerged in the 1980s (*Nicholls et al.*, 2008). Rich fertile land, transport connections, port access, coastal and deep sea fishing have attracted millions of people along the coastal fringes of continents. Many of the world's megacities with population of many millions have been developed along the coasts with little consideration of sea level rise and its impacts. While in global terms relatively small in number, the very existence of small-island nation states makes them more vulnerable to rises in sea level (*Mimura et al.,* 2007, *Nicholls et al.*, 2011). It is estimated that at least 600 million people live within 10m of sea level currently (*McGranahan et al.*, 2007), and these populations are growing more rapidly than global trends and is expected to reach 800 million by the 2080s (*Nicholls et al.,* 2010).

Sea level rise and its resultant coastal impact are one of the main consequences of present day anthropogenic global climate change. Sea level rise from ocean warming and land ice melt is a central part of the Earth's response to increasing greenhouse gas (GHG) concentrations and is therefore identified as the major challenge facing humankind in the 21st century. Though estimates of timescales, magnitudes and rates of future sea level rise vary considerably, partly as a consequence of uncertainties in future emissions and associated climate response, it is expected that the sea level will continue to rise in the near future. This is because, even if the GHG emissions are stabilized, the oceanic thermal inertia and the slow response time of different climate components would still aid in the continuation of sea level rise (*Dutton et al.*, 2015, *IPCC*, 2013, *Levermann et al.*, 2013, *Meehl et al.*, 2012, *Meehl et al.*, 2005, *Wigley*, 2005). Therefore it is imperative to identify and quantify the causes contributing to the present observed

sea level change not only for basic understanding and scientific challenges but also in order that better models can be developed and more reliable predictions can be provided. Furthermore, the study of past sea level changes by making use of historical records and their proxies will also offer means for understanding and quantifying uncertainties, as well as determining how well sea level rise can be monitored in the future. In addition, the Earth has a memory of past events, and the pattern of relative sea-level change, today and in the future, will continue to respond to past events (*Lambeck et al*., 2010).

In this introductory chapter, we provide a brief synthesis of what is known about sea level variations between the paleo and the instrumental era. In addition to this, we also address the main contributors to global mean sea level change since the instrumental era. This chapter does not present the results of the Ph.D. work but rather creates a base for the subjects addressed in the work and explains the framework of my Ph.D. thesis.

1.1 Paleo sea level

Sea level changes have occurred throughout Earth history with magnitudes and timing of the changes being extremely variable. On geological time scales, hundreds of millions of years ago, sea level variations were mainly controlled by changes in the shape and volume of the oceanic basins due to tectonic activities such as formation of oceanic plates at mid-ocean ridges, collision with continents etc. Over the Quaternary period, the oscillations between glacial and inter-glacial climate conditions during the past three millions of years have caused large-scale global mean sea level fluctuations in order > ± 100 m as a result of immense amount of water transferred between oceans and ice sheets (*Lambeck et al.*, 2002). So far there have been 17 such glacial and inter-glacial cycles associated with successive cold (northern hemisphere covered by ice sheets) and warm (equivalent to present conditions) periods. During the last interglacial period around 125,000 years ago, studies have shown that the global mean sea level was at least 5m higher than at present (*Dutton and Lambeck*, 2012, *Kopp et al.*, 2013, *Church et al.,* 2013, *Dutton et al.*, 2015). At the last glacial maximum that took place about ~21,000 years ago following the last interglacial period, the global mean sea level was ~130 m below the current sea level. Since then, subsequent melting of the northern hemisphere ice caps have been causing a sustained sea level rise (*Rohling et al.*, 2009, *Lambeck et al.*, 2002, *Lambeck et al.*, 2010

Fig.1.1). However, several paleo sea level indicators such as microfossils, coral data, beach rocks etc. have shown that the rate of sea level rise was not constant. Episodes of rapid rise of approximately 40 mm/yr have been reported about 14,000 years ago (*Deschamps et al.*, 2012) followed by significant decrease recorded at the beginning of Holocene 11,000 years ago and stabilization between 6,000 and 2,000 years ago (*Bard et al.*, 2010, *Lambeck et al.*, 2010). Over the past 2,000 years, based on salt-marsh microfossil analyses, studies (*Kemp et al.*, 2011, *Lambeck et al.*, 2004, *Lambeck et al.*, 2010) have shown that the sea level rise did not exceed 0.05-0.07 m per century with a large upward sea level trend becoming well apparent since the beginning of industrial era (late 18th to early 19th century, *Lambeck et al.*, 2004, *Kemp et al.*, 2011, *Woodworth et al.*, 2011, *Gehrels and Woodworth*, 2013). This period also corresponds to the beginning of instrumental era that has been allowing direct sea level measurements.

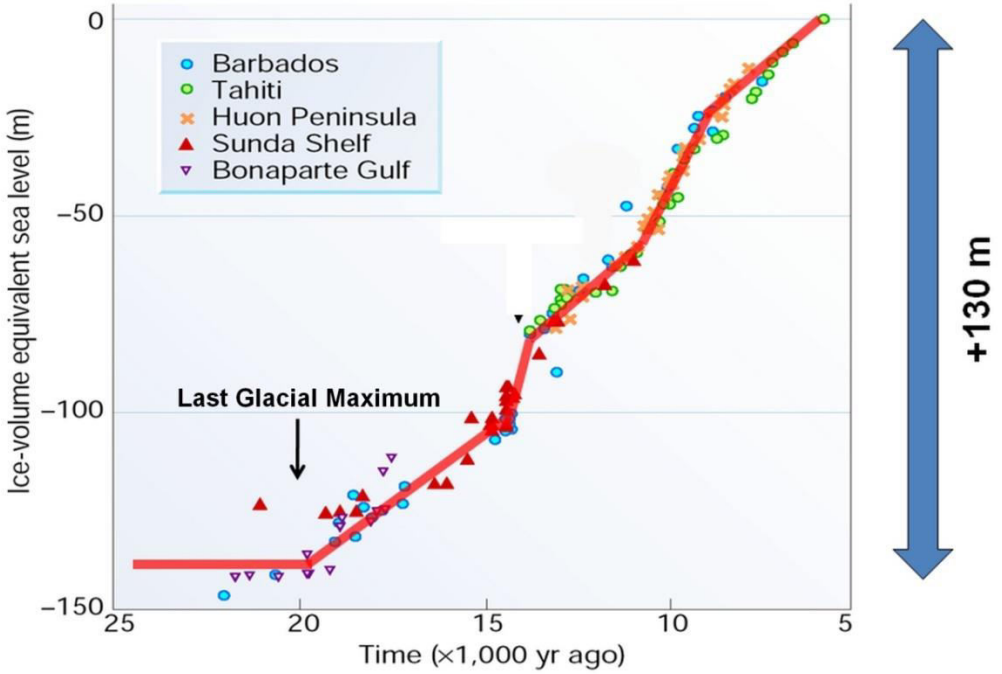

Figure 1.1: Changes in global ice volume in sea level equivalent from the last glacial maximum to present from Lambeck et al., 2002 and Haneburth et al., 2009. The ice-volume equivalent sea level is based on isostatically adjusted sea-level data from different locations. Courtesy: E.Bard

1.2 Instrumental era sea level

The instrumental record of sea level change is comprised of tide gauge measurements and satellite-based radar altimeters since the early 1990s.

1.2.1 Tide gauge records

The first systematic measurements of sea level from direct observations date back to the late 17thcentury mainly to provide information on ocean tides for commercial and military purposes , but it was not until the mid-19th century that the first 'automatic' tide gauges were developed. However, there were only a handful of such tide gauge records spanning the 19th-21st centuries, and most of these long time series come from tide gauges in the northern hemisphere, in specific, northern Europe (*Mitchum et al.,* 2010, *Gehrels and Woodworth*, 2013). In the southern hemisphere, tide gauge records in Australia are among the longest (starting in the late 19th century). Since the 20th century, the tide gauge network extended progressively covering the southern hemisphere. However for long term sea level studies, the number of long term records still remains small and geographically inhomogeneous with a strong density coverage in the northern hemisphere(Fig.1.2).

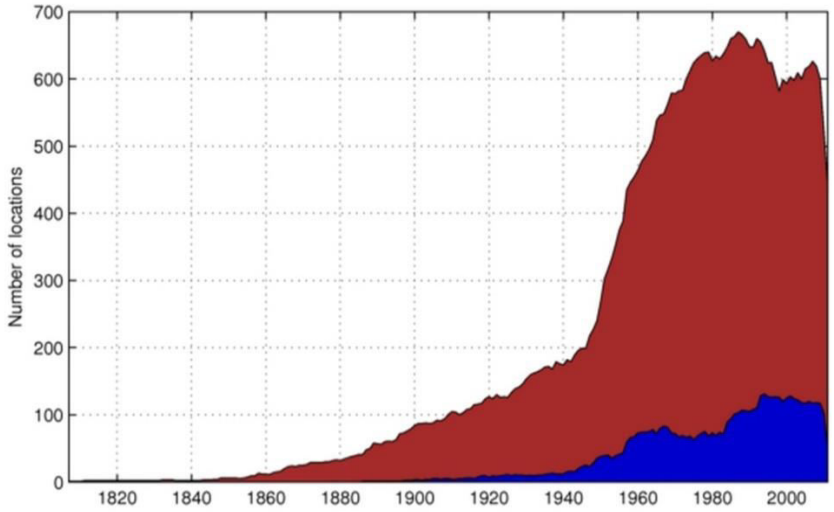

Figure 1.2: number of the tide gauge measurements available since 1807. Brown colour corresponds to the mean sea level data available from Northern Hemisphere and blue colour corresponds to the limited number of mean sea level data available from Southern Hemisphere. Source: PSMSL-http://www.psmsl.org/products/data_coverage/

Besides, tide gauge records often have multi-year or multi-decade long gaps. The sparse and heterogeneous coverage of tide gauge records, both temporally and geographically poses a problem for estimating reliable historical mean sea level variations (*Meyssignac and Cazenave*, 2012). Tide gauges measure sea level relative to the ground, hence monitor ground motions in areas subjected to strong natural (Glacial Isostatic Adjustment (GIA), tectonic/volcanic) or anthropogenic (ground water pumping, oil/gas extraction, sediment loading) ground subsidence. Therefore in order to study the absolute sea level change, the ground motion needs to be removed. Note however that for studying local impacts, the total relative sea level change (climatic sea level change plus vertical land motion) needs to be known (See Section 3.2 of Chapter 3). By developing various strategies, several studies (*Douglas*, 2001, *Church and White*, 2006, *Jevrejeva et al.*, 2006 *Jevrejeva et al.*, 2008, *Church and White*, 2011, *Wöppelmann et al.*, 2007, *Wöppelmann et al.*, 2009) have provided tide gauge based reliable historical sea level time series. In spite of the various approaches used, the results based from these studies are homogeneous and give a mean 20th century sea level rate in the range of 1.6-1.8 mm/yr. Fig.1.3 displays the 20th century global mean sea level curve of Church and White 2011 from tide gauge based past sea level reconstruction (in blue) with the satellite altimetry based sea level curve superimposed in red.

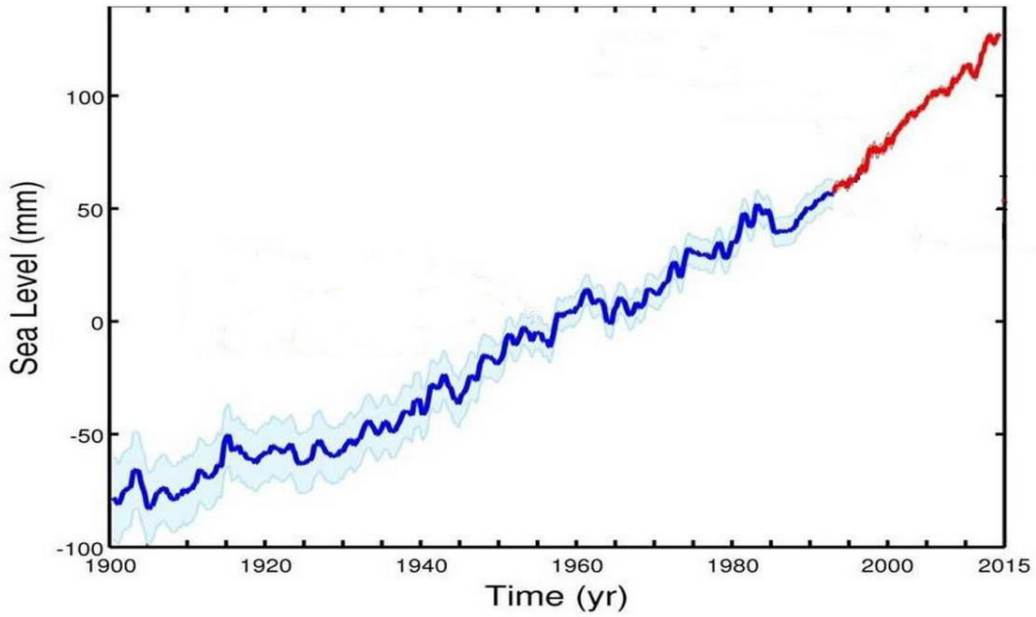

Figure 1.3: 20th century sea level curve (in blue) from tide gauge based past sea level reconstruction of Church and White, 2011and altimetry-based sea level curve (in red) between 1993 and 2015 from AVISO.

1.2.2 Satellite altimetry

Since the early 1990s, high precision satellite altimetry record provides nearly global sea level measurements at regular time intervals (*Fu and Cazenave*, 2001, *Church et al.*, 2013). Chapter 2 of this manuscript discusses the evolution of satellite altimetry, principle of sea surface height (SSH) measurement and the various geophysical and instrumental corrections involved in the precise SSH measurement in detail. The precision of individual SSH measurements based on the various satellite missions has now reached 1-2 cm. Although there are slight differences at interannual time scales in the altimetry-based global mean sea level time series produced by different groups (*Masters et al.*, 2012, *Henry*, 2014, *Dieng et al.*, 2015), there is very good agreement on the 22 year long global mean sea level trend. Over 1993-2015, the multi-satellite altimetry based global mean sea level rate amounts to 3.3 mm/yr. Precision on the global mean sea level rate is in the order of 0.4-0.5 mm/yr which is derived from assessments of all sources of errors affecting the altimetry measurements (*Ablain et al.*, 2009, *Ablain et al.*, 2015) and from tide gauge comparisons (*Beckley et al.*, 2010, *Nerem et al.*, 2010). Fig.1.4 displays the satellite-altimetry based global mean sea level curve obtained from Archiving Validation and Interpretation Satellite Oceanographic (AVISO) center (same as the red curve in Fig.1.3 but enlarged). The altimetry based sea level curve displays a quasi-linear increase over 1993-2015 with temporary interannual anomalies associated with El Niño (1997/1998) and La Niña (2007/2008, 2010/2011) events (e.g. *Nerem et al.,* 2010). The altimetry-based global mean sea level rate of 3.3 mm/yr over 1993-2015 is significantly higher than the mean rate recorded by tide gauges over the 20th century, suggesting sea level rise acceleration since the two recent decades (*Church et al.,* 2013, *Merrifield et al.*, 2009).

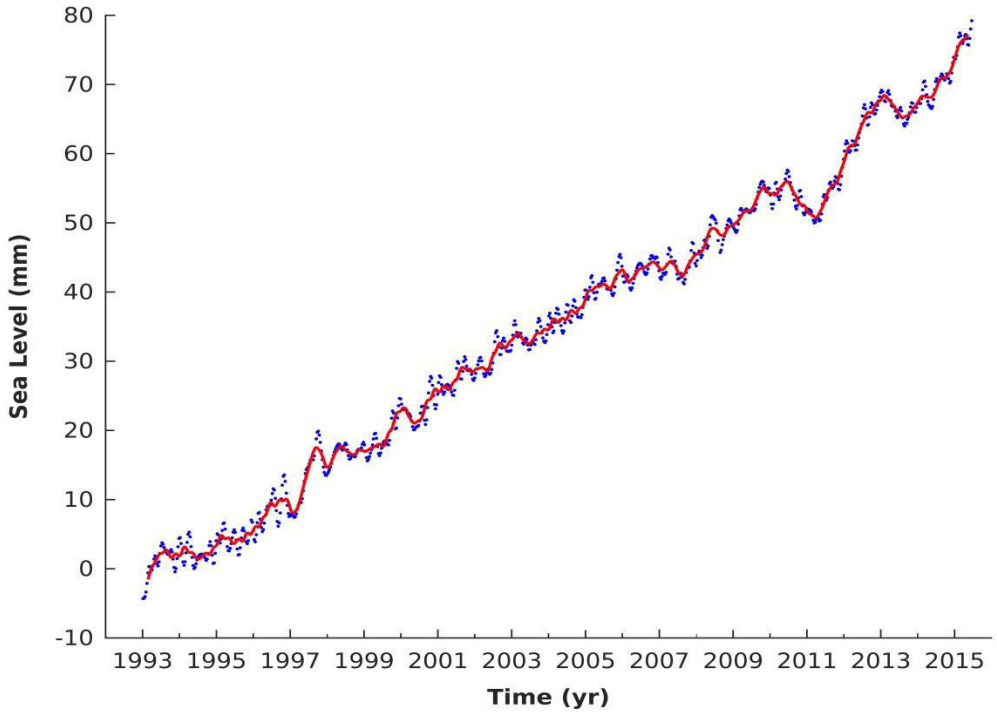

Figure 1.4: Altimetry-based global mean sea level temporal curve since 1993. The post glacial rebound correction of -0.3mm/yr has been applied and the annual, semi-annual signals have been removed. A 6 month filter has been applied on the red curve.

1.3 Contributors to global mean sea level rise during the instrumental era

The two main causes of global mean sea level change are the thermal expansion /contraction of the sea waters in response to ocean warming and the addition of freshwater to ocean basins as a result of land ice loss and water exchange with terrestrial reservoirs (soil and underground reservoirs, lakes, snowpack, etc.).

1.3.1 Ocean temperature and salinity changes

Anomalies in temperature and salinity in the ocean water column change density, which further gives rise to sea level variations (classically called steric variations, or thermosteric or halosteric if associated with only temperature or salinity variations respectively, *Cazenave and*

Llovel, (2010)). Analyses of in situ hydrographic measurements collected by ships over the past 50 years and recently by Argo profiling floats indicate that in terms of global mean, the oceans have warmed significantly since 1950. Over the 1971-2010 period, the 5th Assessment Report of the Intergovernmental Panel on Climate Change (IPCC AR5) shows that the global mean thermosteric sea level (including estimates of deep ocean contribution) trend amounts to 0.8±0.3 mm/yr accounting for about 40% of the observed sea level rise. Over the altimetry period of 1993-2010, the thermosteric sea level trend amounts to 1.1±0.3 mm/yr accounting for about 35% of the total observed sea level rise (*Church et al.,* 2013). Assuming constant total salt content, density changes arising from redistribution of salinity by ocean circulation (halosteric effect) has almost no effect on global mean sea level, although it plays a role at regional scales (*Antonov et al.*, 2002, *Wunsch et al.*, 2007, *von Schuckmann et al.*, 2009, *Cazenave and Llovel*, 2010, *Stammer et al.*, 2013, *Church et al.,* 2013, *Durack et al.*, 2014). For example, for the period 1955-2003, *Ishii et al.*, (2006) estimated a halosteric sea level rate of 0.04±0.02 mm/yr. While it is of interest to quantify this effect, only about 1% of the halosteric expansion contributes to the global sea level rise budget. This is because the halosteric expansion is nearly compensated by a decrease in volume of the added freshwater when its salinity is raised (by mixing) to the mean ocean value; the compensation would be exact for a linear state equation (*Gille*, 2004, *Lowe and Gregory*, 2006). Hence, for global sums of sea level change, halosteric expansion cannot be counted separately from the volume of added land freshwater (*Solomon et al.*, 2007, *Church et al.,* 2013).

1.3.2 Glaciers melting

Being very sensitive to global warming, observations have indicated that since 1970s, mountain glaciers and ice caps are retreating and thinning with noticeable acceleration since the early 1990s. They represent another significant source of freshwater mass to be added to world's oceans thereby raising sea level (*Church et al.,* 2013, *Gardner et al.*, 2013, *Vaughan et al.*, 2013). Contribution of glacier ice melt to sea level has been estimated through mass balance studies of a large number of glaciers (*Marzeion et al.*, 2014, *Gregory et al.*, 2013, *Church et al.,* 2013, *Leclercq et al.*, 2011, *Church et al.*, 2011, *Cogley*, 2009, *Meier et al.*, 2007, *Kaser et al.*, 2006). The mass balance estimates are either based on in situ measurements (monitoring of the annual mean snow accumulation and ice loss from melt) or geodetic techniques (measurements

of surface elevation and area change from airborne altimetry or digital elevation models, *Vaughan et al.,* 2013). The sea level contribution of all glaciers excluding those surrounding the periphery of Greenland and Antarctica ice sheets has been estimated as 0.62±0.37 mm/yr sea level equivalent (SLE) for 1971-2009 in IPCC AR5. For 1993-2009, its contribution amounts to 0.76±0.37 mm/yr, around 25% of the total observed sea level rise (*Church et al.,* 2013, *Church et al.*, 2011).

1.3.3 Ice sheets

The mass balance of ice sheets is a topic of considerable interest in the context of global warming and sea level rise since it is expected that if totally melted, Greenland and West Antarctica would raise sea level by several meters. While little was known on the mass balance of ice sheets before the 1990s mainly because of inadequate observations, since then, different remote sensing techniques (e.g. airborne and satellite radar and laser altimetry, Synthetic Aperture Radar Interferometry-InSAR) and space gravimetry since 2002 (Gravity Recovery and Climate Experiment-GRACE) have enabled the monitoring of ice sheet mass balance. Mass balance estimates from data obtained through the various techniques unambiguously show an accelerated ice mass loss from both the ice sheets in the recent years (*Hanna et al.*, 2013, *Gregory et al.*, 2013, *Fettweis et al.*, 2013, *Church et al.*, 2011, *Chen et al.*, 2009, *Velicogna*, 2009, *Rignot et al.*, 2008, *Hanna et al.*, 2008 and *Vaughan et al.,* 2013 for a review). During 1993-2003, the IPCC AR5 synthesis has shown that only around 13.5% of the total observed sea level rise was explained by the ice sheet mass loss. However, since then this contribution has augmented resulting in approximately 40% during 2003-2004 showing that this is not constant through time. Over the entire 1993-2009 time period, the ice sheet mass loss contribution to sea level was estimated to be 0.7±0.4 mm/yr SLE, that is, ~ 25% of the total observed sea level rise. Of the total ice mass loss contribution, 0.4±0.2 mm/yr SLE and 0.3±0.2 mm/yr SLE were contributed by Greenland and Antarctica respectively (*Church et al.,* 2013).

1.3.4 Land waters

Changes in water storage on land in response to climate change and variability (i.e., water stored in rivers, lakes, wetlands, aquifers and snow pack at high latitudes and altitudes) and from direct human-induced effects (i.e., storage of water in man-made reservoirs along rivers and

ground water pumping) have the potential to contribute to sea level change (*Milly et al.,* 2010). Estimates of climate-related changes in land water storage over the past few decades rely on global hydrological models due to inadequate observational data. Based on hydrological modelling, *Milly et al.*, (2003)and *Ngo-Duc et al.*, (2005) found no long term sea level trend associated with natural land water storage change but interannual to decadal fluctuations, equivalent to several millimeters of sea level. Furthermore, recent studies (*Cazenave et al.*, 2014, *Fasullo et al.*, 2013, *Boening et al.*, 2012, *Cazenave et al.*, 2012, *Llovel et al.*, 2011, *Nerem et al.*, 2010) have shown that interannual variability in observed global mean sea level correlates with El Niño Southern Oscillation (ENSO) indices and is inversely related to ENSO-driven changes of terrestrial water storage. While climate-related changes in land water storage do not show significant long-term sea level trends for the recent decades, direct human (anthropogenic) interventions in land water storage (reservoir impoundment and groundwater depletion) have each contributed at least several tenths of mm of sea level change (*Church et al.,* 2013, *Konikow*, 2013, *Pokhrel et al.*, 2012, *Wada et al.*, 2012, *Konikow*, 2011, *Milly et al.,* 2010, *Chao et al.*, 2008). Reservoir impoundment causes a sea level decrease whereas ground water depletion increases the sea level since most of the water extracted from the ground ends up in one form or another into the oceans. Reservoir impoundment exceeded groundwater depletion for the majority of the 20th century but groundwater depletion has increased and now exceeds current rates of impoundment, contributing to an increased rate of global mean sea level rise. IPCC AR5 estimated the net anthropogenic contribution of land waters to sea level to be 0.12±0.1 mm/yr for 1970-2010. Over 1993-2010, its contribution amounts to 0.38± 0.12 mm/yr, around 12% of the total rate of observed sea level rise (*Church et al.,* 2013).

Fig.1.5 (adapted from *Meyssignac and Cazenave*, 2012) compares the observed global mean sea level rise to different components and their sum over the altimetry era.

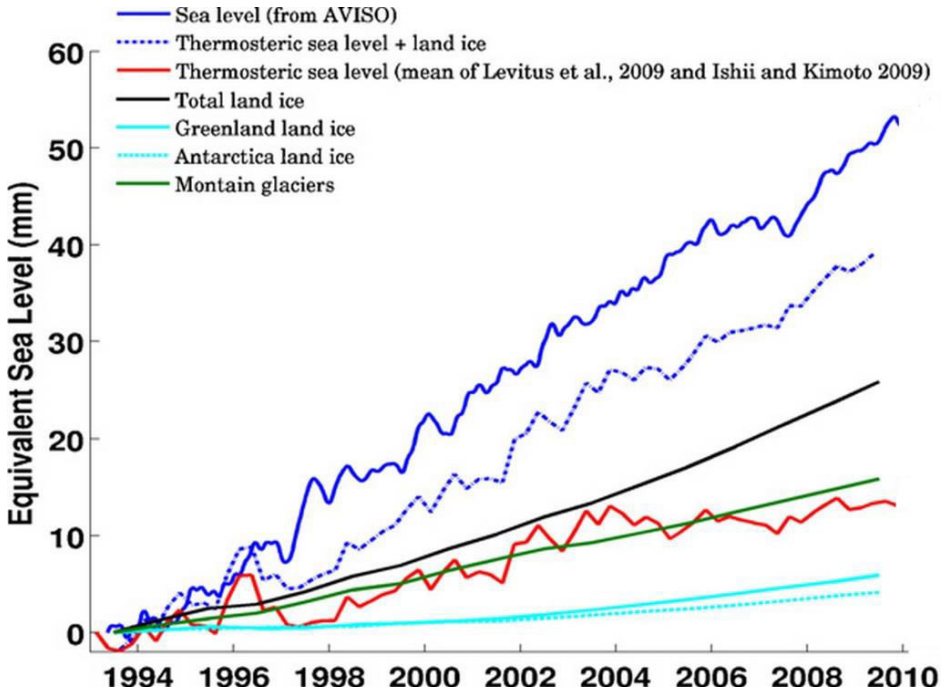

Figure 1.5: Observed sea level from satellite altimetry over 1993–2010 (blue solid curve; thermal expansion (red curve; mean value based on temperature data from Levitus et al., 2009; Ishii and Kimoto, 2009); contribution from Greenland and Antarctica (cyan curves) and glaciers (green curve). The black curve represents the total land ice contribution while the blue dotted curve represents the total climatic contribution (sum of thermal expansion and land ice) (from Meyssignac and Cazenave, 2012).

1.4 Thesis objectives

Sea level is an integrated climate parameter that involves interactions of all components of the climate system (oceans, ice sheets, glaciers, atmosphere, and land water reservoirs) on a wide range of spatial and temporal scales. In the previous sections, we discussed the evolution of global mean sea level over various time scales, factors contributing to global mean sea level changes. Considering the highly negative impact of sea level rise for society, the multidisciplinary aspects of sea level rise remain a major focus of climate research. Monitoring sea level change and understanding its causes has considerably improved in recent years owing to the advent of precise in-situ and remote sensing observations. My thesis contributes to a better estimation and understanding of sea level changes not only at a global scale for the recent decade but also most importantly focusses on regional sea level variability as regional sea level can

substantially deviate from the global mean and can vary on a broad range of spatial and temporal scales. The main objectives and the organization of the thesis are outlined below.

- Chapter 2 of this thesis presents two main works that involve the validation of sea level variations measured by the most recent satellite altimetry mission and the global mean sea level closure budget for the recent decade using various observational data.

In the first part of this chapter, we provide a detailed description on the evolution of different altimetry satellites since the beginning of the altimetry era, principle of SSH measurement and the various geophysical and instrumental corrections involved in the precise SSH measurement. This is then followed by the validation of sea level variations measured by SARAL-AltiKa by comparing them with SSH measurements from JASON-2 and various available tide gauge records. The second part of the chapter attempts to answer the following questions: Can the global mean sea level budget be closed using available observational datasets of sea level and its contributing components over 2003-2012? If not, can the significant residual signal be possibly related to deep ocean contribution and/or signal that corresponds to regions that are not monitored by observing systems or uncertainties in data processing?

- Chapter 3 deals with regional sea level variability, its causes and estimates of total relative sea level change at various vulnerable regions of the world.

In the first part of the chapter, climate-related and non-climatic causes of regional sea level variability over the altimetry era (1993-2013) are discussed in detail. In the second part of the chapter, we then focus our interest on long-term (i.e. at least 60 years) regional sea level variability. By making use of a two dimensional past sea level reconstruction and long term in-situ steric sea level data, the causes of regional sea level variability over 1950-2009 in the Indian Ocean, South China Sea and Caribbean Sea are first discussed. Furthermore, estimates of total relative sea level change (sea level change as felt by the population) since 1950 at several tide gauge locations at the vulnerable coasts and islands of the above mentioned regions obtained using a multidisciplinary approach as in *Becker et al.*, (2012) are then discussed and compared.

- In the final chapter (Chapter 4) we discuss the role of ocean dynamics, internal climate variability and external forcing on regional sea level variability with a special focus on the Pacific Ocean (especially the western tropical Pacific) where the regional sea level trends since the two recent decades are estimated to be three times the global mean sea level rate. This chapter has various sections. The first two sections are dedicated to various well known internal

unforced climate modes and two main sources of externally forced climate variability. This is then followed by a section that focusses on detection and attribution of climate change on global and regional sea level variability where a review of various studies on this subject is performed. The next section focusses on the Pacific Ocean sea level spatial trend patterns over the altimetry era. The contribution of internal climate modes and ocean dynamic processes to the Pacific Ocean sea level trend pattern estimated using observation in-situ data is first discussed. The presence of anthropogenic sea level fingerprint in the Pacific Ocean sea level since 1993 is also studied using observational altimetry and phase 5 of Coupled Model Inter-comparison Project (CMIP5) climate model-based sea level data.

Chapter 2

Multi satellite altimetry record and global mean sea level budget

Satellite altimetry missions have transformed the way we view Earth and its ocean and has been the main tool for continuously and precisely monitoring the sea surface height (SSH) with quasi-global coverage and short revisit time. In Chapter 1, we have seen the evolution of global mean sea level (GMSL) as measured by satellite altimeters since 1993. In this chapter, we first discuss the evolution of various altimetry satellites used for ocean observation, principle behind the altimetry-based SSH measurement and different error corrections involved in precise SSH measurements. We then move on to the estimation of global mean sea level budget since a decade using various observational and in-situ data.

2.1 Evolution of altimetry satellites

Satellite altimetry was developed in the 1960s soon after the flight of artificial satellites became a reality (*Fu and Cazenave*, 2001). The first altimetry satellite, GEOS 3 (Geodynamics Experimental Ocean Satellite) was launched in 1975 and carried instruments to yield useful measurements of sea level and its variability. However, its performance was not good enough to extract useful scientific information from its measurements. This was then followed by Seasat (SEA faring SATellite) and Geosat (GEOdetic SATellite) missions in 1978 and 1985 respectively. While Seasat gave us the first global view of ocean circulation, waves and winds, Geosat was the first mission to provide long-term (over 3 years) of high quality altimetry data. However, until the early 1990s, satellite altimetry has been more useful to marine geophysics rather than oceanography. This is mainly because the orbital error (see section 2.1.2 for details)

for these missions was so large (from several decimeters to ~1m) that the altimetry range uncertainty prevented detection and precise measurements of phenomena associated with ocean dynamics such as dynamic topography, tides, sea level etc. (*Fu and Cazenave*, 2001, *Palanisamy et al.*, 2015a).

The era of precise satellite altimetry dedicated to space oceanography began in the early 1990s with the launch of ERS-1, a European Space Agency (ESA) mission in 1991 and the National Aeronautics and Space Agency (NASA)/ Centre National d'Etudes Spatiales (CNES) joint venture TOPEX/Poseidon in 1992. In fact, TOPEX/Poseidon revolutionized the study of Earth's oceans by providing the first continuous, global coverage of ocean surface topography. Its data made a huge difference in our understanding of the oceans and their effect on global climatic conditions. Its repeat cycle (i.e. the time taken for the satellite to pass vertically over the same location) of ~10 days provided more information than in-situ measurements over hundred years. The mission far exceeded the expectations in terms of both mission duration (initial design life was 5 years but stayed in operation for 13 years) and measurement system performance (*Buis et al.,* 2006).

During the period of TOPEX/Poseidon (1992-2006), several other new altimetry missions were launched: ERS-2 (ESA, 1995-2011), Jason-1 (NASA/CNES, 2001-2012), ENVISAT (ENVIronmental SATellite, ESA, 2002-2012) and Jason-2 (NASA/CNES, 2008-). The combination of several satellites available at the same time enabled a good compromise between the spatial and temporal resolutions for ocean monitoring. For example, while the repeat cycle of TOPEX/Poseidon was ~10 days (good temporal resolution), its inter-track spacing at the Equator was in the order of 315 km; whereas in the case of ENVISAT, its repeat cycle was 30 days with inter-track spacing in the order of 80 km at the Equator (good spatial resolution). Moreover, while TOPEX/Poseidon, Jason-1 and Jason-2 flew at the non- sun synchronous orbit (up to 66°N/S), ENVISAT's polar sun synchronous orbit further enabled high latitude ocean coverage (up to 81.5° N/S) thereby complementing to the other existing missions.

Cryosat-2 and HY-2A are two other satellite altimetry missions launched by ESA and China in 2010 and 2011 respectively. The Cryosat-2 orbit at an inclination of about 92 degree and an altitude of 717 km covers almost all the polar region and henceforth is dedicated to polar observation while HY-2A at sun synchronous and geodetic orbit helps in monitoring the

dynamics of the ocean. Since the beginning of 2013, a new altimetry mission, SARAL-AltiKa, a joint venture between CNES and Indian Space Research Organization (ISRO), now ensures the continuity of high precision sea level data along with the existing Jason-2 measures (*Verron et al.*, 2015). It is the first oceanographic mission using a high frequency Ka band altimeter for improved spatial and temporal resolution and flies in the same orbit as that of ENVISAT (a detailed explanation on SARAL-AltiKa is presented in Section 2.1.4). Another mission, Jason-3 in the framework of a co-operation between CNES, NASA, Eumetsat (EUropean METeorology SATellite) and NOAA (National Oceanic and Atmospheric Administration) is proposed to be launched soon. This mission is similar to those of TOPEX/Poseidon, Jason-1 and Jason-2 with the same kind of payload and orbital parameters.

Since satellite altimetry has proven to be a valuable source of data for ocean monitoring and understanding, several future missions are foreseen such as Sentinel-3 Jason-CS, SWOT (Surface Water Ocean Topography). Continuous monitoring with the help of such satellite altimeters will further enhance our understanding of oceans and their mechanisms.

2.1.1 Principle of satellite altimetry

The radar altimeters on board the satellite transmit signals at high frequency (over 1700 pulses per second) towards the sea surface which is partly reflected back to the satellite. Measurement of the round-trip travel time is then converted to obtain the distance of the satellite above the instantaneous sea surface, called as 'range'. SSH measurement is deduced from the difference between the satellite distance to the Earth's centre of mass (deduced from precise orbitography and called 'satellite/orbit altitude') and the satellite distance (range) above the sea surface (Fig.2.1) Besides sea surface height, wave height and wind speed over the oceans can also be measured from the amplitude and waveform of the return signal.

2.1.2 Corrections involved in Sea Surface Height measurement

The determination of precise SSH measurements from satellite altimetry is influenced by many factors. Amongst the most important are sensor characteristics, long-term stability of the altimeter, and the methods used in altimeter data processing (*Fernandes et al.*, 2006). While the sensor characteristics of the altimeter are pre-determined depending on the altimetry missions,

instrumental and orbital errors, differences in the methodology for processing altimetry data and the corrections involved are crucial for sea level monitoring. High precision SSH measurements require (1) precise orbit determination of the satellite and (2) application of accurate geophysical, corrections to the raw altimetry signal. The latter accounts for the interactions of altimeter signal with the atmosphere and sea surface. Slight differences in the models used or processing approaches for the above mentioned corrections can seriously impact the SSH estimates and corresponding uncertainties. Therefore, from Section 2.1.1, the precise SSH measurement from satellite altimetry can now be expressed as

$$\mathbf{SSH = S - R - Corrections + \varepsilon} \qquad (2.1)$$

where,

S = Orbit altitude

R = Range

Corrections = (orbital + propagation + geophysical + surface) corrections

ε = remaining random and systematic errors

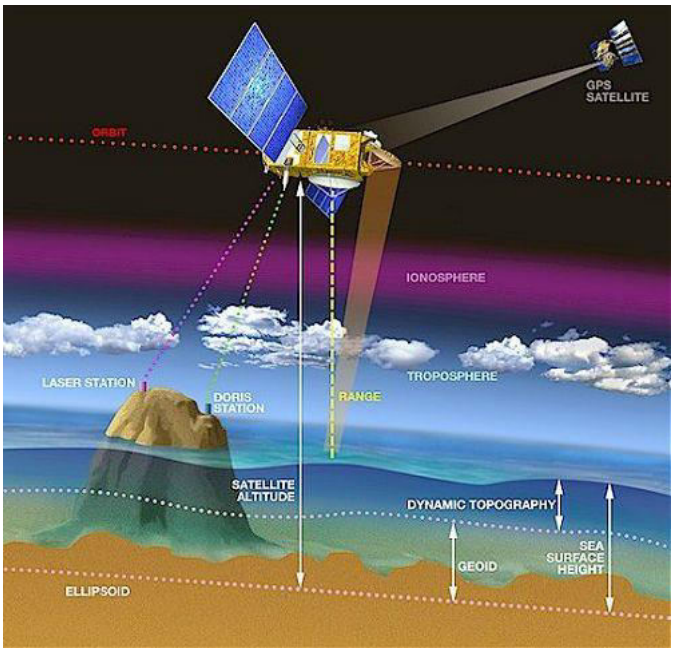

Figure 2.1: Principle of satellite altimetry measurement

In this section, we discuss several of these corrections involved for precise SSH estimation.

1) Orbital correction

The quality of the altimetry data depends on the ability to precisely determine a satellite's position on orbit. Orbital error is caused by imperfect knowledge of the spacecraft position in the radial orbit direction and is the largest error source on altimetry measurements for SSH monitoring. Therefore, a very precise knowledge of the satellite orbit with respect to Earth's reference ellipsoid is essential. The satellite's orbit can be also perturbed by gravitational forces related to the non-uniform distribution of Earth's gravity field, and those caused by the sun, moon and other planets. Forces on the satellite's surface such as atmospheric drag (e.g. low orbit satellites experience more atmospheric drag) and radiative pressure (e.g. solar radiation, Earth's IR radiation etc.) also play a role in the perturbation of the satellite's orbit. This indicates that a detailed knowledge of the satellite and its variations due to maneuvers, fuel consumption, solar panel orientation etc. are also necessary in order to precisely model the above mentioned forces acting on it. Precise orbit determination is done through a combination of satellite tracking and dynamic modelling. Satellite tracking in general involves the use of Satellite Laser Ranging (SLR), Global Positioning System (GPS) and Doppler Orbitography and Radio positioning System (DORIS). A dynamical model taking into account the forces acting on the satellite is then fitted through the tracking data to obtain the precise orbit of the satellite.

2) Propagation corrections

As the radar altimetry signal travels through the atmosphere to the sea surface, it is slowed down due to the presence of various elements in its path. The delay in the propagation of the radar signal thus needs to be corrected in order to estimate the precise range, i.e. the distance between the satellite and sea surface. There are three types of propagation delays that need to be accounted for: (1) ionospheric, (2) wet and (3) dry tropospheric corrections.

a) Ionosphere correction

This correction takes into account the path delay in the radar signal due to the presence of electrons in the ionosphere. The ionosphere is the uppermost layer of the atmosphere (ranging between 60 and 800 km) and the electrons are produced as a result of ionization attributed to solar radiation. As a result, it causes the altimeter to slightly over estimate the range by 1 to 20

cm. This amount can vary with respect to the seasons, solar cycle and occurrences of geomagnetic storms with the maximum influence occurring at the tropical band. Since the range delay due to the presence of electrons is related to electromagnetic radiation frequency, the correction can be estimated using two different radar frequencies (for example, C-band and K_u-band for TOPEX and Jason-1). This correction can also be taken into account from models of the vertically integrated electron density (*Fu and Cazenave*, 2001, *Callahan*, 1984, *Imel*, 1995).

b) Wet troposphere correction

The wet tropospheric correction is the correction for the delay of the radar signal due to the presence of water vapor content in the atmosphere. This is a difficult correction to be accounted for as the wet atmospheric effect highly varies both spatially and temporally with maximum occurring in the tropical convergence zones and magnitudes ranging from 5cm to 30 cm. Over the oceans, the wet tropospheric correction is in general computed using on-board microwave radiometer measurements. But, such radiometric measurements generally fail near the coasts where the signal coming from the surrounding land surface contaminates the radiometer measurements (*Desportes et al.*, 2007). In such cases, the correction is computed from meteorological model outputs such as ECMWF (European Center for Medium Range Weather Forecast) or NCEP (National Centers for Environmental Prediction) models (*Legeais et al.*, 2014).

c) Dry troposphere correction

The mass of dry air molecules in the atmosphere causes a range delay known as the dry tropospheric effect. It is directly proportional to sea level pressure and is the largest adjustment that has to be applied to altimetry measurement as its order of magnitude is about 2.3m. However, its temporal variations are low and range a few centimeters only. The dry tropospheric correction is computed using atmospheric model pressure forecasts such as ECMWF.

3) Geophysical corrections

The gravity forces generated by the Sun and Moon on the Earth can create perturbations on the earth's interior and also sea surface elevations of few meters. These geophysical effects are called as tidal effects and can be classified into four types: (1) ocean, (2) solid Earth, (3) polar tidal and (4) loading effects.

a) Ocean, solid Earth tidal and loading corrections

Ocean tides and their variations are the result of the combined attraction of Sun and Moon and represent more than 80% of the surface variability in open ocean. The tidal periods (half a day or one day) are shorter than the repeat periods of an altimetry satellite. Tidal correction is therefore essential since they contaminate the low frequency altimetry signals. Furthermore, for the estimation of dynamic sea surface height, the magnitude of ocean tides are very large and must therefore be removed as they are considered as noise. Ocean tidal corrections are performed using assimilated hydrodynamic and statistical models that estimate tides globally with high spatial resolution (*Fu and Cazenave*, 2001, *Ray*, 1999).

The gravitational attraction of the Sun and Moon also impacts Earth's interior causing the surface of the Earth beneath the ocean to be slightly deformed. This is called as the solid Earth tidal effect. This effect is nearly in phase with the ocean tide and is corrected using models.

Furthermore, the change in the weight of the water column due to variations in tides causes an elastic loading effect on the sea floor that is also corrected using models.

b) Polar tidal correction

The axis of rotation of the Earth deviates slightly from the Earth's ellipsoidal axis over a period of several moths annually. This as a result causes variations to both solid Earth and oceans and is called as polar tidal effect (*Desai*, 2002, *Wahr*, 1985). The polar tide correction is implemented through modelling that requires precise knowledge on the Earth's axis of rotation.

4) Surface corrections

Apart from propagation and geophysical corrections applied to altimetry signal, there are two types of surface corrections that need to be accounted for: (1) inverse barometric and (2) sea state bias corrections.

a) Inverse barometric (IB) correction

The response of the sea surface to changes in atmospheric pressure has a large effect on measured sea surface height as the ocean responds directly to atmospheric pressure changes. Sea level falls (rises) as the atmospheric pressure loading increases (decreases). For example, an increase in the atmospheric pressure by 1mbar pushes the sea level down by 1 cm. This is called as the isostatic inverse barometric effect (*Wunsch and Stammer*, 1997, *Ponte and Gaspar*, 1999,

Carrère and Lyard, 2003). The magnitude of the IB effect can reach up to ± 15 cm and is corrected using meteorological models such as ECMWF.

b) Sea State Bias (SSB) correction

This correction includes the electromagnetic bias (EM bias) and skewness bias. The EM bias is the correction for bias in measurements due to varying reflectivity of the wave troughs and crests (*Chelton*, 1994). The concave form of wave troughs tends to concentrate and reflect the altimetry signal better than the wave crests that disperse the signal. Therefore the altimetry signal return from the troughs is stronger than from the crests. Furthermore, in the case of wind waves, the wave troughs have a larger surface area than the pointy crests and this is called as skewness bias. Both the EM and skewness bias causes the mean reflecting surface to be shifted towards the troughs. They vary with increasing wind speed and wave height. SSB is estimated using empirical formulas derived from altimeter data analysis and models (*Tran et al.*, 2006). The range correction varies from a few to 30 cm.

5) Other potential errors

Other sources of potential errors in SSH measurements include altimeter instrumental ageing errors. Altimeter parameters are precisely monitored over all the mission life-time to detect instrumental anomalies (*Ablain et al.*, 2009). Based on the instrumental anomalies observed in the satellites, corrections such as for centre of gravity, waveforms etc. are applied.

Over the years, technological developments have considerably decreased the instrumental error down to 1.7 cm for TOPEX/Poseidon and even lesser for Jason-1/2 and other recent missions. Similarly improved satellite orbit determination has reduced the root-mean-squared (rms) orbit error down to the range of 1-2 cm for Jason-1/2. Fig.2.2 displays the evolution of altimetry instrumental and orbital errors. Owing to internationally concerted effort in improved estimates of the geophysical and environmental corrections, the rms error of the various corrections has now been reduced down to ~2.7 cm for a single SSH measurement.

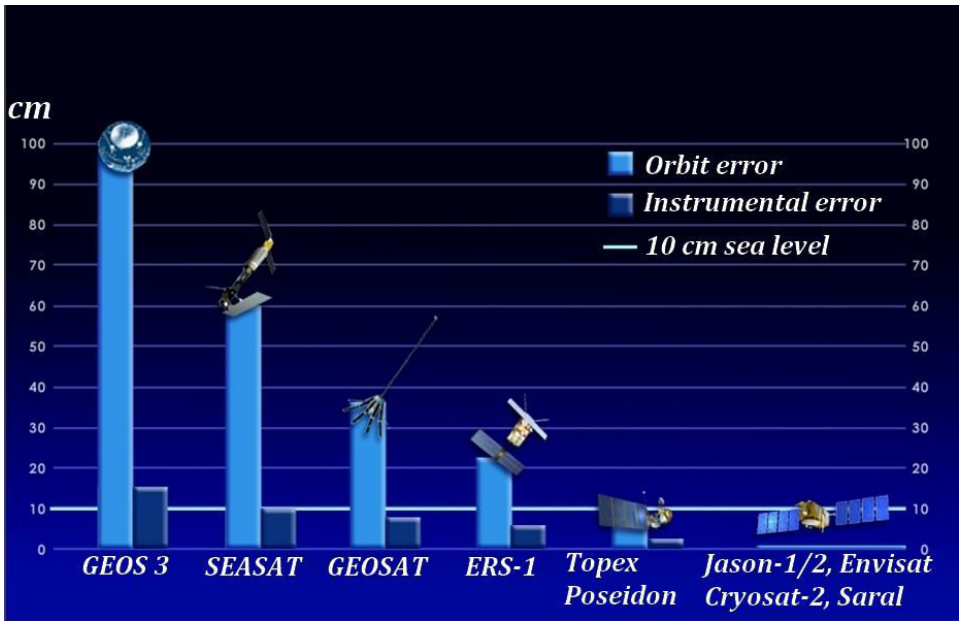

Figure 2.2: Evolution of orbital and instrumental errors in satellite altimetry (Source: AVISO-CNES)

2.1.3 Multi-mission SSH altimetry data

We carried out global and regional sea level studies by making use of multi-mission merged SSH altimetry data. The purpose of using multi-mission altimetry data is to obtain the most stringent accuracy requirements that are needed for climate research. Moreover, as mentioned in Section 2.1, the combination of several satellites enables a better compromise on spatial and temporal resolution. Merging multiple altimeter data sets is not easy. It requires homogenous, inter-calibrated data sets; correcting of orbit error for the less precise altimeter missions; extracting the sea level anomaly using a common reference surface; and combining the data through a mapping (or assimilation) method (*Le Traon et al.*, 1998). After calculating the along track sea level measures for each of the satellite missions, the main steps consists of: combining all missions together, reducing the orbit and the long wavelength errors, computing the gridded sea level anomalies using an objective analysis approach (*Ducet et al.*, 2000, *Le Traon et al.*, 2003), and generating mean sea level products (e.g. GMSL time series, gridded sea level time series) dedicated for climate studies (*Ablain et al.*, 2015). Owing to the homogenization of the altimetry corrections between all the missions, the uncertainty in multi-mission GMSL trend over 1993-2010 is now reduced to 0.5 mm/yr. The main source of this error

remains to be the wet tropospheric correction with a drift uncertainty in the range of 0.2-0.3 mm/yr (*Legeais et al.*, 2014). Orbit error and altimeter parameters error also add an uncertainty in the order of 0.1 mm/yr. Furthermore, imperfect links between various altimetry missions cause a GMSL trend error of about 0.15 mm/yr (*Ablain et al.*, 2015).

2.1.4 SARAL-AltiKa, the new altimetry mission

SARAL-AltiKa mission, launched in February 2013, is an answer to the needs of the oceanographic community, continuity of high accuracy, high resolution, near-real time observations of the ocean surface topography as at least 2 simultaneous altimetry missions are required to fulfill this need. As a consequence, along with the existing Jason-2, SARAL-AltiKa mission is considered as 'gap filler' between ENVISAT (lost in April 2012) and Jason-3/Sentinel-3 (expected in 2015; *Verron et al.*, 2015). This is the first oceanographic mission that uses a high frequency K_a band altimeter (frequency and bandwidth of 35.75 GHz and 500 MHz). The main objective of this mission is to help the oceanographic community to improve knowledge on the ocean meso-scale variability, a class of high energy processes with wavelengths in the range of 50 km to 500 km (*Verron et al.*, 2015). The K_a band frequency of SARAL-AltiKa improves spatial and temporal resolution and thus enables a better observation of the ocean at meso-scale. It is also well suitable for studying mean sea level variations, sea and land ice, wave heights and coastal dynamic processes (as SARAL-AltiKa can reach as close as 8km to the coasts while Jason-2 has managed only up to 15 km), as well as continental water bodies like rivers, lakes, wet lands, etc. (*Palanisamy et al.*, 2015a). Furthermore, SARAL-AltiKa flies at an almost polar (final inclination at 98.55°) sun-synchronous orbit as that of ENVISAT. This enables better observation of polar ice and oceans. With a repeat cycle of 35 days (similar to ENVISAT), SARAL-AltiKa provides a high resolution coverage of the oceanic domain with an inter-track spacing at the equator of 75 km.

In our study, we performed a global and regional validation of the sea level variations measured by SARAL-AltiKa by comparing it with Jason-2 and tide gauge records. This has been published as an article titled 'Sea level variations measured by the new altimetry mission SARAL-AltiKa and its validation based on spatial and temporal curves using Jason-2,tide gauge data and an over view of the annual sea level budget'.

Summary of the article: 'Sea level variations measured by the new altimetry mission SARAL-AltiKa and its validation based on spatial and temporal curves using Jason-2,tide gauge data and an over view of the annual sea level budget' (the original article is inserted at the end of this section).

In the first part of our study, we compared the temporal mean sea level spatial patterns of SARAL-AltiKa with those of Jason-2 over March 2013 to August 2014. At global scale, the temporal mean sea level spatial patterns between SARAL-AltiKa and Jason-2 were found to be very similar. However, differences in the order of ±30 mm were noticed between the two missions (Fig.2.3). Since, SARAL-AltiKa was still in its verification phase at the time the article was written, it was presumed that these differences occurred due to various orbital and geophysical corrections that were not yet completely taken into account in the case of SARAL-AltiKa. For example, from Fig.2.3 we can observe noticeable positive SSH differences between SARAL-AltiKa and Jason-2 in the Southern Hemisphere below 40°S latitudinal range. This is the region with generally high and spontaneous ocean waves that have high significant wave height. Therefore the differences in SSH measurements in this region is probably due to the differences in SSB corrections as the SSB correction in SARAL-AltiKa had not yet been tuned. While in terms of global mean time series, both SARAL-AltiKa and Jason-2 relatively agree well, in terms of regional mean, the difference was found to be maximum at the southern hemisphere extra-tropical latitudinal band. All the preliminary analyses show that the sea level variations measured by SARAL-AltiKa looks very promising.

The second part of the study consisted of comparing SARAL-AltiKa sea level data with Jason-2 and tide gauge records. SARAL-AltiKa and Jason-2 sea level grids were first interpolated within a 1° radius of the tide gauge location and their corresponding time series were compared with that of the tide gauge time series. It was observed that at most tide gauge sites, SARAL-AltiKa time series were well correlated with both tide gauge and Jason-2 time series. There were several locations such as Maloy in the Atlantic and Fremantle in the Indian Ocean that had high amplitudes of sea level variations observed by the tide gauges but not by SARAL-AltiKa and Jason-2. However the high amplitude sea level variations were related to local seasonal phenomena captured by tide gauge records that are not reflected in satellite altimeters.

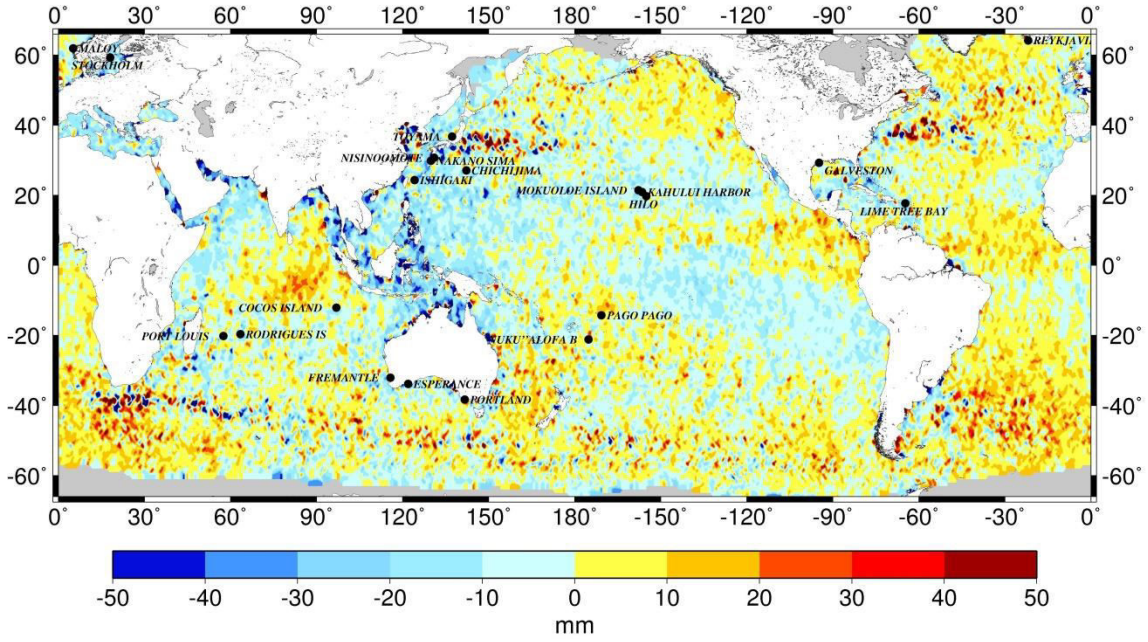

Figure 2.3: Difference between SARAL-AltiKa and Jason-2 temporal mean spatial pattern over March 2013–August 2015. The tide gauge records used in the study are also highlighted (from Palanisamy et al., 2015).

As a last part of this study, we also performed an annual sea level budget (see Section 2.2) by making use of Argo-based steric sea level signal, ocean mass signal from GRACE and SARAL-AltiKa altimetry sea level signal. The seasonal amplitude and phase differences of steric and ocean mass component (i.e., steric +ocean mass) was relatively well comparable with the total sea level signal from SARAL-AltiKa.

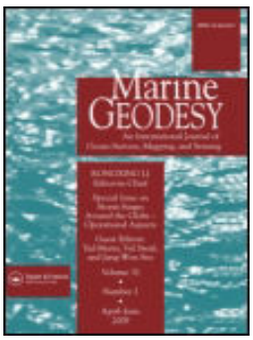

Marine Geodesy

ISSN: 0149-0419 (Print) 1521-060X (Online) Journal homepage: http://www.tandfonline.com/loi/umgd20

Sea-Level Variations Measured by the New Altimetry Mission SARAL/AltiKa and its Validation Based on Spatial Patterns and Temporal Curves Using Jason-2, Tide Gauge Data and an Overview of the Annual Sea Level Budget

H. Palanisamy, A. Cazenave, O. Henry, P. Prandi & B. Meyssignac

To cite this article: H. Palanisamy, A. Cazenave, O. Henry, P. Prandi & B. Meyssignac (2015) Sea-Level Variations Measured by the New Altimetry Mission SARAL/AltiKa and its Validation Based on Spatial Patterns and Temporal Curves Using Jason-2, Tide Gauge Data and an Overview of the Annual Sea Level Budget, Marine Geodesy, 38:sup1, 339-353, DOI: 10.1080/01490419.2014.1000469

To link to this article: http://dx.doi.org/10.1080/01490419.2014.1000469

Marine Geodesy, 38(S1):339–353, 2015

ISSN: 0149-0419 print / 1521-060X online
DOI: 10.1080/01490419.2014.1000469

Taylor & Francis
Taylor & Francis Group

Sea-Level Variations Measured by the New Altimetry Mission SARAL/AltiKa and its Validation Based on Spatial Patterns and Temporal Curves Using Jason-2, Tide Gauge Data and an Overview of the Annual Sea Level Budget

H. PALANISAMY,[1,1] A. CAZENAVE,[1] O. HENRY,[1] P. PRANDI,[2] AND B. MEYSSIGNAC[1]

[1]Laboratoire d'Etudes en Géophysique et Océanographie Spatiale (LEGOS), Centre National d'Etudes Spatiales (CNES), Toulouse, France
[2]Collecte Localisation Satellites (CLS), Ramonville-St.Agne, France

High-precision satellite altimeters help in measuring the variations in sea level since the early 1990s. After a number of such successful altimetry missions such as Topex/Poseidon, Jason-1, Jason-2, and Envisat, SARAL/AltiKa, a high resolution altimetry mission based on the Ka frequency band that can also cover high latitudinal zones, was launched in February 2013. Even though the data set available from this recent mission is not yet suitable for climate research owing to its short duration, in this study we perform a preliminary validation of SARAL/AltiKa sea-level data. The first part of the validation is the comparison of SARAL/AltiKa and Jason-2 sea-level data between March 2013 and August 2014 in terms of temporal mean spatial pattern. Comparisons in terms of global mean sea-level time series and latitudinal band-based mean time series are also performed. The second part of the validation is the comparison of the SARAL/AltiKa sea-level based time series with several tide gauge records covering the period of our study. Finally, an analysis of the annual sea-level budget with SARAL/AltiKa data, steric sea level, and ocean mass is performed. Results of these preliminary comparisons show good agreement with other sea-level data.

Keywords SARAL/AltiKa, preliminary validation, Jason-2, tide gauges, annual sea level budget

1. Introduction

Satellite altimetry is now recognized as the main tool for precisely and continuously monitoring the sea surface height (SSH) with quasi-global coverage and short revisit time. The first altimeter satellite Geos 3 was launched in 1975. Since then, several altimetry missions have flown with the purpose of studying the oceans from space (e.g., Seasat 1978; Geosat 1985–1989). However, until the early 1990s, satellite altimetry has been more useful to marine geophysics than oceanography. In effect, for the early missions,

Received 12 July 2014; accepted 28 November 2014.
Address correspondence to H. Palanisamy, LEGOS/CNES, 18 Avenue Edouard Belin, 31400, Toulouse, France. E-mail: hindumathi.palanisamy@legos.obs-mip.fr

the orbital error was so large (from several decimeters to ∼1 m) that the altimetric range uncertainty prevented detecting and precisely measuring phenomena associated with ocean dynamics (e.g., dynamic topography, tides, sea level). The early 1990s began the era of precise altimetry dedicated to space oceanography (Fu and Cazenave 2001) with the launch of the following missions: ERS-1 in 1991, ERS-2 in 1995, and Envisat in 2002 launched by the European Space Agency (ESA), and the NASA/CNES missions Topex-Poseidon (1992–2006), Jason-1 (2001–2012), and Jason-2 (2008-). Over the years, technological improvements have considerably decreased the instrumental noise, down to 1.7 cm for Topex/Poseidon and Jason-1&2 for point-to-point measurement. Thanks to internationally concerted effort in improved estimates of the geophysical and environmental corrections, the root-mean-squared (rms) error of the various corrections has been reduced down to ∼2.7 cm for a single SSH measurement. Similarly, improved satellite orbit determination has reduced the rms orbit error to ∼2.5 cm. For Jason-1 and Jason-2, the orbit error is even smaller, in the range of 1–2 cm. The total rms measurement accuracy from multisatellite missions is about 4 cm for a single SSH measurement. In terms of global mean sea level, current errors are on the order of 4 mm for a single estimate and about 0.4 mm/yr for interannual to decadal trends (Ablain et al. 2009; Ablain et al. 2014).

The new altimetry mission, SARAL/AltiKa (launched in February 2013), now ensures the continuity of high precision sea-level data, complementing the Jason-2 data set. SARAL/AltiKa is the first oceanographic mission that uses a high frequency Ka band altimeter (frequency and bandwidth of 35.75 GHz and 500MHz, respectively). The Ka band frequency improves the spatial and temporal resolution and thus enables a better observation of the ocean at meso-scale. It is also well suitable for studying mean sea level variations, sea and land ice, wave heights, and coastal dynamic processes (as SARAL/AltiKa can reach as close as 8 km to the coasts while Jason-2 has managed only up to 15 km), as well as continental water bodies such as rivers, lakes, and wet lands. The only drawback of the Ka band frequency is its sensitivity to rain and clouds that can lead to signal attenuation. This could result in data loss in zones with high rainy and cloudy conditions. Furthermore, SARAL/AltiKa flies on the same orbit as Envisat, thus covers high latitude ocean (up to 81.5°N/S), enabling the observation of polar ice and oceans. With the same orbital cycle as Envisat (35 days), SARAL/AltiKa provides a high-resolution coverage of the oceanic domain (with an intertrack spacing at the equator of 75 km).

Global mean sea level (GMSL) is one of the most important variables in climate studies. Sea level is rising in response to global warming at a rate of 3.2 ± 0.4 mm/yr (e.g., Ablain et al. 2015). It should continue to rise because of expected continuing ocean warming and land ice melt, with possible negative impacts in a number of low altitude coastal regions (Cazenave and Cozannet 2014; Church et al. 2013). Therefore, precise measurement and understanding of the GMSL is important and of high scientific interest. The high precision and spatial resolution of SARAL/AltiKa will ensure continuity of sea level measurements, contributing to improved understanding of the evolution of the GMSL.

Even though the available SARAL/AltiKa sea level data are not yet suitable for climate research owing to its relatively recent launch, validation of this product by comparing with other existing products such as Jason-2 and tide gauge sea level data is feasible. Validation of sea level data is an important step that needs to be performed before they can be used for climate studies.

In this article, we perform a preliminary validation of SARAL/AltiKa sea level data using Jason-2 and tide gauge records. The first part of the validation is the comparison of SARAL/AltiKa and Jason-2 sea level data between March 2013 and August 2014 in terms

of temporal mean spatial pattern. Comparisons in terms of GMSL time series and latitudinal band-based mean time series are also performed. The second part of the validation consists of comparing the SARAL/AltiKa-based time series with several tide gauge records. This is done via an interpolation of the sea level data in a 1° radius of the tide gauge site. Once the sea level data have been validated, an analysis of the annual sea level budget with SARAL/AltiKa altimetry sea level, steric sea level and ocean mass is performed.

2. Data

2.1. SARAL/AltiKa Sea Level Product

Two-dimensional gridded SARAL/AltiKa SSH data at regular 1°x1° resolution and monthly interval from March 2013 to August 2014 provided by Archiving Validation and Interpretation of Satellite Oceanographic (AVISO) center were used in this study. In order to produce the 1° × 1° grid, the along-track SSH measurements were first averaged into 1° × 1° grids for each orbital cycle. The averaged SSH grids corresponding to each orbital cycle were then averaged, thereby giving a mean value for each grid corresponding to each month. Corrections applied to SSH measurements include orbit, altimeter instrument bias, and geophysical corrections (i.e., solid earth and ocean tides, dry and wet troposphere, and ionosphere). An advanced dynamic atmospheric correction (DAC) using the MOG2D model has also been applied (Volkov et al. 2007). In the case of the wet troposphere delay correction, two options are available for SARAL/AltiKa SSH: (1) radiometer-based correction through the measurement of atmospheric brightness temperature and a neural network and (2) correction based on ECMWF numerical weather prediction model. The latter is used as a backup and will be used when there is contamination or anomalous radiometer behavior. However, a drift in the radiometer wet tropospheric correction of SARAL/AltiKa appeared during the months of August–October 2013. This was due to a drift in the atmospheric brightness temperature related to the saturation of hot calibration. Even though this drift was corrected by modifying the onboard radiometer database values in late October 2013, since this study includes the months of August, September, and October 2013, we decided to use the SARAL/AltiKa sea level product corrected for the European Center for Medium-Range Weather Forecasts (ECMWF) model-based wet troposphere delay. Since SARAL/AltiKa is still in its verification phase, several corrections need to be accurately tuned. For example, as mentioned above, the radiometer wet troposphere correction has to be well tuned. Also an estimate of the Sea State Bias (SSB) is still not yet fully consolidated. An empirical model as a function of Significant Wave Height (SWH) and wind speed is currently used to interpolate the SSB value and precise SSB tuning is necessary (Bronner et al. 2013; Verron et al. 2013; Verron et al. 2014).

2.2. Jason-2 Sea Level Product

As in the case of SARAL/AltiKa SSH data, Jason-2 monthly SSH 1° × 1° grid was calculated by averaging the along-track SSH measurements in 1° × 1° grids for each orbital cycle. Jason-2 data from March 2013 to August 2014 were used in this study. Orbital, instrumental, and geophysical corrections were also implemented in this data set (see AVISO for more detail on the Jason-2 data processing, http://www.aviso.altimetry.fr/en/data.html).

2.3. Tide Gauge Sea Level Records

The monthly Revised Local Reference (RLR) tide gauge records from the Permanent Service for Mean Sea Level (PSMSL; Woodworth and Player 2003) and from the University of Hawaii Sea Level Center (UHSLC) were also used. While the data from PSMSL are at monthly time scale, UHSLC offers tide gauge data at daily and hourly intervals. In this study, daily tide gauge records from UHSLC have been averaged at monthly interval to be in accordance with the other data sets used. Availability of tide gauge records covering the time span from March 2013 until August 2014 is a challenge because there are not many tide gauge records available for this recent period. Of the available tide gauges covering the period of interest (or at least until May 2014), 21 tide gauges (see Figure 1a for the tide gauge sites) were selected after the editing process (elimination of offsets, discrepancies, and correlation of these tide gauge records with altimetry sea level data over a longer time period between 1993 and 2013). Only those having correlations greater than 0.8 with altimetry data were selected. Most of the tide gauge records used in this study are island tide gauge records located in open oceans. A few stations not located in the open ocean islands (e.g., Stockholm, Fremantle) were also used.

In order to be comparable with altimetry based sea level, tide gauge records need to be corrected for the atmospheric pressure loading. Mean sea level pressure fields from ERA Interim Reanalysis produced by ECMWF (Dee et al. 2011) were used for this correction.

2.4. Argo-based Steric Sea Level

To compute the steric component (i.e., variations in sea level due to changes in temperature and salinity), we used Argo-based gridded temperature (T) and salinity (S) data from the Japan Marine Science and Technology Center (JAMSTEC; Hosoda et al. 2008). These data, available from 2001 to August 2014, cover 27 depth levels from the surface to a maximum depth of 2000 m and are given as $1^\circ \times 1^\circ$ grids at monthly interval. Steric sea level was calculated by integrating the T and S measurements (henceforth called JAMSTEC steric) from the surface down to 1500 m depth.

2.5. GRACE-based Ocean Mass

The time series of the global mean ocean mass component is derived from Gravity Recovery and Climate Experiment (GRACE) satellite data, available from June 2002 to December 2013 at a monthly interval (Johnson and Chambers 2013). We averaged the GRACE ocean mass products processed by three centers: Centre for Space Research (CSR), GeoForschungsZentrum (GFZ), and Jet Propulsion Laboratory (JPL). During the overlapping period of this study and GRACE data availability (i.e., 10 months from March 2013 to December 2013), GRACE data from none of the three centers were available for March, August, and September. Therefore, linear interpolation has been performed to refill data during these missing months. Over November–December 2013, only data from CSR are available. It is to be noted that the presence of missing data and the linear interpolation performed increases the uncertainty in this component.

To facilitate comparisons, all time series used in this study were set to zero-mean.

3. Validation of SARAL/AltiKa Sea Level Data

The validation of the SARAL/AltiKa sea level data was done in three ways: (1) comparison of the spatial patterns of the temporal mean sea level, (2) comparison in terms of global

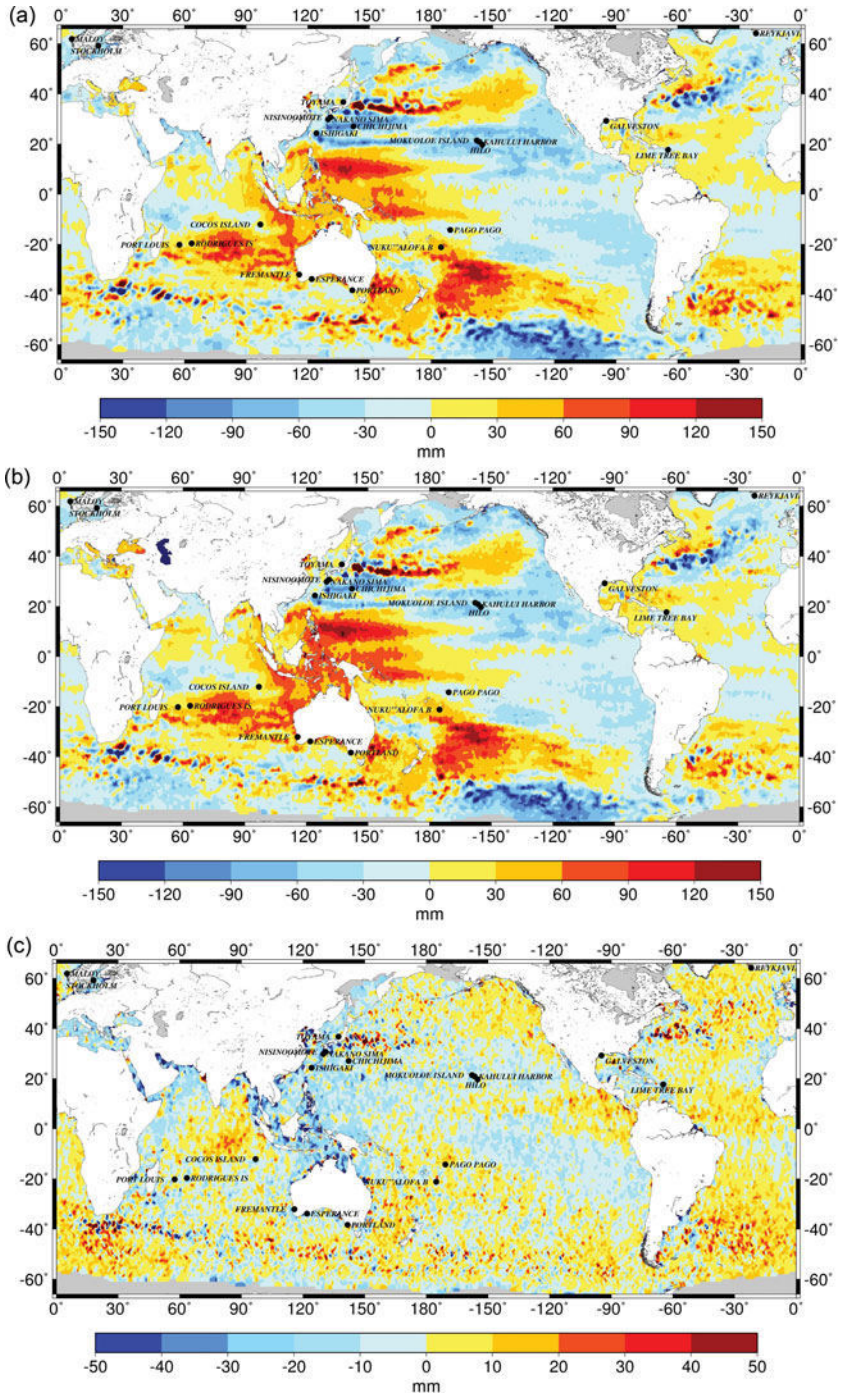

Figure 1. (a) SARAL/AltiKa temporal mean spatial pattern over March 2013–August 2014; (b) Jason-2 temporal mean spatial pattern over March 2013–August 2014; and (c) difference between SARAL/AltiKa and Jason-2 temporal mean spatial pattern over March 2013–August 2014. The tide gauge sites used in this study are also highlighted in the figures.

and latitude-based mean sea level time series, and (3) comparison with tide gauge records. Finally the annual sea level budget making use of SARAL/AltiKa, steric sea level and ocean mass component was also performed.

3.1. Comparison of SARAL/AltiKa with Jason-2

3.1.1. Comparison in terms of sea level spatial pattern. Figures 1a and 1b display SARAL/AltiKa and Jason-2 temporal mean spatial patterns calculated over March 2013–August 2014. Visual inspection shows that, on a global scale, both SARAL/AltiKa and Jason-2 temporal mean sea level spatial patterns are similar. Figures 1a and 1b also display well-known distinct sea level patterns that are related to decadal/interannual climate variability. For example, the v-shaped broad scale positive sea level pattern in the Pacific extending from the central northern Pacific to the central southern Pacific is related to the Pacific Decadal Oscillation (PDO; e.g., Hamlington et al. 2013; Han et al. 2013; Palanisamy et al. 2015; Zhang and Church 2012) while the strong dipole-like pattern with positive and negative sea level anomalies in the western and eastern tropical Pacific are related to interannual El Nino Southern Oscillation (ENSO) events and wind-driven steric sea level changes (McGregor et al. 2012; Stammer et al. 2013; Timmermann et al. 2010). We can also observe in data sets the strong positive east-west spatial pattern in the southern Indian Ocean and two strong positive patterns in the northern and southern Atlantic Ocean.

Even though the temporal mean spatial patterns of SARAL/AltiKa and Jason-2 are similar at the global scale, differences in the order of ± 30 mm between the two sea level data sets are still evident (Figure 1c, showing the difference between SARAL/AltiKa and Jason-2 over March 2013–August 2014). These differences can be due to orbit and geophysical corrections of SARAL/AltiKa that is still in its verification phase. For example, there are noticeable positive SSH differences between SARAL/AltiKa and Jason-2 in the Southern Hemisphere below 40°S latitudinal range. This is the region with generally high and spontaneous ocean waves that have high SWH. Therefore, the differences in SSH measurements in this region are probably due to the differences in SSB corrections since the SSB correction in SARAL/AltiKa is not yet tuned. Noticeable high positive differences can also be found in the northern and southern extra-tropical Atlantic and in the central Indian Ocean. Negative differences are observed in certain regions of the Pacific Ocean (particularly in the tropics and near the islands of Indonesia, Papa New Guinea and Philippines), coastal zones of South China Sea, eastern coast of Bay of Bengal. Whether the origin of these differences are related to orbital or geophysical corrections needs to be verified.

Even though there are differences existing between SARAL/AltiKa and Jason-2-based sea level measurements, at a global scale, spatial sea level patterns are well reproduced by SARAL/AltiKa. Moreover, differences are only in the range of ± 30 mm, that is, less than 20% of the maximum regional signal. Considering that several SARAL/AltiKa corrections still need to be tuned, it is hoped that the differences in sea level will be further reduced.

3.1.2. Comparison in terms of global and latitudinal mean sea level time series. In this section, we first compare SARAL/AltiKa with Jason-2 sea level time series in terms of global mean (Figure 2a) and then perform latitudinal mean-based time series comparison (Figures 2b, c, d, e).

In order to produce GMSL time series, the $1^\circ \times 1^\circ$ gridded SARAL/AltiKa and Jason-2 sea level data have been spatially averaged by applying cosine of latitude weighting. From Figure 2a, we can observe that the two GMSL time series follow each other well; both

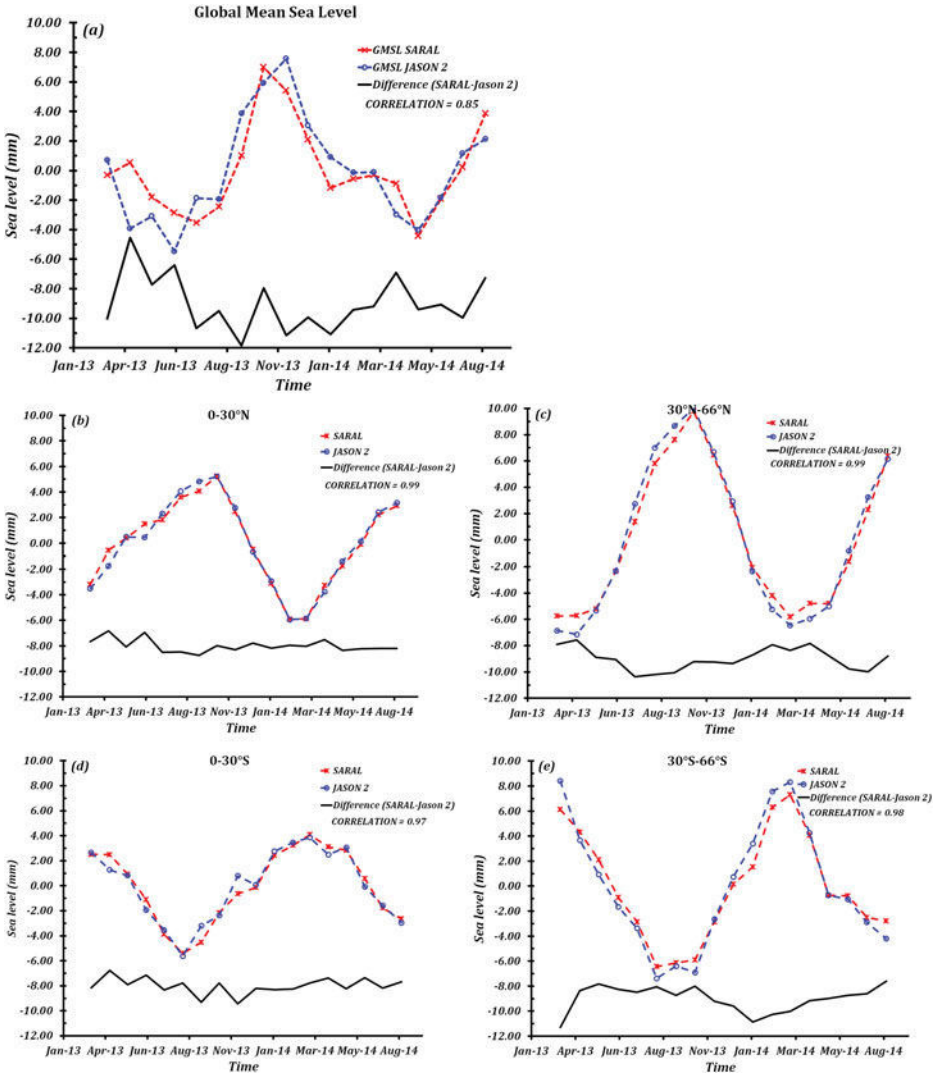

Figure 2. Sea level time series of SARAL/AltiKa (red dashed line with stars), Jason-2 (blue dashed line with circles) and the corresponding SARAL/AltiKa minus Jason-2 time series (black continuous line) in terms of (a) Global, (b) 0°−30°N, (c) 30°N-66°N (d) 0°−30°S, and (e) 30°S-66°S latitudinal bands.

display a clear seasonal variability. The observed seasonal variation in GMSL reaching a maximum of around 5–7 mm between October and November corresponding to North Hemisphere's late summer is in agreement with previous studies on the annual GMSL (e.g., Cazenave et al. 2000; Chen et al. 1998). Even though the magnitude of SARAL/AltiKa time series is slightly less than that of Jason-2, it is highly correlated with Jason-2 (correlation 0.85) GMSL. Figure 2a also displays the difference between SARAL/AltiKa based and Jason-2 based GMSL time series (black curve, with a downward offset of 9 mm for clarity). From this curve, we can observe that there are differences in the order of ∼4 mm occurring between SARAL/AltiKa and Jason-2 in terms of global mean at certain time period. The

standard deviation of the difference curve over March 2013–August 2014 accounts to 1.88 mm. In order to understand at which latitudinal band the difference is maximum, latitude based regional mean is then performed.

Figures 2b-e display the relative contribution of 0–30°N, 30°N-66°N, 0-30°S and 30°S-66°S latitude based regional mean time series from SARAL/AltiKa and Jason-2, respectively. The term "relative contribution" implies that the time series corresponding to each latitudinal band is weighted by the ratio between the surface of the ocean in the latitudinal band considered and the entire global ocean surface (i.e., area weighting). From the figures, we can observe that SARAL/AltiKa highly agrees with Jason-2 sea level time series, with correlations greater than 0.9 in all the 4 cases. The difference between SARAL/AltiKa and Jason-2 regional mean time regional at each latitudinal band is also displayed in Figures 2b–e (black curve with a downward offset of 8 mm for clarity). In the case of the tropical band, that is, 0°–30°N and 0°–30°S latitudinal bands, the standard deviation of the SARAL minus Jason-2 curve accounts to 0.51 mm and 0.66 mm, respectively. For the extra- tropical zones, the standard deviation of the SARAL minus Jason-2 time series in 30°N–66°N latitudinal band is 0.86 mm; for the 30°S–66°S band, it accounts to 1.05 mm. These results indicate that the difference between SARAL/AltiKa and Jason-2 sea level time series is maximum in the extra-tropical latitudinal band of the Southern Hemisphere. As discussed in Section 3.1.1, extra-tropical latitudinal band below 40°S is a region known for high SWH. Therefore, the maximum difference between SARAL/AltiKa and Jason-2 sea level time series could be related to differences in their SSB corrections.

From the latitudinal band-based time series, we can observe that the maxima and minima of the Northern Hemisphere are out of phase with the maxima and minima of the Southern Hemisphere. This is because of the opposite seasonal variations in the Northern and Southern Hemisphere (Leuliette and Miller 2009).

3.2. Comparison with Tide Gauge Records

In order to compare SARAL/AltiKa and Jason-2 sea level data with tide gauge time series, the $1^\circ \times 1^\circ$ sea level grids from both data sets were first interpolated within a 1° radius of the tide gauge site (see Figure 1a for the tide gauge locations). That is, the few SSH measurements falling within a distance of 1° radius (e.g., in the equator $1^\circ \approx 110$km) of the tide gauge site were first selected. These SSH measurements were then averaged thereby giving an estimate of the SSH at each the tide gauge location. The interpolated SARAL/AltiKa and Jason-2 sea level time series were then compared with the tide gauge records. Figure 3 displays the comparison of SARAL/AltiKa and Jason-2 time series with tide gauge records in the Pacific (Figure 3a), Atlantic (Figure 3b), Indian, and Southern Oceans (Figure 3c). Their corresponding correlations are available in Table 1.

From Figures 3a, 3b, and 3c and from Table 1, we can observe that at most tide gauge sites, SARAL/AltiKa is well correlated with both tide gauge and Jason-2 time series. We can also notice that there are several locations, for example, Maloy and Galveston in the Atlantic Ocean, Fremantle in the Indian Ocean, Esperance and Portland in the Southern Ocean where the tide gauge time series show very high sea level amplitudes. Even though the correlations are high between SARAL/AltiKa and tide gauge records at these sites, these high sea level amplitudes appear neither in SARAL/AltiKa nor in Jason-2 based sea level time series. For example, the standard deviation of the tide gauge based sea level times series at Maloy in the North Atlantic is 87 mm whereas that of SARAL and Jason-2-based time series are only 38 mm and 36 mm, respectively. However, the correlation

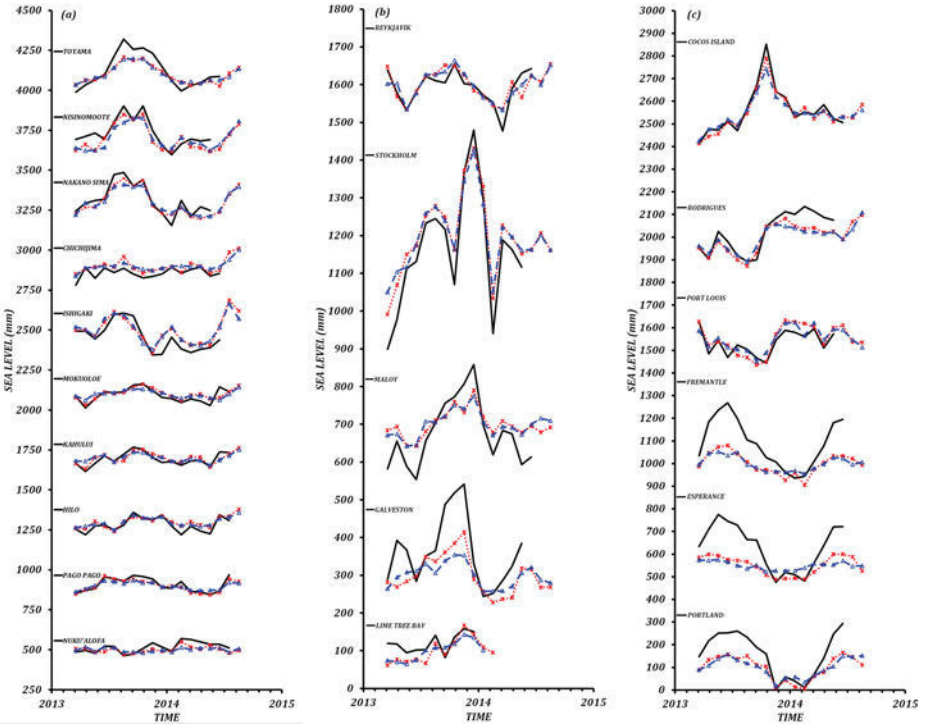

Figure 3. Comparison of sea level time series between tide gauge records (black line), SARAL/AltiKa (red dotted line with stars) and Jason-2 (blue dashed line with triangles) in the (a) Pacific, (b) Atlantic, and (c) Indian and Southern Oceans.

between SARAL and Maloy tide gauge time series is 0.92. The differences in the sea level amplitudes between tide gauge records and observed altimetry time series is mainly due to local seasonal phenomena or impacts such as rainfall, hurricanes, and river water outflow that are captured by the tide gauges but not by satellite altimeters. Apart from these, the tide gauge records can also be impacted by local land motions that are not reflected in satellite altimeters. These differences in amplitudes do not affect the correlation coefficients as they are based on a linear relationship between two variables. A value of 1 implies that a linear equation describes the relationship between variables X and Y perfectly, with all data points lying on a line for which Y increases as X increases. However the magnitude at which Y and X increase is not taken into account. As a result, even though the amplitude of tide gauge sea level time series is higher than the observed altimetry-based sea level time series, the correlations between them remain strong.

The best comparisons between tide gauges and observed-altimetry based sea level time series are only possible after the removal of seasonal signals. However,the availability of only 18 months of SARAL/AltiKa data is still too short for the removal of seasonal cycles. Improved validation of SARAL/AltiKa with tide gauges will be feasible in the future when data over a longer time period will be available. Nevertheless, the already existing high correlations between tide gauges and SARAL/AltiKa sea level time series assure the quality of this new sea level product.

Table 1
Correlation between (Column 1): tide gauge records and SARAL/AltiKa, (Column 2): tide gauge records and Jason-2 and (Column 3): SARAL/AltiKa and Jason-2 sea level time series interpolated at the tide gauge sites

Tide Gauge Stations	SARAL	Jason-2	SARAL & Jason-2
TOYAMA	0.95	0.97	0.97
NISINOMOOTE	0.88	0.84	0.94
NAKANO SIMA	0.94	0.92	0.98
CHICHIJIMA	0.66	0.79	0.89
ISHIGAKI	0.86	0.86	0.97
MOKUOLOE	0.8	0.8	0.9
KAHULUI	0.81	0.78	0.9
HILO	0.86	0.88	0.93
PAGO PAGO	0.94	0.94	0.98
NUKU'ALOFA	0.74	0.54	0.62
REYKJAVIK	0.8	0.86	0.89
STOCKHOLM	0.99	0.98	0.99
MALOY	0.92	0.94	0.91
GALVESTON	0.86	0.88	0.93
LIME TREE BAY	0.83	0.67	0.89
COCOS ISLAND	0.98	0.99	0.99
RODRIGUES	0.94	0.91	0.98
PORT LOUIS	0.88	0.88	0.94
FREMANTLE	0.96	0.94	0.93
ESPERANCE	0.94	0.75	0.79
PORTLAND	0.99	0.96	0.92

4. Sea Level Budget in Terms of Annual Signal

In the previous sections, SARAL/AltiKa sea level data have been compared and validated with Jason-2 sea level data in terms of spatial and temporal mean. Validation with available tide gauge records has further enhanced the confidence of this new sea level product. Having validated the SARAL/AltiKa sea level product, in this section we provide an overview of the annual sea level budget.

In general, observed sea level variations can be explained as two separate physical processes, density changes and water exchange between the ocean, atmosphere, and continents. Changes in salinity and ocean temperature (steric) produce density changes while water exchange between ocean and other reservoirs such as glaciers, ice sheets, land waters, atmosphere results in ocean's total mass variations (e.g., Leuliette and Willis 2011). This can be written as

$$\Delta H_{sea\ level} = \Delta H_{steric} + \Delta H_{ocean\ mass} \tag{1}$$

where $\Delta H_{sea\ level}$ is the observed sea level, ΔH_{steric} is the steric sea level change component and $\Delta H_{ocean\ mass}$ is the ocean mass component in terms of equivalent sea level. Studies (e.g., Church et al. 2011) have shown that ocean warming explains about 30–40% of

the observed sea level rise over the last few decades (1961–2008), while over the satellite altimetry era (1993–2010) its contribution accounts for ~30% (e.g., Cazenave and Cozannet 2014; Church et al. 2013). In terms of regional sea level variability during the altimetry era, studies (e.g., Fukumori and Wang 2013; Köhl and Stammer 2008; Levitus et al. 2012; Lombard et al. 2009; Stammer et al. 2013; Wunsch et al. 2007) have shown that nonuniform ocean thermal expansion and salinity variations explain most of the variability, especially in the case of tropical zones. Therefore, comparison of SARAL/AltiKa's temporal mean sea level spatial pattern with steric sea level pattern should in general result in high correlations in these zones.

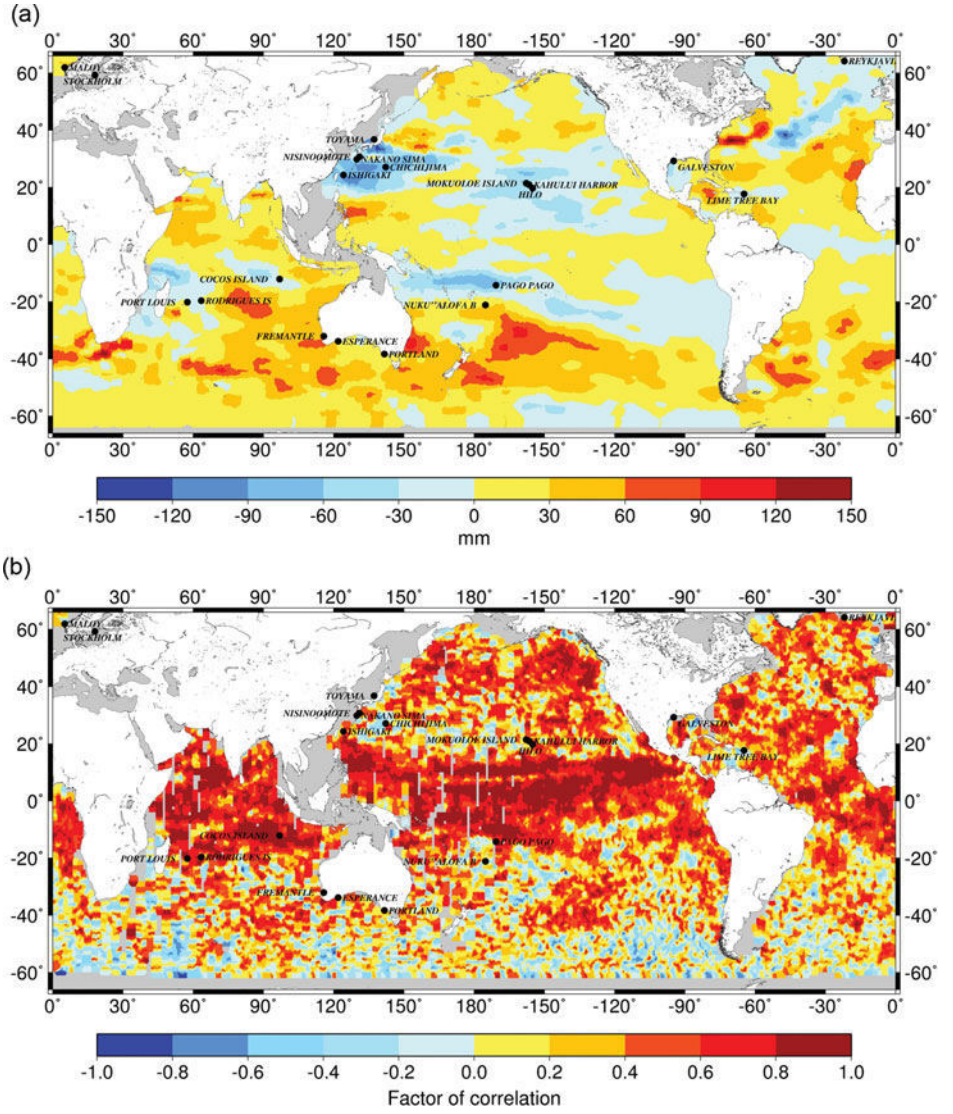

Figure 4. (a) Argo based steric sea level temporal mean spatial pattern. (b) Correlation between SARAL/AltiKa based observed sea level and Argo based steric sea level temporal mean spatial pattern over March 2013–August 2014.

The mean spatial pattern of the JAMSTEC steric sea level over March 2013–August 2014 (Figure 4a) shows good similarities with the observed pattern from SARAL/AltiKa. Positive observed sea level patterns such as the v-shaped broad scale sea level pattern in the Pacific Ocean with the dipole-like signal in the tropics, east to west propagating pattern in the southern Indian Ocean, patterns below Greenland and southern Atlantic are also well represented in the steric-based sea level pattern (compare Figure 1a and Figure 4a). Noticeable differences occur in the northern Indian Ocean, north eastern Atlantic Ocean near the African coasts and in the Southern Ocean where the sea level due to ocean warming appears greater than the observed sea level. Figure 4b displays the correlation between JAMSTEC steric and SARAL/AltiKa temporal mean spatial sea level patterns. As expected, the steric and altimetry-based sea level patterns are highly correlated in the tropical regions.

By making use of SARAL/AltiKa observed sea level, Argo-based steric and GRACE-based ocean mass, an attempt to close the global mean sea level budget (Eq. (1)) can be performed. This is done only in terms of explaining the seasonal patterns of each component with respect to it phase and amplitude. As explained in Section 2.5, GRACE-based ocean mass data available only until December 2013 have been linearly interpolated to replace four months of missing data, thereby increasing the uncertainties. It is also worth to be noted that several orbit and geophysical corrections related to SARAL/AltiKa are not yet completely tuned, further adding uncertainties. Therefore, closing the sea level budget in terms of exact values for a period of one year is not feasible. The global mean SARAL/AltiKa, Argo steric sea level and GRACE ocean mass time series are displayed in Figure 5. We can observe that while the total sea level and ocean mass are in phase with each other, and the steric and ocean mass component of sea level are out of phase. The in-phase and out-of-phase nature of these three components has been noted and studied earlier (e.g., Chambers et al. 2004; Chambers 2006; Leuliette and Miller 2009; Willis et al. 2008) and is due to the uneven

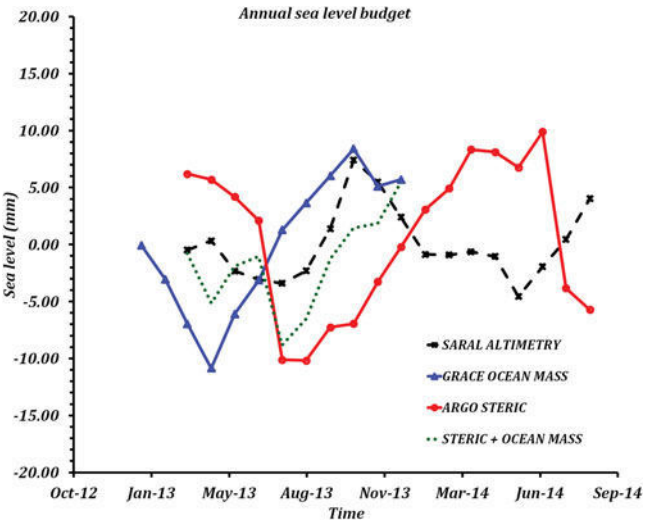

Figure 5. Global mean time series of SARAL/AltiKa observed sea level (black dashes with stars), GRACE ocean mass in terms of equivalent sea level (blue line with triangles), Argo based steric sea level (red line with circles) and total sea level (steric + ocean mass, as dark green dotted line).

distribution of continents in the Northern and Southern Hemispheres and the difference in timing between ocean heating/cooling and fresh water run-off.

The annual mass component (mostly due to the snow pack; e.g., Biancamaria et al. 2011; Cazenave et al. 2000; Chen et al. 1998) has its maximum around September. Therefore, the ocean mass signal is in-phase with the total sea level around this time but at amplitude higher than that of the total sea level. In the case of steric sea level, even though the ocean heating in Northern and Southern Hemisphere tend to cancel out when the global average is performed, since most of the world's ocean is in the Southern hemisphere, the peak amplitude occurs in the late summer of the Southern hemisphere (around March–April). This signal tends to be much larger than the average steric signal and henceforth is still evident in the global mean steric sea level

Therefore, the seasonal amplitude and differences in phase of the steric and the ocean mass component (i.e., steric + ocean mass) tends to compare relatively well with the total sea level signal from SARAL/AltiKa.

5. Conclusion

In this study, we have performed a preliminary validation of SARAL/AltiKa SSH measurements on a global scale by making use of AVISO-based Jason-2 sea level data set. Considering that this mission is quite recent and many algorithms for several corrections are not yet completely tuned, comparisons in terms of sea level temporal mean spatial patterns and global mean time series already look promising. At local scales, SARAL/AltiKa sea level is highly correlated with tide gauge records confirming the quality of SARAL/AltiKa's Ka band altimeter. A preliminary analysis of the annual sea level budget by comparing observed sea level with the sum of the steric and ocean mass components is also highly satisfactory.

The validation of SARAL/AltiKa SSH measurements performed in this study shows that even though there are regional differences in the range of ± 30 mm in the case of comparison with Jason-2, the results are highly in line with other existing sea level data. Over a longer time period with more availability of SARAL/AltiKa sea level data in the future, we are confident that this mission will ensure an improved understanding of the evolution of sea level and its coastal impacts.

Acknowledgements

We thank L. Fenoglio-Marc and an anonymous reviewer for their comments and suggestions.

Funding

H. Palanisamy is supported by a CNES-CLS grant. O. Henry is supported by an ESA Climate Change Initiative grant.

References

Ablain, M., A. Cazenave, G. Larnicol, M. Balmaseda, P. Cipollini, Y. Faugère, M. J. Fernandes, O. Henry, J. A. Johannessen, P. Knudsen, O. Andersen, J. Legeais, B. Meyssignac, N. Picot, M. Roca, S. Rudenko, M. G. Scharffenberg, D. Stammer, G. Timms, and J. Benveniste. 2015.

Improved sea level record over satellite altimetry era (1993–2010) from the Climate Change Initiative project. *Ocean Sciences* 11(1):67–82.

Ablain, M., A. Cazenave, G. Valladeau, and S. Guinehut. 2009. A new assessment of the error budget of global mean sea level rate estimated by satellite altimetry over 1993-2008. *Ocean Science* 5(2):193–201.

Biancamaria, S., A. Cazenave, N. M. Mognard, W. Llovel, and F. Frappart. 2011. Satellite-based high latitude snow volume trend, variability and contribution to sea level over 1989/2006. *Global and Planetary Change* 75(3–4):99–107.

Bronner, E., A. K. Shukla, N. Picot, A. Guillot, J. P. Dumont, V. Rosmorduc, J. Lillibridge, S. Desai, H. Bonekamp, R. Scharroo, and J. Figa. 2013. *SARAL/AltiKa Products Handbook*, Issue 2, France: AVISO, CNES. Available at http://www.aviso.altimetry.fr/fileadmin/documents/data/tools/SARAL_Altika_products_handbook.pdf. Last accessed 28 July 2015.

Cazenave, A., F. Remy, K. Dominh, and H. Douville. 2000. Global ocean mass variation, continental hydrology and the mass balance of the Antarctica ice sheet at the seasonal time scale. *Geophysical Research Letters* 27:3755–3758.

Cazenave, A. and G. Le Cozannet. 2014. Sea level rise and its coastal impacts. *Earth's Future* 2(2):15–34.

Chambers, D. P., J. Wahr, and R. S. Nerem. 2004. Preliminary observations of global ocean mass variations with GRACE. *Geophysical Research Letters* 31:L13310.

Chambers, D. P. 2006. Evaluation of new GRACE time-variable gravity data over the ocean. *Geophysical Research Letters* 33(17):L17603.

Chen, J. L., C. R. Wilson, D. P. Chambers, R. S. Nerem, and B. D. Tapley. 1998. Seasonal global water mass budget and mean sea level variations. *Geophysical Research Letters* 25(19):3555–3558.

Church, J. A., P. U. Clark, A. Cazenave, J. M. Gregory, S. Jevrejeva, A. Levermann, M. A. Merrifield, G. A. Milne, R. S. Nerem, P. D. Nunn, A. J. Payne, W. T. Pfeffer, D. Stammer, and A. S. Unnikrishnan. 2013. Sea level change. In *Climate Change 2013: The Physical Science Basis. Contribution of Working Group I to the Fifth Assessment Report of the Intergovernmental Panel on Climate Change*. Stocker, T. F., D. Qin, G. -K. Plattner, M. Tignor, S. K. Allen, J. Boschung, A. Nauels, Y. Xia, V. Bex, and P. M. Midgley (eds.), Cambridge, UK: Cambridge University Press.

Church, J. A., N. J. White, L. F. Konikow, C. M. Domingues, J. G. Cogley, E. Rignot, J. M. Gregory, M. R.Van denBroeke, A. J. Monaghan, and I. Velicogna. 2011. Revisiting the earth's sea-level and energy budgets from 1961 to 2008. *Geophysical Research Letters* 38(September). doi:10.1029/2011GL048794.

Dee, D. P., S. M. Uppala, A. J. Simmons, P. Berrisford, P. Poli, P. Kobayashi, U. Andrae, M.A. Balmaseda, G. Balsamo, P. Bauer, P. Bechtold, A.C.M. Beljaars, L. van de Berg, J. Bidlot, N. Bormann, C. Delsol, R. Dragani, M. Fuentes, A.J. Geer, L. Haimberger, S.B. Healy, H. Hersbach, E.V. Holm, L. Isaksen, P. Kallberg, M. Kohler, M. Matricardi, A.P. McNally, B.M. Monge-Sanz, J.-J. Morcrette, B.-K. Park, C. Peubey, P. de Rosnay, C. Tavolato, J.-N. Thepaut, and F. Vitart. 2011. The ERA-interim reanalysis: Configuration and performance of the data assimilation system. *Quarterly Journal of the Royal Meteorological Society* 137(656):553–597.

Fu, L. L. and A. Cazenave. 2001. *Satellite Altimetry and Earth Sciences, Vol. 69: A Handbook of Techniques and Applications*. San Diego, CA: Academic Press.

Fukumori, I. and O. Wang. 2013. Origins of heat and freshwater anomalies underlying regional decadal sea level trends. *Geophysical Research Letters* 40(3):563–567.

Hamlington, B. D., R. R. Leben, M. W. Strassburg, R. S. Nerem, and K. -Y. Kim. 2013. Contribution of the Pacific decadal oscillation to global mean sea level trends. *Geophysical Research Letters* 40(19):5171–5175.

Han, W., G. A. Meehl, A. Hu, M. A. Alexander, T. Yamagata, D. Yuan, M. Ishii, P. Pegion, J. Zheng, B.D. Hamlington, X.-W. Quan, and R.R. Leben. 2013. Intensification of decadal and multi-decadal sea level variability in the western tropical Pacific during recent decades. *Climate Dynamics* October:1–23. doi: 10.1007/s00382-013-1951-1.

Hosoda, S., T. Ohira, and T. Nakamura. 2008. A monthly mean dataset of global oceanic temperature and salinity derived from Argo float observations. *JAMSTEC Report of Research and Development* 8:47–59.

Johnson, G. C. and D. P. Chambers. 2013. Ocean bottom pressure seasonal cycles and decadal trends from GRACE release-05: Ocean circulation implications. *Journal of Geophysical Research: Oceans* 118(9):4228–4240.

Köhl, A. and D. Stammer. 2008. Decadal sea level changes in the 50-year GECCO ocean synthesis. *Journal of Climate* 21(9):1876–1890.

Leuliette, E. W. and L. Miller. 2009. Closing the sea level rise budget with altimetry, Argo, and GRACE. *Geophysical Research Letters* 36:04608.

Leuliette, E. W. and J. K. Willis. 2011. Balancing the sea level budget. *Oceanography* 24(2):122–129.

Levitus, S., J. I. Antonov, T. P. Boyer, O. K. Baranova, H. E. Garcia, R. A. Locarnini, A. V. Mishonov, J. R. Reagan, D. Seidov, E. S. Yarosh, and M. M. Zweng. 2012. World ocean heat content and thermosteric sea level change (0–2000 M), 1955–2010. *Geophysical Research Letters* 39(10):L10603.

Lombard, A., G. Garric, T. Penduff, and J. M. Molines. 2009. Regional variability of sea level change using a global ocean model at $^1/_4^\circ$ resolution. *Ocean Dynamics* 3:433–449.

McGregor, S., A. Sen Gupta, and M. H. England. 2012. Constraining wind stress products with sea surface height observations and implications for Pacific Ocean sea level trend attribution. *Journal of Climate* 25(23):8164–8176.

Palanisamy, H., A. Cazenave, T. Delcroix, and B. Meyssignac. 2015. Spatial trend patterns in Pacific Ocean sea level during the altimetry era: The contribution of thermocline depth change and internal climate variability. *Ocean Dynamics.* 1–16, doi:10.1007/s10236-014-0805-7.

Stammer, D., A. Cazenave, R. M. Ponte, and M. E. Tamisiea. 2013. Causes for contemporary regional sea level changes. *Annual Review of Marine Science* 5(September). doi:10.1146/annurev-marine-121211-172406.

Timmermann, A., S. McGregor, and F. -F. Jin. 2010. Wind effects on past and future regional sea level trends in the southern Indo-Pacific. *Journal of Climate* 23(16):4429–4437.

Verron, J., S. Philipps, P. Bonnefond, Y. Faugère, J. Richman, D. Griffin, A. Pascual, F. Birol, L. Aouf, S. Calmant, A. Michel, and J. Tournadre. 2013. *AVISO Users Newsletter, SARAL/AltiKa Special Issue*, 10.

Verron, J., P. Sengenes, J. Lambin, J. Noubel, N. Steunou, A. Guillot, N. Picot, S. Coutin-Faye, R. Gairola, D. V. A. Raghava Murthy, J. Richman, D. Griffin, A. Pascual, F. Rémy, and P. K. Gupta. 2015. The SARAL/AltiKa altimetry satellite mission. *Marine Geodesy* 38(S1): this issue.

Volkov, D. L., G. Larnicol, and J. Dorandeu. 2007. Improving the quality of satellite altimetry data over continental shelves. *Journal Geophysical Research: Oceans* 112(C6). doi: 10.1029/2006JC003765.

Willis, J. K., D. P. Chambers, and R. S. Nerem. 2008. Assessing the globally averaged sea level budget on seasonal to interannual timescales. *Journal of Geophysical Research: Oceans* 113(C6): C06015.

Woodworth, P. L. and R. Player. 2003. The permanent service for mean sea level: An update to the 21st century. Journal of Coastal Research 19:287–295.

Wunsch, C., R. M. Ponte, and P. Heimbach. 2007. Decadal trends in sea level patterns: 1993–2004. *Journal of Climate* 20(24):5889–5911.

Zhang, X. and J. A. Church. 2012. Sea level trends, interannual and decadal variability in the Pacific Ocean. *Geophysical Research Letters* 39(November). doi: 10.1029/2012GL053240.

2.2 Global mean sea level (GMSL) budget since altimetry era

In the previous chapter we have discussed the two main contributors to global mean sea level change: steric changes (density changes due to thermal expansion and salinity changes) and ocean mass changes (due to water exchange between the ocean and other reservoirs such as glaciers, ice caps, ice sheets and ground water. To meaning-fully interpret the causes of sea level change over a particular period, changes in observed sea level should be equal to the sum of changes due to ocean density and mass exchange (*Leuliette and Willis*, 2011). This is called as the sea level budget and can be written as

$$\Delta H_{sea\ level} = \Delta H_{steric} + \Delta H_{ocean\ mass} \qquad (2.2)$$

where $\Delta H_{sea\ level}$ is the observed sea level, ΔH_{steric} is the steric sea level change component and $\Delta H_{ocean\ mass}$ is the ocean mass component in terms of equivalent sea level. Sea level budget closure also indicates that the observations are complete and accurate. Furthermore, quantifying the causes of sea level rise individually is important for predicting how much the sea level will rise in the future and also to understand the magnitude of changes that has already occurred (*Leuliette and Willis*, 2011, *Church et al.*, 2011).

When we consider the satellite altimetry era, the 4th Assessment Report (AR4) of the IPCC estimated the sea level budget over the 1993-2003 time span. The contribution of thermal expansion was estimated at 1.6 ± 0.25 mm/yr (until 700 m depth) while those of glaciers and ice sheets were estimated to be 0.8 ± 0.11 mm/yr and 0.4 ± 0.2 mm/yr respectively. The sum of the contributions, 2.8 ± 0.35 mm/yr was found to be rather in good agreement with the satellite altimetry based GMSL rise of 3.1 ± 0.4 mm/yr with thermal expansion contributing ~50% of the total rate (*Bindoff et al.,* 2007). Over the 1993-2010 time span, IPCC AR5 estimated the sum of contributions amounting to 2.8 ± 0.5 mm/yr, a value slightly lower than the observed sea level rate of 3.2 ± 0.4 mm/yr. During this time span, land ice melt contributed 50% of the total sea level rate while ocean thermal expansion (up to 1500m) and anthropogenic land water storage decrease contributed 35% and 13% respectively (*Church et al.,* 2013).

The contribution of sea level components is in fact not constant through time. Since the last decade, the contribution of ice sheets has accelerated (*Shepherd et al.*, 2012) while the upper

ocean thermal expansion has increased less rapidly (*Lyman et al.*, 2010) than the previous decade. This period of slower upper ocean thermal expansion rate also coincides with the so-called 'pause' in global mean air and sea surface temperature evolution since the early 2000s, popularly called as the 'hiatus' (*Held*, 2013, *Trenberth and Fasullo*, 2013, *Smith*, 2013). However the issue of 'hiatus' remains puzzling because studies (e.g. *Peters et al.*, 2012) have shown that the greenhouse gases have in fact continued to accumulate at an increased rate and the Earth's energy imbalance still remains to be positive in the order of 0.5 -1 W/m^2 (*Hansen et al.*, 2011, *Trenberth et al.*, 2014). Different explanations have been proposed by various studies on this issue that ranges from reduction in radiative forcing due to longer solar minimum, increase in aerosols and volcanic eruptions, stratospheric water vapor changes and enhanced deep ocean heat uptake in the Pacific or Atlantic Ocean. Of all these, the most favored explanation for the hiatus is the deep ocean heat uptake. However, the exact mechanism that causes this still remains an unanswered question (*Solomon et al.*, 2010, *Hansen et al.*, 2011, *Guemas et al.*, 2013, *Trenberth and Fasullo*, 2013, *Kosaka and Xie*, 2013, *Balmaseda et al.*, 2013, *Watanabe et al.*, 2013, *Chen and Tung*, 2014, *England et al.*, 2014, *Goddard*, 2014). Fig.2.4 displays the global mean altimetry based sea level variations and its two main components, ocean mass measure by GRACE and Argo based thermosteric sea level since 2005. The slow rate of ocean thermal expansion is noticeable.

Understanding the contribution of deep ocean heat content to global warming hiatus is possible by means of accurate observations of sea level change and its components (ocean thermal expansion and mass changes, *von Schuckmann et al.*, 2014, *Dieng et al.*, 2015, *Llovel et al.*, 2014). GMSL change from satellite altimetry when corrected for the ocean mass change from GRACE space gravimetry results in an estimate of ocean thermal expansion that also includes the deep ocean contribution. This can then be compared with Argo-based ocean thermal expansion available until a depth of ~ 1500 m and would help in quantifying the deep ocean contribution below 1500 m. We therefore performed such a sea level budget analysis since 2003 with an aim on estimating the deep ocean contribution to sea level change. The 2003-2012 decade corresponds to the hiatus period and also to the availability of new observational systems for ocean thermal expansion (global ocean temperature and salinity measurement until 2000 m of depth by Argo floats) and ocean mass changes (direct ocean mass measurements from GRACE).

This has been published as an article titled 'The sea level budget since 2003: inference on the deep ocean heat content'.

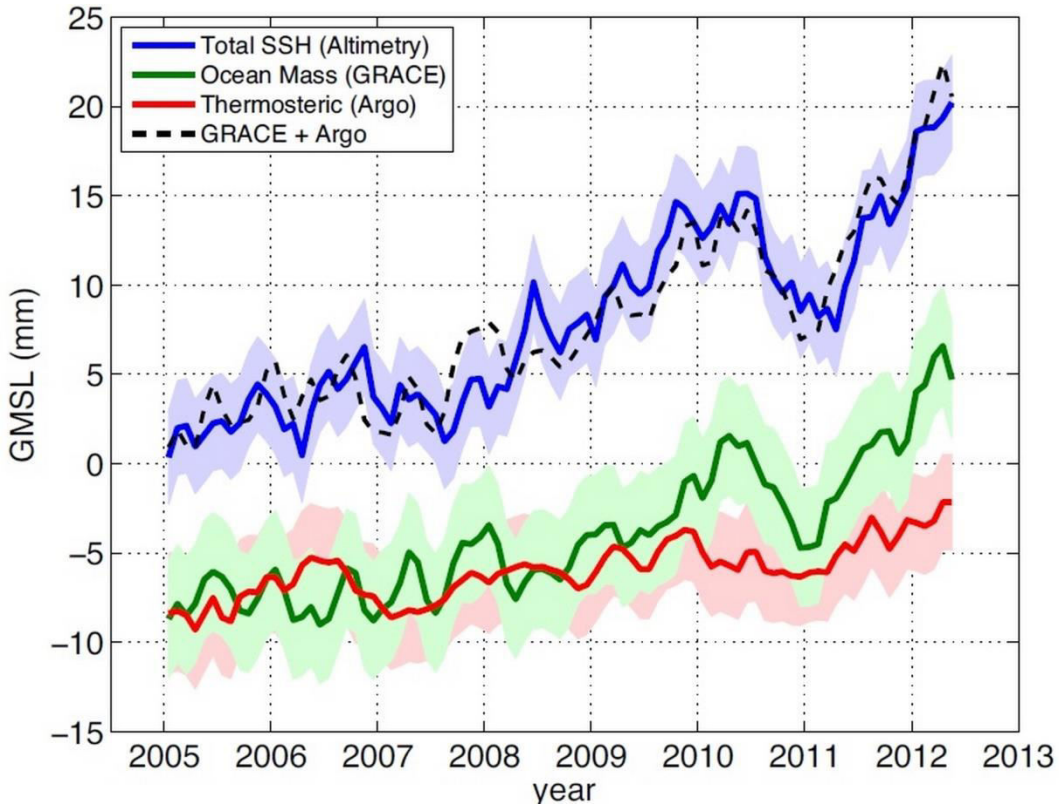

Figure 2.4: Global mean sea level from altimetry from 2005 to 2012 (blue line). Ocean mass changes are shown in green (as measured by GRACE) and thermosteric sea level changes (as measured by the Argo Project) are shown in red. The black line shows the sum of the ocean mass and thermosteric contributions. Adapted from Church et al., 2013.

Summary of the article: 'The sea level budget since 2003: inference on the deep ocean heat content' (the original article is inserted at the end of this section).

In this article, a total of 16 different data sets from various teams (5 for GMSL, 8 for steric sea level and 3 for ocean mass component) were considered to derive constraints on the deep ocean thermal contribution through a sea level budget closure approach during two different time periods: between 2005 and 2012 (P1) and between 2003 and 2012 (P2). The time period 2005-2012 was mainly chosen because before 2005, Argo coverage was incomplete (*von Schuckmann and Le Traon*, 2011). Differences between data sets related to each variable

(observed sea level, ocean mass and steric sea level) were noticed and were mostly attributed to data processing issues. While the large number of datasets can provide 120 different combinations of sea level budget estimates, in this study, the averages of each data type (GMSL, ocean mass and steric sea level) were used and their dispersion ranges were estimated. This provides an insight on the uncertainty range due to variations in processing approach used by different teams.

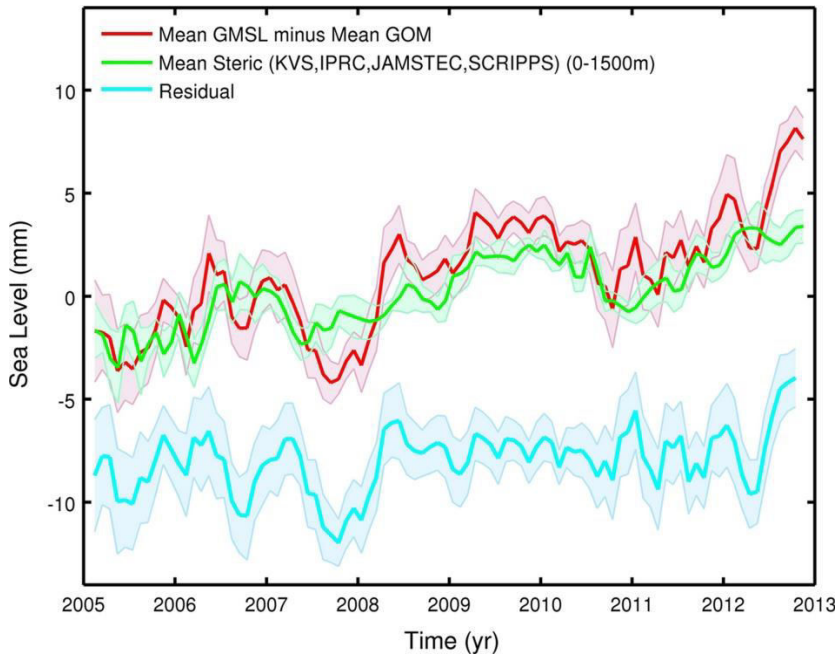

Figure 2.5: Difference time series 'GMSL minus GOM' (based on the averaged curves), mean steric sea level (average of Argo steric) and residual curve ('GMSL minus GOM' minus mean steric sea level, with downward offset of 7.5 mm for clarity over 2005-2012 from Dieng et al., 2015

Over P1 (2005-2012) period, the residual trend value obtained after removing the contribution of Argo based steric (0-1500 m) sea level from the GMSL minus GOM time series accounts to 0.3 ± 0.21 mm/yr (See Fig.2.5 for the corresponding curves). This residual reflects errors affecting all the data sets, errors due to insufficient Argo floats coverage and the potential deep ocean contribution below 1500 m. Similarly, over P2 (2003-2012) period, the residual trend value accounts to 0.55 ± 0.19 mm/yr. In both the cases, the residual curves display important interannual variability. Since direct steric observations below 1500 m depth are very sparse over P1 and P2 time periods (*Purkey and Johnson*, 2010, *Kouketsu et al.*, 2011), in order to obtain the deep ocean steric contribution below this depth, an ocean reanalyses ORAS4 (available until 2009) was also considered in the study. The ORAS4 reanalyses was first compared with the

Argo based steric sea level between 0-1500 m depth and was found to have very good agreement. The ORAS4 based deep ocean steric contribution was then estimated and compared with the 'GMSL minus GOM minus steric' (Fig.2.6). Over the 2003-2009 time span, the ORAS4 steric signal below 1500 m was observed to be smooth with a very small trend value < 0.1 mm/yr. Such a magnitude is in line with estimates of deep ocean contribution based on sparse but direct observations (*Purkey and Johnson*, 2010). This indicates that the residual 'GMSL minus GOM minus steric' curve that displays important interannual variability and associated trend of 0.55 ± 0.19 mm/yr is totally unrealistic in the deep ocean.

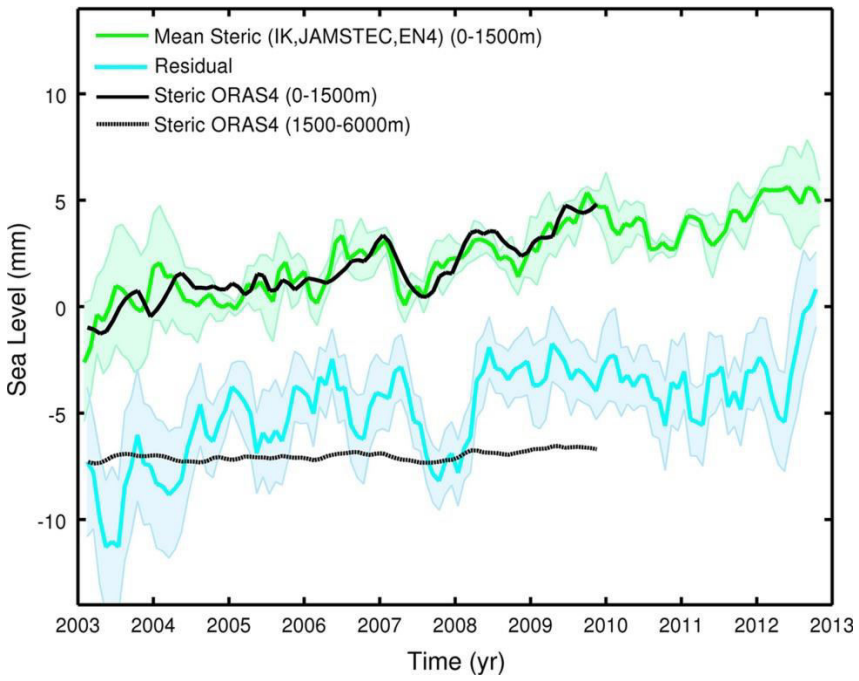

Figure 2.6: Upper curves: Averaged steric sea level (0-1500m) time series from Ishii and Kimoto, Jamstec and EN4 in green and from ORAS4 (0-1500m) in black. Lower curves: GMSL minis GOM minus steric residual in blue with the ORAS4 deep ocean contribution (1500-6000m) in dotted black. Figure adapted from Dieng et al., 2015.

Furthermore, if the systematic errors associated with GMSL (0.4 mm/yr, *Ablain et al.*, 2009,), GOM (0.3 mm/yr, *Chambers and Bonin*, 2012) and steric sea level (0.3 mm/yr) were taken into account, the resulting error in trend based on their quadratic sum accounts to 0.58 mm/yr. This shows that the residual trend (GMSL minus GOM minus steric) is barely significant. While altimetry based sea level and ocean mass signals include the Indonesian region, Argo floats do not cover this region. This implies that the residual trend at least partially reflect this missing steric signal. The steric contribution of the Indonesian region computed using

ORAS4 results in a trend value of ~ 0.3 mm/yr. Therefore, removal of this value from the residual trend (deep ocean) value results in a new residual trend range ~ 0 and 0.25 mm/yr. This range of trend can thus be considered as an upper limit for the deep ocean contribution to recent years sea level rise.

Surv Geophys
DOI 10.1007/s10712-015-9314-6

The Sea Level Budget Since 2003: Inference on the Deep Ocean Heat Content

Habib B. Dieng · Hindumathi Palanisamy · Anny Cazenave · Benoit Meyssignac · Karina von Schuckmann

Received: 26 September 2014 / Accepted: 2 January 2015

Abstract This study provides an overview of the various components of the global mean sea level evolution over two time spans: (1) 2005–2012 (corresponding to the full deployment of the Argo program) and (2) 2003–2012. Using a sea level budget approach, we compare altimetry-based global mean sea level, global ocean mass from GRACE space gravimetry and steric sea level from Argo and other in situ measurements. One goal of this study is to investigate whether it is possible to constrain the deep ocean contribution to the global mean sea level rise over the last decade. This question is particularly relevant, considering the current debate about the 'hiatus,' i.e., the observed recent pause of the global mean air and sea surface temperature evolution while the planet is still in thermal imbalance. We consider a total of 16 different data sets. Differences are noticed between data sets related to each variable (sea level, ocean mass and steric sea level), mostly due to data processing issues. Therefore, we perform the analysis using averages of the available data sets. For each period, we find that, when removing from the global mean sea level, the contributions of the global mean ocean mass and steric sea level (estimated for the 0–1,500 m ocean layer), there remains a residual signal displaying a positive slope of 0.3 ± 0.6 and 0.55 ± 0.6 mm/year over 2005–2012 and 2003–2012, respectively. Comparing with an ocean reanalysis and according to direct (but sparse) ocean temperature measurements below 1,500 m, it seems unlikely that the observed residual signal can be attributed to deep (below 1,500 m) ocean warming, in agreement with other recently published results. We estimate that it possibly reflects, at least partly, the signature of a missing upper ocean steric signal in regions uncovered by current observing systems. Our study also shows a steady warming increase since 2003 of the 700–1,500 m ocean layer (amounting ~ 0.2 mm/year in steric sea level equivalent), confirming previous findings, but seen in our study in each of the eight different steric data sets considered.

H. B. Dieng · H. Palanisamy · A. Cazenave (✉) · B. Meyssignac
LEGOS-CNES, 18 Avenue E. Belin, 31401 Toulouse Cedex 9, France
e-mail: anny.cazenave@legos.obs-mip.fr

K. von Schuckmann
Mediterranean Institute for Oceanography, University of Toulon, Toulon, France

Published online: 28 January 2015

Keywords Sea level rise · Thermal expansion · Ocean mass · Deep ocean warming

1 Introduction

Sea level is an interesting quantity in Earth sciences research as it integrates variations from different climatic and non-climatic variables. For example, in terms of global mean, current sea level rise mostly results from thermal expansion of seawater due to ocean temperature changes and water mass addition into ocean basins due to glacier melting, ice sheet mass loss and land water storage changes of anthropogenic origin (e.g., Leuliette and Willis 2011; Chen et al. 2013; Church et al. 2013). At interannual timescales, in particular during ENSO (El Nino–Southern Oscillation) events, global mean sea level fluctuations are largely due to land–ocean asymmetry in precipitation, causing temporary ocean mass excess (during El Nino) or deficit (during La Nina) (Boening et al. 2012; Cazenave et al. 2012, 2014; Fasullo et al. 2013). While regional variations in absolute sea level mostly result from ocean temperature and salinity variations (and to a lesser extent from direct atmospheric forcing on the sea surface) (Stammer et al. 2013), non-climatic factors also play a role. In effect, the viscous/elastic response of the solid Earth to past (i.e., last deglaciation) and ongoing land ice melt causes complex deformations of ocean basins and changes in the mutual attraction of ice-water bodies, and hence of sea level (e.g., Stammer et al. 2013). Finally, along coastlines, relative sea level changes occur because of a combination of absolute sea level changes and vertical movements of the Earth's crust (Woppelmann et al. 2009).

In the 5th Assessment Report (AR5) of the Intergovernmental Panel on Climate Change (IPCC), it was reported that over the 1993–2010 time span (corresponding to the high-precision satellite altimetry era), the rate of global mean sea level (GMSL) rise is due to the combined effects of land ice melt (50 %), ocean thermal expansion (37 %) and anthropogenic land water storage decrease (13 %) (Church et al. 2013). The sum of these contributions amounts to 2.8 ± 0.5 mm/year, a value only slightly lower than the rate of sea level rise observed by altimeter satellites, of 3.2 ± 0.4 mm/year. Although of the same order of magnitude as associated uncertainties, the difference may also reflect other contributions either not or incompletely accounted for, e.g., the deep ocean (below 700–1,000 m depth where the coverage of available data is poor or non-existent).

In the IPCC 4th Assessment Report (AR4), the sea level budget was estimated over the 1993–2003 time span (Bindoff et al. 2007). Over that decade, the thermal expansion contribution was $\sim$50 % the rate of sea level rise, i.e., significantly larger than the 1993–2010 average (note, however, that in AR4, thermal expansion estimates were contaminated by Expandable Bathy Thermographers—XBT biases). In fact, the sea level components are not constant through time. During the last 10–15 years, the land ice (mostly the ice sheets) component has accelerated (i.e., Shepherd et al. 2012; see also IPCC AR5 and references herein) while the upper ocean thermal expansion has increased less rapidly than during the 1993–2003 decade (Lyman et al. 2010). This recent slower rate in thermal expansion of the upper ocean coincides with the pause (also called the 'hiatus,' e.g., Held 2013) in global mean air and sea surface temperature evolution observed since the early 2000s (e.g., Trenberth and Fasullo 2013; Smith 2013). The current global warming hiatus is puzzling because greenhouse gases have

continued to accumulate at an increased rate (Peters et al. 2012) and the Earth's energy imbalance at the top of the atmosphere is estimated to still be positive, on the order of 0.5–1 Wm^{-2} (e.g., Hansen et al. 2011; Trenberth et al. 2014). This issue has been the object of considerable attention in the very recent years, and different explanations have been proposed, ranging from reduced radiative forcing due to prolonged solar minimum, increased aerosols and numerous volcanic eruptions, changes in stratospheric water vapor, enhanced heat uptake in the deep ocean, either in the Pacific or Atlantic regions (e.g., Trenberth and Fasullo 2010, 2013; Hansen et al. 2011; Solomon et al. 2010; Guemas et al. 2013; Kosaka and Xie 2013 Balmaseda et al. 2013a; Watanabe et al. 2013; England et al. 2014; Chen and Tung 2014). While deep ocean heat uptake is currently the favored explanation of the hiatus, no consensus yet exists on the exact mechanism at work and on the place where deep ocean warming may occur (e.g., Goddard 2014; Trenberth et al. 2014; Chen and Tung 2014).

Accurate observations of sea level rise and its components (ocean thermal expansion and ocean mass change) can, in principle, help to constrain the problem (e.g., von Schuckmann et al. 2014). In particular satellite altimetry-based GMSL rise corrected for ocean mass change (e.g., using GRACE space gravimetry data over the oceans) provides an estimate of the total (full depth integrated) ocean thermal expansion (or equivalently ocean heat content). Comparison with observed Argo-based ocean thermal expansion (down to $\sim$1,500 m depth) may help to quantify any deep ocean contribution (below 1,500 m) and geographically localize any ocean warming. The first issue is addressed in the present study. Our analysis focusses on the 2003–2012 decade which corresponds to the hiatus period and the availability of new observing systems for estimating thermal expansion and ocean mass (nearly full ocean temperature and salinity coverage down to 2,000 m from Argo floats and direct ocean mass measurements from GRACE space gravimetry). Time series of satellite altimetry-based sea level, thermal expansion and ocean mass components are currently constructed by different groups (see Sect. 2) so that several data sets of each variable are available. But as we will see below, for some of them, in particular ocean thermal expansion, significant discrepancies are noticed between the data sets. Thus, part of our study consists of discussing the differences observed between the different records and estimate the uncertainty of each component. We further address the question: Can we close the sea level budget with available data sets for sea level and components or, if not, can we extract a significant residual possibly related to the deep ocean contribution? The present study deals with global mean time series. Contributions from oceanic regions will be presented in another study. Inside the 2003–2012 time span, two subperiods are considered: period P1 covering January 2005 to December 2012, corresponding to quasi global coverage of Argo data (before 2005, the Argo coverage is incomplete, e.g., von Schuckmann and Le Traon 2011), and period P2 covering January 2003 to December 2012 where GRACE data are available, as well as several steric data sets and ocean reanalyses products (in general available over a longer time span, e.g., 1950–present). In the following, we study periods P1 (2005–2012) and P2 (2003–2012).

While our manuscript was under review, another study by Llovel et al. (2014) was published on the same issue. Llovel et al. (2014) consider the 2005–2013 time span, and not as many data sets as in the present study, but their conclusion is not at odds with ours. In the last section, we discuss their results and compare them with ours.

2 Data

2.1 Sea Level Data

We used five different products from five processing groups for the altimetry-based sea level data:

1. Archiving Validation and Interpretation Satellite Oceanographic Center (AVISO; http://www.aviso.altimetry.fr/en/data/products/ocean-indicators-products/actualitesindicateurs-des-oceansniveau-moyen-des-mersindexhtml.html)
2. Colorado University (CU Release 3; http://sealevel.colorado.edu/)
3. Goddard Space Flight Center (GSFC version 2; http://podaac-ftp.jpl.nasa.gov/dataset/MERGED_TP_J1_OSTM_OST_GMSL_ASCII_V2)
4. National Oceanographic and Atmospheric Administration (NOAA; http://www.star.nesdis.noaa.gov/sod/lsa/SeaLevelRise/LSA_SLR_timeseries_global.php)
5. Commonwealth Scientific and Industrial Research Organization (CSIRO; www.cmar.csiro.au/sealevel/sl_data_cmar.html).

All five sea level data sets are based on Topex/Poseidon, Jason-1 and Jason-2 data averaged over the 66°S–66°N domain, except for the CSIRO data averaged between 65°S and 65°N. For each product, a set of instrumental and geophysical corrections is applied (details are given on the websites of each data set). In addition, the effect of glacial isostatic adjustment (GIA, i.e., a small correction of −0.3 mm/year, Peltier 2004) is accounted for in each sea level time series except in the NOAA data set. We thus corrected the latter sea level data for the GIA effect, using the −0.3 mm/year value. The five sea level time series (AVISO, CU, GSFC, NOAA and CSIRO) are obtained either by directly averaging the along-track sea surface height data (e.g., CU) or by firstly gridding the unevenly distributed along-track data and then performing grid averaging (e.g., AVISO and NOAA). In all cases, an area weighting is applied. In addition to the geographical averaging method, other differences exist between the GMSL data sets because of the applied geophysical and instrumental corrections and the number of satellites considered (discussion on these differences can be found in Masters et al. 2012 and Henry et al. 2014). The sea level time series used in this study cover the period January 2003–December 2012.

Recently, in the context of the European Space Agency (ESA) Climate Change Initiative (CCI) 'Sea Level' project (ftp.esa-sealevel-cci.org/Products/SeaLevel-ECV/V1_11092012/), a new, improved product, combining the Topex/Poseidon and Jason-1/2 with the ERS-1/2 and Envisat missions, has been computed (Ablain et al. 2014). However, at the date of writing it is available until December 2010 only. Even if, for the sea level budget, we will not use the CCI data set as it does not yet extend to 2012, we will compare the CCI-based GMSL with the other data sets during their overlapping time span (January 2003–December 2010) (see Sect. 3.1).

2.2 Ocean Mass Data

For estimating the ocean mass component, we used three different data sets: The GRACE Release 05 products from the Center for Space Research from Texas University (CSR RL05), the German GeoForschungsZentrum (GFZ RL05) and the Jet Propulsion Laboratory (JPL RL05). To study the ocean mass evolution, a specific processing has been carried out by D. Chambers, using the GRACE Release 05 data sets over the oceans. In effect, as warned on the http://grace.jp.nasa.gov Web site, gridded Release 05 data cannot be used to

compute ocean mass changes because they have the global mean removed. In this study, we used the Chambers' ocean data. They are provided as global mean (averaged over the 90°S–90°N domain) time series with associated uncertainty. They are publicly available from https://dl.dropboxusercontent.com/u/31563267/ocean_mass_orig.txt. The processing methodology is described in Johnson and Chambers (2013) (see also Chambers and Schroeter 2011; Chambers and Bonin 2012). The GIA component has been subtracted from each GRACE ocean mass time series using the GIA correction computed in Chambers et al. (2010).

2.3 Steric Data

The steric component is estimated using in situ ocean temperature and salinity data sets. We considered seven different datasets, including four Argo products, plus an ocean reanalysis.

2.3.1 Period P1: Argo Data

We used Argo temperature and salinity data sets provided by four different groups:

- the International Pacific Research Center (IPRC),
- the Japan Agency for Marine-Earth Science and Technology (Jamstec),
- the Scripps Institution of Oceanography (SCRIPPS).

These data sets are available at monthly intervals on a global $1° \times 1°$ grid down to 2,000 m, over the period January 2005–December 2012. They can be downloaded from the http://www.argo.ucsd.edu/Gridded_fields Web site.

Using these data sets, we computed the steric sea level time series (and associated uncertainty; but note that only Jamstec provides errors), integrating the data over the 0–1,500 m depth range. The gridded steric time series from IPRC, Jamstec and SCRIPPS are estimated over the 62.5°S–64.5°N, 60.5°S–70.5°N and 61.5°S–64.5°N domains, respectively (i.e., corresponding to the data availability). An area weighting is applied when computing the global mean time series.

We also used an updated version of the global mean steric time series computed by von Schuckmann and Le Traon (2011) (0–1,500 m ocean layer). This monthly time series is based on a weighted box averaging scheme of Argo data, within the 60°S–60°N domain. In the following, this data set is called KvS.

Therefore, a total of four steric data sets are considered over period P1.

2.3.2 Period P2

In addition to the Jamstec data set, we also used other steric data sets to study the sea level budget over period P2 (since 2003): an updated version of Ishii and Kimoto (2009), the NOAA data set from Levitus et al. (2012) and the EN4 data set (Good et al. 2013). In addition, we also used the ORAS4 reanalysis from Balmaseda et al. (2013b). Over the recent years, these data sets integrate Argo data. Prior to Argo, most data are based on XBT devices and other in situ measurements (see Abraham et al. 2013). A few details on these data sets are given below:

- Ishii and Kimoto (2009) data set (called IK hereinafter): We used the updated 6.13 version available at http://rda.ucar.edu/datasets/ds285.3/. It is based on the World

Ocean Database 2005 and World Ocean Atlas 2005 (WOD05 and WOA05), the Global Temperature-Salinity dataset in the tropical Pacific from the Institut de Recherche pour le Development (IRD, France) and the Centennial in situ Observation Based Estimates (COBE) sea surface temperature. The XBT depth bias correction is applied in the current version. The temperature and salinity data are available at monthly intervals over 24 depth levels ranging from the ocean surface down to 1,500 m depth, on a global 1° × 1° grid from January 1945 to December 2012 (see Ishii and Kimoto 2009 for details).

- NOAA data set: Available at https://www.nodc.noaa.gov/OC5/3M_HEAT_CONTENT. As described in Levitus et al. (2012), this 1° × 1° data set uses the World Ocean Database 2009 (WOD09) plus additional data processed since 2009. Bias corrections are applied to the MBT (Mechanical BathyThermographs) and XBT data as described by Levitus et al. (2009). The temperature and salinity grids below 700 m are not available prior to January 2005. Thus, for the P2 time span, we computed the NOAA steric time series considering data down to 700 m only. Data are given at 3-month interval. Therefore, we interpolated the NOAA time series at monthly intervals to be consistent with the other steric time series.
- EN4 data set: We used the EN4.0.2 version from the Met Office Hadley Centre (http://www.metoffice.gov.uk/hadobs/en4/download-en4-0-2.html). This data set is based on the quality controlled subsurface ocean temperature and salinity profiles and objective analyses. The EN4.0.2 data set is an incremental development of the previous EN2 and EN3 versions. Data sources include the WOD09, Global Temperature and Salinity Profile Program (GTSPP) and Argo data from Argo Global Data Assembly Centres (GDACs). The EN4.0.2 temperature and salinity data are corrected for the XBT and MBT bias. The temperature and salinity data are available at monthly intervals over 40 depth levels ranging from the ocean surface down to 5,350 m depth, on a global 1° × 1° grid from January 1900 to December 2013. Details on the data processing are given in Good et al. (2013).
- The ORAS4 reanalysis from Balmaseda et al. (2013b) (https://icdc.zmaw.de/easy_init_ocean.html?&L=1#c2231). It is based on the Nucleus for European Modelling of the Ocean (NEMO) ocean circulation model (version 3.0) with data assimilation. Assimilated data include temperature and salinity profiles from EN3 version 2a (1958–2009), along-track altimetry-based sea level anomalies and global sea level trend from AVISO, sea surface temperature and sea ice from the ERA-40 archive (prior to November 1981), from NCEP (National Centers for Environmental Prediction) OI version 2 (1981 until December 2009) and from OSTIA (Operational Sea Surface Temperature and Sea Ice Analysis; January 2010 onwards). The ORAS4 temperature and salinity data are available at monthly intervals over 42 depth levels ranging from the ocean surface down to 5,350 m depth, on a global 1° × 1° grid from January 1958 to December 2009. Details on the data processing are given in Balmaseda et al. (2013b).

Except for NOAA for which steric sea level grids are directly available, we computed the steric sea level time series and associated errors for the P2 period, integrating the data over the 0–1,500 m depth range. The global mean steric time series were further estimated by geographically averaging the gridded data (area weighting applied).

For the whole set of time series, annual and semiannual cycles were removed and residual time series were smoothed using a 3-month moving window.

3 Data Analysis

3.1 Global Mean Sea Level and Ocean Mass Time Series

Figure 1a shows plots of the GMSL time series without the CCI data over 2003–2012. We note that the CU and GSFC sea level curves are very close, as are the NOAA and AVISO curves. The CSIRO curve agrees better with NOAA and AVISO than with the other two, at least for the second part of the study time span. Some differences are observed between the time series on short time spans (<2–3 years). In terms of trends, differences up to $\sim$0.35 mm/year are noticed between the AVISO, CSIRO, NOAA groups on the one hand, and CU and GSFC on the other hand, the latter groups giving slower rates. As shown in Masters et al. (2012) and Henry et al. (2014), most of these differences (for both inter-annual fluctuations and trends) result from the mapping process adopted by the different groups. Table 1 gives the GMSL trend estimates for the five time series and their means, over P1 and P2 periods.

Figure 1b plots the same five GMSL time series as in Fig. 1a, together with the CCI GMSL over January 2003–December 2010 time span. Slight differences are observed between the CCI and other GMSL time series at interannual timescales. Table 1 also gives the GMSL trends over January 2003–December 2010. We note that the CCI trend (2.75 mm/year) is equal to the mean trend of the other five time series (2.71 mm/year) over this time span. In the following, we will only consider the mean GMSL time series based on averaging the AVISO, CU, NOAA, GSFC and CSIRO time series.

Figure 1c shows the three ocean mass time series over 2003–2012. The global ocean mass (GOM) curves agree well, both in terms of trend and interannual variability. The year-to-year discrepancies between the three curves remain within the error bars of each time series. GOM trends for each data set and means, over P1 and P2 periods are given in Table 1.

Note that the reasonably good agreement among the GMSL and GOM products does not imply anything on their absolute accuracy. However, for the GMSL, external calibration with tide gauge data and assessment of all sources of errors acting on the satellite altimetry system allows us to estimate the GMSL trend and the year-to-year mean sea level anomalies accurate to $\sim$0.4 mm/year and 1–2 mm (Ablain et al. 2009, 2014). For the ocean mass component, it is not possible to do external calibration. Although the GRACE-based ocean mass could be compared to the sum of individual mass components (glacier melting, ice sheet mass loss, land water storage change, atmospheric water vapor change), the latter are still too uncertain to perform any reliable calibration at a global scale. The GRACE-based ocean mass precision has been estimated to 1.5 mm for individual monthly gridded values (Wahr et al. 2006; Chambers and Bonin 2012). In terms of trend, the main uncertainty comes from the GIA correction (estimated at the 0.3 mm/year level, Chambers et al. 2010).

Figure 2 plots mean GMSL (average of the five products), mean GOM (average of the three products) and difference 'GMSL minus GOM' (based on the above averaged curves) with associated uncertainty. For the mean GMSL, the uncertainty is based on the dispersion of each time series with respect to the mean. For the mean GOM, it is based on the quadratic sum of individual errors. Estimating the uncertainty of the mean GOM curve from the dispersion of individual curves gives exactly the same result.

Over P2 (2003–2012), the linear trends amount to 2.82 $\pm$ 0.10 mm/year for the mean GMSL, 1.70 $\pm$ 0.10 mm/year for the mean GOM and 1.12 $\pm$ 0.13 mm/year for the difference. Uncertainties quoted here are formal errors (1 standard deviation, SD). More realistic errors are discussed below (Sect. 4). The GMSL minus GOM time series

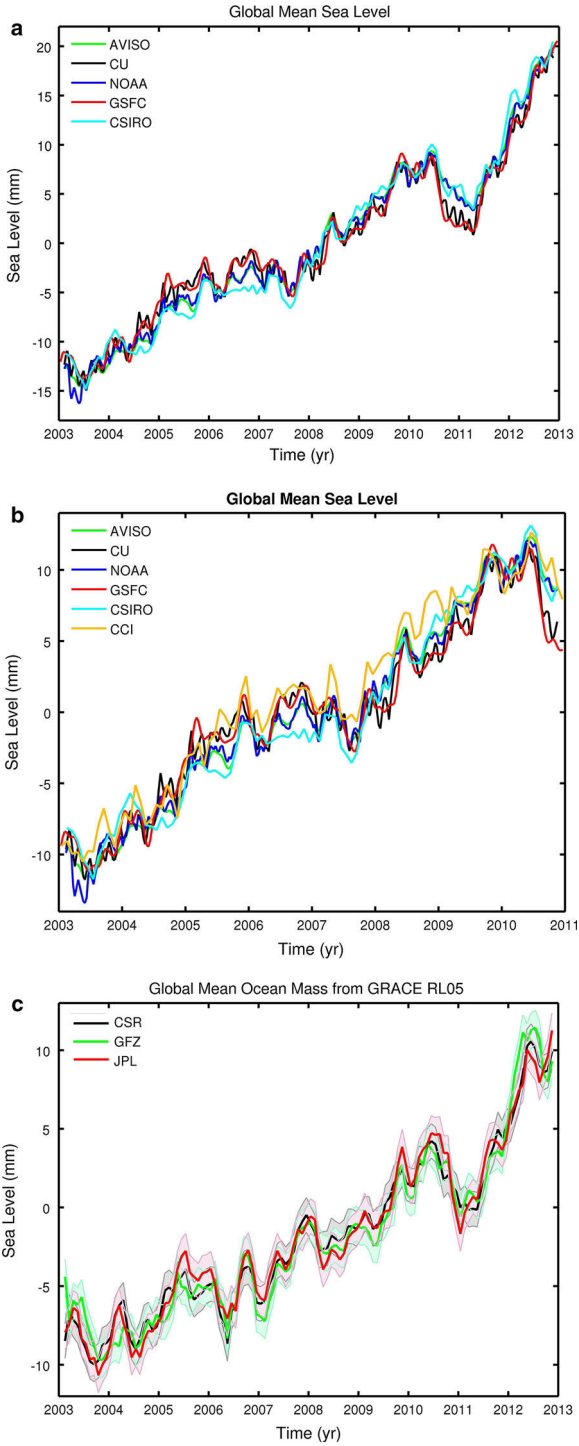

Fig. 1 **a** Global mean sea level (GMSL) time series (January 2003–December 2012) from the five satellite altimetry processing groups (AVISO, CU, CSIRO, GSFC and NOAA). **b** Global mean sea level (GMSL) time series (January 2003–December 2010) from the five satellite altimetry processing groups (AVISO, CU, CSIRO, GSFC and NOAA) and CCI. **c** Global mean ocean mass time series (January 2003–December 2012) from GRACE based on the data from CSR, GFZ and JPL (data provided by D. Chambers)

>**Table 1** Estimated trends for individual GMSL, ocean mass and steric sea level (for 700 and 1,500 m integration depth) time series, as well as their mean over the P1 and P2 periods

Trend estimates	January 2003–December 2010	P1: January 2005–December 2012		P2: January 2003–December 2012	
GMSL (mm/year)					
AVISO	2.90	2.97		2.97	
CU	2.55	2.57		2.66	
NOAA	2.85	2.89		2.91	
GSFC	2.46	2.51		2.61	
CSIRO	2.81	3.18		2.99	
MEAN	2.71 ± 0.10	2.81 ± 0.10		2.82 ± 0.10	
CCI	2.75	–		–	
Ocean mass (OM) (mm/year)					
CSR		1.85 ± 0.12		1.71 ± 0.08	
GFZ		1.94 ± 0.12		1.68 ± 0.08	
JPL		1.81 ± 0.12		1.72 ± 0.08	
MEAN		1.87 ± 0.11		1.70 ± 0.10	
Mean GMSL minus mean OM		0.94 ± 0.16		1.12 ± 0.13	
		0–700 m	0–1,500 m	0–700 m	0–1,500 m
Steric sea level Argo (mm/year)					
KvS		–	0.51 ± 0.15	–	–
IPRC		0.42	0.62	–	–
JAMSTEC		0.53 ± 0.13	0.77 ± 0.16	0.65 ± 0.14	0.92 ± 0.17
SCRIPPS		0.41	0.63	–	–
MEAN		–	0.63 ± 0.12	–	–
Residual (mean GMSL − mean OM mean − steric sea level)		–	0.29 ± 0.21	–	–
Steric sea level (mm/year)					
IK		0.40 ± 0.13	0.67 ± 0.14	0.39 ± 0.11	0.61 ± 0.16
EN4		–	–	0.00 ± 0.14	0.15 ± 0.17
NOAA		–		0.29	–
MEAN		–	–	0.32 ± 0.11	0.56 ± 0.14
Residual (mean GMSL − mean OM mean − steric sea level)		–	–	–	0.55 ± 0.19
ORAS4 Reanalysis (mm/year)	ORAS4 (Jan. 2003–Dec. 2009): 0–1,500 m = 0.65; 1,500–6,000 m = 0.07				

Uncertainties of mean trends correspond to 1 SD. Residual (mean GMSL − mean ocean mass − mean steric sea level) trends are also provided. ORAS4-based steric trends are also given over 2003–2009

displayed in Fig. 2 shows a positive slope between 2003 and 2007, followed by a temporary negative anomaly of several mm (coinciding with the 2007–2008 La Nina). Since mid-2008, the residual trend is lower than during 2003–2007 but still slightly positive. In addition to systematic errors of each observing system, the residual curve represents in principle the total (full depth) steric component.

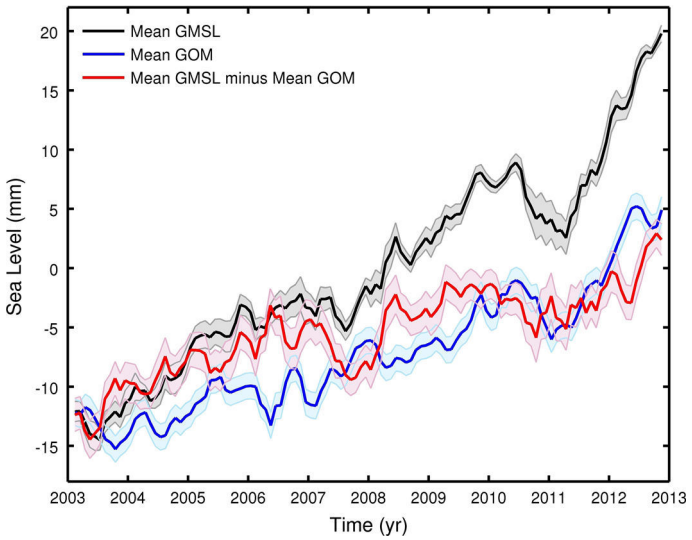

Fig. 2 Averaged GMSL, averaged global mean ocean mass (GOM) and difference time series (January 2003–December 2012)

3.2 Steric Sea Level Time Series: Comparison Between the 'GMSL Minus GOM' Residual Time Series and Steric Sea Level

3.2.1 Period P1 (2005–2012; Argo Time Series)

Figure 3 shows the four Argo steric time series over 2005–2012 for the 0–1,500 depth range. Uncertainties (available only for the KvS and Jamstec data sets) are also shown. Important discrepancies of several mm are noticed at interannual timescales between the four curves. As discussed in detail in Abraham et al. 2013 (see also Lyman and Johnson 2014; von Schuckmann and Le Traon 2011), these differences come from several factors, i.e., quality control, infilling gaps in data coverage, choice of the climatology, gridding process. So far no best processing method can be proposed, and we continue here with a mean Argo time series (as shown in Fig. 4), i.e., the average of the four time series shown in Fig. 3 (called 'mean steric' in the following) and its associated uncertainty (based on the dispersion of individual time series with respect to the mean). We then compare then 'mean steric' curve to the 'GMSL minus GOM' curve (Fig. 4). The mean steric curve displays significant interannual variability that roughly follows that of the 'GMSL minus GOM' curve. Superimposed on the interannual fluctuations, there is positive steric trend amounting to 0.29 ± 0.21 mm/year. Figure 4 also shows the residual 'GMSL minus GOM' minus mean steric curve (called 'residual' hereinafter; with a downward offset of 7.5 mm, for clarity). The residual curve reflects errors affecting all data sets (altimetry-based sea level, GRACE-based ocean mass, GIA, Argo data). It also includes the effect of gaps in Argo data coverage (e.g., in the Indonesian region) as well as a potential contribution from the deep ocean below 1,500 m. Interpretation of this residual curve is not straightforward. The early part of the record is characterized by year-to-year oscillations of about 2–4 mm (peak to peak) amplitude, followed by a strong negative anomaly late 2007. Then, from early 2008 to early 2012, the residual curve is rather flat.

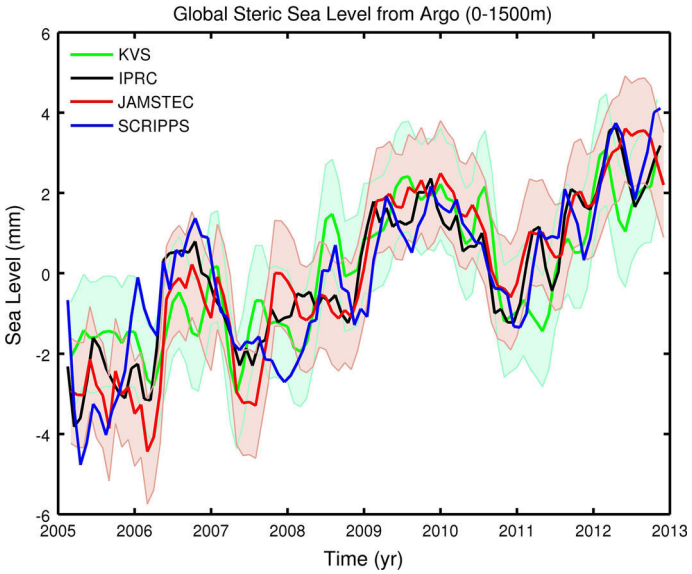

Fig. 3 Argo-based global mean steric sea level from four processing groups (KvS, IPRC, Jamstec and SCRIPPS; January 2005–December 2012)

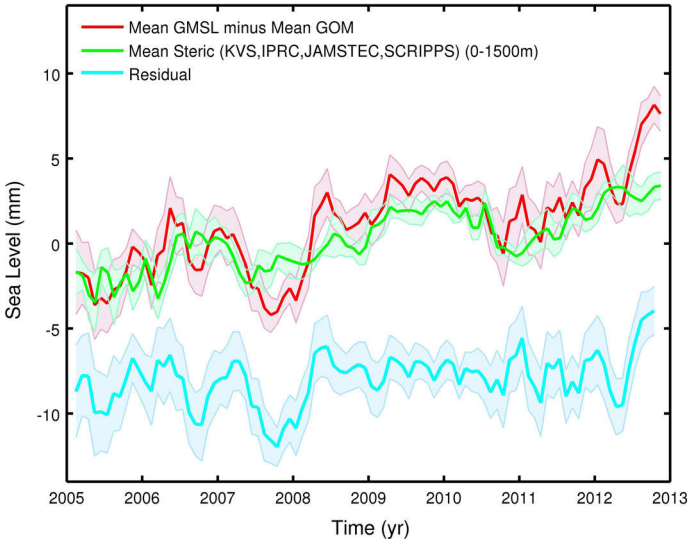

Fig. 4 Difference time series 'GMSL minus GOM' (based on the averaged curves), mean steric sea level (average of KvS, IPRC, Jamstec and SCRIPPS) and residual curve ('GMSL minus GOM' minus mean steric sea level, with downward offset of 7.5 mm for clarity; January 2005–December 2012)

After mid-2012, the 'GMSL minus GOM' curve increases abruptly, unlike the mean steric curve, causing a steep increase in the residual. Overall, what this residual shows is some step-like rise (around early 2008) preceded and followed by a plateau. Another step-like rise is suggested at the end of the period.

Table 1 gives the steric trends estimated over the P1 period for each Argo time series (integration down to 1,500 m) and mean steric trend. Trends of 'mean GMSL minus mean GOM' and residual time series over P1 are also given.

3.2.2 Period P2 (2003–2012; Other Steric Products)

Over the 2003–2005 time span, only the IK, Jamstec and EN4 data sets provide data over the 0–1,500 m depth range (however, we must keep in mind the limited raw data available below 700 m over this time span). So we present below the steric curves for the 0–700 and 0–1,500 m depth ranges separately.

Figure 5a shows the IK, Jamstec, NOAA and EN4 steric curves for the 0–700 m depth range, with associated uncertainties for IK, Jamstec and EN4. Very large errors affect the early part of the time span (2003–2005), and strong discrepancies are noticed between the four curves. These differences predominantly occur from data processing methodologies, in particular different gap filling methods. Moreover, prior to 2005—where the data source is mostly based on XBT measurements—differences in the XBT bias correction add to the discrepancies (see Lyman et al. 2010; Abraham et al. 2013; Lyman and Johnson 2014). Figure 5b shows the IK, Jamstec and EN4 steric curves for the 1,500 m depth range. Similar comments apply as for the 0–700 m depth range. In both cases, the EN4 curve is almost flat over the whole time span (its trend over 2003–2012 is 0.0 ± 0.14 and 0.15 ± 0.17 mm/year for 700 and 1,500 m integration depths, respectively). This is unlike the IK and Jamstec curves that display larger positive trends. Over P2, the IK trend amounts 0.39 ± 0.11 and 0.61 ± 0.16 mm/year down to 700 and 1,500 m, respectively, while the Jamstec trend amounts 0.65 ± 0.14 and 0.92 ± 0.17 mm/year for the same two integration depth. The behavior of the EN4 time series is puzzling and needs further investigation. However, we still consider this data set in our analysis.

Figure 6 shows the mean of IK, Jamstec, NOAA and EN4 for 0–700 m and mean of IK, Jamstec and EN4 for 0–1,500 m depth range (the NOAA data down to 1,500 m are available only as of 2005) for the 2003–2012 time span (P2 period). Interannual variability is very similar for the 700 and 1,500 m cases, as expected since it is essentially due to the upper ocean layers. The main difference between the two curves is a 0.24 mm/year short-term trend increase, from 700 to 1,500 m.

Steric trends estimated over P2 for each time series (0–700 and 0–1,500 m depth ranges) and means are given in Table 1. Trends of 'mean GMSL minus mean GOM' and residual time series over P2 are also given.

Figure 7 shows the 'GMSL minus GOM' curve and mean steric curve (average of IK, Jamstec and EN4) for the 0–1,500 m depth, as well as the residual curve ('GMSL minus GOM' minus mean steric curve; with a downward offset of 7.5 mm, for clarity). Over 2005–2012, the residual curve is very similar to that shown in Fig. 4 when using Argo data, with similar behavior though time. Over 2003–2012 (P2 period), the residual curve displays a positive trend of 0.55 ± 0.19 mm/year.

4 Mid-Ocean and Deep Ocean Contribution

Comparing the upper 700 and 1,500 m steric contributions and their evolution through time shows an interesting behavior. As expected, the 1,500 m steric contribution is larger than the 700 m steric one. But, more interestingly, the difference seems to increase linearly with time. This implies that more and more heat reaches the ocean below 700 m. This is

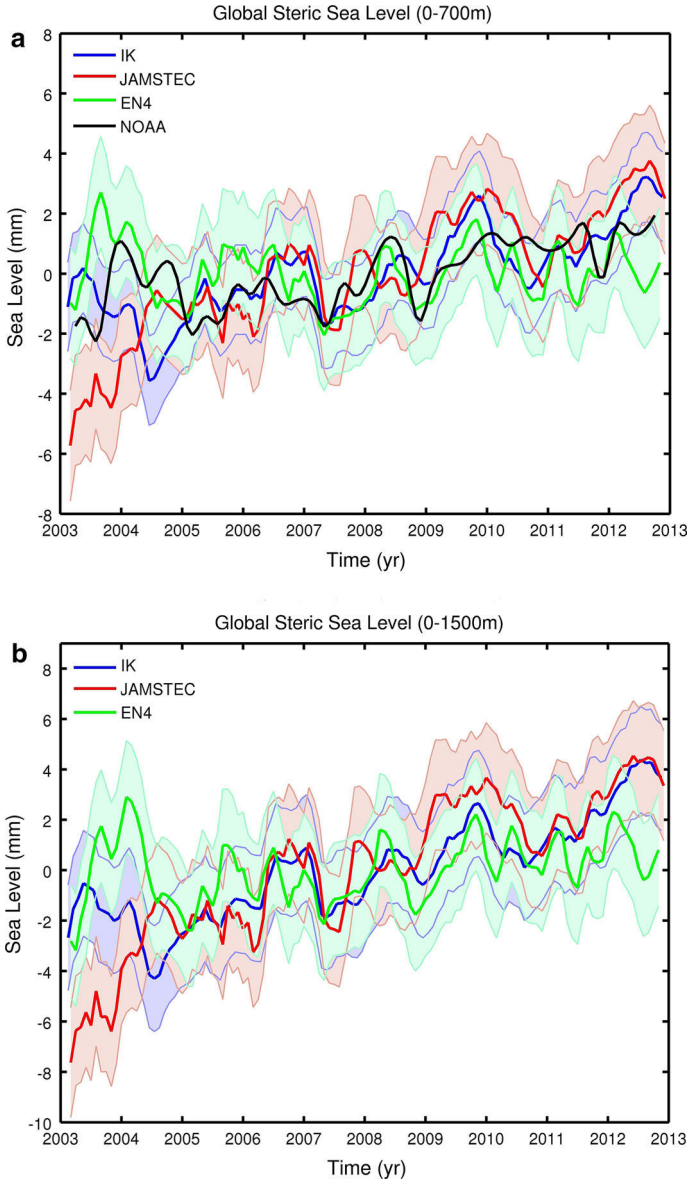

Fig. 5 **a** Global mean steric sea level time series (January 2003–December 2012; 0–700 m); data from IK, NOAA, Jamstec and EN4. **b** Global mean steric sea level time series (January 2003–December 2012; 0–1,500 m); data from IK, Jamstec and EN4

observed for all data sets, although not exactly with the same intensity (ranging from 0.15 to 0.27 mm/year). This is illustrated in Fig. 8, showing the evolution over 2005–2012 of the steric sea level for a few data sets (IPRC, Jamstec, and IK) as well as for their mean (the NOAA and EN4—not shown—show similar behavior). To highlight this time-increasing difference, the 700 and 1,500 m curves start from the same (arbitrary) value.

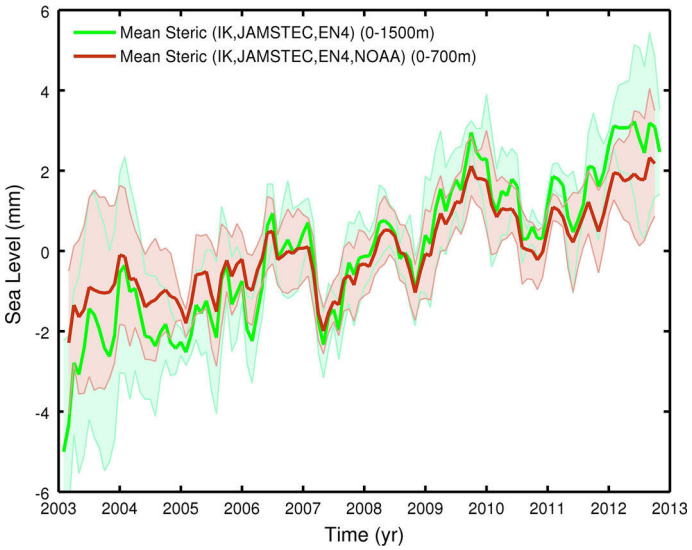

Fig. 6 Averaged steric sea level time series (January 2003–December 2012) for 0–700 m (average of IK, NOAA, Jamstec and EN4) and 0–1,500 m (average of IK, Jamstec and EN4)

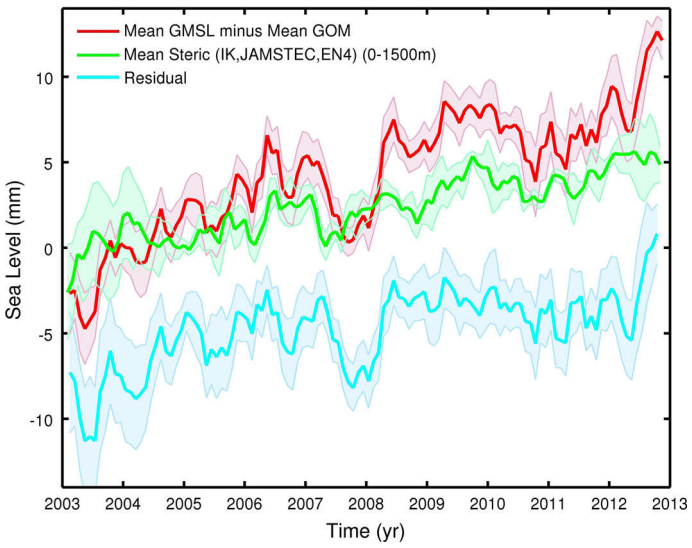

Fig. 7 Difference time series 'GMSL minus GOM' (based on the averaged curves), mean steric sea level for 0–1,500 m (average of IK, Jamstec and EN4) and residual curve ('GMSL minus GOM' minus mean steric sea level, with downward offset of 7.5 mm for clarity; January 2003–December 2012)

Figure 8 clearly shows that the layers below 700 m have gained heat over the last few years. This observation is in agreement with previous results from Levitus et al. (2012) based on the NOAA data set, and Balmaseda et al. (2013a) based on the ORAS4 reanalysis. The latter study showed an increasing warming trend below 700 m. However, it did not

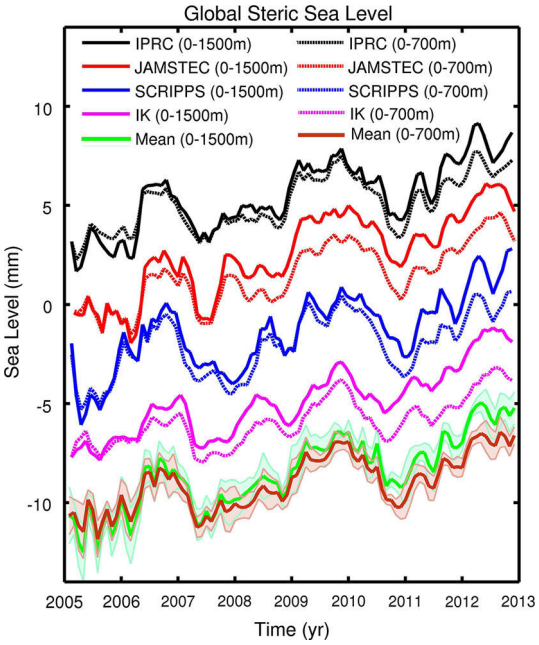

Fig. 8 Steric sea level curves for 0–700 and 0–1,500 m for IK, IPRC, Jamstec and SCRIPPS (January 2005–December 2012)

specify in which layers (likely, it is in the 700–1,500 m depth range; see discussion below). A similar behavior was found by Llovel et al. (2014) between 700 and 2,000 m with Argo data.

The residual curves shown in Figs. 4 and 7, i.e., the 'mean GMSL minus mean GOM' minus mean steric down to 1,500 m, reflect errors of all data sets plus missing contributions. For the latter, one candidate is the steric contribution from the deep ocean (below 1,500 m). Direct steric observations below 1,500 m are very sparse (e.g., Purkey and Johnson 2010; Kouketsu et al. 2011) and not available over the P1 and P2 time spans. However, we can use the ORAS4 reanalysis to compare the deep ocean contribution based on the residual "'GMSL minus GOM' minus steric down to 1,500 m" estimated from observations and the ORAS4 reanalysis (Fig. 9). The ORAS4 data set available to us ends in December 2009. So the comparison is performed over 2003–2009 only. Figure 9 superimposes the mean steric and ORAS4 for 0–1,500 m depth range (upper curves). Very good agreement is found between the two curves. The bottom curves of Fig. 9 correspond to the residual "'GMSL minus GOM' minus steric down to 1,500 m" and the ORAS4 steric contribution for the 1,500–6,000 m depth range. Over the 2003–2009 time span, the ORAS4 steric signal below 1,500 is very small, with a trend of <0.1 mm/year. This is unlike the residual curve "'GMSL minus GOM' minus steric down to 1,500 m" that displays important variability and a large positive trend of 0.55 ± 0.19 mm/year (over 2003–2012). The question whether this trend is significant or not is a difficult one. To the ~ 0.2 mm/year formal error, we must add systematic errors associated with each observing system. We can assume systematic errors of 0.4 mm/year for the GMSL (Ablain et al. 2009, 2014), 0.3 mm/year for GOM (Chambers and Bonin 2012) and 0.3 mm/year for the steric sea level. The latter estimate is likely an upper bound, since summing quadratically the total trend errors given for the steric data gives 0.28 mm/year. Therefore, the resulting (more realistic) error of the residual trend based on the quadratic sum of individual errors is

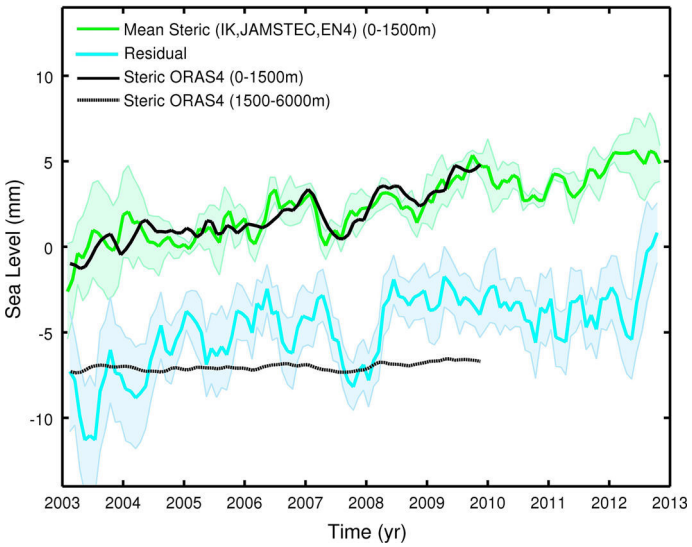

Fig. 9 *Upper curves* averaged steric sea level for 0–1,500 m (average of IK, Jamstec and EN4; January 2003–December 2012) with steric sea level (0–1,500 m) from ORAS4 superimposed. *Lower curves* residual curve ('GMSL minus GOM' minus mean steric sea level)—same as in Fig. 7—with the steric sea level (1,500–6,000 m) from ORAS4 superimposed

0.58 mm/year. So the residual trend (of 0.55 mm/year) is barely significant (the large negative anomalies seen in the residual curve prior to mid-2004 are suspect and likely due to data errors).

5 Discussion and Conclusions

In this study, we have considered 16 different data sets (5 for the GMSL, 3 for the ocean mass and 8 for the steric sea level) to compare the observed GMSL to the sum of components (ocean mass plus steric sea level) and tried to derive constraints on the deep ocean contribution through a sea level closure budget approach. This large number of different data sets would allow 120 different combinations to study the sea level budget. With such an approach, it would always be possible to find some combinations allowing closure of the sea level budget, or inversely leading to nonzero deep ocean contribution. Instead, we used averages of each type of data (GMSL, ocean mass, steric sea level) and estimated their dispersion range. This gives insight into the precision of the different estimates and provides an uncertainty range due to the variants in processing approaches developed by the different groups. On top of this, systematic errors of each observing system have also to be considered.

The main result of our study is that, for the limited time span considered here, the total uncertainty on the "'GMSL minus GOM' minus steric 0–1,500 m" is quite large (0.58 mm/year), preventing us from bringing a realistic constraint on the deep (below 1,500 m) ocean contribution (as previously noticed in von Schuckmann et al. 2014).

In addition, over both P1 (2005–2012) and P2 (2003–2012) periods, the residual curves (Figs. 4, 7) display important interannual variability that is totally unrealistic in the deep

ocean. Very likely, it reflects errors at interannual timescales in one of the components (GMSL, ocean mass or steric sea level) or in all of them. Previous studies (e.g., Cazenave et al. 2012; Masters et al. 2012; Henry et al. 2014; Ablain et al. 2014) showed that at interannual timescales, the (detrended) GMSL time series displays 2–4 mm differences from one data set to another. Thus, it is quite possible that the year-to-year fluctuations seen here in the residual curves are at least partly due to errors in the GMSL. Current efforts conducted in the context of the ESA Climate Change Initiative 'sea level' project already provide improved sea level data (Ablain et al. 2014), but assessment of this new product is still an ongoing work. Moreover, gaps in coverage in the steric data, in particular Argo data (e.g., in the Indonesian region), and the associated missing steric signal very likely impact the residual time series at interannual timescales.

The short-term trends displayed by the residual curves for both P1 and P2 periods are also very likely contaminated by uncertainties in interannual variability as well as by longer-term systematic errors. As shown in Cazenave et al. (2014), ENSO events cause temporary positive or negative sea level anomalies (mostly of mass origin, but also in the steric component) that significantly alter estimates of the rate of sea level rise. However, even if the short-term variability is removed, the trend estimated from the filtered residual curves (not shown) remain unrealistically large to be attributed to the deep ocean (>1,500 m) contribution. As shown in Fig. 9, the ORAS4 reanalysis estimates the 1,500–6,000 m steric trend to $\sim$0.1 mm/year. Such a magnitude is in line with estimates based on sparse, but direct observations. For example, Purkey and Johnson (2010) report a (non uniform) deep ocean contribution of the order of 0.1 mm/year for the 1990–2000 decade. For the same time span, Kouketsu et al. (2011) also find observational support for a deep ocean warming, but not larger than 0.1 mm/year (in steric sea level equivalent) for layers below 3,000 m. Such values agree well with the ORAS4 reanalysis (the ORAS4 steric sea level trend amounts to 0.17 mm/year for the 1993–2003 decade and 1,500–6,000 m depth range). Although it can be expected that more heat has reached the deep ocean since the early 2000s, the residual values reported here for the P1 and P2 periods appear anomalously large.

We suspect that gaps in steric data coverage, like in the Indonesian region, and the associated missing signal, contribute to the residual curves over the P1 and P2 periods. For example, in the oceanic region covering the China Sea, Indonesian region and north of Australia, satellite altimetry shows strong positive spatial trends over these two time spans (also observed over the whole altimetry era). As regional sea level trends are mainly of steric origin (e.g., Stammer et al. 2013), it is possible that the residual curves shown in Figs. 4 and 7 reflect at least partly the missing steric signal. To check this, we computed the altimetry-based sea level trend associated with the Indonesian region over the P1 and P2 periods and found that it contributes by $\sim$0.3 mm/year, hence about 10 % the total sea level trend. Since this region has been considered in the GMSL (as well as in the ocean mass; but a rough estimate indicates a very small mass contribution to the residual trend, less than 0.05 mm/year), but not is the steric data due to the gap in data coverage (since 2005 but also earlier), we conclude that the steric trend has been underestimated because of these missing data. To investigate this issue somewhat further, we computed the steric contribution of the Indonesian region (considering an area covering the Indonesian region, the Timor Sea plus the South China Sea; see Fig. 10) using the ORAS4 data. The steric contribution of this area to the residual trend is estimated to 0.29 and 0.31 mm/year over 2003–2009 and 2005–2009, respectively (after weighting by the ratio of the area to the total ocean surface between 66°S and 66°N). Assuming that the Indonesian steric trend remains more or less constant over the whole P1 and P2 periods and subtracting it (using a

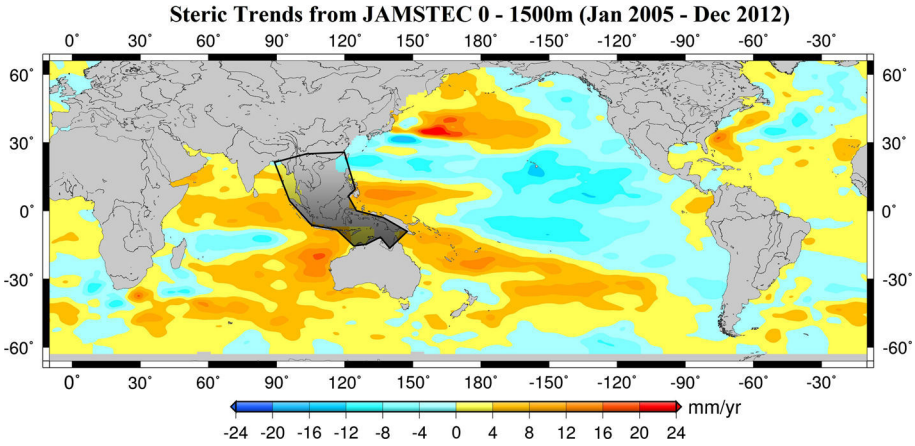

Fig. 10 Steric trend map based on Jamstec data over January 2005–December 2012 showing the Argo data gap in the Indonesian region and the contours (*black line*) of the area considered in this study to estimate—using the ORAS4 reanalysis—its contribution to the global mean steric trend

value of 0.3 mm/year) from the above estimated residual trends, we find new residual trends of $\sim$0 and 0.25 mm/year for P1 and P2, respectively. We consider such a range (0–0.25 mm/year) as an upper limit for the deep ocean contribution to recent years sea level rise.

The recently published study by Llovel et al. (2014) uses different data sets (Colorado University/CU altimetry and CSR GRACE data) for the GMSL and ocean mass. They also integrate Argo data down to 2,000 m (instead of 1,500 m in our study) and consider the January 2005–December 2013 time span. They come up with a residual trend (GMSL rise corrected for GRACE ocean mass and 0–2,000 m Argo steric trends) of -0.13 ± 0.72 mm/year. That their residual trend is lower than ours (amounting 0.29 mm/year over 2005–2012; see Table 1) is largely due to the fact that the CU GMSL trend over P1 is lower by $\sim$0.25 mm/year than the mean GMSL trend used in our study (see Table 1). The remaining difference (on the order of 0.15 mm/year) arises because of differences in the integration depth and study period. Llovel et al. (2014) further consider the upper value of the $\pm$0.72 mm/year uncertainty range to derive an upper bound for the GMSL rise due to deep ocean warming below 2,000 m. Doing this, they estimate at 0.59 mm/year the maximum contribution of the deep ocean warming for the period from 2005 to 2013. This is more than twice our estimate after correcting for the data gap effect. Clearly, more investigations are needed on this important issue.

Probably, the most reliable result of our study is the evidence of a continuing warming of the 700–1,500 m ocean layer. While reported earlier by Levitus et al. (2012) and von Schuckmann et al. (2014) using the NOAA and KvS steric data sets, respectively, Balmaseda et al. (2013a) using the ORAS4 reanalysis, as well as Llovel et al. (2014) using Argo data since 2005, here we observe a similar behavior for each of the eight steric data sets considered over the P1 and P2 periods, indicating that the result is most probably robust. Expressed in steric sea level equivalent, the trend contribution of the 700–1,500 m layer is on the order of 0.2 mm/year.

As discussed in the introduction, the favored candidate for explaining the current hiatus in global warming is deep ocean heat uptake. In the absence of direct deep ocean

temperature measurements, the sea level budget approach may in principle help to constrain the problem. But as shown here and in previous studies (e.g., Abraham et al. 2013; von Schuckmann et al. 2014), uncertainties due to data processing approaches and systematic errors of the different observing systems still prevent us from obtaining accurate enough results, even when using almost all available data sets—as done here, instead of just a selection of them. Besides, regional gaps in the steric coverage of the upper ocean, like in the Indonesian region, complicate the sea level budget approach.

Priority for future work is to improve the data processing of each observing system. Systematic intercomparisons of observational products (i.e., sea level, ocean mass and steric sea level—including ocean reanalyses) should be implemented in an international context in order to better understand the causes of the reported differences and define a best processing methodology (if possible). The following step should be a global reprocessing of all data sets, following the approach of the ESA Climate Change Initiative program. In parallel, implementation of new observing systems (e.g., deep Argo) should be a sustained goal of the scientific community and institutional organizations.

Priority in terms of observing systems is definitely the development of a deep Argo program and improved coverage of the upper ocean temperature and salinity measurements, as advocated in a number of recent articles (e.g., Abraham et al. 2013).

Acknowledgments We thank Don Chambers and two anonymous referees for their constructive reviews. We also thank William Llovel for interesting discussions about our respective studies. H.B.D. PhD is funded by the European Space Agency in the context of the Climate Change Initiative Sea Level Project. H.P. is supported by a joint CNES-CLS PhD grant.

References

Ablain M, Cazenave A, Valladeau G, Guinehut S (2009) A new assessment of the error budget of global mean sea level rate estimated by satellite altimetry over 1993–2008. Ocean Sci 5(2):193–201

Ablain M et al (2014) Improved Sea Level record over the satellite altimetry era 1 (1993–2010) from the Climate Change Initiative project. *Ocean Sci* (in press)

Abraham JP et al (2013) A review of global ocean temperature observations: implications for ocean heat content estimates and climate change. Rev Geophys 51:450 2013RG000432

Balmaseda MA, Trenberth K, Kallen E (2013a) Distinctive climate signals in reanalysis of global ocean heat content. Geophys Res Lett 40:1–6. doi:10.1002/grl.50382

Balmaseda MA, Mogensen K, Weaver A (2013b) Evaluation of the ECMWF ocean reanalysis ORAS4. Q J R Meteorol Soc. doi:10.1002/qj.2063

Bindoff N, Willebrand J, Artale V, Cazenave A, Gregory J, Gulev S, Hanawa K, Le Quéré C, Levitus S, Nojiri Y, Shum CK, Talley L, Unnikrishnan A (2007) Observations: oceanic climate and sea level. In: Solomon S, Qin D, Manning M, Chen Z, Marquis M, Averyt KB, Tignor M, Miller HL (eds) Climate change 2007: the physical science basis. Contribution of Working Group I to the fourth assessment report of the intergovernmental panel on climate change. Cambridge University Press, Cambridge and New York

Boening C, Willis JK, Landerer FW, Nerem RS (2012) The 2011 La Nina: so strong, the oceans fell. Geophys Res Lett 39:L19602. doi:10.1029/2012GL053055

Cazenave A, Henry O, Munier S, Meyssignac B, Delcroix T, Llovel W, Palanisamy H, Becker M (2012) ENSO influence on the global mean sea level over 1993–2010. Mar Geod 35(S1):82–97

Cazenave A, Dieng H, Meyssignac B, von Schuckmann K, Decharme B, Berthier E (2014) The rate of sea level rise. Nat Clim Change. doi:10.1038/NCLIMATE2159

Chambers DP, Bonin JA (2012) Evaluation of Release-05 GRACE time variable gravity coefficients over the ocean. Ocean Sci 8:859–868. doi:10.5194/os-8-859-2012
Chambers DP, Schroeter J (2011) Measuring ocean mass variations from satellite gravimetry. J Geodyn 52:333–343
Chambers DP, Wahr J, Tamisiea ME, Nerem RS (2010) Ocean mass from GRACE and glacial isostatic adjustment. J Geophys Res 115:B11415. doi:10.1029/2010JB007530
Chen X, Tung K-K (2014) Varying planetary heat sink led to global warming slowdown and acceleration. Science 345:897–903
Chen JL, Wilson CR, Tapley BD (2013) Contribution of ice sheet and mountain glacier melt to recent sea level rise. Nat Geosci 6:549–552
Church JA, Clark PU, Cazenave A, Gregory JM, Jevrejeva S, Levermann A, Merrifield MA, Milne GA, Nerem RS, Nunn PD, Payne AJ, Pfeffer WT, Stammer D, Unnikrishnan AS (2013) Sea Level Change. In: Stocker TF, Qin D, Plattner G-K, Tignor M, Allen SK, Boschung J, Nauels A, Xia Y, Bex V, Midgley PM (eds) Climate change 2013: the physical science basis. Contribution of Working Group I to the fifth assessment report of the intergovernmental panel on climate change. Cambridge University Press, Cambridge and New York
England MH et al (2014) Recent intensification of wind-driven circulation in the pacific and the ongoing warming hiatus. Nat Clim Change 4:222–227
Fasullo JT, Boening C, Landerer FW, Nerem RS (2013) Australia's unique influence on global mean sea level in 2010–2011. Geophys Res Lett 40(16):4368–4373. doi:10.1002/grl.50834
Goddard L (2014) Heat hide and seek. Nat Clim Change 4:158161
Good SA, Martin MJ, Rayner NA (2013) EN4: quality controlled ocean temperature and salinity profiles and monthly objective analyses with uncertainty estimates. J Geophys Res Oceans 118:6704–6716. doi:10.1002/2013JC009067
Guemas V, Doblas-Reyes FJ, Andreu-Burillo I, Asif M (2013) Retrospective prediction of global warming slowdown in the past decade. Nat Clim Change 3:649–653
Hansen J, Sato M, Kharecha P, von Schuckmann K (2011) Earth's energy imbalance and implications. Atmos Chem Phys 11:13421–13449. doi:10.5194/acp-11-13421-2011
Held IM (2013) The cause of the pause. Nature 501:318–319
Henry O, Ablain M, Meyssignac B, Cazenave A, Masters D, Nerem S, Leuliette E, Garric G (2014) Investigating and reducing differences between the satellite altimetry-based global mean sea level time series provided by different processing groups. J Geod 88:351–361. doi:10.1007/s00190-013-0687-3
Ishii M, Kimoto M (2009) Reevaluation of historical ocean heat content variations with time-varying XBT and MBT depth bias corrections. J Oceanogr 65(3):287–299. doi:10.1007/s10872-009-0027-7
Johnson GC, Chambers DP (2013) Ocean bottom pressure seasonal cycles and decadal trends from GRACE Release-05: ocean circulation implications. J Geophys Res Oceans 118:4228–4240. doi:10.1002/jgrc.20307
Kosaka Y, Xie S-P (2013) Recent global warming hiatus tied to equatorial Pacific surface cooling. Nature 501:403–407
Kouketsu S et al (2011) Deep ocean heat content changes estimated from observation and reanalysis product and their influence on sea level change. J Geophys Res 116:C03012
Leuliette EW, Willis JK (2011) Balancing the sea level budget. Oceanography 24:122–129
Levitus S et al (2009) Global ocean heat content 1955–2008 in light of recently revealed instrumentation problems. Geophys Res Lett 36:L07608. doi:10.1029/2008GL037155
Levitus S, Antonov JI, Boyer TP, Baranova OK, Garcia HE, Locarnini RA, Mishonov AV, Reagan JR, Seidov D, Yarosh ES, Zweng MM (2012) World ocean heat content and thermosteric sea level change (0–2000 m), 1955–2010. Geophys Res Lett 39:L10603. doi:10.1019/2012GL051106
Llovel W, Willis JK, Landerer FW, Fukumori I (2014) Deep-ocean contribution to sea level and energy budget not detectable over the past decade. Nat Clim Change. doi:10.1038/NCLIMATE2387
Lyman JM, Johnson GC (2014) Estimating global ocean heat content changes in the upper 1800 m since 1950 and the influence of climatology choice. J Clim. doi:10.1175/JCLIM-D-12-00752.1
Lyman JM, Godd SA, Gouretski VV, Ishii M, Johnson GC, Palmer MD, Smith DM, Willis JK (2010) Robust warming of the global upper ocean. Nature 465:334–337. doi:10.1038/nature09043
Masters D, Nerem RS, Choe C, Leuliette E, Beckley B, White N, Ablain M (2012) Comparison of global mean sea level time series from TOPEX/Poseidon, Jason-1, and Jason-2. Mar Geod 35:20–41
Peltier WR (2004) Global glacial isostasy and the surface of the ice-age Earth: the ICE-5G (VM2) model and GRACE. Annu Rev Earth Planet Sci 32:111–149
Peters GP, Marland G, Le Queré C, Boden T, Canadell JG, Raupach MR (2012) Rapid growth in CO2 emissions after the 2008–2009 global financial crisis. Nat Clim Change 2:2–4

Purkey S, Johnson GC (2010) Warming of global abyssal and deep southern ocean waters between the 1990s and 2000s: contributions to global heat and sea level rise budget. J Clim 23:6336–6351

Shepherd A et al (2012) A reconciled estimate of ice sheet mass balance. Science 338(6111):1183–1189. doi:10.1126/science.1228102

Smith D (2013) Has global warming stalled? Nat Clim Change 3:618–6919

Solomon S, Rosenlof K, Portmann R, Daniel J, Davis S, Sanford T, Plattner G-K (2010) Contributions of stratospheric water vapour to decadal changes in the rate of global warming. Science. doi:10.1126/science.1182488

Stammer D, Cazenave A, Ponte RM, Tamisiea ME (2013) Causes for contemporary regional sea level changes. Annu Rev Mar Sci 5:21–46. doi:10.1146/annurev-marine-121211-172406

Trenberth KE, Fasullo JT (2010) Tracking Earth's energy. Science 328:316–317

Trenberth KE, Fasullo JT (2013) An apparent hiatus in global warming? Earth's Future. doi:10.102/2013EF000165

Trenberth KE, Fasullo JT, Balmaseda MA (2014) Earth's energy imbalance. J Clim 27:3129–3144. doi:10.1175/JCLI-D-13-00294.1

Von Schuckmann K, Le Traon PY (2011) How well can we derive Global Ocean Indicators from Argo data? Ocean Sci 7(6):783–791. doi:10.5194/os-7-783-2011

Von Schuckmann K, Sallée JB, Chambers D, Le Traon PY, Cabanes C, Gaillard C, Speich S, Hamon M (2014) Consistency of the current global ocean observing systems from an Argo perspective. Ocean Sci 10:547–557. doi:10.5194/os-10-547-2014

Wahr J, Swenson S, Velicogna I (2006) Accuracy of GRACE mass estimates. Geophys Res Lett 33:L06401. doi:10.1029/2005GL025305

Watanabe M, Kamae Y, Yoshimori M, Oka A, Sato M, Ishii M, Mochizuki T, Kimoto M (2013) Strengthening of ocean heat uptake efficiency associated with the recent climate hiatus. Geophys Res Lett 40:3175–3179. doi:10.1002/grl.50541

Woppelmann G, Letetrel C, Santamaria A, Bouin MN, Collilieux X, Altamimi Z, Williams SDP, Miguez BM (2009) Rates of sea-level change over the past century in a geocentric reference frame. Geophys Res Lett. doi:10.1029/2009gl038720

2.2.1 Future needs

In our study, we have shown how the sea level budget can help constraint the problem of sparse temperature measurements to estimate the deep ocean contribution. However, uncertainties due to data processing approaches and systematic errors of different observing systems still prevent us from obtaining accurate results (*Dieng et al.*, 2015a, *Von Schuckmann et al.*, 2014, *Abraham et al*, 2013). Besides we have also shown that incomplete steric data coverage of the upper ocean such as in the Indonesian region further complicates the sea level budget approach.

Of late, studies have worked on investigating the sources causing differences in observational climate variables (GMSL in specific) that are processed by different institutions. For example, Masters et al., (2012) investigated the effects of different GMSL computation methodologies and different geophysical corrections applied to satellite altimetry data by five different groups (Colorado University, AVISO, National Oceanic and Atmospheric Administration-NOAA, National Aeronautics and Space Agency-NASA, Commonwealth Scientific and Industrial Research Organization-CSIRO). This study suggested that the main source of difference is caused by the choice of averaging method used to estimate GMSL from along-track SSH data. Following this, Henry et al., (2014) attempted to identify the main cause of difference found in the short-term (<10 years) GMSL trends based on altimetry data from AVISO and CU processing groups over Jason-1 operating period (2002–2009) by considering an ocean circulation model as reference and studying the impacts of averaging methods, bathymetry and grid resolution. In agreement with Master et al., (2012), they also showed that the essential trend difference arises from the averaging methods adopted by the groups. In a very recent study, by studying the role of data errors in the closure of global mean sea level budget over 2005-2013, *Dieng et al.*, 2015b have shown that the main source of trend uncertainty comes from the altimetry-based sea level data processing; while at sub-seasonal to multi-annual time scales, the main source of uncertainty comes from short-terms errors in GRACE and Argo data.

All these studies imply that there is a prior need to improve data processing methodologies of each observational products followed by systematic comparisons between various teams. This has to be implemented in an international context in order to understand the

causes for the differences and to define a best methodology. One such attempt has already been made by ESA. Since 2010, ESA has developed a new program, the Climate Change Initiative (CCI), dedicated to reprocessing a set of 13 essential Climate Variables (ECVs) currently observed from space; among them, the satellite altimetry-based sea level being one of the main ECVs. The objective of the CCI sea level project is to produce a consistent and precise sea level record covering the past two decades, based on the reprocessing of all satellite altimetry data available from all missions. In the framework of this project, a new validation protocol has been brought into use in order to develop new altimeter corrections and algorithms that can be applied for precise sea level calculation (*Ablain et al.*, 2015). This protocol focusses on three main objectives: (1) global internal analyses with the aim of checking the internal consistency of a specific mission-related altimetry system by analyzing the computed sea level, its instrumental parameters (from altimeter and radiometer) and associated geophysical corrections, (2) global multi mission comparisons in order to evaluate the coherence between two different altimetry missions and (3) altimetry in-situ data comparison dedicated to the computation of sea level differences between altimetry data and in-situ sea level measurements such as tide gauges, Argo steric etc. as in *Valladeau et al.*, (2012). As a result, the newly developed CCI sea level products exhibit improvements at different levels of importance for climate studies. In fact, *Dieng et al.,* (2015b) have shown that the observed altimetry based GMSL from the CCI program shows less GMSL short term errors when compared to other data sets. Therefore, such international programs if implemented for steric and ocean mass components also can largely help in minimizing their uncertainties.

Furthermore, as mentioned in our study and in various recent studies, there is a need for deep Argo and improved coverage of upper ocean temperature and salinity measurements. For example, *Durack et al.*, (2014a) have shown that there has been an underestimation of the long-term upper ocean warming due to poor sampling of the Southern Hemisphere. The need for improved coverage is not only essential for ocean observational variables but also for other variables such as surface temperature. In fact, very recently, using an updated global surface temperature analysis, *Karl et al.*, (2015) have shown that the global surface temperature trend in the recent decade is higher and suggest that the global warming hiatus is an artifact due biases in temperature observation networks.

Therefore, scientific community and institutional organizations should consider all these factors as high priority for better understanding of climate change.

Chapter 3

Regional sea level variability and total relative sea level change

In the previous chapters we have discussed sea level variations at global scale, their causes and the various missions/ instruments that help in the continuous sea level monitoring. Though sea level has been rising at a rate of 1.6-1.8 mm/yr over the twentieth century (*Jevrejeva et al.*, 2008, *Wöppelmann et al.*, 2009, *Church and White*, 2011) and at a rate of 3.2 mm/yr since the altimetry era (*Nerem et al.*, 2010), this rate is far from being spatially uniform (*Stammer et al.*, 2013, *Church et al.*, 2013, *Cazenave and Cozannet*, 2014). Prior to the altimetry era, tide gauge records at various locations suggested the non-uniform sea level variations (*Douglas*, 2001). Since the altimetry era, the quasi global coverage of the satellite altimeters enables us to study the regional sea level variability precisely. Fig.3.1 displays the altimetry-based sea level spatial trend patterns between 1993 and 2013 after having removed the uniform global mean trend of 3.2 mm/yr. We can observe that in certain regions such as the western and northern Pacific, south of Greenland in the Atlantic Ocean and southern Indian Ocean and the southern Austral Ocean, sea level rates reach up to three times the global mean rate. There are also regions such as the eastern Pacific Ocean that face sea level rates lower than the global mean rate. In fact, the regional sea level variability superimposes on the GMSL thereby either reducing or amplifying the regional sea level rate. This implies that different parts of the world face different range of sea level risks (*Palanisamy et al.*, 2015b). Therefore it becomes highly essential to understand the regional sea level variability and its driving forces. In this chapter, first we discuss the various causes of regional sea level variability and then move on to the estimate of

long term (i.e. over 50-60 years) sea level rates and coastal impacts at three main vulnerable zones.

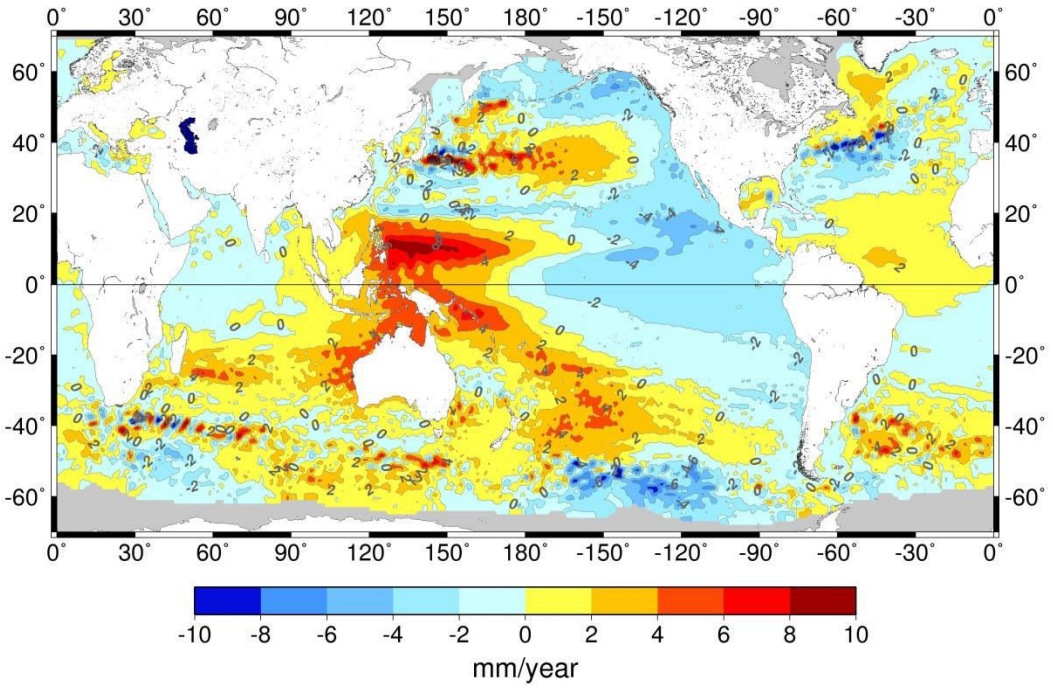

Figure 3.1: Satellite altimetry based sea level spatial trend pattern over 1993-2013 (uniform global mean trend of 3.2 mm/yr removed)

3.1 Regional sea level trend variability: Causes

The complexity and non-uniformity of the regional sea level trend variability is mainly driven by ocean dynamic processes due to thermal expansion/contraction, salinity changes and fresh water influx induced ocean mass and circulation changes. Quasi-static effects such as Earth's response to present and past ice mass loss and other coastal processes also play a secondary role at a regional scale and at various time scales. In this section, we briefly discuss the various causes that contribute to the regional sea level variability.

3.1.1 Climate related regional sea level variability

1) Thermal expansion and salinity changes

The ocean thermal expansion and salinity changes not only have an impact on the GMSL change but also on regional variability. The main contribution to regional sea level variability results from the changes in the density structure of the ocean due to non-uniform thermal expansion (thermosteric) and salinity changes (halosteric, *Bindoff et al.*, 2007). Studies using in-situ hydrographic measures (*Ishii and Kimoto*, 2009, *Levitus et al.*, 2009, *Levitus et al.*, 2012, *Lombard et al.*, 2005) and ocean circulation models (*Carton and Giese*, 2008, *Köhl and Stammer*, 2008) have shown that the regional sea level trends during the altimetry era mostly result from non-uniform thermal expansion of the ocean. Salinity changes also play a non-negligible role in the regional sea level evolution such as in the North Atlantic and Arctic Ocean as they can either enhance or compensate for the thermosteric changes (*Wunsch et al.*, 2007, *Landerer et al.*, 2007, *Köhl and Stammer*, 2008, *Durack and Wijffels*, 2010, *Stammer et al.*, 2013, *Durack et al.*, 2014). This compensation can amount to 25% of the thermosteric contribution (*Wunsch et al.*, 2007). While model simulations (*Lowe and Gregory*, 2006, *Pardaens et al.*, 2011) have suggested that the halosteric changes can dominate sea level change in the Arctic Ocean, recent observation studies (eg. *Morison et al.*, 2012) suggest that this might already be the case.

Fig.3.2a displays an updated version, V6.13, of Ishii and Kimoto, 2009 based steric (thermosteric plus halosteric) sea level spatial trend patterns over the altimetry period of 1992-2013. The steric sea level anomaly was calculated between the depth of 0 to 700 m and the uniform global mean steric sea level trend of mm/yr has been removed. Comparing Fig.3.2a with Fig.3.1, we can see that the observed altimetry based and steric regional sea level trends agree very well both in amplitude and regional location. Fig.3.2b displays the map of sea level trend difference between the altimetry based seal level signal (as in Fig.3.1) and steric sea level signal. The range of difference is relatively smaller (value) when compared to the actual range of the altimetry and steric sea level signals (in the order of 10 mm/yr). This indicates that the upper ocean (0-700 m) steric variations dominate the regional sea level variability during the altimetry era. The residual (altimetry-steric) signal can also give us an idea on the contribution of deep

ocean (>700 m) heat content and ocean mass variations. Over longer time period (i.e. since mid-1950s), by making use of observational ocean temperature data, *Lombard et al.*, (2005), has shown that the regional thermosteric sea level trends are not only non- uniform but they also fluctuate in both time and space in response to internal climate modes like ENSO, Interdecadal Pacific Oscillation (IPO)/ Pacific Decadal Oscillation (PDO) etc. This indicates that the non-uniform regional sea level trends also fluctuate in space and time.

Regional steric sea level changes in different ocean basins are attributed to differential heating and freshening of various ocean layers and associated physical processes such as air-sea interaction, lateral and vertical mixing or advective processes (*Yin et al.*, 2010) with ocean circulation changes playing a major role (*Stammer et al.*, 2013). *Fukumori and Wang*, (2013) showed that the internal re distribution of pre-existing heat and salt anomalies accounts for most of the regional sea level trends in regions of strong currents except in the western tropical Pacific where external sources dominate the sea level. This is in agreement with studies (*Merrifield*, 2011, *Merrifield and Maltrud*, 2011, *Palanisamy et al.*, 2015b) that showed that the high sea level trends in this region during the altimetry era are related to the deepening of the thermocline in response to intensified trade winds.

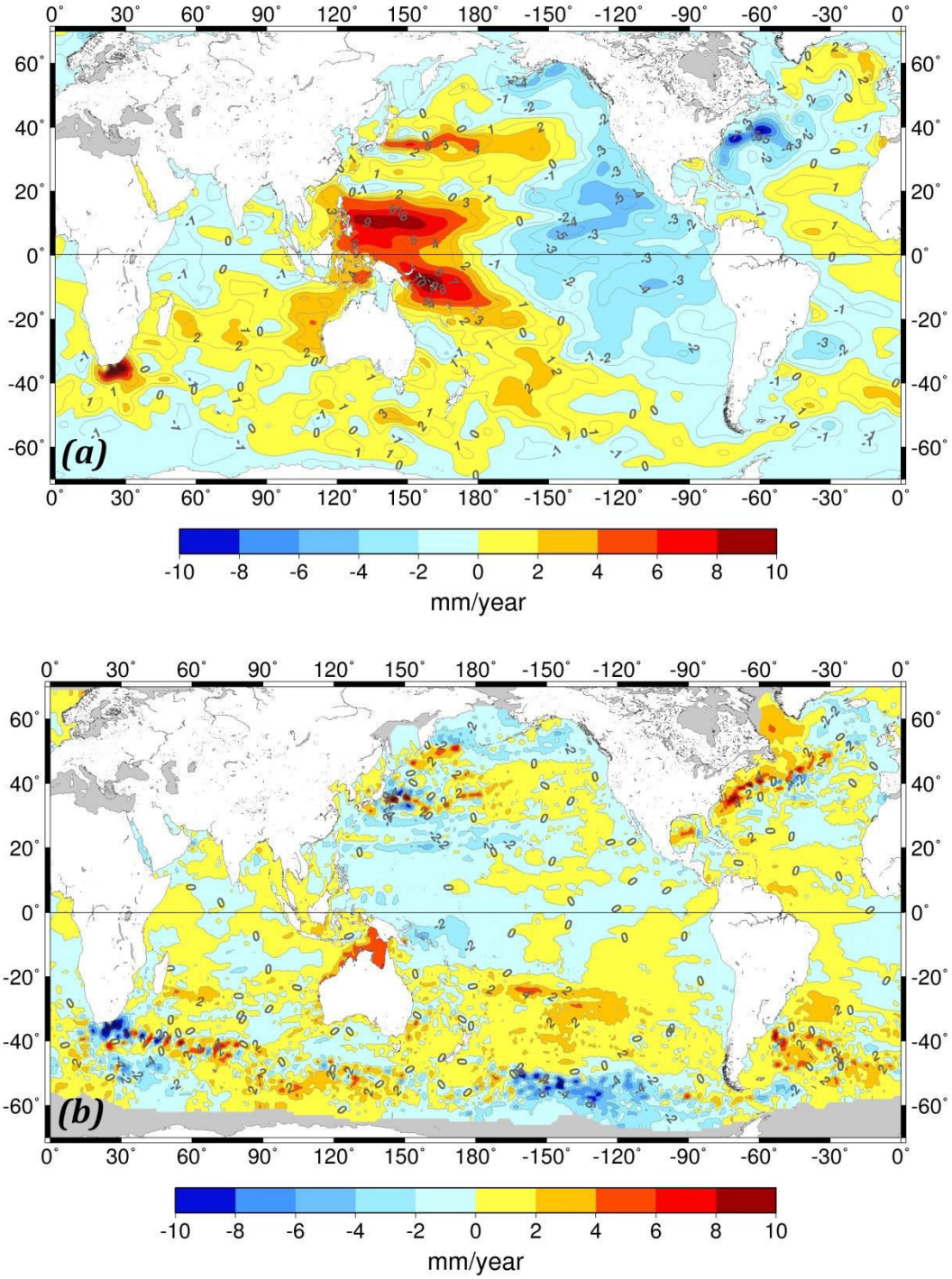

Figure 3.2: (a) Ishii and Kimoto, 2009 steric sea level spatial trend pattern (uniform global mean trend removed), (b) difference between altimetry-based and steric sea level trend patterns over 1993-2013.

2) Ocean mass changes

Changes in ocean mass due to present day continental ice melt and land water exchanges also play a role in the regional sea level trend variability. Unlike steric changes that fluctuate on relatively small spatial scales, ocean mass varies on large, slow, basin-wide scales (*Johnson and Chambers*, 2013). The fresh water input from continents change the density structure of the ocean water column at a localized scale (i.e. at the entry point to the ocean) thereby modifying the ocean circulation. As a result, there is a regional dynamic sea level adjustment occurring at interannual and multi decadal time scales (*Stammer*, 2008, *Stammer et al.*, 2011, *Okumura et al.*, 2009). However, any addition in ocean mass from changes in freshwater storage between ocean and land will redistribute uniformly throughout the global oceans within days (*Lorbacher et al.*, 2012). Apart from the dynamic effect of land ice loss, it can also cause a quasi-static effect on regional sea level variability (see Section 3.1.2).

Regional ocean mass changes can be estimated following the sea level budget by removing the steric sea level (including deep ocean) contribution from altimetry based sea level signal. Regional ocean mass addition can also be estimated directly using GRACE measures. However low signal to noise ratio of GRACE over the ocean can hinder accurate estimation of regional ocean mass variations. Recently by making use of both the sea level budget and GRACE estimates, *Purkey et al.*, (2014) compared the global and regional ocean mass trends. They showed that both the methods capture similar large scale mass variation patterns with higher rates of mass addition in the North Pacific, South Atlantic and Indo-Atlantic sector of the Southern Ocean. Lower mass addition trends were observed in the Indian, North Atlantic, South Pacific and the Pacific sector of the Southern Ocean.

3.1.2 Non climatic causes for regional sea level variability

Continental water mass redistribution due to present day and past land ice loss causes a quasi-static effect on regional sea level variability (*Milne et al.*, 2009, *Tamisiea and Mitrovica*, 2011, *Stammer et al.*, 2013). This is because the melted water from the present and past does not get redistributed uniformly over the oceans. This is a result of several processes such as self-gravitation between ice and water masses, gravity change and solid Earth's deformation due to elastic/visco-elastic response, changes in Earth's rotation due to water mass redistribution

(*Peltier*, 2004, 2009, *Chambers et al.*, 2010, *Tamisiea et al.*, 2010, *Spada et al.*, 2013, *Cazenave and Cozannet*, 2014). While the present day ice melt produces an elastic response of the Earth, the last deglaciation that started approximately 20,000 years ago produces a visco-elastic response (GIA) of the Earth. Even though the impact due to present day and past ice melt is broad-scale, their regional fingerprint is different depending on the melting source (i.e. Greenland, Antarctica, glaciers or last glaciation ice sheets, (*Mitrovica et al.*, 2001, *Lambeck et al.*, 2010, *Riva et al.*, 2010, *Cazenave and Cozannet*, 2014). Fig.3.3a and Fig.3.3b display the numerical prediction (ICE5G-VM, *Peltier et al.*, 2009) of the present-day impact of GIA on relative sea level as measured by tide gauges and altimetry respectively. From Fig.3.3a, we can observe that near the loading centers such as northern Europe and northern American continents, relative sea level is falling due to continued uplift of the crust. Surrounding these loading centers, the crust is subsiding thereby causing an increase in the relative sea level. The relative sea level as measured by altimetry due to GIA (Fig.3.3b) is much smoother than that measured by tide gauges.

It is to be noted that the regional sea level variability due to present day land ice loss is still negligible and difficult to detect in altimetry based observations (*Kopp et al.*, 2010, *Meyssignac and Cazenave*, 2012). However with the accelerating rate of land ice loss, it is expected that this will become a major contributor in the future (*Slangen et al.*, 2011).

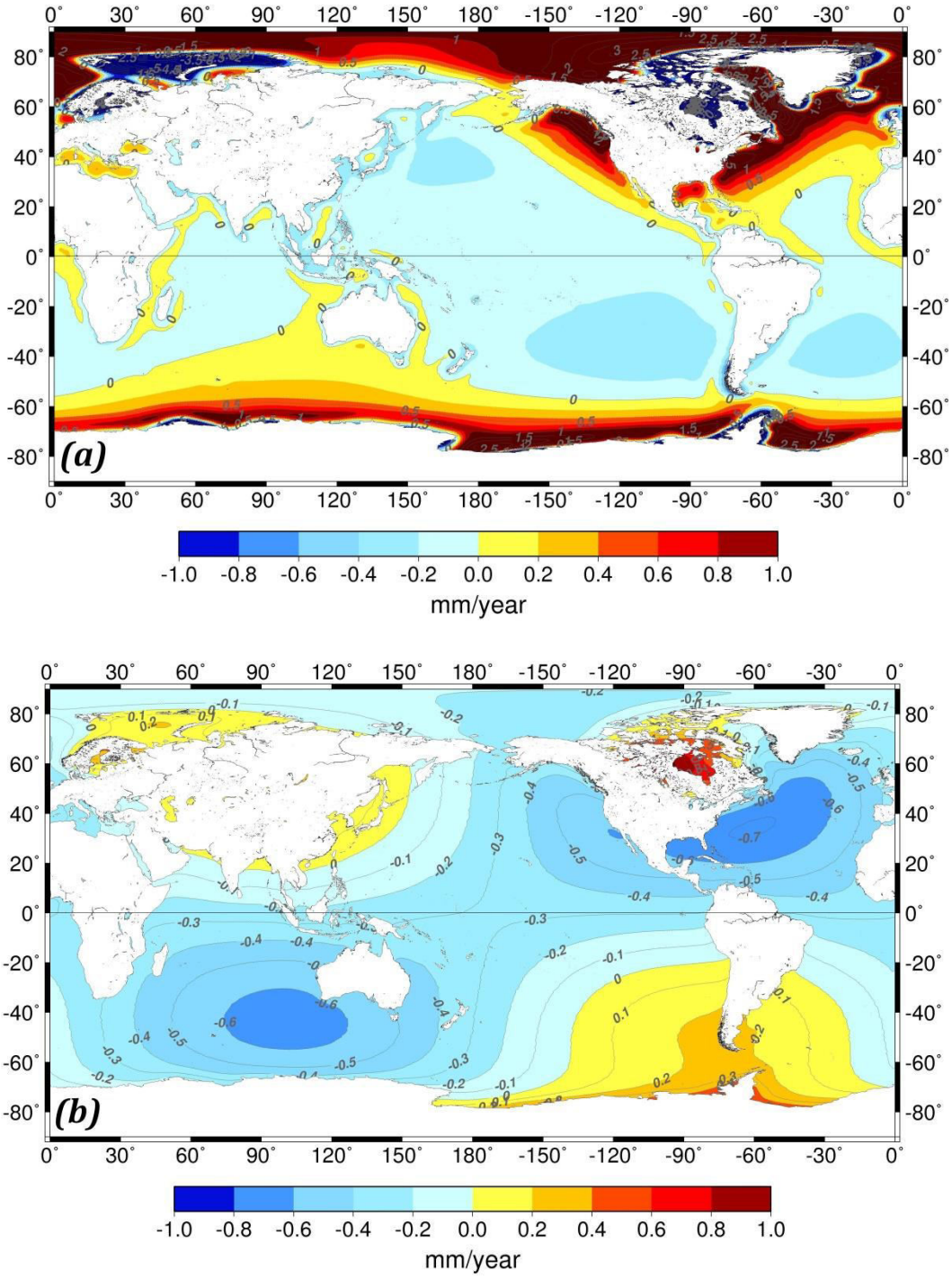

Figure 3.3: ICE5G-VM model based GIA contribution to relative sea level as measured by (a) tide gauges, (b) satellite altimetry

3.1.3 Vertical Land Motions

There are other coastal and tectonic processes that result in vertical land motion (VLM) that can cause highly localized sea level changes. VLM is either an uplift or subsidence of the ground due to natural (such as GIA, sediment loading, tectonic and volcanic activities) or anthropogenic (such as ground water pumping, oil/gas extraction, mining etc.) causes and produces sea level variations relative to the ground(*Ballu et al.*, 2011, *Wöppelmann and Marcos*, 2012). These localized phenomena may either reduce or amplify the climate related sea level variations. For example, ground subsidence in the Mississippi delta due to Holocene sediment compaction (*Törnqvist et al.*, 2008) and oil/gas mining (*Morton et al.*, 2006) has resulted in ground subsidence along the Gulf Coast of the United States in the range of 5-10 mm/yr (*Ericson et al.*, 2006). Similarly, ground subsidence due to groundwater withdrawal from deltaic regions has resulted in subsidence of megacities such as Tokyo by 5m, Shanghai and Bangkok by 3 m and 2 m respectively (*Nicholls*, 2010, *Stammer et al.*, 2013). All these imply the importance of understanding the role of vertical land motion in the estimation of local relative sea level change.

3.2 Long term regional sea level variability, total relative sea level change and coastal impacts

Sea level rise due to human induced global warming has been seen as a major threat to low-lying coastal and island regions. The immediate effect of sea level rise is the submergence and increased flooding of coastal land as well as salt water intrusion into surface waters. Longer term impacts of sea level rise include wetland loss, changes in response to higher water tables and increasing salinity, erosion of beaches, salt water intrusion into groundwater etc. (*Nicholls et al.*, 2007, 2010, 2011, *Nicholls and Cazenave*, 2010). These longer term impacts can further interact with immediate effects of sea level rise and exacerbate them. For example, erosion of sedimentary features will result in the degradation or disappearance of natural protection such as mangroves, salt marshes etc. This will increase the vulnerability of such regions to coastal flooding (*Nicholls*, 2011). There is also increasing concern about higher extreme sea levels due to more intense storms superimposed on these mean rises, especially for areas affected by tropical storms (*Meehl et al.*, 2007). These possible storms would exacerbate the impacts of sea level rise, particularly the risk of more damaging floods and storms (*Nicholls*, 2011). Sea level

rise also has an impact on the socio-economic development of a region. For example, flooding can cause serious damages to coastal infrastructures, agricultural properties etc. Therefore estimating the impact of sea level rise at localized scale is as important as understanding its causes.

As a part of the French ANR project CECILE, in my Ph.D., we focused on understanding the long-term (over 5 decades between 1950-2009) regional sea level variability and estimating the total relative sea level rate (i.e. sea level change relative to the coast) at three of the main vulnerable coastal and island regions: Indian Ocean, Caribbean and South China Sea, as identified by *Nicholls and Cazenave*, (2010).

A multidisciplinary approach as in *Becker et al.*, (2012) used for the tropical Pacific was also used in these studies to estimate the total relative sea level change. The total relative sea level change is estimated as the sum of 2 main components: (1) the climate-related component i.e. global mean sea level plus the regional variability and (2) local vertical land motions (VLM, including natural components such as the GIA, tectonic/volcanic activity and anthropogenic components such as ground water pumping).

In section 3.1.1, we mentioned that the regional sea level variability is not only 'non-uniform' but also fluctuates in space and time. Therefore in order to study and understand the evolution of sea level change with respect to the coasts and its impact, it's important that we estimate the total relative sea level change over longer time period and not only over the altimetry era of 20 years. One method of estimating long-term total relative sea level change prior to the altimetry era is by using tide gauge records. However, very sparse availability of tide gauges with records over more than at least 30 years hinder the possibility of long-term sea level change estimation. Even if some tide gauges in the regions of our interest exist since the beginning of the 20th century, very significant data gaps (due to instrumental errors/ discontinued monitoring) make such records unfit for the study. Another approach to get information on long term regional sea level variability is by using Ocean General Circulation Models (OGCMs) and ocean reanalyses (OGCMs with data assimilation) (*Carton and Giese*, 2008, *Köhl and Stammer*, 2008, *Balmaseda et al.*, 2013). OGCMs and ocean reanalyses deduce sea level from the steric component, to which a small barotropic component is added. This allows mapping the spatio-

temporal behaviour of both temperature and salinity contributions to the sea level under a prescribed external meteorological forcing (*Meyssignac and Cazenave*, 2012).

A new approach (called past sea level reconstruction) was developed in the recent years that combine information from tide gauge data with spatial patterns from altimetry and/or OGCMs (*Church et al.*, 2004, *Berge-Nguyen et al.*, 2008, *Llovel et al.*, 2009, *Church and White*, 2011, *Hamlington et al.*, 2011, *Ray and Douglas*, 2011, *Meyssignac et al.*, 2012a). Since this method uses tide gauge records, it is expected to carry more information on regional sea level variability than OGCMs and is complimentary to the latter (*Meyssignac et al.*, 2012a, *Meyssignac and Cazenave*, 2012). The reconstruction methodology is based on the reduced optimal interpolation described by *Kaplan et al.,* (2000). It consists of combining long tide gauge records with a time-varying linear combination of Empirical orthogonal Function (EOF) based (*Preisendorfer*, 1988, *Toumazou and Cretaux*, 2001) spatial patterns derived from2-D sea level grids (in general of shorter duration than the tide gauge records). These sea level grids are based on either satellite altimetry or outputs from an OGCM. The method has 2 steps. In the first step, an EOF decomposition of the sea level grids is performed over their time span of availability. This decomposition allows separating the spatially well resolved signal of the gridded data into spatial modes (EOFs) and associated temporal amplitudes. The second step consists of computing new temporal amplitudes of the EOFs over the longer period covered by the selected tide gauge records. This is done through a least-squares optimal procedure that minimizes the difference between the reconstructed fields and the tide gauge records at the tide gauge locations. Reconstructions are then evaluated and validated by comparison with independent tide gauge records that were not used in the reconstruction process (*Meyssignac et al.,* 2012a, *Palanisamy et al.,* 2014).

In our studies, to estimate the climatic component of the total relative sea level, we have used one such past sea level reconstruction developed by *Meyssignac et al.*, (2012a). This sea level reconstruction is based on 91 long (up to 60 years) but sparsely distributed tide gauge records. It also uses gridded sea level data from two OGCMs, the DRAKKAR/NEMO (Nucleus of European Modelling of the Ocean) model (*Penduff et al.*, 2010) without data assimilation and the SODA (Simple Ocean Data Assimilation) ocean reanalyses (*Carton and Giese*, 2008) over 1958-2009, and satellite altimetry data over 1993-2009. This sea level reconstruction is the mean

of the three different global reconstructions derived from the three above mentioned sea level grids (*Meyssignac et al.*, 2012a, *Palanisamy et al.*, 2014). Fig.3.4 displays the sea level spatial trend pattern between 1950 and 2009 obtained from the mean reconstruction based sea level data. The uniform global mean trend of 1.8 mm/yr has been removed. On comparing Fig.3.4 with Fig.3.1 (altimetry-based sea level trend pattern without its global mean trend), we can observe that the sea level trend patterns in both the cases are different (both in terms of pattern and magnitude) confirming once again that the regional sea level trend variability fluctuates in time and space.

In addition to the past sea level reconstruction data used for estimating the climate-related sea level component, satellite altimetry, long-term (with no data gaps greater than 4 years) good quality tide gauge and steric data sets were also used in the studies. While altimetry and tide gauge records were used to validate the sea level reconstruction over their overlapping time period, steric data spanning over the entire period of study (1950-2009) allowed us to discuss the regional sea level variability. Very few measures are available to estimate VLM, i.e., the second component of the total relative sea level change. While global GIA models such as ICE5G (*Peltier*, 2004,2009, and also see Fig. 3.3) can be used for the estimation of VLM due to the last deglaciation, VLM estimates due to other local effects such as tectonic/volcanic activities, ground water pumping are difficult to obtain. Wherever available, precise positioning data from GPS or DORIS were used to obtain the total VLM estimate.

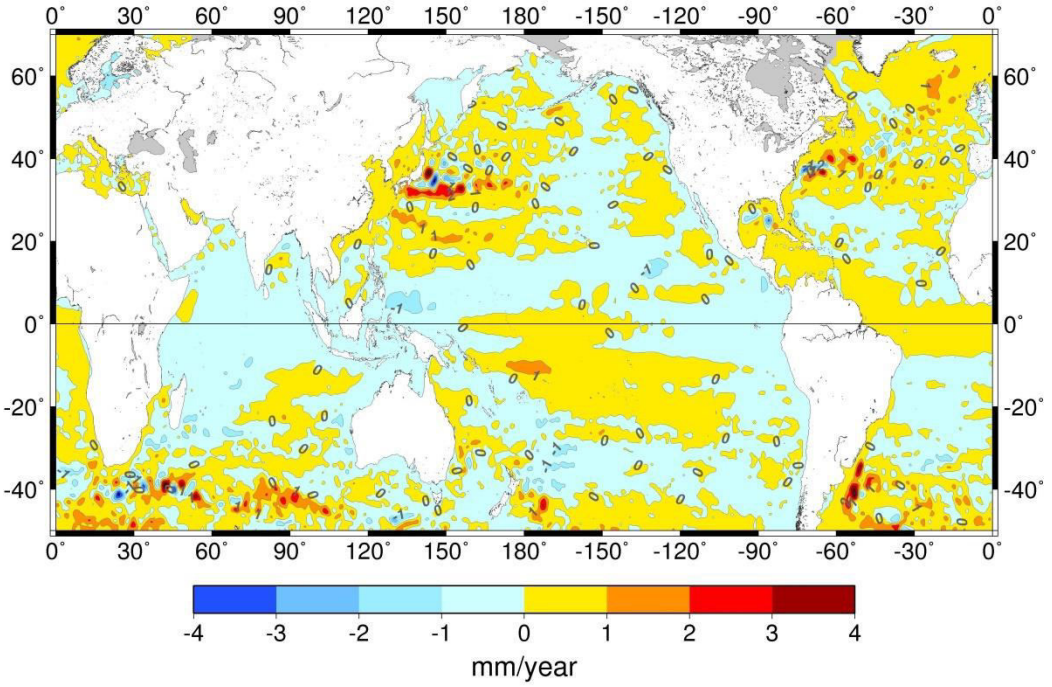

Figure 3.4: Mean reconstruction based sea level spatial trend pattern over 1950-2009 (uniform global mean trend of 1.8 mm/yr removed)

3.2.1 Indian Ocean

Indian Ocean is the home to highly populated coastal regions such as Bangladesh, India and many tropical low lying islands such as Mauritius, Seychelles, Maldives, and Lakshadweep etc. These regions have been gaining a lot of attention during the recent years owing to sea level rise and its impacts. For example, the Maldives Islands are often used as case studies within research into the impacts of potential future sea level changes (*Woodworth*, 2005). There have been several recent studies that have used geological evidences (*Woodroffe*, 2005), tide gauge records and other sea level products (*Church et al.*, 2006, *Unnikrishnan and Shankar*, 2007, *Dunne et al.*, 2012) to infer rate of sea level rise in the island and coastal regions of the Indian Ocean. All these studies show increased sea level rates that would therefore cause serious problems for the inhabitants in the future.

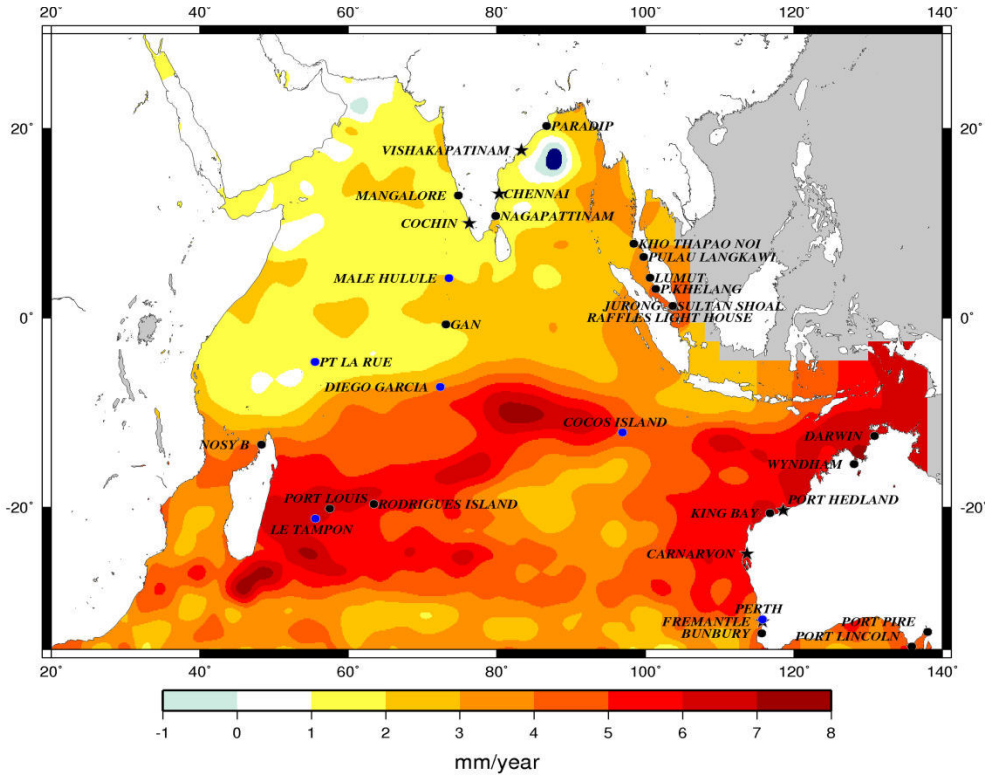

Figure 3.5: Altimetry based Indian Ocean sea level spatial trend pattern over 1993-2009 from Palanisamy et al., 2014.

Over the altimetry period between 1993 and 2009, sea level trends in most part of the Indian Ocean remain positive with the regional average amounting to 3.4 ± 0.7 mm/yr and with trend patterns exceeding 4 mm/yr (thereby exceeding the global mean rise of 3.2 mm/yr) in regions below the 15°S latitude (Fig.3.5). However the short altimetry time period is not sufficient enough to understand the evolution of the Indian Ocean sea level. We therefore studied sixty years of regional sea level variability in the Indian Ocean and estimated the total relative sea level changes at different tide gauge locations based on the methodology described in Section 3.2. This has been published as an article titled 'Regional sea level variability, total relative sea level rise and its impacts on islands and coastal zones of Indian Ocean over the last sixty years'.

Summary of the article: 'Regional sea level variability, total relative sea level rise and its impacts on islands and coastal zones of Indian Ocean over the last sixty years' (the original article is inserted at the end of this section)

In this article, we analyzed the regional sea level variability and estimated the total relative sea level change in the Indian Ocean since 1950. To start with, good quality tide gauge

records from the data archive of Permanent Service Mean Sea Level (PSMSL) were first analyzed. Based on their geographical location, the tide gauges were all regionally grouped into four zones: (1) Indian Ocean island zone, coastal regions of (2) India, (3) South East Asia, and (4) Western Australia. The tide gauge based coastal 'mean' sea level and their corresponding uncertainties based on data availability over time were estimated. It was observed that in three among the four regions of study, the uncertainties are larger between 1950s and 1970s indicating the very sparse availability of tide gauge records during this time period. Therefore, to estimate the six decades of climate-related sea level change, mean past sea level reconstruction (MRESL) data of *Meyssignac et al.*, (2012) was used in this study. VLM estimates were obtained from the latest ULR5 (*Santamaría-Gómez et al.*, 2012) GPS solution and International DORIS Service (IDS) based DORIS (*Willis et al.*, 2010) solutions.

Over the period of 60 years, the climate-related mean sea level trend in the Indian Ocean amounts to 1.5±0.5 mm/yr, a value lesser (although not statistically different) from the global mean sea level rise of 1.8±0.5 mm/yr as obtained by *Church and White*, (2011) and *Meyssignac et al.*, (2012). The spatial-temporal characteristics of the regional sea level variability since 1950 show high correlation with those of steric sea level variability. Distinct positive-negative dipole patterns between the western and eastern parts of Indian Ocean also show good correlation with the Dipole Mode Index (DMI), a proxy of the internal climate mode called the Indian Ocean Dipole (IOD; *Saji et al.*, 1999, *Behera and Yamagata*, 2001, *Saji and Yamagata*, 2003). This validates that the regional sea level variability in the Indian Ocean is driven by steric changes in response to surface wind and Ekman pumping velocity changes as mentioned by *Han et al.*, (2010) and oscillates in response to the IOD. Total climate-related sea level change was also studied in the four different regions of the Indian Ocean mentioned above and was found that in most cases, they lie well within or lesser than the range of global mean sea level rise over 60 years. The mean sea level trends over 60 years in the coastal Indian subcontinent and in the Indian Ocean islands amount to 1.5 mm/yr each. In the South East Asian coasts and Western Australian coasts they amount to 1.4 mm/yr and 1.3 mm/yr respectively. However, over the two recent decades, South East Asian and Western Australian coasts were found to exhibit high sea level trend values of 3.5 mm/yr and 5.5 mm/yr respectively presumably linked to the western tropical Pacific trade wind intensification (*Merrifield*, 2011, *Merrifield and Maltrud*, 2011,

Merrifield et al., 2012). The results obtained in this study were also found to be consistent to those obtained by *Church et al.*, (2006).

Estimation of total relative sea level change over 60 years with the help of VLM data from GPS and DORIS showed that in two islands, Cocos Island and Diego Garcia, the rates are the same as that of the global mean sea level rise. Whereas in the case of Malé Hulule (Maldives), le Tampon (Reunion) and Perth (Australia) , the values exceed the global mean rate with subsidence playing an important role. The contribution of subsidence at Malé Hulule and Le Tampon exceed 50% while at Perth, it exceeds 70%. Ground water extraction has been suggested (*Featherstone et al.*, 2012) as the main contributor to subsidence in Perth. Therefore it is likely that the long term total- relative sea level change at this location is overestimated.

Global and Planetary Change 116 (2014) 54–67

Contents lists available at ScienceDirect

Global and Planetary Change

journal homepage: www.elsevier.com/locate/gloplacha

Regional sea level variability, total relative sea level rise and its impacts on islands and coastal zones of Indian Ocean over the last sixty years

H. Palanisamy [a,*], A. Cazenave [a], B. Meyssignac [a], L. Soudarin [b], G. Wöppelmann [c], M. Becker [d]

[a] LEGOS/CNES, Toulouse, France
[b] CLS, Ramonville Saint-Agne, France
[c] LIENSs, UMR7266, CNRS, University of La Rochelle, France
[d] UAG, UMR ESPACE-DEV (IRD, UM2, UAG, UR), Cayenne, France

ARTICLE INFO

Article history:
Received 2 June 2013
Received in revised form 31 January 2014
Accepted 1 February 2014
Available online 8 February 2014

Keywords:
Regional sea level variability
Mean Reconstructed Sea Level
Altimetry
Tide gauge
Vertical land motion
Indian Ocean
Indian Ocean Dipole

ABSTRACT

Indian Ocean is the home to many tropical low lying islands and highly populated coastal zones. Since a few recent decades, many of these zones have been gaining a lot of international attention due to fears of sea level rise and possible submersions of islands. In this study we estimate sea level rise and regional sea level variability in Indian Ocean (20°E–140°E, 30°N–35°S) over a period of 60 years from 1950 until 2009. We determine the climatic factors that influence the sea level change and variability in this region. We find that the changes in the Indian Ocean sea level are of steric origin and are also driven by short-term Indian Ocean Dipole events. The trend in this region over 60 years amounts to 1.5 mm/yr, a value lesser (although not statistically different) than the global mean sea level rise over the same period. There is also an east–west increase in sea level trend pattern below 15°S latitude which is more amplified since the two recent decades. Climate-related sea level changes are also studied at different sites in the Indian ocean corresponding to the existence of tide gauge records and has been found that over the long term period (60 years), the sea level trend at most of the individual locations are well within the global mean sea level rise. Total relative sea level change which is the sum of climate-related sea level change and vertical land motion is also estimated at 5 locations with the help of GPS and DORIS measures.

1. Introduction

High precision satellite altimetry available since the early 1990s has for the first time provided sea level time series over the whole oceanic domain. This invaluable data set has confirmed that in terms of global mean, the rate of sea level rise during the last 20 years is twice larger than during the previous longer multidecadal time period (e.g., Nerem et al., 2010; Church and White, 2011). It also revealed high regional variability in the rates of sea level change (e.g., Cazenave and Llovel, 2010). Sea level trend patterns over the past 20 years show high sea level rates in the western tropical Pacific (up to 3 times the global mean), in the northern Atlantic and Austral oceans. While the main cause of last 20 years global mean sea level rise (GMSLR) is land ice melt (~55%), followed by ocean thermal expansion (~30%) (Church et al., 2011; Meyssignac and Cazenave, 2012; Hanna et al., 2013), the regional sea level trends mostly result from non-uniform ocean thermal expansion and salinity variations (Lombard et al., 2005; Levitus et al., 2012) related to ocean circulation changes (e.g., Bindoff et al., 2007; Stammer et al., 2013). There are other processes causing regional variability in sea level rates, among these are deformations of ocean basins and self-gravitational changes due to glacial isostatic adjustment (GIA) resulting from the last deglaciation and due to present-day land ice melt, respectively (e.g., Milne et al., 2009; Stammer et al., 2013). However so far, their contribution is small compared to ocean temperature and salinity changes. In the recent years, growing attention has been given in the literature to the regional variability in sea level rates (see Stammer et al., 2013 for a review). In fact this regional sea level variability superimposes on the GMSLR, either amplifying or reducing it. When studying the impacts of sea level rise, what does matter locally is indeed the sum of the GMSLR plus the regional variability (and including the effect of vertical land motions, see below). There are also raising concerns whether the shoreline erosion reported today in many coastal regions of the world is mostly due to sea level rise (e.g., Bruun, 1962; Bird, 1996; Zhang et al., 2004) or whether it also results from other factors, including urbanization, coastal management, reduced sediment transport, etc. To answer these questions, the estimate of the 'total relative' sea level change at local scale is needed (e.g., Le Cozannet et al., 2013). The term 'total relative' here means total 'climatic' sea level change, i.e., GMSLR plus the regional trend in sea level, plus eventual vertical

* Corresponding author at: 18. Avenue Edouard Belin, 31400 Toulouse, France. Tel.: +33 5 61 33 29 72.
E-mail address: hindumathi.palanisamy@legos.obs-mip.fr (H. Palanisamy).

http://dx.doi.org/10.1016/j.gloplacha.2014.02.001
0921-8181 http://dx.doi.org/10.1016/j.gloplacha.2014.02.001

land motion. In order to estimate the total climatic sea level change and its coastal impacts, knowledge on past regional sea level trend patterns is important. In fact, several studies have shown that spatial trend patterns in sea level are not stationary but evolve in space and time in response to the main modes of internal variability of the ocean–atmosphere system (Lombard et al., 2005; Bindoff et al., 2007; Meyssignac et al., 2012a; Stammer et al., 2013). For example, in the tropical Pacific, sea level oscillates west–east in responses to ENSO (El Nino-Southern Oscillation) events (Wyrtki, 1984; Busalacchi and Cane, 1985; Zebiak and Cane, 1987; Chao et al., 1993; Hendricks et al., 1996; Zhang and Levitus, 1996; Delcroix, 1998;Becker et al., 2012). In addition, studies have shown that in the Pacific, the spatial trend patterns have a life time of 20–30 years (Meyssignac et al., 2012a) and that associated fluctuations are driven by the Pacific Decadal Oscillation (PDO) (Meyssignac et al., 2012a; Hamlington et al., 2013).

The regional variability is measured by satellite altimetry over the last two decades only. To determine the spatial trend patterns prior to the altimetry era, several approaches have been developed: (1) numerical ocean modeling from OGCMs (Ocean General Circulation Models) forced by meteorological data, either assimilating ocean data (e.g., ocean temperature and salinity data) or not; (2) past sea level reconstructions combining long, good quality tide gauge records of limited distribution with short records of global gridded sea level time series from satellite altimetry or OGCMs (Church et al., 2004; Llovel et al., 2009; Hamlington et al., 2011; Ray and Douglas, 2011; Meyssignac et al., 2012b). These two-dimensional sea level reconstructions allow mapping sea level trend patterns over a time span about 3 times longer than the altimetry period. In three previous studies, we estimated the total 'climatic' sea level changes since 1950 at several sites from three different regions: the western tropical Pacific (Becker et al., 2012), the Caribbean region (Palanisamy et al., 2012) and the South China Sea (Peng et al., 2013).

In these studies, we used the most recent reconstruction from Meyssignac et al. (2012b) to estimate the total 'climatic' sea level (i.e., global mean sea level plus regional variability) at different sites of the studied regions. The present study uses a similar approach to those three studies in order to determine the total 'climatic' sea level change since 1950 at several coastal sites of East Asia, India and Western Australia in the Indian Ocean, as well as at several Indian Ocean islands. When available, precise positioning data from GPS (Global Positioning System) or DORIS (Doppler Orbitography and Radiopositioning Integrated by Satellite) are used to estimate vertical land motion allowing us to estimate the total relative sea level change.

Section 2 describes the data sets used in the study. In addition to the reconstructed sea level data, we also analyze available tide gauge records in the Indian Ocean region as well as satellite altimetry data and steric sea level data. Altimetry data are used to validate the sea level reconstruction over their overlapping time span while steric data spanning over the whole studied period (1950–2009) allow us to discuss the regional variability of the Indian Ocean sea level. In Section 3 we show the few tide gauge records available along the Indian Ocean coastlines and islands. Section 4 presents the sea level reconstruction and its validation. In Section 5 we analyze the regional variability over the whole Indian Ocean over the past 20 years and 60-year long time span using Empirical Orthogonal Function (EOF) decomposition of the altimetry-based, reconstructed and steric sea level grids to highlight the dominant modes of natural/internal variability in this region. Section 6 provides the best estimates of total climate-related sea level trends at individual locations in the coastal and island regions of the Indian Ocean. In Section 7, we discuss the rate of vertical land motion at locations with GPS and DORIS data whereas in Section 8 we deal with the estimation of total relative sea level change at selected locations by making use of climatic-related sea level change and vertical land motion. Section 9 is the summary and general conclusion on the contribution of the regional variability and land motions to the local sea level changes.

2. Data

This section presents the five datasets used in studying the climate-related sea level changes and variability: (1) the 2-D past sea level reconstruction from Meyssignac et al. (2012b), (2) satellite altimetry data, (3) steric data (representing effects of ocean temperature and salinity on sea level), (4) tide gauges and (5) GPS/DORIS vertical land motion measures.

2.1. Ensemble 2D past sea level reconstruction

Many studies have been developed to perform two dimensional past sea level reconstruction on time spans longer than the altimetry era (starting in 1993) (Church et al., 2004; Llovel et al., 2009; Hamlington et al., 2011; Ray and Douglas, 2011; Meyssignac et al., 2012b). The main advantage of past sea level reconstructions is that they provide estimates of regional and global variations of sea level, as well as time series of estimated sea level at any location over a period longer than the 2-D altimetry record and many individual tide gauge records (Church et al., 2004). The general approach consists of computing spatial modes from the gridded fields using an Empirical Orthogonal Function decomposition and computing new EOF temporal amplitudes through a least-squares optimal interpolation that minimize the difference between reconstructed fields and tide gauge records at tide gauge locations. In this study, we make use of an ensemble two dimensional past sea level reconstruction over the period 1950 to 2009 at yearly interval with a resolution of 0.5° × 0.5° developed by Meyssignac et al. (2012b). The sea level reconstruction is based on 91 long (up to 60 years) but sparsely distributed tide gauge records as described in Meyssignac et al. (2012b). It also uses gridded sea level data from two numerical ocean models, the DRAKKAR/NEMO model (Penduff et al., 2010) without data assimilation and the SODA ocean reanalysis (Carton and Giese, 2008) over 1958–2009, and satellite altimetry data over 1993–2009. It is the mean of the three different global reconstructions derived from the three above mentioned sea level grids. (See Section 4 for a detailed presentation of the reconstruction).

2.2. Satellite altimetry

DT-MSLA "Ref" altimetry data provided by Collecte Localisation Satellite (CLS) has been used in this study. It is a 0.25° × 0.25° Mercator projection grid at weekly interval. The data is used over a time span from January 1993 to December 2009. Even though the available data set extends into April 2012, the gridded dataset only until December 2009 has been used in most of this study in order to be compared with the 2D sea level reconstruction grid. However in cases where the altimetry data is superimposed to reconstructed sea level and tide gauge records at several individual locations in order to study the total climate related sea level change (Section 6), the time period is extended. The DT-MSLA "Ref" global grid is a merge of several altimetry missions, namely TOPEX/Poseidon, Jason-1 and Jason-2, Envisat and ERS-1 and 2. It is a global, homogenous, intercalibrated dataset based on global crossover adjustment (Le Traon and Ogor, 1998) using TOPEX/Poseidon and followed by Jason 1 as reference missions. Geophysical corrections like the solid Earth, ocean and pole tides, wet and dry troposphere, and ionosphere (updates from Ablain et al., 2009) have been performed. An advanced dynamic atmospheric correction (DAC) using the MOG2D model has also been applied (Volkov et al., 2007). In the altimetry data, the annual and semi-annual signals have been removed through a least square fit of 12 month and 6 month period. In order to be consistent with the temporal resolution of the 2-D past sea level reconstruction data, the weekly altimetry data has been averaged to obtain the annual temporal resolution.

2.3. Steric sea level data

In this study, we use steric sea level global grid from 1950 to 2009 with 1° × 1° resolution until the depth of 700 m computed from the global gridded temperature (T) and salinity (S) monthly data set of Ishii and Kimoto (2009), version 6.12, henceforth IK12. Even though the data covers the depth of 0-1500 m, depths below 700 m are not advisable to be used before the Argo period (since the early 2000s), especially in the Indian Ocean region where the Expendable Bathythermograph (XBT) profiles in the past were very minimal. As in the case of altimetry data, the annual and semi-annual signals from the steric data have also been removed. The monthly steric data has been averaged to annual data.

2.4. Tide gauge records

Tide gauge records from the data archive of the Permanent Service Mean Sea Level (PSMSL) Revised Local Reference (RLR) monthly mean sea level is used in this study. There are many long term tide gauge records found along the coasts of the Indian Ocean. However most of these records are not continuous and have time gaps of more than 5 years. Among the very few long tide gauge records with more than 30 years of data availability and without significant gaps, 7 have been used in the reconstruction of the global sea level grid. These are Fremantle, Port Hedland and Carnarvon in the Western Australian coast, Mumbai, Cochin, Chennai, and Vishakhapatnam along the coasts of the Indian sub-continent (marked as stars in Fig. 1). The number of long term good quality tide gauge records available in the open Indian Ocean is very limited. Most of the tide gauges in this zone do not extend prior to 1980s with an exception of Port Louis in Mauritius but with a time gap of more than 20 years (data availability: 1942–1965 and 1986–2011). Even though there are some tide gauge records starting in the 1950s (example: Nosy Be, Madagascar), the last recorded measurements end in the early 1970s and hence are too short for the study. In the case of Reunion Island, the tide gauge record at Pointe des Galets is highly intermittent and hence useless for this study. The geographical locations of the tide gauge records used in this study in the Indian Ocean region are shown in Fig. 1. The tide gauge records have been corrected for the Inverse Barometric correction using the surface pressure grids from the National Centre for Environmental Prediction (NCEP) (Kalnay et al., 1996). Tide gauge data were also corrected for the GIA effect using ICE5G-VM4 from Peltier (2004). Adopting the methodology of Becker et al. (2012), linear interpolation was performed to introduce missing data in the gaps whenever gaps were lesser or equal to 4 consecutive years. The outliers were removed making use of the Rosner's test (Rosner, 1975). Annual and semi-annual signals have been removed and the monthly records have been averaged to obtain the yearly time series.

2.5. GPS and DORIS data

In the Indian Ocean, the number of GPS and DORIS stations co-located with existing tide gauge records is very few (5 and 3 in the case of GPS and DORIS respectively). GPS and DORIS sites are shown in Fig. 1 as blue circles. In our study we make use of the latest version of GPS solution, ULR5 (Santamaría-Gómez et al., 2012) provided through the SONEL (www.sonel.org) data service. This recent version makes use of ITRF2008 (Altamimi et al., 2011) as the terrestrial reference frame and directly gives the vertical rates. More realistic uncertainties on the GPS velocities are obtained by using the maximum likelihood estimation (MLE) technique. For details on the methodologies applied for the vertical rate calculations and error estimation of the GPS velocities, please refer to Santamaría-Gómez et al. (2012). Based on the ULR5 version of GPS data, there are 5 stations co-located with tide gauge records: Cocos Island, the island of Diego Garcia, Mahé in Seychelles, Malé in the islands of Maldives and Hillary along the eastern coast of Australia. A GPS station is also located in the Reunion Islands but with no tide gauge record existing. However sea level time

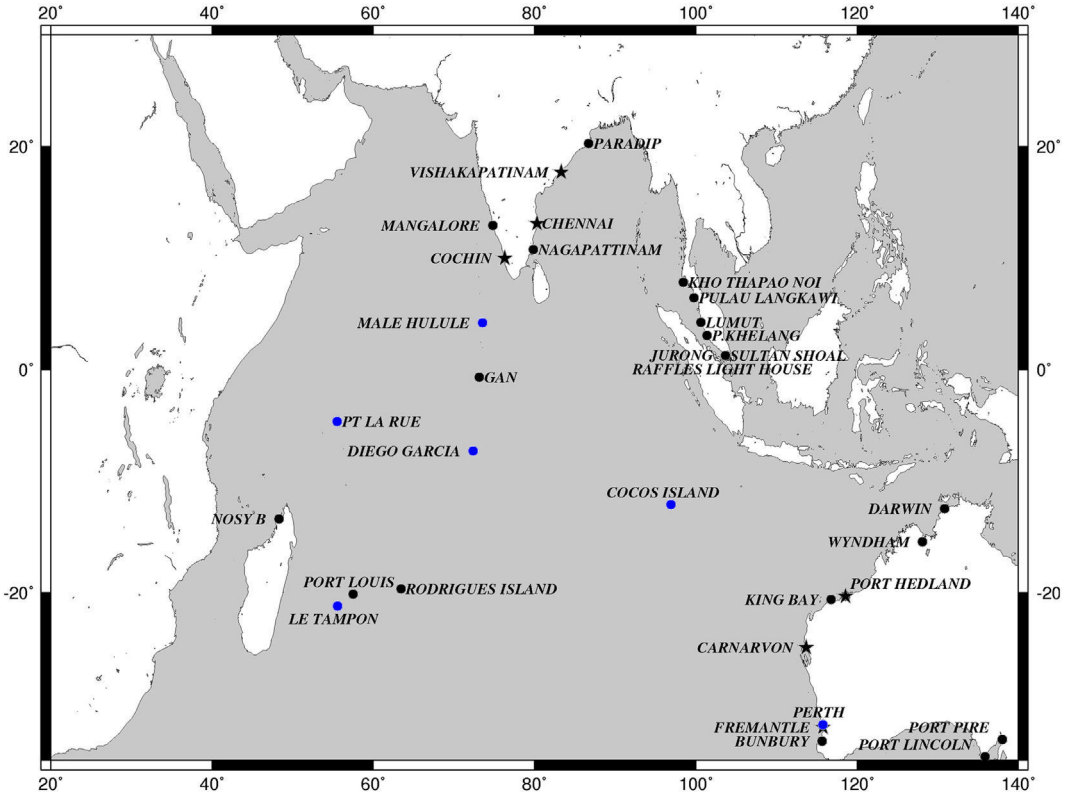

Fig. 1. Map showing the geographical locations of the tide gauge sites used in this study. Co-located GPS and DORIS stations are also represented in blue whereas black stars indicate the tide gauge records used in the global reconstruction grid. (For interpretation of the references to color in this figure legend, the reader is referred to the web version of this article.)

series from the reconstructed sea level grid (Fig. 7b) has been interpolated nearest this GPS record.

DORIS solutions located in islands of Indian Ocean are obtained from the International DORIS Service (IDS) database (www.ids-doris.org) (Willis et al., 2010a) which offers 4 individual DORIS solutions. Here we make use of 2 such solutions:

1. ign11wd01 from the combined analysis center of Institut Géographique National (IGN) and Jet Propulsion Laboratory (JPL), (Willis et al., 2010b).
2. lca11wd02 from the analysis center of Collecte Localisation Satellites (CLS) and Centre National des Etudes Spatiales (CNES), (Soudarin and Crétaux, 2006).

Both of these solutions use ITRF2008 as their terrestrial reference frame and hence are comparable with the ULR5 version of GPS. In the Indian Ocean, there are DORIS solutions at 3 sites, Mahé in Seychelles, Malé in Maldives and in the Reunion Islands.

3. Coastal sea level at tide gauge sites

The tide gauge based coastal 'mean' sea level during the 1950–2009 time span is displayed (represented as black curves) in Fig. 2 at four different zones of the Indian Ocean: 1) the Western Australian coast, 2) South East Asian coast, 3) coasts along the Indian subcontinent and 4) coasts of some Indian Ocean Islands. The individual tide gauge records are also displayed as several colored curves in the same figure. The 'mean' coastal sea level time series are based on averages of individual tide gauge time series at each of its zone. The uncertainties in the zonally averaged time series correspond to the ratio (expressed in terms of percentage) of the number of 'no data' tide gauges at each point of time to the total number of tide gauges available in each zone, i.e., lesser the number of tide gauges available in a particular zone at a particular time, larger is the displayed uncertainty in terms of percentage. From Fig. 2, it can be observed that in three regions, the uncertainties are larger in the 'mean' sea level time series between 1950s and 1970s indicating very sparse availability of tide gauge records during this time period. In the case of the South East Asian coasts, the tide gauges commence only in the 1970s.

At each zone, the coastal mean sea level trend was calculated over time spans that correspond to the availability of at least 50% of the total number of zonal tide gauge records. Along the western coasts of the Australian continent, the mean sea level trend between 1966 and 2010 amounts to 1.66 ± 0.45 mm/yr and amounts to 5.68 ± 1.6 mm/yr between 1990 and 2010. This sharp rise in sea level along the Western Australian coast from the early 1990s can be observed in Fig. 2. The mean coastal sea level trend in the South East Asian zone amounts to 1.5 ± 0.5 mm/yr between 1980 and 2010 with an increase in the trend value by 1 mm/yr between 1990 and 2010. The mean coastal sea level trends along the coasts of the Indian subcontinent and several islands of the Indian Ocean amount to 1.22 ± 0.3 mm/yr between 1966 and 2010 and 4.4 ± 0.62 between 1990 and 2010 respectively. Both of these zones also show a marked increase in sea level since the early 1990s. The above results show the evolution of sea level trend at various zones of the Indian Ocean. However, as it can be observed from Fig. 1 and as it has already been discussed in Section 2.4, the unavailability of tide gauge records over a longer time period in the Indian Ocean is an issue that hinders the study of long term regional sea level changes. As this is the main objective of our study, we make use of the ensemble mean of three reconstructed sea level grids computed by Meyssignac et al. (2012b) to replace short or erroneous tide gauge records in this study.

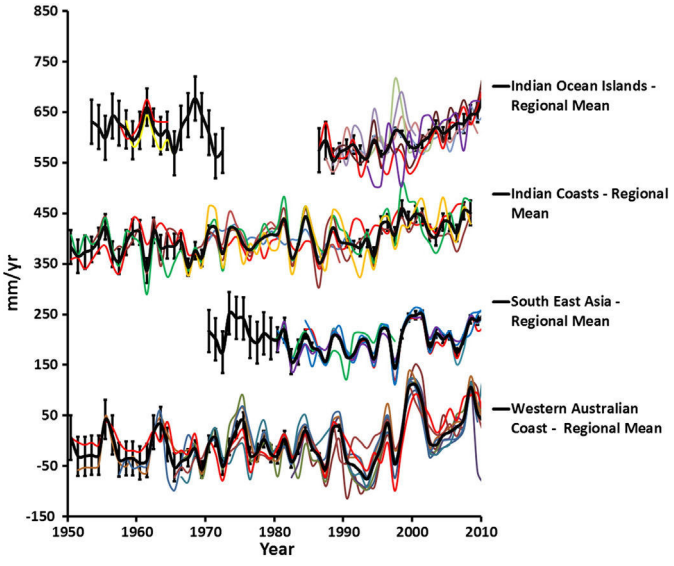

Fig. 2. Mean coastal sea level time series estimated from tide gauge records in four different zones of the Indian Ocean. Mean time series in black, individual tide gauge records in color. (For interpretation of the references to color in this figure legend, the reader is referred to the web version of this article.)

4. Past sea level reconstruction: brief description

The reconstruction methodology is based on the reduced optimal interpolation described by Kaplan et al. (2000). It consists of combining long tide gauge records with a time-varying linear combination of EOF-based (Preisendorfer, 1988; Toumazou and Cretaux, 2001) spatial patterns derived from 2-D sea level grids (in general of shorter duration than the tide gauge records). These sea level grids are based on either satellite altimetry or outputs from an OGCM. The method has 2 steps. In the first step, an EOF decomposition of the sea level grids is performed over their time span of availability. This decomposition allows separating the spatially well resolved signal of the gridded data into spatial modes (EOFs) and associated temporal amplitudes. The second step consists of computing new temporal amplitudes of the EOFs over the longer period covered by the selected tide gauge records. This is done through a least-squares optimal procedure that minimizes the difference between the reconstructed fields and the tide gauge records at the tide gauge locations. Some reconstructions use altimetry-based sea level grids (e.g., Church et al., 2004, 2011; Hamlington et al., 2013) while others used OGCM outputs (e.g., Llovel et al., 2009; Ray and Douglas, 2011). The option of using OGCM outputs rather than satellite altimetry grids was driven by the fact that spatial sea level patterns observed during the relatively short altimetry time span are likely not stationary in time but fluctuate at frequencies related to the internal modes of variability of the climate system (e.g., ENSO, PDO and NAO — North Atlantic Oscillation). To correctly capture the decadal/multidecadal variability of the spatial patterns, it is preferable to use sea level grids of longer duration than available from satellite altimetry. Meyssignac et al. (2012b) performed three different reconstructions based on three different gridded products: (1) from the ORCA025-B83 version of NEMO OGCM grids (1/4° resolution, no data assimilation, DFS4.1 atmospheric forcing described in Brodeau et al., 2010; run over 1958–2007), (2) the Carton and Giese (2008) reanalysis over 1958–2007 and (3) the sea level grids from satellite altimetry over 1993–2009. 91 long tide gauge records from the PSMSL were used for the reconstruction. One problem with tide gauge records is that measurements are made with respect to a local datum that is different from one site to another. By working with derivatives, this problem can be overcome. In Meyssignac et al. (2012b), a different approach was chosen, consisting of subtracting from each sea level record a mean value computed over the 1950–2009 time span (note that most of the 91 tide gauge records are almost complete over this 60-year long time span; when gaps were observed, linear interpolation was applied to fill the gaps). The tide gauge data were corrected for the inverted barometer and GIA. Annual and semi-annual cycles were also removed

and yearly-averages were computed. Each of the three reconstructions was validated at global scale by comparison with independent tide gauges not used in the reconstruction process. To do this, for each case (i.e., for each gridded product), 91 new reconstructions were performed, leaving out successively each one of the 91 tide gauge records (thus each of these new 91 reconstructions now uses a set of 90 tide gauges). For each deleted tide gauge, the reconstructed sea level time series at the tide gauge site was compared with the observed data. The validation results are discussed in detail in Meyssignac et al. (2012b). 70% of the reconstructed sea level time series present a correlation coefficient with the observed sea level greater than 0.8 (95% confidence level) (28% have a correlation between 0.5 and 0.7). The root mean squared (rms) differences between (detrended) reconstructed sea levels and observed sea level time series were compared. 75% of the rms differences between detrended tide gauge-based and reconstructed sea level time series are below 30 mm. The uncertainty of reconstructed sea level trends over the 1950–2009 time span was found on the order of 0.5 mm/yr. This uncertainty was based on the sum of errors due to the least-squares method and errors of the tide gauge records. This latter error was estimated from a bootstrap method (Efron and Tibshirani, 1993) for standard errors of the tide gauge records for each year (significant at the 95% level). Another way to check the validity of the new reconstruction was to look at reconstructed sea level trends over the altimetry period (here 1993–2009) and compare with altimetry data for which the spatial trend patterns are trusted. As shown in Meyssignac et al. (2012b), spatial trend maps agree well over their overlapping periods. Finally, the study of Becker et al. (2012) compared reconstructed sea level time series with tide gauge records in the tropical Pacific region not used in the reconstruction and showed very good agreement between the two sets of data.

Meyssignac et al. (2012b) computed an ensemble mean of the three reconstructions as well as a map of the associated uncertainty. It is this reconstruction, called the Mean REconstructed Sea Level, henceforth MRESL, which we use in the following study.

In the absence of long-term tide gauge records in the Indian Ocean, the validity of the MRESL in the Indian Ocean was checked by comparing the MRESL spatial trend pattern over the altimetry period (here 1993–2009) with the altimetry based spatial trend pattern (Meyssignac et al., 2012b). This is illustrated in Fig. 3a, b and c which present the altimetry based and reconstruction based sea level spatial trend patterns along with the correlation plot. The correlation between the two spatial trend patterns is 0.64 with level of significance greater than 95%. Visual inspection also indicates that the spatial trend patterns agree well. The altimetry based trend map shows slightly higher amplitude when compared to the reconstruction based trend map. This is mainly due to the fact that the reconstruction is developed based on limited set of EOF modes and this act as low pass filter. Nevertheless, since the reconstruction uses long-term (~50 years) spatial information from two OGCMs, the decadal natural modes of regional sea level variability in the Indian Ocean are assumed to be well represented and therefore suitable for this study.

5. Regional variability of the Indian Ocean

In this section we discuss the spatial trend patterns observed in sea level and steric data over different time spans.

5.1. Spatial trend patterns over the satellite altimetry period (1993–2009) and 60-year long time span (1950–2009)

Over the 1993–2009 time span, the sea level trends in most part of the Indian Ocean remain positive (Fig. 3a and b). The Indian Ocean mean sea level trend over 1993–2009 amounts to 3.4 ± 0.7 mm/yr from observed altimetry and 3.0 ± 0.5 mm/yr from reconstruction. There is also a noticeable high sea level trend pattern below 15°S latitude extending from east to west. This could be attributed to the intensification of trade winds in the Western Tropical Pacific since the recent two decades (Merrifield and Maltrud, 2011), which as a result has its impact in the Indian Ocean also. Knowing that the spatial trend patterns are not stationary but evolve in space and time, sea level spatial trend patterns in the Indian Ocean over 60 years is studied.

Fig. 4 shows the reconstructed spatial trend patterns in the Indian Ocean between 1950 and 2009. As in Fig. 3a and b but at smaller magnitude, we can also observe patterns of high sea level trend (with maximum of 3.5 mm/yr) below 15°S latitude along the Eastern Indian Ocean propagating westward. There are also patterns of higher sea level trend values along the eastern coasts of African continent and in central Bay of Bengal and Northern Arabian Sea. Patterns of relatively lower sea level trends are also seen in the western part of the central Indian Ocean. Over the period of 60 years, the mean sea level trend in the Indian Ocean amounts to 1.5 ± 0.5 mm/yr, a value lesser (although not statistically different) than the global mean sea level rise of 1.8 ± 0.5 mm/yr over the same period as obtained from (Church and White, 2011; Meyssignac et al., 2012b).

Han et al. (2010) have attributed the regional sea level changes in the Indian Ocean to steric changes in response to surface wind and Ekman pumping velocity changes. These changes are due to enhancement of Indian Ocean regional Hadley and Walker cells as a result of Indo-Pacific warming pool. As a result there is a marked pattern of positive trend values extending from the east toward the west below 15°S latitude and negative values above (Fig. 1, middle panel of Han et al. (2010)). This pattern is also exhibited in the MRESL spatial trend map in Fig. 4 calculated between 1950 and 2009. Since the period of study in Han et al. (2010) is between 1961 and 2008, MRESL spatial trend pattern was calculated for the same time period (not shown in this study) and was found to exhibit similar pattern as that of Han et al. (2010).

5.2. Steric and Indian Ocean Dipole impact on the Indian Ocean sea level variability

As steric sea level is the main cause of regional variability of observed sea level, here we analyze the evolution of the steric spatial patterns.

EOF decomposition of the MRESL and IK12 steric sea level grid for the Indian Ocean over the 1950–2009 time periods was performed in order to capture the characteristics of the regional sea level variability. The mean sea level trend of 1.5 ± 0.5 mm/yr over the Indian Ocean and the mean steric Indian Ocean trend of 0.2 ± 0.04 mm/yr were removed from the MRESL and IK12 grids respectively before performing the EOF decomposition. The MRESL EOF mode with 15% of total variance shows high correlation (correlation 0.8 with significance > 95%) with the IK12 EOF mode with 17% of total variance (Fig. 5a). This further validates that the regional sea level variability in the Indian Ocean is driven by steric changes in response to surface wind and Ekman pumping velocity changes as mentioned by Han et al. (2010).

In both EOF spatial patterns, we also clearly observe the negative–positive dipole patterns between the eastern and western parts of the Indian Ocean indicating the influence of the Indian Ocean Dipole (IOD) events. IOD event is a coupled ocean–atmosphere phenomenon which evolves with an east–west dipole Sea Surface Temperature (SST) anomaly (Saji et al., 1999; Behera and Yamagata, 2001). SST anomalies during the IOD events are strongly coupled to surface wind anomalies in the central equatorial Indian Ocean (Saji et al., 1999; Saji and Yamagata, 2003). However the IOD is a short term event and usually begins to develop during the summer of the northern hemisphere, reaches its maximum in fall and ends in winter as a result of strong seasonal winds (Behera and Yamagata, 2001; Black et al., 2003; Hastenrath, 2007). Even though the spatial patterns in Fig. 5a capture the IOD events well, the temporal curves being averaged on an annual scale do not capture the short term IOD events. This is a minor constraint of MRESL grid available only on annual time scale. In order to capture the short term

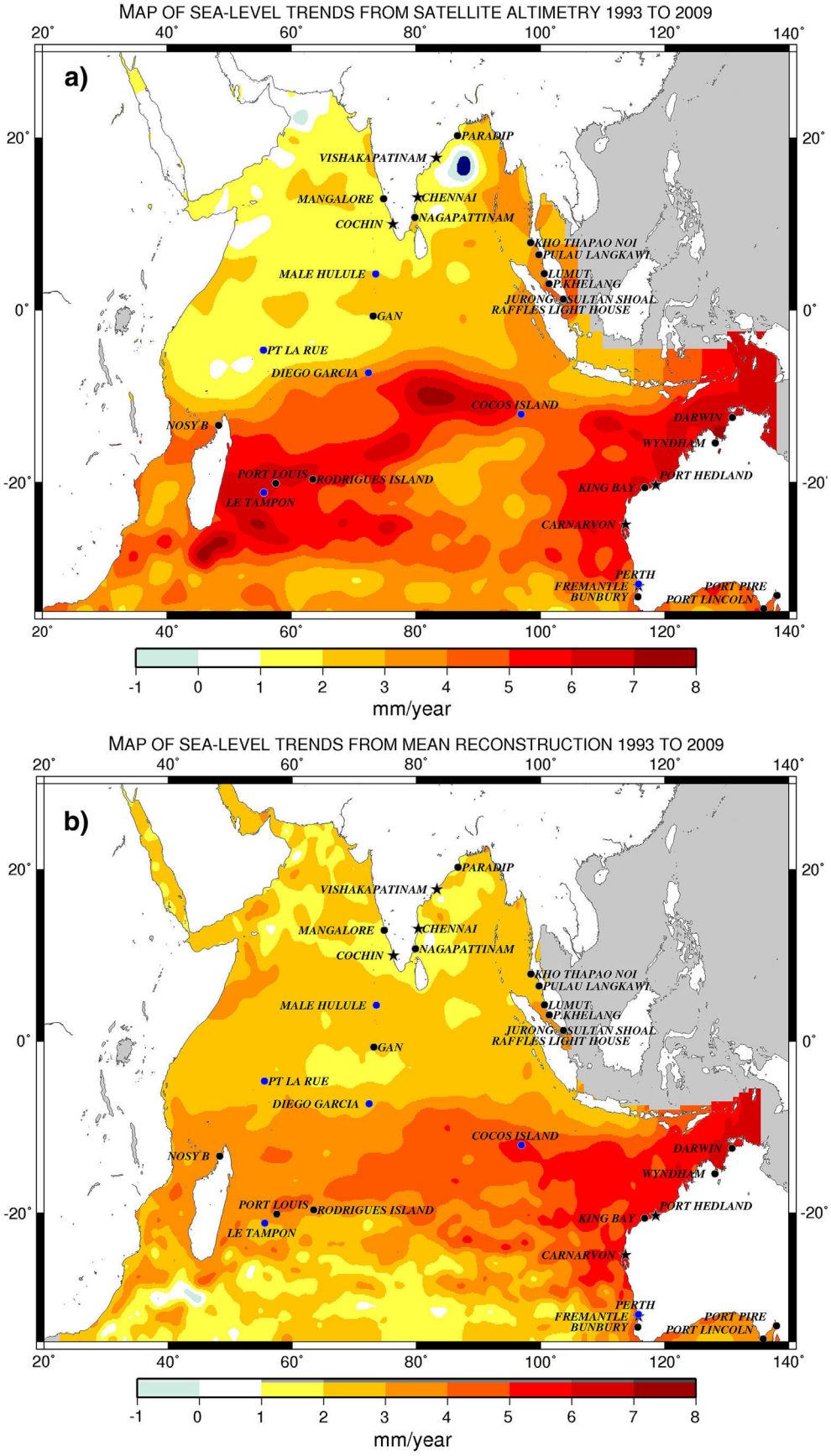

Fig. 3 (a): Map of sea level trend pattern from observed altimetry during 1993 and 2009. (b): Map of reconstruction based sea level trend pattern during 1993 and 2009. Tide gauge locations are superimposed and marked in black in both the maps. The stars indicate tide gauge records used in mean reconstruction of global sea level grid. The blue circles indicate co-located GPS and DORIS stations. (c): Correlation plot between reconstruction and altimetry based spatial sea level trends. (For interpretation of the references to color in this figure legend, the reader is referred to the web version of this article.).

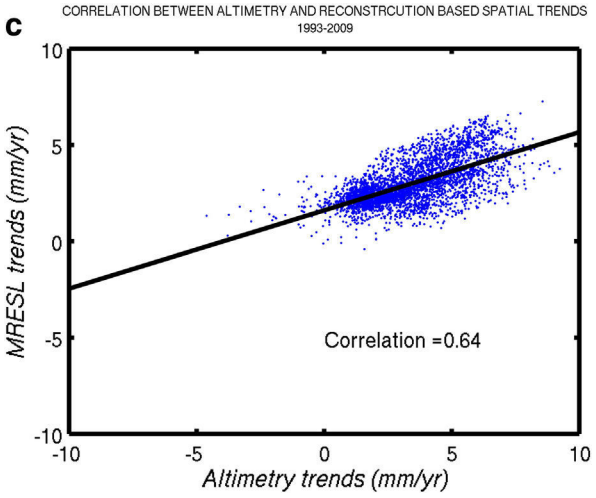

Fig. 3 (*continued*).

IOD events on the temporal curve, EOF analysis was performed on the monthly IK12 steric sea level grid over the Indian Ocean. Fig. 5b shows spatial pattern and temporal curve of the first EOF mode of the monthly IK12 steric sea level over 1950–2009. The IOD signals appear stronger in the first EOF spatial pattern obtained from the monthly data than from that of the annual IK12 data set. Fig. 5b also shows the correlation (correlation = 0.5 with level of significance > 95%) between the monthly temporal (with a smoothing of 3 months) curve of IK12 EOF first mode and the Dipole Mode Index (DMI), implying the link between the short-term IOD events and steric sea level variability. DMI is a measure of the anomalous zonal SST gradient across the equatorial Indian Ocean. It is defined as the difference in SST anomaly between the tropical western Indian Ocean (50°E ± 70°E, 10°S ± 10°N) and the tropical south-eastern Indian Ocean (90°E ± 110°E, 10°S — Equator) (Saji et al., 1999).

6. Total climate-related sea level change at coastal and island sites of the Indian Ocean

In this section, we study the total 'climate' related sea level change at several sites in the Indian Ocean. For this purpose, we take into account several sites along the coasts of the Indian sub-continent, South-East Asian coast, Western Australian coast and islands of the Indian Ocean. Sites with existing tide gauge records were chosen as the points of interest in each of the region of study. As already discussed in Section 3, tide gauge records do not sufficiently cover the 60 year time period that is the interest of this study. Therefore, MRESL grid interpolated within a 1° radius of the tide gauge location is used to compute the long-term climate-related sea level change at those locations. Estimates from tide gauge records and observed altimetry are also discussed at each of the zones whenever feasible. Similar to the MRESL grid, the observed altimetry grid has also been interpolated within a 1° radius of each tide gauge site thereby giving the observed altimetry sea level time series at each location.

Figs. 6 and 7 show the interpolated climate-related sea level time series obtained from MRESL at several zones of the Indian Ocean. The corresponding tide gauge records and interpolated altimetry time series are also superimposed over the MRESL time series. The figures also display certain sites with no tide gauge time series. These are the sites where the sea level recorded by the tide gauges show very high fluctuations (in certain cases as high as 30 cm), and/or highly intermittent. Some of these do not have data extending into the altimetry period and hence cannot be verified. Individual case study on each of these tide gauges is beyond the scope of this study. Hence three such dubious tide gauge records have been discarded and only the MRESL and altimetry time series have been studied at these sites.

It can be observed in Figs. 6 and 7 that there are some discrepancies between the MRESL and tide gauge time series, in terms of interannual/decadal variability in certain cases and trend values in other cases (as shown in Table 1). The discrepancies may arise due to the fact that when the tide gauge records are short (i.e., when data availability is limited to few years), they are highly dominated by signals related to interannual variability like ENSO or IOD. These signals mask out the long term decadal sea level trends whereas MRESL, due to its 60 year time span, captures the low frequency long term decadal sea level trends. So tide gauges with longer records agree better with MRESL trends (e.g., Cochin, Vishakaptinam, Paradip, Port Hedland, Bunbury etc.). Apart from this, even though the GIA related vertical land motion has been corrected for the tide gauge records, local ground motion impacts like subsidence due to ground water/hydrocarbon extraction are reflected in tide gauge records while the MRESL does not contain this signal. These could further add to the differences in the trend values.

6.1. Coastal zones of Indian sub-continent

Fig. 6a shows the sea level time series obtained by interpolating the MRESL corresponding to several sites chosen along the coastal regions of the Indian sub-continent. Available tide gauge records and the interpolated observed altimetry time series have also been superimposed to the MRESL time series. The mean rms difference between tide gauges and MRESL in this zone amounts to 2.9 cm. We observe that the magnitude of the interannual variability exhibited by the sites located on the western coast is lesser than that of the sites on the eastern coast. This was mathematically quantified by calculating the standard deviation of the interannual anomalies of the sites located on the western and eastern coasts. The mean of the standard deviations of the MRESL time series of the sites on the western coast is 26 mm against the mean standard deviation value of 30 mm on the eastern coasts. The sea level trend over a period of 60 years (1950–2009) along the Indian coasts ranges between 1.3 mm/yr and 1.7 mm/yr with the maximum trend rate of 1.7 mm/yr observed at Chennai on the eastern coast. Table 1 lists the different locations and the trend values that have been studied.

6.2. South East Asian coasts

Fig. 6b shows the MRESL, tide gauge and observed altimetry sea level time series at various locations on the coastal zones of South East Asia. The mean rms difference between MRESL and tide gauges amounts to 2.8 cm. Over 60 years, the sea level rate calculated from MRESL at these sites range between 1.4 mm/yr and 1.6 mm/yr. However, since the two recent decades, the sites at the South East Asian coasts exhibit an increased rate of sea level. For example, between 1950 and 2009, the MRESL trend at Sultan Shoal amounts to 1.5 ± 0.5 mm/yr whereas at the same location, the MRESL trend over 1992–2009 period is 4.0 ± 0.7 mm/yr. The tide gauge sea level trend at Sultan Shoal between 1992 and 2009 is 1.8 mm/yr. For the same time period, at Sultan Shoal, altimetry data also exhibits high sea level trend of 3.9 ± 1.3 mm/yr which is consistent with the MRESL trend value. The higher rate of sea level rise since two decades in South East Asia is similar to that exhibited in the Western Tropical Pacific as in Merrifield and Maltrud (2011) thereby indicating the influence of Western Tropical Pacific trade wind intensification along the coastal zones of South East Asia.

6.3. Western Australian coast

Fig. 7a shows individual MRESL sea level time series over 60 years with tide gauge records and observed altimetry time series superimposed at sites along the Western Australian coast. The mean rms difference between the tide gauges and MRESL is 2.8 cm. In Fig. 7a, we can

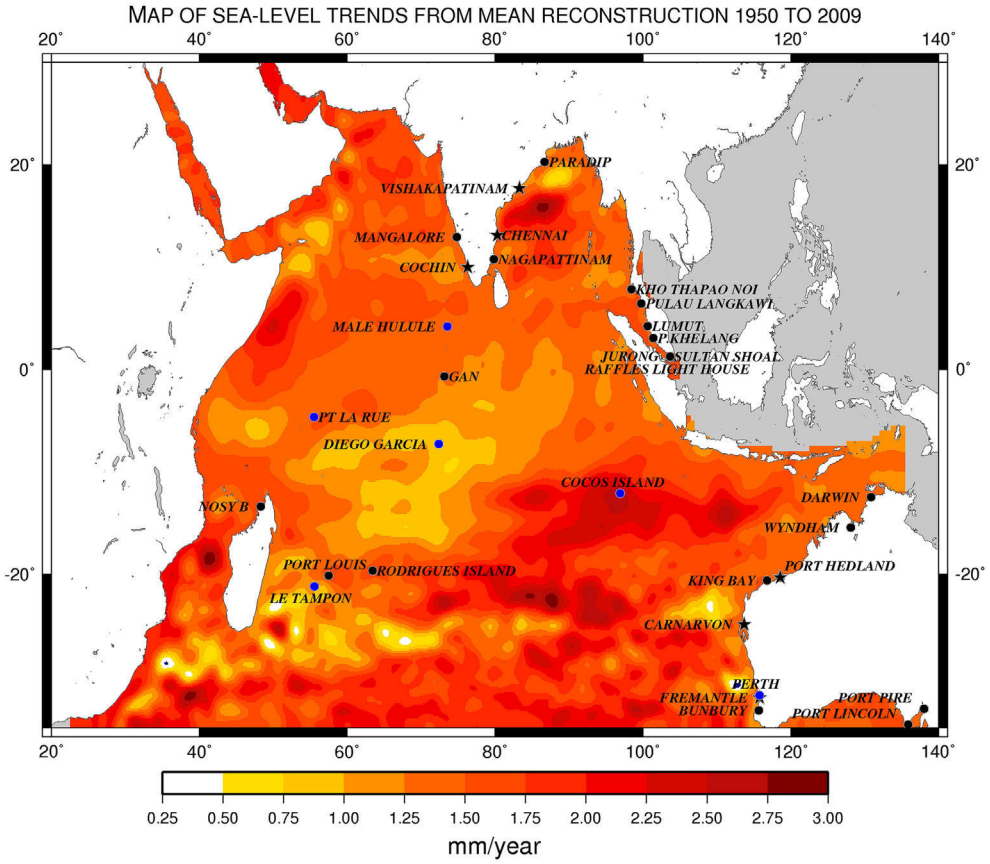

Fig. 4. Map of sea level trend patterns from Mean Reconstructed Sea Level grid during 1950–2009 with tide gauge sites superimposed as black circles. Co-located GPS and DORIS stations are represented in blue whereas black stars indicate the tide gauge records used in the global reconstruction grid. (For interpretation of the references to color in this figure legend, the reader is referred to the web version of this article.)

observe that between 1950 and the beginning of 1990s, the sea level trend at every site is almost flat whereas from the 1990s, there is a steep increase in the sea level rise rates in all the stations. To verify this, mean sea level trends were calculated prior to and after 1990s from available tide gauges and MRESL time series. Mean sea level trend from tide gauges available between 1966 (as most of the records start only in the1960s) and 1991 amounts to 0.6 ± 0.8 mm/yr, whereas between 1992 and 2009 (100% availability of tide gauges), the mean trend amounts to 5.5 ± 1.6 mm/yr. The tide gauge records clearly show a marked increase in sea level rate since 1990s. The mean of MRESL trend values along the western coast during 1950–1991 amounts to 0.8 ± 0.3 mm/yr. Between 1992 and 2009, the mean MRESL trend value amounts to 5.5 ± 1.7 mm/yr. Over the same time period, the mean altimetry sea level trend at this zone is 5.6 ± 2 mm/yr. The trend values from MRESL and altimetry are consistent with each other. As in the case of tide gauges, the MRESL also shows a marked increase in sea level trend since the 1990s when compared to the previous decades. This is also consistent with the spatial trend patterns showing high sea level trends during 1992–2009 along the Western Australian coasts observed in Fig. 3a and b. And as discussed in Section 5, the sudden increase in the sea level trend seen in these sites since the two recent decades is attributed to the enhancement in the Walker and Hadley cells Indo Pacific warm pool warming (Han et al., 2010). Moreover, the interannual sea level variability along the Western Australian coasts prior to 1970 is lesser than that of the variability after 1970. The mean of the standard deviation of interannual anomalies at the individual stations prior to 1970 is 14 mm whereas after 1970 it is 42 mm as calculated from the MRESL. This remains true with the standard deviation values obtained from tide gauge records wherever they extend prior to 1970s. Similar phenomenon has also been observed in the western tropical Pacific as noted by Church et al. (2006) and Becker et al. (2012).

6.4. Indian Ocean Islands

Fig. 7b shows the long term sea level time series of Indian Ocean islands. Even though lacking a tide gauge site, MRESL time series has been interpolated at Le Tampon in the Reunion Island as there are GPS and DORIS measures at this site and henceforth are useful in the estimation of total relative sea level change (Section 8). The tide gauges and MRESL exhibit a mean rms difference of 3.5 cm. Rodrigues Island, Port Louis (Mauritius), Le Tampon (Reunion) lying below the 15°S and Nosy Be (Madagascar) at 13°S show very similar sea level variability (correlation exceeding 0.9 with significance greater than 95%) over the entire period between 1950 and 2009 estimated from the MRESL time series. This similarity in sea level variability is consistent with the results of Church et al. (2006) between Port Louis and Rodrigues Island. Church et al. (2006) mention a lag of 2 months between the two sites which however is not visible in our result as the data used in this study is at an annual sampling. In order to verify the MRESL results and also to confirm the 2 months lag mentioned by Church et al. (2006), we studied the monthly tide gauge records at Rodrigues Island and Port Louis between 1988 and 2009. The two tide gauge time series are highly correlated (correlation 0.9 with significance greater than 95%) with Port Louis tide gauge time series lagging Rodrigues by 2 months. This is consistent with MRESL results and Church et al. (2006).

The location of Rodrigues, Port Louis, Le Tampon and Nosy Be below the 15°S latitude band also corresponds to the pattern of high sea level

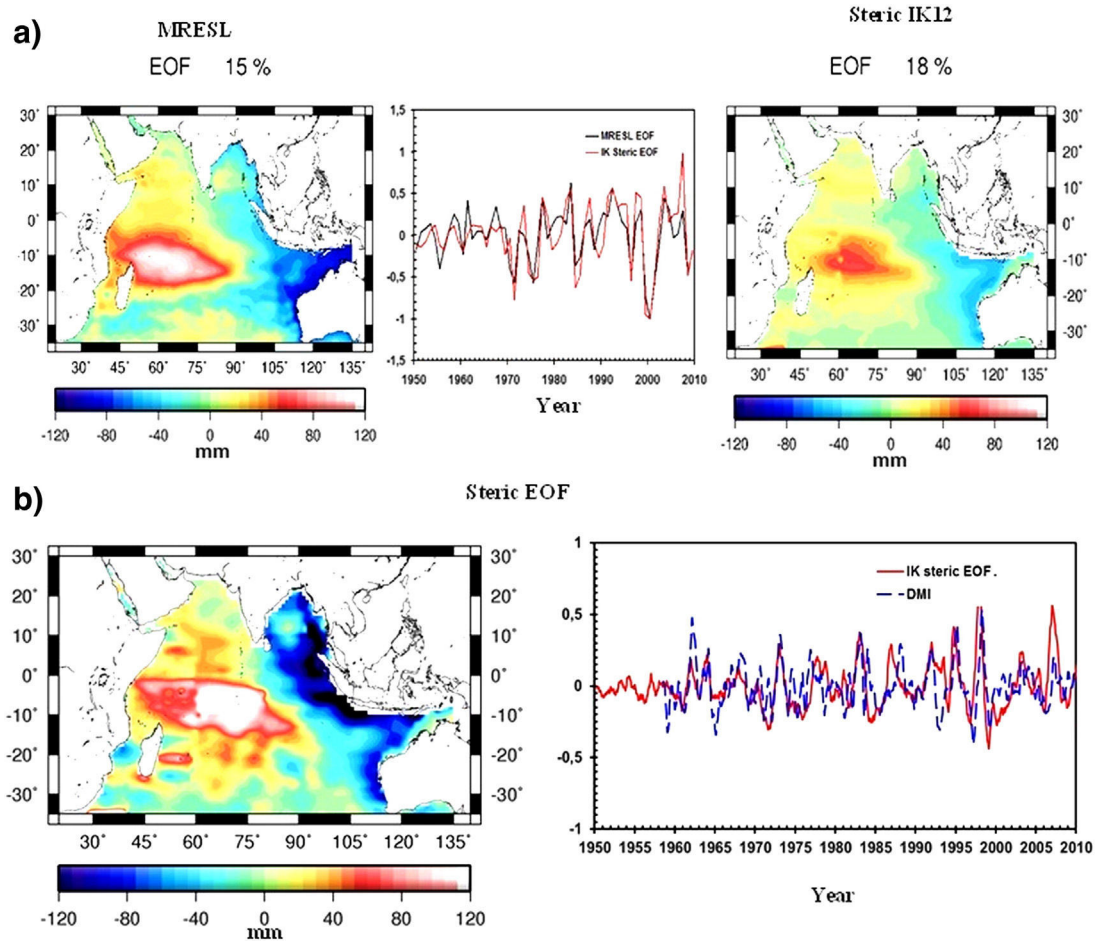

Fig. 5. Top panel: (a): EOF modes of MRESL and IK12 steric sea level over 1950–2010. Bottom panel: (b): first mode of EOF from monthly steric IK12 sea level data compared with Dipole Mode Index (DMI).

trend extending from the east to the west discussed in Section 5. The rates of sea level rise at these four locations range between 1.2 mm/yr and 1.7 mm/yr (Table 1) over 60 years and are below the global mean sea level rise. A similarity in the sea level variability time series (correlation 0.8 with 95% significance) is also seen between Diego Garcia (British Indian Ocean Territory) and Point la Rue (Seychelles) with Diego Garcia leading Pointe la Rue by a year. This was again confirmed by comparing the individual tide gauge time series at Diego Garcia and Pointe La Rue between 1993 and 2000 (correlation 0.6, significance of 90%). The values of climate-related sea level trend at these two locations over 60 years obtained from MRESL are 0.9 and 1.5 mm/yr respectively. The unavailability of tide gauges in this zone prior to 1990s hinder the tide gauge based long term sea level change estimation.

6.4.1. Rate of sea level change in Maldives

Maldives has been the subject of great interest socially and politically when questions of sea level rise arise and hence has been the focus of many scientific studies (e.g., Woodworth, 2005; Church et al., 2006). This is mainly because of its low lying lands and thereby the fear of storm surges, sea salt water intrusion in the already dwindling fresh water supply and outgrowing population. There are three tide gauge records in the islands of Maldives: Hanimaadhoo, Malé and Gan. The record at Hanimaadhoo is too short (1991–2002) and therefore is of little interest in this study. While Malé and Gan have records over 20 years, they are also not sufficient to study long term variations over 60 years.

Sea level variability from MRESL in Gan and Malé (Fig. 7b), both located in the equatorial band and belonging to the island of Maldives are strongly correlated (0.95). However when the tide gauge records at Malé and Gan are compared between 1989 and 2009, the correlation reduces to 0.6 (95% significant). The potential causes for the discrepancies between the tide gauge records and MRESL time series have been mentioned in the general Section 6. At Malé and Gan, comparisons between MRESL and altimetry data are convincing (See Table 1) and henceforth study has been carried out using the MRESL time series.

Of all the Indian Ocean islands taken for this study, Maldives shows the lowest sea level variability. Mean of the standard deviation of the MRESL sea level time series over Malé and Gan over 60 years is 26 mm whereas the mean of the same over the rest of the islands in the Indian Ocean show a value of 32 mm. This has also been noted by Church et al. (2006). The rates of sea level rise between 1950 and 2009 at the two sites are 1.3 ± 0.4 and 1.4 ± 0.4 mm/yr respectively. At the same two locations, Church et al. (2006) show the sea level rise rates between 1950 and 2001 to be 1.0 mm/yr each. Like in most of the Indian Ocean islands, the rate of climate-related sea level rise in the Maldives also lies well within the global mean sea level rise rate. However this does not mean that the islands are not impacted by sea level rise. There are other factors that can further magnify the impact of sea level rise even if the rise is at the same scale as the global mean. For example, Woodworth (2005) has mentioned the threats posed by inundations in the low lying Maldives. Also the islands being located in an active tectonic zone are prone to high vertical land motions. The increasing demand for freshwater due to increasing population in

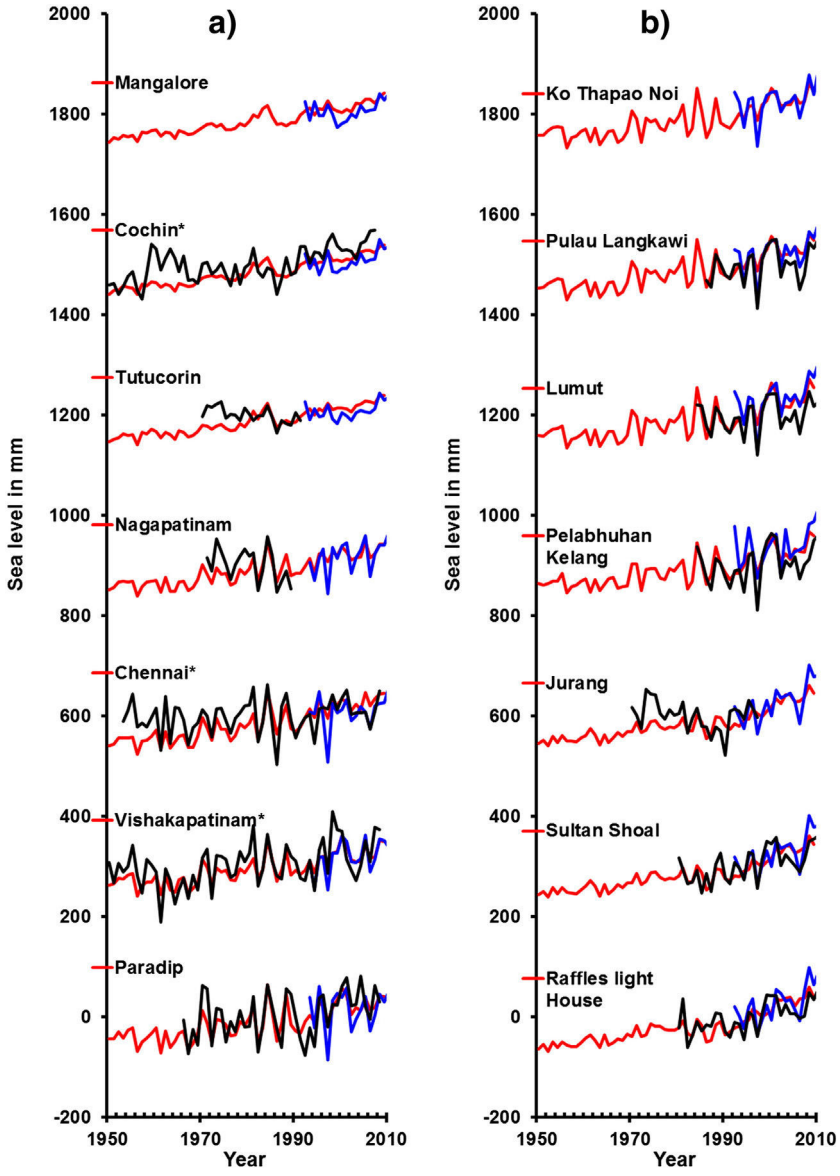

Fig. 6. Sea level time series at tide gauge sites in the (a) Indian sub-continent and (b) South East Asia. MRESL in red, tide gauge in black and altimetry in blue. (For interpretation of the references to color in this figure legend, the reader is referred to the web version of this article.)

these islands can also cause local subsidence which can have a huge impact in terms of relative sea level change. Therefore measuring the rate of vertical land motion at these sites is equally important as estimating the climate-related sea level change.

7. Vertical land motions

The rates of vertical land motion (henceforth VLM) from GPS and DORIS data located at the sites are directly provided by SONEL and IDS. Even though GPS and DORIS trends are estimated only with limited years of data, following the studies of Wöppelmann et al. (2007) and Becker et al. (2012), we assume that these short term trend values (minimum 6 years of data) reflect long term VLM rates at the coast.

The vertical rates and their associated uncertainties from GPS and DORIS records are given in Table 2. At Cocos Island, the estimated VLM rate over 17 years obtained from GPS is 0.79 ± 0.27 mm/yr (time series available on http://www.sonel.org/-GPS-.html). Having no discontinuities in the time series, this value is considered in the estimation of the total relative sea level rate. The VLM rate at Diego Garcia between 1996 and 2010 accounts to -0.89 ± 0.19 mm/yr and this indicates subsidence. Even though there are some minor discontinuities in the GPS time series at this station, the VLM rate is considered. Malé in Maldives has both GPS and DORIS measures. The GPS estimate dates between 1999 and 2006 with a VLM rate of 0.01 ± 0.71 mm/yr. DORIS dates between 2005 and 2012 with VLM rates of -1.63 ± 0.24 mm/yr and -1.32 ± 0.38 mm/yr as provided by the two different teams. While the two DORIS VLM rates agree well and indicate subsidence, the VLM rate from GPS is estimated to be nearly zero. Considering that both the DORIS solutions and GPS use the same terrestrial reference frame (ITRF2008), the weighted mean VLM rate computed from GPS and two DORIS estimates (average of the three rate values weighted by their respective inverse square uncertainty) at this station was used. At Mahé, Seychelles, the GPS time series show very high spurious jumps in the beginning of the time series followed by large discontinuities all through the time series. The VLM rates obtained from the DORIS station by the two analysis centers also highly differ (-3.1 ± 0.16 mm/yr and 0.85 ± 0.32 mm/yr). With no proper means to validate the rates, the VLM rates at this station were discarded. In the Reunion Island, the VLM estimate from GPS accounts to -4.3 ± 0.68 mm/yr between 1998 and 2010. However the VLM estimates from the two DORIS

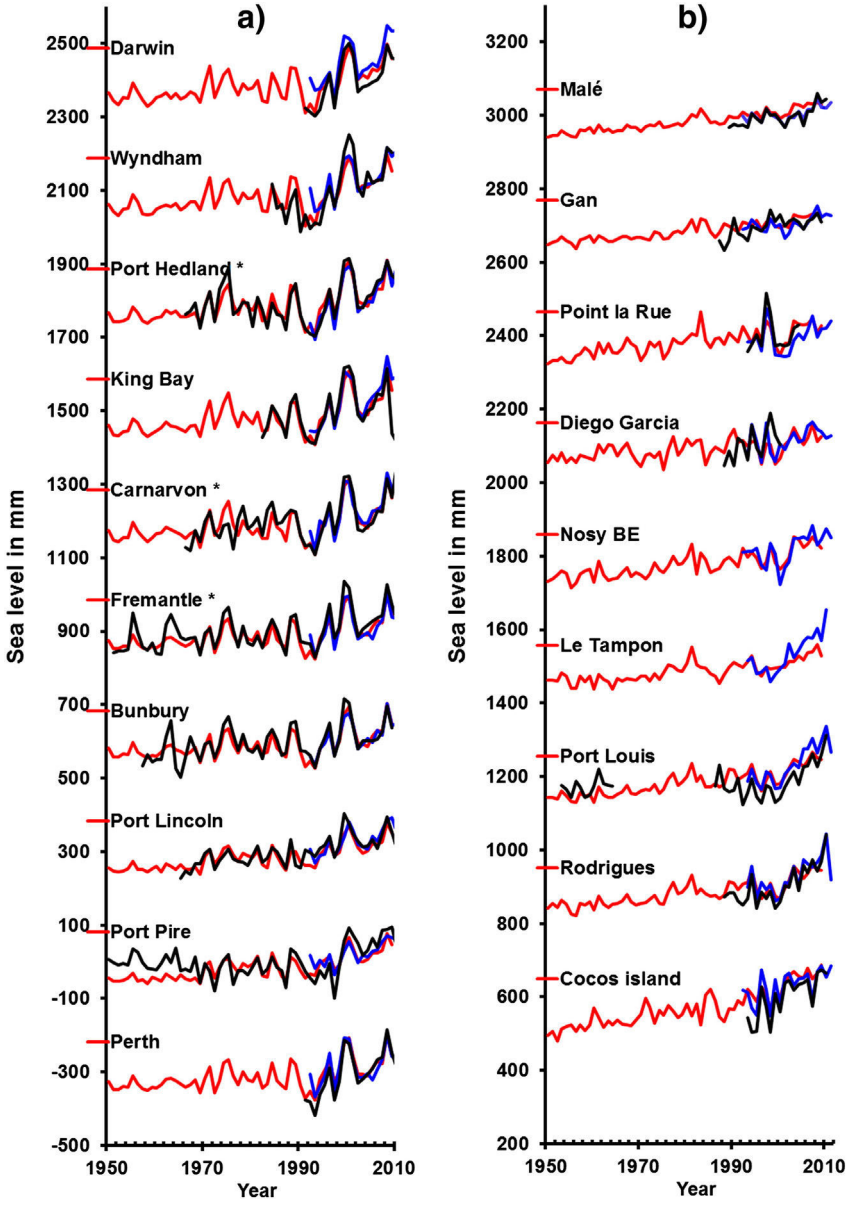

Fig. 7. Sea level time series at tide gauge sites in the (a) Western Australian coast and (b) Indian Ocean Islands. MRESL in red, tide gauge in black and altimetry in blue. (For interpretation of the references to color in this figure legend, the reader is referred to the web version of this article.)

analysis centers over 1999 and 2012 account to -1.27 ± 0.12 mm/yr and -1.51 ± 0.13 mm/yr. The discrepancy between DORIS and GPS rates at this island could be due to different VLM at those particular sites. The reliability of GPS time series in the Reunion island is questioned as the time series is nonlinear and exhibits two sudden dips in height level (which could either be instrumental error or volcanic instabilities or even anthropogenic causes) even after the position offsets have been corrected. Therefore the GPS based VLM rate at this station is discarded and the weighted mean VLM rate from the two DORIS analysis centers is considered in this study. At Perth, Australia, the rate of VLM estimates from the GPS data over 17 years accounts to -2.98 ± 0.34 mm/yr.

8. Total relative sea level change

As discussed in the previous sections, the total relative sea level change is given by the sum of the climatic-component of the sea level change (obtained from MRESL time series) and changes in vertical land motion (obtained from GPS and DORIS). Fig. 8 shows the total relative sea level change over 60 years at four locations in Indian Ocean. We see that at Cocos Island and Diego Garcia, the total relative sea level trend values account to 1.8 ± 0.3 mm/yr, a value identical to the global mean sea level rise over 60 years. Malé Hulule in the Maldives and Le Tampon in the Reunion Island shows total relative sea level trend values of 2.8 ± 0.1 mm/yr and of 2.6 ± 0.4 mm/yr respectively. These values are almost 1.5 times the long term global mean sea level trend. More than 50% of the total relative sea level rise at these two locations is contributed by subsidence. Total relative sea level trend at Perth in Australia over 60 years reaches a value of 4.2 ± 0.6 mm/yr with subsidence contributing around 71% to the total. This is more than twice the global mean sea level rise over the long term period. The factors contributing to high subsidence rates at this region are a subject of investigation by geophysicists. Featherstone et al. (2012) attribute subsidence at this region to ground water extraction in Yarragadee aquifers and show a subsidence rate of 4.6 mm/yr over 14 years with a subsidence rate of 6.1 mm/yr between 2000 and 2005. If this is the case, the subsidence in this region is anthropogenic in nature. This puts into question if the total-relative sea level change

Table 1
Locations of tide gauge records in Indian Ocean with their respective trend and error values. Trends and error values are also obtained from observed altimetry between 1992 and 2009 and MRESL records over 1950–2010, tide gauge time span and altimetry time span. The stars indicate the sites used in developing the MRESL grids. The symbol * replaces values that could not be calculated due to tide gauge records that were intermittent/absent. CF corresponds to Correlation Factor, which is a measure of correlation existing between two data sets.

Station name	Tide gauge					Altimetry (1992–2009)		MRESL 1950–2009		MRESL (tide gauge time span)			MRESL (altimetry time span)		
	Longitude	Latitude	Time span	Trend	Error	Trend	Error	Trend	Error	Trend	Error	CF	Trend	Error	CF
Chennai⋆	80.30	13.10	1950–2008	0.4	0.3	0.87	1.5	1.70	0.51	1.63	0.52	0.58	2.04	0.75	0.55
Cochin⋆	76.27	9.97	1950–2007	1.2	0.2	2.18	0.77	1.40	0.51	1.39	0.51	0.66	1.81	0.60	0.68
Mangalore	74.80	12.92	1976–2000	*	*	1.56	0.82	1.40	0.51	1.41	0.61	*	1.72	0.63	0.50
Nagapattinam	79.85	10.77	1971–1989	−2.4	1.3	2.28	1.46	1.40	0.51	1.53	1.00	0.56	1.87	0.76	0.59
Paradip	86.70	20.27	1966–2008	1.3	0.5	0.28	1.9	1.40	0.54	1.58	0.59	0.74	1.84	0.93	0.54
Tutucorin	78.20	8.75	1964–1991	−1.3	0.4	1.64	0.65	1.40	0.51	0.98	0.65	−0.02	1.70	0.58	0.56
Vishakapattinam⋆	83.28	17.68	1957–2008	1.1	0.3	2.86	1.46	1.30	0.51	1.24	0.52	0.77	2.18	0.95	0.78
Ko Taphao Noi	98.43	7.83	1950–2010	*	*	2.51	1.5	1.40	0.54	1.40	0.52	*	2.80	0.84	0.68
Pulau Langkawi	99.77	6.43	1986–2010	1.80	0.90	2.72	1.55	1.50	0.54	3.11	0.73	0.70	2.93	0.87	0.73
Lumut	100.62	4.23	1984–2010	1.00	0.80	3.79	1.60	1.50	0.54	2.28	0.85	0.74	3.38	0.99	0.73
Pelabhuhan Kelang	101.37	3.05	1984–2010	1.50	0.90	3.25	1.57	1.40	0.51	2.10	0.79	0.75	3.29	0.97	0.61
Jurang	103.72	1.30	1970–1997	−0.90	0.70	4.57	1.39	1.50	0.51	0.71	0.58	0.26	4.03	0.64	0.72
Sultan Shoal	103.65	1.23	1969–2011	2.10	0.53	3.90	1.32	1.50	0.51	2.73	0.59	0.64	4.04	0.64	0.71
Raffles light house	103.75	1.17	1973–2011	0.40	0.50	4.21	1.38	1.60	0.51	2.92	0.59	0.65	3.99	0.67	0.67
Darwin	130.85	−12.47	1991–2011	6.90	1.90	7.44	2.35	1.40	0.58	7.49	1.58	0.94	6.91	1.71	0.90
Wyndham	128.10	−15.45	1984–2010	6.20	1.70	6.69	2.13	1.40	0.58	3.74	1.25	0.88	6.89	1.77	0.91
Port Hedland⋆	118.57	−20.32	1966–2010	1.60	0.60	5.91	2.52	1.40	0.58	1.57	0.71	0.93	5.79	2.15	0.96
King Bay	116.75	−20.62	1982–2010	2.30	1.30	7.77	2.40	1.50	0.58	3.99	1.15	0.90	6.49	2.14	0.95
Carnarvon⋆	113.65	−24.90	1965–2010	2.10	0.56	6.16	2.40	1.30	0.58	1.63	0.71	0.83	6.02	2.24	0.97
Fremantle⋆	115.75	−32.07	1897–2010	1.40	0.30	3.85	2.34	1.20	0.54	1.18	0.55	0.93	4.91	1.90	0.93
Hillarys/Perth	115.74	−31.83	1991–2011	7.20	1.80	4.92	1.83	1.20	0.54	6.55	1.76	0.96	4.91	1.90	0.92
Bunbury	115.66	−33.32	1957–2010	1.34	0.37	4.34	1.87	1.10	0.54	1.22	0.58	0.86	4.99	1.85	0.97
Port Lincoln	135.87	−34.72	1965–2010	2.10	0.30	4.48	1.31	1.40	0.54	1.55	0.58	0.86	4.00	1.29	0.90
Port Pire	138.01	−33.18	1950–2010	0.80	0.30	4.57	1.01	1.40	0.54	1.42	0.53	0.65	3.98	1.20	0.84
Male-B Hulule	73.53	4.18	1989–2010	2.90	0.60	2.07	0.82	1.40	0.51	1.98	0.61	0.72	2.07	0.70	0.74
Gan	73.15	−0.68	1987–2009	2.80	0.64	1.79	0.96	1.30	0.51	1.81	0.60	0.43	1.76	0.71	0.65
Point la Rue	55.53	−4.67	1993–2004	1.85	4.10	1.51	1.94	1.50	0.54	0.88	2.71	0.76	1.65	1.38	0.74
Diego Garcia	72.40	−7.28	1988–2000	6.41	2.78	3.26	1.64	0.90	0.54	−4.10	1.85	−0.02	2.21	1.29	0.56
Nosy B	48.28	−13.40	1958–1972	*	*	4.11	1.81	1.50	0.54	−0.59	1.05	*	2.65	1.25	0.89
Le Tampon	55.57	−21.21	*	*	*	7.50	1.50	1.20	0.65	*	*	*	1.72	1.21	0.32
Port Louis	57.50	−20.15	1986–2011	2.60	1.08	7.25	1.32	1.70	0.51	2.80	0.81	0.68	3.81	1.13	0.82
Rodrigues Island	63.42	−19.67	1986–2011	3.60	1.10	5.09	1.57	1.60	0.51	2.46	0.96	0.81	3.21	1.27	0.73
Cocos island	96.89	−12.12	1993–2011	8.29	1.89	4.20	1.40	2.60	0.54	5.36	1.19	0.84	5.50	1.08	0.74

over 60 years calculated in this study at Perth is overestimated since subsidence is anthropogenic in nature. A detailed study is needed in this zone to analyze the rates of subsidence over longer time period. For now, considering the fact that the GPS estimated VLM rate at Perth covers a period of 17 years, we use the same to calculate the total-relative sea level change. However it is highly probable that this estimation of total relative sea level change over the long term period at Perth is overestimated and may not reflect the exact scenario of the past.

9. Summary and conclusion

The Indian Ocean is the home to many tropical low lying islands like Maldives, Seychelles, Mauritius, and Reunion and highly populated coastal regions like Bangladesh which have been gaining a lot of attention during the recent years owing to sea level rise and its impacts. In this work, we studied the long term regional sea level variability in the Indian Ocean. We find that the mean sea level rise over this region between 1950 and 2009 amounts to 1.5 mm/yr, a value lesser (although not statistically different) than the global mean sea level rise of 1.8 mm/yr. The long term spatial trend patterns show eastward to westward increase in regional sea level trend below 15°S latitude. This pattern grows stronger from 1993 thereby confirming the influence of Western Tropical Pacific trade wind intensification propagating into the Indian Ocean also. We also determined that the steric and Indian Ocean Dipole events play an important role in driving the climatic component of the sea level change in the Indian Ocean. Total climate-related sea level change is also studied in different regions within the Indian Ocean between 1950 and 2009 and was found that in most cases, the total climate-related sea level change lies well within or lesser than the range of global mean sea level rise over 60 years. The mean sea level trends in the coastal Indian-subcontinent, South-East Asian coasts, Western Australian coasts and Indian Ocean Islands are 1.4 mm/yr, 1.5 mm/yr, 1.3 mm/yr and 1.5 mm/yr respectively. However South-East Asian locations and Western Australian coast showed very high sea level trends during the two recent decades (3.5 mm/yr in the case of South East Asia and 5.5 mm/yr in the case of Western Australia) presumably linked to Western Tropical Pacific trade wind intensification.

A special focus was also made in the case of Maldives Island to estimate the total-climate related sea level change. It was found that even though there is a positive sea level trend at this location over 60 years, the variability of interannual sea level at this island was found lower than those in the rest of the Indian Ocean considered in this study. The results obtained at this location were also consistent with those obtained by Church et al. (2006).

In this study, we also estimated the total relative sea level change at 5 locations: Cocos and Diego Garcia Islands (British Indian Ocean Territory), Le Tampon in Reunion Islands and Perth in Western Australia. In Cocos Island and Diego Garcia, the total relative sea level rise is equal to the global mean sea level rise over 60 years whereas in the case of Malé Hulule, Le Tampon and Perth, the values exceed the global mean. The contribution of subsidence at Malé Hulule and Le Tampon exceed 50% while at Perth, it exceeds 70%. Studies (e.g. Featherstone et al., 2012) suggest ground water extraction as the main contributor to the land subsidence in Perth indicating the cause of subsidence to be anthropogenic in nature. Therefore it is likely that the long term total-relative sea level change at this location is overestimated.

Overall, this study demonstrates the importance of regional sea level variability. Our results show that during 1950–2009, the climate-related sea level change in Indian Ocean is in the same order as that of the global

Table 2
GPS (from ULR 5) and DORIS (from lca11wd02 and ign11wd01) rates with their respective error values and weighted mean vertical land motion rates at few available sites in the Indian Ocean. The symbol * corresponds to DORIS unavailability.

Colocalised tide gauge station	GPS						DORIS						Weighted mean	
	Acronym of the GPS sites	Lon	Lat	ULR5			Acronym of DORIS sites	lca11wd02			ign11wd01			
				Years	Vertical velocity (mm/yr)	Error (mm/yr)		Years	Vertical velocity (mm/yr)	Error (mm/yr)	Years	Vertical velocity (mm/yr)	Error (mm/yr)	Vertical velocity (mm/yr)	Error (mm/yr)
Cocos island	COCO	96.8	−12.2	1994–2010	0.79	0.27	*	*	*	*	*	*	*	0.79	0.27
Diego garcia	DGAR	72.4	−7.3	1996–2010	−0.89	0.19	*	*	*	*	*	*	*	−0.89	0.19
Male hulule	MALD	73.5	4.2	1999–2006	0.01	0.71	MALB	2005–2012	−1.63	0.24	2005–2012	−1.32	0.38	−1.42	0.04
Pt la Rue/Mahe	SEY1	55.5	−4.7	1995–2010	−3.15	0.67	MAHB	2001–2012	−3.77	0.22	2003–2012	0.85	0.32	*	
Le tampon/reunion	REUN	55.6	−21.2	1998–2010	−4.3	0.68	REUB	1999–2012	−1.27	0.12	1998–2013	−1.51	0.13	−1.38	0.01
Hillary/Perth	PERT	115.9	−31.8	1993–2010	−2.98	0.34	*	*	*	*	*	*	*	−2.98	0.34

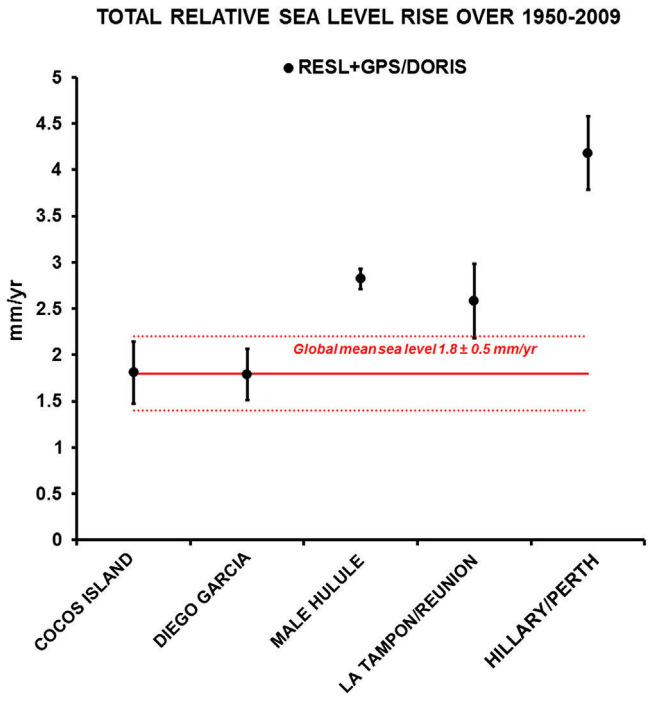

Fig. 8. Total relative sea level change estimated over 1950–2010 in the Indian Ocean.

mean sea level rise. This does not mean that the coastal and island zones of Indian Ocean do not face sea level rise impact. In addition to the climatic component of sea level change, vertical land motions pose higher threats to coastal zones and islands. In this article, a study on the vertical land motion rates and henceforth the total relative sea level change has been performed along the Western Australian coast and central Indian Ocean islands. Our results show the impact of vertical land motions on sea level change and also indicate the importance of understanding the nature of such land motions in order to be able to study local sea level change over the past.

Acknowledgments

The authors would like to thank the reviewers for their comments and suggestions that led to significant improvement of the manuscript. H. Palanisamy was successively supported by ANR CNRS grant number ANR-09-CEP-001-01 (Project CECILE) and a PhD grant from CNES and CLS. The altimetry products were produced by SSALTO/DUACS and distributed by AVISO. We also acknowledge the SONEL and IDS database for providing comprehensive access to GPS and DORIS data sets.

References

Ablain, M., Cazenave, A., Valladeau, G., Guinehut, S., 2009. A new assessment of the error budget of global mean sea level rate estimated by satellite altimetry over 1993–2008. Ocean Sci. 5 (2), 193–201.

Altamimi, Z., Collilieux, X., Metivier, L., 2011. ITRF2008, an improved solution of the International Terrestrial Reference Frame. J. Geod. 85 (8), 457–473. http://dx.doi.org/10.1007/s00190-011-0444-4.

Becker, M., Meyssignac, B., Letetrel, C., Llovel, W., Cazenave, A., Delcroix, T., 2012. Sea level variations at tropical pacific islands since 1950. Glob. Planet. Chang. 80–81, 85–98. http://dx.doi.org/10.1016/j.gloplacha.2011.09.004.

Behera, S.K., Yamagata, T., 2001. Subtropical SST dipole events in the Southern Indian Ocean. Geophys. Res. Lett. 28 (2), 327–330. http://dx.doi.org/10.1029/2000GL011451.

Bindoff, N.L., Willebrand, J., Artale, V., Cazenave, A., Gregory, J., Gulev, S., Hanawa, K., Le Quere, C., Levitus, S., Nojiri, Y., et al., 2007. "Observations: oceanic climate change and sea level". Climate change 2007: the physical science basis. In: Solomon, S., Qin, D. (Eds.), Contribution of Working Group I to the Fourth Assessment Report of

the Intergovernmental Panel on Climate Change. M. Cambridge University Press, Cambridge.
Bird, E.C.F., 1996. Coastal erosion and rising sea level. In: Millimann, J.D., Haq, B.U. (Eds.), Sea Level Rise and Coastal Subsidence. Kluwer Academic Publishers, Dordrecht, the Netherlands, pp. 87–103.
Black, E., Slingo, J., Sperber, K.R., 2003. An observational study of the relationship between excessively strong short rains in coastal East Africa and Indian Ocean SST. Mon. Weather Rev. 131 (1), 74–94. http://dx.doi.org/10.1175/1520-0493(2003) 131.
Brodeau, L., Barnier, B., Treguier, A.M., Penduff, T., Gulev, S., 2010. An ERA40-based atmospheric forcing for global ocean circulation models. Ocean Model. 31, 88–104.
Bruun, P., 1962. Sea-level rise as a cause of shoreline erosion. J. Waterw. Harb. Div. 88 (1–3), 117–130.
Busalacchi, A.J., Cane, M.A., 1985. Hindcasts of sea level variations during the 1982–83 El Niño. J. Phys. Oceanogr. 15, 213–221.
Carton, J.A., Giese, B.S., 2008. A reanalysis of ocean climate using Simple Ocean Data Assimilation (SODA). Mon. Weather Rev. 136 (8), 2999–3017. http://dx.doi.org/10.1175/2007MWR1978.1.
Cazenave, A., Llowel, W., 2010. Contemporary sea level rise Annual Review of Marine Science 2, 145–173.
Chao, Y., Halpern, D., Perigaud, C., 1993. Sea surface height variability during 1986–1988 in the Tropical Pacific Ocean. J. Geophys. Res. 98 (C4), 6947–6959. http://dx.doi.org/10.1029/92JC02984.
Church, J.A., White, N.J., 2011. Sea-level rise from the late 19th to the early 21st century. Surv. Geophys. 32 (4–5), 585–602. http://dx.doi.org/10.1007/s10712-011-9119-1.
Church, J.A., White, N.J., Coleman, R., Lambeck, K., Mitrovica, J.X., 2004. Estimates of the regional distribution of sea level rise over the 1950–2000 period. J. Clim. 17, 2609–2625.
Church, J.A., White, N.J., Hunter, J.R., 2006. Sea-level rise at tropical Pacific and Indian Ocean islands. Glob. Planet. Chang. 53 (3), 155–168. http://dx.doi.org/10.1016/j.gloplacha.2006.04.001.
Church, J.A., Gregory, J.M., White, N.J., Platten, S.M., Mitrovica, J.X., 2011. Understanding and projecting sea level change. Oceanography 24 (2), 130–143.
Delcroix, T., 1998. Observed surface oceanic and atmospheric variability in the tropical Pacific at seasonal and ENSO timescales: a tentative overview. J. Geophys. Res. 103 (C9), 18611–18633.
Efron, B., Tibshirani, R.J., 1993. An Introduction to the Bootstrap. Chapman & Hall.
Featherstone, W.E., Filmer, M.S., Penna, N.T., Morgan, L.M., Schenk, A., 2012. Anthropogenic land subsidence in the Perth Basin: challenges for its retrospective geodetic detection. J. R. Soc. West. Aust. 95, 53–62.
Hamlington, B.D., Leben, R.R., Nerem, R.S., Han, W., Kim, K.-Y., 2011. Reconstructing sea level using cyclostationary empirical orthogonal functions. J. Geophys. Res. Oceans 116. http://dx.doi.org/10.1029/2011JC007529.
Hamlington, B.D., Leben, R.R., Strassburg, M.W., Nerem, R.S., Kim, K.-Y., 2013. Contribution of the Pacific Decadal Oscillation to global mean sea level trends. Geophys. Res. Lett. 40, 5171–5175. http://dx.doi.org/10.1002/grl.50950.
Han, W., Meehl, G.A., Rajagopalan, B., Fasullo, J.T., Hu, A., Lin, J., Large, W.G., et al., 2010. Patterns of Indian Ocean sea-level change in a warming climate. Nat. Geosci. 3 (8), 546–550. http://dx.doi.org/10.1038/ngeo901.
Hanna, E., Navarro, F.J., Pattyn, F., Domingues, C., Fettweis, X., Ivins, E., Nicholls, R.J., Ritz, C., Smith, B., Tulaczyk, S., Whitehouse, P., Zwally, J., 2013. Ice-sheet mass balance and climate change. Nature 498, 51–59. http://dx.doi.org/10.1038/nature12238.
Hastenrath, S., 2007. Circulation mechanisms of climate anomalies in East Africa and the Equatorial Indian Ocean. Dyn. Atmos. Oceans 43 (1–2), 25–35. http://dx.doi.org/10.1016/j.dynatmoce.2006.06.002.
Hendricks, J.R., Leben, R.R., Born, G.H., Koblinsky, C.J., 1996. Empirical orthogonal function analysis of global TOPEX/POSEIDON altimeter data and implications for detection of global sea level rise. J. Geophys. Res. 101 (C6), 14,131–14,145. http://dx.doi.org/10.1029/96JC00922.
Ishii, M., Kimoto, M., 2009. Reevaluation of historical ocean heat content variations with time-varying XBT and MBT depth bias corrections. J. Oceanogr. 65 (3), 287–299. http://dx.doi.org/10.1007/s10872-009-0027-7.
Kalnay, E., Kanamitsu, M., Kistler, R., Collins, W., Deaven, D., Gandin, L., Iredell, M., et al., 1996. The NCEP/NCAR 40-year reanalysis project. Bull. Am. Meteorol. Soc. 77 (3), 437–471. http://dx.doi.org/10.1175/1520-0477(1996) 077.
Kaplan, A., Kushnir, Y., Cane, M.A., 2000. Reduced space optimal interpolation of historical marine sea level pressure: 1854–1992. J. Clim. 13, 2987–3002.
Le Cozannet, G., Garcin, M., Petitjean, L., Cazenave, A., Becker, M., Meyssignac, B., Walker, P., Devilliers, C., Le Brun, O., Lecacheux, S., Baills, A., Bulteau, T., Yates, M., Wöppelmann, G., 2013. Exploring the relation between sea level rise and shoreline erosion using sea level reconstructions: an example in French Polynesia. J. Coast. Res. Special Issue No. 65, 2137–2142 (ISSN 0749-0208).
Le Traon, P.-Y., Ogor, F., 1998. ERS-1/2 orbit improvement using TOPEX/POSEIDON: the 2 cm challenge. J. Geophys. Res. 103 (C4), 8045. http://dx.doi.org/10.1029/97JC01917.
Levitus, S., Antonov, J.I., Boyer, T.P., Baranoval, O.K., Garcia, H.E., Locarnini, R.A., Mishonov, A.V., Reagan, J.R., Seidov, D., Yarosh, E.S., Zweng, M.M., 2012. World ocean heat content and thermosteric sea level change (0–2000 m), 1955–2010. Geophys. Res. Lett. 39, L10603. http://dx.doi.org/10.1029/2012GL051106.
Llovel, W., Cazenave, A., Rogel, P., Lombard, A., Bergé-Nguyen, M., 2009. 2-D reconstruction of past sea level (1950–2003) using tide gauge records and spatial patterns from a general ocean circulation model. Clim. Past Discuss. 5 (2), 1109–1132. http://dx.doi.org/10.5194/cpd-5-1109-2009.
Lombard, A., Cazenave, A., Le Traon, P.Y., Ishii, M., 2005. Contribution of thermal expansion to present-day sea-level change revisited. Glob. Planet. Chang. 47 (1), 1–16. http://dx.doi.org/10.1016/j.gloplacha.2004.11.016.
Merrifield, M.A., Maltrud, M.E., 2011. Regional sea level trends due to a Pacific trade wind intensification. Geophys. Res. Lett. 38. http://dx.doi.org/10.1029/2011GL049576.
Meyssignac, B., Cazenave, A., 2012. Sea level: a review of present-day and recent-past changes and variability. J. Geodyn. 58, 96–109. http://dx.doi.org/10.1016/j.jog.2012.03.005.
Meyssignac, B., Llovel, W., Cazenave, A., Salas-Melia, D., Becker, M., 2012a. Tropical Pacific spatial trend patterns in observed sea level: internal variability and/or anthropogenic signature? Clim. Past 8, 787–802. http://dx.doi.org/10.5194/cp-8-787-2012.
Meyssignac, B., Becker, M., Llovel, W., Cazenave, A., 2012b. An assessment of two-dimensional past sea level reconstructions over 1950–2009 based on tide gauge data and different input sea level grids. Surv. Geophys. 33 (5), 945–972. http://dx.doi.org/10.1007/s10712-011-9171-x.
Milne, G.A., Gehrels, W.R., Hughes, C.W., Tamisiea, M.E., 2009. Identifying the causes of sea-level change. Nat. Geosci. http://dx.doi.org/10.1038/ngeo544.
Nerem, R.S., Chambers, D.P., Choe, C., Mitchum, G.T., 2010. Estimating mean sea level change from the TOPEX and Jason altimeter missions. Mar. Geod. 33, 435–446. http://dx.doi.org/10.1080/01490419.2010.491031.
Palanisamy, H., Becker, M., Meyssignac, B., Henry, O., Cazenave, A., 2012. Regional sea level change and variability in the Caribbean Sea since 1950. J. Geod. Sci. 2, 125–133. http://dx.doi.org/10.2478/v10156-011-0029-4.
Peltier, W.R., 2004. Global glacial isostasy and the surface of the ice-age Earth: the ICE-5G(VM2) model and GRACE. Ann. Rev. Earth Planet. Sci. 32, 111–149.
Penduff, T., Juza, M., Brodeau, L., Smith, G.C., Barnier, B., Molines, J.-M., Treguier, A.-M., Madec, G., 2010. Impact of global ocean model resolution on sea-level variability with emphasis on interannual time scales. Ocean Sci. 6 (1), 269–284. http://dx.doi.org/10.5194/os-6-269-2010.
Peng, D., Palanisamy, H., Cazenave, A., Meyssignac, B., 2013. Interannual sea level variations in South China Sea over 1950–2009. Mar. Geod. 36 (2), 164–182. http://dx.doi.org/10.1080/01490419.2013.771595.
Preisendorfer, R.W., 1988. Principal component analysis in meteorology and oceanography. Developments in Atmospheric Science, vol. 17. Elsevier (425 pp.).
Ray, R.D., Douglas, B.C., 2011. Experiments in reconstructing twentieth-century sea levels. Prog. Oceanogr. 91 (4), 496–515. http://dx.doi.org/10.1016/j.pocean.2011.07.021.
Rosner, B., 1975. On the detection of many outliers. Technometrics 17 (2), 221. http://dx.doi.org/10.2307/1268354.
Saji, N.H., Yamagata, T., 2003. Possible impacts of Indian Ocean Dipole mode events on global climate. Clim. Res. 25, 151–169. http://dx.doi.org/10.3354/cr025151.
Saji, N.H., Goswami, B.N., Vinayachandran, P.N., Yamagata, T., 1999. A dipole mode in the tropical Indian Ocean. Nature 401 (6751), 360–363. http://dx.doi.org/10.1038/43854.
Santamaría-Gómez, A., Gravelle, M., Collilieux, X., Guichard, M., Martín Míguez, B., Tiphaneau, P., Wöppelmann, G., 2012. Mitigating the effects of vertical land motion in tide gauge records using a state-of-the-art GPS velocity field. Glob. Planet. Chang. 98–99, 6–17. http://dx.doi.org/10.1016/j.gloplacha.2012.07.007 (*Science* 2, 145–173.).
Soudarin, L., Crétaux, J.F., 2006. A model of present-day tectonic plate motions from 12 years of DORIS measurements. J. Geod. 80 (8–11), 609–624. http://dx.doi.org/10.1007/s00190-006-0090-4.
Stammer, D., Cazenave, A., Ponte, R.M., Tamisiea, M.E., 2013. Causes for contemporary regional sea level changes. Ann. Rev. Mar. Sci. 5. http://dx.doi.org/10.1146/annurev-marine-121211-172406.
Toumazou, V., Cretaux, J.F., 2001. Using a Lanczos eigensolver in the computation of empirical orthogonal functions. Mon. Weather Rev. 129, 1243–1250.
Volkov, D.L., Larnicol, G., Dorandeu, J., 2007. Improving the quality of satellite altimetry data over continental shelves. J. Geophys. Res. Oceans 112 (C6). http://dx.doi.org/10.1029/2006JC003765.
Willis, P., Fagard, H., Ferrage, P., Lemoine, F.G., Noll, C.E., Noomen, R., Otten, M., Ries, J.C., Rothacher, M., Soudarin, L., Tavernier, G., Valette, J.J., 2010a. The International DORIS Service, toward maturity. Adv. Space Res. 45 (12), 1408–1420. http://dx.doi.org/10.1016/j.asr.2009.11.018.
Willis, P., Boucher, C., Fagard, H., Garayt, B., Gobinddass, M.-L., 2010b. Contributions of the French Institut Géographique National (IGN) to the International DORIS Service. Adv. Space Res. 45 (12), 1470–1480. http://dx.doi.org/10.1016/j.asr.2009.09.019.
Woodworth, P.L., 2005. Have there been large recent sea level changes in the Maldive Islands? Glob. Planet. Chang. 49 (1–2), 1–18. http://dx.doi.org/10.1016/j.gloplacha.2005.04.001.
Wöppelmann, G., Martin Miguez, B., Bouin, M.-N., Altamimi, Z., 2007. Geocentric sea-level trend estimates from GPS analyses at relevant tide gauges world-wide. Glob. Planet. Chang. 57 (3–4), 396–406. http://dx.doi.org/10.1016/j.gloplacha.2007.02.002.
Wyrtki, K., 1984. The slope of sea level along the equator during the 1982/1983 El Niño. J. Geophys. Res. 89 (C6), 10,419–10,424. http://dx.doi.org/10.1029/JC089iC06p10419.
Zebiak, S.E., Cane, M.A., 1987. A model El Niño-southern oscillation. Mon. Weather Rev. 115, 2262–2278.
Zhang, R.H., Levitus, S., 1996. Structure and evolution of interannual variability of the tropical Pacific upper ocean temperature. J. Geophys. Res. 101 (C9), 20,501–20,524. http://dx.doi.org/10.1029/96JC01805.
Zhang, K.Q., Douglas, B.C., Leatherman, S.P., 2004. Global warming and coastal erosion. Clim. Chang. 64, 1–2.

3.2.2 Caribbean Sea

The Caribbean Sea, located between 9°N-22°N latitudes and 60°W-89°W longitudes is bound by the South American continent in the south, Central America in the west. The Caribbean region, situated largely on the Caribbean plate comprises more than 7000 islands, islets, reefs and cays. They separate the Caribbean Sea from the Atlantic Ocean. Most of these islands lie close to the Caribbean tectonic plate and hence are geologically active with earthquakes and volcanic eruptions. Situated in the tropical zone, this region is also highly impacted by tropical hurricanes. The Caribbean islands are considered to be one of the vulnerable islands under future se level rise (*Nicholls and Cazenave*, 2010) with more than 50% of the population living within 1.5km of the shore (*Mimura et al*., 2007). Sea level rise in this region poses various threats that can be related to increase in both frequency and intensity of the tropical hurricanes, bleaching and changed calcification rates of coral reefs etc.

Using 11 tide gauge time series from South America and Caribbean region with records over 10 years, *Aubrey et al.*, (1988) showed varying sea level trend in the Caribbean region with changes in vertical land motion dominating the coastal trends. However, absence of good quality tide gauges hinder long-term sea level analysis in the Caribbean region. *Jury*, (2011) studied the long term sea level variability and trend in the Caribbean Sea from 1958 to 2007 by making use of ocean reanalysis data and found that the sea level rates in this region are similar to that of the global mean rates with higher values off Venezuela and Cuba. In our study, by making use of past sea level reconstruction data of *Meyssignac et al*., (2012), long-term regional sea level variability in the Caribbean Sea between 1950 and 2009 was also analyzed. However, estimation of total relative sea level change was not feasible in this region due to the non-availability of GPS/DORIS measures at the time the study was performed. Therefore, only the climatic component (global mean sea level + regional variability) of the sea level was analyzed. This study has been published as an article titled 'Regional sea level change and variability in the Caribbean Sea since 1950'. Following this study, another new study (*Torres and Tsimplis*, 2013) has also been performed in the Caribbean region using tide gauges and satellite altimetry data. At time periods that overlap to the period of our study, they have shown that sea level rates in the Caribbean are consistent to that of our study. Furthermore, with access to certain GPS data in the Caribbean region, *Torres and Tsimplis*, (2013) have also shown that subsidence plays an

important role in the total relative sea level change with certain locations subsiding at the rate of - 2.4 mm/yr.

Summary of the article: 'Regional sea level change and variability in the Caribbean Sea since 1950' (the original article is inserted at the end of this section).

In this study, as mentioned above, we analyzed the long-term climatic component of sea level change in the Caribbean Sea using the ensemble mean sea level reconstruction data. Only 10 tide gauge records (7 records having more than 30 years of data) were available in the region of our study. Therefore these records were mainly used for the validation of the reconstruction based sea level time series interpolated at the tide gauge locations. Over the altimetry era, the mean sea level trend averaged over the Caribbean Sea amounts to 1.7±0.6 mm/yr with strong positive trend patterns in the range of 4 mm/yr to5 mm/yr occurring along the coastal region of the South American continent. Negative sea level trend values in the range of -1 mm/yr to -2mm/yr were observed in the central Caribbean Sea. Over the 1950-2009 period, mean reconstruction based regional sea level trend value amounts to 1.8±0.1 mm/yr, a value similar to that of the global mean rate over 60 years.

Good correlations of the Caribbean interannual sea level time series with the ENSO indices such as NINO3.4 and CAR (Caribbean SST index) especially since 1985 indicates that the interannual sea level variability in this region is influenced by and responds to ENSO events. Furthermore, Northern Caribbean (that includes the island nations of Cayman, Cuba, Haiti, Dominican Republic, Jamaica, and Puerto Rico etc.) was found to exhibit interannual variability at magnitudes higher than those of the Southern or Eastern Caribbean regions. This coincides with the studies of *Goldenberg et al.*, (2001) and *Pielke et al.*,(2003) who have shown increase in hurricane activity and intensity in the Northern Caribbean when compared to the other Caribbean regions. The increased activity and intensity of the tropical hurricanes have been attributed to the simultaneous increases in the North Atlantic Sea Surface Temperature (SST) and decrease in the vertical wind shear. It is possible that this also explains a part of the Caribbean interannual sea level variability. Future studies are however needed to investigate this.

Journal of Geodetic Science

• 2(2) • 2012 • 125-133 DOI: 10.2478/v10156-011-0029-4 •

Regional sea level change and variability in the Caribbean sea since 1950

Research Article

H. Palanisamy[1]*, M. Becker[2], B. Meyssignac[1], O. Henry[1], A. Cazenave[1]

1 *LEGOS/OMP, Toulouse, France*
2 *UMR 228 ESPACE-DEV/UAG, Cayenne, French Guiana*

Abstract:
We investigate the regional variability in sea level in the Caribbean Sea region over the past 60 years (1950-2009) using an Empirical Orthogonal Function (EOF)-based 2-dimensional past sea level reconstruction (a mean of 3 reconstructions based on few long tide gauge records and different sea level grids from satellite altimetry and ocean circulation models) and satellite altimetry data for the last two decades. We find that over the past 60 years, the mean rate of sea level rise in the region was similar to the global mean rise (∼1.8 mm/yr). The interannual mean sea level of the placeCaribbean region appears highly correlated with El Nino-Southern Oscillation (ENSO) indices. Interpolation of the sea level reconstruction grid at different sites, in particular at the Caribbean Islands where tide gauge records are either very short or inexistent, shows that locally, the sea level trend is on the order of 2 mm/yr, i.e. only slightly larger than the mean trend over the region. Besides, correlation with ENSO is in general good, especially since the mid-1980s. We also find a significant correlation between the interannual variability in sea level and hurricane activity, especially over the past decade during which hurricane intensity and sea level interannual variability have both increased.

Keywords:
Caribbean Sea • sea level variability • 2-D past sea level reconstruction • satellite altimetry • tide gauge • ENSO • hurricane

Received 23-03-2012 ; accepted 06-04-2012

1. Introduction

Sea level is a very sensitive indicator of climate change and variability as it integrates the responses of all components of the climate system to natural and human-induced forcing. Sea level also reflects the natural variability of the climate system. During the 20th century, the global mean sea level (GMSL) has risen at an average rate of ∼1.8 mm/yr (e.g., Church and White, 2011). Since the early 1990s, sea level is routinely measured by high-precision satellite altimetry which indicates a GMSL rise of 3.2 mm/yr since over 1993-2011. Sea level budget studies conducted over the altimetry era (since 1993) have shown the GMSL rise results from ocean thermal expansion (contributing by ∼30%) and land ice loss from glaciers and the Greenland and Antarctica ice sheets (contributing in total to ∼55%-60%) (e.g., Church et al., 2011, Cazenave and Llovel, 2010, Cazenave and Remy, 2011).

Satellite altimetry has revealed high regional variability in the rates of sea level rise, with faster rates (up to 3 times than the global mean) in the western Pacific, North Atlantic and southern oceans. The main cause of regional variability over the altimetry era is non uniform ocean heat content as well as salinity variations (e.g., Lombard et al., 2005, 2009). 2-dimensional past sea level reconstructions developed to study the regional variability in sea level prior to the altimetry era (e.g., Church et al., 2004, Llovel et al., 2009, Ray and Douglas, 2011, Meyssignac et al., 2012a) have shown that the spatial trend patterns are not stationary but fluctuate in time and space in responses to the natural modes of the ocean-atmosphere coupled system like El Nino-Southern Oscillation (ENSO), Pacific Decadal Oscillation (PDO), North Atlantic Oscillation (NAO) (e.g., Meyssignac et al, 2012a, b). This indicates that, at regional scale,

*E-mail: hindu@legos.obs-mip.fr, 18, Av. E. Belin, 31400 Toulouse, France, tel. +33 5 61 33 29 72

there is a low-frequency (multidecadal) component of the regional variability that superimposes to the GMSL rise. This component may either amplify or reduce the GMSL rise. When investigating the effective rate of sea level change in selected regions, it is of primary importance to account for this regional component in addition to the global mean rise. In a previous study focusing on the western tropical Pacific islands, (Becker et al., 2012) found that at Funafuti, an island in the Tropical Pacific belonging to the nation of Tuvalu, because of the low-frequency regional variability component, the total (absolute) sea level rise is almost three times the global mean rate of sea level rise over the past half century (i.e., $\sim$5 mm/yr versus 1.8 mm/yr over 1950-2010). This shows the importance of estimating the rate of sea level rise not only globally but also in terms of regional variability in order to understand the level of impacts that the sea level rise can have on the local population.

In the present study, we focus on the Caribbean Sea, a region surrounded by highly populated countries and islands, and develop an approach similar to that of (Becker et al., 2012) to determine the total sea level change (i.e., GMSL plus regional variability) in this area since 1950.

The Caribbean Sea, located between 9°N and 22°N latitude and between 60°W and 89°W longitude is bound by South America to the South, Central America to the West. The Antilles, a chain of islands, separate the Caribbean Sea from the Atlantic Ocean to the North and East and from the Gulf of Mexico to the South West. The Caribbean region, situated largely on the Caribbean plate comprises more than 7000 islands, islets, reefs and cays. Most of the Caribbean islands lie close to the boundaries of the Caribbean plate and hence are geologically active with earthquakes from time to time and a number of volcanic activities. The Caribbean islands are considered to be one of the vulnerable islands under future sea level rise (Nicholls and Cazenave, 2010) with more than 50% of the population living within 1.5 km of the shore (Mimura et al., 2007).

To estimate the low-frequency regional sea level variability in the Caribbean, we make use of an Empirical Orthogonal Function (EOF)-based (Preisendorfer, 1988) 2-dimensional past sea level reconstruction (Meyssignac et al., 2012a). This is a mean of 3 reconstructions that combines nearly one hundred long tide gauge records (1950-2009) with different sea level grids of shorter duration. The Caribbean does not possess many good quality tide gauge records and even the few available (about 10) do not cover the whole 60 years period. Of the available records, only Magueyes has been used in the global sea level reconstruction. Thus the reconstruction is an important tool to study the regional sea level variability. To understand what drives the Caribbean Sea regional variability, we estimate the effects of ocean temperature and salinity on the observed sea level variations and also compare the sea level with different climatic indices, in particular ENSO indices. We also investigate a potential link between sea level variability and hurricane activity in the Caribbean region.

2. Data

2.1. Satellite Altimetry

We use the DT-MSLA "Ref" series of satellite altimetry data provided by Collecte Localisation Satellite (http://www.aviso.oceanobs.com/en/data/products/sea-surface-height-products/global/msla/index.html). The data set is based on the combination of several altimetry missions namely Topex/Poseidon (T/P), Jason-1 and 2, Envisat and ERS 1 and 2. It is a global homogenous inter-calibrated dataset based on a global crossover adjustment that considers T/P and then Jason-1/2 as reference missions. Usual geophysical corrections are applied: solid Earth, ocean and pole tides, wet and dry troposphere, ionosphere (see Ablain et al., 2009 for details) and inverted barometric correction (Carrere and Lyard, 2003). The altimetry data set is used over the time span from January 1993 until December 2009. It is available as 0.25° x 0.25°Mercator projection grids at weekly intervals.

2.2. Tide gauges

Revised Local Reference monthly mean sea level data of the Permanent Service for the Mean Sea Level (PSMSL; Woodworth and Player, 2003; http://www.psmsl.org/) are used in this study. As mentioned above, the tide gauge coverage in the Caribbean Sea region is rather poor. Only 7 tide gauges have $>$30 years of data between 1950 and 2009. In this study, we have made use of 10 tide gauge records: 7 having $>$ 30 years of data and 3 having data only between 15 to 20 years but of good quality. Linear interpolation was performed to introduce missing data in the gaps whenever the gaps are $\leq$ 4 consecutive years (otherwise the record is not considered). Gaps and discontinuities occur in the tide gauge records due to natural factors like earthquakes or changes in instrumentation or even due to anthropogenic factors. Fig. 1 (as star symbols) shows the location of the tide gauges and their characteristics are given in Table 1 (in Fig. 1 -as blue dots- and Table 1 are also listed a few additional tide gauges with shorter records, records with time gaps exceeding 4 consecutive years or incorrect tide gauge data. In view of the poor quality of the tide gauge records, only the past sea level reconstruction (see Section 2.3), and observed altimetry data have been considered in these locations in order to study the past and recent sea level variability.

The tide gauge time series have been corrected for the inverted barometric response of sea level to atmospheric pressure forcing using the surface pressure grids from the National Centre for Environmental Prediction (NCEP, Kalnay et al., 1996). Glacial Isostatic Adjustment (GIA) is very small in the placeCaribbean region and henceforth the tide gauge records have not been corrected for GIA. In order to concentrate only on the interannual variability, the seasonal cycles have been filtered through a least-squares fit of 12-month and 6-month period sinusoids.

Table 1. Tide gauge locations, MRESL and altimetry trends at the tide gauge locations, correlation coefficients between the detrended tide gauge and detrended MRESL and between detrended tide gauge and detrended altimetry. Also shown is the correlation existing between detrended MRESL and detrended altimetry-based sea level over 1993-2009.

Tide Gauge Stations	Tide Gauge							MRESL 1950-2009			Observed Altimetry 1993-2009	
	Start	End	Span (yr)	Trend (mm/yr)	Error	Corr.Coeff with MRESL	Corr.Coeff with Obs.alti	Trend (mm/yr)	Error	Corr.Coeff with Obs.alti	Trend (mm/yr)	Error
Cabo San Antonio	1971	2009	39	3,5	0,7	0,6	0,5	2,1	0,1	0,7	0,8	1,5
Gibara	1974	2009	36	1,5	0,5	0,7	1,0	2,3	0,1	0,7	0,5	1,5
Port Royal	1954	1969	16	1,1	2,1	0,7	-	2,0	0,1	0,7	1,5	1,6
Magueyes	1955	2010	56	1,4	0,2	0,8	1,0	1,7	0,1	0,8	2	1,1
San Juan	1962	2010	49	1,6	0,3	0,7	1,0	1,7	0,1	0,8	1,7	1,2
Lima Tree Bay	1977	2010	34	1,0	0,5	0,6	1,0	1,6	0,1	0,8	2,4	1,3
Cartagena	1950	1992	43	5,6	0,2	0,3	-	2,0	0,1	0,5	2,5	0,7
Cristobal	1950	1980	31	2,5	0,4	0,2	-	2,0	0,1	0,5	1,9	0,6
Puerto Limon	1950	1968	19	2,2	0,6	0,5	-	2,0	0,1	0,7	2	0,8
Puerto Cortes	1950	1968	19	9,3	0,9	0,5	-	2,0	0,1	0,5	0,9	0,9
North Sound	1976	1996	21	-	-	-	-	2,3	0,1	0,7	0,9	1,7
Port Au Prince	1950	1961	12	-	-	-	-	1,9	0,1	0,6	0,2	1,0
Port of Spain	1983	1992	10	-	-	-	-	1,9	0,1	0,9	3,1	0,7
Marigot	-	-	-	-	-	-	-	1,6	0,1	0,8	2,4	1,2
Gustavia	-	-	-	-	-	-	-	1,6	0,1	0,8	2,4	1,1
Pointe-a-Pitre	1991	2010	20	-	-	-	-	1,7	0,1	0,6	1,9	0,8
Fort de France	-	-	-	-	-	-	-	2,0	0,1	0,3	1,5	0,8

2.3. Sea level reconstruction

Satellite altimetry since 1993 shows that sea level rise is not uniform and that it follows a characteristic spatial pattern. However this mostly reflects the interannual-decadal variability and the low frequency trends cannot be captured because the altimetry record is still short. Numerical ocean models and ocean reanalyses tools can produce the regional sea level trends on a longer time span (e.g., Carton and Giese., 2008; Kohl and Stammer, 2008; Penduff et al., 2010). To retrieve past regional variability in sea level prior to the altimetry era, other approaches can be made use. These approaches called reconstruction techniques combine long tide gauge records of limited spatial coverage with shorter, global gridded sea level data, either from satellite altimetry or from numerical ocean models (Church et al., 2004, Hamlington et al., 2011; Llovel et al., 2009; Meyssignac et al., 2012a; Ray and Douglas, 2011). Most of these studies interpolate in an optimal way (see Kaplan et al., 2000 for more details) the long tide gauge records with the principal EOF modes of ocean variability deduced from the altimetry-based gridded sea level data or ocean model outputs. Results do depend on underlying assumptions, i.e., that the principal modes of variability of the ocean are well captured by the relatively short altimetry record or from imperfect ocean models, and thus are representative over the longer time span of the reconstructed period (generally since the early 1950s). Here we use a mean of 3 different global reconstructions developed by Meyssignac et al. (2012a) over 1950-2009. These reconstructions are derived from 2-D sea level grids from the ocean circulation model DRAKKAR (Penduff et al., 2010), the SODA reanalysis (Carton et al., 2008) and from satellite altimetry (data from AVISO). For more details, (refer to Meyssignac et al., 2012a)

In the following, we call the mean reconstruction as MRESL.

2.4. Steric sea level (effects of ocean temperature and salinity changes)

Changes in the climate system's energy budget are predominantly revealed in ocean temperatures (Levitus et al., 2005, Bindoff et al., 2007) and the associated thermal expansion contribution to sea-level rise (Bindoff et al., 2007). Anomalies in temperature and salinity in the ocean water column change density, which further gives rise to sea level variations. In this study, we have used the annual-mean steric sea level anomalies for the period 1950-2009 computed from the global gridded temperature (T) and salinity (S) data set of Ishii and Kimoto, 2009 (version 6.12). Steric sea level anomalies were computed over the range of 0-700 m depth. The annual and semi-annual signals were removed and the annual average was performed.

3. Spatial Trend Patterns in the placeCaribbean Sea

3.1. Trend patterns from satellite altimetry and the mean sea level reconstruction over 1993-2009

Over the period from 1993 to 2009, the altimetry-based mean sea level trend averaged over the Caribbean Sea region – see Fig. 1a for the area contours– amounts to 1.7 $\pm$ 0.6 mm/yr. The spatial trend patterns over 1993-2009 in the region are shown in Fig. 1a. Strong positive trends are observed along the coast of the South American continent with trend maxima in the range of 4-5 mm/yr around 10°N and 60°W to 70°W, an area containing the Lesser Antilles islands of La Tortuga, Curaçao and Aruba. High trends are also observed around 10°N and 80°W to 83°W. Smaller trends of about 2 mm/yr are observed around the Greater Antilles islands of Jamaica, Cayman and around the islands of the Lesser Antilles in the eastern Caribbean.

For comparison, Fig. 1b shows the spatial trend patterns in the Caribbean Sea during 1993 to 2009 as derived from the mean re-

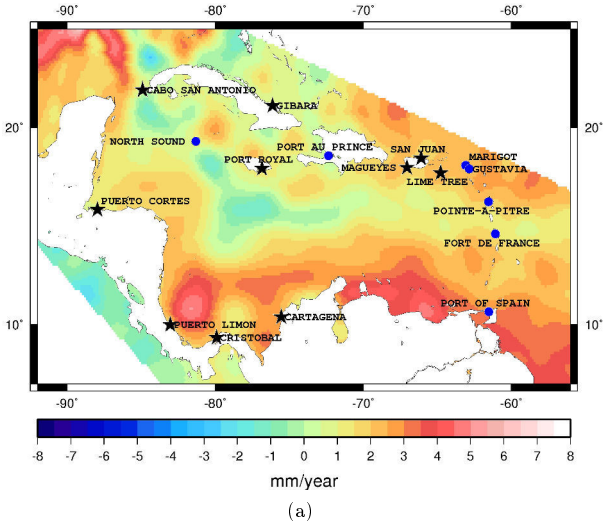

(a)

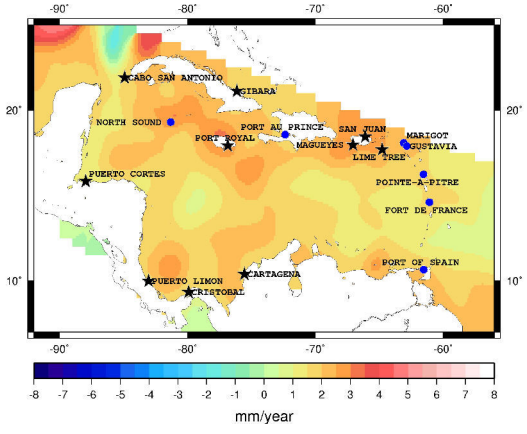

(b)

Figure 1. (a) Map of altimetry based sea level trends from 1993 to 2009 with the tide gauge locations superimposed. (b) Map of sea level trends from Mean Reconstruction from 1993 to 2009. Stars correspond to the 10 tide gauges used in the study while the blue dots correspond to other locations with only MRESL and altimetry data.

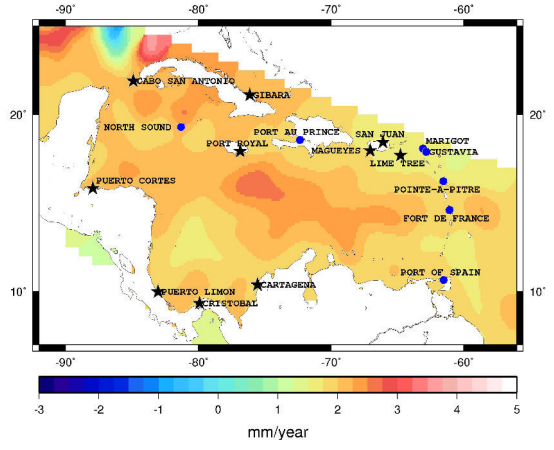

Figure 2. Map of sea level trends from the mean reconstruction over 1950-2009.

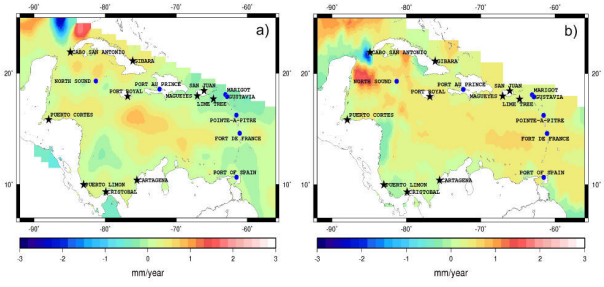

Figure 3. (a) Map of MRESL trend over 1950-2009 with the global mean trend (∼1.8 mm/yr) removed. (b) Map of steric sea level trend over 1950-2009 with the global mean trend of 0.3 mm/yr removed.

construction sea level (MRESL). We can observe that the spatial trend patterns between the satellite altimetry and MRESL are well correlated spatially but the altimetry-based trend amplitudes are larger, especially along the coasts of South America.

Fig. 2 shows the spatial sea level trend pattern from 1950 to 2009 over the Caribbean Sea based on the MRESL. As expected the spatial patterns are different from those on the shorter period (altimetry era) (see the difference in colour scale). Over 1950-2009, the mean sea level trend over the region amounts to 1.8 $\pm$ 0.1 mm/yr, a value very similar to the global mean sea level rate ($\approx$ 1.8 $\pm$ 0.5 mm/yr) for the past 60 years as obtained from Church and White (2011) and Meyssignac et al. (2012a). In Fig. 2, we also note a local maximum reaching 3 mm/yr in the central Caribbean Sea.

3.2. Steric effects on the placeCaribbean sea level

Fig 3a and Fig 3b show the spatial trend pattern of the MRESL and steric sea level (sum of thermal expansion and salinity effects) over the Caribbean Sea between 1950 and 2009 after having removed the global mean trend of each data set (i.e., 1.8 mm/yr and 0.3 mm/yr for MRESL and steric sea level respectively). Both figures show similar positive trend above 1 mm/yr in the centre of the Caribbean Sea with the trend more concentrated below the Jamaican island in the case of MRESL, whereas the concentration is more towards the Lesser Antilles in the case of the steric sea level. Positive trend patterns to the south of the Cuban island are also clearly visible in both the MRESL and steric sea level. We observe a strong dipole-like positive-negative trend pattern in the steric sea level at the mouth of the Caribbean Sea opening to the placeGulf of Mexico. Similar pattern, however not inside the placeCaribbean region is also observed in the MRESL above the island of Cuba.

Fig. 4 shows the interannual sea level variability over the Caribbean Sea obtained by geographically averaging the MRESL over the Caribbean from 1950 to 2009. The mean trend of 1.8 mm/yr has

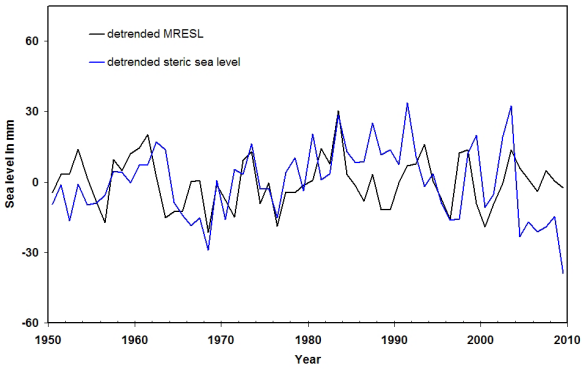

Figure 4. Comparison between detrended MRESL (in mm) and detrended steric sea level (in mm) over the placeCaribbean region from 1950 to 2009.

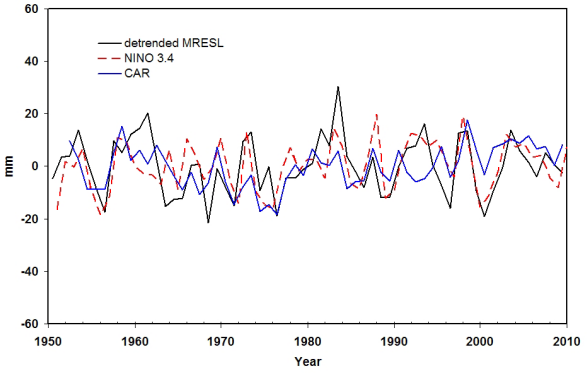

Figure 5. Comparison between detrended MRESL in mm, NINO 3.4 and CAR from 1950 to 2009.

been removed. The detrended steric sea level has been superimposed to the detrended MRESL curve. We observe that the maxima and minima of the steric sea level and MRESL curves are well correlated, suggesting that the same processes drive the interannual variability of the sea level and its steric component.

3.3. Interannual sea level variability and climate indices

In this section, we investigate what are the main climate modes that drive the interannual to multidecadal variability in sea level in the Caribbean region.

Fig. 5 shows the comparison between detrended MRESL and climate index NINO3.4. NINO3.4 index is one of the several ENSO proxies. It is based on sea surface temperature (SST) anomalies averaged in the region bound by 5°N to 5°S and from 170°W to 120°W. It is to be noted that there is a time lag of 6 months between NINO3.4 and MRESL (NINO3.4 leads MRESL) and this lag has been corrected. Though there is no significant correlation between NINO3.4 and MRESL over the entire time period, the correlation is equal to 0.6 between 1985 and 2009. Fig. 5 also shows the climate index CAR superimposed to the detrended MRESL. CAR-Caribbean SST index is the time series of SST anomalies averaged over the Caribbean (Penland and Matrosova, 1998). Overall we note a correlation of 0.5 between CAR and MRESL over the whole time span. Neglecting the temporary anti-correlation in the early 1990s, the correlation increases to 0.7 between 1985 and 2009. The reasonably good correlations existing between MRESL, NINO3.4 and CAR indices indicate that the interannual sea level variability in the Caribbean is influenced by and responds to ENSO events.

In order to capture the characteristics of the Caribbean Sea level variability, an EOF decomposition of the MRESL was performed over the Caribbean for the 1950-2009 time span. Fig. 6a, b show the 1st and 2nd modes of MRESL EOF decomposition respectively. The EOF mode 1 with 88% of the total variance captures the trend over the Caribbean. Indeed, the spatial map on Fig. 6a corresponds well

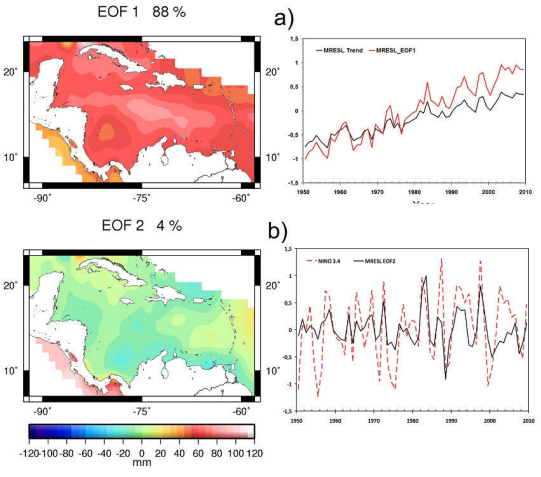

Figure 6. (a) EOF 1st mode of decomposition of the MRESL over 1950-2009 with the mean trend superimposed to the temporal curve of EOF1. (b) EOF 2nd mode of decomposition of the MRESL over 1950-2009 with NINO3.4 climate index superimposed to the temporal curve.

to the trend map on Fig. 1b. Fig. 6a also shows the geographically averaged trend over the Caribbean superimposed to the temporal curve corresponding to the EOF mode 1. Both the temporal curves are highly correlated (correlation equal to 1). The temporal curve corresponding to the 2nd EOF mode with 4% of total variance has a correlation of 0.6 with NINO 3.4 climate index as shown in Fig. 6b.

4. Sea level variability from tide gauge, MRESL and observed altimetry at various locations in the placeCaribbean region.

Sea level variability at different locations in the Caribbean was analysed by making use of tide gauge data, MRESL and observed altimetry at the tide gauge sites. Though there are many tide gauges available in the Caribbean, only ten sites could be used in the

study. In effect, the selection of the tide gauges from the available records was performed based on the time period of availability of the data, time gap between the discontinuities and the quality of their data. The chosen records were then compared with the MRESL and in certain cases, with observed altimetry data depending on the availability of the tide gauge data during the altimetry era. Table 1 summarizes tide gauge as well as reconstructed and altimetry trends, correlation coefficients between detrended tide gauge, reconstructed and altimetry time series.

In Fig. 7 is shown the comparison of the detrended tide gauge series (in red) with the detrended MRESL (in black) and altimetry series (in blue) interpolated at the corresponding tide gauge locations. Except for two tide gauges (Cartagena and Cristobal), the rest of the (detrended) tide gauges records have correlations ($\geq$ 0.5) with detrended MRESL. Magueyes, located in Puerto Rico is the only tide gauge site that has been used in the 2-D global sea level reconstruction of Meyssignac et al. (2012a). So, when possible, comparison between other tide gauges and the reconstruction is a validation of the reconstruction, allowing us to assess its quality (at least in terms of interannual variability).

Between 1950 and 2009, the individual mean sea level trend from MRESL at several tide gauge sites is in the range of 1.9 to 2.3 mm/yr. In few cases (Magueyes, San Juan, Lime Tree Bay, Marigot, Gustavia and Pointe-a-Pitre), it is even lesser than the global mean trend (1.8 mm/yr).

4.1. North, South and the Eastern Caribbean

As we have seen in Fig. 7 and Table 1, there is overall good correlation between available tide gauge records and reconstructed sea level on interannual time scale. Thus, the tide gauge records could be replaced by the MRESL in the Caribbean in order to provide information on the sea level variability at islands and coastal zones that do not have long term tide gauge records. Fig. 8 shows the detrended mean reconstructed sea level (in black) over the last 60 years in three different zones: 1) the Southern Caribbean comprising the Central and South American countries of Costa Rica, Guatemala, Honduras, Panama, Colombia and Venezuela; 2) the Northern Caribbean containing the island nations of Cayman Islands, Cuba, Dominican Republic, Haiti, Jamaica, Puerto Rico, U.S Virgin islands and 3) Eastern Caribbean with islands of Guadeloupe, Martinique, Saint Barthélemy and St.Martin. The altimetry based detrended sea level (in blue) between 1993 and 2009 is also superimposed to the detrended MRESL. The difference between Fig. 7 and Fig. 8 is that in Fig. 7, only locations with the availability of tide gauges (star symbols in trend maps) are considered whereas in Fig. 8 few other stations (blue dots in trend maps) where only the MRESL and altimetry are available are also included in order to study the 3 above mentioned zones. In Fig. 8, we can observe that on a longer time scale, the interannual sea level variability in the North Caribbean is higher than in the Southern Caribbean while the Eastern Caribbean shows greater interannual variability during the recent decades. Both the Northern and Eastern Caribbean

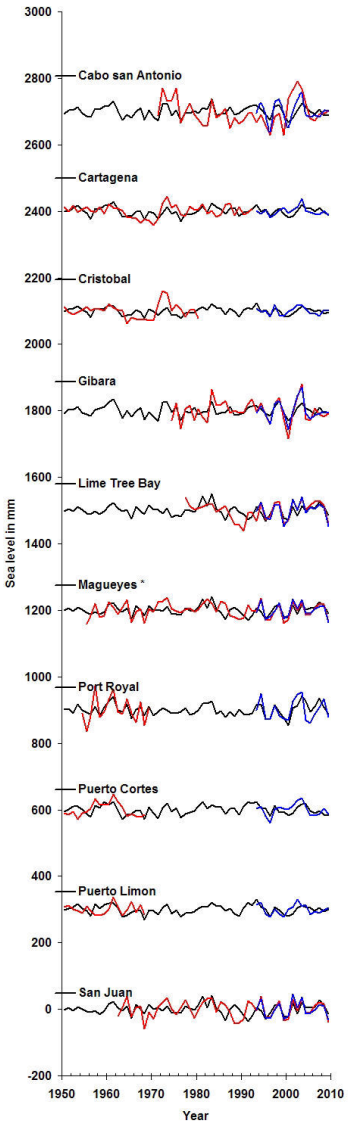

Figure 7. Detrended MRESL and altimetry sea level curves in mm, interpolated at the tide gauge locations since 1950. MRESL in black, tide gauge in red and observed altimetry in blue. The star symbol indicates the station used in 2-D past sea level reconstruction.

show prominent peak during 1982, roughly coinciding with the El Niño event in 1982.

4.2. Sea level variability and hurricanes

Klotzbach (2011) showed that the interannual variability of hurricanes in the Caribbean region is driven by ENSO and that more activity occurs with La Nina conditions than with El Nino conditions. The last two decades (in particular since 1999) have recorded more La Niña events (in particular in 1999/2000, 2007/2008 and

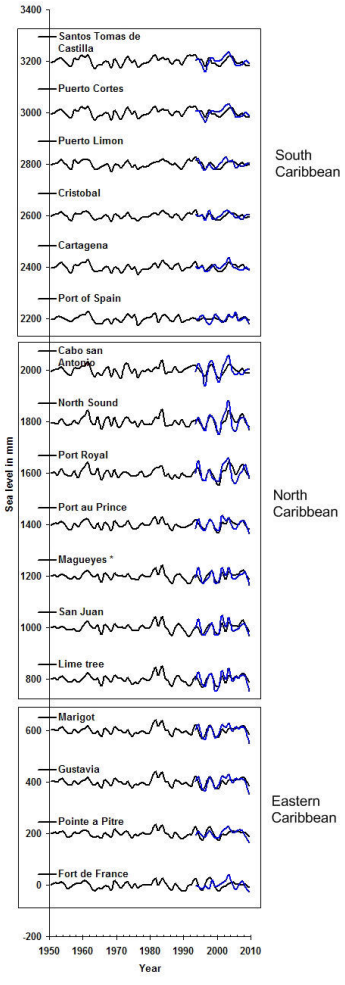

Figure 8. Detrended MRESL (in black) and altimetry sea level (in blue) curves in mm since 1950 at the tide gauge locations arranged based on their location: Southern Caribbean, Northern Caribbean and Eastern Caribbean.

2010/2011) than before. Furthermore, Goldenberg et al. (2001) showed that the years 1995 to 2000 have seen a 2.5 fold increase in major hurricane activity and a fivefold increase in hurricane activity affecting the Caribbean due to simultaneous increases in North Atlantic sea surface temperatures and decreases in vertical wind shear. These authors also showed that this phenomenon is likely to persist for an additional 10 to 40 years. In section 3.2 we have seen that the NINO3.4, a proxy of El Nino and La Nina events and CAR, an index based on the Caribbean SST correlate well with MRESL over the Caribbean since 1985. This period also corresponds to the increased frequency of La Niña events and hurricane activity.

Pielke et al. (2003) showed that between 1944 and 1999, the Northern Caribbean hurricanes (hurricanes hitting Bahamas, British Virgin Islands, Cayman Islands, Cuba, Dominican Republic, Haiti, Jamaica, Puerto Rico etc.) show high interannual variability as well as large multi decadal changes with a long term average of 1.0 hurricane strike per year. The Eastern Caribbean experiences hurricanes at a lower rate than the Northern Caribbean with 0.4 hurricane strike per year, whereas the hurricanes hitting the Central and South American part of the Caribbean show small decadal changes with only 0.2 strike per year. The pattern is very similar to the interannual variability in sea level observed in the Northern and Southern Caribbean as discussed in section 4.1, i.e. Northern Caribbean showing higher interannual sea level variability than the Southern. This seems to suggest that both the sea level interannual variability and hurricane activity in the placeCaribbean are related. Further investigation is needed to understand the link between the sea level variability and hurricane activity in that region.

5. Conclusion

In this study, we have analysed the sea level variability in the Caribbean since 1950 by making use of the mean of a mean 2-D past sea level reconstruction, observed satellite altimetry and tide gauge records wherever available. We observe that the spatial trend pattern in sea level during 1950 -2009 is quite different from that during the altimetry era (since 1993). Moreover the mean sea level trend in the Caribbean is very similar to the global mean sea level rise rate thereby indicating that the Caribbean is not facing a sea level rise larger than the global mean rise (unlike at some islands of the western tropical Pacific, as shown by Becker et al., 2012). Our results also show that the increase in the number of hurricanes during the recent decades have caused so far more damages to the coastal areas than the sea level rise itself. However, projected sea level rise in the future decades in response to global warming will represent an additional threat in this region.

Acknowledgements

Hindumathi Palanisamy is supported by the 'CECILE' project of the Agence Nationale de la Recherche (ANR) while Olivier Henry is supported by the European project MONARCH.

References

Ablain M., Cazenave A., Guinehut S. and Valladeau G., 2009, A new assessment of global mean sea level from altimeters highlights a reduction of global slope from 2005 to 2008 in agreement with in-situ measurements Ocean Sciences, 5, 193-201.

Becker M., Meyssignac B., Llovel W., Cazenave A. and Delcroix T., 2012, Sea level variations at Tropical Pacific Islands during 1950-2009, Glob. Planet. Chan., 80/81, 85-98.

Bindoff N.L., Willebrand J., Artale V., Cazenave A., Gregory J., Gulev S., Hanawa K., Le Quéré C., Levitus S., Nojiri Y., Shum C.K., Talley L.D. and Unnikrishnan A., 2007, Observations:

Oceanic Climate Change and Sea Level. In: Climate Change 2007: The Physical Science Basis. Contribution of Working Group I to the Fourth Assessment Report of the intergovernmental Panel on Climate Change [Solomon, S., D. Qin, M. Manning, Z. Chen, M. Marquis, K.B. Averyt, M. Tignor and H.L. Miller (eds.)]. Cambridge University Press, Cambridge, United Kingdom and New York, NY, USA.

Carrere L. and Lyard F., 2003, Modeling the barotropic response of the global ocean to atmospheric wind and pressure forcing -comparisons with observations, Geophys. Res. Lett., 30, 6, 1275, DOI:10.1029/2002GL016473.

Carton J.A. and Giese B.S., 2008, A reanalysis of ocean climate using Simple Ocean Data Assimilation (SODA), Mon. Weath. Rev., 136, 2999–3017.

Cazenave A. and Llovel W., 2010, Contemporary sea level rise, Ann. Rev. Marine Sci., 2, 145-173.

Cazenave A. and Remy F., 2011, Sea level and climate: measurements and causes of changes, Interdisciplinary Reviews: Climate Change, 2, 5, 647–662, DOI:10.1002/wcc.139.

Church J.A., White N.J., Konikow L.F., Domingues C.M., Cogley J.C., Rignot E., Gregory J. M., van den Broeke M. R., Monaghan A. J., and Velicogna I., 2011, Revisiting the Earth's sea-level and energy budgets from 1961 to 2008, Geophys. Res. Lett., 38, L18601, DOI: 10.1029/2011GL048794.

Church J.A., White N.J., Coleman R., Lambeck K. and Mitrovica J.X., 2004, Estimates of the regional distribution of sea level rise over the 1950–2000 period, J Climat., 17, 2609–2625.

Church J.A. and White N.J., 2011, Changes in the rate of sea level rise from the late 19th to the early 21st century, Surv. Geophys., 1–18, DOI:10.1007/s10712-011-9119-1.

Goldenberg S.B., Landsea C. W., Mestas-Nunez A.M., and Gray W.M., 2001, The recent increase in Atlantic hurricane activity: Causes and implications, Science, 293, 474–79

Hamlington B.D., Leben R., Nerem S., Han W. and Kim K.Y., 2011, Reconstructing sea level using cyclostationary empirical orthogonal functions, J Geophys. Res., 116, C12, DOI: 10.1029/2011JC007529.

Ishii M. and Kimoto M., 2009, Reevaluation of historical ocean heat content variations with varying XBT and MBT depth bias corrections, J Oceanog., 65, 287-299.

Kalnay E.C., Kanamitsu M., Kistler R., Collins W., Deaven D., Gandin L., Iredell M., Saha S., White G., Woollen J., Zhu Y., Leetmaa A., Reynolds B., Chelliah M., Ebisuzaki W., Higgins W., Janowiak J., Mo K. C., Ropelewski C., Wang J., Jenne R. and Dennis J., 1996, The NCEP/NCAR 40-year reanalysis project. Bull. American Meteo. Soci., 77, 437–472.

Kaplan A., Kushnir Y. and Cane M.A., 2000, Reduced space optimal interpolation of historical marine sea level pressure: 1854–1992, J Climat., 13, 2987–3002.

Klotzback P.J., 2011, The influence of El Nino-southern oscillation and the atlantic multidecadal oscillation on Caribean tropical cyclone activity, J Climat., 721-731.

Kohl A. and Stammer D., 2008, Decadal sea level changes in the 50-year GECCO ocean synthesis. J Climat., 21, 1876–90.

Levitus S., Antonov J. and Boyer T., 2005, Warming of the world ocean, 1955–2003, Geophys. Res. Lett., 32, L02604, DOI:10.1029/2004GL021592.

Llovel W., Cazenave A., Rogel P. and Berge-Nguyen M., 2009, 2-D reconstruction of past sea level (1950-2003) using tide gauge records and spatial patterns from a general ocean circulation model, Climat. Past, 5, 1-11.

Lombard A., Cazenave A., DoMinh K., Cabanes C., Nerem R., 2005, Thermosteric sea level rise for the past 50 years; comparison with tide gauges and inference on water mass contribution. Global and Planetary Change, 48, 303-312.

Lombard A., Cazenave A., Le Traon P.Y. and Ishii M., 2005, Contribution of thermal expansion to present-day sea level rise revisited, Glob. Planet. Chan., 47, 1-16.

Lombard A., Garric G., Penduff T. and Molines J.M., 2009, Regional variability of sea level change using a global ocean model at 1/4_ resolution, Ocean Dyn., DOI: 10.1007/s10236-009-0161-6.

Meyssignac B., Llovel W., Becker M. and Cazenave A., 2012, An assessment of two-dimensional past sea level reconstructions over 1950 - 2009 based on tide gauge data and different input sea level grids, Surv. Geophys., in press, DOI:10.1007/s10712-011-9171-x.

Meyssignac B., Salas y Melia D., Becker M., Llovel W., and Cazenave A., 2012, Tropical Pacific spatial trend patterns in observed sea level: internal variability and/or anthropogenic signature?, Climat. Past, in press, DOI: 10.5194/cpd-8-349-2012.

Mimura N., Nurse L., McLean R.F., Agard J., Briguglio L,

Lefale P., et al., 2007, Small islands. Climate Change, 2007: Impacts, Adaptation and Vulnerability. Contribution of Working Group II to the Fourth Assessment Report of the Intergovernmental Panel on Climate Change, M.L. Parry, O.F. Canziani, J.P. Palutikof, P.J. van der Linden and C.E. Hanson, Eds., Cambridge University Press, Cambridge, UK, 687-716.

Nicholls R. and Cazenave A., 2010, Sea level change and the impacts in coastal zones, Science, 328, 1517-1520.

Peltier W.R., 2010, Global glacial isostasy and the surface of the ice-age Earth: The ICE-5G (VM2) model and GRACE, Ann. Rev. Earth Planet. Sci., 32, 111-149.

Penduff T., Juza M., Brodeau L., Smith G., Barnier B., Molines J., Treguier A.-M., and Madec G., 2010, Impact of global ocean model resolution on sea-level variability with emphasis on interannual time scales, Ocean Sci., 6, 269-284.

Penland C. and Matrosova L., 1998, Prediction of tropical Atlantic sea surface temperatures using linear inverse modeling, J Climat., 483-496.

Pielke A.J., Rubiera J., Landsea C., Fernandez M.L. and Klein R., 2003, Hurricane Vulnerability in Latin America and the Caribbean: Normalized Damage and Loss Potentials. Nat. Haz. Rev., 4, 3, DOI: 10.1061/(ASCE)1527- 6988(2003)4:3(101).

Preisendorfer R.W., 1988, Principal component Analysis in Meteorology and oceanography, Develop. Atmos. Sci., 17, Elsevier, 425pp.

Ray R. and Douglas B., 2011, Experiments in reconstructing twentieth-century sea levels. Prog. Oceanog., 91, 4, 496-515.

Woodworth P.L. and Player R., 2003, The permanent service for mean sea level: an update to the 21st century, J Coas. Res., 19, 287-295.

3.2.3 South China Sea

South China Sea, a region sometimes called as the Asian Mediterranean, located between western Pacific and eastern Indian Ocean, is the largest semi-enclosed marginal sea in the northwest Pacific Ocean. Three major rivers namely Mekong, Red and Pearl drain into the South China Sea. The sea level in this region has presented significant changes over the recent decades and this deviates greatly from those in is adjacent and global oceans (*Nidheesh et al.*, 2013). Its bottom topography is characterized by two extended continental shelves with water depth less than 200 m along the north and southwest coasts and a deep basin with a maximum water depth of about 5000 m in the central region (See Fig.3.6). Its coastal sub regions are home to about 270 million people and have been one of the fastest developing and most vibrant economies on Earth. Rising sea level would therefore severely threaten the coastal zones (*Peng et al.*, 2013).

A number of previous studies have investigated South China Sea level trends over the satellite altimetry era. In our study, we analyzed the long-term (60 years) sea level variability in the South China Sea using the past sea level reconstruction data set. Only the climate-related sea level component was studied due to the inaccessibility of GPS measures in the region of South China Sea for the VLM estimates. However, anthropogenic land subsidence plays a major role in this region. For example, the Bangkok megacity has subsided by 2 m due to ground water withdrawal (*Nicholls*, 2010, *Stammer et al.*, 2013). Our study has been published as an article titled ‘Interannual sea level variations in the South China Sea over 1950-2009’.

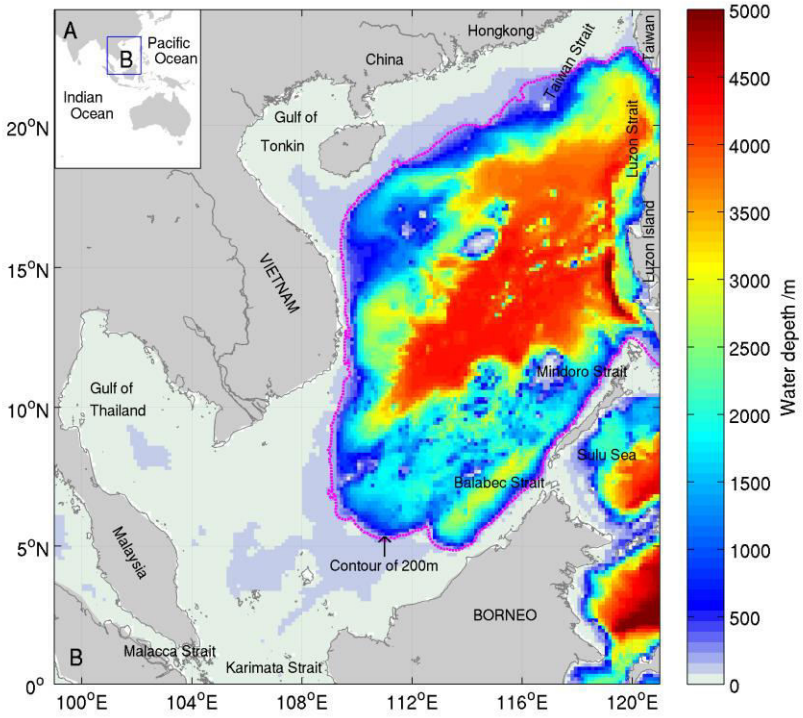

Figure 3.6: Bathymetric map of South China Sea, adapted from Peng et al., 2012

Summary of the article: Interannual sea level variations in the South China Sea over 1950-2009' (the original article is inserted at the end of this section).

In this study, we analyzed South China Sea (SCS) regional sea level variability, total climate-related sea level change at several locations within the region between 1950 and 2009. During the altimetry era (1993-2009), the regional mean sea level rate amounts to 3.9 ± 0.6 mm/yr with considerable spatial trend variability. Positive sea level spatial trend variability was observed in the central SCS basin with water depth greater than 200 m while over the continental shelves, the spatial trend variability was found to be below average. It was also observed that the trend minima occur at three locations where the major rivers, Mekong, Red and Pearl drain into the sea. Between 1950 and 2009, the regional sea level trend value amounts to 1.7±0.1 mm/yr, a value slightly smaller than the global mean rate of 1.8 mm/yr.

In terms of spatial trend patterns, interestingly, it was noted that the sea level over the continental shelves (along the coasts of China and North Vietnam) is rising faster than the deep

water region which is almost the reverse case during the satellite altimetry era. This once again shows that satellite altimetry cannot capture low-frequency trend signals owing to its short time period. Comparison of the long-term regional sea level trend patterns with those of upper steric (0-700 m) regional trend patterns showed that while in the central SCS basin, the patterns are similar; it is not the case in the northern SCS region. This suggests that the sea level variability in the north SCS is either caused by the ocean water mass contribution or by the thermal expansion of the shallow water (considering the shallow bathymetry of the region). If it is the latter, the inability of the upper steric sea level to produce this signal could be due to the lack of complete coverage of temperature and salinity data in this region. Good correlation of long-term interannual sea level time series with the ENSO NINO3.4 index indicates that the interannual sea level variability in SCS is driven by ENSO events. Estimation of long-term total climate-related sea level change at different locations in SCS showed that in the northern SCS, several locations exhibit sea level change at rates higher than that of the global mean rate.

Marine Geodesy, 36:164–182, 2013

ISSN: 0149-0419 print / 1521-060X online
DOI: 10.1080/01490419.2013.771595

Taylor & Francis
Taylor & Francis Group

Interannual Sea Level Variations in the South China Sea Over 1950–2009

DONGJU PENG,[1,2] HINDUMATHI PALANISAMY,[2]
ANNY CAZENAVE,[2] AND BENOIT MEYSSIGNAC[2]

[1]Shanghai Astronomical Observatory, CAS, Shanghai, China
[2]LEGOS/OMP, Toulouse, France

Spatial patterns of interannual sea level variations in the South China Sea (SCS) are investigated by analyzing an EOF-based 2-dimensional past sea level reconstruction from 1950 to 2009 and satellite altimetry data from 1993 to 2009. Long-term tide gauge records from 14 selected stations in this region are also used to assess the quality of reconstructed sea levels and determine the rate of sea level along the coastal area. We found that the rising rate of sea levels derived from merged satellite altimetry data during 1993–2009 and past sea level reconstruction over 1950–2009 is about 3.9 ± 0.6 mm/yr and 1.7 ± 0.1 mm/yr, respectively. For the longer period, this rate is not significantly different from the global mean rate (of 1.8 ± 0.3 mm/yr). The interannual mean sea level of the SCS region appears highly correlated with Niño 4 indices (a proxy of El Niño-Southern Oscillation/ENSO), suggesting that the interannual sea level variations over the SCS region is driven by ENSO events. Interpolation of the reconstructed sea level data for 1950–2009 at sites where tide gauge records are of poor quality (either short or gapped) show that sea level along the Chinese coastal area is rising faster than the global mean rate of 1.8 mm/yr. At some sites, the rate is up to 2.5 mm/yr.

Keywords Sea level variations, South China Sea, 2-D past sea level reconstruction, ENSO

Introduction

Sea level rise represents one of the potentially catastrophic consequences of climate change. It has received much attention since the emergence of concerns about human-induced global warming in the 1980s (e.g., Church et al. 2010). Sea level has been rising at a rate of 1.8 ± 0.3 mm/yr during the last century (Church et al. 2011), while satellite altimetry-based estimation indicates that sea level risen to a even faster rate of 3.2 ± 0.4 mm/yr during 1993–2012 (Nicholls and Cazenave 2010). The fact that geographically sea level is not rising uniformly has been revealed by many studies (e.g., Cazenave and Nerem 2004; Stammer and Gregory 2011). Over 1993–2012, in some regions such as the tropical Western Pacific, rates are up to 3–4 times higher than the global rate of 3.3 ± 0.4 mm/yr (Cazenave and Remy 2011). Considering the potential impacts of rapid sea-level rise in vulnerable coastal areas, it is of great importance to estimate and understand the regional variability of sea level change.

Received 21 July 2012; accepted 14 January 2013.
Address correspondence to Dongju Peng, 80 Nandan Road, Shanghai 200030, China. E-mail: pdongju@shao.ac.cn

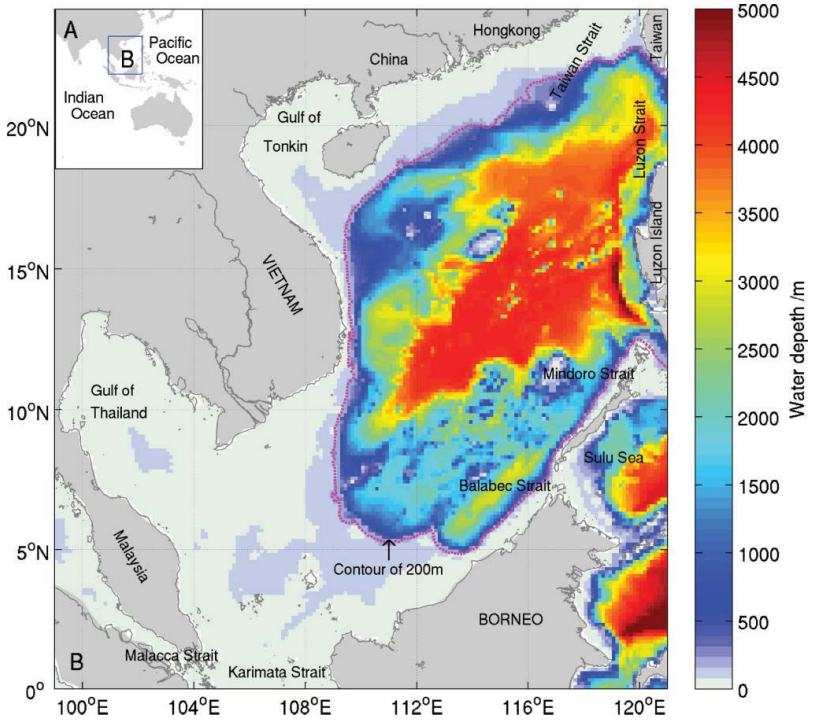

Figure 1. (A) Location of the South China Sea (SCS). (B) Bathymetric map of the SCS, the bottom topography and coastlines presented in this figure are based on 5-min Earth Topography (ETOPO5) data set. (Color figure available online.)

In the present study, we focus on the South China Sea (SCS), a region sometimes referred to as the Asian Mediterranean. Located between the western Pacific and the eastern Indian oceans, the SCS is the largest marginal sea in the southeast Asia covering an area from equator to 24°N and from 99°E to 121°E (see Fig. 1 for location). The SCS is a semi-enclosed basin, connecting with the East China Sea to the northeast through the Taiwan Strait, the Pacific Ocean and the Sulu Sea to the east through Luzon Strait, Balabec and Mindoro Straits, respectively, Java Sea to the South through Karimata Strait, and the Indian Ocean to the west through the Malacca Strait. Its bottom topography is characterized by two extended continental shelves with water depth less than 200 m along the north and southwest coasts and a deep basin with a maximum water depth of about 5,000 m in the central region. Its costal subregions are home to about 270 million people that have had some of the fastest developing and most vibrant economies on Earth. Rising sea levels would therefore severely threaten the costal zones of the SCS due to high density population and fast growing economies.

Because of its geographical location, between the north tropical Pacific and Indian oceans, the SCS has considerable seasonal, interannual and decadal sea level variability associated with the El Niño-Southern Oscillation (ENSO), the East Asian monsoon and phenomena such as the Indian Ocean Dipole. The seasonal variations of sea level in the SCS respond to seasonally reversing monsoon winds, as demonstrated by Shaw et al. (1999) and Ho et al. (2000) using TOPEX/Poseidon (T/P) satellite altimetry data. They showed in particular that the SCS sea level is higher during summer and lower during winter. The interannual variations of sea level response to ENSO were successfully identified by Rong

et al. (2007). Based on satellite altimeter observations over 1993–2004, these authors found that the correlation between interannual SCS mean sea level anomalies and SOI (Southern Oscillation Index, a proxy of ENSO) reaches 0.78, with SOI leading the mean sea level anomalies by 4 months.

Sea level trends in the SCS have been investigated in a number of previous studies (Li et al. 2002; Cheng and Qi 2007; Rong et al. 2007). These studies were based on satellite altimeter data over a short time period, that is, less than 15 years. Using satellite altimetry data from 1993 to 2006, Cheng and Qi (2007) reported that SCS mean sea level rose at a rate of 11.3 mm/yr during 1993–2000 and then fell at a rate of 11.8 mm/yr during 2001–2005. As revealed by recent studies, the altimetry-based spatial trend patterns are not long-lived features, they mostly reflects the interannual-decadal variability and the low frequency trends cannot be captured since the altimetry record is still too short. However, it has become increasingly important to take account of long-term trends in sea level, extreme surges and extreme waves in ensuring the protection of life and property in coastal regions.

To retrieve past regional variability in sea level prior to the altimetry era, other approaches can be made use. These approaches include the use of Ocean General Circulation Models (OGCMs) and ocean reanalyzes (i.e., OGCMs with data assimilation) as well as two-dimensional (2-D) past sea level reconstructions (Church et al. 2004; Llovel et al. 2009; Ray and Douglas 2011; Meyssignac et al. 2012). Meyssignac et al. (2012) suggest that being partly based on tide-gauge observations, the reconstructions may in principle carry more information on the regional variability factors than OGCMs. The past sea level reconstruction method has been successfully used by several previous studies to investigate long-term sea level rise over tropical Pacific Ocean (Church et al. 2006; Becker et al. 2012), Caribbean Sea (Palanisamy et al. 2012) and Indian Ocean (Church et al. 2006).

Improving our understanding of sea level rise and variability, as well as reducing the associated uncertainties, critically depends on the availability of adequate observations. Currently, longer time period of sea level measurements (over the past ~60 years) are available from tide gauge, satellite altimetry, past 2-D reconstruction and steric data to study sea level variations. These data can not only improve the accuracy and credibility of observed sea level variation rate, but they also can reveal sea level variability over a wider range of time scales. In the present study, satellite altimetry observed sea level for the last two decades, 60-year-long reconstructed and steric sea level, as well as tide gauge records are employed to examine the interannual sea level variations in the SCS.

Data Sets

The data used to investigate the interannual sea level variations over the SCS in the present study contain satellite altimetry, tide gauge records, 2-D past sea level reconstructions and steric (effects of ocean temperature and salinity on sea level) data. As we are only interested in the interannual sea level variability, all the data presented here have had a seasonal (annual plus semi-annual) signal removed by fitting 6-month and 12-month sinusoids.

Satellite Altimetry Data

Satellite altimetry provides direct, near-global observations of the rate of sea-level rise and its temporal and spatial variability; it has been widely used to study the global and regional sea level variations since the launch of the first oceanographic satellite T/P in 1992. In the present study, we use DT-MSLA "Ref" series satellite altimetry data provided by Collecte Localisation Satellite (CLS) space oceanography Division (http://www.aviso.oceanobs.com/en/data/products/sea-surface-height-products/global/msla/index.html). The data set is a merged sea level anomaly product based on

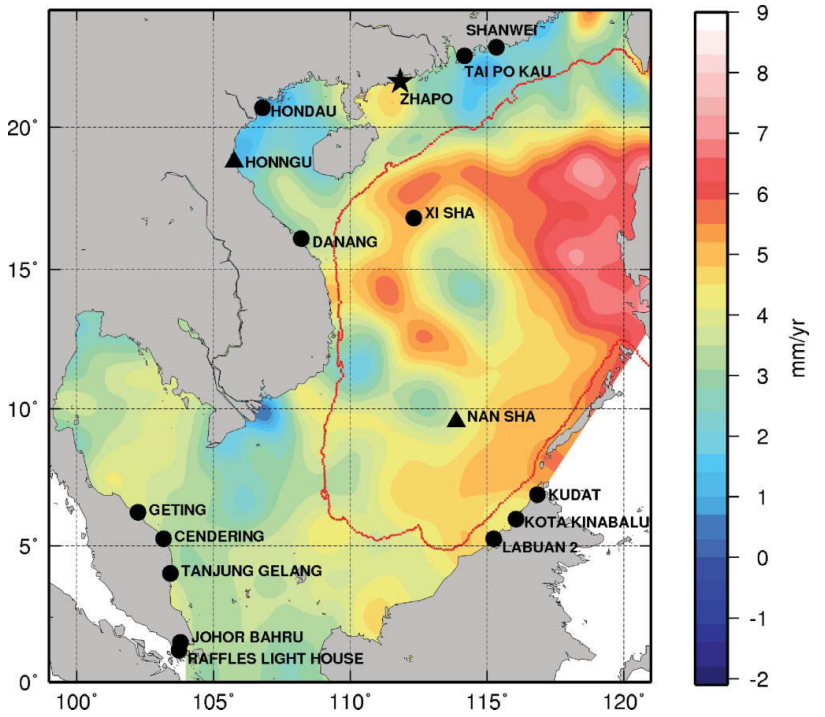

Figure 2. Map of satellite altimetry observed sea level trends over the SCS during 1993–2009 with tide gauge superimposed. (Color figure available online.)

several altimetry missions, namely T/P, Jason-1 and 2, Envisat and ERS-1 and 2. It is a global homogeneous inter-calibrated data set based on a global crossover adjustment that considers T/P and then Jasn-1/2 as reference missions. Usual geophysical corrections including solid Earth, ocean and pole tides, wet and dry troposphere, ionosphere and inverted barometric corrections have been applied to the altimeter measurements. The sea level anomaly data are available as $0.25^\circ \times 0.25^\circ$ Mercator projection grids at weekly intervals. In this study, these weekly data are first averaged to produce monthly mean data. To be consistent with the other data used in this study, the altimeter data over January 1993 to December 2009 are used and annual average is performed accordingly.

Tide Gauge

Tide gauge measurement is one of the essentially two types of observations that measure sea level directly. They have been used to measure sea level change along continental coastline and Mid-ocean Island since the mid-19th century (Douglas 1991, 2001; Church et al. 2006, 2011; Jevrejeva et al. 2006, 2008; Holgate 2007; Bakitz and Shum 2010; Ding et al. 2004). Tide gauge data used here are monthly mean sea level from the data archive of the Permanent Service for Mean Sea level (PSMSL; http://www.pol.ac.uk/psmsl) (Woodworth and Player 2003). Although there are about 70 tide gauge stations in the SCS region, only 14 records could be used in this study. The main criteria of selecting tide gauges are data length and data quality with respect to reconstructed/satellite altimetry observed sea levels. The location of those selected tide gauge stations are displayed in Fig. 2 and the correspondingly specific information is listed in Table 1.

Table 1

Tide gauge locations, time span, and sea level trends from tide gauge record, past sea level reconstruction, and satellite altimetry. The Corr. Coef. (correlation coefficient) is given for the tide gauge and satellite altimetry span. Stars ★ and triangles ▲ correspond to tide gauge used in the reconstruction and tide gauge either with short data record or poor data quality.

				tide gauge							RESL 1950–2009			ALTI 1993–2009	
						Span	Trend	Error	Corr. Coef.		Trend	error	Corr. Coef.	trend	error
Station group	Name	lon	Lat	start	end	(yr)	(mm/yr)	(mm/yr)	RESL	ALTI	(mm/yr)	(mm/yr)	Coef. with ALTI	(mm/yr)	(mm/yr)
SCS1	XI SHA	112.333	16.833	1990	2011	22	3.0	1.4	0.36	0.94	1.1	0.2	0.54	5.2	1.7
	NAN SHA▲	113.883	9.533	1998	2011	14	—	—	—	—	1.8	0.1	0.50	3.9	1.1
SCS2	SHANWEI	115.350	22.750	1975	1994	20	1.4	0.7	0.45	—	2.4	0.1	0.72	2.5	1.1
	TAI PO KAU	114.184	22.442	1963	2010	48	2.9	0.5	0.49	0.30	2.5	0.1	0.74	2.5	1.1
	ZHAPO★	111.833	21.583	1959	2011	53	2.2	0.3	0.64	0.80	2.2	0.1	0.85	4.5	1.0
	HONDAU	106.800	20.667	1957	2001	45	2.5	0.4	0.55	0.75	2.3	0.1	0.70	1.1	1.1
	HONNGU▲	105.767	18.800	1962	2001	40	—	—	—	—	2.5	0.1	0.58	1.4	1.0
	DANANG	108.217	16.100	1978	2001	24	4.3	0.8	0.27	0.90	2.3	0.1	0.72	3.0	1.1
SCS3	GETING	102.250	6.233	1987	2010	24	2.0	0.7	0.35	0.79	1.6	0.1	0.57	3.9	0.8
	CENDERING	103.183	5.267	1984	2010	27	2.2	0.4	0.39	0.68	1.5	0.1	0.49	3.3	0.8
	TANJUNG GELANG	103.433	3.983	1984	2010	27	2.1	0.4	0.49	0.79	1.5	0.1	0.47	3.4	0.8
	JOHOR BAHRU	103.800	1.467	1984	2010	27	2.0	0.4	0.43	0.68	1.6	0.1	0.37	4.0	1.2
	RAFFLES LIGHT HOUSE	103.750	1.167	1973	2011	39	1.8	0.5	0.38	0.55	1.6	0.1	0.38	4.0	1.2
	LABUAN 2	115.250	5.267	1996	2010	15	1.8	2.2	0.81	0.95	1.6	0.1	0.67	4.6	1.3
	KOTA KINABALU	116.067	5.983	1988	2010	23	3.6	0.9	0.66	0.94	1.7	0.1	0.73	4.1	1.5
	KUDAT	116.850	6.883	1996	2010	15	2.9	2.1	0.87	0.98	1.7	0.1	0.75	5.0	1.6

In terms of data processing, we first correct the tide gauge data for the inverse barometer effect (i.e., the response of sea level to the atmospheric perturbations) using surface pressure grid from the National Centers for Environmental Prediction (NECP) reanalysis (Kalnay et al. 1996). The surface atmospheric pressure grids are available as monthly means on a 2.5° grid. We assign to each tide gauge the sea level pressure value of the nearest grid point. In addition, Glacial Isostatic Adjustment (GIA) correction (Peltier 2004) has not been applied to tide gauge records since it is small in the SCS region and can be neglected in the present study. Second, we removed annual and semi-annual signals for each record through a least-squares fit of 12- and 6-month period sinusoids. Gaps and discontinuities due to changes in instrumentation, earthquakes or other natural or anthropogenic factors may affect the tide gauge time series. When small gaps ($\leq$4 consecutive years) were noticed in the tide gauge record, we reintroduced missing data by linearly interpolating the time series. Outliers were detected using the ROSNER's test (see Becker et al. 2012). In a last step to be consistent with the time resolution of the sea level reconstruction, we averaged monthly tide gauge time series to obtain annual averages.

Past Sea Level Reconstruction

The main advantage of past sea level reconstruction is that it provides estimates of regional and global variations of sea level, as well as time series of estimated sea level at any locality over a longer period than is often available from individual tide gauge records alone (Church et al. 2006). As mentioned above, several studies have developed past sea level reconstructions either globally or regionally. Here, we use the global sea level reconstruction at yearly intervals on a 1/2° grid over 1950–2009 developed by Meyssignac et al. (2012).

The general approach of past sea level reconstruction consists of computing spatial modes from the gridded fields using an Empirical Orthogonal Function (EOF) decomposition and computing new EOF temporal amplitudes through a least-squares optimal interpolation that minimize the reconstructed filed and the tide gauge records at the tide gauge locations. The sea level reconstruction used in the study is based on 91 long-term (up to 60 years) but sparsely distributed tide gauge records and gridded sea level data from two numerical ocean models (the DRAKKAR/NEMO model (Penduff et al. 2011) without data assimilation and the SODA ocean reanalysis (Carton and Giese 2008) over 1958–2008, and satellite altimetry data over 1993–2009. It is a mean of the 3 different global reconstructions derived from the 3 above mentioned sea level grids. For more details, please refer to Meyssignac et al. (2012). Hereafter, mean reconstructions will be abbreviated as MRESL.

Steric Sea Level

Steric effect is the most important cause of regional variability in sea level trends (e.g., Lombard et al. 2005). It represents sea level change due to ocean volume change that results from temperature (thermosteric) and salinity (halosteric) variations. In this study, an updated version (version 6.12) of monthly 1° × 1° gridded temperature and salinity data set from Ishii and Kimoto (2009) is used to compute thermosteric and halosteric sea level anomalies from 1950 to 2009 over the range of 0–700 m in the SCS. To be consistent with time resolution of MRESL, annual average of steric sea level was performed after removing seasonal signals. Note that the steric contribution from deep-ocean (water depth more than 700 m) has not been accounted for in this study. However, recent studies have revealed that it actually cannot be ignored. For example, using Conductivity-Temperature-Depth data, Purkey and Johson (2010) estimate the 1,000–4,000 m deep contribution to 0.14 ±

0.08 mm/yr from the early 1990s to mid-2000s around the Antarctica area. Using an ocean general circulation model, Song and Colberg (2011) propose a much larger deep ocean contribution, of about 1 mm/yr over the altimetry era at global scale. Unfortunately, there are not enough deep-ocean measurements available in the SCS region; the steric sea level in the study only represents the upper ocean (0∼700 m) component.

Patterns of Sea Level Rise over the SCS

Spatial Trends Pattern in Observed Sea Level over 1993–2009 and 1950–2009

Owing to its quasiglobal coverage of the oceans, satellite altimetry allows us to estimate regional trends in sea level. The spatial trend pattern of sea level derived from the satellite altimeter over the SCS during 1993–2009 is presented in Fig. 2. Even though altimetry data show increasing trend in the whole SCS basin, there is considerable spatial variability ranging from 0 to ∼8 mm/yr. Sea level trends over the central basin of the SCS, with water depth more than 200 m, are higher than elsewhere, with a ridge of large positive trends extending from west of Luzon Island to east of Vietnam across the highest rate area around 118.5E, 18.5N. Over the continental shelves, the rates of rising sea levels are generally below average during the 1993–2009 timespan. Three locations with trend minima around 0 to ∼1 mm/yr are observed. Those are located near the major rivers draining into the SCS, namely Mekong River, Red River and Pearl River.

For comparison, Fig. 3 shows the spatial trend patterns over the SCS during the same time period (1993–2009) as derived from reconstruction (MRESL). We observe that the

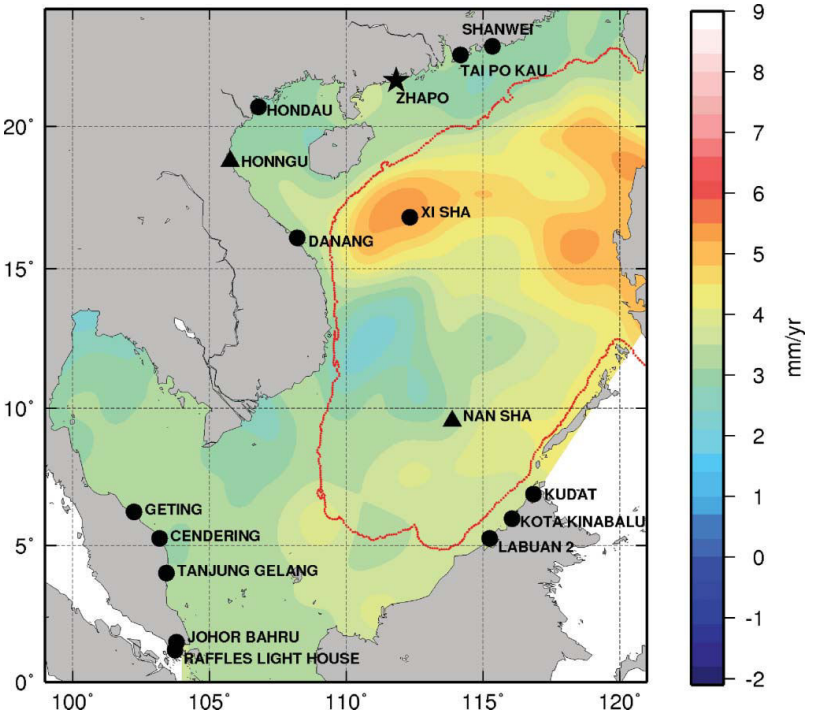

Figure 3. Map of reconstructed sea level trends over the SCS during 1993–2009. (Color figure available online.)

spatial trend patterns from satellite altimetry and reconstruction are well correlated spatially but the altimetry-based trend amplitudes are larger, especially around Luzon Island. The mean seal level trends derived from satellite altimetry and MRESL during 1993–2009 over the SCS are similar and equal to 3.9 ± 0.6 mm/yr, and 3.6 ± 0.4 mm/yr, respectively. We therefore infer that MRSL captured the main features of spatial trend patterns over the SCS and it could be used to analyze the long-term features of sea level trend over the SCS.

Figure 4 shows the spatial sea level trend patterns from 1950 to 2009 over the SCS based on reconstruction. It is worth to be noted that spatial patterns are different from those on the shorter period of 1993–2009 (satellite altimetry era), confirming that altimetry data are still too short to capture the low-frequency trends. Over 1950–2009, the mean sea level trend over the region amounts to 1.7 ± 0.1 mm/yr, It is slightly smaller than the global mean sea level rate of ∼1.8 ± 0.3 mm/yr over the same time span (Church et al. 2011; Meyssignac et al. 2012). It is interesting to note that sea level along the coasts of China and northern Vietnam is rising faster (>2 mm/yr) than the deep seawater region, which is almost the reverse case during the satellite altimetry era. This low frequency regional trend thus affects several major mega cities such as Hongkong and Guangzhong. Its origin is still unclear and needs to be investigated further. Note that what Fig. 4 shows is essentially the climatic component of the (absolute) sea level trend. Locally vertical crustal motions due to groundwater withdrawal for example may superimpose to the absolute component, eventually giving rise to larger relative sea level rise.

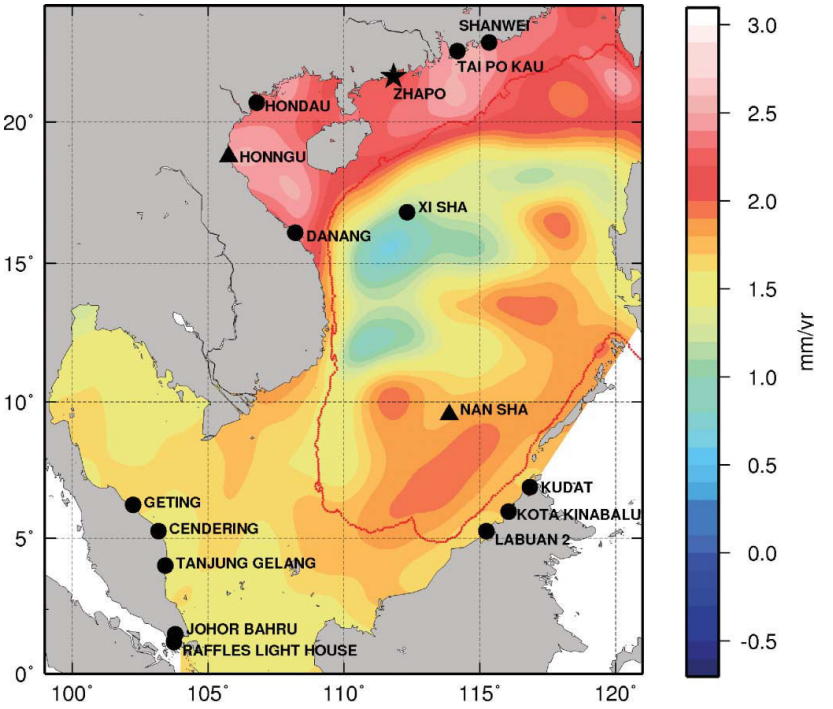

Figure 4. Map of reconstructed sea level trend over the SCS during 1950–2009. (Color figure available online.)

Steric Contributions on Sea Level Variations

There are two major components of sea level changes. One is the steric component, due to changes in the sea water temperature and salinity at all depths. In terms of global average, the other component is related to water-mass change as a result of the net transport of freshwater mass to the oceans from melting ice sheets and mountain glaciers, and from terrestrial water reservoirs. At regional scale, however the ocean mass change is related to precipitation, evaporation and inflow/outflow from the considered region. The viscoelastic/elastic response of the solid Earth to water mass redistribution may also play some role (e.g., Milne et al. 2009). Figure 5 shows the geographical distribution of upper (above 700 m) steric sea level trend for the period 1993–2009. The mean upper steric sea level trend over the region amounts to 2.2 ± 0.3 mm/yr, representing 56% of the total sea level rise derived from satellite altimetry. Note that the upper steric sea level trends are positive all over the basin. A peak center around 118°N, 18.5°E reveals a highest rising rate of 8 mm/yr. We observe that the spatial patterns in upper steric sea level trends over the deep seawater area are similar to those in altimetry-based observed sea level trends (compare with Fig. 2), but they are not perfectly correlated since the SCS is not a closed basin. Besides the steric contribution from deep oceans (below 700 m), the mass change component may also play a role in the sea level changes. The latter depends on precipitation and evaporation above the SCS, as well as inflow and outflow into and out from the sea. It is beyond the scope of this study to quantify this component.

The rate of sea level rise since 1950 caused by the upper steric effect is about 0.4 ± 0.1 mm/yr, which is much lower than the reconstructed mean trend of the SCS region. It

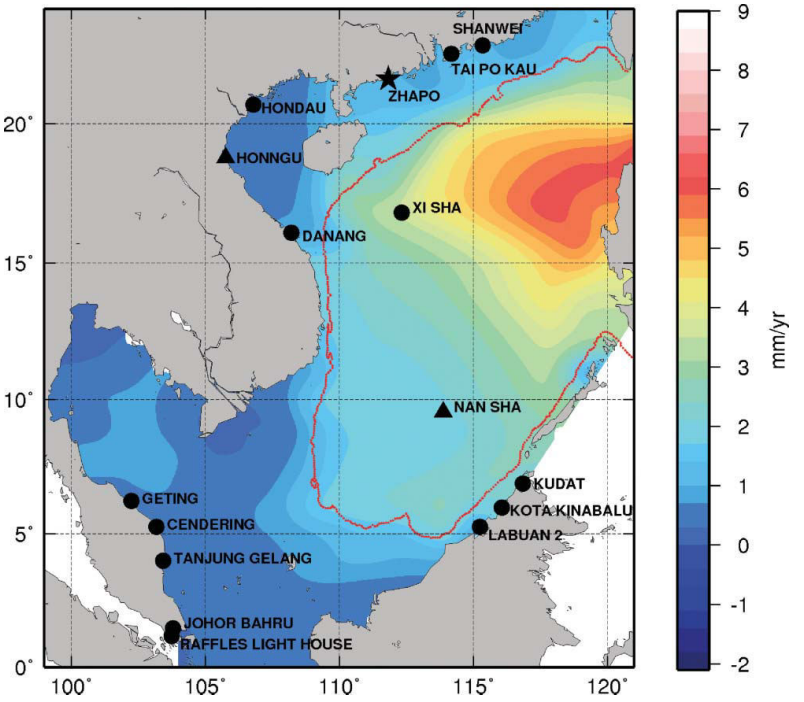

Figure 5. Map of steric sea level trends over the SCS during 1993–2009. (Color figure available online.)

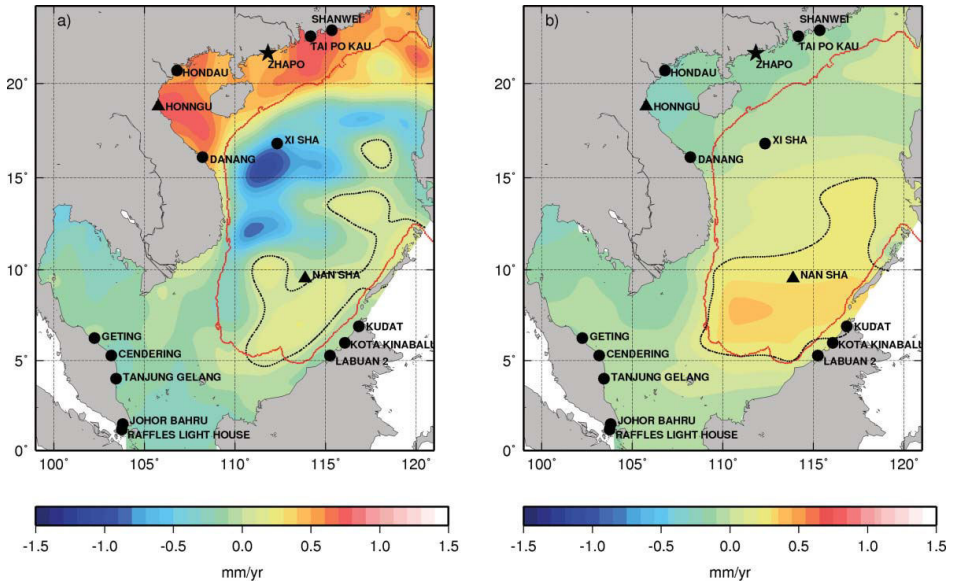

Figure 6. (a) Map of MRESL trend over 1950–2009 with the global mean (∼1.8 mm/yr) trend removed. (b) Map of steric sea level trend over 1950–2009 with the global mean trend of 0.3 mm/yr removed. (Color figure available online.)

only represents 24% of the reconstructed sea level rise. To check if there are similar regional trend patterns in the reconstructed and upper steric sea level in the SCS since 1950, we remove the global mean trend of each data set (1.8 mm/yr for MRESL and 0.3 mm/yr for steric sea level trends). Fig. 6a and 6b show the regional sea level trends in the SCS derived from MRESL and upper steric sea level, respectively. Both figures show a positive rising trend to the southeast of the region, especially in the deeper part of the SCS. Elsewhere, the correlation is poor. The difference between upper steric and reconstructed regional sea level trends suggests that in the SCS, the ocean water mass contribution is substantial.

Interannual Variations of the SCS Sea Level and ENSO

ENSO is the most important natural coupled ocean-atmosphere phenomenon causing global climate variability on interannual time scales. The SCS is embedded between the western Pacific Ocean and the eastern Indian Ocean. Its variations are thus influenced by ENSO. The linkage between El Niño and the SCS is believed to be through an atmospheric bridge of atmospheric circulation changes (Qu 2000; Qu et al. 2004; Wang et al. 2006). In this section, we investigate which are the main climate modes that drive the interannual to multidecadal variability in sea level over the SCS by analyzing the correlation between the Niño 4 index (defined as the mean sea surface temperature averaged over the 5° S-5° N, 160° E - 150° W area of central tropical Pacific; NINO4 hereafter) and the short-term and long-term sea level variations derived from satellite altimetry and reconstruction.

Satellite altimetry data, steric sea level and NINO4 are available at monthly intervals. As for sea level data, we smooth the NINO4 data using a one-year low pass band filter. Figure 7a shows the low-pass filtered NINO4 and the interannual altimetry-based and steric mean sea level over the SCS region. Correlations corresponding to different lag times

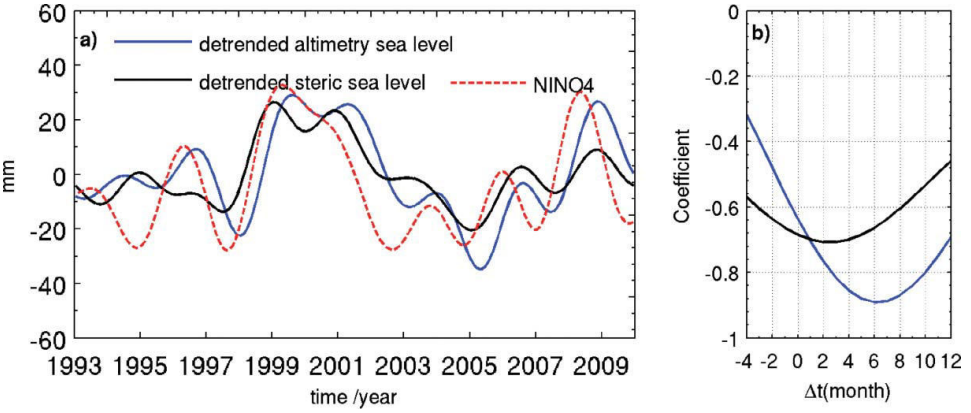

Figure 7. (a) Satellite altimetry observed and steric mean sea level time series for 1993–2009. The detrended satellite altimetry observed sea level is in the blue line. The detrended steric sea level is in black line. The inverse NINO4 index is superimposed in red. (b) Correlation coefficient corresponding to different lag times between detrended altimetry-observed/steric sea level and NINO4. (Color figure available online.)

between NINO4 and SLA are shown in Fig. 7b, the positive value of $\triangle$t denotes NINO4 lead of $\triangle$t months. In Fig. 7a, the sea level time series appears dominated by interannual fluctuations, with strong signals in 1999–2000 and 2007–2008 when NINO4 is minimum. These dates correspond to La Niña events. This clearly demonstrates that mean sea level and its steric component over the SCS is strongly responding to ENSO. The correlation between the observed and steric (interannual) sea level and NINO4 is 0.89 and 0.71, with NINO4 leading the observed and steric sea level by 6 months and 3 months, respectively (see Table 2).

Figure 8 shows geographically averaged MRESL over the SCS between 1950 and 2009 after removing the 1.7 mm/yr mean trend over the region. Fig. 8 also presents the detrended steric sea level averaged over the SCS. We note a high correlation ($r = 0.74$) at interannual time scale between detrended MRESL and steric sea level. The NINO4 index is superimposed on Figure 8. Over the entire period, the MRESL and steric sea levels are anti-correlated with NINO4 ($r = -0.46$). After 1970, both MRESL and steric sea level show a higher correlation with NINO4 ($r = -0.52$). This significant correlation confirms that interannual variability of both observed and steric sea level during the last 60 years is driven by ENSO.

Table 2
Correlation Coefficients

	Correlation Coefficient	
SLA	$r(t = 0)$	r_{max}
Satellite altimetry	-0.64	$r(t = 6) = -0.89$
Steric sea level	-0.68	$r(t = 3) = -0.71$

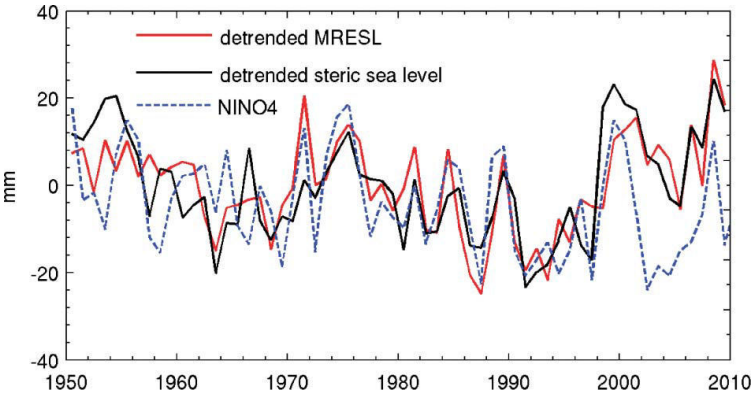

Figure 8. MRESL and steric mean sea level time series for 1950–2009. The detrended MRESL is in the red line. The detrended steric sea level is in black line. The inverse NINO4 index is superimposed in blue. (Color figure available online.)

To capture the characteristics of the SCS sea level variability, an EOF decomposition (Preisendorfer 1988) of the reconstructed sea level was performed over the SCS for the 1950–2009 timespan. Figures 9 and 10 show the first and second modes of RESL EOF decomposition, respectively. The EOF mode 1 with 92% of the total variance captures the sea level trend over SCS. The spatial map in Figure 9 corresponds well to the observed trend map shown in Figure 8. Fig. 9 also shows the geographically averaged trend over the SCS superimposed to the temporal curve corresponding to EOF mode 1. Both the temporal curves are highly correlated. The temporal curve corresponding to the second EOF mode with 4% of the total variance has a significant correlation of 0.7 with NINO4 climate index as shown in Fig. 10. The comparison between the principal component (temporal curve) and NINO4 again confirms that the interannual variability of the SCS sea level is highly correlated with ENSO.

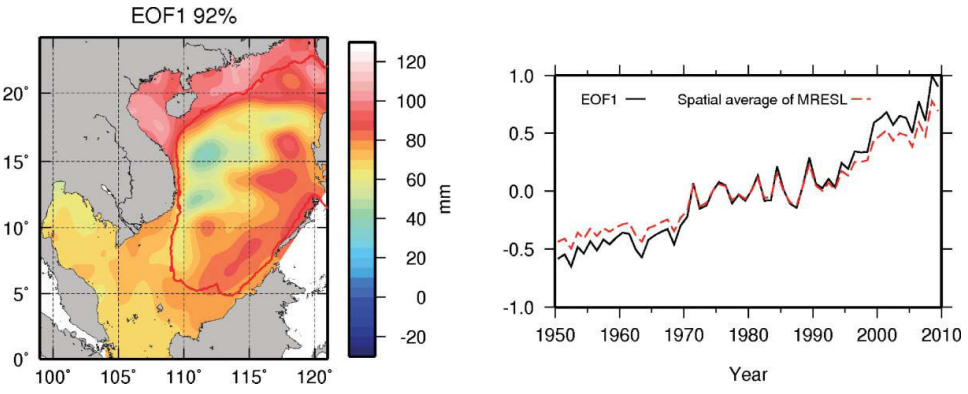

Figure 9. EOF1 decomposition of mean reconstructed sea level for 1950–2009. Left panels show the spatial patterns of the first MRESL EOF modes. In the left panel, temporal time series of the first EOF modes are plotted in black and in red for spatial averaged sea level. (Color figure available online.)

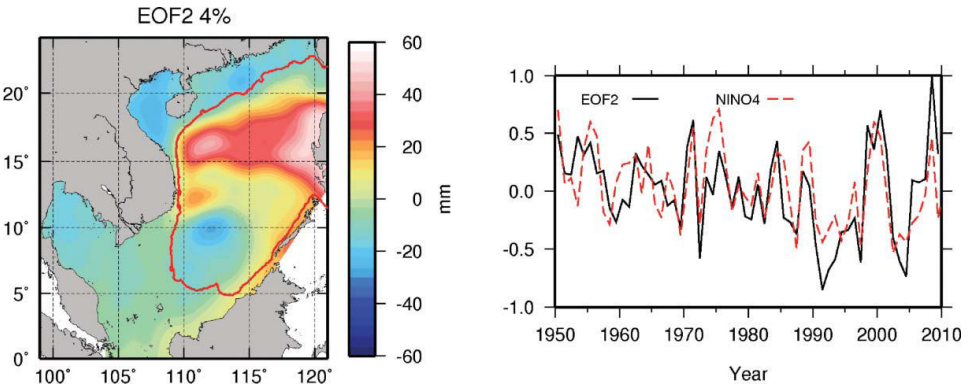

Figure 10. EOF2 decomposition of mean reconstructed sea level for 1950–2009. Left panels show the spatial patterns of the second MRESL EOF modes. In the left panel, temporal time series of the two first EOF modes are plotted in black and in red for NINO4. (Color figure available online.)

Sea Level Variability from Tide Gauge, MRESL, Satellite Altimetry at Tide Gauge Sites

We now consider the tide gauge data (see Figure 2 for location) along with the reconstructed sea levels and the corresponding merged satellite altimetry data. In Fig. 11, we superimpose tide gauge-based and reconstructed sea level time series over their respective timespans. We also superimpose altimetry-based sea level interpolated at tide gauges sites since 1993. Oceanographic considerations as well as trend patterns from Fig. 4 lead us to consider three groups of sea level stations as follows: deep seawater area with water depth more than 200m, northern continental shelf [15°N–24°N] along the Chinese and northern Vietnamese coasts, and southern continental shelf from equator to 15°N. The three sub-regions are called hereafter: SCS1, SCS2 and SCS3 respectively. As noted above, only one tide gauge record (ZHAPO site) in the SCS region was used in the global reconstruction of Meyssignac et al. (2012) while the remaining 15 tide gauge were not used. Thus at those 15 sites, we can test the quality of the reconstruction looking at the correlation with the tide gauge and satellite altimetry data. Table 1 summarizes correlations as well as sea level trends from the MRESL, satellite altimetry observed sea levels and tide gauge data sets.

Generally, the tide gauge records have good correlation with MRESL and satellite altimetry-based sea level, demonstrating the ability of the reconstruction technique to reproduce the interannual variability in the SCS. During 1950–2009, the individual mean sea level trend from MRESL at tide gauges is in the range of 1.1 to 2.5 mm/yr.

Figure 12 shows MRESL trends and associated uncertainty over 1950–2009 at the tide gauge sites. In Fig. 12, the global mean sea level trend (1.8 mm/yr) and its uncertainty are also shown (horizontal red solid line). From Fig. 12 (see also Table 1), we note that only at XI SHA is the sea level trend based on MRESL lower than the global mean sea level rise of the past 60 years, while trends at the six tide gauges sites (SHANWEI, TAI PO KAU, ZHAPO, HONDAU, HONNGU, DANANG) over the SCS1 region are slightly higher. At the seven remaining sites, trends are similar as the global mean sea level rise within its associated uncertainty.

XI SHAN and NAN SHAN are located in the SCS1 sub-region. Since the tide gauge record of NAN SHA is very short (14 years), we interpolate the MRESL at this location to complete the tide gauge records. We then compare the sea level derived from MRESL

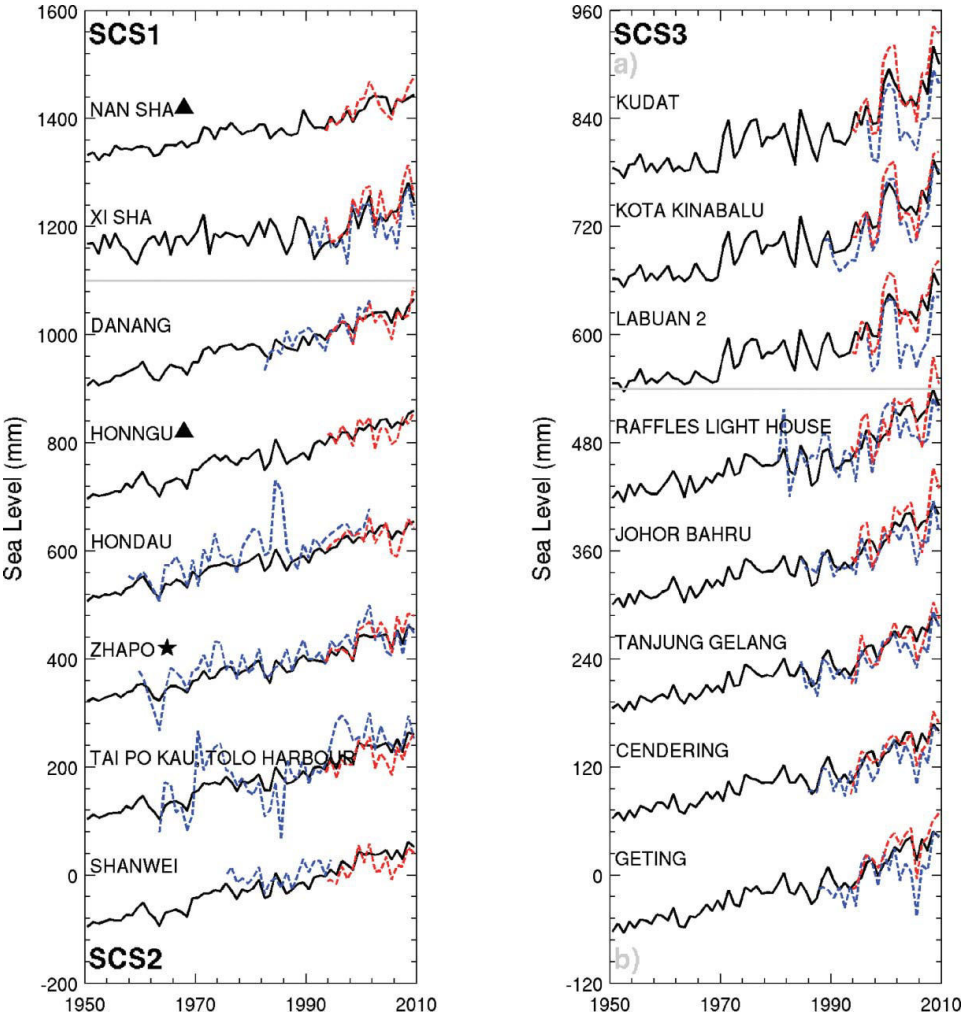

Figure 11. Sea level curves at tide gauge sits since 1950. Time series of MRESL (black), tide gauge (blue), and altimetry-based sea level (red). The time series were arranged in 3 groups: SCS1, SCS2, and SCS3. (Color figure available online.)

and satellite altimetry observed sea level as a mean of validating the reconstruction. The average correlation between MRESL and altimetry-based sea level is 0.52. We observe that the amplitude of sea level variability at XI SHA is larger than that at NAN SHA, while the rate of sea level rising at XI SHA during the last 60 years is 1.1 ± 0.2 mm/yr, smaller than that of 1.8 ± 0.1 mm/yr at NAN SHA. It is evident that sea level in the SCS1 subregion is not rising uniformly. The spatial average (detrended) of MRESL time series for the SCS1 subregion is shown in Fig. 13a (MRESL mean rise over 1950–2009 over SCS1 region amounts to 1.6 ± 0.1 mm/yr). We observe a clear negative correlation ($r = -0.53$) between detrended mean sea level and NINO4 over 1950–2009.

In the SCS2 subregion, which includes SHANWEI, TAI PO KAU, ZHAPO, HONDAU, HONNGU and DANANG, the average correlation between MRESL and tide gauge (not used in reconstruction) sea level is 0.44 (Table 1). The data quality at HONNGU is not

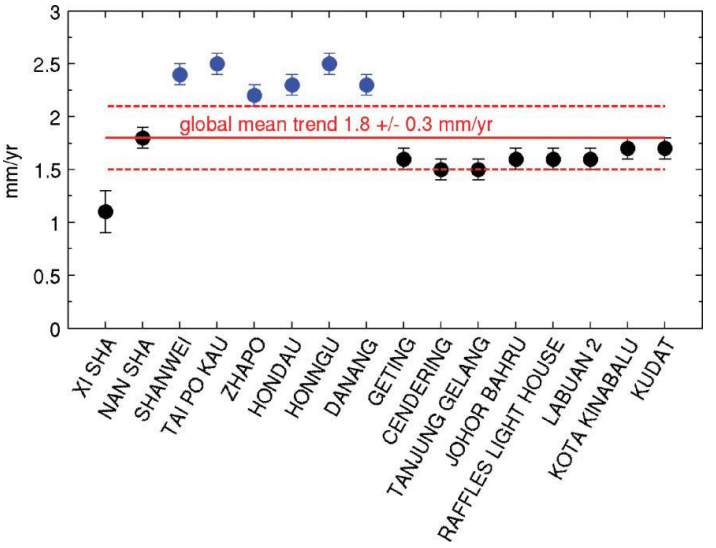

Figure 12. Sea level variations at tide gauge sites along the SCS coastal area since 1950; tide gauges in the SCS2 subregion are in blue and others are in black. (Color figure available online.)

good, although it has a long-time record. We therefore did not superimpose the tide gauge records. The mean MRESL trend over the SCS2 region amounts to 2.3 ± 0.1 mm/yr for 1950–2009. Fig. 13b shows the spatial average (detrended) of MRESL time series superimposed with NINO4 for the SCS2 subregion. We note over the whole 60-year period that MRSL and NINO4 in the SCS2 subregion are not strongly correlated ($r = -0.21$), while over a shorter period of 1970–2000 the variability in sea level derived from MRESL is indeed corresponding to ENSO ($r = -0.52$).

We further divide the SCS3 subregion into two parts according to geographical locations of tide gauges (a) western SCS3 including LABUAN 2, KOTA KINABALU and KUDAT and (b) eastern SCS3 including GETING, CENDERING, TANJUNG GELANG, JOHOR BAHRU and RAFFLES LIGHT HOUSE. The average correlation between detrended MRESL (mean MRESL trend in SCS3 region amounts to 1.6 ± 0.1 mm/yr over 1950–2009) and tide gauge-based sea level is about 0.55. The spatial average of the (detrended) MRESL time series for the SCS3 subregion is shown in Fig. 13c. Similarly to the SCS2 sub-region, we note a high correlation between MRESL and NINO4 over the period of 1970–2009 ($r = -0.66$).

In the SCS3 (a) subregion, although the three sites (LABUAN 2, KOTA KINABALU, and KUDAT) each have short records, starting in 1988 and 1996, reconstructions well represent the interannual variability, as seen in comparing with the tide gauge records and altimetry-based sea level. We then use the reconstruction to examine the long-term interannual sea level variability in this sub-region. It is to be noted that the three locations are well correlated with each other at interannual time scales: the correlation coefficients are about 0.99, suggesting that interannual variability in sea level at those three locations are driven by the same process. We observe that interannual variability in sea level derived from MRESL at these three sites prior to 1970 is much smaller than that of the post 1970 data. For example, at LABUAN 2, the trend over 1950–1970 is about 0.2 ± 0.2 mm/yr

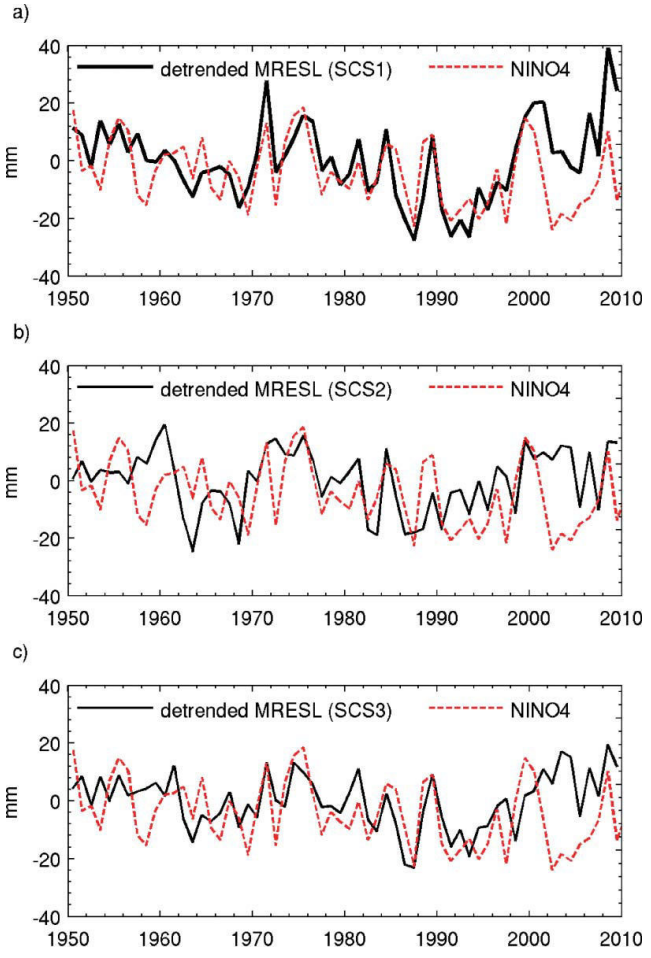

Figure 13. Detrended MRESL curves in each of the 3 regions: (a) SCS1: depth of sea water more than 200 m, (b) SCS2: northern continental shelf, and (c) SCS3: southern continental shelf with the superimposed inverse NINO4. (Color figure available online.)

while the sea level rate amounts to 1.8 ± 0.2 mm/yr during 1970–2009. This difference in variability is similar to that displayed by the NINO4 index.

For the SCS3 (b) subregion, we observe that there is a sudden increase in interannual sea level trend after 1990 for all the five tide gauge sites. For example, at CENDERING location the trends of sea level derived from MRSL amounts to 1.3 ± 0.2 mm/yr over 1950–1990 while it is 3.1 ± 0.3 mm/yr during 1990–2009, consistent with the rising rate of 3.3 ± 0.8 mm/yr derived from satellite altimetry.

Conclusions

In this study, we have examined the sea level variability in the SCS since 1950 by analyzing a 2-D past sea level reconstruction, observed satellite altimetry data and tide gauge records wherever available. For 1993 to 2009, the altimeter data and reconstructed sea levels show the average sea level trend in the SCS region at about 3.6 mm/yr, similar to but

slightly smaller than the regional satellite altimetry trend of about 3.9 mm/yr. We observe that spatial trends in sea level during 1950–2009 are quite different from those reported over the altimetry era (1993–2009). Over the 1950–2009 timespan, sea level in the SCS region is characterized by a strong positive pattern, particularly over the SCS2 subregion [15°N–23°N] along Chinese and northern Vietnamese coastlines. We find that interannual variability of sea level in the SCS and its steric component are driven by ENSO events. However, this regional variability has different characteristics depending on the subregions. For the SCS1 sub-region, the reconstructed sea level rise over 1950–2009 amounts to 1.6 ± 0.1 mm/yr. In this subregion (central basin of the SCS with water depth more than 200 m), we observe a clear negative correlation between detrended mean sea level and NINO4 index over the last 60 year. For the SCS2 subregion where some major cities such as Hongkong and Guangzhou are located, the reconstructed sea level trend amounts to 2.3 ± 0.1 mm/yr for 1950–2009. In this coastal area, sea level is rising faster than elsewhere in the region. The reason for such a behavior is unclear. However, we have a suspicion that it might be caused by the thermal expansion in this shallow area, since this signal could not be captured by the Ishii and Kimoto (2009) steric sea level due to lack of complete coverage of temperature and salinity data, while it is successfully reproduced in the reconstructions. Further investigations are needed to figure out its origins. Over 1970–2000, the interannual variability in sea level is highly correlated with NINO4 index ($r = -0.53$). Similar to SCS2 subregion, the reconstructed sea level trend in the SCS3 subregion [from equator to 15°N] over 1950–2009 is about 1.6 ± 0.1 mm/yr and the correlation coefficient between MRESL and NINO4 over 1970–2000 reaches $-0.66.0$

Acknowledgements

We are grateful to Dr. Jianli Chen of CSR, United States, for constructive suggestions. Thanks are also extended to two anonymous reviewers for their valuable comments. Dongju Peng was supported by the CAS Scholarship Council and National Natural Science Foundation of China (No. 11003036). Hindumathi Palanisamy benefited from a grant of the ANR CECILE project. This work is part of the ANR CECILE project.

References

Becker, M., B. Meyssignac, C. Letetrel, W. Llovel, A. Cazenave, and T. Delcroix, 2012. Sea level variations at tropical Pacific islands since 1950. *Global and Planetary Change* 80/81:85–98.

Bakitz, H., and C. K. Shum, 2010. Mean sea level variation in the South China Sea from four decades of tidal records in Hongkong. *Marine Geodesy* 23:221–233.

Carton, J. A., and B. S. Giese. 2008, A reanalysis of ocean climate using Simple Ocean Data Assimilation (SODA). *Month Weather Review* 136:2999–3017.

Cazenave, A., and R. S. Nerem, 2004. Present-day sea level change: Observations and causes. *Reviews of Geophysics* 42:RSCS3001.

Cazenave, A., and F. Remy, 2011. Sea level and climate: Measurements and causes of changes. *WIREs Climate Change* 2:647–662.

Cheng, X., and Y. Qi, 2007. Trends of sea level variations in the South China Sea from the merged altimetry data. *Global and Planetary Change* 57:371–382.

Church, J. A., N. J. White, R. Coleman, K. Lambeck, and J. X. Mitrovica, 2004. Estimates of the regional distribution of sea level rise over the 1950 to 2000 period. *Journal of Climate* 17(13):2609–2625.

Church, J. A., N. J. White, and J. R. Hunter, 2006. Sea-Level rise at tropical Pacific and Indian Ocean islands. *Global and Planetary Change* 53:155–168.

Church, J. A., N. J. White, L. Konikow, C. Domingues, J. Goley, and E. Rignot, 2011. Revisiting the Earth's sea level and energy budget from 1961 to 2008. *Geophysical Research Letters* 38: L18601.

Church, J. A., P. Woodworth, T. Aarup, and W. S. Wilson. 2010. *Understanding sea-level rise and variability*. London: Wiley.

Ding, X., D. Zheng, W. T. Wong, K. W. Li, W. Chen, and P. Zhong, 2004. Recent sea level variations in Southern China from tide gauge observations. Proceedings of the Asia-Pacific Space Geodynamics Symposium, Singapore, 6–8 July 2004, 126–136.

Douglas, B. C. 1991. Global sea level rise. *Journal of Geophysical Research* 96(C4):6981–6992.

Douglas, B. C. 2001. Sea level change in the era of the recording tide gauge. *International Geophysics* 75:37–64.

Ho, C., Q. Zheng, Y. Soong, N. Kuo, and J. Hu, 2000. Seasonal variability of sea surface height in the South China Sea observed with TOPEX/Poseidon altimeter data. *Journal of Geophysical Research* 105:13981–13990.

Holgate, S. 2007. On the decadal rates of sea level change during the twentieth century. *Geophysical Research Letters* 34:L01602.

Ishii, M., and M. Kimoto, 2009. Reevaluation of historical ocean heat content variations with varying XBT and MBT depth bias corrections. J*ournal of Oceanography* 65:287–299.

Jevrejeva, S., A. Grinsted, J. Moore, and S. Holgate, 2006. Nonlinear trends and multiyear cycles in sea level records. *Journal of Geophysical Research* 111:C09012.

Jevrejeva, S., J. Moore, A. Grinsted, and P. Woodworth, 2008. Recent global sea level acceleration started over 200 years ago? *Geophysical Research Letters* 35:L08715.

Kalnay, E., M. Kanamitsu, R. Kistler, W. Collins, D. Deaven, L. Gandin, M. Iredell, S. Saha, G. White, J. Woollen, Y. Zhu, M. Chelliah, W. Ebisuzaki, W. Higgins, J. Janowiak, K. C. Mo, C. Ropelewski, J. Wang, A. Leetmaa, R. Reynolds, R. Jenne, and D. Joseph, 1996. The NCEP/NCAR 40-year reanalysis project. *Bulletin of the American Meteorological Society* 77:437–472.

Li, L., J. Xu, and R. Cai, 2002. Trends of sea level rise in the South China Sea during 1990s: An altimetry result. *Chinese Science Bulletin* 47:582–585.

Llovel, W., A. Cazenave, P. Rogel, A. Lombard, and M. Berge-Nguyen. 2009. Two-dimensional reconstruction of past sea level (1950–2003) from tide gauge and Ocean General Circulation Model. *Climate of the Past* 5:217–227.

Lombard, A., A. Cazenave, P. Y. Le Traon, and M. Ishii, 2005. Contribution of thermal expansion to present-day sea-level change revisited. *Global and Planetary Change* 47:1–16.

Meyssignac, B., W. Llovel, M. Becker, and A. Cazenave, 2012. An assessment of two-dimensional past sea level reconstructions over 1950–2009 based on tide gauge data and different input sea level grids. *Surveys in Geophysics* 33:945–972.

Milne, G., W. Gehrels, C. Hughes, and M. Tamisiea, 2009. Identifying the causes of sea-level change. *Nature Geoscience* 2(7):471–478.

Nicholls, R. J., and A. Cazenave, 2010. Sea-level rise and its impact on coastal zones. *Science* 328:1517–1520.

Palanisamy, H., M. Becker, B. Meyssignac, O. Henry, and A. Cazenave, 2012. Regional sea level change and variability in the Caribbean Sea since 1950. *Journal of Geodetic Science* 2/2:125–133.

Peltier, W. R. 2004. Global glacial isostasy and the surface of the ice-age Earth: The ICE-5G (VM2) model and GRACE. *Annual Review of Earth and Planetary Sciences* 32:111–149.

Penduff, T., M. Juza, L. Brodeau, G. Smith, B. Barnier, J.-M. Molines, A.-M. Treguier, and G. Madec, 2011. Impact of global ocean model resolution on sea-level variability with emphasis on interannual time scales. *Ocean Science* 6:269–284.

Preisendorfer, R. W. 1988. Principal component analysis in meteorology and oceanography. *Developments in Atmospheric Science* 17.

Purkey, S., and G. C. Johnson, 2010. Warming of global abyssal and deep southern ocean waters between the 1990s and 2000s: Contributions to global heat and sea level rise budget. *Journal of Climate* 23:6336–6351.

Qu, T. 2000. Upper-layer circulation in the South China Sea. *Journal of Physical Oceanography* 30:1450–1460.

Qu, T., Y. Y. Kim, M. Yaremchuk, T. Tozuka, A. Ishida, and T. Yamagata. 2004. Can Luzon strait transport play a role in conveying the impact of ENSO to the South China Sea? *Journal of Climate* 17:3644–3657.

Ray, R., and B. Douglas, 2011. Experiments in reconstructing twentieth-century sea levels. *Progress in Oceanography* 91(4):496–515.

Rong, Z., Y. Liu, H. Zong, and Y. Cheng, 2007. Interannual sea level variabilty in the South China Sea and its response to ENSO. *Global and Planetary Change* 55:257–272.

Shaw, P., S. Chao, and L. Fu, 1999. Sea surface height in the South China Sea from satellite altimetry. *Oceanologica Acta* 22(1):1–17.

Song, Y. T., and F. Colberg, 2011. Deep ocean warming assessed from altimeters, gravity recovery and climate experiment, in situ measurements, and a non-Boussinesq ocean general circulation model. *Journal of Geophysical Research* 116:C02020.

Wang, C., W. Wang, D. Wang, and Q. Wang, 2006. Interannual variability of the South China Sea associated with El Niño. *Journal of Geophysical Research* 111:C030203.

Woodworth, P., and R. Player, 2003. The permanent service for mean sea level: An update to the 21st century. *Journal of Coastal Research* 19:287–295.

3.2.4 The vulnerable zones: a synthesis

In the section, we put into perspective, the results obtained on climate-related and total relative sea level change over 1950-2009 in four regions of study: tropical Pacific (*Becker et al.*, 2012), Indian Ocean (*Palanisamy et al.*, 2014, Caribbean (*Palanisamy et al.*, 2012) and South China Sea (*Peng et al.*, 2013). Fig.3.7 displays the long term total climate-related sea level change over the four study regions. The figure clearly shows that the sea level variations are not uniform globally and that the tropical Pacific shows highest variability in sea level trends when compared to the Caribbean Sea, South China Sea or the Indian Ocean. Over the period of 60 years, several sites at the Tropical Pacific, for example Honiara, Funafuti, etc. have sea level trend values higher than the global mean sea level rise (including its error bars) with Funafuti having a value more than twice the global mean value. There are also very few sites in the Tropical Pacific (example Noumea) where the sea level trend is lesser than the global mean sea level. In the case of the Caribbean Sea, the sea level trends over 60 years at different sites are in the same range as the global mean sea level rise with few stations (example: Gibara, North Sound) having values slightly higher than the global mean rise but well within the error bars. This is the same in the case of South China Sea and Indian Ocean where most of the sites have sea level trend values lesser than or the same as that of the global mean sea level rise between 1950 and 2009.

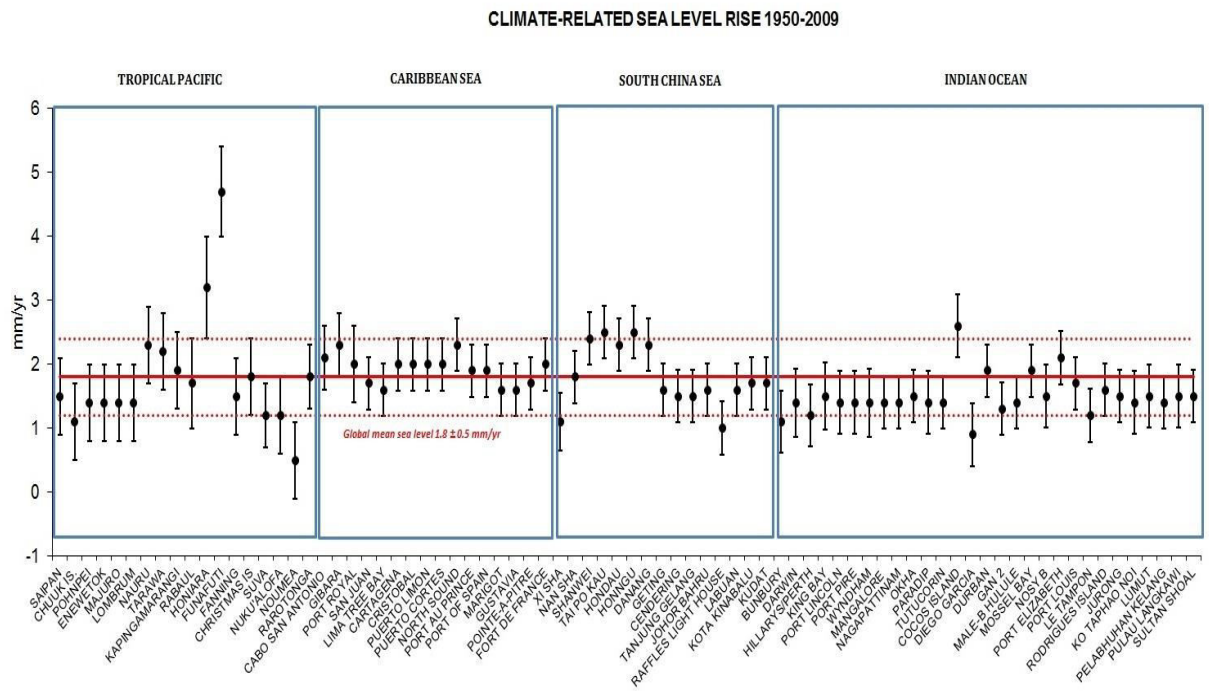

Figure 3.7: Climate-related sea level changes at different locations of the vulnerable zone over 1950-2009

Fig.3.8 displays the long-term total relative sea level change estimated with the help of VLM measures from GPS and DORIS in the tropical Pacific and Indian Ocean. Funafuti in the Tropical Pacific shows very high relative sea level trend (5.1 ± 0.7 mm/yr) followed by Perth in the eastern Indian Ocean with a trend of 4.2 ± 0.6 mm/yr. In both of these cases, subsidence plays a very important role. From the figure we can also observe that there are several other sites in the tropical Pacific and Indian Ocean with total relative sea level trend values higher than the global mean sea level rise.

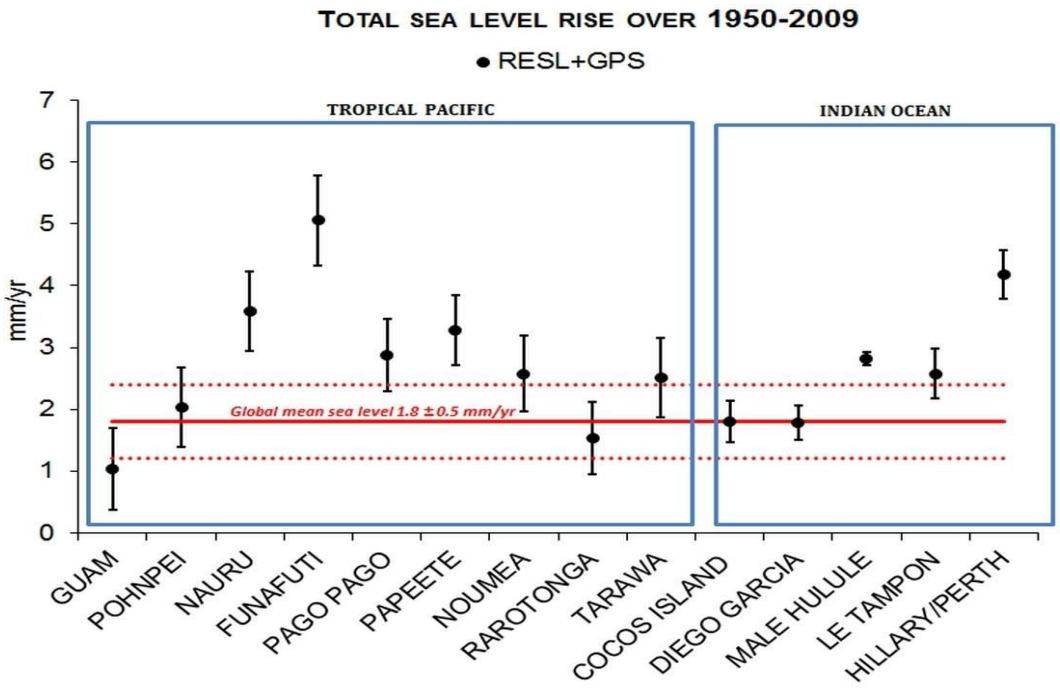

Figure 3.8: Total relative sea level change at different locations in the tropical Pacific and Indian Ocean over 1950-2009.

All the above results demonstrate the importance and contribution of regional sea level variability and land motions to local sea level changes in the tropical islands and coastal zones: regions that are highly impacted by climate-change. These results corroborate that sea level rise as felt by the population is no longer a question. The question that needs to be addressed now would be how well are we all prepared in this scenario of sea level risks.

Chapter 4

The role of internal climate variability and external forcing on regional sea level variations

In chapter 3, we have discussed the various causes that contribute to regional sea level variability with non-uniform thermosteric and halosteric changes being the most important contributor. In fact, the spatial and temporal variability of steric sea level changes is tightly linked to complex ocean dynamic processes that are also related to internal climate modes such as ENSO, IPO/PDO etc. While the internal climate modes are in general natural climate variability not resulting from human (i.e. anthropogenic) influences, understanding the impact of external anthropogenic influences (i.e. climate change) on regional sea level variability and on internal climate modes has so far remained a great challenge for sea level and climate scientists. For studies on global warming and climate change, it is important to distinguish between internally generated and externally-forced climate variability. In this chapter, we first provide a detailed explanation on the roles of internal climate variability and external forcing in regional sea level variability. We then discuss our two main works related to this thematic applied on the Pacific Ocean.

4.1 Internal climate variability

Internal climate variability refers to what is frequently called 'unforced' climate changes or 'modes' of variability that do not involve changes in Earth's net radiative balance. *Hunt*, (2006) called the unforced internal climate variability as that which occurs solely due to internal interactions such as complex ocean-atmosphere dynamics within the climate system without any

external forcing. The climate may vary naturally even in the absence of external forcing, because, in a system of components with very different response times and non-linear interactions, the components are never in equilibrium and are constantly varying. These can occur over various spatial (regional, hemispheric or global) and temporal scales (e.g. seasonal, inter-annual, decadal etc.) and can have significant global impacts. The unforced modes of climate variability can further be affected by feedbacks, i.e. the results of the varying processes affecting the original state of the climate system thereby amplifying or reducing the original state.

Regional climate is generally much more variable than climate on a hemispheric or global scale because variations in one region are compensated for by opposite variations elsewhere (*Houghton et al.,* 2001). The spatial structure of regional climate variability shows that it occurs predominantly in preferred large-scale and geographically anchored spatial patterns. Such patterns result from interactions between the atmospheric circulation and land and ocean. Though geographically anchored, their amplitude can change in time. A well-known example of an internal climate mode is the ENSO phenomenon caused by atmosphere-ocean interaction in the tropical Pacific. The resulting El Nino and La Nina events have world-wide impacts on weather and climate (*Houghton et al.,* 2001). Internal climate modes play a significant role in influencing regional sea level variability at both shorter and longer time scales (e.g. *Levitus et al.*, 2005, *Lombard et al.*, 2005, *Lozier et al.*, 2010, *Di Lorenzo et al.*, 2010, *Zhang and Church*, 2012, *Stammer et al.*, 2013). In this section, we first address four main internal climate modes affecting the world ocean even though we will further focus only on the Pacific region.

4.1.1 El Niño-Southern Oscillation (ENSO)

The El Niño-Southern Oscillation mode of variability originates in the tropical Pacific Ocean through dynamic interaction between ocean and atmosphere causing El Niño ‘warm’ and La Niña ‘cold’ events every two to eight years and is the strongest interannual climate mode. Initially ‘El Niño’ was a term that was used by the Peruvian fishermen to indicate a warm seasonal southward coastal current that appeared along the Peruvian coasts around Christmas. Later on, *Hildebrandssan,* (1897), *Walker, (1928 and references therein), Walker and Bliss, (1937 and references therein)* discovered out of phase surface atmospheric pressure fluctuations

between the western and eastern halves of the tropical Pacific and the term Southern Oscillation was henceforth used to portray the east-west seesaw. The link between El Nino and Southern Oscillation was established by *Bjerknes*, (1969, 1966) and hence the name El Niño-Southern Oscillation (ENSO).

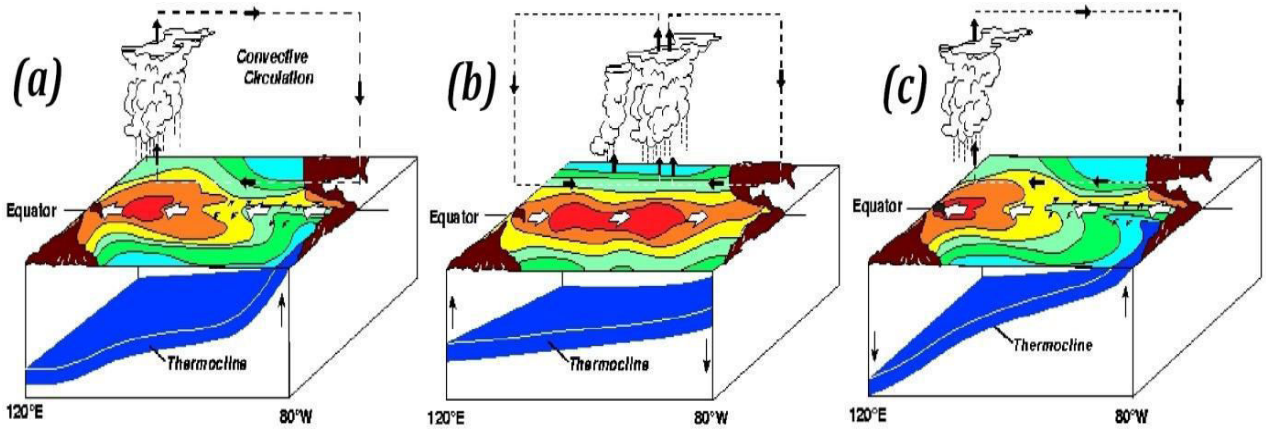

Figure 4.1: Schematic plots of the state of the tropical Pacific during (a) normal, (b) El Niño, and (c) La Niña conditions. The contour plots illustrate the sea surface temperature with red (blue) denoting warmer (cooler) temperatures. Thick black (white) arrows denote the wind (surface currents) direction. Source: http://www.pmel.noaa.gov/tao/elnino/nino-home.html

Under normal conditions, strong easterly trade winds (north easterly in the northern and south easterly in the southern hemisphere) blow over central tropical Pacific and they intensify the North and South Equatorial Currents thereby resulting in the accumulation of warm water in the western equatorial Pacific. This causes an east-west thermocline slope (Fig.4.1a) with sea level higher in the western than in the eastern tropical Pacific. During the onset of El Niño event, the easterly trade winds weaken with the arrival of strong westerlies in the western equatorial Pacific resulting in an eastward release of the accumulated water. This results in anomalous warm SSTs occupying the central and Eastern Equatorial Pacific (EEP) causing the deepening of the thermocline in the EEP thereby decreasing the normal east-to-west tilt (Fig 4.1b) and reversed slope in sea level. La Niña 'cool' events are the opposite of El Nino events that occur due to 'more than normal' intensified easterly trade winds. As a result, the SST warming is unusually weak. The warm water is pushed further into the far western equatorial Pacific thereby strengthening the east-west tilt of the thermocline depth (Fig.4.1c) and therefore the increased sea level in western tropical Pacific. The relation between thermocline depth and sea level is discussed in Section 4.4.

Several indices, such as, Multivariate ENSO Index (MEI), Southern Oscillation Index (SOI), Niño 3.4, Niño 3.1 SST indices can be used to characterize the phase and intensity of ENSO events. The variables that are used to calculate these indices differ. For example, while SOI is calculated based on sea level pressure difference between Tahiti and Darwin, the MEI index is calculated using six different variables: sea level pressure, zonal and meridional components of surface wind, SST, surface air temperature and cloudiness. A comparison between some of these indices can be found in *Hanley et al.*, (2003), *Deser and Wallace*, (1987).

4.1.2 Pacific Decadal Oscillation (PDO)/ Interdecadal Pacific Oscillation (IPO)

The Pacific Decadal Oscillation (PDO), a robust ocean-atmosphere Pacific climate variability often described as a long-lived El Nino-like pattern (*Zhang et al.*, 1997) was first identified through the relationship between decadal SSTs and oceanic ecosystem variability (Alaskan salmon production) by *Mantua et al.*, (1997). The PDO pattern is marked by widespread variations in the Pacific basin and North American climate with a periodicity of around 20 to 30 years. It exhibits two extreme phases that can be classified as either warm or cool phases as defined by ocean temperature anomalies in the northeast and tropical Pacific Ocean. The PDO is termed positive and warm when SSTs are anomalously cool in the interior North Pacific and warm along the Pacific Coast, and when sea level pressures are below average over the North Pacific (Fig.4.2a). When the climate anomaly patterns are reversed, with warm SST anomalies in the interior and cool SST anomalies along the North American coast, or above average sea level pressures over the North Pacific, the PDO is in its cold/negative phase (Fig.4.2b, *Zhang et al.*, 1997, *Mantua et al.*, 1997). Its timing, phase and amplitude can be quantified by the PDO index defined as the leading principal component of the North Pacific (poleward of 20° N) monthly sea surface temperature (SST) variability (*Mantua et al.* 1997, *Zhang et al.* 1997). The Interdecadal Pacific Oscillation (IPO) is (almost) Pacific-wide equivalent of the PDO with as much variance in the South Pacific (at least to 55°S) as in the North Pacific (*Folland et al., 1999*). Shifts in the IPO/PDO phase can have significant implications for global climate such as affecting Pacific and Atlantic hurricane activity, droughts and flooding around the Pacific basin, the productivity of marine ecosystems, and global land temperature patterns and regional sea level.

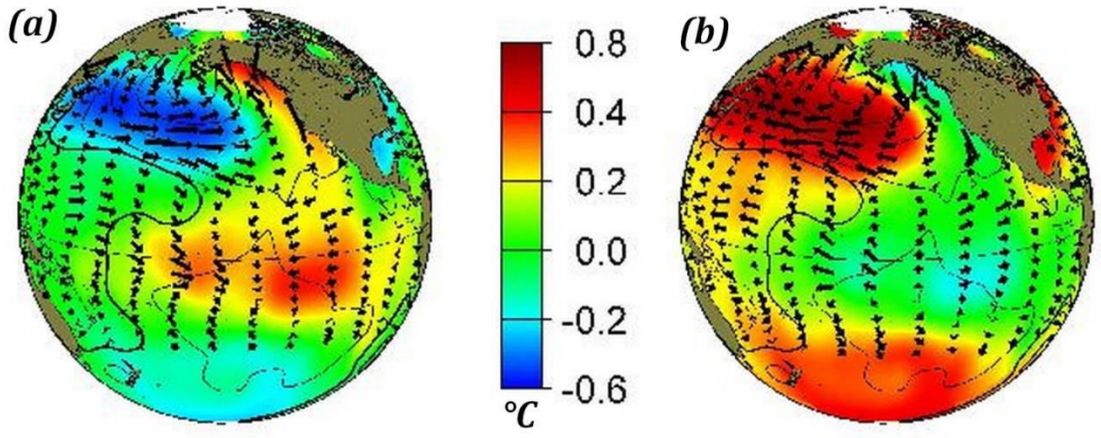

Figure 4.2: Typical winter time Sea Surface Temperature (colors), Sea Level Pressure (contours) and surface wind stress (arrows) anomaly patterns during* (a) *warm and* (b) *cool phases of PDO. Source: http://research.jisao.washington.edu/pdo/

Several studies (e.g. *Mantua and Hare*, 2002, *Deser et al.*, 2004, *Power et al.*, 2006, *Verdon and Franks*, 2006, *McGregor et al.*, 2007, *Zhang and Church*, 2012) have tried to explain the relation between ENSO and IPO/PDO. They have shown that IPO/PDO is could essentially be the low frequency residual of ENSO variability occurring at multi decadal time scales. Furthermore, *Verdon and Franks*, (2006) have also shown that positive PDO/IPO phase triggers more El Niño events while negative phase triggers more La Niña events. However, two main characteristics distinguish PDO/IPO from ENSO: first, PDO/IPO events generally persist for 20-to-30 years, while typical ENSO events persist for 6 to 18 months; second, the climatic fingerprints of the PDO/IPO are most visible in the extra-tropics, especially the North Pacific/ North American sector, while secondary signatures exist in the tropics, and the opposite is true for ENSO (*Zhang et al.*, 1997, *Mantua et al.*, 1997, *Minobe*, 1997, *NRC, 1998*). Moreover, *Schneider and Cornuelle*, (2005) and *Pierce*, (2001) have also shown that IPO is not a mode of variability linked only to ENSO but is in fact a blend of several other phenomena such as zonal advection in the Kuroshio-Oyashio Extension, Aleutian low anomalies etc.

Evidence of four IPO phase changes since the 20th century, i.e. two warm phases during 1925-1946, 1977-1997 and two cold phases during 1947-1976 and since 1998 have been recorded so far (*Deser et al.*, 2004, *Yasunaka and Hanawa*, 2003, *Hare and Mantua*, 2000). The IPO index which is defined as the leading principal component of the Pacific (from the North

Pacific until at least 55°S) monthly SST variability is in general used to characterize the intensity of IPO events. The influence of IPO on sea level will be discussed in Section 4.4.

4.1.3 Indian Ocean Dipole (IOD) mode

The Indian Ocean Dipole (IOD) is a coupled ocean-atmosphere phenomenon occurring in the equatorial Indian Ocean that affects the climate of Australia and other countries that surround the Indian Ocean basin and is a significant contributor to rainfall in this region (*Saji et al.*, 1999). The IOD involves aperiodic east-west oscillation of SST between 'positive', 'neutral' and 'negative' phases and are strongly coupled to surface wind anomalies in the central equatorial Indian Ocean (*Saji et al.*, 1999, *Behera and Yamagata*, 2001, *Saji and Yamagata*, 2003). A positive IOD period is characterized by anomalous SST cooling in the south eastern equatorial Indian Ocean and anomalous SST warming in the western equatorial Indian Ocean (Fig.4.3a). As a result, the normal convection situated over the eastern Indian Ocean warm pool shifts to the west. This brings heavy rainfall over east Africa, decrease in rainfall over central and southern Australia and severe droughts over the Indonesian regions. Conversely, negative IOD period is characterized by anomalous SST warming in the south eastern equatorial and cooling in the western equatorial Indian Ocean (Fig.4.3b) resulting in more rainfall in the Indonesian and Australian regions and drought in east Africa.

IOD is a short term event and usually begins to develop during the summer of the Northern Hemisphere, reaches its maximum in fall and ends in winter as a result of seasonal winds (*Behera and Yamagata*, 2001, *Black et al.*, 2003, *Hastenrath*, 2007). Several IOD events have occurred simultaneously with ENSO events and there is a significant debate on whether IOD is an independent climate variability occurring in the Indian Ocean or whether it is triggered by ENSO (*Reason et al.*, 2000, *Allan et al.*, 2001). Positive IOD events are often associated with El Niño events and negative IOD with La Niña events. The link between IOD and ENSO is thought to be through the extension of the Walker circulation to the west and associated Indonesian through flow i.e. the flow of warm tropical ocean water from the Pacific into the Indian Ocean. Studies (e.g. *Deser et al.*, 2004, *Clark et al.*, 2003) have also shown good correlations between inter-decadal and decadal variability of SST-based IOD, ENSO and IPO/PDO indices, raising the issue of coupled mechanisms governing IOD, ENSO and

IPO/PDO. Recently, *Han et al.*, (2013) found that while IOD based variability correlated well with IPO on decadal time scales until the mid-1980s, this correlation reversed sign afterwards. The mechanism that has caused this sudden sign reversal is yet to be understood.

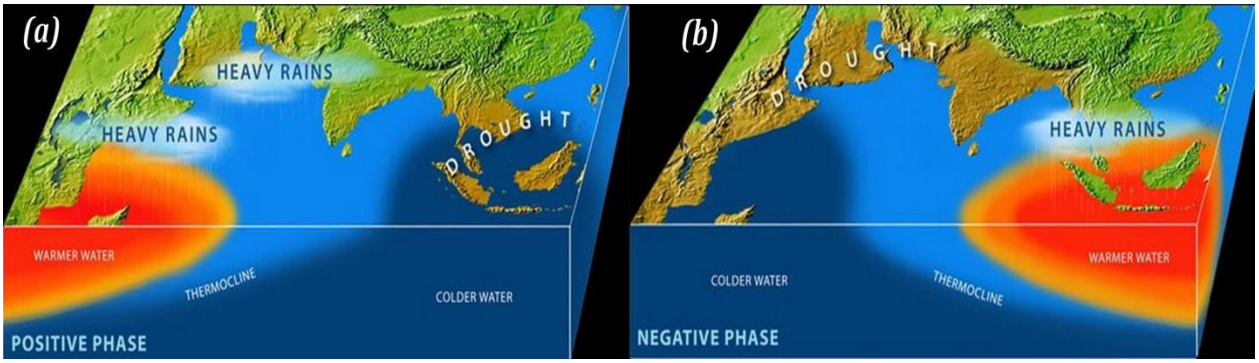

Figure 4.3: Indian Ocean Dipole (a) positive and (b) negative phases. Source: Woods Hole Oceanographic Institution with illustration by E. Paul Oberlander.

Several studies have shown that the interannual sea level variability in the Indian Ocean is driven by mechanisms that involve IOD events (*Palanisamy et al.*, 2014, *Nidheesh et al.*, 2013, *Aparna et al.*, 2012, *Sreenivas et al.*, 2012). Performing an EOF decomposition on the Indian Ocean sea level signal to capture the characteristics of the sea level variability clearly shows the east-west dipole pattern related to IOD events (See *Palanisamy et al.*, 2014 and Section 3.2.1 of this manuscript).

4.1.4 North Atlantic Oscillation (NAO)

The North Atlantic Oscillation (NAO) is one of the most prominent and recurrent patterns of intra-seasonal atmospheric circulation variability that dictates climate variability from the eastern United States to Siberia and from the Arctic to subtropical Atlantic (*Hurrell et al.*, 2003). NAO refers to the redistribution of atmospheric mass between the Arctic and the subtropical Atlantic and swings from one phase to another.

The positive phase of the NAO reflects below-normal sea surface heights and pressure across the high latitudes of the North Atlantic and above-normal sea surface heights and pressure over the central North Atlantic, the eastern United States and Western Europe. NAO strong positive phases can be associated with above-normal temperatures in eastern United States and northern Europe and below-normal temperatures in Greenland and across southern Europe and

the Middle East. They are also associated with above-normal precipitation over northern Europe and Scandinavia and below-normal precipitation over southern and central Europe (Fig.4.4a). The negative phase reflects an opposite pattern of height and pressure anomalies over these regions with patterns of temperature opposite to that of positive NAO being observed over land (Fig.4.4b). Both phases of the NAO are associated with basin-wide changes in the intensity and location of the North Atlantic jet stream and storm track, and in large-scale modulations of the normal patterns of zonal and meridional heat and moisture transport (*Hurrell*, 1995), which in turn results in changes in temperature and precipitation patterns often extending from eastern North America to western and central Europe (*Walker and Bliss*, 1932, *van Loon and Rogers*, 1978, *Rogers and Van Loon*, 1979).

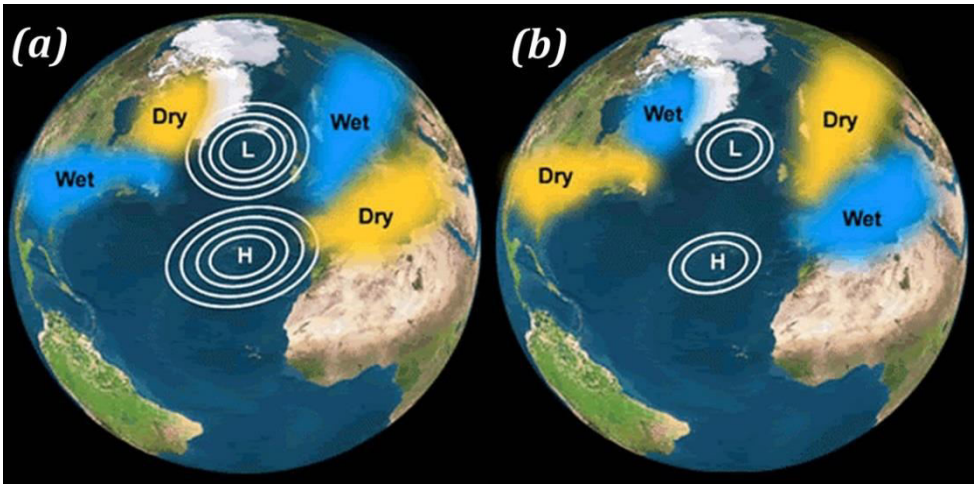

Figure 4.4: North Atlantic Oscillation (a) positive and (b) negative phases. The contours 'L' and 'H' indicate high and low pressure anomalies respectively. Source: http://nc-climate.ncsu.edu/climate/patterns/NAO.html

Studies (*Tsimplis and Josey*, 2001, *Woolf et al.*, 2003, *Wakelin et al.*, 2003, *Tsimplis et al.*, 2006) have been performed on the impact of NAO on sea level. They show that a linear relationship between the winter sea-level anomalies and the NAO index can be used to explain most of the variability in the North Sea, Mediterranean and the eastern parts of the North Atlantic. While wind is the major forcing factor affected by NAO in the shallow North Sea (*Wakelin et al.*, 2003), atmospheric pressure changes remain as the major contributor over the Mediterranean (*Tsimplis and Josey*, 2001) and Atlantic coasts of Europe (*Wakelin et al.*, 2003, *Tsimplis et al.*, 2006).

4.1.5 Other modes of internal climate variability

Many other patterns of internal climate variability have also been identified over the years occurring at various time scales such as the Atlantic Multi-decadal Oscillation (AMO, *Kerr*, 2000, *McCarthy et al.*, 2015), Antarctic Circumpolar Wave (ACW, *White et al.*, 1998, *Venegas*, 2003), Arctic Oscillation or Northern Annular Mode (NAM, *Lorenz*, 1951, *Thompson and Wallace*, 1998, *Ripesi et al.*, 2012), Southern Annular Mode (SAM, *Hartmann and Lo*, 1998, *Abram et al.*, 2014), Madden-Julian Oscillation (MJO, *Madden and Julian*, 1971, *Madden and Julian*, 1994, *Zhang et al.*, 1997) etc. In this manuscript, I have focused on four of the main internal climate modes that have major impacts on regional sea level variability.

4.2 Externally-forced climate variability

Externally-forced climate variability refers to variations over time in one or more measures of climate caused by some factors outside the climate system. These factors include both natural and anthropogenic sources. Examples of natural external forcing include solar variability and volcanic eruptions. Examples of anthropogenic forcing are from changing concentrations of greenhouse gases and aerosols and land use produced by human activities.

The magnitude of externally- forced variability depends on the extent of the forcing involved and the sensitivity of the climate system to the forcing. Therefore the response time of various components of the climate system to external forcing highly varies. Within the atmosphere, the response time of the troposphere to external forcing is relatively shorter, only from days to weeks, whereas the stratosphere comes into equilibrium only within a time period of few months. In the case of oceans, due to their large heat capacity, they have a much longer response time, typically decades but also up to centuries. The response time of the strongly coupled surface-troposphere system is therefore slow compared with that of the stratosphere, and is mainly determined by the oceans. Therefore the climate system may respond to variations in external forcing on a wide range of space- and time-scales (*Houghton et al.,* 2001). In this section, we briefly explain the two sources of external forcing that impact the climate.

4.2.1 Natural external forcing

Several natural external drivers of climate change operate on multiple time scales (*Myhre et al.*, 2013). For example, solar variability takes place at many time scales that include centennial and millennial time scales as the radiant energy output of the Sun changes (*Helama et al.*, 2010). Furthermore, variations in Earth's orbital and rotational parameters result in redistribution of incoming solar radiation and trigger glacial and interglacial cycles. While these occur at very large time scales, Earth's revolution around the sun and rotation results in seasonal and daily cycle changes respectively. All the mentioned natural external forcings are gradual and do not produce drastic changes at short time scale thereby enabling different components of the climate system to retain their equilibrium. However this is not the case with forcing that produces immediate changes or consists of short-lived impulse such as volcanic eruptions (*Philander*, 2012).

Volcanic eruptions that inject substantial amounts of SO_2 gas (sulphate aerosols) into the stratosphere are the dominant natural cause of externally forced climate change on the annual to multi-decadal time scales, both because of the multi-decadal variability of eruptions and the time scale of the climate system response. Volcanic eruptions and solar variability can explain much of the pre-industrial climate change of the last two millennia (*Schneider et al.*, 2009, *Brovkin et al.*, 2010; *Legras et al.*, 2010; *Miller et al.*, 2012). Though sulphate aerosols remain in the troposphere only for a few weeks, those in the stratosphere from tropical eruptions have a lifetime of about one year. Those from high latitude eruptions can last several months. Thus, mostly major eruptions such as the eruption of Mt. Pinatubo (Philippines) in 1991 can penetrate the lower stratosphere and can have significant impact on global climate. The aerosols generated by major volcanic eruptions result in the reduction of incoming solar radiation incident on the Earth's surface largely through the process of scattering back the incident solar radiation. This results in the cooling of the Earth's atmosphere and surface. The duration of the cooling of the Earth following major volcanic eruptions is longer than the duration of the presence of aerosols in the stratosphere and can last several years. This is due to the interaction of the ocean mixed layer and its large heat capacity. More time is needed for the layer to regain the heat lost due to air-sea temperature imbalance while the aerosols were in the atmosphere. The Earth returns back to its pre-eruption level only when the equilibrium of the ocean is restored (*Philander*, 2012).

4.2.2 Anthropogenic external forcing

Human beings, more than any other living organisms, have always influenced the environment. Human activity has caused a variety of changes that has played a direct/ indirect role in climate change. However, it is only since the beginning of the Industrial Era, mid-18th century that the impact of human activities has begun to extend to a much larger scale. Substantial increase of anthropogenic greenhouse gases has occurred over the Industrial Era and this has had complex and diverse influences on climate change. The Earth has a natural greenhouse effect where certain atmospheric gases known as the greenhouse gases (GHGs) such as water vapor, carbon dioxide (CO_2), methane (CH_4), nitrous oxide (N_2O), chlorofluorocarbons (CFCs) etc. absorb part of infrared heat radiation back from the Earth's surface. Due to the heat absorbed by these gases, Earth's average surface temperature remains around 14°C instead of -19°C.

However, since the start of the industrial era, human activity has increased the amount of GHGs emitted into the atmosphere. This increased amount of GHGs absorb more infrared heat which leads to more heat being retained in the lower atmosphere and thus an increase in global average surface temperature. This is called as the enhanced greenhouse effect. The increase in temperature is known as global warming, although additional effects on the climate system are also observed. Together, these affects are known as anthropogenic climate change. The IPCC AR5 (*IPCC*, 2013) states with high confidence that the anthropogenic GHG emissions since the pre-industrial era have driven large increases in the atmospheric concentrations of carbon dioxide, methane and nitrous oxide. Between 1750 and 2011, about 40% of these emissions have remained in the atmosphere, while the rest was removed from the atmosphere and stored on land (in plants and soils) and in the ocean. While the process of emission is called as source, the process of absorption is called as sink. The ocean has absorbed about 30% of the emitted anthropogenic CO_2. About half of the anthropogenic CO_2 emissions between 1750 and 2011 have occurred in the last 40 years. Over the last 40 years between 1970 and 2010, large absolute increases in the total anthropogenic GHG emissions occurred between 2000 and 2010 (Fig.4.5). Emissions of CO_2 from fossil fuel combustion and industrial processes contributed 78% of the total GHG emissions increase from 1970 to 2010 with a similar percentage contribution for the increase during 2000 to 2010 (*IPCC,* 2013).

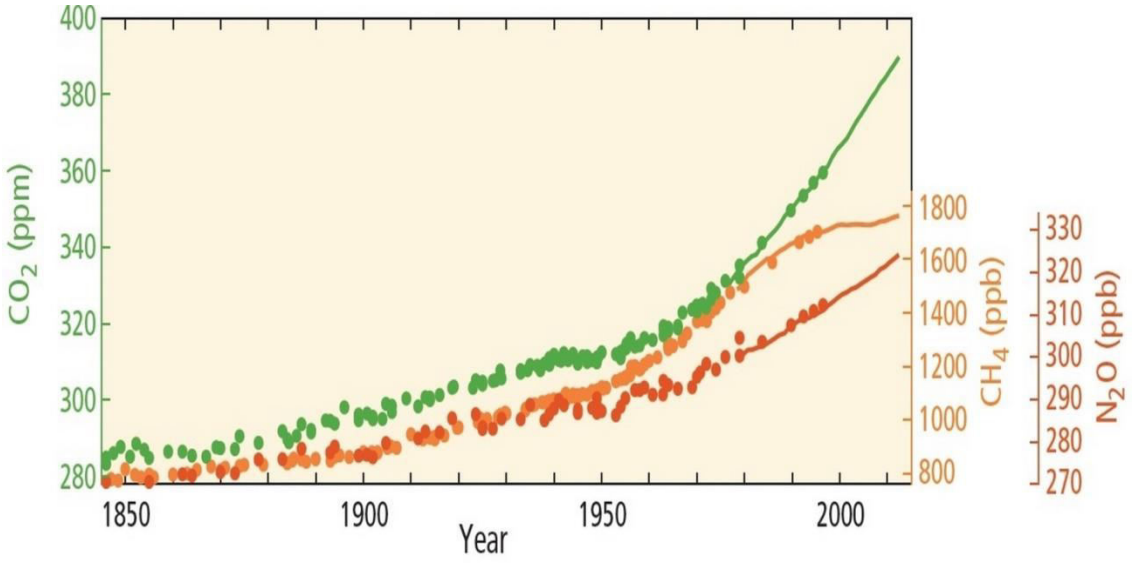

Figure 4.5: Globally averaged atmospheric concentrations of greenhouse gases: carbon dioxide (CO_2, green), methane (CH_4, orange) and nitrous oxide (N_2O, red) from ice core data (dots) and direct atmospheric measurements (lines). Adapted from IPCC, 2013.

The increase in anthropogenic aerosol concentrations in the atmosphere also plays a role in climate change. Human activity contributes to the amount of aerosol present in the atmosphere in several ways: biomass burning, various industrial processes, and exhaust emissions from transports etc. The direct effect is the scattering of part of the incoming solar radiation back into space. This causes a negative radiative forcing which may partly, and locally even completely, offset the enhanced greenhouse effect. However, due to their short atmospheric lifetime, the radiative forcing is very inhomogeneous in space and in time. This complicates their effect on the highly non-linear climate system. Some aerosols, such as soot, absorb solar radiation directly, leading to local heating of the atmosphere, or absorb and emit infrared radiation, thus adding to the enhanced greenhouse effect (*Houghton et al.,* 2001).

Aerosols also affect the properties of clouds. In fact, clouds play a key role in the understanding of climate change. Low, thick clouds primarily reflect solar radiation and cool the surface of the Earth. High, thin clouds primarily transmit incoming solar radiation; at the same time, they trap some of the outgoing infrared radiation emitted by the Earth and radiate it back downward, thereby warming the surface of the Earth. Whether a given cloud will heat or cool the surface depends on several factors, including the cloud's altitude, its size, and the make-up of the particles that form the cloud. In the presence of high amounts of aerosols, clouds will have more

droplets than normal, with droplets tending to be smaller than usual. Because the droplets are smaller and more numerous, the clouds last longer reflect more sunlight thereby cooling the Earth. Owing to physical complexity of cloud processes, they remain one of the largest uncertainties *(Boucher et al.,* 2013) in climate modelling.

Furthermore, land-use change due to urbanization, human forestry (deforestation in particular) and agricultural practices also affect the physical and biological properties of the Earth's surface. Such effects have a potential impact on regional and global climate as they change the surface albedo and act as both source and sink of CO_2. In addition, human activity may change the water cycle through irrigation and power plant cooling, and also generate direct input of heat to the atmosphere by consuming energy. Land use change, and in particular deforestation, also has significant impacts on GHG emissions (*Myhre et al.*, 2013, *Houghton et al.,* 2001). Fig.4.6 shows the temporal evolution of CO_2 sources and sinks since 1870.

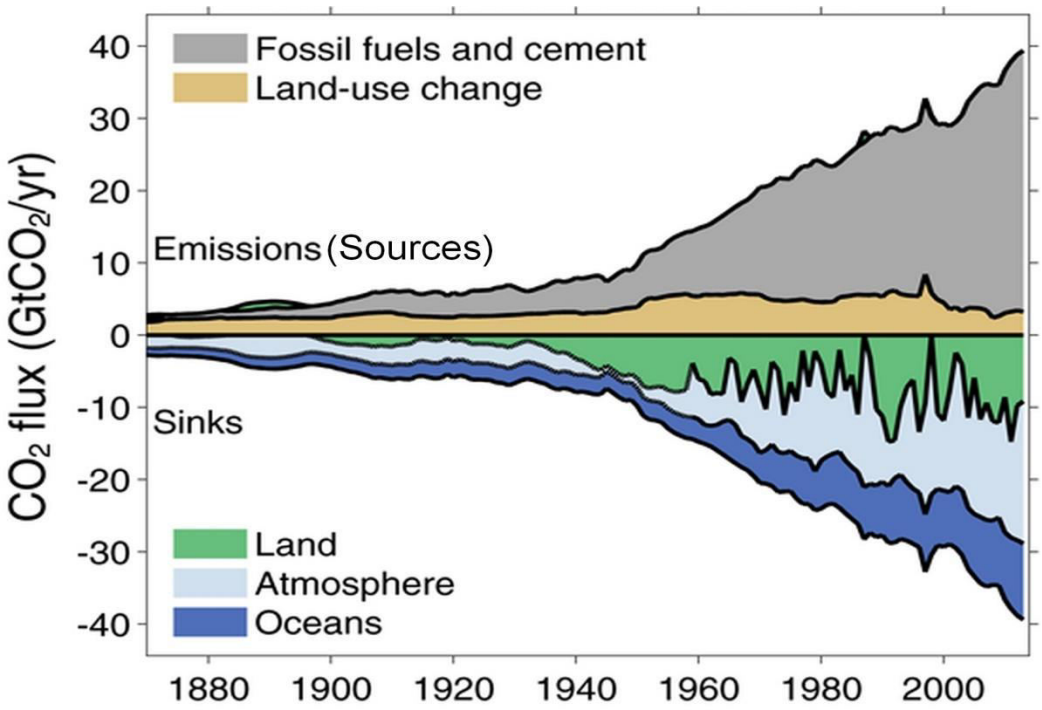

Figure 4.6: Temporal evolution of CO2 sources and sinks (in Gt CO2/yr) since 1870. Source: NOAA-ESRL, Houghton et al 2012, Giglio et al 2013, Joos et al 2013, Khatiwala et al 2013, Le Quéré et al 2014

4.3 Detection and attribution of climate change

There is little doubt that global warming will continue and even increase during the future decades as GHG emissions, the main contributor to anthropogenic global warming will likely continue to grow in the future (*Myhre et al.*, 2013, *IPCC,* 2013). The response of the climate system to anthropogenic external forcing occurs against a backdrop of natural internal and externally forced climate variability that can occur on similar temporal and spatial scales. This implies that the detection and attribution of anthropogenic climate change becomes a statistical 'signal-in-noise' problem where the unforced internal variability is the noise. Detection is the process of demonstrating that an observed change is significantly different from changes due to unforced internal variability only, while attribution evaluates the causes for the observed changes (*Hegerl et al;* 2010).

Although observational evidence for detectable human influence on climate was still weak at the time of the IPCC first assessment report (AR1) in 1990 (*Houghton et al.,* 1990), since then, observational data and more numerical analyses have multiplied and the first detection/attribution (D&A) studies were performed on the global atmospheric temperature. Based on these results, the IPCC third assessment report (AR3) in 2001 (*Houghton et al.,* 2001) concluded that the signal corresponding to GHG was weakly detectable in Earth's global atmospheric temperature and that the majority of the global warming signal observed since the last 50 years was 'probably' of anthropogenic origin. Following this, by making use of models and simulations from the Phase 3 of CMIP (CMIP3), D&A studies were performed on other parameters such as SST, surface wind, precipitation etc. Based on these results, IPCC AR3 and the IPCC forth assessment report (AR4, *Solomon et al.,* 2007) concluded that it was 'highly probable' that the majority of global warming signal observed both in oceans and continents since the last 50 years was due to anthropogenic GHG emissions. Since 2007, D&A studies are also being performed on other parameters such as sea level pressure (e.g. *Gillett and Stott*, 2009), sea ice (*Kay et al.*, 2011, *Jahn et al.*, 2011), ice sheets and glaciers (e.g. *Hanna et al.*, 2008, *Marzeion et al.*, 2014a, *Marzeion et al.*, 2014b), ocean salinity (e.g. *Terray et al.*, 2012, *Pierce et al.*, 2012, *Durack et al.*, 2014), ocean heat content and sea level (see Section 4.3.1). Based on these results, the IPCC fifth assessment report (AR5) in 2013 (*IPCC*, 2013) has concluded that anthropogenic influences have 'very likely' contributed to Arctic sea-ice loss since 1979 and

have 'very likely' made a substantial contribution to increases in global upper ocean heat content (0–700 m) and to global mean sea level rise observed since the 1970s.

4.3.1 Detection and attribution on global mean sea level variations

Global mean sea level is an important indicator of climate change. Only few studies quantifying the contribution of external anthropogenic forcing on sea level directly at global and regional scales exist so far. However, when the global mean sea level change is considered, there exist many D&A studies on each of the main sea level contributors (thermal expansion, glaciers, sea ice, and ice sheets). For example, a number of D&A studies have been performed on ocean heat content (OHC), one of the two main contributors to sea level change. Studies (e.g. *Domingues et al.*, 2008, *Levitus et al.*, 2012, *Gleckler et al.*, 2012) have shown that the upper ocean layer between 0-700m depth has been warming up since the 1950s. This ocean warming represents ~93% of the total Earth's energy increase. This is in accordance with the Earth's energy imbalance which shows that during the same time period, the Earth received more solar energy than it had reflected back to the space (*Church et al.*, 2011, *Hansen et al.*, 2011).

Barnett et al., (2001, 2005) compared a climate model driven by external anthropogenic and natural forcings on observed OHC changes and showed evidence of anthropogenic influence on observed OHC in the upper 700m layer of the ocean. Studies (*Church et al.*, 2005, *AchutaRao et al.*, 2006, *Gregory et al.*, 2006, *Domingues et al.*, 2008) have also shown that models that take into account only the anthropogenic GHG emission forcing (without considering external natural forcing such as volcanic eruptions) in fact have underestimated the inter-decadal ocean warming variability and overestimated the OHC trend over the last 50 years. This is because of the ocean's response to volcanic eruption that results in a sudden cooling of its upper layer that can last for few decades. This was further confirmed by *Gleckler et al.*, (2012) and *Gregory et al.*, (2013) who by making use of CMIP3 models showed that only the models that take both the anthropogenic GHG emissions and natural volcanic eruptions into account represent the global warming signal in the upper 700m of the ocean layer better.

In the case of global mean sea level rise, *Jevrejeva et al.*, (2010) utilized a statistical semi-empirical method to relate global mean sea level rise rate from observational data to different external natural and anthropogenic forcing. They found that before 1800, the global

mean sea level variations were explained only by the external natural forcing whereas since 1800, external natural forcing contributes only 25% to global mean sea level rise while 75% is contributed by external anthropogenic effects. Recently, *Gregory et al.*, (2013) performed a sea level closure budget over the twentieth century by summing up different sea level contributors and arrived to a conclusion that the relationship between global temperature change and global mean sea level rise rate is weak or absent in the twentieth century. However the reason for this weak link was related to the recovery of sea level from large volcanic eruptions that occurred in the later part of 19th century and also in the late 20th century (since 1960s) that were not well taken into account in the pre-industrialized control runs of CMIP3 models.

Recently, *Marcos and Amores*, (2014) performed D&A studies on CMIP5 based thermosteric sea level changes using signal-to-noise maximizing empirical orthogonal function technique for the period 1950–2005. Their study concluded that about 87% of the observed warming-related sea level rise in the 0-700m of the global ocean is of anthropogenic in origin. Similarly, *Slangen et al.*, (2014) compared three different full-depth observational thermosteric sea level changes with 28 different CMIP5 models for the period 1950-2005. CMIP5 models driven by various single external forcings such as natural only, anthropogenic only, GHG only and aerosol only were compared with historical simulations, pre-industrialized control runs (for internal climate variability) and observational data. They concluded that the observed thermosteric sea level change cannot be explained by models driven by internal climate variability and natural forcing alone. Furthermore, the observed thermosteric sea level changes were not solely caused by GHG forcing either, because the GHG experiments overestimated the observed change. The observed global mean thermosteric sea level change, including the observed trends over various time periods, were best explained by using a combination of natural and anthropogenic forcings to drive the models. The anthropogenic forcing was found to be the leading factor in explaining the magnitude of the observed sea level change, while most of the variability in the models was caused by natural forcing.

A recent study of *Becker et al.*, (2014) used a statistical approach developed by *Lennartz and Bunde*, (2009) to provide evidence of anthropogenic forcing in global mean sea level change. They concluded that the rate of global mean sea level change is beyond its unforced internal variability by exceeding the 99% confidence interval. Furthermore, their statistical

analysis showed that more than half of the total observed global sea level trend during the 20th century was of anthropogenic origin. Similarly, very recently, *Dangendorf et al.*, (2015) concluded that it was virtually certain that at least 45% of the observed 21st century global mean sea level change is of anthropogenic origin.

4.3.2 Detection and attribution on regional sea level variability

As seen in Chapter 3, the physical processes which determine global mean sea level rise and regional sea level change are not identical, although they are related. While D&A studies at global scales (i.e. in terms of global mean sea level) have been feasible, performing similar studies on regional sea level is highly challenging. One main reason is that the internal climate variability introduces strong changes in regional sea level on time scales from years to decades and makes the signal to noise ratio very unfavorable to detect the forced response above the unforced internal variability (*Richter and Marzeion*, 2014, *Palanisamy et al.,* 2015c). For example, the regional sea level changes in the tropical Pacific Ocean are governed by natural climates modes such as ENSO, PDO/IPO at interannual and decadal time scales respectively (e.g. *Stammer et al.*, 2013, *Zhang and Church*, 2012, *Han et al.*, 2013, *Hamlington et al.*, 2014a *and references therein*). The internal sea level variability related to such climate modes of the order of ± 10-20 cm can therefore mask sea level changes due to externally forced signal (*Palanisamy et al.*, 2015c). Moreover, the patterns of regional sea level variations before the altimetry era (i.e. before 1990s) are known mainly from tide gauge records that are relatively few in number existing only along coastlines and from OGCMs and sea level reconstructions. Therefore the short record of regional sea level change imposes a limit on the statistical significance of detection and attribution studies (*Bilbao et al.*, 2015).

Recently, in line with D&A studies, a number of 'Time of Emergence (ToE)' studies (*Lyu et al.*, 2014, *Jordà*, 2014, *Richter and Marzeion*, 2014,*Bilbao et al.*, 2015) have been performed on regional sea level variability. ToE is defined as the time when the ratio of the climate change signal to the noise of natural variability exceeds a particular threshold and emerges from the natural climate variability at regional scale. *Lyu et al.*, (2014) find that relative to the 1986-2005 reference period, under RCP4.5and RCP8.5 scenarios, the externally forced trend would be detectable in both steric and dynamic sea level by early to mid-2040s in 50% of

all the oceans. The RCP refers to Representative Concentration Pathway, new key scenarios used in CMIP5 models. The RCPs describe a wide range of potential futures for the main drivers of climate change such as greenhouse gas and air pollutant emissions and land use and are expressed in terms of net radiative forcing (e.g. RCP8.5 = +8.5 W/m^2). The RCP4.5 is a stabilization scenario where GHG emissions peak around 2040 and is later stabilized before 2100 by employment of a range of technologies and strategies for reducing greenhouse gas emissions. The RCP8.5 scenario assumes continuous GHG emissions throughout the 21st century and can also be considered as a representative extrapolation of the present day emission (*IPCC,* 2013). In a ToE study similar to that of *Lyu et al.*, (2014), *Richter and Marzeion*, (2014) also find that the externally forced signal is detectable in the early 2030s relative to 1990 in 50% of the world oceans. These regions include the South Atlantic Ocean, Arctic Ocean, eastern Pacific Ocean and most parts of the Indian Ocean. Furthermore *Jordà*, (2014) has shown that on an average, it would require a minimum time period of 40 years to identify the externally forced signal at regional scale. However in regions with strong decadal and interannual sea level variability, the emergence time increases up to 60-80 years. These results are also in agreement to that of *Richter and Marzeion*, (2014) and *Lyu et al.*, (2014). Recently *Bilbao et al.*, (2015) have used pattern scaling method to study the time of emergence of regional sea level change. The assumption underlying this method is that the local response of a climate variable (sea level in this case) is linearly related to a global variable called the predictor (e.g. global mean surface air temperature, global mean sea surface temperature, ocean volume mean temperature etc.) with the geographical pattern of the change independent of the forcing. Choosing ocean volume mean temperature over the total ocean depth as predictor, *Bilbao et al.*, (2015) have shown that the local sea level change will emerge first or may have already emerged in the northern latitudes of the Southern Ocean and in the tropical Atlantic where the unforced internal variability is smaller. While in the case of the southern latitudes of the Southern Ocean, it may not emerge until after 2100. Interestingly, they note that the local time of emergence is independent of the RCP scenarios, since the local sea level signal emerges in the early 21st century when the RCP scenarios have not yet significantly varied.

While D&A studies on the patterns of regional sea level variability are still lacking, at regional scale, few studies do exist. For example, apart from D&A analysis on global mean upper layer (0-700 m) thermosteric sea level change, *Marcos and Amores*, 2014 also performed

D&A analysis on ocean basin- based regional mean upper layer thermosteric sea level for 1970-2005 period. They concluded that at regional scale the impact of anthropogenic forcing was highly variable with the impact being particularly large in the North Atlantic. *Becker et al.*, (2014), using the same method applied for their global mean sea level study, also performed D&A studies at very local scale. They considered long term good quality tide gauge records available wherever possible all over the world in their study. It was concluded that strong anthropogenic sea level trend contributed to more than 80% of the total observed trend at places located in the extreme western Baltic Sea and at least as much as 67% in New York and more than 50% in Baltimore, Marseille, Mumbai etc. Overall, the presence of significant anthropogenic trends was found in two thirds of the longest century- scale tide gauge records.

4.4 The case of the Pacific Ocean

Pacific Ocean has always been a subject of keen interest among the climate and sea level community as the largest sea level trends over the altimetry period (since 1993) are observed here (See Fig.3.1 of Chapter 3). In fact, we have also discussed in Chapter 3 (Section 3.2.4 and also Fig.3.7) that the tropical Pacific displays the highest climate-related regional sea level trend variability when compared to other regions not only during the altimetry era but also at longer time scales (for the past 6 decades at least). Understanding the origin and mechanisms involved in the Pacific Ocean sea level spatial trend patterns over the altimetry era has been the subject of interest of several recent studies. When we consider the spatial patterns of Pacific Ocean sea level trend (with the global mean removed) since 1993 (Fig.4.7), we can clearly observe two distinct patterns: (1) a V-shaped broad-scale positive trend pattern extending from about 30°–50° N in the central basin to the western equatorial Pacific and then 30°–50° S in the central–eastern basin and (2) a well-pronounced strong dipole-like pattern with positive trends in the western tropical Pacific (with two relative maxima near 10° N and 10° S) and negative trends in the central–eastern tropical Pacific (with relative minima trapped in the equatorial band) limited to about 30° N and 20° S (*Palanisamy et al.*, 2015b).

Bindoff et al., (2007), *Levitus et al.*, (2009), *Becker et al.*, (2012), *Stammer et al.*, (2013) have shown that the strong dipole-like pattern with a positive (negative) trend in the western (eastern) tropical Pacific during the altimetry era is mainly of thermosteric (0-700m) origin and

have related this to the ENSO events. Furthermore, using numerical ocean models, *Carton et al.*, (2005), *Köhl et al.*, (2007), and *Timmermann et al.*, (2010), *Merrifield*, (2011) for example, have shown that in these regions, the thermosteric sea level trends are driven by surface wind stress and changes in circulation. In particular, *Merrifield*, (2011), by making use of tide gauges in the western Pacific, showed that the sea level trend in this region has highly increased since the 1990s when compared to the previous years in the past. *McGregor et al.*, (2012), *Merrifield*, (2011), *Merrifield and Maltrud*, (2011), *Merrifield et al.*, (2012), and *Nidheesh et al.*, (2013) have attributed the high sea level trends in the western tropical Pacific during the last two decades to the intensification of trade winds and/or wind stress curl variations.

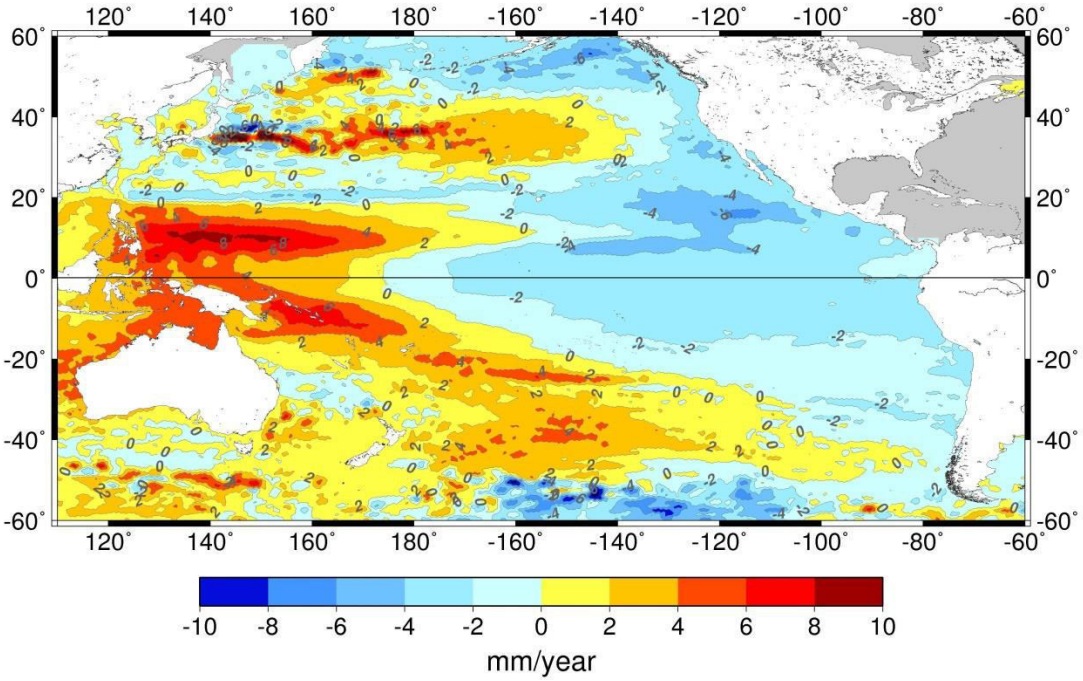

Figure 4.7: Observed altimetry based Pacific Ocean sea level spatial trend pattern over 1993-2012 (uniform global mean has been removed) from Palanisamy et al., 2015.

While the strong dipole-like sea level trend pattern in the tropical Pacific has been related to the ENSO internal climate variability, the V-shaped broad-scale positive trend pattern extending towards the entire Pacific Ocean has been linked with the decadal IPO/PDO climate variability (*Zhang and Church*, 2012, *Han et al.*, 2013, *England et al.*, 2014, *Hamlington et al.*, 2014). In particular, *Zhang and Church*, (2012), studied the regional sea level variability patterns in the Pacific Ocean during the altimetry era by making use of a multiple linear regression model. Interannual and decadal climate indices similar to ENSO and IPO were defined and their

relationships with the regional sea level were studied. It was concluded that the interannual variability pattern could be explained by ENSO while the decadal patterns could be explained by IPO. Moreover they also showed that combining these two modes explains about 60 % of the total sea level variance in the Pacific Ocean over the altimetry era. This leads us to question if the observed regional sea level trend pattern in the Pacific Ocean is the result of only natural unforced interannual and decadal climate variability or if there is a role of anthropogenic forcing too. If that is the case, how successfully can we separate the anthropogenic signal from the signal due to internal climate variability? This has been the study subject of *Meyssignac et al.*, (2012b) who by making use of CMIP3 models concluded that over the short altimetry record (17 year at the time of their study), the amplitude of the noise represented by the internal climate variability has been so strong in the tropical Pacific that it prevents the detection of anthropogenic forcing on the regional variability of the sea level trends in this region. However, in a more recent study, *Hamlington et al.*, (2014), attempted to remove the contribution of IPO from Pacific Ocean sea level signal and related the residual signal to anthropogenic warming of the tropical Indian Ocean (*Han et al.*, 2013). They concluded that the anthropogenic fingerprint was already visible in the Pacific Ocean regional sea level trend pattern over altimetry era.

The contradictory results lead us to wonder if the regional sea level spatial trend pattern in the Pacific Ocean has been well understood. Therefore one of the main focuses of my Ph.D. work was on explaining the regional sea level patterns in the Pacific Ocean (in specific, the tropical Pacific) in terms of the ocean dynamic processes involved, the role of internal climate variability (with main focus on IPO) and finally the possible role of anthropogenic forcing. An article has been published based on our work that focuses on the ocean dynamic processes and internal climate variability in the 'Ocean Dynamics' journal whereas another article on the detection of anthropogenic fingerprint in the Pacific Ocean has been published in the 'Environmental Research Letters'. Our work published in the two articles has been resumed in the following pages.

Summary of the article: 'Spatial trend patterns in the Pacific Ocean sea level during the altimetry era: the contribution of thermocline depth change and internal climate variability' (the original article is inserted at the end of this section)

In this article, we first focused on explaining the tropical Pacific regional sea level trend patterns in terms of the ocean dynamic processes involved. As mentioned above, several studies have already related the observed sea level trend patterns of the tropical Pacific to 0-700m thermosteric/steric-related sea level changes. However, only the integrated steric contribution (down to 700 m) to observed trends has been studied so far. In this study by making use of in-situ ocean temperature and salinity data (data from *Ishii and Kimoto*, 2009), we quantified the contribution of the thermocline depth changes (which affect the vertical thermal structure) to the sea level trend patterns, focusing in the tropical Pacific (20° N–20° S) where the largest trends are observed (see Fig.4.7).

Tropical oceans can be considered as a two-layer system with a warm upper layer and a cold deeper layer separated by the thermocline defined as the depth of the maximum vertical temperature gradient. In the tropical ocean, 20°C isotherm has been broadly used to define the depth of the thermocline (*Kessler*, 1990, *Swenson and Hansen*, 1999, *Durand and Delcroix*, 2000). Therefore in our study, we first estimated the time-varying thermocline depth corresponding to the depth of 20°C isotherm within the 20°N-20°S tropical Pacific latitudinal bands. The contribution of changes in thermocline depth to sea level can then be expressed in terms of equivalent sea level by estimating the changes in the 0-700m steric with respect to changes in thermocline depth (D20). This can take place in three possible ways: between (1) the surface and the mean thermocline depth, (2) the mean thermocline depth and time-varying thermocline depth, and (3) the time-varying thermocline depth and 700m, expressed as a mathematical equation below

$$\mathrm{SSL}(0,700\mathrm{m}) = \int_{0}^{z=\mathrm{D20mean}} \frac{\Delta\rho(T,S,p)dz}{\rho_0(p)} + \int_{z=\mathrm{D20mean}}^{z=\mathrm{D20}(t)} \frac{\Delta\rho(T,S,p)dz}{\rho_0(p)} + \int_{z=\mathrm{D20}(t)}^{700\mathrm{m}} \frac{\Delta\rho(T,S,p)dz}{\rho_0(p)} \tag{4.1}$$

where SSL is the steric sea level, z is depth for which the steric sea level is estimated, and $\Delta\rho$ is the change in density with respect to the reference density ρ_0. We studied the thermocline depth contribution by estimating the steric sea level spatial trend pattern that corresponds to each of the above mentioned three terms. It was found that the combined contributions of the first two right

hand sided terms of Eq.(4.1) explained most of the 0-700 m steric sea level changes in the tropical Pacific. This indicates that over 1993-2012 period, it is essentially the thermocline attributed upper steric layer due to time-varying vertical movement of the thermocline (i.e. between the surface and D20 (t)) that governs most of the observed sea level changes and trends in the tropical Pacific.

In the next part of the study, we focused on the mechanism responsible for the time-varying vertical thermocline movement that explains the sea level changes in the tropical Pacific. Studies using wind stress forced models (e.g. *McGregor et al.*, 2012, *Merrifield et al.*, 2012, *Merrifield and Maltrud*, 2011) have shown that the recent sea level intensification in the western tropical Pacific is due to the intensification of trade winds. Therefore, in our study, we studied the relationship between wind stress, thermocline and the thermocline attributed upper layer steric sea level following the physical equations of *Meyers*, (1979), *Garzoli and Katz*, (1983), *Kessler*, (1990, see equations.(2), (3) and(4) in *Palanisamy et al.*, 2015b). In the equatorial band (5°N-5°S latitudes), the slope of the thermocline was calculated along 130°E to 90°W and was compared with the zonal wind stress averaged over the same latitudinal and longitudinal bands (Fig.4.8). The thermocline slope and zonal wind stress were highly (anti) correlated (anti-correlation because the conventional sign of zonal wind stress is positive towards the east). Furthermore, the presence of negative trend in the zonal wind stress further confirms the intensification of west-ward blowing trade winds which thereby deepens the thermocline further (as seen by positive trend in thermocline slope). Away from the equatorial bands (i.e. between 5°-15° north and south latitudes), direct comparison of the thermocline attributed upper layer steric sea level with zonal wind stress showed good (anti) correlations between the two with time lags of around 3 to 4 months that is consistent with the time taken for the wind stress-generated Rossby waves to propagate towards the west. These results show that in the equatorial band, the changes in the upper ocean thermal structure are in direct response to the zonal wind stress whereas away from the equatorial band (say, within 5°–15° latitude),the changes in the upper ocean thermal structure are consistent with the wind stress-generated Rossby waves.

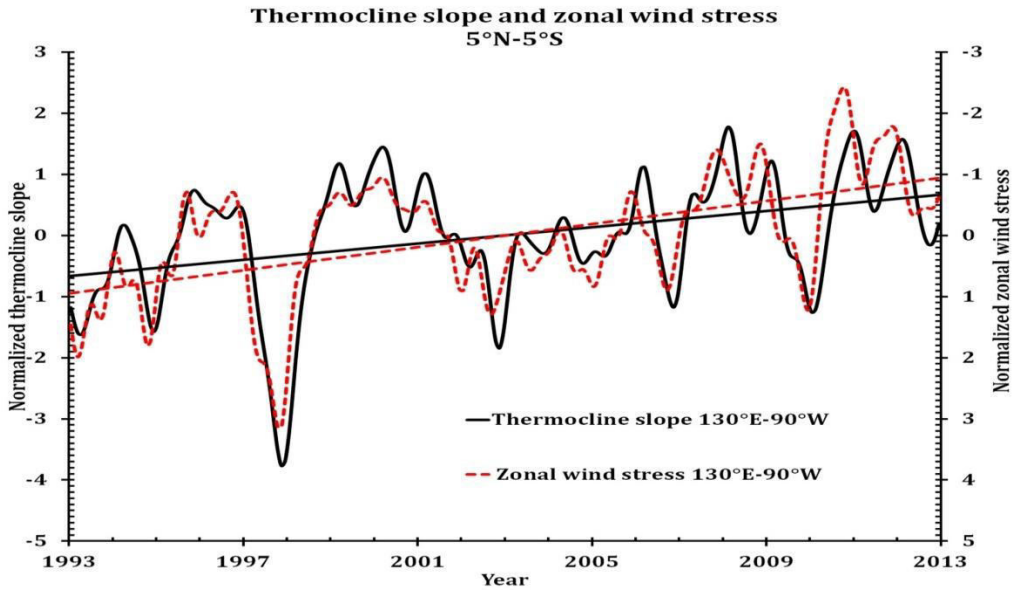

Figure 4.8: Normalized thermocline slope (black) and zonally averaged zonal wind stress (red dotted) computed from 130° E to 90° W and averaged within 5° N–5° S. The solid black and dashed red lines denote their respective linear trends. Figure adapted from Palanisamy et al., 2015.

In the last part, we studied the contribution of IPO-related internal climate variability on the upper layer steric sea level by performing a linear regression of the IPO climatic index on the upper layer steric sea level. We showed that while IPO is responsible for explaining most of the sea level trend in the tropical Pacific, removal of its contribution from the sea level results in some significant residual trend signal. This wind forced residual closely resembles to that found by *Hamlington et al.,* (2014) which was attributed as the response of tropical Pacific to anthropogenic warming in the tropical Indian Ocean. However we concluded that it is possible that the residual pattern could also reflect some non-linear internal climate modes that have not been totally removed. Therefore a detailed study on this was the focus of our next following study.

Ocean Dynamics
DOI 10.1007/s10236-014-0805-7

Spatial trend patterns in the Pacific Ocean sea level during the altimetry era: the contribution of thermocline depth change and internal climate variability

H. Palanisamy · A. Cazenave · T. Delcroix · B. Meyssignac

Received: 11 July 2014 / Accepted: 16 December 2014

Abstract This study investigates the spatial trend patterns and variability of observed sea level and upper ocean thermal structure in the Pacific Ocean during the altimetry era (1993–2012), and the role of thermocline depth changes. The observed sea level trend pattern in this region results from the superposition of two main signals: (1) a strong broad-scale V-shaped positive trend anomaly extending to mid-latitudes in the central Pacific and (2) another very strong positive trend anomaly located in the western tropical Pacific within about 120° E–160° E and 20° S–20° N latitude. In this study, we focus on the tropical Pacific (20° N–20° S) where the strongest trends in sea level are observed. By making use of in situ observational data, we study the impact of thermocline depth changes on steric sea level between the surface and 700 m and its relation with the altimetry-based observed sea level changes. This is done by calculating the time-varying thermocline depth (using the 20 °C isotherm depth as a proxy) and estimating the sea level trend patterns of the thermocline-attributed individual steric components. We show that it is essentially the vertical movement of the thermocline that governs most of the observed sea level changes and trends in the tropical Pacific. Furthermore, we also show that in the equatorial band, the changes in the upper ocean thermal structure are in direct response to the zonal wind stress. Away from the equatorial band (say, within 5°–15° latitude), the changes in the upper ocean thermal structure are consistent with the wind stress-generated Rossby waves. We also estimate the contribution of the Interdecadal Pacific Oscillation (IPO) on the vertical thermal structure of the tropical Pacific Ocean. Removing the IPO contribution to the upper layer steric sea level provides a non-negligible residual pattern, suggesting that IPO-related internal ocean variability alone cannot account for the observed trend patterns in the Pacific sea level. It is likely that the residual signal may also reflect non-linear interactions between different natural modes like El Niño Southern Oscillation (ENSO), IPO, etc.

Keywords Tropical Pacific · Wind-driven thermocline depth changes · Upper layer steric sea level contribution · Internal climate variability · Interdecadal Pacific Oscillation

1 Introduction

Since the early 1990s, satellite altimetry has become the main tool for precisely and continuously measuring sea level with quasi-global coverage and short revisit time. Analyses of altimetry data have shown that since 1993, sea level is rising at a global mean rate of 3.2±0.4 mm/year (Nerem et al. 2010), but the rate is far from being spatially uniform (e.g., Cazenave and Cozannet 2014; Stammer et al. 2013; Church et al. 2013). In regions like the western tropical Pacific, north Atlantic around Greenland, and southern Austral Ocean, rates up to three times the global mean rate are observed over the altimetry period, while other regions like the eastern tropical Pacific face lower rates of sea level rise (Bromirski et al. 2011; Thompson et al. 2014). The regional sea level variability superimposes on the global mean sea level rate and thus amplifies or reduces the sea level rate. This implies that different parts of the world do not face the same extent of sea level risks. This shows the importance of regional

Responsible Editor: Richard John Greatbatch

H. Palanisamy (✉) · A. Cazenave · B. Meyssignac
LEGOS/CNES, 18 Avenue Edouard Belin, 31400 Toulouse, France
e-mail: hindumathi.palanisamy@legos.obs-mip.fr

T. Delcroix
LEGOS/IRD, 18 Avenue Edouard Belin, 31400 Toulouse, France

Published online: 08 January 2015

variability in sea level trends in the estimation of relative sea level and its potential impact on low-lying coasts and islands. It is thus important to understand the causes that drive the regional sea level trend patterns. Many previous studies have shown that the regional sea level trends over the altimetry era mostly result from non-uniform ocean thermal expansion and salinity variations (Lombard et al. 2005a; 2009; Levitus et al. 2005, 2012; Wunsch et al. 2007; Köhl and Stammer 2008; Fukumori and Wang 2013), thus at least to first order reflect ocean circulation changes. Theoretical studies have shown that other phenomena such as gravitational and deformational effects of solid Earth in response to glacial isostatic adjustment (GIA) also contribute to the regional variability in sea level rates (e.g., Milne et al. 2009; Stammer et al. 2013), but their effects are small in the last decades when compared to thermosteric and halosteric changes.

The largest regional variations in sea level trends over the altimetry period (since 1993) are observed in the Pacific Ocean (as illustrated in Fig. 1 showing the spatial trend patterns over 1993–2012, with the global mean trend removed), with two distinctive patterns: (1) a V-shaped broad-scale positive trend pattern extending from about 30°–50° N in the central basin to the western equatorial Pacific and then 30°–50° S in the central–eastern basin and (2) a well-pronounced strong dipole-like pattern with positive trends in the western tropical Pacific (with two relative maxima near 10° N and 10° S) and negative trends in the central–eastern tropical Pacific (with relative minima trapped in the equatorial band) limited to about 30° N and 20° S.

Bindoff et al. (2007), Levitus et al. (2009), Becker et al. (2012), and Stammer et al. (2013) have shown that the strong dipole-like pattern with a positive (negative) trend in the western (eastern) tropical Pacific during the altimetry era is mainly of thermosteric origin and have related this to the El Niño Southern Oscillation (ENSO) events. Furthermore, using numerical ocean models, Carton et al. 2005, Köhl et al. 2007, and Timmermann et al. 2010, for example, have shown that in these regions, the thermosteric sea level trends are driven by surface wind stress and changes in circulation. McGregor et al. (2012), Merrifield (2011), Merrifield and Maltrud (2011), Merrifield et al. (2012), and Nidheesh et al. (2013) have attributed the high sea level trends in the western tropical Pacific during the last two decades to the intensification of trade winds and/or wind stress curl variations. Making use of wind stress forced models, Timmermann et al. (2010) and McGregor et al. (2012) have further shown that the positive–negative dipole-like sea level trend patterns in the tropical Pacific since 1993 are consistent with the wind-driven thermocline depth variability associated with ENSO.

The first level of explanation relies on comparing observed sea level and steric trend patterns and investigating the forcing factors that cause the regional changes. The following step consists of asking whether the observed changes mostly result from internal/natural variability of the ocean–atmosphere coupled system or not, and how to separate the natural modes from the longer term signal possibly related to anthropogenic global warming. These issues have been the object of other studies (e.g., Zhang and Church 2012; Meyssignac et al. 2012; Han et al. 2013; Hamlington et al. 2013, 2014; Marcos and Amores 2014; Becker et al. 2014; Slangen et al. 2014). For example, Zhang and Church (2012) quantified the contribution of natural modes of interannual/decadal variability—like ENSO and Pacific Decadal Oscillation (PDO) or Interdecadal

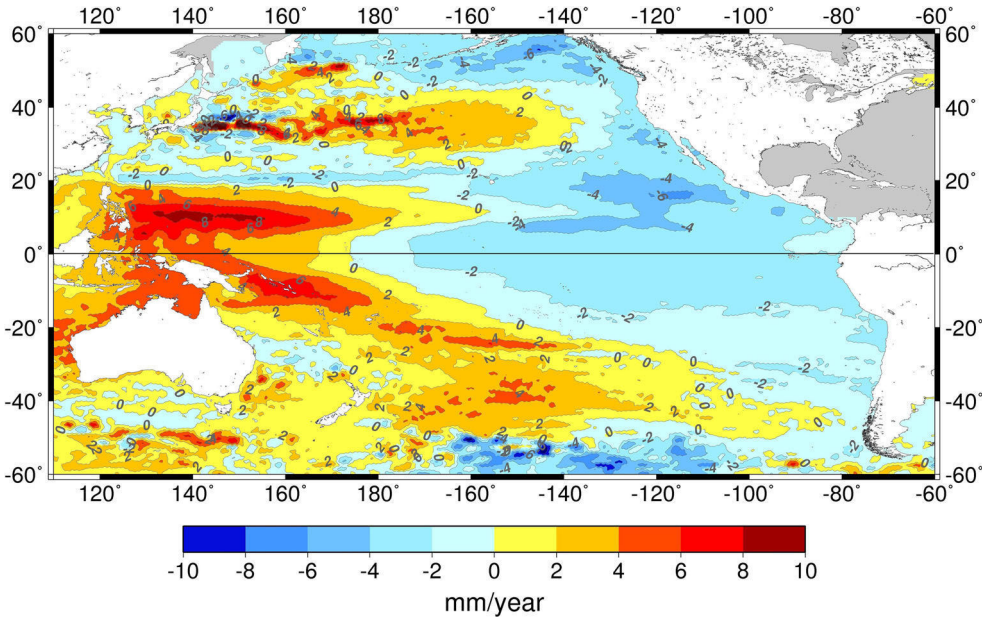

Fig. 1 Observed altimetry-based Pacific sea level spatial trend pattern over 1993–2012 (global mean trend removed)

Pacific Oscillation (IPO)—to the Pacific sea level trends. They showed that combining these modes explains about 60 % of the total sea level variance over the altimetry era. Moreover, as discussed in several studies (see Hamlington et al. 2013; 2014 and the references therein), the PDO contributes not only to regional trends but also to the global mean sea level trend, highlighting the importance of the interannual/decadal variability when estimating sea level trends.

The present study builds on these previous studies and focuses on the spatial trend patterns in sea level of the tropical Pacific Ocean (up to 20° N/S) over 1993–2012, but from a different and complementary perspective. As discussed above, in the tropical Pacific, several studies have already related the observed sea level trend patterns (Fig. 2a as in Fig. 1) to 0–700-m steric-related sea level changes (Fig. 2b, correlation between observed altimetry and steric sea level in terms of trend is greater than 0.9). However, only the integrated steric contribution (down to 700 m) to observed trends has been studied so far. In this study, we quantify the contribution of the thermocline depth changes (which affect the vertical thermal structure) to the sea level trend patterns, focusing in the tropical Pacific (20° N–20° S) where the largest trends are observed (Fig. 1). Previous studies mentioned above have used models to show that the positive (negative) sea level trend patterns in the western (eastern) tropical Pacific are due to the wind-driven thermocline deepening (shoaling). Here, by making use of in situ ocean temperature data, we analyze mechanisms accounting for changes in the thermocline depth, hence quantify the main contribution of changes in the vertical thermal structure of the upper ocean to the observed sea level spatial trend pattern in the tropical Pacific. We also try to estimate the influence of the natural internal variability (IPO) on the observed upper ocean thermal structure, remove this influence over the study period, and study the residual pattern.

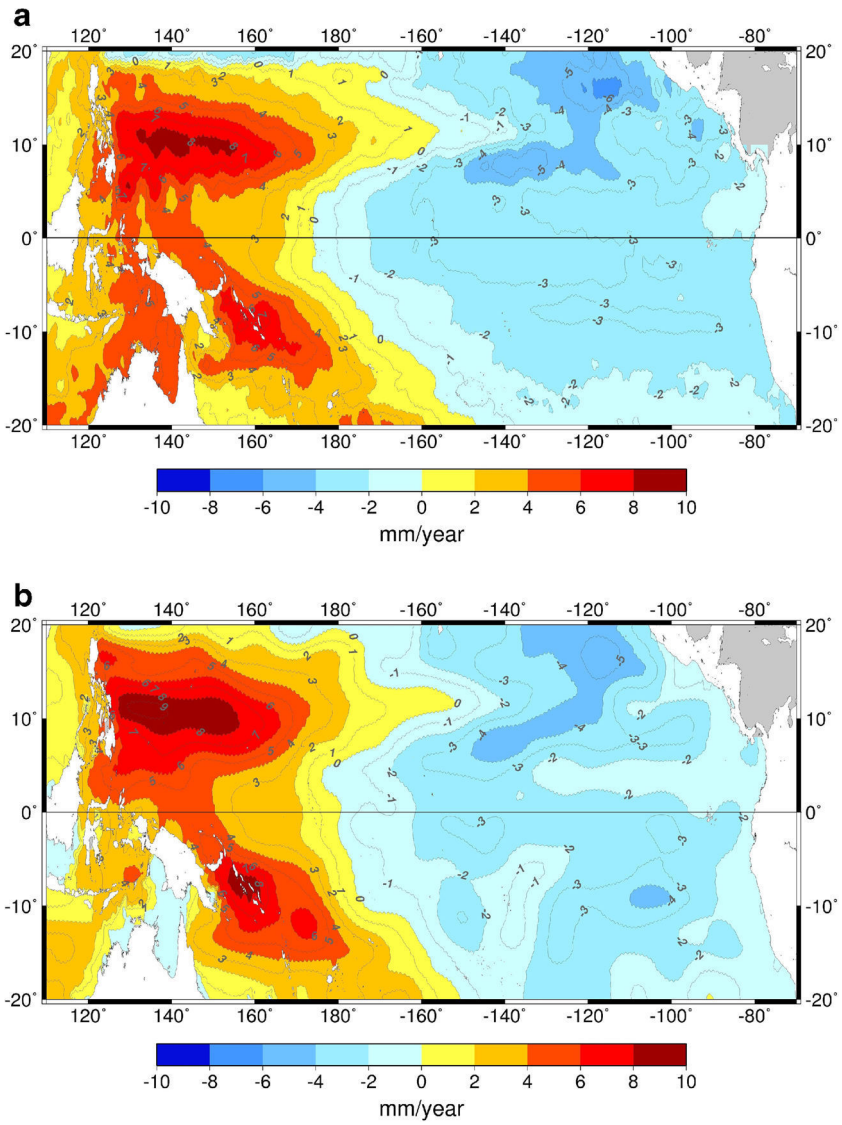

Fig. 2 **a** Altimetry-based sea level spatial trend pattern (global mean removed), as in Fig. 1; **b** steric sea level (0–700 m) spatial trend pattern (global mean removed) in the tropical Pacific over 1993–2012

2 Data

Different datasets and climate indices are used in this study. These are briefly presented below.

2.1 Satellite altimetry sea level data (1993–2012)

Altimetry-based 2-D gridded sea level anomalies from AVISO were used in this study. This data is available on a weekly interval as a ¼° regular grid from January 1993 to December 2012. We used the DT-MSLA "Ref" series computed at Collecte Localisation Satellite (CLS) by merging several altimeter missions, namely TOPEX/Poseidon, Jason-1 and Jason-2, Envisat, and ERS-1 and ERS-2. It is a global, homogenous, intercalibrated dataset based on global crossover adjustment (Le Traon and Ogor 1998) using TOPEX/Poseidon and followed by Jason-1 as reference missions. Corrections for long wavelength orbital errors, ocean tides, and wet/dry troposphere and ionosphere have been performed (Ablain et al. 2009). In order to minimize the aliasing effects, inverted barometer (IB) correction has also been applied (Volkov et al. 2007) through the MOG2D barotropic model correction that includes the dynamic ocean response to short-period (<20 days) atmospheric wind and pressure forcing and the static IB correction at periods above 20 days (see Carrère and Lyard 2003 for more details). The annual and semi-annual signals have been removed through a least squares fit of 12- and 6-month periods. In order to be consistent with the other datasets used in this study, the altimetry sea level data at weekly interval has been averaged to monthly scale.

2.2 In situ ocean temperature and salinity data

We used the gridded temperature (T) and salinity (S) data from Ishii and Kimoto (2009) (updated version 6.13, hereafter denoted IK6.13). These data are available at depths of 0, 10, 20, 30, 50, 75, 100, 125, 150, 200, 250, 300, 400, 500, 600, and 700 m (16-depth levels) with a 1°×1° horizontal resolution, at monthly intervals from January 1945 to December 2012. Ocean temperature has principally been measured by mechanical bathythermographs (MBT) in the 1950s, then by expendable bathythermographs (XBTs) from the mid-1970s, and Conductivity–Temperature–Depth (CTD) and Argo (from 2003) data. XBT depth biases due to assumed particular fall rates of the XBT measures which result in positive temperature biases from long-term XBT observations (Gouretski and Koltermann 2007) have been corrected for in the gridded dataset and are available at monthly scales. In order to be able to capture the thermocline depths that correspond to the 20 °C isotherm depths in the tropics (see below), the T (and S) measures that are available only at the standard depths have then been linearly interpolated with respect to the vertical depth profiles. Even though T and S measures are available deeper than 700 m (until 1500 m in the case of IK6.13), the number of these available measures is very scarce until the period of Argo profiles (i.e., until 2003). Therefore, estimation of steric sea level changes below the depth of 700 m prior to 2003 may not yield accurate results. The time period of study in our case being 1993–2012, 0–700 m has been used as the reference depth for steric sea level changes. As in the case of altimetry data, the annual and semi-annual signals have also been removed from this dataset using the least squares fit of 12- and 6-month periods.

2.3 Wind data

Wind stress fields were calculated using the wind components (U component and V component) and wind speed at 10 m dataset from ERA-Interim (produced by the European Centre for Medium-Range Weather Forecast (ECMWF)). These data are available on a global 1°×1° resolution at a monthly time scale from 1979. The forecast model, data assimilation method, and input datasets for ERA-Interim are described in (Dee et al. 2011). The annual and semi-annual signals have also been removed from the wind stress fields.

2.4 Climate indices

PDO is a Pacific climate variability pattern on decadal time scales and is characterized by changes in large-scale atmospheric and oceanic circulation, physical, and biological changes. Its timing and amplitude can be quantified by the PDO index defined as the leading principal component of the North Pacific (poleward of 20° N) monthly sea surface temperature (SST) variability (Mantua et al. 1997; Mantua and Hare 2002; Zhang et al. 1997). The IPO is (almost) the Pacific-wide equivalent of the PDO, with as much variance in the Southern Hemisphere Pacific (at least to 55° S) as in the Northern Hemisphere (Folland et al. 1999). In our study, similar to several other studies (Power et al. 1999; Deser et al. 2004; Han et al. 2013; Meehl et al. 2013; England et al. 2014), we use an updated version of the IPO index available from 1871 to mid-2014 (kindly provided by C.K. Folland).

3 Method

In general, the tropical ocean can be considered as a two-layer system with a warm upper layer and a cold deeper layer that are separated by the thermocline. Theoretically, the thermocline depth is defined as the depth of the maximum vertical temperature gradient (Pedlosky 2006; Yang and Wang 2009). In general, the depth of the thermocline is often determined by means of a representative isotherm within the thermocline

layer (Kessler 1990; Yang and Wang 2009). In the tropical Pacific, the depth of the 20 °C isotherm has been broadly used to define the thermocline depth as it occurs near the center of the main or permanent thermocline (e.g., Kessler 1990; Swenson and Hansen 1999; Durand and Delcroix 2000). In order to illustrate the choice of 20 °C isotherm as the thermocline depth in the tropical Pacific, Fig. 3a–c shows the 1993–2012 time mean and latitude (20° N–5° N, 5° N–5° S, and 5° S–20° S, respectively) averaged temperature in the longitude–depth plane between 130° E and 90° W. The 20 °C isotherm (represented as a solid black line) occurs at depths corresponding to the maximum vertical temperature gradient. The choice of 20 °C depth is hereafter considered apt to represent the thermocline depth (henceforth referred to as D20).

In an ideal two-layer system with an upper layer of depth H, density $\rho 1$, and temperature $T1$ and a motionless lower layer of density $\rho 2 = \rho 1 + \Delta\rho$ and temperature $T2$, changes in sea level Δh and changes in the upper layer depth ΔH are related by $\Delta h = \Delta H \cdot \Delta\rho/\rho$ (where ΔH is positive downward). With this hypothesis, in the tropical ocean, the fluctuations in sea level are chiefly determined by the thermocline depth fluctuations (Wyrtki and Kendall 1967; Chaen and Wyrtki 1981; Rebert et al. 1985; McGregor et al. 2012). Applying this concept, Rebert et al. (1985) analyzed the relations between sea level, 20 °C isotherm depth, heat content, and dynamic height by making use of in situ observations (temperature profiles from XBT near certain island tide gauges in the tropical Pacific) and have inferred that the sea level changes are highly correlated to the steric (or dynamic height) and thermocline depth changes. Rebert et al. (1985) showed that the value of $\rho/\Delta\rho$ is of the order of 180, meaning that a deepening of 18 m in thermocline depth (D20) corresponds to an increase of 10 cm in sea level. Furthermore, this relationship has been the principle behind several wind stress-forced shallow water models (SWMs) used to study the impact of surface wind stress on sea level changes in the tropical Pacific (e.g., McGregor et al. 2007; McGregor et al. 2008; Timmermann et al. 2010; McGregor et al. 2012 etc.). The SWMs simulate the thermocline anomalies due to surface wind stress in the tropical Pacific. These thermocline anomalies are then converted to equivalent sea level response, thereby providing an estimate of the effect of surface wind stress on sea level.

Benefitting from the fact that the tropical ocean can be reasonably simplified as a two-layer structure separated by a thermocline, at least within about 20° N–20° S, we first estimate the time-varying thermocline depth. The sea level trend patterns in the tropical Pacific are then explained by estimating the main changes in the thermocline depth.

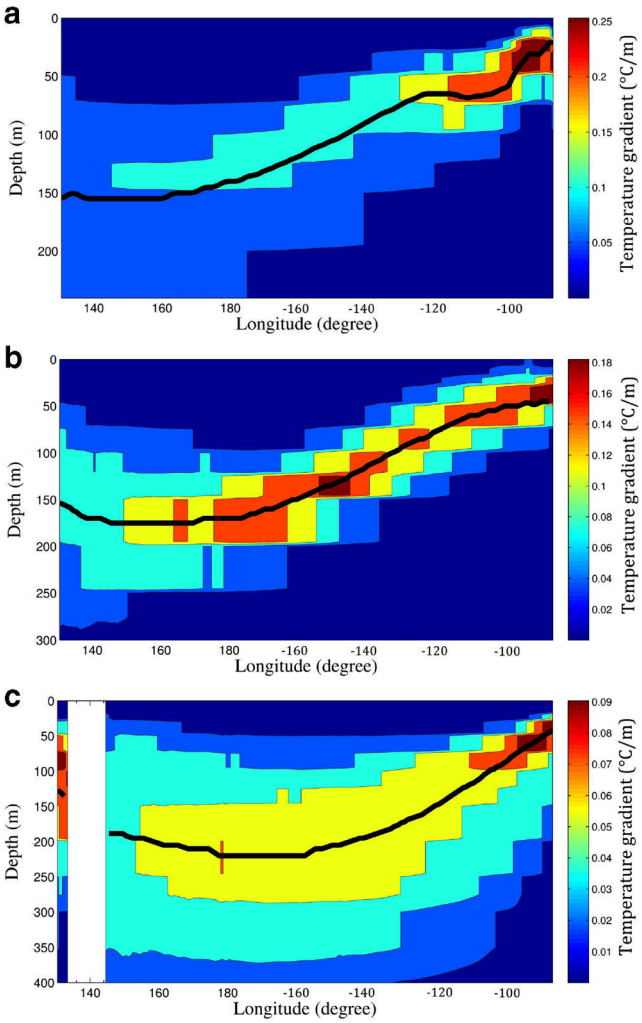

Fig. 3 Longitude–depth distribution of the 20° N–5° N (**a**), 5° N–5° S (**b**), and 5° S–20° S (**c**) averaged temperature vertical gradient (*color contours*) over 1993–2012. The 20 °C isotherm mean position is represented as a *solid black line* in the figure. The *white stripe* in (**c**) corresponds to the continental surface

4 Analysis of sea level trend patterns in the tropical Pacific Ocean

4.1 Thermocline depth and its spatial trend pattern in the tropical Pacific

The mean thermocline depth and its spatial trend pattern over 1993–2012 are illustrated in Fig. 4a, b. Figure 4a shows that D20 is deeper in the western tropical Pacific when compared to that in the east. This is consistent with the fact that under normal conditions, the trade winds blowing from the east to the west along the equator pile up the water in the west and make a deep warm layer, thereby pushing the thermocline deeper in the west while in the east the thermocline is shallow. In general, the locations of the mean thermocline maxima and minima in the western tropical Pacific correspond to the locations of major ridges and troughs that define the boundaries of the zonal geostrophic currents, respectively (Kessler 1990). There are two distinct D20 maxima found to the east of

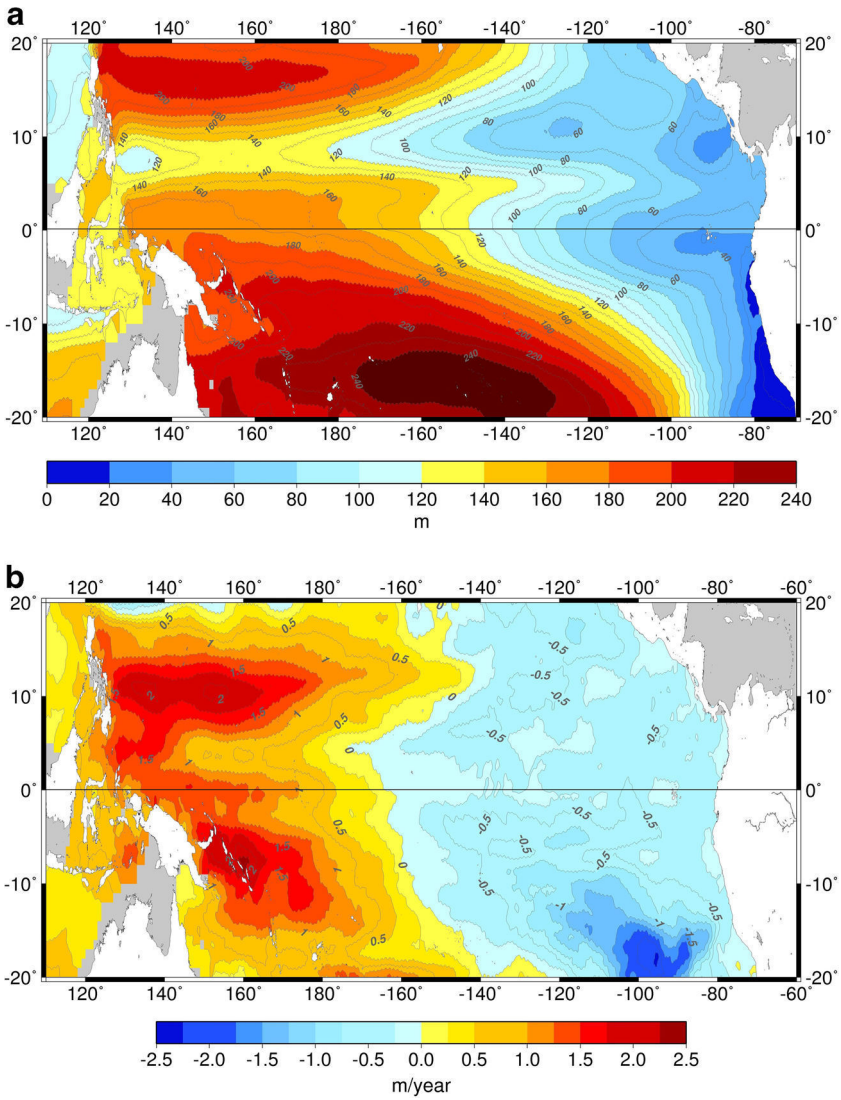

Fig. 4 **a** Mean thermocline depth and **b** spatial trend pattern of thermocline variations in the tropical Pacific over 1993–2012

the Philippines (~10° N–20° N, ~120° E–160° W) and northeastern Australia (~5° S–20° S, ~150° E–100° W) with the maximum depth exceeding 200 m. These two maxima are located in the North Equatorial Ridge (NER) and South Equatorial Ridge (SER) and mark the centers of the subtropical gyres in each of the hemispheres. The shallowest thermocline depth occurring between 8° and 10° N in the western tropical Pacific corresponds to the location of the Countercurrent Trough. Our mean thermocline depth pattern is consistent with that of studies published years ago with smaller datasets (Kessler 1990; Durand and Delcroix 2000).

As in the case of the temporal mean, the thermocline spatial trend pattern over 1993–2012 (Fig. 4b) is also maximum in the western tropical Pacific. Maximum trend values are shifted towards the equator compared to the maximum depths. The shift in the occurrence of maximum thermocline trend indicates that the maximum variation in the depth of the thermocline over time does not actually occur at the centers of the subtropical gyres (i.e., NER and SER) but in between the ridges and the Equatorial Trough (ET) in both hemispheres.

The longitude–depth distribution of the latitude-averaged (i.e., 20° N–5° N, 5° N–5° S, and 5° S–20° S) temperature trends (Fig. 5a–c) confirms that the largest changes are centered at the mean thermocline depth (solid black line in the figure), positive in the western half of the basin and negative in the eastern half.

4.2 Thermocline-attributed steric sea level spatial trend patterns

The contribution of changes in thermocline depth to sea level can be expressed in terms of equivalent sea level by estimating the changes in the 0–700-m steric sea level with respect to changes in the thermocline depth (D20). This contribution could take place through changes in temperature and salinity

between (1) the surface and the mean thermocline depth, (2) the mean thermocline depth and the time-varying thermocline depth, and (3) the time-varying thermocline depth and 700 m (terms 1, 2, and 3 in the right-hand side of Eq. (1), respectively). In terms of mathematical equations, the above three criteria can be expressed as

$$\mathrm{SSL}(0,700\mathrm{m}) = \int_{0}^{z=\mathrm{D20mean}} \frac{\Delta\rho(T,S,p)dz}{\rho_0(p)} + \int_{z=\mathrm{D20mean}}^{z=\mathrm{D20}(t)} \frac{\Delta\rho(T,S,p)dz}{\rho_0(p)} + \int_{z=\mathrm{D20}(t)}^{700\mathrm{m}} \frac{\Delta\rho(T,S,p)dz}{\rho_0(p)} \quad (1)$$

where SSL is the steric sea level, z is depth for which the steric sea level is estimated, and $\Delta\rho$ is the change in density with respect to the reference density ρ_0.

The thermocline depth contribution is first studied by estimating the spatial trend pattern in steric sea level between the surface and $\mathrm{D20}_{\mathrm{mean}}$ (Fig. 6a) and between $\mathrm{D20}_{\mathrm{mean}}$ and D20(t) (Fig. 6b) over 1993–2012 (i.e., the first and the second terms in the right-hand sides of Eq. (1)). The spatial trend patterns in both the cases display the positive–negative dipole-like pattern in the tropical Pacific with the positive trend corresponding to the regions of deep thermocline (in the west) and negative trend pattern in the east where the thermocline remains shallow. From Fig. 6a, b, we can observe that both steric sea level trend patterns exhibit the two prominent positive trend regions in the east of the Philippines and Papua New Guinea. However, Fig. 6b, i.e., the pattern due to changes in steric sea level between $\mathrm{D20}_{\mathrm{mean}}$ and D20(t), shows a greater amplitude than Fig. 6a and remains highly comparable to sea level spatial trend patterns from observed altimetry (Fig. 2a) and steric between the surface and 700 m (Fig. 2b and henceforth referred to as "total steric" sea level). In terms of mean trend, the regionally (20° N–20° S, 120° E–90° W) averaged steric sea level trend estimated between the surface and $\mathrm{D20}_{\mathrm{mean}}$ accounts to 0.4±0.07 mm/year while that between $\mathrm{D20}_{\mathrm{mean}}$ and D20(t) accounts to 0.69±0.05 mm/year. These significant sea level trend patterns and values show that the density changes above the mean thermocline (from 0 to $\mathrm{D20}_{\mathrm{mean}}$) alone cannot fully explain the steric sea level of the upper layer (from 0 to D20(t)). The vertical movement (i.e., deepening/shoaling) of the thermocline (i.e., from $\mathrm{D20}_{\mathrm{mean}}$ to D20(t)) also plays a significant role.

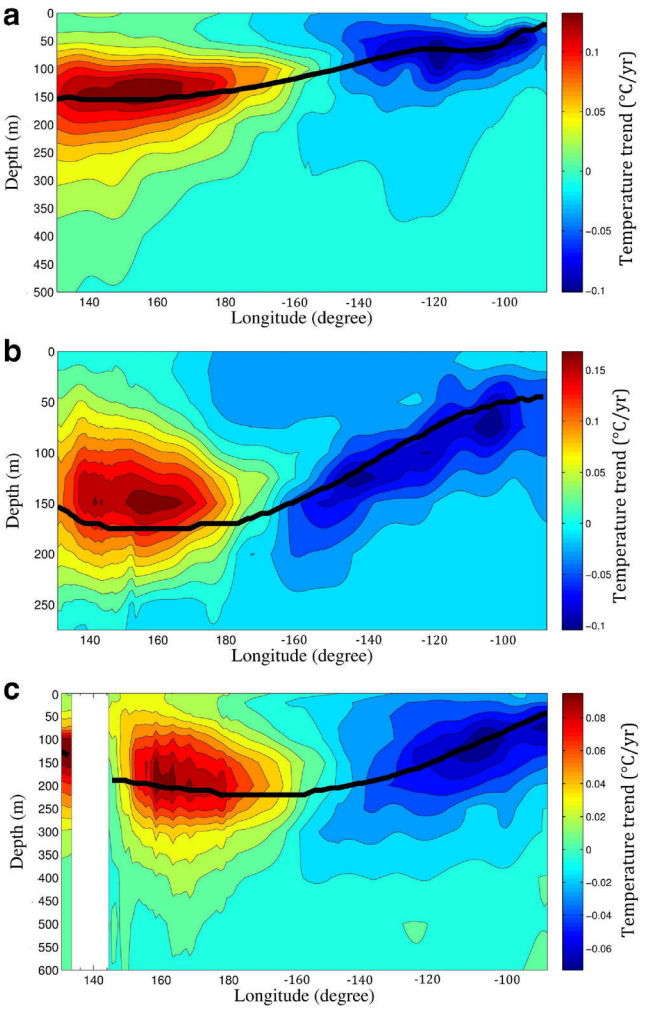

Fig. 5 Longitude–depth distribution of the 20° N–5° N (**a**), 5° N–5° S (**b**), and 5° S–20° S (**c**) averaged temperature trend pattern (*color contours*) over 1993–2012. The 20 °C isotherm mean position is represented as a *solid black line* in the figure. The *white stripe* in (**c**) corresponds to the continental surface

The total contribution of the time-varying vertical movement of the thermocline to the upper steric sea level changes (i.e., terms 1 and 2 in the right-hand side of Eq. (1) put together which gives changes from 0 to D20(t)) is shown in Fig. 7a. It also displays a dipole-like high positive trend in the western and negative trend pattern in the eastern tropical Pacific with a fulcrum near 160° W. In some areas, for example east of the Philippines and Papua New Guinea, the upper layer steric sea level trend exceeds 10 mm/year over the study period. The basin-scale (20° N–20° S, 120° E–90° W) averaged steric sea level trend contributed by the time-varying upper layer over the 1993–2012 time period accounts to 1.14 ±0.1 mm/year.

Figure 7b shows the contribution of the lower layer, i.e., between D20(t) and 700 m (term 3 in the right-hand side of

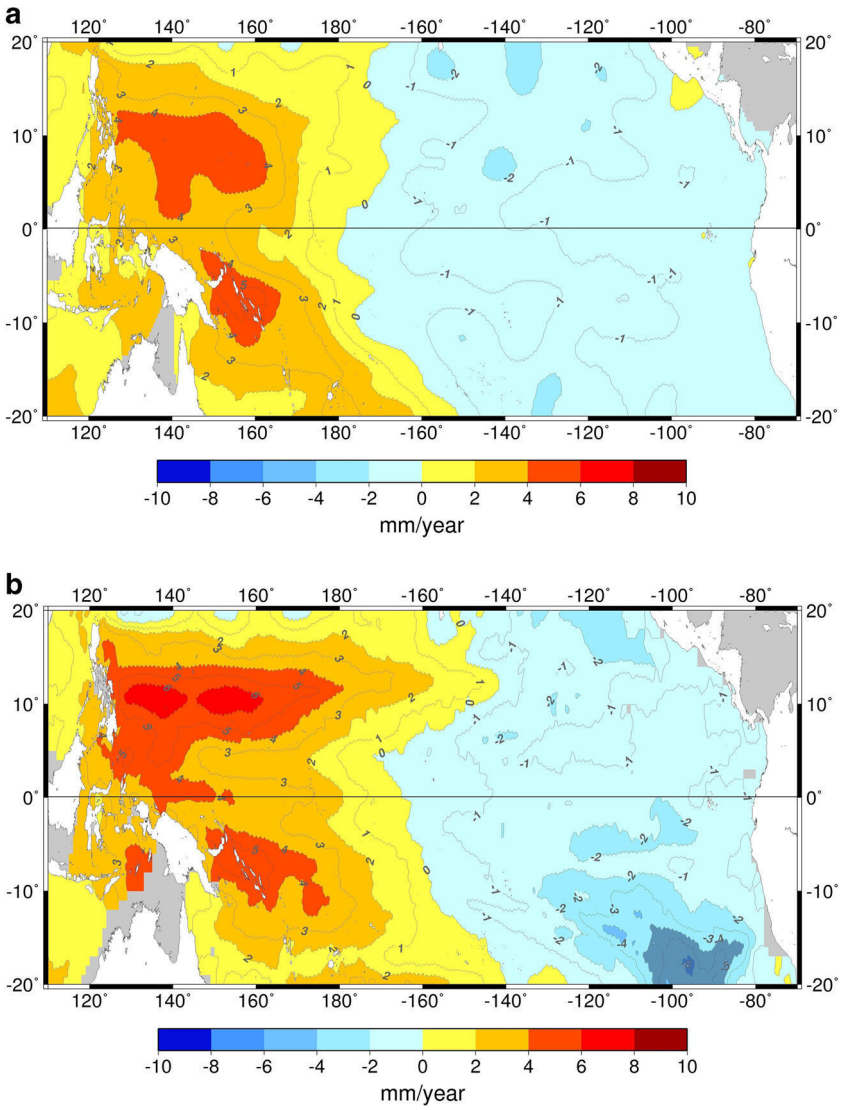

Fig. 6 Steric sea level spatial trend pattern between the surface and $D20_{mean}$ (**a**) and between $D20_{mean}$ and $D20(t)$ (**b**) in the tropical Pacific over 1993–2012 (see Eq. 1 for the definitions of $D20_{mean}$ and D20(t))

Eq. (1)), to the spatial trend pattern in steric sea level. The dipole-like positive/negative patterns are reversed with a negative pattern in the west and a positive pattern in the east. The magnitude of the trend values in this case remains low, probably within the error bars, noting that positive/negative values appear consistent over two large regions (each covering about half of the basin). The basin-scale averaged steric sea level trend contributed by this lower layer accounts to −0.19± 0.03 mm/year. The change in sign of the steric sea level trend value between the surface and D20(*t*) (positive) and between D20(*t*) and 700 m (negative) is because an increased thickness of the upper tropical ocean layer implies a reduced thickness of the lower tropical ocean layer. Moreover, in the equatorial band, this dipole reversal could also be related to the strengthening of the trade winds over the last two decades (England et al. 2014). As discussed below, such a strengthening induces an increased tilt of the thermocline, hence a stronger Equatorial Undercurrent (EUC) that in general brings heat from the western to the eastern tropical Pacific in the deeper layers. Further analysis would be needed to test this assumption.

The basin-scale steric sea level trend estimates in the upper (1.14±0.1 mm/year) and lower (−0.19±0.03 mm/year) thermocline layers imply that most of the changes in the total (0–700 m) steric sea level (net trend=0.94±0.09 mm/year) in the tropical Pacific are contributed by changes in the upper layer of the time-varying thermocline.

To further highlight the different contributions, Fig. 8 compares the basin-scale averaged steric sea level changes due to the various thermocline cases discussed above with the 0–700-m steric sea level changes. It is to be noted that when the steric sea level due to changes in thermocline depth is compared with the total steric (i.e., between the surface and 700 m), the global steric sea level trend should be included in the latter. This is because the steric sea level changes due to vertical thermocline movement contain the global steric

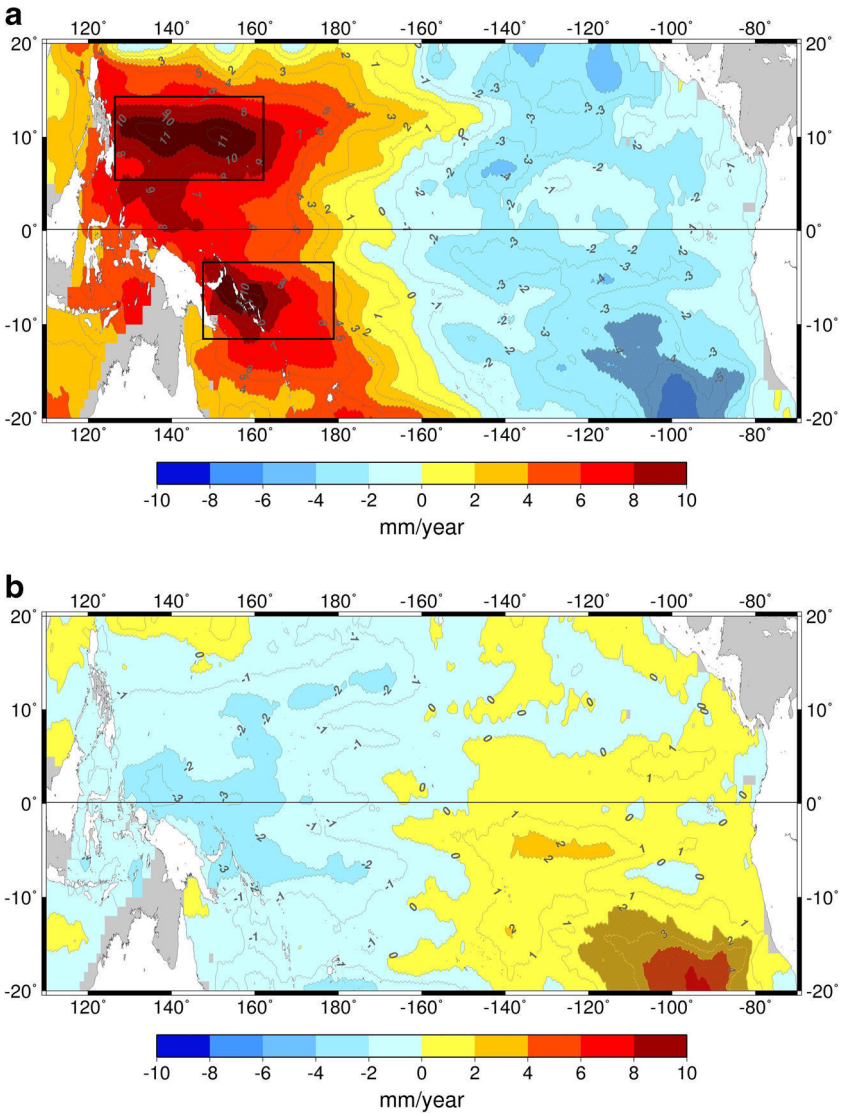

Fig. 7 Steric sea level spatial trend pattern between (**a**) the surface and D20(t) and (**b**) D20(t) and 700 m in the tropical Pacific over 1993–2012 (see Eq. (1) for the definitions of D20(*t*))

signal. Elimination of this signal which in general is calculated for a fixed depth between 0 and 700 m is not possible as the thermocline-attributed steric is calculated between varying thermocline depths. From Fig. 8, we clearly observe that the upper layer steric sea level curve is highly correlated with the total steric sea level curve (black and red curves in Fig. 8).

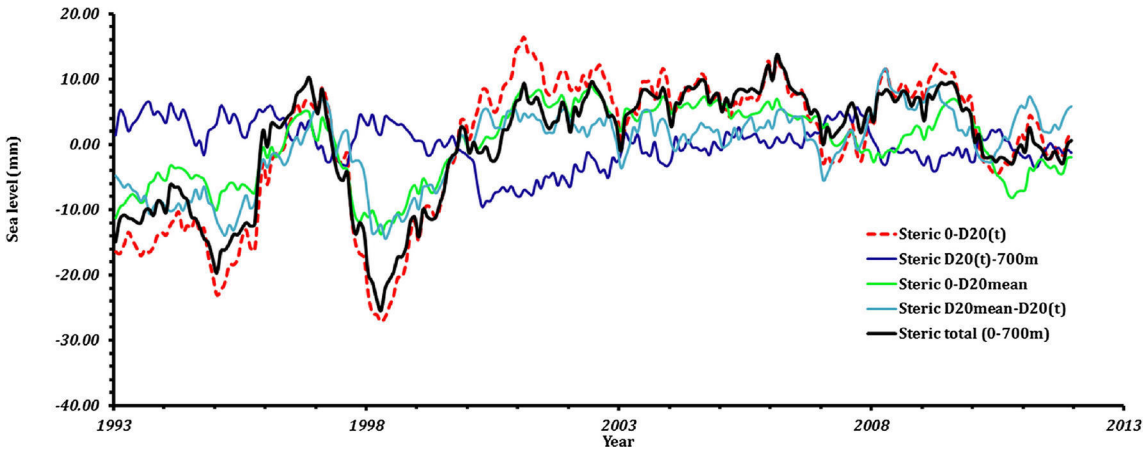

Fig. 8 Time series of different contributions of the steric sea level averaged over the tropical Pacific (20° N–20° S, 120° E–90° W)

Furthermore, Table 1 lists the correlation between the total steric (0–700 m) and the individual steric components. We can observe that among various steric components, the maximum correlation with the total steric occurs in the case of the upper layer steric (0-D20(t)). In terms of variance, the upper layer steric explains most of the variance of the total steric signal. These once again confirm that in the tropical Pacific, most of the signal corresponding to the steric sea level change can be explained by the vertically moving thermocline and associated vertical density structure changes. The spatial trend pattern of the upper layer steric sea level also shows high correlation (correlation>0.9 and significance>95 %, not shown here) with the observed altimetry sea level spatial trend pattern.

4.3 Relation between upper layer steric sea level and wind stress

From previous sections, we have seen that the sea level trend pattern during 1993–2012 in the tropical Pacific is essentially due to steric variations related to the changes in the vertical movement of the thermocline. Therefore, understanding the mechanism of the vertical thermocline movement is necessary when we focus on sea level variations in the tropical Pacific.

The low-frequency changes in the tropical thermocline depth are mainly caused by wind stress anomalies that alter the horizontal pressure gradient, the Ekman pumping, and the resulting westward-propagating oceanic Rossby waves (Meyers 1979; Kessler 1990; McGregor et al. 2012). In terms of physical equations, this can be expressed as

$$\frac{dH}{dx} = \tau_x \tag{2}$$

$$\frac{dH}{dt} - c_r \frac{dH}{dx} = -\mathrm{curl}(\tau/\rho.f) \tag{3}$$

where H is the thermocline depth (also called D20 here), τ the wind stress vector (τ_x positive to the east and τ_y to the north), ρ the density of sea water, and c_r the long gravity Rossby wave phase speed equals $\sqrt{(\beta c^2/f^2)}$ where c is the first baroclinic mode phase speed (of the order of 2.8 m/s), β the meridional (y) derivative of f, and f the Coriolis parameter. Equation (2) applies in the equatorial band only and denotes the equilibrium between the zonal thermocline slope and the zonal wind stress (Sverdrup 1947), and Eq. (3) applies about 5° off the equator only and denotes the quasi-geostrophic vorticity equation (Meyers 1979; Garzoli and Katz 1983; Kessler 1990).

The Ekman pumping term in Eq (3) can be written as

$$\mathrm{curl}(\tau/\rho.f) = (\mathrm{curl}(\tau) + (\beta/f).\tau_x)/(\rho.f) \tag{4}$$

indicating that its magnitude, at a given latitude (and so f), is thus determined both by the wind stress curl and the zonal wind stress (Delcroix and Hénin 1989).

Therefore, from Eqs. (2) and (3), we can expect an impact of the zonal wind stress on the thermocline both in the equatorial band (Eq. (2)) and away from the equatorial band (Eq. (3)). In order to confirm this, we first focus on the equatorial band and thus compare the two terms of Eq. (2). The left-hand side term was computed at each time step as a linear regression of D20 along each degree latitude from 130° E to 90° W and then averaged within 5° N–5° S. The right-hand side term was computed at each time step as the average of the zonal wind stress within 130° E–90° W and 5° N–5° S. The comparison is shown in Fig. 9. Both the thermocline slope and zonal wind stress were low-pass filtered with half a year cutoff frequency and normalized by their respective standard deviations to ease comparison. We find that the thermocline slope and zonal wind stress are highly correlated (significance>95 %), with the highest correlation (−0.92) occurring when the thermocline slope lags behind the zonal wind stress by 2 months (the correlation at 0 lag is −0.85). The thermocline slope and zonal wind stress are anti-correlated because the conventional sign of zonal wind stress is positive

Table 1 Correlation between total steric (0–700 m) and individual components of the steric sea level time series in the tropical Pacific over 1993–2012

Steric components	Total steric (0–700 m)
0-D20$_{mean}$	0.90
0-D20$_{mean}$-D20(t)	0.86
0-D20(t)	0.96
D20-700 m	−0.40

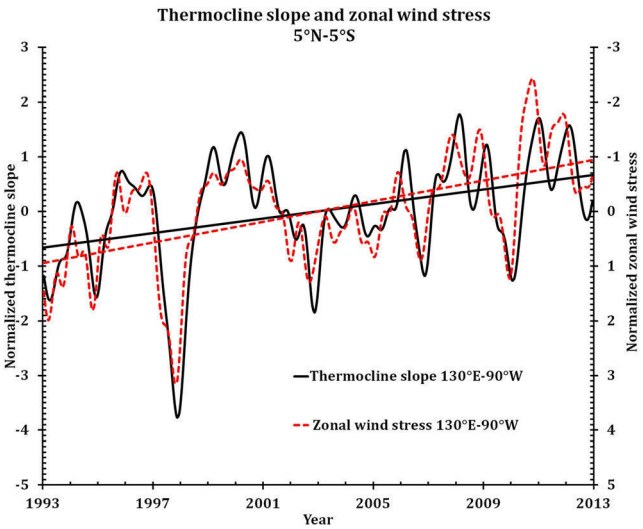

Fig. 9 Normalized thermocline slope (*black*) and zonally averaged zonal wind stress (*red dotted*) computed from 130° E to 90° W and averaged within 5° N–5° S. The *solid black and dashed red lines* denote their respective linear trends. The thermocline slope and the zonal wind stress time series have been low-pass filtered with half a year cutoff frequency for clarity

towards the east. This implies that an increase in the eastward wind causes a decrease in the westward slope of the thermocline and vice versa. Similar results were obtained over the 1968–1987 (Kessler 1990) and 1980–1994 (Delcroix 1998) time periods, using different in situ datasets.

From Fig. 9, the ENSO variability is clearly visible in both the temporal curves, for example, the 1997–1998 and 2009–2010 El Niño and the 2007–2008 and 2010–2011 La Niña. We can also observe that the thermocline slope and zonal wind stress curves exhibit positive and negative trends, respectively indicating intensification. The negative zonal wind stress trend (also see Fig. 10 for zonal wind stress spatial trend pattern) over 1993–2012 confirms the results of previous studies (e.g., Han et al. 2013; England et al. 2014) on the intensification of trade winds in the western–central tropical Pacific over the past two decades. Interestingly, parts of the trends in Fig. 9 are clearly due to the respective frequency occurrences of El Niño and La Niña events as well as to their non-symmetric characters. For example, removal of the main El Niño 1997–1998 event (i.e., removing these 2 years only out of a 20-year study period) results in a reduction of approximately 30 and 15 % of the trend of both the thermocline slope and zonal wind stress, respectively. This indicates the influence of ENSO events not only in terms of interannual variability but also in terms of trend.

Figure 9 confirms that the zonal wind stress impacts the thermocline slope in the equatorial Pacific. Since in this region, the changes in the vertical movement of the thermocline explain most of the sea level variations, we obtained similar correlation values (not shown here) when comparing the zonally averaged zonal wind stress and the upper layer (0-D20(t)) steric sea level slope. Therefore, now focusing away from the equatorial band and using Eqs. (3) and (4), we have chosen to directly compare zonal wind stress and upper layer sea level.

For this purpose, we chose to focus on the upper layer steric sea level at two regions in the western tropical Pacific (130–160° E, 5° N–15° N and 150–180° E, 5° S–15° S, boxed areas in Fig. 7a) where the upper layer steric sea level trend is maximum. Each of these regional mean steric sea level time series was then correlated with a moving regional mean zonal wind stress and wind curl (first and second right-hand side terms in Eq. 4) time series in each hemisphere. The choice of the region for the wind was made by starting with the same region as that of the upper layer steric sea level and then zonally incrementing the wind stress region by 10° to the east while maintaining the same surface area (boxed area in Fig. 10). That is to say, to start with, in the northern hemisphere, the regional mean upper layer steric sea level between 130 and 160° E was first correlated with the regional mean wind curl and zonal wind stress between 130 and 160° E (both within 5° N–5° S). Following this, the upper layer steric time series was then correlated with the wind curl and zonal wind stress time series between 140 and 170° E (with an increment of 10° zonally) and so on. Correlations at several such windows were estimated covering an overall range between 130° E and 90° W in the northern and between 150° E and 90° W in the southern hemispheres.

Figure 11a, b shows the correlation between the upper layer steric sea level and regionally varying zonal wind stress (second right-hand side term in Eq. 4) time series in the northern and southern tropical Pacific, respectively. Both the upper layer steric sea level and zonal wind stress time series were low-pass filtered with a cutoff frequency of half a year to ease comparison. In the northern tropical Pacific, the correlation between the upper layer steric sea level and zonal wind stress is high (correlation between −0.68 and −0.74 with significance>95 %) with a time lag of around 4 to 5 months between 155° E (the middle of the 140°–170° E box) and 165° W (the middle of the 180°–150° W box). In the southern tropical

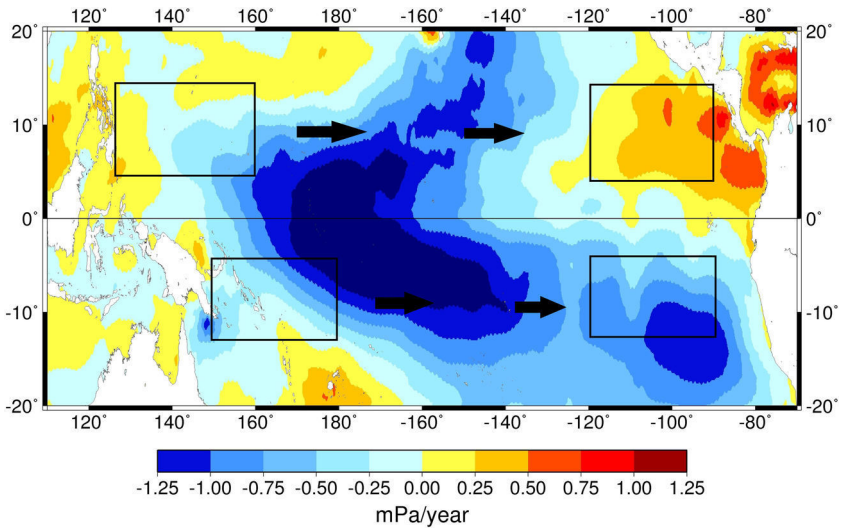

Fig. 10 Zonal wind stress spatial trend pattern in the tropical Pacific over 1993–2012. The *boxed* areas show the regions used to compute the correlation between zonal wind stress and steric sea level as in Fig. 11. The *arrows* display the direction of the eastward-moving zonal wind stress boxes

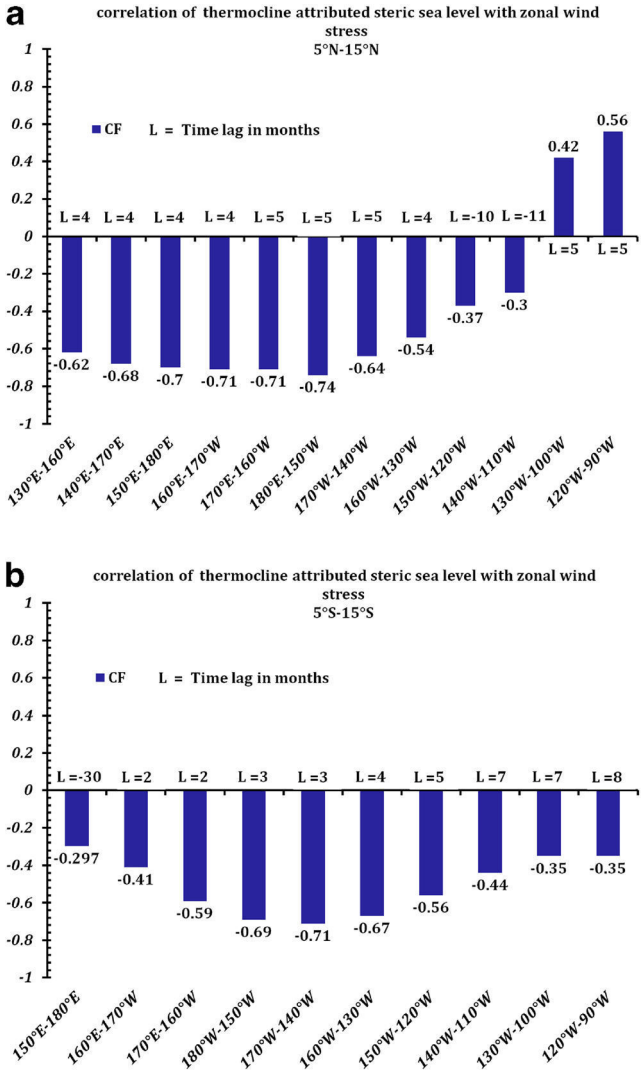

Fig. 11 Correlation between thermocline-attributed steric sea level and regionally varying zonal wind stress in the northern (**a**) and southern (**b**) tropical Pacific boxes (see Fig. 10) over 1993–2012

Pacific, the upper layer steric sea level is still highly correlated (correlation between −0.69 and −0.71 with >95 % significance) with the zonal wind stress between 165° W and 145° W. As in the northern tropical, the best correlations are obtained when the steric sea level lags behind the zonal wind stress by around 3 to 4 months. The time lag in the upper layer steric sea level variation is overall consistent with the time taken for the wind stress-generated Rossby waves to propagate towards the west at 10° latitude (i.e., in between our 5°–15° band). The theoretical Rossby wave phase speed at 10° N is actually of the order of 40 cm/s (e.g., White et al. 1985), which corresponds to about 40° longitude in 4 months. Performing a similar correlation analysis with detrended zonal wind stress and upper layer steric sea level time series (not shown here) resulted in the same values of correlation and lags. This once again indicates that the trends in steric sea level are mainly due to the changes in the tropical zonal wind stress and are influenced by the occurrences of non-symmetric El Niño and La Niña interannual variability.

To fully exploit Eq. (4), the zonal wind stress was then replaced by the wind stress curl (first right-hand side term in Eq. 4) and the correlation analysis was performed. In that latter case, we found that the curl fluctuations were weakly correlated (R of the order of −0.3) with the upper layer steric sea level. This somewhat disagrees with part of the results of Nidheesh et al. (2013), possibly because of the high sensitivity of the wind stress curl calculations to different wind products, as demonstrated by these authors. Nevertheless, the high correlation between the zonal wind stress and upper layer steric sea level is remarkably consistent with previous studies that have related the intensification of the zonal wind to high sea level rates in the western tropical Pacific during 1993–2012.

4.4 Relation between thermocline-attributed steric sea level and IPO

The contribution of decadal climate variability (PDO/IPO) to sea level can be derived from a regression of the climatic index on sea level. Defining new decadal and interannual climatic indices based on PDO and Multivariate ENSO Index (MEI), Zhang and Church (2012) used multiple linear regressions to discriminate between anthropogenic climate change and natural/internal variability to explain regional sea level changes observed since 1993 in the Pacific Ocean. They concluded that 60 % of the observed sea level variance results from internal climate modes (ENSO and PDO). In a recent detection and attribution study, Hamlington et al. (2014) attempted to estimate the sea level rise pattern associated with anthropogenic warming from satellite altimetry-based regional sea level data from the last 20 years. For that purpose, they removed the contribution of the PDO and explained—at least partly—the residual sea level trends as the signature of anthropogenic forcing. In particular, using a modeling approach, they found qualitative good agreement between the residual sea level trends in the tropical Pacific and those predicted in response to anthropogenically forced tropical Indian Ocean warming (see also Han et al. 2013).

In the previous sections, we have studied in detail the wind-related mechanisms responsible for most of the observed upper layer steric sea level trend pattern in the tropical Pacific. We now estimate the contribution of natural/internal modes to the thermocline-attributed (upper and lower layer) steric sea level trend pattern by regressing the IPO on the upper and lower layer steric sea level. Instead of using the PDO index as in previous studies, in our case, we use the IPO index. This is because the PDO index takes into account only the Northern Hemisphere (north of 20° N). Therefore, this may not necessarily account for the variability in the Southern Hemisphere unlike IPO which extends at least until 55° S. The

regression of IPO on steric sea level is performed by applying a multiple linear regression of IPO and its corresponding Hilbert transform. The Hilbert transform will also take the phase of the IPO associated with propagating signal into account.

Figure 12a, b shows the IPO contribution to the upper (0-D20(t)) and lower (D20(t)-700 m) layer steric sea level trend pattern over 1993–2012, respectively. Figure 12a exhibits the same positive–negative east–west tropical dipole pattern as in the observations (i.e., the 0-D20 steric sea level trend; see Fig. 7a), with high sea level trends in the east of the Philippines and Papa New Guinea. In the case of the lower layer steric sea level contributed by IPO, its trend pattern is similar to that of the observed lower layer steric sea level (compare Figs. 7b and 12b). However, most of the IPO-contributed trend values in this layer remain non-significant (p value >0.05). This shows that the sea level changes due to IPO occur mainly in the upper ocean layer. This leads us to focus more on the IPO-contributed upper layer steric sea level.

From Fig. 12a, we can also observe that the magnitude of the IPO-related upper layer steric sea level trend in the western tropical Pacific ranges only between 6 and 8 mm/year, while the total upper layer steric trend in this region is between 9 and 11 mm/year. This suggests that there is still a significant residual trend (in the order of 2–4 mm/year) that cannot be explained only by the IPO contribution. This can be seen in Fig. 13a which displays the residual trend pattern after removing the IPO contribution. The residual upper steric sea level trend (i.e., Fig. 13a) is comparable, though with a smaller amplitude, to the residual after the removal of the IPO contribution from the altimetry-based sea level trend pattern (Fig. 13b). This shows that natural/internal variability alone cannot totally explain the residual sea level trends of the western tropical Pacific. This result is in line with the

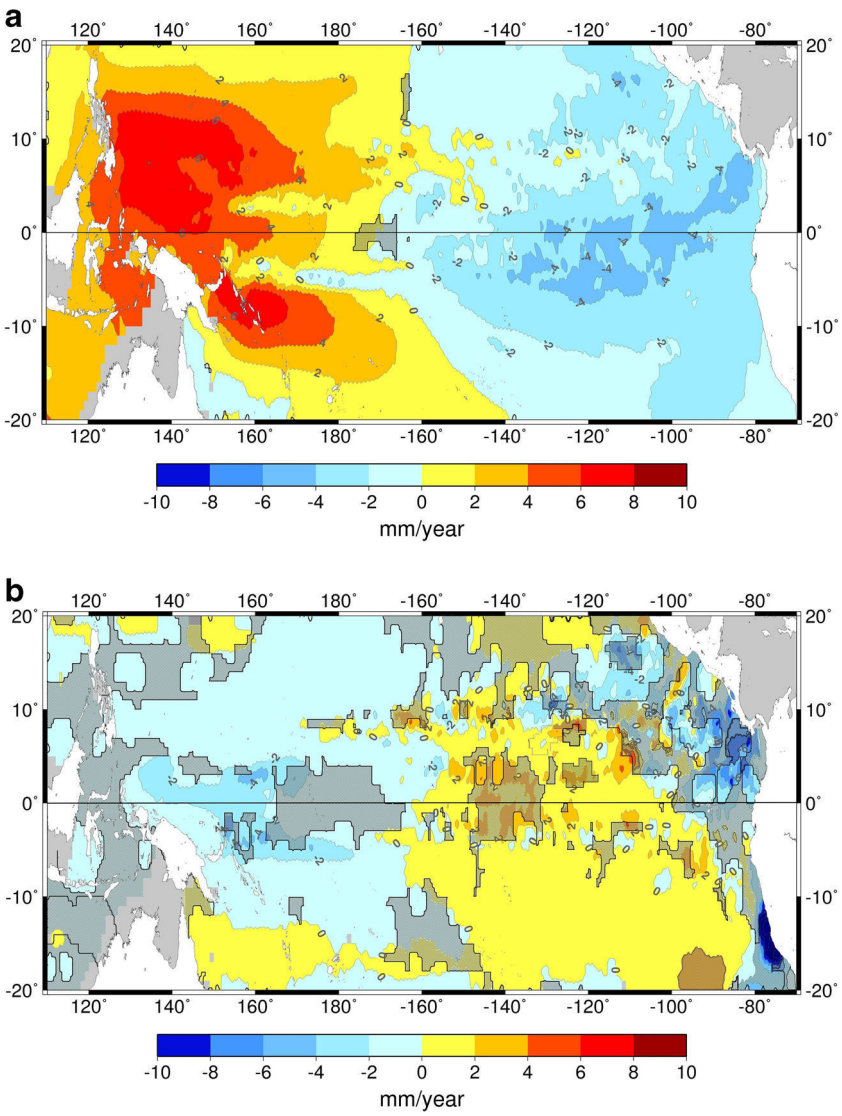

Fig. 12 IPO-contributed upper (0-D20(t)) layer (**a**) and lower (D20(t)-700 m) layer (**b**) steric sea level trend in the tropical Pacific over 1993–2012. The *hatched regions* correspond to non-significant trends (p value >0.05)

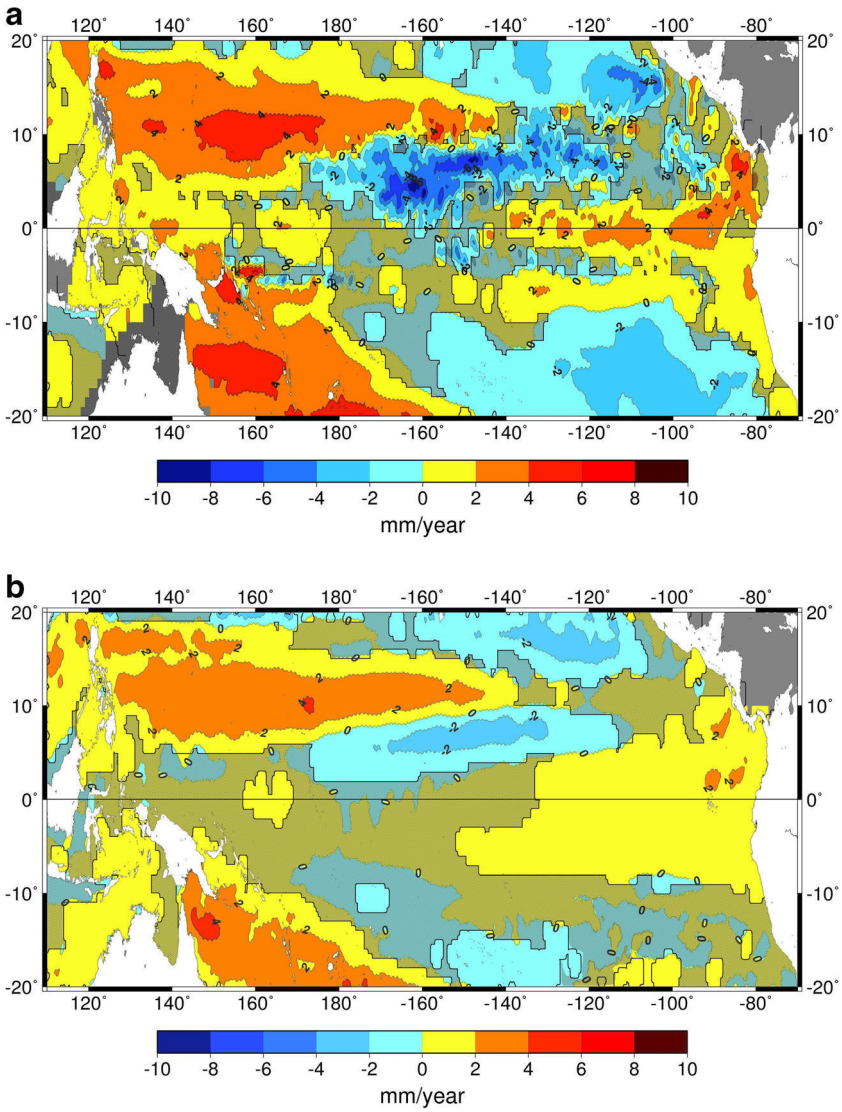

Fig. 13 **a** Upper layer steric and **b** observed altimetry-based (global mean observed sea level trend removed and global mean steric trend added) sea level trend pattern in the tropical Pacific over 1993–2012 without IPO contribution. The *hatched regions* correspond to non-significant trends (p value >0.05)

conclusion of Zhang and Church (2012) and Hamlington et al. (2014).

5 Conclusion

In this study, the mechanism that contributes to the observed sea level changes in the tropical Pacific has been studied. Using an observational dataset, we have shown that between 1993 and 2012, most of the observed sea level trend pattern in the tropical Pacific can be related to the vertically moving thermocline which affects the upper layer (i.e., above thermocline) steric sea level. The largest changes in the upper layer steric sea level in the tropical Pacific result mainly from the zonally averaged wind stress in the equatorial band (5° N–5° S) and from the upstream zonal wind stress away from the equatorial band (say within 5° and 15° latitudes), in relation to interannual (ENSO) changes and long-term trends.

The contribution of IPO-related internal climate variability to the upper layer steric sea level which is responsible for the observed sea level changes is also studied. We show that removal from the upper layer steric sea level trends of the natural/internal climate variability associated with the IPO leaves some significant residual signal. This wind-forced residual signal closely resembles that found by Hamlington et al. (2014) and attributed by these authors as the response of the tropical Pacific to anthropogenic warming of the tropical Indian Ocean (Han et al. 2013). However, we cannot exclude the fact that the residual signal may also reflect nonlinear interactions between different natural climate modes like ENSO, PDO, etc. This will be the focus of our future study. Besides, further progress in understanding our results should also rely on modeling using climate models from CMIP5 with and without anthropogenic forcing (Slangen

et al. 2014), through an appropriate detection and attribution analysis.

References

Ablain M, Cazenave A, Valladeau G, Guinehut S (2009) A new assessment of the error budget of global mean sea level rate estimated by satellite altimetry over 1993–2008. Ocean Sci 5(2):193–201

Becker M, Meyssignac B, Letetrel C, Llovel W, Cazenave A, Delcroix T (2012) Sea level variations at tropical Pacific islands since 1950. Glob Planet Chang 80–81:85–98. doi:10.1016/j.gloplacha.2011.09.004

Becker M, Karpytchev M, Lennartz-Sassinek S (2014) Long-term sea level trends: natural or anthropogenic?. Geophys Res Lett 41(15), 2014GL061027, doi: 10.1002/2014GL061027

Bindoff NL, Willebrand J, Artale V, Cazenave A, Gregory J, Gulev S, Hanawa K, Le Quéré C, Levitus S, Nojiri Y, Shum CK, Talley LD, Unnikrishnan A (2007) Observations: oceanic climate change and sea level. In: Solomon S, Qin D, Manning M, Chen Z, Marquis M, Averyt KB, Tignor M, Miller HL (eds) Climate change 2007: the physical science basis. Contribution of working group I to the fourth assessment report of the intergovernmental panel on climate change. Cambridge University Press, Cambridge

Bromirski PD, Miller AJ, Flick RE, Auad G (2011) Dynamical suppression of sea level rise along the Pacific coast of North America: indications for imminent acceleration. J Geophys Res Oceans 116(C7), n/a–n/a, doi: 10.1029/2010JC006759.

Carrère L, Lyard F (2003) Modeling the barotropic response of the global ocean to atmospheric wind and pressure forcing—comparisons with observations. Geophys Res Lett 30(6), n/a–n/a, doi: 10.1029/2002GL016473

Carton JA, Giese BS, Grodsky SA (2005) Sea level rise and the warming of the oceans in the Simple Ocean Data Assimilation (SODA) ocean reanalysis. J Geophys Res Oceans 110(C9), n/a–n/a, doi: 10.1029/2004JC002817

Cazenave A, Cozannet GL (2014) Sea level rise and its coastal impacts. Earths Future 2(2):15–34. doi:10.1002/2013EF000188

Chaen M, Wyrtki K (1981) The 20 °C isotherm depth and sea level in the western equatorial pacific. J Oceanogr Soc Jpn 37(4):198–200. doi:10.1007/BF02309057

Church JA, Clark PU, Cazenave A, Gregory JM, Jevrejeva S, Levermann A, Merrifield MA, Milne GA, Nerem RS, Nunn PD, Payne AJ, Pfeffer WT, Stammer D, Unnikrishnan AS (2013) Sea level change. In: Stocker TF, Qin D, Plattner G-K, Tignor M, Allen SK, Boschung J, Nauels A, Xia Y, Bex V, Midgley PM (eds) Climate change 2013: the physical science basis. Contribution of working group I to the fifth assessment report of the intergovernmental panel on climate change. Cambridge University Press, Cambridge

Dee DP et al (2011) The ERA-Interim reanalysis: configuration and performance of the data assimilation system. Q J R Meteorol Soc 137(656):553–597. doi:10.1002/qj.828

Delcroix T (1998) Observed surface oceanic and atmospheric variability in the tropical Pacific at seasonal and ENSO timescales: a tentative overview. J Geophys Res Oceans 103(C9):18611–18633. doi:10.1029/98JC00814

Delcroix T, Hénin C (1989) Mechanisms of subsurface thermal structure and sea surface thermohaline variabilities in the southwestern tropical Pacific during 1975–85. J Mar Res 47:777–812

Deser C, Phillips AS, Hurrell JW (2004) Pacific interdecadal climate variability: linkages between the tropics and the North Pacific during boreal winter since 1900. J Clim 17(16):3109–3124. doi:10.1175/1520-0442(2004)017<3109:PICVLB>2.0.CO;2

Durand F, Delcroix T (2000) On the variability of the tropical pacific thermal structure during the 1979–96 period, as deduced from XBT sections. J Phys Oceanogr 30(12):3261–3269. doi:10.1175/1520-0485(2000)030<3261:OTVOTT>2.0.CO;2

England MH, McGregor S, Spence P, Meehl GA, Timmermann A, Cai W, Gupta AS, McPhaden MJ, Purich A, Santoso A (2014) Recent intensification of wind-driven circulation in the Pacific and the ongoing warming hiatus. Nat Clim Chang 4(3):222–227. doi:10.1038/nclimate2106

Folland CK, Parker DE, Colman A, Washington R (1999) Large scale modes of ocean surface temperature since the late nineteenth century. In: Navarra A (ed) Beyond El Nino: decadal and interdecadal climate variability. Springer, Berlin, Refereed book: chapter 4, pp 73–102

Fukumori I, Wang O (2013) Origins of heat and freshwater anomalies underlying regional decadal sea level trends. Geophys Res Lett 40(3):563–567. doi:10.1002/grl.50164

Garzoli SL, Katz EJ (1983) The forced annual reversal of the Atlantic north equatorial countercurrent. J Phys Oceanogr 13(11):2082–2090. doi:10.1175/1520-0485(1983)013<2082:TFAROT>2.0.CO;2

Gouretski V, Koltermann KP (2007) How much is the ocean really warming?. Geophys Res Lett 34(1), n/a–n/a, doi: 10.1029/2006GL027834

Hamlington BD, Leben RR, Strassburg MW, Nerem RS, Kim K-Y (2013) Contribution of the Pacific Decadal Oscillation to global mean sea level trends. Geophys Res Lett 40(19):5171–5175. doi:10.1002/grl.50950

Hamlington BD, Strassburg MW, Leben RR, Han W, Nerem RS, Kim K-Y (2014) Uncovering an anthropogenic sea-level rise signal in the Pacific Ocean. Nat Clim Chang 4(9):782–785. doi:10.1038/nclimate2307

Han W et al (2013) Intensification of decadal and multi-decadal sea level variability in the western tropical Pacific during recent decades. Clim Dyn 1–23. doi: 10.1007/s00382-013-1951-1

Ishii M, Kimoto M (2009) Reevaluation of historical ocean heat content variations with time-varying XBT and MBT depth bias corrections. J Oceanogr 65(3):287–299. doi:10.1007/s10872-009-0027-7

Kessler WS (1990) Observations of long Rossby waves in the northern tropical Pacific. J Geophys Res Oceans 95(C4):5183–5217. doi:10.1029/JC095iC04p05183

Köhl A, Stammer D (2008) Decadal sea level changes in the 50-year GECCO ocean synthesis. J Clim 21(9):1876–1890. doi:10.1175/2007JCLI2081.1

Köhl A, Stammer D, Cornuelle B (2007) Interannual to decadal changes in the ECCO global synthesis. J Phys Oceanogr 37(2):313–337. doi:10.1175/JPO3014.1

Le Traon P-Y, Ogor F (1998) ERS-1/2 orbit improvement using TOPEX/POSEIDON: the 2 cm challenge. J Geophys Res 103(C4):8045. doi:10.1029/97JC01917

Levitus S, Antonov J, Boyer T (2005) Warming of the world ocean, 1955–2003. Geophys Res Lett 32(2) doi: 10.1029/2004GL021592

Levitus S, Antonov JI, Boyer TP, Locarnini RA, Garcia HE, Mishonov AV (2009) Global ocean heat content 1955–2008 in light of recently revealed instrumentation problems. Geophys Res Lett 36(7), n/a–n/a, doi: 10.1029/2008GL037155

Levitus S et al (2012) World ocean heat content and thermosteric sea level change (0–2000 m), 1955–2010. Geophys Res Lett 39(10), L10603. doi:10.1029/2012GL051106

Lombard A, Cazenave A, Le Traon P-Y, Ishii M (2005) Contribution of thermal expansion to present-day sea-level change revisited. Glob Planet Chang 47(1):1–16. doi:10.1016/j.gloplacha.2004.11.016

Lombard A, Garric G, Penduff T (2009) Regional patterns of observed sea level change: insights from a ¼° global ocean/sea-ice hindcast. Ocean Dyn 59(3):433–449. doi:10.1007/s10236-008-0161-6

Mantua NJ, Hare SR (2002) The Pacific Decadal Oscillation. J Oceanogr 58(1):35–44. doi:10.1023/A:1015820616384

Mantua NJ, Hare SR, Zhang Y, Wallace JM, Francis RC (1997) A pacific interdecadal climate oscillation with impacts on salmon production. Bull Am Meteorol Soc 78(6):1069–1079. doi:10.1175/1520-0477(1997)078<1069:APICOW>2.0.CO;2

Marcos M, Amores A (2014) Quantifying anthropogenic and natural contributions to thermosteric sea level rise. Geophys. Res. Lett., 41(7) 2014GL059766, doi: 10.1002/2014GL059766

McGregor S, Holbrook NJ, Power SB (2007) Interdecadal sea surface temperature variability in the equatorial Pacific Ocean. Part I: the role of off-equatorial wind stresses and oceanic Rossby waves. J Clim 20(11):2643–2658. doi:10.1175/JCLI4145.1

McGregor S, Holbrook NJ, Power SB (2008) Interdecadal sea surface temperature variability in the equatorial pacific ocean. Part II: the role of equatorial/off-equatorial wind stresses in a hybrid coupled model. J Clim 21(17):4242–4256. doi:10.1175/2008JCLI2057.1

McGregor S, Gupta AS, England MH (2012) Constraining wind stress products with sea surface height observations and implications for Pacific Ocean sea level trend attribution*. J Clim 25(23) 8164–8176, doi: 10.1175/JCLI-D-12-00105.1

Meehl GA, Hu A, Arblaster JM, Fasullo J, Trenberth KE (2013) Externally forced and internally generated decadal climate variability associated with the Interdecadal Pacific Oscillation. J Clim 26(18):7298–7310. doi:10.1175/JCLI-D-12-00548.1

Merrifield MA (2011) A shift in western tropical Pacific sea level trends during the 1990s. J Clim 24(15):4126–4138. doi:10.1175/2011JCLI3932.1

Merrifield MA, Maltrud ME (2011) Regional sea level trends due to a Pacific trade wind intensification. Geophys Res Lett 38. doi: 10.1029/2011GL049576

Merrifield MA, Thompson PR, Lander M (2012) Multidecadal sea level anomalies and trends in the western tropical Pacific. Geophys Res Lett 39. doi: 10.1029/2012GL052032

Meyers G (1979) On the annual Rossby wave in the tropical North Pacific Ocean. J Phys Oceanogr 9(4):663–674. doi:10.1175/1520-0485

Meyssignac B, Salas y Melia D, Becker M, Llovel W, Cazenave A (2012) Tropical Pacific spatial trend patterns in observed sea level: internal variability and/or anthropogenic signature? Clim Past 8(2):787–802. doi:10.5194/cp-8-787-2012

Milne GA, Gehrels WR, Hughes CW, Tamisiea ME (2009) Identifying the causes of sea-level change. Nat Geosci. doi:10.1038/ngeo544

Nerem RS, Chambers DP, Choe C, Mitchum GT (2010) Estimating mean sea level change from the TOPEX and Jason altimeter missions. Mar Geod 33:435–446. doi:10.1080/01490419.2010.491031

Nidheesh AG, Lengaigne M, Vialard J, Unnikrishnan AS, Dayan H (2013) Decadal and long-term sea level variability in the tropical Indo-Pacific Ocean. Clim Dyn 41(2):381–402. doi:10.1007/s00382-012-1463-4

Pedlosky J (2006) A history of thermocline theory. In: Jochum M, Murtugudde R (eds) Physical oceanography. Springer, New York, pp 139–152

Power S, Casey T, Folland C, Colman A, Mehta V (1999) Inter-decadal modulation of the impact of ENSO on Australia. Clim Dyn 15:319–324. doi:10.1007/s003820050284

Rebert JP, Donguy JR, Eldin G, Wyrtki K (1985) Relations between sea level, thermocline depth, heat content, and dynamic height in the tropical Pacific Ocean. J Geophys Res Oceans 90(C6):11719–11725. doi:10.1029/JC090iC06p11719

Slangen ABA, Church JA, Zhang X, Monselesan D (2014) Detection and attribution of global mean thermosteric sea level change. Geophys Res Lett n/a–n/a, doi: 10.1002/2014GL061356

Stammer D, Cazenave A, Ponte RM, Tamisiea ME (2013) Causes for contemporary regional sea level changes. Annu. Rev. Mar. Sci, 5. doi: 10.1146/annurev-marine-121211-172406

Sverdrup HU (1947) Wind-driven currents in a baroclinic ocean; with application to the equatorial currents of the eastern pacific. Proc Natl Acad Sci U S A 33(11):318–326

Swenson MS, Hansen DV (1999) Tropical Pacific Ocean mixed layer heat budget: the pacific cold tongue. J Phys Oceanogr 29(1):69–81. doi:10.1175/1520-0485(1999)029<0069:TPOMLH>2.0.CO;2

Thompson PR, Merrifield MA, Wells JR, Chang CM (2014) Wind-driven coastal sea level variability in the northeast Pacific. J Clim 27(12):4733–4751. doi:10.1175/JCLI-D-13-00225.1

Timmermann A, McGregor S, Jin F-F (2010) Wind effects on past and future regional sea level trends in the southern Indo-Pacific*. J. Clim., 23(16), 4429–4437, doi: 10.1175/2010JCLI3519.1

Volkov DL, Larnicol G, Dorandeu J (2007) Improving the quality of satellite altimetry data over continental shelves. J. Geophys. Res. Oceans 112(C6), n/a–n/a, doi: 10.1029/2006JC003765

White W, Meyers G, Donguy JR, Pazan S (1985) Short-term climatic variability in the thermal structure of the Pacific Ocean during 1979–82. J Phys Oceanogr 15:917–935

Wunsch C, Ponte RM, Heimbach P (2007) Decadal trends in sea level patterns: 1993–2004. J Clim 20(24):5889–5911. doi:10.1175/2007JCLI1840.1

Wyrtki K, Kendall R (1967) Transports of the Pacific equatorial countercurrent. J Geophys Res 72(8):2073–2076

Yang H, Wang F (2009) Revisiting the thermocline depth in the equatorial Pacific*. J. Clim., 22(13) 3856–3863. doi: 10.1175/2009JCLI2836.1

Zhang X, Church JA (2012) Sea level trends, interannual and decadal variability in the Pacific Ocean. Geophys Res Lett 39. doi: 10.1029/2012GL053240

Zhang Y, Wallace JM, Battisti DS (1997) ENSO-like interdecadal variability: 1900–93. J Clim 10(5):1004–1020. doi:10.1175/1520-0442(1997)010<1004:ELIV>2.0.CO;2

Summary of the article: 'Is anthropogenic sea level fingerprint already detectable in the Pacific Ocean?' The original article is inserted at the end of this section.

In this study, we focused on verifying if the observed regional sea level trend pattern in the Pacific Ocean over the altimetry period is the result of only natural unforced interannual and decadal climate variability or if there is also a role of anthropogenic forcing. One method for determining the externally forced signal in sea level at regional scale will be to remove the internal variability signal from the observed sea level at the region of interest and relate any residual signal to an externally forced signal (as in *Hamlington et al.,* 2014 and *Palanisamy et al*., 2015b). Since IPO/PDO is the main internal climate mode in the Pacific Ocean (*Han et al.*, 2013, *Hamlington et al.,* 2014), following *Palanisamy et al*., (2015b), in this study, the contribution of decadal IPO climate variability was first derived by linearly regressing the IPO climate index on observed altimetry based Pacific Ocean sea level signal. The IPO contributed observed sea level spatial trend pattern thus obtained was also found to be similar to the decadal sea level fingerprint of *Zhang and Church*, (2012) and that of *Hamlington et al.,* (2014). While *Zhang and Church*, 2012 used multiple variable linear regression (defining 'new' interannual and decadal climatic indices based on PDO and Multivariate ENSO Index (MEI)) to discriminate the interannual, decadal and longer term trend, *Hamlington et al.*, (2014) estimated the PDO contribution by an EOF analysis of sea level reconstruction based 20 year trend patterns from 1950 to 2010. These indicate that the IPO contributed observed sea level trend pattern is hardly sensitive to the methodologies used.

Observed altimetry-based sea level trend pattern without IPO contribution (Alti-IPO) was then estimated by subtracting the IPO contributed sea level signal from the altimetry based sea level signal. The Alti-IPO sea level trend pattern (Fig.4.9) was estimated to be insignificant in most of the regions of the Pacific Ocean with exceptions in the western tropical and southern central Pacific. Though weaker, the positive trend pattern in the western tropical Pacific (especially near 10°N/S) is in the order of 2-4 mm/yr. A simple Empirical orthogonal Function (EOF) analysis was then performed on the Alti-IPO residual signal and the mode with the maximum variance was then analyzed. The spatial pattern corresponding to the first EOF mode was found to closely resemble pattern associated with El Niño Modoki, a central Pacific ENSO event (*Ashok et al.*, 2007, *Bosc and Delcroix*, 2008). Furthermore, a very good correlation was

also found between the EOF1 temporal curve and the El Niño Modoki index (EMI). The presence of El Niño Modoki signal in the Alti-IPO residual indicates that there is in fact some ENSO-related internal variability still remaining even after the removal of IPO. As a next step, the signal corresponding to El Niño Modoki was further removed from the Alti-IPO signal by once again performing a linear regression of EMI on Alti-IPO (henceforth called Alti-IPO-EMI). An EOF analysis of Alti-IPO-EMI resulted in the first EOF mode closely resembling the eastern Pacific ENSO event in terms of spatial pattern with the evident strong 1997/1998 El Nino event clearly visible in the temporal curve. Therefore, all the analyses performed on the altimetry sea level residual without IPO and EMI contribution finally showed that that attempts to separate/ remove both decadal and interannual climate modes from observed altimetry based sea level signal through the method of linear regression (as shown in this study) or the methodology of *Hamlington et al.*, 2014 do not in fact totally eliminate the internal sea level variability. Some non-linear internal variability related to intense ENSO events such as the 1997/1998 El Nino still remains in the residual.

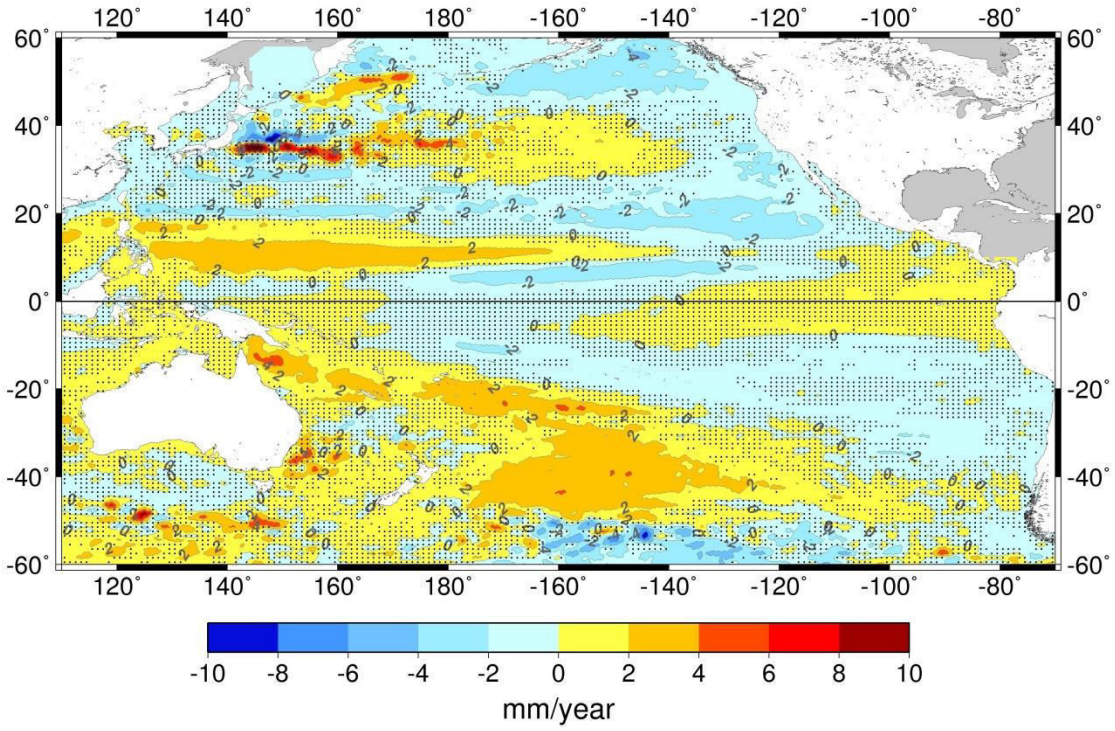

Figure 4.9: Altimetry based Pacific Ocean sea level spatial trend pattern without the contribution of IPO over 1993-2013 (uniform global mean has been removed from both before performing the regression) Stippling indicates regions of non-significant trend (p-value > 0.05). Adapted from Palanisamy et al., 2015c.

In order to further confirm our results, we then worked on 21 CMIP5 models. Performing a Multi Model Ensemble (MME) of the 21 CMIP5 models would in general average out/ reduce the sea level signal due to internal climate modes. The MME containing only the expected sea level response to external forcings (natural and anthropogenic) can then be compared with the Alti-IPO and Alti-IPO-EMI residual sea level trend patterns. Before a direct comparison of the sea level trend patterns, the presence of any internal climate modes in the MME was first verified by performing EOF decomposition on the MME based global and Pacific Ocean sea level signal between 1900 and 2098 and the corresponding spatial and temporal patterns were studied. This would enable us to verify the effectiveness of MME in reducing the impact of internal climate modes not only in the Pacific but also in the other oceans. Furthermore, such verification would also give us an idea on regions where the impact of external forcing is the maximum and the structure of their corresponding spatial patterns. The first EOF mode of the global MME signal explains a total variance of 96%. In terms of spatial pattern, this increase in sea level appears in the northern high latitudinal bands, North Atlantic Ocean south of Greenland and also in the southern latitudinal bands. Regions of positive sea level patterns also occur in the western extra-tropical Pacific Ocean and in western Indian and central Atlantic oceans. Region of negative sea level change appears in the Southern Ocean beyond the 50°S latitudinal band. This is in agreement with the results from *Bilbao et al.*, (2015). Performing the same EOF analysis only on the Pacific Ocean, we obtain the same Pacific Ocean spatial pattern (with a variance of 93%). The temporal curves of both the global and Pacific Ocean EOF1 mode are almost flat until 1970 after which there is an increase that continues over time implying accelerated dynamic sea level change. These are in agreement with studies showing increased anthropogenic forcing since 1970s. Small amplitude oscillations displayed in both EOF1 temporal curves were removed by performing a spline smoothing (*Ribes et al.*, 2009). The smoothed global EOF1 temporal curve was then regressed on to the CMIP5 MME sea level signal.

Analysis of the regressed CMIP5 MME based Pacific Ocean sea level spatial trend pattern over 1993-2013 period (Fig.4.10) showed that in the western tropical Pacific it was not comparable with the Alti-IPO-EMI based residual trend pattern. Contrary to the Alti- IPO and Alti-IPO-EMI trend patterns, the CMIP5 MME based positive trend pattern that appears in the western tropical Pacific extending towards the east between 10°N to 20°N and 120°E to 120°W is only in the range of 0.1 mm/yr to 0.3 mm/yr. The absence of significantly high positive sea

level trend in the western tropical Pacific over the altimetry era from the regressed CMIP5 MME based data shows that the residual trend patterns observed in the altimetry signal after having removed IPO and EMI contribution cannot be attributed to anthropogenic forcing. Furthermore, our results also show that the methodology of removing one main internal climate mode (i.e. IPO in this case) through linear regression may not successfully remove the modes that do not linearly co-vary with it. The most important of all, the amplitude of the regressed CMIP5 MME based sea level trend pattern in the tropical Pacific is significantly lower than the expected error in trend patterns from satellite al timetry (in the order of 2 mm/yr to 3 mm/yr, *Ablain et al.*, 2015, *Couhert et al.*, 2015) and suggest that satellite altimetry measurement is still not accurate enough to detect the anthropogenic signal in the 20 year tropical Pacific sea level trends.

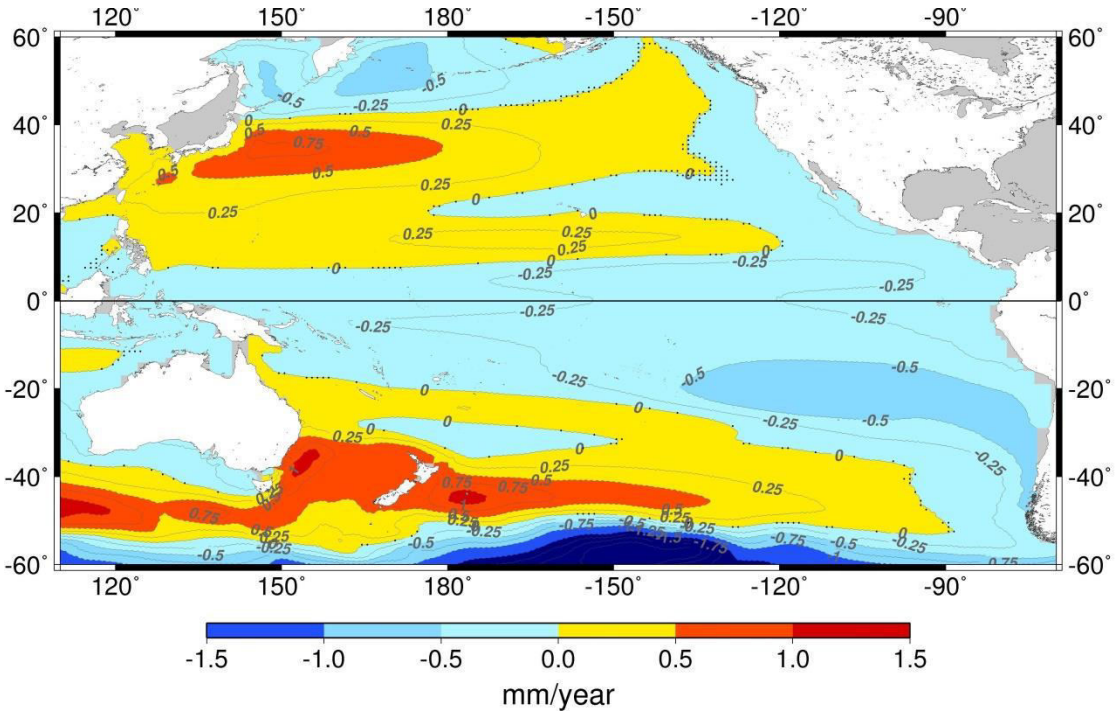

Figure 4.10: Pacific Ocean sea level spatial trend pattern estimated 735 from regressed CMIP5 MME sea level data over 1993-2013. Stippling indicates regions of non-significant trend (p-value > 0.05). Adapted from Palanisamy et al.,2015b.

Environmental Research Letters

LETTER

Is anthropogenic sea level fingerprint already detectable in the Pacific Ocean?

H Palanisamy[1], B Meyssignac[1], A Cazenave[1,2] and T Delcroix[1]

[1] LEGOS-UMR5566, Toulouse, France
[2] ISSI, Bern, Switzerland

E-mail: hindumathi.palanisamy@legos.obs-mip.fr

Keywords: tropical Pacific Ocean, internal climate mode, anthropogenic sea level fingerprint, altimetry based sea level, CMIP5 dynamic sea level

OPEN ACCESS

RECEIVED
15 April 2015

ACCEPTED FOR PUBLICATION
30 July 2015

PUBLISHED
25 August 2015

Abstract

Sea level rates up to three times the global mean rate are being observed in the western tropical Pacific since 1993 by satellite altimetry. From recently published studies, it is not yet clear whether the sea level spatial trend patterns of the Pacific Ocean observed by satellite altimetry are mostly due to internal climate variability or if some anthropogenic fingerprint is already detectable. A number of recent studies have shown that the removal of the signal corresponding to the Pacific Decadal Oscillation (PDO)/Interdecadal Pacific Oscillation (IPO) from the observed altimetry sea level data over 1993–2010/2012 results in some significant residual trend pattern in the western tropical Pacific. It has thus been suggested that the PDO/IPO-related internal climate variability alone cannot account for all of the observed trend patterns in the western tropical Pacific and that the residual signal could be the fingerprint of the anthropogenic forcing. In this study, we investigate if there is any other internal climate variability signal still present in the residual trend pattern after the removal of IPO contribution from the altimetry-based sea level over 1993–2013. We show that subtraction of the IPO contribution to sea level trends through the method of linear regression does not totally remove the internal variability, leaving significant signal related to the non-linear response of sea level to El Niño Southern Oscillation (ENSO). In addition, by making use of 21 CMIP5 coupled climate models, we study the contribution of external forcing to the Pacific Ocean regional sea level variability over 1993–2013, and show that according to climate models, externally forced and thereby the anthropogenic sea level fingerprint on regional sea level trends in the tropical Pacific is still too small to be observable by satellite altimetry.

1. Introduction

Sea level change is one of the most concerning consequences of climate change. Since the early 1990s, sea level is rising at a rate of 3.2 ± 0.4 mm yr^{-1} (e.g. Church *et al* 2013, Ablain *et al* 2015). Though a recent study, Watson *et al* (2015), has shown that the sea level rate over the altimetry period might be lower than previously estimated, all studies agree that sea level will continue to rise in the future because of expected continuing ocean warming and land-ice melt (Church *et al* 2013). Sea level rise is far from being uniform and exhibits significant spatial variations regionally mainly related to non-uniform thermal expansion and salinity variations of the ocean (e.g., Cazenave and Cozannet 2014, *Stammer et al* 2013, Church *et al* 2013, Levitus *et al* 2012, Fukumori and Wang 2013). For example, since 1993, rates up to three times the global mean rise are observed in regions like the western tropical Pacific (e.g. Merrifield and Maltrud 2011), north Atlantic around Greenland and southern Austral Ocean while other regions like the eastern tropical Pacific face lower rates of sea level rise (Bromirski *et al* 2011, Thompson *et al* 2014). Regional steric sea level changes in different ocean basins are attributed to differential heating and freshening of various ocean layers and associated physical processes such as air-sea interaction, lateral and vertical mixing or advective

processes (Yin *et al* 2010) with ocean circulation changes playing a major role (Stammer *et al* 2013). In addition other phenomena such as net ocean mass changes from melting land-ice as well as gravitational and solid earth responses due to Glacial Isostatic Adjustment (GIA) also contribute to regional sea level variability (e.g. Milne *et al* 2009, Stammer *et al* 2013), however their effects are small over the two recent decades. In the tropical Pacific, Merrifield, 2011, Merrifield and Maltrud, 2011 and Palanisamy *et al* 2015 showed that the high sea level trends in this region during the altimetry era are essentially due to the heat redistribution in the ocean related to the deepening of the thermocline in response to intensified trade winds.

The different contributors to sea level and thus sea level itself respond to unforced internal variability and forced variability of the climate system. While the unforced internal variability is spontaneously generated by the climate system in the absence of changes in the climate forcing, the forced variability is in response to external climate forcing which includes anthropogenic signal as well as natural forcing such as volcanic eruptions or solar variability. While at the global scale (i.e. in terms of global mean sea level), detecting and separating the internally generated climate modes from externally forced signals in sea level has been feasible (Marcos and Amores 2014, Slangen *et al* 2014), performing similar studies on regional sea level is highly challenging. This is because the internal climate variability introduces strong changes in regional sea level on time scales from years to decades (Richter and Marzeion 2014) and makes the signal to noise ratio very unfavorable in the detection of the forced response above the unforced internal variability. For example, the regional sea level changes in the tropical Pacific Ocean are governed by natural climates modes such as El Niño Southern Oscillation (ENSO) and Pacific Decadal Oscillation (PDO)/Interdecadal Pacific Oscillation (IPO) at interannual and decadal time scales, respectively (e.g. Stammer *et al* (2013), Zhang and Church (2012), Han *et al* (2013) Hamlington *et al* (2014a) and references therein). The internal sea level variability related to such climate modes of the order of ±10–20 cm can therefore mask sea level changes due to externally forced signals.

Recently, making use of climate models from the fifth phase of the Coupled Model Intercomparison Project (CMIP5), studies (Lyu *et al* 2014, Jordà 2014, Richter and Marzeion 2014, Bilbao *et al* 2015) have determined the time of emergence, that is, the time when the anthropogenic climate change signal exceeds and emerges from the natural climate variability at a regional scale. Lyu *et al* (2014) find that relative to the 1986–2005 reference period, under RCP4.5 and RCP8.5 scenarios, the externally forced trend would be detectable in both steric and dynamic sea levels by the early to mid-2040s in 50% of the ocean. Similarly Richter and Marzeion (2014) also find that the externally forced signal is detectable in the early 2030s relative to 1990 in 50% of the ocean. These regions include the South Atlantic Ocean, Arctic Ocean, eastern Pacific Ocean and most parts of the Indian Ocean. Furthermore Jordà (2014) has shown that on average, it would require a minimum time period of 40 years to identify the externally forced signal at the regional scale. However in regions with strong decadal and interannual sea level variability, the emergence time increases up to 60–80 years. These results are also in agreement to that of Richter and Marzeion (2014) and Lyu *et al* (2014). This shows that the presence of strong internal variability can mask the long-term forced trend for several decades.

One method for determining the externally forced signal in sea level at the regional scale will be to remove the internal variability signal from the observed sea level at the region of interest and relate any residual signal to an externally forced signal. This has been the subject of two recent studies, Hamlington *et al* (2014a) and Palanisamy *et al* (2015) in the tropical Pacific. Since PDO/IPO is the main natural climate mode in this region (Han *et al* 2013, Hamlington *et al* 2014a), Hamlington *et al* (2014a) removed its contribution to sea level from the altimetry-based sea level signal over 1993–2012 and showed a residual trend pattern in the tropical Pacific that, in general, cannot be due to PDO. Using a modelling approach, this study also showed that the residual pattern after having removed the influence of PDO could be linked to anthropogenic warming of the tropical Indian Ocean (see Han *et al* (2013) for details). By removing the contribution of IPO from the mechanism that contributes to sea level changes in this region (i.e. the thermocline attributed steric sea level), Palanisamy *et al* (2015) showed a similar residual trend pattern in the tropical Pacific, but concluded that this residual pattern may alternately reflect the signature of other natural climate modes or some non-linear PDO signatures that were not properly removed in the process.

In this study we investigate this issue further. We perform a detailed analysis on the residual sea level trend pattern after having removed the IPO contribution in the tropical Pacific to verify if the origin of the residual is externally forced signal or a signal due to internal climate modes of variability. To do so, we use two approaches: (1) a simple Empirical Orthogonal Function (EOF) analysis on the residual altimetry signal without IPO and (2) comparison of the residual signal with CMIP5 based climate models.

2. Data and methods

2.1. Satellite altimetry sea level (1993–2013)

In this study, we used the altimetry-based 2D gridded sea level anomalies from AVISO. This data is available on a weekly interval as a ¼° regular grid from January 1993 to December 2013. This is the DT-MSLA 'Ref'

series computed at Collecte Localisation Satellite (CLS) by merging several altimeter missions namely: Topex/Poseidon, Jason-1 and Jason-2, Envisat, ERS-1 and ERS-2. This dataset has undergone geophysical and orbital corrections. Detailed information on the dataset and processing can be found in Ablain *et al* (2009). In order to be consistent with the other data sets used in this study, the altimetry sea level data at weekly intervals has been averaged to a monthly scale. The annual and semi-annual signals have been removed through a least-square fit of twelve and six month period sinusoids. Since the focus of our study is regional sea level trend patterns, the uniform global mean sea level has been removed from the altimetry data.

The contribution of decadal climate variability (i.e. IPO) to sea level can be derived from a regression of the climatic index on sea level (Palanisamy *et al* 2015). Here we make use of an updated version of the IPO index available from 1871 until mid-2014 (kindly provided by C K Folland). This index is similar to that of PDO which is defined as the leading principal component of the North Pacific (poleward of 20°N) monthly sea surface temperature (SST) variability (Mantua *et al* 1997, Mantua and Hare 2002, Zhang *et al* 1997). The IPO is the Pacific-wide equivalent of the PDO, with as much variance in the Southern Hemisphere Pacific (at least to 55°S) as in the Northern Hemisphere (Folland *et al* 1999). Using the IPO index, we perform a multiple linear regression of IPO and its corresponding Hilbert transform on altimetry based observed sea level. The Hilbert transform will also take the phase of the IPO associated with propagating signal into account (Palanisamy *et al* 2015). The IPO contributed sea level signal obtained as a result is then removed from the observed altimetry-based sea level.

2.2. 2D past sea level reconstruction (1960–2013)

The limited time length of the altimetry data can become an issue when evaluating low frequency variability in terms of trends (Frankcombe *et al* 2014). IPO is a low frequency natural climate oscillation with a periodicity of around two to three decades. Several studies (Deser *et al* 2004, Yasunaka and Hanawa 2003, Hare and Mantua 2000) have shown evidence of four IPO phase changes since the 20th century: two warm phases during 1925–1946, 1977–1997 and two cold phases during 1947–1976 and since 1998. Performing regression of IPO index on the observed altimetry sea level signal since 1993 implies that we take into account only one complete phase of the IPO climate mode, i.e., the current negative IPO phase since 1998. This can result in trend aliasing (Frankcombe *et al* 2014), i.e. the incomplete separation of the trend and low frequency IPO variability since the period of the internal variability is longer than the altimetry period. The inability to distinguish between the trend and low frequency variability results in the low frequency variability itself to be aliased as a trend. Frankcombe *et al* (2014) have shown that around 50 years of time series is required to extract low frequency variability from the sea level signal. However, it is to be noted that exact quantification of signal related to internal variability using finite records still remains a challenge. For example, Wittenberg (2009) has shown that there is no guarantee that 150 year historical SST records can be used to determine a full representative for ENSO modulation. Furthermore, Bordbar *et al* (2015) have mentioned that the lack of long-term observations poses a challenge in quantifying long-term internal variability as it can introduce considerable uncertainty on the future evolution of regional sea level.

In our study, in order to verify if the residual trend pattern in the tropical Pacific after having removed the IPO contribution from altimetry sea level is due to aliasing effect or not, we also used the updated version of a 2D past sea level reconstruction from Meyssignac *et al* (2012a) available from 1960 to 2013. This 2D past sea level reconstruction is an optimal interpolation of long tide gauge records with Empirical Orthogonal Function (EOF) deduced from the sea level output of 3 different ocean reanalyses, namely GECCO2 (Köhl, 2015), SODA 2.1.6 (Carton and Giese 2008) and ORAS4 (Balmaseda *et al* 2013). This approach uses EOFs to combine 134 long tide gauge records of limited spatial coverage and 2D sea level patterns based on ocean reanalysis. Three different past sea level reconstructions based on EOFs from each ocean reanalysis were performed and then merged in a unique mean reconstruction following Meyssignac *et al* 2012a. Compared to previous reconstructions available in the literature, these updated reconstructions are not global reconstructions based on global EOFs. They are based on regional reconstructions over the Pacific-Indian Basin and the Atlantic Basin which were further concatenated into global reconstructions. By separating the Indian-Pacific region from the Atlantic region, it is expected that EOFs are more consistent with the regional climate modes of the basins (ENSO and PDO in the Indo-Pacific region and NAO in the Atlantic) to interpolate the tide gauge records. It yields a better reconstruction of the sea level over the last decades in comparison with independent tide gauge records (see Meyssignac *et al* 2015).

The linear regression of IPO is then performed on this data with a time length of 53 years and IPO contribution is then removed from the reconstruction-based sea level signal. Comparison of reconstruction based residual trend pattern with altimetry-based residual trend pattern over 1993–2013 would reveal the presence of aliasing if any.

2.3. CMIP5 climate models (1860–2098)

To investigate changes in sea level due to external forcing, we also analyzed the dynamic sea surface

Table 1. List of CMIP5 dynamic sea level models and the corresponding number of realizations used in the study.

Dynamic sea level data	
CMIP5 models	No. of realizations
ACCESS1.0	1
ACCESS1.3	1
CanESM2	5
CCSM4	6
CNRM-CM5	5
CSIRO-Mk3.6.0	10
GFDL-CM3	1
GFDL-ESM2M	1
HadGEM2-CC	1
HadGEM2-ES	4
INM-CM4	1
IPSL-CM5A-LR	4
IPSL-CM5A-Mr	1
MIROC5	3
MIROC-ESM	1
MIROC-ESM-CHEM	1
MPI-ESM-LR	3
MPI-ESM-Mr	1
MRI-CGCM3	1
NorESM1-M	1
NorESM1-ME	1
Total no. of realizations	53
Total no. of models	21

height from 21 climate models from CMIP5 (Taylor *et al* 2012). Table 1 displays the list of CMIP5 models used. The dynamic sea surface height includes changes in the thermohaline and wind-driven circulations (Richter and Marzeion 2014). The CMIP5 climate models do not include the net ocean mass changes from melting ice sheets and glaciers as well as associated gravitational and solid earth responses. But this term is almost uniform over the last 20 years and likely negligible (Landerer *et al* 2014, Yin *et al* 2010) in terms of spatial variability in regional sea level trends. Hence it is not important for our study. We used the historical 'all forcing' CMIP5 climate simulations available from 1850/1860. These simulations are forced by natural forcing agents (solar radiation, volcanic aerosols) and anthropogenic forcing agents (e.g. greenhouse gas, anthropogenic aerosols, and ozone etc, Taylor *et al* 2012). CMIP5 historical simulations in general end in 2005. Since our period of interest corresponds to that of the satellite altimetry era from 1993 until 2013, we therefore extended the historical simulations by concatenating the 21st century projections under the Representative Concentration Pathway (RCP) 8.5 scenario (2006–2098/2100) to the historical simulations. The RCP8.5 scenario assumes continuous anthropogenic GHG emission throughout the 21st century and can also be considered as a representative of the present scenario (IPCC 2013).

Among the 21 models, some models provide multiple realizations of the historical experiment. For example, CMIP5 historical runs initialized from different times of a control run would be identified as 'r1','r2', etc. The RCP simulation is assigned the same realization number as the historical run from which it was initiated (information on CMIP5 data reference syntax can be found at http://cmip-pcmdi.llnl.gov/cmip5/output_req.html). In our study, all possible realizations that correspond to the Historical+RCP8.5 simulations were taken into account (see table 1). As a result, 53 realizations were used in this study. The data is at yearly resolution and the spatial fields are remapped to a regular $1^\circ \times 1^\circ$ resolution. All climate models are corrected for the model drift (Gregory *et al* 2001, Sen Gupta *et al* 2012) by removing the quadratic trend in the time series of the accompanying pre-industrial control run. The global mean was removed from the dynamic sea level data at every time step.

The temporal phases of the internal climate variability in the CMIP5 models are not reproduced. This is because in Global Coupled Models (GCMs), the unforced internal climate modes (e.g. ENSO, IPO) are not constrained to be synchronized to real-world occurrence (Landerer *et al* 2014). Furthermore, the ability of climate models to accurately reproduce the internal climate modes has been a questionable subject. Since the interest of this study is to look for externally forced sea level signals, performing a multi-model ensemble (MME) of several such CMIP5 models will in general average out/reduce signals related to internal climate variability thereby reflecting the forced signal mostly due to external forcings. To avoid bias to models with more realizations, in this study, the realizations of each model are first averaged to obtain the model mean and then the 21 models are averaged (as in Yin, 2012).Taking into account one realization per model (instead of averaging all realizations of each model first) produces the same results.

3. Results

3.1. Observation based Pacific Ocean sea level trend pattern and internal climate modes

Figure 1(a) displays the observed altimetry based sea level spatial trend pattern over 1993–2013 (with the global mean sea level (GMSL) removed) and figure 1 (b) displays the contribution of IPO to Pacific Ocean sea level trend over 1993–2013 based on the regression of IPO index on sea level signal. Stippling indicates regions where the trends are non-significant (p-value > 0.05). The IPO contributed sea level trend pattern exhibits similar broad scale positive v-shaped trend pattern and east-west tropical dipole as the observed altimetry-based sea level trend pattern. This trend pattern is also similar to the decadal sea level fingerprint of Zhang and Church (2012) (see their figure 4(b)) and the PDO contributed sea level trend

pattern of Hamlington *et al* (2014a) (see their figure 1 (b)). Their methodology of calculation of the decadal sea level fingerprint somewhat differs from the methodology used in this study. Zhang and Church (2012) used multiple variable linear regression (defining 'new' interannual and decadal climatic indices based on PDO and Multivariate ENSO Index (MEI)) to discriminate the interannual, decadal and longer term trend. On the other hand, Hamlington *et al* (2014a) estimated the PDO contribution by an EOF analysis of sea level reconstruction (Hamlington *et al* 2014b) based 20 year trend patterns from 1950 to 2010. Based on the results obtained in this study and studies of Zhang and Church (2012) and Hamlington *et al* (2014a), we can observe that the IPO contributed observed sea level spatial trend pattern is hardly sensitive to the methodologies used.

Observed altimetry-based sea level trend pattern without IPO contribution (figure 2(a)) and henceforth called the (Alti-IPO) residual signal, is estimated by subtracting the IPO contributed sea level signal from the altimetry based sea level signal. The Alti-IPO sea level trend pattern is insignificant in most of the regions of the Pacific Ocean with exceptions in the western tropical and southern central Pacific. Though weaker, the positive trend pattern in the western tropical Pacific (especially near 10°N/S) is in the order of 2–4 mm yr^{-1}. The residual sea level trend pattern is similar to figure 1(c) of Hamlington *et al* (2014a) that has been attributed to an anthropogenic sea level fingerprint.

In order to verify if the residual trend pattern is due to aliasing of IPO and sea level signal as a result of short time length of study, we used the 2D reconstruction based Pacific Ocean (until 40°S latitude as the reconstruction data is not available further south) sea level spatial trend pattern over 1993–2013 without IPO contribution (figure 2(b)). As described in section 2.2, this is obtained by performing a regression of IPO on reconstruction based sea level signal over 53 years and removing its contribution. The residual trend patterns in both figure 2(a) (Alti-IPO) and figure 2(b) (reconstruction-IPO) at the region of interest, i.e the western tropical Pacific are very similar. This implies that the trend pattern of the Alti-IPO residual signal is likely not a result of the aliasing effect.

3.1.1. Analysis of Alti-IPO residual signal

As the next step, we tried to verify if Alti-IPO residual pattern can be related to any physical processes. So an EOF analysis was first performed on the Alti-IPO residual signal and the mode with the maximum variance was analyzed. Figures 3(a) and (b) show the spatial pattern and corresponding temporal curve of the first EOF mode of Alti-IPO sea level signal, respectively. The maximum variance explained by the first EOF mode of the Alti-IPO residual is only 6%. Performing an EOF analysis directly on the Pacific Ocean observed altimetry based sea level results in a first mode with a variance of 17% (not shown here). The reduction in the maximum variance explained by the Alti-IPO EOF implies the significant role of IPO in the Pacific Ocean sea level. From figure 3(a), we can observe that the spatial pattern very closely resembles the central Pacific ENSO event, also called the El Niño Modoki. While conventional El Niño is characterized by strong anomalous warming in the eastern tropical Pacific, El Niño Modoki is associated with strong anomalous warming in the central tropical Pacific and cooling in the eastern and western tropical Pacific (Ashok *et al* 2007, also see figure 14 of Bosc and Delcroix (2008)).

The temporal curve that corresponds to EOF1 was then analyzed. Firstly, it was correlated with the El Niño Modoki Index (EMI). The index is calculated as the area averaged sea surface temperature anomaly (SSTA) over 3 regions: (1) 165°E–140°W, 10°S–10°N, (2) 110°W–70°W, 15°S–5°N, and (3) 125°E–145°E, 10°S–20°N (see Ashok *et al* (2007) for more details). Over 1993–2013, we find a correlation of 0.7 between the temporal curve and the EMI index. If we consider only the time period between 1993 and 2008 (since from figure 3(b), we can observe deterioration between the two temporal curves after 2008), the correlation increases to 0.8. The correlations are all significant at the 95% confidence level. One possible reason for the deterioration of correlation after 2008 (correlation $= -0.2$) could be related to the occurrence of two extreme La Niña events (2007–2008 and 2010–2011). However this needs to be further investigated. Even though this mode represents only 6% of the total variance, it can have an impact on sea level trends. For example, the positive trend observed in the temporal curve between 2004 and 2008/2009 is related to the period of El Niño Modoki events (see figure 1 of Singh *et al* (2011)). As a result, during this time period, the central tropical Pacific experienced increased sea level rates.

On performing a power spectral analysis on the EOF1 temporal curve over 1993–2013, we obtain a periodicity of approximately 3 years. This corresponds to the periodicity of ENSO events that ranges between 3 and 8 years.

The presence of El Niño Modoki signal in the Alti-IPO residual indicates that there is in fact some ENSO-related (in specific El Niño Modoki until 2008) internal variability still remaining even after the removal of IPO.

3.1.2. Analysis of Alti-IPO-EMI residual signal

To further analyze the residual trend pattern, we then removed the El Niño Modoki contributed signal from the Alti-IPO residual signal (henceforth called Alti-IPO-EMI) by once again performing a linear regression of EMI on Alti-IPO. Figure 4 displays the sea level spatial trend pattern in the Pacific Ocean from observed altimetry without IPO and El Niño Modoki related internal variability. On comparison with Alti-

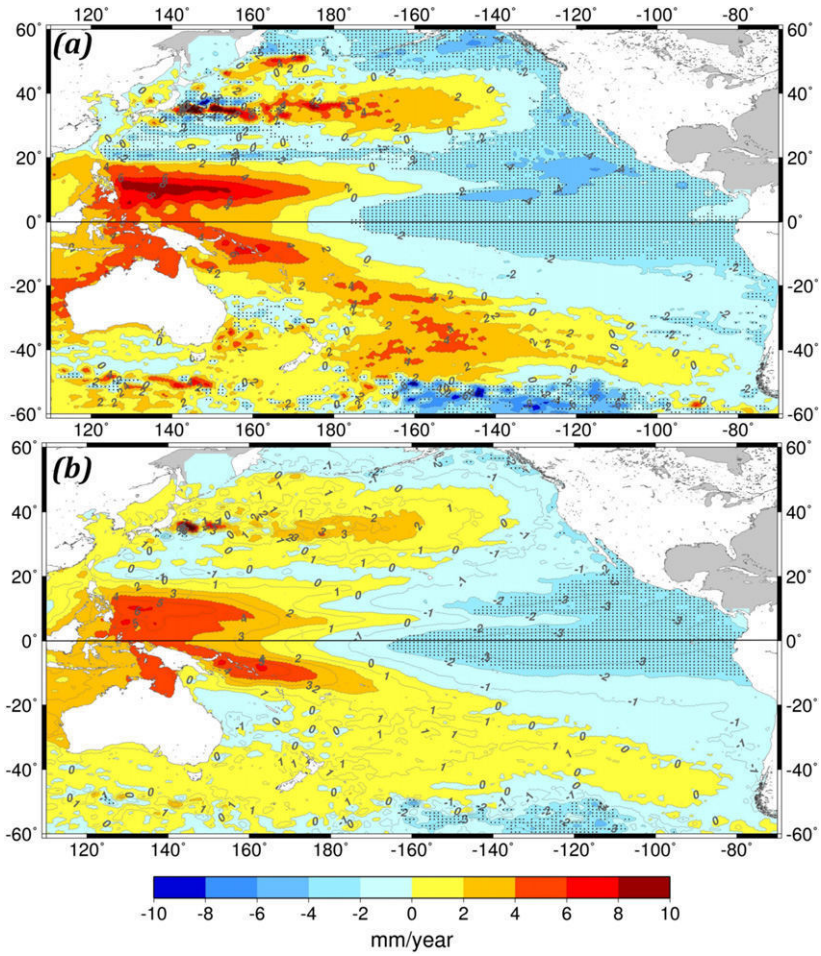

Figure 1. (a) Observed altimetry based sea level spatial trend pattern and (b) IPO contributed sea level spatial trend pattern (uniform global mean has been removed) in the Pacific Ocean over 1993–2013. Stippling indicates regions of non-significant trend (p-value $>$ 0.05).

IPO residual sea level trend pattern in figure 2(a), we can observe that the removal of the El Niño Modoki signal from Alti-IPO results only in a small decrease in magnitude of the residual sea level trend with no significant changes in the trend pattern. Furthermore, in figure 4, we can observe meridionally alternating positive and negative sea level trend patterns within 20°N and 20°S with mostly positive trend patterns at the equatorial band. These patterns suggest accumulation of a warm water volume in the equatorial band and a reduction in the north and south equatorial counter currents which all together are a reminiscent of a strong El Niño situation (Meinen and McPhaden 2000, Kessler and Taft 1987). However, since the trend patterns in this region are not significant, it is difficult to have a robust conclusion on this. An EOF analysis on the Alti-IPO-EMI sea level signal results in the first EOF mode closely resembling the eastern Pacific ENSO event in terms of spatial pattern (figure 5(a)) with the evident strong 1997/1998 El Niño event clearly visible in the temporal curve (figure 5(b)). The periodicity of the temporal curve is around 3–4 years and this once again corresponds to the ENSO periodicity.

All the above discussed results show that attempts to separate/remove both decadal and interannual climate modes from observed altimetry based sea level signal through the method of linear regression (as shown in this study) or the methodology of Hamlington *et al* (2014a) do not in fact totally eliminate the internal sea level variability. Some non-linear internal variability related to intense ENSO events such as the 1997/1998 El Niño still remains in the residual.

3.2. CMIP5 model based sea level spatial trend pattern and internal climate modes

3.2.1. Multi model ensemble (MME) and internal climate modes

As mentioned in section 2.3, performing a Multi Model Ensemble (MME) of the 21 CMIP5 models would in general average out/reduce sea level signal due to internal climate modes. The MME containing only the expected sea level response to external forcings (natural and anthropogenic) can then be compared with the Alti-IPO and Alti-IPO-EMI residual sea level trend patterns. If the sea level spatial trend pattern of MME is similar to that of the above mentioned two residual trend patterns, we can

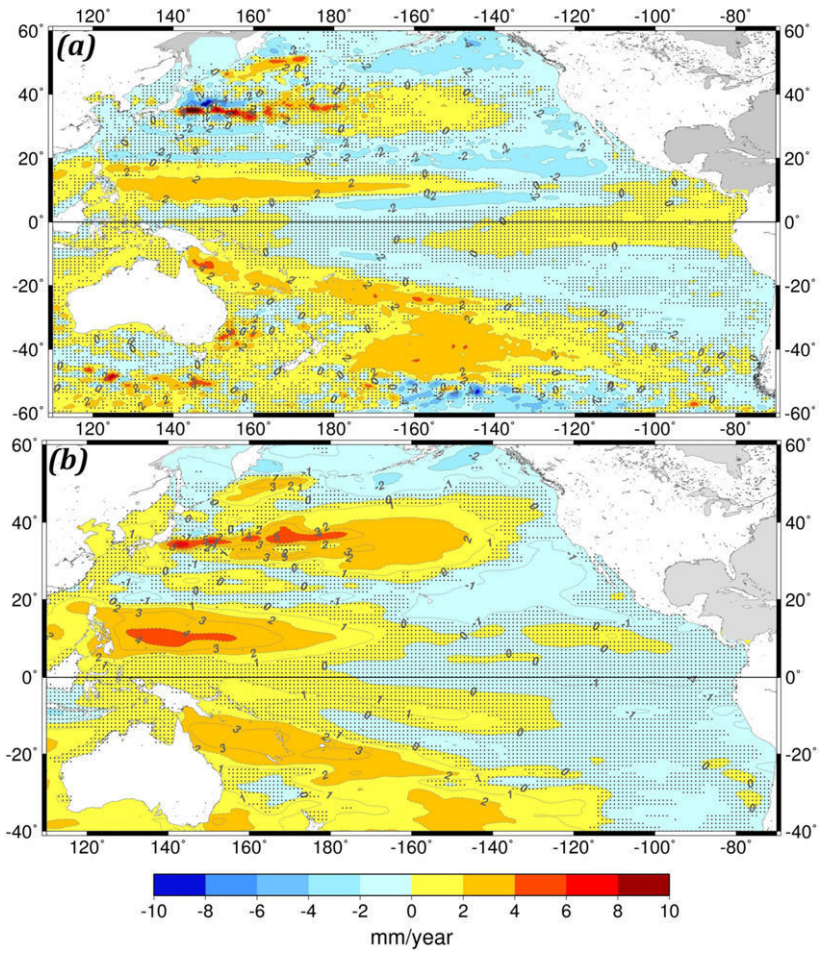

Figure 2. (a) Altimetry and (b) 2D reconstruction-based Pacific Ocean sea level spatial trend pattern without IPO over 1993–2013 (uniform global mean has been removed from both before performing the regression. In the case of 2D reconstruction, regression was performed over 1960–2013 and the result is plotted over 1993–2013). Stippling indicates regions of non-significant trend (p-value $>$ 0.05).

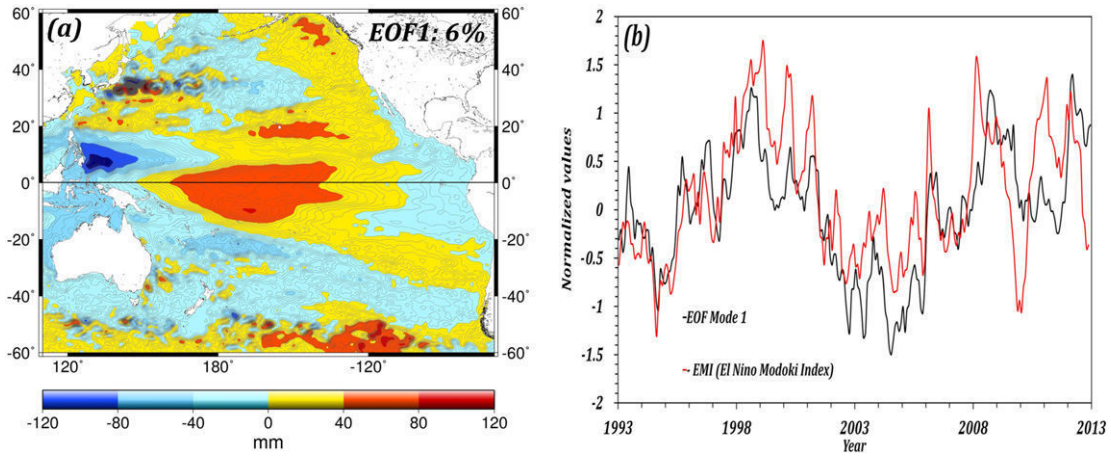

Figure 3. (a) Spatial pattern and (b) its corresponding time curve of the first EOF mode of Altimetry-IPO residual signal over 1993–2013. The EMI index is represented as the red curve.

conclude the presence of externally forced sea level signal in the Pacific Ocean over the 2 recent decades.

Before a direct comparison of the sea level trend patterns, the presence of any internal climate modes in the MME was first verified. EOF decomposition was performed on the MME-based sea level signal between 1900 and 2098, and the corresponding spatial and temporal patterns were studied. Even though the main

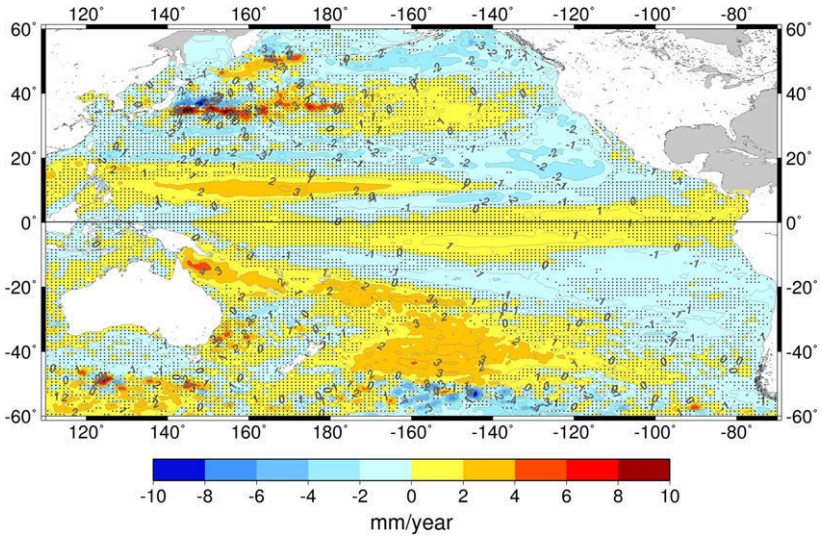

Figure 4. Altimetry based Pacific Ocean sea level spatial trend pattern without IPO and EMI contribution over 1993–2013. Stippling indicates regions of non-significant trend (p-value $>$ 0.05).

region of interest of our study is the Pacific Ocean, for this verification, we chose the global ocean. This would enable us to verify the effectiveness of MME in reducing the impact of internal climate modes not only in the Pacific but also in the other oceans. Furthermore, such verification would also give us an idea on regions where the impact of external forcing is the maximum and the structure of their corresponding spatial patterns.

Figure 6(a) and the black curve in figure 6(b) display the spatial pattern and temporal curve of the first EOF mode of the MME sea level with total variance of 96%. The second and third EOF modes contribute 3% and 1% of the total variance and do not exhibit any significant spatial patterns or temporal curves (not shown here). From figure 6(b), we can observe that the temporal curve is almost flat until 1970 after which there is an increase that continues over time implying an accelerated dynamic sea level change. Skeie *et al* (2011) (figure 1(a)) and Myhre *et al* (2013) (figure 8.18) have shown that the radiative forcing from CO_2 and other well-mixed greenhouse gases (WMGHG) has rapidly increased since the 1950s with the CO_2 emission being the largest contributor to the increased anthropogenic forcing since 1960s. These are in agreement with the time series in figure 6(b) showing an increased signal since 1970.

In terms of spatial pattern, this increase in sea level appears in the northern high latitudinal band between 70°N and 85°N, North Atlantic Ocean south of Greenland between 30°N and 60°N and also in the southern latitudinal band between 40°S and 45°S. Regions of positive sea level patterns also occur in the western extra-tropical Pacific Ocean between 30°N and 40°N and in western Indian and central Atlantic oceans. Region of negative sea level change appears in the Southern Ocean beyond the 50°S latitudinal band. This is in agreement with the results from Bilbao *et al* (2015). Performing the same EOF analysis only on the Pacific Ocean (boxed region in figure 6(a)), we obtain the same Pacific Ocean spatial pattern (with a variance of 93%) as in figure 6(a). The temporal curve that corresponds to the Pacific Ocean first EOF mode (blue curve in figure 6(b)) is very similar to that of the global EOF1 temporal curve. On close observation of both EOF1 temporal curves, we can also notice that while the global curve exhibits small amplitude oscillations, the curve corresponding to the Pacific Ocean exhibits higher amplitude oscillations throughout the time period. Presence of oscillations in both the curves which do not correspond to oscillations in the external forcing (due to volcanic forcing or solar forcing) indicates that performing the multi-model mean may not average out the entire signal that corresponds to internal variability and there may still remain some residual internal variability. Since, in general the internal variability exhibits stronger amplitude oscillations regionally than globally, even the residual of the Pacific Ocean internal variability obtained (blue curve in figure 6(b)) tends to be greater at regional scale.

In order to effectively obtain the temporal curve and spatial pattern that corresponds to external forcing only, we performed a spline smoothing (Ribes *et al* 2010) on the global EOF1 temporal curve to remove the small amplitude oscillations. The smoothed temporal curve (red dotted curve in figure 6(b) with an upward offset of 0.1 for clarity) is then regressed on to the CMIP5 MME sea level dataset and the sea level pattern that corresponds to the smoothed temporal curve is obtained. On calculating the variance, the CMIP5 MME sea level signal thus obtained after regression (hereafter called regressed CMIP5 MME) explains 97% of the total CMIP5 MME signal. The regressed CMIP5 MME sea level signal can

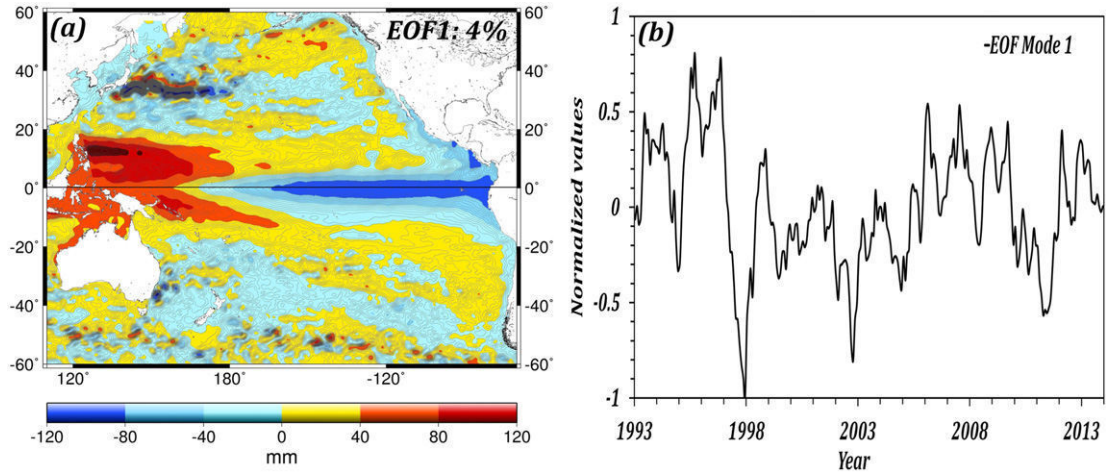

Figure 5. (a) Spatial pattern and (b) its corresponding time curve of the first EOF mode of Altimetry-IPO-EMI residual signal over 1993–2013.

now be considered to contain mainly externally forced sea level signal.

3.2.2. MME-based sea level spatial trend pattern over altimetry period

As mentioned in section 3.2.1, the regressed CMIP5 MME sea level signal that contains mainly externally forced signal can be compared with Alti-IPO and Alti-IPO-EMI residual sea level spatial trend patterns to verify if the two latter residual patterns are linked to external forcing. Figure 7 displays the regressed MME-based sea level spatial trend pattern in the Pacific Ocean between 1993 and 2013. Stippling indicates regions where the trends are insignificant (p-value $>$ 0.05). The externally forced sea level spatial trend pattern is positive in the north-west and south-west Pacific Ocean between the sub-tropical latitudes of 20°N–40°N and 20°S-40°S. In the north-west Pacific, the positive trend values are in the order between 0.2 mm yr^{-1} and 0.7 mm yr^{-1} while in the south-west the trend values range between 0.2 mm yr^{-1} and 1.6 mm yr^{-1}. Interestingly, from the Alti-IPO (figure 2(a)) and Alti-IPO-EMI (figure 4) residual patterns, we can clearly notice that in the western tropical Pacific, the residual sea level trend patterns are not comparable with the regressed CMIP5 MME based trend pattern in figure 7 (Note that the color scale is not the same as in figure 2(a) and 4). Contrary to the Alti-IPO and Alti-IPO-EMI trend patterns, the positive trend pattern that appears in the western tropical Pacific extending towards the east between 10°N to 20°N and 120°E to 120°W is only in the range of 0.1 mm yr^{-1} to 0.3 mm yr^{-1}. The absence of significantly high positive sea level trend in the western tropical Pacific over the altimetry era from the regressed CMIP5 MME based data shows that the residual trend patterns observed in the altimetry signal after having removed IPO and EMI contribution is not consistent with the CMIP5 MME based expected sea level response to external forcing. This once again suggests that the residual Alti-IPO/ Alti-IPO-EMI patterns cannot be attributed to anthropogenic signal. However in the Pacific Ocean east of the Australian continent between 20°S and 40°S latitudes, we can observe that the Alti-IPO and Alti-IPO-EMI trend patterns are consistent with that of the CMIP5 MME. This indicates the possible sea level response to external forcing in this region.

3.3. Discussion and conclusion

Several earlier studies (e.g. Zhang and Church 2012, McGregor *et al* 2007, Verdon and Franks 2006, Power *et al* 2006 Deser *et al* 2004, Mantua and Hare 2002) have tried to understand and explain the relation between ENSO and IPO/PDO. They have shown that PDO/IPO is essentially the low frequency residual of ENSO variability occurring at multi-decadal time scales. Furthermore, Verdon and Franks, (2006) have shown that an increased occurrence of El Nino events during positive phase of PDO/IPO whereas negative PDO/IPO triggers more La Niña events.

While the above mentioned studies have shown that PDO/IPO and ENSO are inter-related, several studies (e.g. Schneider and Cornuelle 2005, Pierce 2001) have also shown that the former is not a mode of variability linked only to ENSO but is a blend of several other phenomena like the zonal advection in the Kuroshio-Oyashio Extension, Aleutian low anomalies and others. All these studies lead us to question if attempts to remove the decadal natural climate mode (PDO/IPO, if assumed that they are adequately sampled using existing historical and observational records) from the sea level signal could also effectively remove all other internal natural climate modes.

In this study, we analyzed the observed altimetry based sea level spatial trend patterns in the Pacific Ocean after having removed IPO contribution through linear regression. On performing a simple

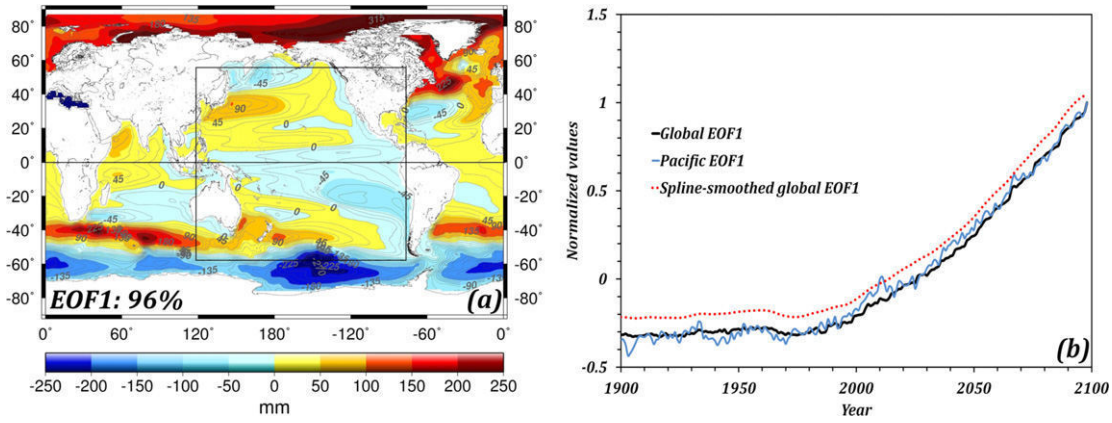

Figure 6. (a) Spatial pattern of the first EOF mode of CMIP5 MME sea level over 1900–2098; (b) its corresponding temporal curve (black curve). The red dotted curve corresponds to the spline-smoothed EOF1 temporal curve (with an upward offset of 0.1 for clarity) and the blue curve corresponds to the Pacific Ocean EOF1 temporal curve estimated over the boxed region in (a).

EOF analysis on the residual (Alti-IPO) sea level signal, we found the presence of ENSO-related El Nino Modoki (Central Pacific) signal in the residual. Further efforts to remove the El Niño Modoki signal from Alti-IPO signal through linear regression still resulted in the presence of Eastern Pacific ENSO signal in the residual. This indicates that linearly regressing IPO on observed sea level and removing its contribution does not totally remove the entire internal sea level variability. Nonlinear ENSO-related variability that does not linearly co-vary with IPO still remains in the residual sea level signal. Our results show that the methodology of removing the main decadal natural climate mode from sea level signal and analyzing the residual is not an effective way to explain the contribution of external anthropogenic sea level fingerprint.

The range of altimetry-based regional sea level trend uncertainties/error estimate should also be considered in these studies as the residual sea level trend pattern after removing IPO and ENSO contributions should be compared to the pattern of uncertainty. A detailed comparison is beyond the scope of this study as further investigations are needed to obtain accurate altimetry-based trend error patterns at regional scale. However we expect that the patterns of regional altimetry error do not coincide to those in figure 2(a) (Alti-IPO) and figure 4 (Alti-IPO-EMI) as the errors are mainly large spatial patterns at hemispherical scale in the order of 2 mm yr^{-1} to 3 mm yr^{-1} with orbital errors contributing the most (Ablain *et al* 2015, Couhert *et al* 2015).

Furthermore, regressed CMIP5 MME-based sea level spatial trend pattern in the tropical Pacific over the altimetry period do not display any positive sea level trend values that are comparable to the altimetry based sea level signal after having removed the contribution of the decadal natural climate mode. This suggests that the residual positive trend pattern observed in the western tropical Pacific is not externally forced and thereby not anthropogenic in origin. In addition the amplitude of the sea level spatial trend pattern from regressed CMIP5 MME is low over the altimetry period in the tropical Pacific. This amplitude is significantly lower than the expected error in trend patterns from satellite altimetry (in the order of 2 mm yr^{-1} to 3 mm yr^{-1}, Ablain *et al* 2015, Couhert *et al* 2015) and suggest that satellite altimetry measurement is still not accurate enough to detect the anthropogenic signal in the 20 year tropical Pacific sea level trends.

Our results are also in agreement with studies of Richter and Marzeion (2014), Lyu *et al* (2014), Jordà (2014), Frankcombe *et al* (2014), Bilbao *et al* (2015) who have shown that in regions of high internal variability, the trend due to externally forced signal is masked during longer time spans than in regions of low internal variability. This is the case of tropical Pacific which is a region highly impacted by internal variability. Studying the residual sea level signal after separating/removing the internal climate modes over a short time period of 20 years in this region may not yield significant results with respect to external forcing. This is also in agreement with Meyssignac *et al* (2012b) who have shown that over the 17 years altimetry period, the tropical Pacific observed sea level spatial trend pattern is mainly due to internal variability.

Our study suggests that detection/attribution studies should be focused on other regions such as Northern and Southern Oceans, North Atlantic, Southern Pacific to the east of Australia. Based on CMIP5 MME (see figures 6 and 7), these are the regions that show significant externally forced sea level signals. Detailed studies on these regions could help us understand the role of externally forced signal on sea level.

Lastly, another important factor to consider would be the impact of external anthropogenic forcing on the natural internal climate modes. In the previous studies (Hamlington *et al* 2014b, Palanisamy *et al* 2015) and this current study, it has been assumed that the natural

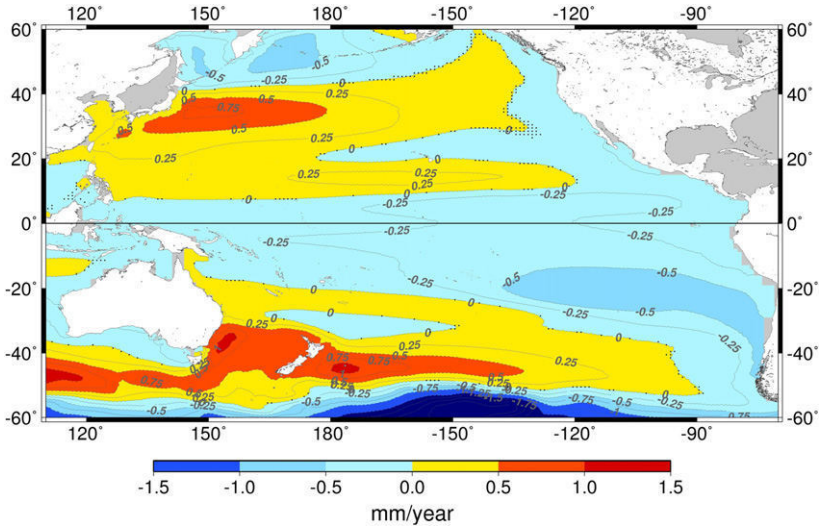

Figure 7. Pacific Ocean sea level spatial trend pattern estimated from regressed CMIP5 MME sea level data over 1993–2013. Stippling indicates regions of non-significant trend (p-value $>$ 0.05).

internal climate mode is independent of the external anthropogenic forcing. Attempts have then been made to separate/remove the internal climate mode from the sea level signal and attribute the residual to be anthropogenic in origin. However it should not be forgotten that the anthropogenic global warming signal may not only appear as a constant increasing pattern in response to greenhouse gas emissions (as seen in figure 6(b)) but could also change the behavior of the internal climate modes. Recently, using CMIP5 models, Dong *et al* (2014) have shown that in the twentieth century, the Pacific Decadal Variability is not only dominated by internal variability but also significantly affected by external forcing (combined effects of greenhouse gases and anthropogenic aerosols). While the greenhouse gas forcing induces strong surface downward shortwave radiation over the tropical Pacific resulting in stronger warming, the anthropogenic aerosol forcing induces stronger cooling in the North Pacific due to reduced surface downward shortwave radiation (Dong *et al* 2014). Furthermore, in terms of ENSO events, studies such as Cai *et al* (2015), Cai *et al* (2014), Power *et al* (2013 and references therein) have shown an increase in the frequency of extreme El Niño and La Niña events occurring due to increasing greenhouse warming while Yeh *et al* (2009) show an increase in El Niño Modoki events. Though possibly model dependent, all the above mentioned studies show the role of external anthropogenic forcing on internal climate modes. Therefore by removing/separating the internal climate mode from sea level signal, it is highly probable that we also remove a part of (if not all) the external anthropogenic forcing.

This also indicates that we cannot totally deny the role of external forcing in the western tropical Pacific sea level changes over the two recent decades. Indeed the recent sea level intensification in this region could be a result of very high internal variability driven by intensified trade winds which could have partly been driven by the anthropogenic forcing itself (e.g. England *et al* 2014). Therefore in future, it is important to first understand how anthropogenic forcing can impact the mechanisms that drive the internal climate modes.

Acknowledgments

We thank Dr Aurelien Ribes for his useful suggestions on CMIP5 models analysis. We also thank the anonymous reviewers for their comments and suggestions. We acknowledge AVISO for making available the satellite altimetry sea level product. We also acknowledge the World Climate Research Programme's Working Group on Coupled Modelling, which is responsible for CMIP5 and we thank the climate modeling groups for producing and making available their model output. Support for CMIP5 is provided by the US Department of Energy. H Palanisamy is supported by a CNES/CLS PhD grant.

References

Ablain M *et al* 2015 Improved sea level record over the satellite altimetry era (1993–2010) from the climate change initiative project *Ocean Sci* **11** 67–82

Ablain M, Cazenave A, Valladeau G and Guinehut S 2009 A new assessment of the error budget of global mean sea level rate estimated by satellite altimetry over 1993–2008 *Ocean Sci.* **5** 193–201

Ashok K, Behera S K, Rao S A, Weng H and Yamagata T 2007 El Niño Modoki and its possible teleconnection *J. Geophys. Res. Oceans* **112** C11007

Balmaseda M A, Mogensen K and Weaver A T 2013 Evaluation of the ECMWF ocean reanalysis system ORAS4 *Q. J. R. Meteorol. Soc.* **139** 1132–61

Bilbao R A F, Gregory J M and Bouttes N 2015 Analysis of the regional pattern of sea level change due to ocean dynamics

and density change for 1993–2099 in observations and CMIP5 AOGCMs *Clim. Dyn.* 1–20
Bordbar M H, Martin T, Latif M and Park W 2015 Effects of long-term variability on projections of twenty-first century dynamic sea level *Nat. Clim. Change* **5** 343–7
Bosc C and Delcroix T 2008 Observed equatorial Rossby waves and ENSO-related warm water volume changes in the equatorial Pacific Ocean *J. Geophys. Res. Oceans* **113** C06003
Bromirski P D, Miller A J, Flick R E and Auad G 2011 Dynamical suppression of sea level rise along the Pacific coast of North America: indications for imminent acceleration *J. Geophys. Res. Oceans* **116** C07005
Cai W *et al* 2014 Increasing frequency of extreme El Nino events due to greenhouse warming *Nat. Clim. Change* **4** 111–6
Cai W *et al* 2015 Increased frequency of extreme La Nina events under greenhouse warming *Nat. Clim. Change* **5** 132–7
Carton J A and Giese B S 2008 A reanalysis of ocean climate using simple ocean data assimilation (SODA) *Mon. Weather Rev.* **136** 2999–3017
Cazenave A and Cozannet G L 2014 Sea level rise and its coastal impacts *Earths Future* **2** 15–34
Church J A *et al* 2013 Sea level change *Climate Change 2013: The Physical Science Basis. Contribution of Working Group I to the Fifth Assessment Report of the Intergovernmental Panel on Climate Change* ed T F Stocker, D Qin, G-K Plattner, M Tignor, S K Allen, J Boschung, A Nauels, Y Xia, V Bex and P M Midgley (Cambridge, United Kingdom:: Cambridge University Press)
Couhert A, Cerri L, Legeais J-F, Ablain M, Zelensky N P, Haines B J, Lemoine F G, Bertiger W I, Desai S D and Otten M 2015 Towards the 1 mm/y stability of the radial orbit error at regional scales *Adv. Space Res.* **55** 2–23
Deser C, Phillips A S and Hurrell J W 2004 Pacific interdecadal climate variability: linkages between the tropics and the north pacific during boreal winter since 1900 *J. Clim.*, **17** 3109–24
Dong L, Zhou T and Chen X 2014 Changes of Pacific decadal variability in the twentieth century driven by internal variability, greenhouse gases, and aerosols *Geophys. Res. Lett.* **41** 8570–7
England M H, McGregor S, Spence P, Meehl G A, Timmermann A, Cai W, Gupta A S, McPhaden M J, Purich A and Santoso A 2014 Recent intensification of wind-driven circulation in the Pacific and the ongoing warming hiatus *Nat. Clim. Change* **4** 222–7
Folland C K, Parker D E, Colman A and Washington R 1999 Large scale modes of ocean surface temperature since the late nineteenth century Refereed book: ch 4, pp 73–102 *of Beyond El Nino: Decadal and Interdecadal Climate Variability* ed A Navarra (Berlin: Springer)
Frankcombe L M, McGregor S and England M H 2014 Robustness of the modes of Indo-Pacific sea level variability *Clim. Dyn.* 1–18 doi:10.1007/s00382-014-2377-0
Fukumori I and Wang O 2013 Origins of heat and freshwater anomalies underlying regional decadal sea level trends *Geophys. Res. Lett.* **40** 563–7
Gregory J M *et al* 2001 Comparison of results from several AOGCMs for global and regional sea-level change 1900–2100 *Clim. Dyn.* **18** 225–40
Hamlington B D, Strassburg M W, Leben R R, Han W, Nerem R S and Kim K-Y 2014a Uncovering an anthropogenic sea-level rise signal in the Pacific Ocean *Nat. Clim. Change* **4** 782–5
Hamlington B D, Leben R R, Strassburg M W and Kim K-Y 2014b Cyclostationary empirical orthogonal function sea-level reconstruction *Geosci. Data J.* **1** 13–9
Han W *et al* 2013 Intensification of decadal and multi-decadal sea level variability in the western tropical Pacific during recent decades *Clim. Dyn.* 1–23 doi:10.1007/s00382-013-1951-1
Hare S R and Mantua N J 2000 Empirical evidence for North Pacific regime shifts in 1977 and 1989 *Prog. Oceanogr.* **47** 103–45
IPCC 2013 *Climate Change 2013: The Physical Science Basis. Contribution of Working Group I to the Fifth Assessment Report of the Intergovernmental Panel on Climate Change* ed T F Stocker, D Qin, G-K Plattner, M Tignor, S K Allen, J Boschung, A Nauels, Y Xia, V Bex and P M Midgley (Cambridge, United Kingdom: Cambridge University Press) 1535 doi:10.1017/CBO9781107415324
Jordà G 2014 Detection time for global and regional sea level trends and accelerations *J. Geophys. Res. Oceans* **119** 7164–74
Kessler W S and Taft B A 1987 Dynamic heights and zonal geostrophic transports in the central tropical Pacific during 1979-84 *J. Phys. Oceanogr.* **17** 97–122
Köhl A 2015 Evaluation of the GECCO2 ocean synthesis: transports of volume, heat and freshwater in the Atlantic *Q. J. R. Meteorol. Soc.* **141** 166–81
Landerer F W, Gleckler P J and Lee T 2014 Evaluation of CMIP5 dynamic sea surface height multi-model simulations against satellite observations , *Clim. Dyn.* **43** 1271–83
Levitus S *et al* 2012 World ocean heat content and thermosteric sea level change (0–2000 m), 1955–2010 *Geophys. Res. Lett.* **39** L10603
Lyu K, Zhang X, Church J A, Slangen A B A and Hu J 2014 Time of emergence for regional sea-level change *Nat. Clim. Change* **4** 1006–10
Mantua N J and Hare S R 2002 The pacific decadal oscillation *J. Oceanogr.* **58** 35–44
Mantua N J, Hare S R, Zhang Y, Wallace J M and Francis R C 1997 A Pacific interdecadal climate oscillation with impacts on salmon production *Bull. Am. Meteorol. Soc.* **78** 1069–79
Marcos M and Amores A 2014 Quantifying anthropogenic and natural contributions to thermosteric sea level rise *Geophys. Res. Lett.* **41** 2014GL059766
McGregor S, Holbrook N J and Power S B 2007 Interdecadal sea surface temperature variability in the equatorial pacific ocean: I. the role of off-equatorial wind stresses and oceanic rossby waves *J. Clim.* **20** 2643–58
Meinen C S and McPhaden M J 2000 Observations of warm water volume changes in the equatorial pacific and their relationship to El Niño and La Niña *J. Clim.* **13** 3551–9
Merrifield M A 2011 A shift in western tropical Pacific Sea level trends during the 1990s *J. Clim.* **24** 4126–38
Merrifield M A and Maltrud M E 2011 Regional sea level trends due to a Pacific trade wind intensification *Geophys. Res. Lett.* **38** L21605
Meyssignac B, Henry O, Palanisamy H and Cazenave A 2015 Advances in understanding regional sea level variations from 2D sea level reconstructions based on tide gauge records, in preparation
Meyssignac B, Becker M, Llovel W and Cazenave A 2012a An assessment of two-dimensional past sea level reconstructions over 1950–2009 based on tide-gauge data and different input sea level grids *Surv. Geophys.* **33** 945–72
Meyssignac B, Salas y Melia D, Becker M, Llovel W and Cazenave A 2012b Tropical Pacific spatial trend patterns in observed sea level: internal variability and/or anthropogenic signature? *Clim. Past* **8** 787–802
Milne G A, Gehrels W R, Hughes C W and Tamisiea M E 2009 Identifying the causes of sea-level change *Nat. Geosci.* **2** 471–8
Myhre G *et al* 2013 Anthropogenic and natural radiative forcing *Climate Change 2013: The Physical Science Basis. Contribution of Working Group I to the Fifth Assessment Report of the Intergovernmental Panel on Climate Change* ed T F Stocker, D Qin, G-K Plattner, M Tignor, S K Allen, J Boschung, A Nauels, Y Xia, V Bex and P M Midgley (Cambridge, United Kingdom: Cambridge University Press)
Palanisamy H, Cazenave A, Delcroix T and Meyssignac B 2015 Spatial trend patterns in the Pacific Ocean sea level during the altimetry era: the contribution of thermocline depth change and internal climate variability *Ocean Dyn.* **65** 341–56
Pierce D W 2001 Distinguishing coupled ocean-atmosphere interactions from background noise in the North Pacific *Prog. Oceanogr.* **49** 331–52
Power S, Delage F, Chung C, Kociuba G and Keay K 2013 Robust twenty-first-century projections of El Nino and related precipitation variability *Nature* **502** 541–5

Power S, Haylock M, Colman R and Wang X 2006 The predictability of interdecadal changes in ENSO activity and ENSO teleconnections *J. Clim.* **19** 4755–71

Ribes A, Azaïs J-M and Planton S 2010 A method for regional climate change detection using smooth temporal patterns *Clim. Dyn.* **35** 391–406

Richter K and Marzeion B 2014 Earliest local emergence of forced dynamic and steric sea-level trends in climate models *Environ. Res. Lett.* **9** 114009

Schneider N and Cornuelle B D 2005 The forcing of the pacific decadal oscillation* *J. Clim.* **18** 4355–73

Sen Gupta L C, Muir J N, Brown S J, Phipps P J, Durack D, Monselesan and Wijffels S E 2012 Climate drift in the CMIP3 models *J. Clim.* **25** 4621–40

Singh A, Delcroix T and Cravatte S 2011 Contrasting the flavors of El NINO-SOUTHERN OSCILLATION USINg sea surface salinity observations *J. Geophys. Res.* **116** 1–16

Skeie R B, Berntsen T K, Myhre G, Tanaka K, Kvalevåg M M and Hoyle C R 2011 Anthropogenic radiative forcing time series from pre-industrial times until 2010 *Atmos Chem Phys.* **11** 11827–57

Slangen A B A, Church J A, Zhang X and Monselesan D 2014 Detection and attribution of global mean thermosteric sea level change *Geophys. Res. Lett.* **41** 5951–9

Stammer D, Cazenave A, Ponte R M and Tamisiea M E 2013 Causes for contemporary regional sea level changes *Annu. Rev. Mar. Sci.* **5** 21–46

Taylor K E, Stouffer R J and Meehl G A 2012 An overview of CMIP5 and the experiment design *Bull. Am. Meteorol. Soc.* **93** 485–98

Thompson P R, Merrifield M A, Wells J R and Chang C M 2014 Wind-driven coastal sea level variability in the northeast pacific *J. Clim.* **27** 4733–51

Verdon D C and Franks S W 2006 Long-term behaviour of ENSO: Interactions with the PDO over the past 400 years inferred from paleoclimate records *Geophys. Res. Lett.* **33** L06712

Watson C S, White N J, Church J A, King M A, Burgette R J and Legresy B 2015 Unabated global mean sea-level rise over the satellite altimeter era *Nat. Clim. Change* **5** 565–8

Wittenberg A T 2009 Are historical records sufficient to constrain ENSO simulations? *Geophys. Res. Lett.* **36** L12702

Yasunaka S and Hanawa K 2003 Regime shifts in the northern hemisphere SST field: revisited in relation to tropical variations *J. Meteorol. Soc. Jpn. Ser II* **81** 415–24

Yeh S-W, Kug J-S, Dewitte B, Kwon M-H, Kirtman B P and Jin F-F 2009 El Niño in a changing climate *Nature* **461** 511–4

Yin J 2012 Century to multi-century sea level rise projections from CMIP5 models *Geophys. Res. Lett.* **39** 17709

Yin J, Griffies S M and Stouffer R J 2010 Spatial variability of sea level rise in twenty-first century projections *J. Clim.* **23** 4585–607

Zhang X and Church J A 2012 Sea level trends, interannual and decadal variability in the Pacific Ocean *Geophys. Res. Lett.* **39**

Zhang Y, Wallace J M and Battisti D S 1997 ENSO-like interdecadal variability: 1900–93 *J. Clim.* **10** 1004–20

4.5 Role of external anthropogenic forcing on internal climate modes – A synthesis

From our results we have shown that it is not yet possible to detect anthropogenic sea level fingerprint in the tropical Pacific, a region known for high internal variability. This is also in agreement with *Meyssignac et al.*, (2012b) who have shown that over 17 years of altimetry period, the tropical Pacific observed sea level spatial trend pattern is mainly due to internal variability. Furthermore, studies of *Richter and Marzeion*, (2014), *Lyu et al.*, (2014), *Jordà*, (2014), *Frankcombe et al.*, (2014*)*, *Bilbao et al.*, (2015) have also shown that in regions of high internal variability, the trend due to externally forced signal is masked during longer time spans than in regions of low internal variability.

Another most important factor that needs to be considered in D&A studies is the role of external anthropogenic forcing on internal climate modes. So far, most of the D&A studies have assumed that the natural internal climate mode is independent of the external anthropogenic forcing. Attempts have then been made to separate/remove the internal climate mode from the sea level signal and attribute the residual to be anthropogenic in origin. However it should not be forgotten that the anthropogenic global warming signal may not only appear as a constant increasing pattern in response to greenhouse gas emissions but could also change the behavior of the internal climate modes (*Palanisamy et al.*, 2015c). Considering this into account, some recent studies have shown that the external anthropogenic forcing in fact has an impact on driving/ changing the behavior of different internal climate modes. Using CMIP5 models, *Dong et al.*, (2014) have shown that in the twentieth century, the Pacific decadal variability is not only dominated by internal variability but also significantly affected by external. Furthermore, in terms of ENSO events, studies such as *Cai et al.*, (2014), *Cai et al.*, (2015), *Power et al.*, (2013 and references therein) have shown an increase in the frequency of extreme El Niño and La Niña events occurring due to increasing greenhouse warming while *Yeh et al.*, (2009) show an increase in El Niño Modoki events. Though possibly model dependent, all the above mentioned studies show the possible role of external anthropogenic forcing on internal climate modes (*Palanisamy et al.*, 2015c). This also indicates that the role of external forcing cannot be completely denied in the case of western tropical Pacific sea level changes over the two recent

decades. Indeed the recent sea level intensification in this region could be a result of very high internal variability driven by intensified trade winds which could have partly been driven by the anthropogenic forcing itself (e.g. *England et al.*, 2014).

4.6 Internal climate variability uncertainty in CMIP5 models

Since several years, it has been a common practice for climate change and sea level community to use CMIP3/CMIP5 models not only for D&A studies but also for the projection of future sea level changes. Therefore, characterizing and quantifying uncertainties in these climate models is of fundamental importance for such studies. There are three main uncertainties in climate models: (1) model uncertainty which arises because of an incomplete understanding of the physical processes and the limitations of implementation of the understanding, (2) scenario uncertainty arising because of incomplete information about future emissions and (3) internal variability modelling uncertainty that arises because the complex processes intrinsic to the atmosphere, ocean and the ocean-atmosphere coupling are highly aleatoric and cannot be easily modelled (*Yip et al.*, 2011, *Deser et al.*, 2010, *Hawkins and Sutton*, 2009). While the influence of these uncertainties are largely variable, internal variability uncertainty plays an important role in D&A studies as the main objective of such studies are to separate the signal (i.e. anthropogenic forcing) from the noise (i.e. internal variability).

Of late, there have been few studies that have focused on the role of internal variability uncertainty in future sea level changes. By making use of a 40 member ensemble of the Community Climate System Model version 3 (CCSM3), *Hu and Deser*, (2013) isolated uncertainty in 2000-2060 regional sea level trends. They concluded that the uncertainty in the projected trends were mainly due to unpredictable internal climate fluctuations that can vary by a factor of two depending on the region, with coastal areas bordering the North Pacific and Atlantic showing the greatest range. More recently, *Bordbar et al.*, (2015) demonstrated that in the case of centennial regional dynamic sea level projections, uncertainty in long term internal variability plays as great a part as external forcing. Furthermore, the study also mentions that the lack of long term observations poses a challenge in quantifying the long term internal variability thereby adding on to the uncertainty. Subsequently, *Carson et al.*, 2014 have also shown that internal variability can be a substantial portion of the model spread for both short and long-term

regional sea level projections. *Little et al.*, (2015), in a very detailed and exhaustive work partitioned the different sources of uncertainty over two projection periods, 2040 and 2090 using different RCP scenarios and various models of CMIP5 archive. They concluded that the three sources of uncertainty play a role in future sea level projection. The internal variability uncertainty was attributed to differences in the representation of internal variability among the various CMIP5 models. They further stress the importance of characterization of internal variability along two fronts: 1) developing alternate techniques to capture the representation of internal variability in models and 2) model–data comparison aimed at determining whether model-based methods capture observed modes of sea level variability, particularly those relevant to long-term climate changes.

As a work in progress, we are currently studying the capability of CMIP5 models on capturing 'realistic' decadal climate variability. As the study is not yet completed, we therefore do not include it in this Ph.D. manuscript.

Conclusion and perspectives

There is no doubt that global warming will continue during the future decades owing to continuous GHG emissions, the main contributor to anthropogenic global warming. An important consequence of global warming and thereby climate change over the next few decades is sea level rise and its impacts. Theoretical estimations of sea level projections in the future are regularly being proposed by climate scientists based on different scenarios of global mean temperature rise in response to increasing GHG concentration. All the scenarios correspond to an increase in global mean sea level during the 21st century and beyond because of expected continuing ocean warming and land ice loss. Using climate models, for the high emission scenario (RCP8.5) that can also be considered as a representative extrapolation of the present day emission, IPCC AR5 now predicts the likely range of global mean sea level rise between 52cm and 98cm by the year 2100 with a median value of 74 cm. This would threaten the survival of several coastal cities and entire low-lying island nations. Even with aggressive emissions reductions, for the RCP2.6 scenario (peak in global annual GHG emissions between 2010-2020 followed by a substantial decline thereafter), a rise of 28-61 cm by 2100 is predicted indicating that even under the highly optimistic scenario we might see over half a meter of sea-level rise. In all scenarios, thermal expansion is predicted to be the largest contributor accounting for about 30 to 55% of the projections. Glaciers are the next largest, accounting for 15-35% of the projections. By 2100, 35 to 85% of the present volume of glaciers outside Antarctica is projected to be eliminated under RCP8.5 scenario (*Church et al.,* 2013).

Despite these recent updates, uncertainties in sea level projections remain very large (±25 cm in the case of global mean sea level). They come from the difficulty of climate models to precisely simulate the global mean sea level contributors (ocean thermal expansion, melting of glaciers and polar ice sheets, and land water storage) in a realistic manner. While this is the case for future sea level projections, uncertainty in different sea level contributors also play an

important role in the present sea level changes especially in understanding thermal expansion contribution from the deep ocean and/or the precise role of internal climate modes. During the course of the thesis, attempts were made to close the global mean sea level budget and estimate the deep ocean contribution by using sea level observations from satellite altimetry, GRACE based ocean mass changes and Argo-based ocean thermal expansion since 2003. We showed that uncertainties due to data processing approaches and systematic errors of different observing systems still prevent us from obtaining accurate results. Absence of observations in certain regions further adds on to the uncertainty thereby complicating accurate estimations. Our work emphasized the importance of systematic inter-comparisons of observational products in order to better understand the causes of the differences. This would further result in a better understanding of various global mean sea level rise contributors that can be applied for future projections.

In this thesis, we were particularly interested in regional sea level trends and variability and have put in evidence the importance of regional sea level changes by a better estimate of its signal since 1950 in different vulnerable regions. Our results showed that sea level variations are not uniform globally and that they are highly dominated by regional variability at both interannual and decadal time scales. Estimates of local long-term total relative sea level change further demonstrated the importance of not only regional sea level variability but also the role of vertical land motion, in particular land subsidence that exacerbates the sea level rise impact leading us to question sea level risks in the future. The results obtained during the course of the thesis indicate the importance of regional sea level change estimation for better coastal management for the present and in future. The IPCC AR5 projections indicate stronger regional sea level variability than at present by the end of 2100 largely dominated by increased heat uptake and changes in wind forcing. The IPCC AR5 sea level projections towards the end of 21st century from CMIP5 models reveal a clear regional pattern in dynamic sea level change with largest sea level rise in the North Atlantic, Arctic and in the tropical oceans. In terms of regional relative sea level change, CMIP5 model estimates resulting from GIA, glacier and land-ice melting during 2081-2100 relative to 1986-2000 suggest that for the 21st century, past, present and future loss of land-ice mass will very likely be an important contributor to spatial patterns in relative sea level change, leading to rates of maximum rise at low-to-mid latitudes. It is very likely that over about 75% of world oceans, regional relative sea level rise will be positive, while

most regions that will experience sea level fall are located near current and former glaciers and ice sheets (*Church et al.,* 2013).

Regions showing enhanced relative sea level changes towards the end of 21st century from CMIP5 estimates also coincide with those showing the largest uncertainty indicating strong differences in between different climate models. Sea level contribution due to Earth's visco-elastic response strongly depends on the magnitude of the melting ice which highly differs from one model to another. In addition, climate models poorly simulate land water storage due to groundwater depletion in aquifers. Therefore, uncertainty hinders accurate projections of regional relative sea level changes. Knowing the importance of regional relative sea level changes emphasized in this thesis and in other studies, if we want a better estimation of sea level rise impacts and risks in 2100, it is crucial to reduce uncertainty in assessing, understanding and modelling of regional relative sea level rise and variability.

Another main focus of this thesis was to analyze respective roles of ocean dynamic processes, internal climate modes and external anthropogenic forcing on regional sea level spatial trend patterns in the tropical Pacific Ocean over the altimetry observational era. Building up on the relationship between thermocline and sea level in the tropical region, we showed that most of the observed sea level spatial trend pattern in the tropical Pacific can be explained by the wind driven vertical thermocline movement. By performing detection and attribution study on sea level spatial trend patterns in the tropical Pacific and attempting to eliminate signal corresponding to the main internal climate mode, we further showed that the remaining residual sea level trend pattern does not correspond to externally forced anthropogenic sea level signal and that some non-linear internal climate modes still remain as residual. In addition, the amplitude of the residual trend pattern is significantly lower than the expected error in trend patterns from satellite altimetry (in the order of 2 mm/yr to 3 mm/yr) and therefore suggests that satellite altimetry measurement is still not accurate enough to detect the anthropogenic signal in the 20 year tropical Pacific sea level trends.

While the thesis has helped in answering sea level-related questions and in having a better understanding of regional sea level variability, there are numerous subjects that still need to be addressed in the near future. Few of the subjects that will be studied by the sea level team of LEGOS are listed below:

- Cross validation of ESA CCI ECVs involved in the sea level budget.

In the context of ESA CCI, this work will involve inter-comparisons of various observational products of altimetry sea level, ocean mass and steric sea level in order to better understand existing differences in sea level closure budget studies and identify a best processing methodology that can be implemented to minimize the differences. Furthermore, statistical approaches will be developed to identify best combination from among different set of components that will enable the closure of global mean sea level budget with accurate estimations of each of its contributing components. Similar studies will also be performed at regional scale.

- Validation of CMIP5 climate models based on their ability to characterize decadal internal climate variability.

This study will involve model–data comparison aimed at determining whether CMIP5 model-based methods capture observed modes of sea level variability, particularly those relevant to long-term climate changes over the 20th century. Various OGCMs and ocean reanalyses such as DRAKKAR, SODA, GECCO, ORAS4 and two dimensional past sea level reconstructions will be used in this study along with 21 CMIP5 based climate models. Regional patterns of decadal sea level variability estimated from ocean models and reanalyses since 1950 will be compared with those from CMIP5 based control run and historical simulations. The ultimate aim of this work will be to select climate models that realistically reproduce observed long term sea level variability which can later be used for regional sea level projections. This is currently an ongoing work and preliminary results are already interesting.

- Projections of 21st sea level rise using CMIP5 climate models under different warming scenarios.

It is intended to develop sea level projections until 2100 at various coastal locations by making use of the CMIP5 climate models under different warming scenarios validated in the above mentioned previous study. While CMIP5 climate models mainly represent the steric sea level component, collaborations with other scientific community will help in obtaining land ice melt (glaciers and ice sheets) contribution which will then be included along with the steric contribution from CMIP5 models. Furthermore, sea level variations due to post glacial rebound (GIA) and other solid Earth response to ice/water mass redistribution caused by future land ice

melt will also be considered. Sea level changes thus computed from CMIP5 models over 1950 to present will be compared with observations such as tide gauges and GPS for relative sea level variations and vertical land motions, satellite altimetry for absolute sea level variations. This will allow us to calibrate the CMIP5 models to obtain future sea level projections at various vulnerable regions.

Conclusion générale (en français)

Il ne fait aucun doute que le réchauffement climatique se poursuivra pendant les décennies à venir en raison des émissions de gaz à effet de serre, le principal contributeur au réchauffement climatique anthropique. Une conséquence importante du réchauffement de la planète actuel et futur est l'élévation du niveau de la mer et ses impacts. Des estimations théoriques de projections du niveau de la mer dans le futur sont régulièrement proposées par les scientifiques en fonction de différents scénarios d'augmentation des gaz à effet de serre. Quel que soit le scénario, du plus optimiste au plus pessimiste, donne lieu à une augmentation du niveau moyen de la mer au cours du 21e siècle et même au-delà en raison de la poursuite attendue du réchauffement de l'océan et de la perte de masse des calottes polaires et des glaciers. En utilisant des modèles climatiques, pour le scénario d'émission élevée (RCP8.5), le 5ème rapport du GIEC prédit désormais une élévation moyenne globale du niveau de la mer comprise entre 52 cm et 98 cm à l'horizon 2100, avec une valeur médiane de 74cm. De telles valeurs menaceraient de nombreuses villes côtières et les nations insulaires de faible altitude. Même avec les réductions d'émissions agressives, comme pour le scénario RCP2.6, une hausse de 28-61 cm d'ici 2100 est prévue, indiquant que même dans ce scénario très optimiste, nous pourrions voir plus de un demi-mètre d'élévation du niveau de la mer. Dans tous les scénarios, la contribution de l'expansion thermique de l'océan à la hausse future de la mer domine, dans une proportion de 30 à 55%. La seconde contribution provient des glaciers (pour 15 à 35%). On estime qu'en 2100, 35 à 85% des glaciers hors de l'Antarctique pourraient avoir disparu dans le cas du scénario RCP8.5 (*Church et al.,* 2013).

En dépit des mises à jour récentes, les incertitudes sur les projections future du niveau de la mer restent très importantes (± 25 cm dans le cas de niveau moyen global). Celle-ci provient des imperfections des modèles climatiques et leur inaptitude à simuler précisément et de façon réaliste les différentes contributions à la hausse future de la mer. Pour les variations actuelles de

la mer, l'incertitude sur les différentes composantes joue également un rôle important, en particulier dans la compréhension de la contribution de l'expansion thermique de l'océan profond et /ou le rôle précis de modes climatiques internes. Au cours de ma thèse, des tentatives ont été faites pour fermer le bilan du niveau moyen de la mer et estimer la contribution de l'océan profond utilisant des observations issues de l'altimétrie satellitaire (missions altimétrique Jason-1, Jason-2 et Envisat), de la mission GRACE, et des profils de température et salinité de l'océan par les flotteurs Argo depuis 2003. Nous avons montré que les incertitudes dues au traitement des données et aux erreurs systématiques des différents systèmes d'observation nous empêchent encore d'obtenir des résultats précis sur cette contribution. L'absence d'observations dans certaines régions océaniques ajoute encore de l'incertitude, ce qui empêche d'obtenir des estimations précises des différents termes du bilan. Notre travail a souligné l'importance des inter-comparaisons systématiques de produits d'observation afin de mieux comprendre les causes des différences observées entre les différents jeux de données.

Dans cette thèse, nous avons été particulièrement intéressés par les tendances et la variabilité régionale du niveau de la mer. Nos résultats ont montré que les variations du niveau de la mer ne sont pas uniformes à l'échelle mondiale, même sur des périodes longues (par exemple les soixante dernières années), et qu'ils sont fortement dominés par les modes de variabilité internes au système couplé océan-atmosphère, à des échelles de temps interannuelles et décennales. L'estimation de la hausse locale du niveau de la mer relatif a démontré l'importance non seulement de la variabilité régionale, mais aussi le rôle des mouvements verticaux du sol, en particulier la subsidence qui exacerbe l'impact de l'élévation du niveau de la mer d'origine climatique. De toutes les régions étudiées, c'est le Pacifique tropical qui présente la plus forte amplitude des variations du niveau de la mer depuis 1950.

Dans la dernière partie de cette thèse, nous nous sommes concentrés sur le Pacifique tropical, puisque c'est la région qui montre la plus forte hausse de la mer. Nous avons analysé, sur les 20 dernières années, les rôles respectifs de la dynamique océanique, des modes de variabilité interne du climat et du forçage anthropique sur les structures de la variabilité régionale du niveau de la mer. Nous avons montré qu'une partie importante de la variabilité régionale du niveau de la mer du Pacifique tropical peut être expliquée par le mouvement vertical de la thermocline en réponse à l'action du vent. En estimant la contribution du signal correspondant

aux modes de variabilité interne du climat à la hausse régionale observée du niveau de la mer dans le Pacifique tropical, nous avons montré que le signal résiduel (c'est-à-dire le signal total moins le signal de variabilité interne) ne correspond probablement pas encore à l'empreinte externe du forçage anthropique. De ces études, nous concluons que le signal régional actuel, notamment celui observé par les satellites altimétriques depuis 25 ans, est encore dominé par la variabilité interne du système climatique.

Alors que cette thèse a contribué à répondre aux questions liées au niveau de la mer, en particulier à mieux comprendre la variabilité régionale du niveau de la mer et ses cause, de nombreuses questions scientifiques demeurent non résolues, en particulier sur les projections futures. Certains de ces sujets sont déjà à l'étude par l'équipe travaillent sur le niveau de la mer au LEGOS.

Bibliography

Ablain, M. et al. (2015), Improved sea level record over the satellite altimetry era (1993–2010) from the Climate Change Initiative project, *Ocean Sci*, *11*(1), 67–82, doi:10.5194/os-11-67-2015.

Ablain, M., A. Cazenave, G. Valladeau, and S. Guinehut (2009), A new assessment of the error budget of global mean sea level rate estimated by satellite altimetry over 1993-2008, *Ocean Sci.*, *5*(2), 193–201.

Abraham et al. (2013), A review of global ocean temperature observations: Implications for ocean heat content estimates and climate change, *Rev. Geophys.*, *51*, 450–483, doi:10.1002/rog.20022.

Abram, N. J., R. Mulvaney, F. Vimeux, S. J. Phipps, J. Turner, and M. H. England (2014), Evolution of the Southern Annular Mode during the past millennium, *Nat. Clim. Change*, *4*(7), 564–569, doi:10.1038/nclimate2235.

AchutaRao, K. M., B. D. Santer, P. J. Gleckler, K. E. Taylor, D. W. Pierce, T. P. Barnett, and T. M. L. Wigley (2006), Variability of ocean heat uptake: Reconciling observations and models, *J. Geophys. Res. Oceans*, *111*(C5), C05019, doi:10.1029/2005JC003136.

Allan, R. J., D. Chambers, W. Drosdowsky, H. Hendon, M. Latif, N. Nicholls, I. Smith, R. C. Stone, and Y. Tourre (2001), Is there an Indian Ocean dipole and is it independent of the El Niño-Southern Oscillation?, *CLIVAR Exch.*, *6*(3 (no.), 18–22.

Antonov, J. I., S. Levitus, and T. P. Boyer (2002), Steric sea level variations during 1957–1994: Importance of salinity, *J. Geophys. Res. Oceans*, *107*(C12), 8013, doi:10.1029/2001JC000964.

Aparna, S. G., J. P. McCreary, D. Shankar, and P. N. Vinayachandran (2012), Signatures of Indian Ocean Dipole and El Niño–Southern Oscillation events in sea level variations in the Bay of Bengal, *J. Geophys. Res. Oceans*, *117*(C10), C10012, doi:10.1029/2012JC008055.

Ashok, K., S. K. Behera, S. A. Rao, H. Weng, and T. Yamagata (2007), El Niño Modoki and its possible teleconnection, *J. Geophys. Res. Oceans*, *112*(C11), C11007, doi:10.1029/2006JC003798.

Aubrey, D. G., K. O. Emery, and E. Uchupi (1988), Changing coastal levels of South America and the Caribbean region from tide-gauge records, *Tectonophysics*, *154*(3–4), 269–284, doi:10.1016/0040-1951(88)90108-4.

Ballu, V., M.-N. Bouin, P. Siméoni, W. C. Crawford, S. Calmant, J.-M. Boré, T. Kanas, and B. Pelletier (2011), Comparing the role of absolute sea-level rise and vertical tectonic motions in coastal flooding, Torres Islands (Vanuatu), *Proc. Natl. Acad. Sci.*, *108*(32), 13019–13022, doi:10.1073/pnas.1102842108.

Balmaseda, M. A., K. E. Trenberth, and E. Källén (2013), Distinctive climate signals in reanalysis of global ocean heat content, *Geophys. Res. Lett.*, *40*(9), 1754–1759, doi:10.1002/grl.50382.

Balmaseda, M. A., K. Mogensen, and A. T. Weaver (2013), Evaluation of the ECMWF ocean reanalysis system ORAS4, *Q. J. R. Meteorol. Soc.*, *139*(674), 1132–1161, doi:10.1002/qj.2063.

Bard, E., B. Hamelin, and D. Delanghe-Sabatier (2010), Deglacial Meltwater Pulse 1B and Younger Dryas Sea Levels Revisited with Boreholes at Tahiti, *Science*, *327*(5970), 1235–1237, doi:10.1126/science.1180557.

Barnett, T. P., D. W. Pierce, and R. Schnur (2001), Detection of anthropogenic climate change in the world's oceans, *Science*, *292*(5515), 270–274, doi:10.1126/science.1058304.

Barnett, T. P., D. W. Pierce, K. M. AchutaRao, P. J. Gleckler, B. D. Santer, J. M. Gregory, and W. M. Washington (2005), Penetration of Human-Induced Warming into the World's Oceans, *Science*, *309*(5732), 284–287, doi:10.1126/science.1112418.

Becker, M., B. Meyssignac, C. Letetrel, W. Llovel, A. Cazenave, and T. Delcroix (2012), Sea level variations at tropical Pacific islands since 1950, *Glob. Planet. Change*, *80–81*, 85–98, doi:10.1016/j.gloplacha.2011.09.004.

Becker, M., M. Karpytchev, and S. Lennartz-Sassinek (2014), Long-term sea level trends: Natural or anthropogenic?, *Geophys. Res. Lett.*, *41*(15), 2014GL061027, doi:10.1002/2014GL061027.

Beckley, B. D., N. P. Zelensky, S. A. Holmes, F. G. Lemoine, R. D. Ray, G. T. Mitchum, S. D. Desai, and S. T. Brown (2010), Assessment of the Jason-2 Extension to the TOPEX/Poseidon, Jason-1 Sea-Surface Height Time Series for Global Mean Sea Level Monitoring, *Mar. Geod.*, *33*(sup1), 447–471, doi:10.1080/01490419.2010.491029.

Behera, S. K., and T. Yamagata (2001), Subtropical SST dipole events in the southern Indian Ocean, *Geophys. Res. Lett.*, *28*(2), 327–330, doi:10.1029/2000GL011451.

Berge-Nguyen, M., A. Cazenave, A. Lombard, W. Llovel, J. Viarre, and J. F. Cretaux (2008), Reconstruction of past decades sea level using thermosteric sea level, tide gauge, satellite altimetry and ocean reanalysis data, *Glob. Planet. Change*, *62*(1–2), 1–13, doi:10.1016/j.gloplacha.2007.11.007.

Bilbao, R. A. F., J. M. Gregory, and N. Bouttes (2015), Analysis of the regional pattern of sea level change due to ocean dynamics and density change for 1993–2099 in observations and CMIP5 AOGCMs, *Clim. Dyn.*, 1–20, doi:10.1007/s00382-015-2499-z.

Bindoff, N., et al. (2007), Observations: Oceanic climate and sea level, in *Climate Change 2007: The Physical Science Basis. Contribution of Working Group I to the Fourth Assessment Report of the Intergovernmental Panel on Climate Change*, edited by S. Solomon, D. Qin, M. Manning, Z. Chen, M. Marquis, K. B. Averyt, M. Tignor, and H. L. Miller, Cambridge Univ. Press, Cambridge, U. K.

Bjerknes, J. (1966), A possible response of the atmospheric Hadley circulation to equatorial anomalies of ocean temperature, *Tellus*, *18*(4), 820–829, doi:10.1111/j.2153-3490.1966.tb00303.x.

Bjerknes, J. (1969), Atmospheric teleconnections from the equatorial pacific1, *Mon. Weather Rev.*, *97*(3), 163–172, doi:10.1175/1520-0493(1969)097<0163:ATFTEP>2.3.CO;2.

Black, E., J. Slingo, and K. R. Sperber (2003), An Observational Study of the Relationship between Excessively Strong Short Rains in Coastal East Africa and Indian Ocean SST, *Mon. Weather Rev.*, *131*(1), 74–94, doi:10.1175/1520-0493(2003)131<0074:AOSOTR>2.0.CO;2.

Boening, C., J. K. Willis, F. W. Landerer, R. S. Nerem, and J. Fasullo (2012), The 2011 La Niña: So strong, the oceans fell, *Geophys. Res. Lett.*, *39*(19), L19602, doi:10.1029/2012GL053055.

Bordbar, M. H., T. Martin, M. Latif, and W. Park (2015), Effects of long-term variability on projections of twenty-first century dynamic sea level, *Nat. Clim. Change*, *5*(4), 343–347, doi:10.1038/nclimate2569.

Bosc, C., and T. Delcroix (2008), Observed equatorial Rossby waves and ENSO-related warm water volume changes in the equatorial Pacific Ocean, *J. Geophys. Res. Oceans*, *113*(C6), C06003, doi:10.1029/2007JC004613.

Boucher, O., D. Randall, P. Artaxo, C. Bretherton, G. Feingold, P. Forster, V.-M. Kerminen, Y. Kondo, H. Liao, U. Lohmann, P. Rasch, S.K. Satheesh, S. Sherwood, B. Stevens and X.Y. Zhang, 2013: Clouds and Aerosols. In: Climate Change 2013: The Physical Science Basis. Contribution of Working Group I to the Fifth Assessment Report of the Intergovernmental Panel on Climate Change [Stocker, T.F., D. Qin, G.-K. Plattner, M. Tignor, S.K. Allen, J. Boschung, A. Nauels, Y. Xia, V. Bex and P.M. Midgley (eds.)]. Cambridge University Press, Cambridge, United Kingdom and New York, NY, USA.

Brovkin, V., S. J. Lorenz, J. Jungclaus, T. Raddatz, C. Timmreck, C. H. Reick, J. Segschneider, and K. Six (2010), Sensitivity of a coupled climate-carbon cycle model to large volcanic eruptions during the last millennium, *Tellus B*, *62*(5), doi:10.3402/tellusb.v62i5.16620.

Cai, W. et al. (2014), Increasing frequency of extreme El Nino events due to greenhouse warming, *Nat. Clim. Change*, *4*(2), 111–116, doi:10.1038/nclimate2100.

Cai, W. et al. (2015), Increased frequency of extreme La Nina events under greenhouse warming, *Nat. Clim. Change*, *5*(2), 132–137, doi:10.1038/nclimate2492.

Callahan, P. S. (1984), Ionospheric Variations Affecting Altimeter Measurements: A Brief Synopsis, *Mar. Geod.*, *8*(1-4), 249–263, doi:10.1080/15210608409379505.

Carrère, L., and F. Lyard (2003), Modeling the barotropic response of the global ocean to atmospheric wind and pressure forcing - comparisons with observations, *Geophys. Res. Lett.*, *30*(6), n/a–n/a, doi:10.1029/2002GL016473.

Carson, M., A. Köhl, and D. Stammer (2014), The Impact of Regional Multidecadal and Century-Scale Internal Climate Variability on Sea Level Trends in CMIP5 Models, *J. Clim.*, *28*(2), 853–861, doi:10.1175/JCLI-D-14-00359.1.

Carton, J. A., and B. S. Giese (2008), A reanalysis of ocean climate using Simple Ocean Data Assimilation (SODA), *Mon. Weather Rev.*, *136*(8), 2999–3017, doi:10.1175/2007MWR1978.1.

Carton, J. A., B. S. Giese, and S. A. Grodsky (2005), Sea level rise and the warming of the oceans in the Simple Ocean Data Assimilation (SODA) ocean reanalysis, *J. Geophys. Res. Oceans*, *110*(C9), n/a–n/a, doi:10.1029/2004JC002817.

Cazenave, A., and G. L. Cozannet (2014), Sea level rise and its coastal impacts, *Earths Future*, *2*(2), 15–34, doi:10.1002/2013EF000188.

Cazenave, A., and W. Llovel (2010), Contemporary Sea Level Rise, *Annu. Rev. Mar. Sci.*, *2*(1), 145–173, doi:10.1146/annurev-marine-120308-081105.

Cazenave, A., H.-B. Dieng, B. Meyssignac, K. von Schuckmann, B. Decharme, and E. Berthier (2014), The rate of sea-level rise, *Nat. Clim. Change*, *4*(5), 358–361, doi:10.1038/nclimate2159.

Cazenave, A., O. Henry, S. Munier, T. Delcroix, A. L. Gordon, B. Meyssignac, W. Llovel, H. Palanisamy, and M. Becker (2012), Estimating ENSO Influence on the Global Mean Sea Level, 1993–2010, *Mar. Geod.*, *35*(sup1), 82–97, doi:10.1080/01490419.2012.718209.

Chambers, D. P., and J. A. Bonin (2012), Evaluation of Release-05 GRACE time-variable gravity coefficients over the ocean, *Ocean Sci*, *8*(5), 859–868, doi:10.5194/os-8-859-2012.

Chambers, D. P., J. Wahr, M. E. Tamisiea, and R. S. Nerem (2010), Ocean mass from GRACE and glacial isostatic adjustment, *J. Geophys. Res. Solid Earth*, *115*(B11), B11415, doi:10.1029/2010JB007530.

Chao, B. F., Y. H. Wu, and Y. S. Li (2008), Impact of Artificial Reservoir Water Impoundment on Global Sea Level, *Science*, *320*(5873), 212–214, doi:10.1126/science.1154580.

Chelton, D. B. (1994), The sea state bias in altimeter estimates of sea level from collinear analysis of TOPEX data, *J. Geophys. Res. Oceans*, *99*(C12), 24995–25008, doi:10.1029/94JC02113.

Chen, J. L., C. R. Wilson, D. Blankenship, and B. D. Tapley (2009), Accelerated Antarctic ice loss from satellite gravity measurements, *Nat. Geosci.*, *2*(12), 859–862, doi:10.1038/ngeo694.

Chen, X., and K.-K. Tung (2014), Varying planetary heat sink led to global-warming slowdown and acceleration, *Science*, *345*(6199), 897–903, doi:10.1126/science.1254937.

Church JA, Clark PU, Cazenave A, Gregory JM, Jevrejeva S, Levermann A, Merrifield MA, Milne GA, Nerem RS, Nunn PD, Payne AJ, PfefferWT, Stammer D, Unnikrishnan AS (2013) Sea level change. In: Stocker TF, Qin D, Plattner G-K, Tignor M, Allen SK, Boschung J, Nauels A, Xia Y, Bex V, Midgley PM(eds) Climate change 2013: the physical science basis. Contribution of working group I to the fifth assessment report of the intergovernmental panel on climate change. Cambridge University Press, CambridgeChurch, J. A., and N. J. White (2006), A 20th century acceleration in global sea-level rise, *Geophys. Res. Lett.*, *33*(1), L01602, doi:10.1029/2005GL024826.

Church, J. A., and N. J. White (2011), Sea-Level Rise from the Late 19th to the Early 21st Century, *Surv. Geophys.*, *32*(4-5), 585–602, doi:10.1007/s10712-011-9119-1.

Church, J. A., N. J. White, and J. M. Arblaster (2005), Significant decadal-scale impact of volcanic eruptions on sea level and ocean heat content, *Nature*, *438*(7064), 74–77, doi:10.1038/nature04237.

Church, J. A., N. J. White, and J. R. Hunter (2006), Sea-level rise at tropical Pacific and Indian Ocean islands, *Glob. Planet. Change*, *53*(3), 155–168, doi:10.1016/j.gloplacha.2006.04.001.

Church, J. A., N. J. White, L. F. Konikow, C. M. Domingues, J. G. Cogley, E. Rignot, J. M. Gregory, M. R. van den Broeke, A. J. Monaghan, and I. Velicogna (2011), Revisiting the Earth's sea-level and energy budgets from 1961 to 2008, *Geophys. Res. Lett.*, *38*, doi:10.1029/2011GL048794.

Church, J. A., N. J. White, L. F. Konikow, C. M. Domingues, J. G. Cogley, E. Rignot, J. M. Gregory, M. R. van den Broeke, A. J. Monaghan, and I. Velicogna (2011), Revisiting the Earth's sea-level and energy budgets from 1961 to 2008, *Geophys. Res. Lett.*, *38*, doi:10.1029/2011GL048794.

Church, J. A., N. J. White, R. Coleman, K. Lambeck, and J. X. Mitrovica (2004), Estimates of the Regional Distribution of Sea Level Rise over the 1950–2000 Period, *J. Clim.*, *17*(13), 2609–2625, doi:10.1175/1520-0442(2004)017<2609:EOTRDO>2.0.CO;2.

Clark, C. O., P. J. Webster, and J. E. Cole (2003), Interdecadal Variability of the Relationship between the Indian Ocean Zonal Mode and East African Coastal Rainfall Anomalies, *J. Clim.*, *16*(3), 548–554, doi:10.1175/1520-0442(2003)016<0548:IVOTRB>2.0.CO;2.

Cogley, J. G. (2009), Geodetic and direct mass-balance measurements: comparison and joint analysis, *Ann. Glaciol.*, *50*(50), 96–100, doi:10.3189/172756409787769744.

Couhert, A., L. Cerri, J.-F. Legeais, M. Ablain, N. P. Zelensky, B. J. Haines, F. G. Lemoine, W. I. Bertiger, S. D. Desai, and M. Otten (2015), Towards the 1 mm/y stability of the radial orbit error at regional scales, *Adv. Space Res.*, *55*(1), 2–23, doi:10.1016/j.asr.2014.06.041.

Dangendorf, S., M. Marcos, A. Müller, E. Zorita, R. Riva, K. Berk, and J. Jensen (2015), Detecting anthropogenic footprints in sea level rise, *Nat. Commun.*, *6*, doi:10.1038/ncomms8849.

Desai, S. D. (2002), Observing the pole tide with satellite altimetry, *J. Geophys. Res. Oceans*, *107*(C11), doi:10.1029/2001JC001224.

Deschamps, P., N. Durand, E. Bard, B. Hamelin, G. Camoin, A. L. Thomas, G. M. Henderson, J. Okuno, and Y. Yokoyama (2012), Ice-sheet collapse and sea-level rise at the Bolling warming 14,600 years ago, *Nature*, *483*(7391), 559–564, doi:10.1038/nature10902.

Deser, C., A. Phillips, V. Bourdette, and H. Teng (2010), Uncertainty in climate change projections: the role of internal variability, *Clim. Dyn.*, *38*(3-4), 527–546, doi:10.1007/s00382-010-0977-x.

Deser, C., A. S. Phillips, and J. W. Hurrell (2004), Pacific Interdecadal Climate Variability: Linkages between the Tropics and the North Pacific during Boreal Winter since 1900, *J. Clim.*, *17*(16), 3109–3124, doi:10.1175/1520-0442(2004)017<3109:PICVLB>2.0.CO;2.

Deser, C., and J. M. Wallace (1987), El Niño events and their relation to the Southern Oscillation: 1925–1986, *J. Geophys. Res. Oceans*, *92*(C13), 14189–14196, doi:10.1029/JC092iC13p14189.

Desportes, C., E. Obligis, and L. Eymard (2007), On the Wet Tropospheric Correction for Altimetry in Coastal Regions, *IEEE Trans. Geosci. Remote Sens.*, *45*(7), 2139–2149, doi:10.1109/TGRS.2006.888967.

Di Lorenzo, E., K. M. Cobb, J. C. Furtado, N. Schneider, B. T. Anderson, A. Bracco, M. A. Alexander, and D. J. Vimont (2010), Central Pacific El Nino and decadal climate change in the North Pacific Ocean, *Nat. Geosci.*, *3*(11), 762–765, doi:10.1038/ngeo984.

Dieng, H. B., H. Palanisamy, A. Cazenave, B. Meyssignac, and K. von Schuckmann (2015a), The Sea Level Budget Since 2003: Inference on the Deep Ocean Heat Content, *Surv. Geophys.*, *36*(2), 209–229, doi:10.1007/s10712-015-9314-6.

Dieng, H. B., A. Cazenave, K. von Schuckmann, M.Ablain, B. Meyssignac (2015b), Sea level budget over 2005-2013: Missing contributions and data errors, *Ocean Sciences,* Accepted.

Domingues, C. M., J. A. Church, N. J. White, P. J. Gleckler, S. E. Wijffels, P. M. Barker, and J. R. Dunn (2008), Improved estimates of upper-ocean warming and multi-decadal sea-level rise, *Nature*, *453*(7198), 1090–1093, doi:10.1038/nature07080.

Dong, L., T. Zhou, and X. Chen (2014), Changes of Pacific decadal variability in the twentieth century driven by internal variability, greenhouse gases, and aerosols, *Geophys. Res. Lett.*, *41*(23), 2014GL062269, doi:10.1002/2014GL062269.

Douglas, B.C., (2001), Sea level change in the era of the recording tide gauge, in Sea Level Rise: History and Consequences, Douglas, B.C., Kearney, M.S., and Leatherman, S.P., eds., International Geophysics Series, vol. 75, New York, Academic Press, pp. 37–62.

Douglas, B.C., (2001), Sea level change in the era of the recording tide gauge, in Sea Level Rise: History and Consequences, Douglas, B.C., Kearney, M.S., and Leatherman, S.P., eds., International Geophysics Series, vol. 75, New York, Academic Press, pp. 37–62.

Ducet, N., P. Y. Le Traon, and G. Reverdin (2000), Global high-resolution mapping of ocean circulation from TOPEX/Poseidon and ERS-1 and -2, *J. Geophys. Res. Oceans*, *105*(C8), 19477–19498, doi:10.1029/2000JC900063.

Dunne, R. P., S. M. Barbosa, and P. L. Woodworth (2012), Contemporary sea level in the Chagos Archipelago, central Indian Ocean, *Glob. Planet. Change*, *82–83*, 25–37, doi:10.1016/j.gloplacha.2011.11.009.

Durack, P. J., and S. E. Wijffels (2010), Fifty-Year Trends in Global Ocean Salinities and Their Relationship to Broad-Scale Warming, *J. Clim.*, *23*(16), 4342–4362, doi:10.1175/2010JCLI3377.1.

Durack, P. J., P. J. Gleckler, F. W. Landerer, and K. E. Taylor (2014a), Quantifying underestimates of long-term upper-ocean warming, *Nat. Clim. Change*, *4*(11), 999–1005, doi:10.1038/nclimate2389.

Durack, P. J., S. E. Wijffels, and P. J. Gleckler (2014b), Long-term sea-level change revisited: the role of salinity, *Environ. Res. Lett.*, *9*(11), 114017, doi:10.1088/1748-9326/9/11/114017.

Durand, F., and T. Delcroix (2000), On the Variability of the Tropical Pacific Thermal Structure during the 1979–96 Period, as Deduced from XBT Sections, *J. Phys. Oceanogr.*, *30*(12), 3261–3269, doi:10.1175/1520-0485(2000)030<3261:OTVOTT>2.0.CO;2.

Dutton, A., A. E. Carlson, A. J. Long, G. A. Milne, P. U. Clark, R. DeConto, B. P. Horton, S. Rahmstorf, and M. E. Raymo (2015), Sea-level rise due to polar ice-sheet mass loss during past warm periods, *Science*, *349*(6244), aaa4019, doi:10.1126/science.aaa4019.

Dutton, A., and K. Lambeck (2012), Ice Volume and Sea Level During the Last Interglacial, *Science*, *337*(6091), 216–219, doi:10.1126/science.1205749.

England, M. H., S. McGregor, P. Spence, G. A. Meehl, A. Timmermann, W. Cai, A. S. Gupta, M. J. McPhaden, A. Purich, and A. Santoso (2014), Recent intensification of wind-driven circulation in the Pacific and the ongoing warming hiatus, *Nat. Clim. Change*, *4*(3), 222–227, doi:10.1038/nclimate2106.

Ericson, J. P., C. J. Vörösmarty, S. L. Dingman, L. G. Ward, and M. Meybeck (2006), Effective sea-level rise and deltas: Causes of change and human dimension implications, *Glob. Planet. Change*, *50*(1–2), 63–82, doi:10.1016/j.gloplacha.2005.07.004.

Fasullo, J. T., C. Boening, F. W. Landerer, and R. S. Nerem (2013), Australia's unique influence on global sea level in 2010–2011, *Geophys. Res. Lett.*, *40*(16), 4368–4373, doi:10.1002/grl.50834.

Featherstone, W.E., Filmer,M.S., Penna, N.T.,Morgan, L.M., Schenk, A., 2012. Anthropogenic land subsidence in the Perth Basin: challenges for its retrospective geodetic detection. J. R. Soc. West. Aust. 95, 53–62.

Fernandes, M. J., S. Barbosa, and C. Lázaro (2006), Impact of Altimeter Data Processing on Sea Level Studies, *Sensors*, *6*(3), 131–163.

Fettweis, X., B. Franco, M. Tedesco, J. H. van Angelen, J. T. M. Lenaerts, M. R. van den Broeke, and H. Gallée (2013), Estimating the Greenland ice sheet surface mass balance contribution to future sea level rise using the regional atmospheric climate model MAR, *The Cryosphere*, *7*(2), 469–489, doi:10.5194/tc-7-469-2013.

Folland CK, Parker DE, Colman A, Washington R (1999) Large scale modes of ocean surface temperature since the late nineteenth century. In: Navarra A (ed) Beyond El Nino: decadal and interdecadal climate variability. Springer, Berlin, Refereed book: chapter 4, pp 73–102.

Frankcombe, L. M., S. McGregor, and M. H. England (2014), Robustness of the modes of Indo-Pacific sea level variability, *Clim. Dyn.*, 1–18, doi:10.1007/s00382-014-2377-0.

Fu, L.-L., and A. Cazenave (2001), *Satellite Altimetry and Earth Sciences, Volume 69: A Handbook of Techniques and Applications*, 1st edition., Academic Press, San Diego, CA.

Fukumori, I., and O. Wang (2013), Origins of heat and freshwater anomalies underlying regional decadal sea level trends, *Geophys. Res. Lett.*, *40*(3), 563–567, doi:10.1002/grl.50164.

Gardner, A. S. et al. (2013), A Reconciled Estimate of Glacier Contributions to Sea Level Rise: 2003 to 2009, *Science*, *340*(6134), 852–857, doi:10.1126/science.1234532.

Garzoli, S. L., and E. J. Katz (1983), The Forced Annual Reversal of the Atlantic North Equatorial Countercurrent, *J. Phys. Oceanogr.*, *13*(11), 2082–2090, doi:10.1175/1520-0485(1983)013<2082:TFAROT>2.0.CO;2.

Gehrels, W. R., and P. L. Woodworth (2013), When did modern rates of sea-level rise start?, *Glob. Planet. Change*, *100*, 263–277, doi:10.1016/j.gloplacha.2012.10.020.

Gille, S. T. (2004), How nonlinearities in the equation of state of seawater can confound estimates of steric sea level change, *J. Geophys. Res.*, *109*(C3), doi:10.1029/2003JC002012.

Gillett, N. P., and P. A. Stott (2009), Attribution of anthropogenic influence on seasonal sea level pressure, *Geophys. Res. Lett.*, *36*(23), L23709, doi:10.1029/2009GL041269.

Gleckler, P. J. et al. (2012), Human-induced global ocean warming on multidecadal timescales, *Nat. Clim. Change*, *2*(7), 524–529, doi:10.1038/nclimate1553.

Goddard, L. (2014), Heat hide and seek, *Nat. Clim. Change*, *4*(3), 158–161, doi:10.1038/nclimate2155.

Goldenberg, S. B., C. W. Landsea, A. M. Mestas-Nuñez, and W. M. Gray (2001), The Recent Increase in Atlantic Hurricane Activity: Causes and Implications, *Science*, *293*(5529), 474–479, doi:10.1126/science.1060040.

Gregory, J. M. et al. (2013), Twentieth-Century Global-Mean Sea Level Rise: Is the Whole Greater than the Sum of the Parts?, *J. Clim.*, *26*(13), 4476–4499, doi:10.1175/JCLI-D-12-00319.1.

Gregory, J. M., J. A. Lowe, and S. F. B. Tett (2006), Simulated Global-Mean Sea Level Changes over the Last Half-Millennium, *J. Clim.*, *19*(18), 4576–4591, doi:10.1175/JCLI3881.1.

Guemas, V., F. J. Doblas-Reyes, I. Andreu-Burillo, and M. Asif (2013), Retrospective prediction of the global warming slowdown in the past decade, *Nat. Clim. Change*, *3*(7), 649–653, doi:10.1038/nclimate1863.

Hamlington, B. D., M. W. Strassburg, R. R. Leben, W. Han, R. S. Nerem, and K.-Y. Kim (2014), Uncovering an anthropogenic sea-level rise signal in the Pacific Ocean, *Nat. Clim. Change*, *4*(9), 782–785, doi:10.1038/nclimate2307.

Hamlington, B. D., R. R. Leben, R. S. Nerem, W. Han, and K.-Y. Kim (2011), Reconstructing sea level using cyclostationary empirical orthogonal functions, *J. Geophys. Res.-Oceans*, *116*, doi:10.1029/2011JC007529.

Han, W. et al. (2010), Patterns of Indian Ocean sea-level change in a warming climate, *Nat. Geosci.*, *3*(8), 546–550, doi:10.1038/ngeo901.

Han, W. et al. (2013), Intensification of decadal and multi-decadal sea level variability in the western tropical Pacific during recent decades, *Clim. Dyn.*, 1–23, doi:10.1007/s00382-013-1951-1.

Hanley, D. E., M. A. Bourassa, J. J. O'Brien, S. R. Smith, and E. R. Spade (2003), A Quantitative Evaluation of ENSO Indices, *J. Clim.*, *16*(8), 1249–1258, doi:10.1175/1520-0442(2003)16<1249:AQEOEI>2.0.CO;2.

Hanna, E. et al. (2013), Ice-sheet mass balance and climate change, *Nature*, *498*(7452), 51–59, doi:10.1038/nature12238.

Hanna, E., P. Huybrechts, K. Steffen, J. Cappelen, R. Huff, C. Shuman, T. Irvine-Fynn, S. Wise, and M. Griffiths (2008), Increased Runoff from Melt from the Greenland Ice Sheet: A Response to Global Warming, *J. Clim.*, *21*(2), 331–341, doi:10.1175/2007JCLI1964.1.

Hansen, J., M. Sato, P. Kharecha, and K. von Schuckmann (2011), Earth's energy imbalance and implications, *Atmos Chem Phys*, *11*(24), 13421–13449, doi:10.5194/acp-11-13421-2011.

Hare, S. R., and N. J. Mantua (2000), Empirical evidence for North Pacific regime shifts in 1977 and 1989, *Prog. Oceanogr.*, *47*(2–4), 103–145, doi:10.1016/S0079-6611(00)00033-1.

Hartmann, D. L., and F. Lo (1998), Wave-Driven Zonal Flow Vacillation in the Southern Hemisphere, *J. Atmospheric Sci.*, *55*(8), 1303–1315, doi:10.1175/1520-0469(1998)055<1303:WDZFVI>2.0.CO;2.

Hastenrath, S. (2007), Circulation mechanisms of climate anomalies in East Africa and the equatorial Indian Ocean, *Dyn. Atmospheres Oceans*, *43*(1–2), 25–35, doi:10.1016/j.dynatmoce.2006.06.002.

Hawkins, E., and R. Sutton (2009), The Potential to Narrow Uncertainty in Regional Climate Predictions, *Bull. Am. Meteorol. Soc.*, *90*(8), 1095–1107, doi:10.1175/2009BAMS2607.1.

Hegerl, G. C., O. Hoegh-Guldberg, G. Casassa, M. Hoerling, S. Kovats, C. Parmesan, D. Pierce, and P. Stott (2010), Good practice guidance paper on detection and attribution related to anthropogenic climate change, in *Meeting Report of the Intergovernmental Panel on Climate Change Expert Meeting on Detection and Attribution of Anthropogenic Climate Change*, edited by T. Stocker et al., IPCC Working Group I Technical Support Unit, Univ. of Bern, Bern, Switzerland.

Helama, S., M. M. Fauria, K. Mielikäinen, M. Timonen, and M. Eronen (2010), Sub-Milankovitch solar forcing of past climates: Mid and late Holocene perspectives, *Geol. Soc. Am. Bull.*, B30088.1, doi:10.1130/B30088.1.

Held, I. M. (2013), Climate science: The cause of the pause, *Nature*, *501*(7467), 318–319, doi:10.1038/501318a.

Henry (2014), Effect of the processing methodology on satellite altimetry-based global mean sea level rise over the Jason-1 operating period, *J. Geod.*, *88*(4), 351–361, doi:10.1007/s00190-013-0687-3.

Hildbrand Hildebrandsson, H. (1897), Quelques recherches sur les centres d'action de l'atmosphère. *L'Académie Royale des Sciences de Suède 29(3)*.

Houghton, J., G. Jenkins, and J. Ephraums (Eds.), *Report prepared for Intergovernmental Panel on Climate Change by Working Group I*, Cambridge University Press, Cambridge, United Kingdom and New York, NY, USA, 1990.

Houghton, J., Y. Ding, D. Griggs, M. Noguer, P. van der Linden, X. Dai, K. Maskell, and C. Johnson (Eds.),(2001), *Contribution of Working Group I to the Third Assessment Report of the Intergovernmental Panel on Climate Change, 2001*, Cambridge University Press, Cambridge, United Kingdom and New York, NY, USA, 2001.

Hu, A., and C. Deser (2013), Uncertainty in future regional sea level rise due to internal climate variability, *Geophys. Res. Lett.*, *40*(11), 2768–2772, doi:10.1002/grl.50531.

Hunt, B. G. (2006), Climatological Extremes of Simulated Annual Mean Rainfall, *J. Clim.*, *19*(20), 5289–5304, doi:10.1175/JCLI3921.1.

Hurrell, J. W. (1995), Decadal Trends in the North Atlantic Oscillation: Regional Temperatures and Precipitation, *Science*, *269*(5224), 676–679, doi:10.1126/science.269.5224.676.

Hurrell, J. W., Y. Kushnir, G. Ottersen, and M. Visbeck (2003), An Overview of the North Atlantic Oscillation, in *The North Atlantic Oscillation: Climatic Significance and Environmental Impact*, edited by J. W. Hurrell, Y. Kushnir, G. Ottersen, and rtin Visbeck, pp. 1–35, American Geophysical Union.

Imel, D. A. (1995), Evaluation of the TOPEX/POSEIDON dual-frequency ionosphere correction, *J. Geophys. Res. Atmospheres*, *99*(C12), doi:10.1029/94JC01869.

IPCC, 2013: Climate Change 2013: The Physical Science Basis. Contribution of Working Group I to the Fifth Assessment Report of the Intergovernmental Panel on Climate Change, Stocker, T.F., D. Qin, G.-K. Plattner, M. Tignor, S.K. Allen, J. Boschung, A. Nauels, Y. Xia, V. Bex and P.M. Midgley (eds.). Cambridge University Press, Cambridge, United 548 Kingdom and New York, NY, USA, 1535 pp, doi:10.1017/CBO9781107415324.

Ishii, M., and M. Kimoto (2009), Reevaluation of historical ocean heat content variations with time-varying XBT and MBT depth bias corrections, *J. Oceanogr.*, *65*(3), 287–299, doi:10.1007/s10872-009-0027-7.

Ishii, M., M. Kimoto, K. Sakamoto, and S.-I. Iwasaki (2006), Steric sea level changes estimated from historical ocean subsurface temperature and salinity analyses, *J. Oceanogr.*, *62*(2), 155–170, doi:10.1007/s10872-006-0041-y.

Jahn, A. et al. (2011), Late-Twentieth-Century Simulation of Arctic Sea Ice and Ocean Properties in the CCSM4, *J. Clim.*, *25*(5), 1431–1452, doi:10.1175/JCLI-D-11-00201.1.

Jevrejeva, S., A. Grinsted, J. C. Moore, and S. Holgate (2006), Nonlinear trends and multiyear cycles in sea level records, *J. Geophys. Res. Oceans*, *111*(C9), C09012, doi:10.1029/2005JC003229.

Jevrejeva, S., J. C. Moore, A. Grinsted, and P. L. Woodworth (2008), Recent global sea level acceleration started over 200 years ago?, *Geophys. Res. Lett.*, *35*(8), L08715, doi:10.1029/2008GL033611.

Johnson, G. C., and D. P. Chambers (2013), Ocean bottom pressure seasonal cycles and decadal trends from GRACE Release-05: Ocean circulation implications, *J. Geophys. Res. Oceans*, *118*(9), 4228–4240, doi:10.1002/jgrc.20307.

Jordà, G. (2014), Detection time for global and regional sea level trends and accelerations, *J. Geophys. Res. Oceans*, *119*(10), 7164–7174, doi:10.1002/2014JC010005.

Jury, M. R. (2011), Long-Term Variability and Trends in the Caribbean Sea, *Int. J. Oceanogr.*, *2011*, e465810, doi:10.1155/2011/465810.

Kaplan, A., Kushnir, Y., Cane,M.A., 2000. Reduced space optimal interpolation of historical marine sea level pressure: 1854–1992. J. Clim. 13, 2987–3002.

Karl, T. R., A. Arguez, B. Huang, J. H. Lawrimore, J. R. McMahon, M. J. Menne, T. C. Peterson, R. S. Vose, and H.-M. Zhang (2015), Possible artifacts of data biases in the recent global surface warming hiatus, *Science*, aaa5632, doi:10.1126/science.aaa5632.

Kaser, G., J. G. Cogley, M. B. Dyurgerov, M. F. Meier, and A. Ohmura (2006), Mass balance of glaciers and ice caps: Consensus estimates for 1961–2004, *Geophys. Res. Lett.*, *33*(19), L19501, doi:10.1029/2006GL027511.

Kay, J. E., M. M. Holland, and A. Jahn (2011), Inter-annual to multi-decadal Arctic sea ice extent trends in a warming world, *Geophys. Res. Lett.*, *38*(15), L15708, doi:10.1029/2011GL048008.

Kemp, A. C., B. P. Horton, J. P. Donnelly, M. E. Mann, M. Vermeer, and S. Rahmstorf (2011), Climate related sea-level variations over the past two millennia, *Proc. Natl. Acad. Sci.*, *108*(27), 11017–11022, doi:10.1073/pnas.1015619108.

Kerr, R. A. (2000), A North Atlantic Climate Pacemaker for the Centuries, *Science*, *288*(5473), 1984–1985, doi:10.1126/science.288.5473.1984.

Kessler, W. S. (1990), Observations of long Rossby waves in the northern tropical Pacific, *J. Geophys. Res. Oceans*, *95*(C4), 5183–5217, doi:10.1029/JC095iC04p05183.

Köhl, A., and D. Stammer (2008), Decadal Sea Level Changes in the 50-Year GECCO Ocean Synthesis, *J. Clim.*, *21*(9), 1876–1890, doi:10.1175/2007JCLI2081.1.

Köhl, A., D. Stammer, and B. Cornuelle (2007), Interannual to Decadal Changes in the ECCO Global Synthesis, *J. Phys. Oceanogr.*, *37*(2), 313–337, doi:10.1175/JPO3014.1.

Konikow, L. F. (2011), Contribution of global groundwater depletion since 1900 to sea-level rise, *Geophys. Res. Lett.*, *38*(17), L17401, doi:10.1029/2011GL048604.

Konikow, L. F. (2013), Overestimated water storage, *Nat. Geosci.*, *6*(1), 3–3, doi:10.1038/ngeo1659.

Kopp, R. E., F. J. Simons, J. X. Mitrovica, A. C. Maloof, and M. Oppenheimer (2013), A probabilistic assessment of sea level variations within the last interglacial stage, *Geophys. J. Int.*, *193*(2), 711–716, doi:10.1093/gji/ggt029.

Kopp, R. E., J. X. Mitrovica, S. M. Griffies, J. Yin, C. C. Hay, and R. J. Stouffer (2010), The impact of Greenland melt on local sea levels: a partially coupled analysis of dynamic and static equilibrium effects in idealized water-hosing experiments, *Clim. Change*, *103*(3-4), 619–625, doi:10.1007/s10584-010-9935-1.

Kosaka, Y., and S.-P. Xie (2013), Recent global-warming hiatus tied to equatorial Pacific surface cooling, *Nature*, *501*(7467), 403–407, doi:10.1038/nature12534.

Kouketsu, S. et al. (2011), Deep ocean heat content changes estimated from observation and reanalysis product and their influence on sea level change, *J. Geophys. Res. Oceans*, *116*(C3), C03012, doi:10.1029/2010JC006464.

Lambeck, K., C. D. Woodroffe, F. Antonioli, M. Anzidei, W. R. Gehrels, J. Laborel, and A. J. Wright (2010), Paleoenvironmental Records, Geophysical Modeling, and Reconstruction of Sea-Level Trends and Variability on Centennial and Longer Timescales, in *Understanding Sea-Level Rise and Variability*, edited by J. A. Church, P. L. W. former D. Chairman, T. A. S. P. Specialist, and W. S. W. S. Scientist, pp. 61–121, Wiley-Blackwell.

Lambeck, K., M. Anzidei, F. Antonioli, A. Benini, and A. Esposito (2004), Sea level in Roman time in the Central Mediterranean and implications for recent change, *Earth Planet. Sci. Lett.*, *224*(3–4), 563–575, doi:10.1016/j.epsl.2004.05.031.

Lambeck, K., T. M. Esat, and E.-K. Potter (2002), Links between climate and sea levels for the past three million years, *Nature*, *419*(6903), 199–206, doi:10.1038/nature01089.

Landerer, F. W., J. H. Jungclaus, and J. Marotzke (2007), Regional Dynamic and Steric Sea Level Change in Response to the IPCC-A1B Scenario, *J. Phys. Oceanogr.*, *37*(2), 296–312, doi:10.1175/JPO3013.1.

Le Traon, P. Y., F. Nadal, and N. Ducet (1998), An Improved Mapping Method of Multisatellite Altimeter Data, *J. Atmospheric Ocean. Technol.*, *15*(2), 522–534, doi:10.1175/1520-0426(1998)015<0522:AIMMOM>2.0.CO;2.

Le Traon, P. Y., Y. Faugère, F. Hernandez, J. Dorandeu, F. Mertz, and M. Ablain (2003), Can We Merge GEOSAT Follow-On with TOPEX/Poseidon and ERS-2 for an Improved Description of the Ocean Circulation?, *J. Atmospheric Ocean. Technol.*, *20*(6), 889–895, doi:10.1175/1520-0426(2003)020<0889:CWMGFW>2.0.CO;2.

Leclercq, P. W., J. Oerlemans, and J. G. Cogley (2011), Estimating the Glacier Contribution to Sea-Level Rise for the Period 1800–2005, *Surv. Geophys.*, *32*(4-5), 519–535, doi:10.1007/s10712-011-9121-7.

Legeais, J.-F., M. Ablain, and S. Thao (2014), Evaluation of wet troposphere path delays from atmospheric reanalyses and radiometers and their impact on the altimeter sea level, *Ocean Sci*, *10*(6), 893–905, doi:10.5194/os-10-893-2014.

Legras, B., O. Mestre, E. Bard, and P. Yiou (2010), A critical look at solar-climate relationships from long temperature series, *Clim Past*, *6*(6), 745–758, doi:10.5194/cp-6-745-2010.

Lennartz, S., and A. Bunde (2009), Trend evaluation in records with long-term memory: Application to global warming, *Geophys. Res. Lett.*, *36*(16), L16706, doi:10.1029/2009GL039516.

Leuliette, and J. K. Willis (2011), Balancing the Sea Level Budget, *Oceanography*, *24*(2), 122–129, doi:10.5670/oceanog.2011.32.

Levermann, A., P. U. Clark, B. Marzeion, G. A. Milne, D. Pollard, V. Radic, and A. Robinson (2013), The multimillennial sea-level commitment of global warming, *Proc. Natl. Acad. Sci.*, *110*(34), 13745–13750, doi:10.1073/pnas.1219414110.

Levitus, S. et al. (2012), World ocean heat content and thermosteric sea level change (0–2000 m), 1955–2010, *Geophys. Res. Lett.*, *39*(10), L10603, doi:10.1029/2012GL051106.

Levitus, S., J. Antonov, and T. Boyer (2005), Warming of the world ocean, 1955-2003, *Geophys. Res. Lett.*, *32*(2), doi:10.1029/2004GL021592.

Levitus, S., J. I. Antonov, T. P. Boyer, R. A. Locarnini, H. E. Garcia, and A. V. Mishonov (2009), Global ocean heat content 1955–2008 in light of recently revealed instrumentation problems, *Geophys. Res. Lett.*, *36*(7), n/a–n/a, doi:10.1029/2008GL037155.

Little, C. M., R. M. Horton, R. E. Kopp, M. Oppenheimer, and S. Yip (2015), Uncertainty in Twenty-First-Century CMIP5 Sea Level Projections, *J. Clim.*, *28*(2), 838–852, doi:10.1175/JCLI-D-14-00453.1.

Llovel, W., A. Cazenave, P. Rogel, A. Lombard, and M. Bergé-Nguyen (2009), 2-D reconstruction of past sea level (1950–2003) using tide gauge records and spatial patterns from a general ocean circulation model, *Clim. Past Discuss.*, *5*(2), 1109–1132, doi:10.5194/cpd-5-1109-2009.

Llovel, W., J. K. Willis, F. W. Landerer, and I. Fukumori (2014), Deep-ocean contribution to sea level and energy budget not detectable over the past decade, *Nat. Clim. Change*, *4*(11), 1031–1035, doi:10.1038/nclimate2387.

Llovel, W., M. Becker, A. Cazenave, S. Jevrejeva, R. Alkama, B. Decharme, H. Douville, M. Ablain, and B. Beckley (2011), Terrestrial waters and sea level variations on interannual time scale, *Glob. Planet. Change*, *75*(1–2), 76–82, doi:10.1016/j.gloplacha.2010.10.008.

Lombard, A., A. Cazenave, K. DoMinh, C. Cabanes, and R. S. Nerem (2005), Thermosteric sea level rise for the past 50 years; comparison with tide gauges and inference on water mass contribution, *Glob. Planet. Change*, *48*(4), 303–312, doi:10.1016/j.gloplacha.2005.02.007.

Lorbacher, K., S. J. Marsland, J. A. Church, S. M. Griffies, and D. Stammer (2012), Rapid barotropic sea level rise from ice sheet melting, *J. Geophys. Res. Oceans*, *117*(C6), C06003, doi:10.1029/2011JC007733.

Lorenz, E. N. (1951), Seasonal and irregular variations of the northern hemisphere sea-level pressure profile, *J. Meteorol.*, *8*(1), 52–59, doi:10.1175/1520-0469(1951)008<0052:SAIVOT>2.0.CO;2.

Lowe, J. A., and J. M. Gregory (2006), Understanding projections of sea level rise in a Hadley Centre coupled climate model, *J. Geophys. Res. Oceans*, *111*(C11), C11014, doi:10.1029/2005JC003421.

Lozier, M. S., V. Roussenov, M. S. C. Reed, and R. G. Williams (2010), Opposing decadal changes for the North Atlantic meridional overturning circulation, *Nat. Geosci.*, *3*(10), 728–734, doi:10.1038/ngeo947.

Lyman, J. M., S. A. Good, V. V. Gouretski, M. Ishii, G. C. Johnson, M. D. Palmer, D. M. Smith, and J. K. Willis (2010), Robust warming of the global upper ocean, *Nature*, *465*(7296), 334–337, doi:10.1038/nature09043.

Lyu, K., X. Zhang, J. A. Church, A. B. A. Slangen, and J. Hu (2014), Time of emergence for regional sea-level change, *Nat. Clim. Change*, *4*(11), 1006–1010, doi:10.1038/nclimate2397.

Madden, R. A., and P. R. Julian (1971), Detection of a 40–50 Day Oscillation in the Zonal Wind in the Tropical Pacific, *J. Atmospheric Sci.*, *28*(5), 702–708, doi:10.1175/1520-0469(1971)028<0702:DOADOI>2.0.CO;2.

Mantua, N. J., and S. R. Hare (2002), The Pacific Decadal Oscillation, *J. Oceanogr.*, *58*(1), 35–44, doi:10.1023/A:1015820616384.

Mantua, N. J., S. R. Hare, Y. Zhang, J. M. Wallace, and R. C. Francis (1997), A Pacific Interdecadal Climate Oscillation with Impacts on Salmon Production, *Bull. Am. Meteorol. Soc.*, *78*(6), 1069–1079, doi:10.1175/1520-0477(1997)078<1069:APICOW>2.0.CO;2.

Marcos, M., and A. Amores (2014), Quantifying anthropogenic and natural contributions to thermosteric sea level rise, *Geophys. Res. Lett.*, *41*(7), 2014GL059766, doi:10.1002/2014GL059766.

Marzeion, B., A. H. Jarosch, and J. M. Gregory (2014b), Feedbacks and mechanisms affecting the global sensitivity of glaciers to climate change, *The Cryosphere*, *8*(1), 59–71, doi:10.5194/tc-8-59-2014.

Marzeion, B., J. G. Cogley, K. Richter, and D. Parkes (2014a), Attribution of global glacier mass loss to anthropogenic and natural causes, *Science*, *345*(6199), 919–921, doi:10.1126/science.1254702.

Masters, D., R. S. Nerem, C. Choe, E. Leuliette, B. Beckley, N. White, and M. Ablain (2012), Comparison of Global Mean Sea Level Time Series from TOPEX/Poseidon, Jason-1, and Jason-2, *Mar. Geod.*, *35*(sup1), 20–41, doi:10.1080/01490419.2012.717862.

McCarthy, G. D., I. D. Haigh, J. J.-M. Hirschi, J. P. Grist, and D. A. Smeed (2015), Ocean impact on decadal Atlantic climate variability revealed by sea-level observations, *Nature*, *521*(7553), 508–510, doi:10.1038/nature14491.

McGranahan, G., D. Balk, and B. Anderson (2007), The rising tide: assessing the risks of climate change and human settlements in low elevation coastal zones, *Environ. Urban.*, *19*(1), 17–37, doi:10.1177/0956247807076960.

McGregor, S., A. S. Gupta, and M. H. England (2012), Constraining Wind Stress Products with Sea Surface Height Observations and Implications for Pacific Ocean Sea Level Trend Attribution*, *J. Clim.*, *25*(23), 8164–8176, doi:10.1175/JCLI-D-12-00105.1.

McGregor, S., N. J. Holbrook, and S. B. Power (2007), Interdecadal Sea Surface Temperature Variability in the Equatorial Pacific Ocean. Part I: The Role of Off-Equatorial Wind Stresses and Oceanic Rossby Waves, *J. Clim.*, *20*(11), 2643–2658, doi:10.1175/JCLI4145.1.

Meehl, G. A., A. Hu, C. Tebaldi, J. M. Arblaster, W. M. Washington, H. Teng, B. M. Sanderson, T. Ault, W. G. Strand, and J. B. W. Iii (2012), Relative outcomes of climate change mitigation related to global temperature versus sea-level rise, *Nat. Clim. Change*, *2*(8), 576–580, doi:10.1038/nclimate1529.

Meehl, G. A., W. M. Washington, W. D. Collins, J. M. Arblaster, A. Hu, L. E. Buja, W. G. Strand, and H. Teng (2005), How Much More Global Warming and Sea Level Rise?, *Science*, *307*(5716), 1769–1772, doi:10.1126/science.1106663.

Meehl, G.A., T.F. Stocker, W.D. Collins, P. Friedlingstein, A.T. Gaye, J.M. Gregory, A. Kitoh, R. Knutti, J.M. Murphy, A. Noda, S.C.B. Raper, I.G. Watterson, A.J. Weaver and Z.-C. Zhao, (2007): Global Climate Projections. In: Climate Change 2007: The Physical Science Basis. Contribution of Working Group I to the Fourth Assessment Report of the Intergovernmental Panel on Climate Change [Solomon, S., D. Qin, M. Manning, Z. Chen, M. Marquis, K.B. Averyt, M. Tignor and H.L. Miller (eds.)]. Cambridge University Press, Cambridge, United Kingdom and New York, NY, USA.

Meier, M. F., M. B. Dyurgerov, U. K. Rick, S. O'Neel, W. T. Pfeffer, R. S. Anderson, S. P. Anderson, and A. F. Glazovsky (2007), Glaciers Dominate Eustatic Sea-Level Rise in the 21st Century, *Science*, *317*(5841), 1064–1067, doi:10.1126/science.1143906.

Merrifield, M. A. (2011), A Shift in Western Tropical Pacific Sea Level Trends during the 1990s, *J. Clim.*, *24*(15), 4126–4138, doi:10.1175/2011JCLI3932.1.

Merrifield, M. A., and M. E. Maltrud (2011), Regional sea level trends due to a Pacific trade wind intensification, *Geophys. Res. Lett.*, *38*, doi:10.1029/2011GL049576.

Merrifield, M. A., P. R. Thompson, and M. Lander (2012), Multidecadal sea level anomalies and trends in the western tropical Pacific, *Geophys. Res. Lett.*, *39*, doi:10.1029/2012GL052032.

Merrifield, M. A., S. T. Merrifield, and G. T. Mitchum (2009), An Anomalous Recent Acceleration of Global Sea Level Rise, *J. Clim.*, *22*(21), 5772–5781, doi:10.1175/2009JCLI2985.1.

Meyers, G. (1979), On the Annual Rossby Wave in the Tropical North Pacific Ocean, *J. Phys. Oceanogr.*, *9*(4), 663–674, doi:10.1175/1520-0485(1979)009<0663:OTARWI>2.0.CO;2.

Meyssignac, B., and A. Cazenave (2012), Sea level: A review of present-day and recent-past changes and variability, *J. Geodyn.*, *58*, 96–109, doi:10.1016/j.jog.2012.03.005.

Meyssignac, B., D. Salas y Melia, M. Becker, W. Llovel, and A. Cazenave (2012b), Tropical Pacific spatial trend patterns in observed sea level: internal variability and/or anthropogenic signature?, *Clim. Past*, *8*(2), 787–802, doi:10.5194/cp-8-787-2012.

Meyssignac, B., M. Becker, W. Llovel, and A. Cazenave (2012a), An Assessment of Two-Dimensional Past Sea Level Reconstructions Over 1950-2009 Based on Tide-Gauge Data and Different Input Sea Level Grids, *Surv. Geophys.*, *33*(5), 945–972, doi:10.1007/s10712-011-9171-x.

Miller, G. H. et al. (2012), Abrupt onset of the Little Ice Age triggered by volcanism and sustained by sea-ice/ocean feedbacks, *Geophys. Res. Lett.*, *39*(2), L02708, doi:10.1029/2011GL050168.

Milly, P. C. D., A. Cazenave, and C. Gennero (2003), Contribution of climate-driven change in continental water storage to recent sea-level rise, *Proc. Natl. Acad. Sci.*, *100*(23), 13158–13161, doi:10.1073/pnas.2134014100.

Milly, P. C. D., et al., 2010: Terrestrial water-storage contributions to sea-level rise and variability. In: Understanding Sea-Level Rise and Variability [J. A. Church, P. L. Woodworth, T. Aarup and W. S. Wilson (eds.)]. Wiley-Blackwell, Hoboken, NJ, USA, pp. 226–255.

Milne, G. A., W. R. Gehrels, C. W. Hughes, and M. E. Tamisiea (2009), Identifying the causes of sea-level change, *Nat. Geosci.*, *2*(7), 471–478, doi:10.1038/ngeo544.

Mimura N., Nurse L., McLean R.F., Agard J., Briguglio L, Lefale P., et al., 2007, Small islands. Climate Change, 2007: Impacts, Adaptation and Vulnerability. Contribution of Working Group II to the Fourth Assessment Report of the Intergovernmental Panel on Climate Change, M.L. Parry, O.F. Canziani, J.P. Palutikof, P.J. van der Linden and C.E. Hanson, Eds., Cambridge University Press, Cambridge, UK, 687-716.

Minobe, S. (1997), A 50–70 year climatic oscillation over the North Pacific and North America, *Geophys. Res. Lett.*, *24*(6), 683–686, doi:10.1029/97GL00504.

Mitchum, G. T., R. S. Nerem, M. A. Merrifield, andW. R. Gehrels (2010), Modern sea level change estimates, in *Understanding Sea-Level Rise and Variability*, edited by J. A. Church, P. L. Woodworth, T. Aarup, and W. S. Wilson, pp. 122–142, Wiley-Blackwell.

Mitrovica, J. X., M. E. Tamisiea, J. L. Davis, and G. A. Milne (2001), Recent mass balance of polar ice sheets inferred from patterns of global sea-level change, *Nature*, *409*(6823), 1026–1029, doi:10.1038/35059054.

Morison, J., R. Kwok, C. Peralta-Ferriz, M. Alkire, I. Rigor, R. Andersen, and M. Steele (2012), Changing Arctic Ocean freshwater pathways, *Nature*, *481*(7379), 66–70, doi:10.1038/nature10705.

Morton, R. A., J. C. Bernier, and J. A. Barras (2006), Evidence of regional subsidence and associated interior wetland loss induced by hydrocarbon production, Gulf Coast region, USA, *Environ. Geol.*, *50*(2), 261–274, doi:10.1007/s00254-006-0207-3.

Myhre, G., D. Shindell, F.-M. Bréon, W. Collins, J. Fuglestvedt, J. Huang, D. Koch, J.-F. Lamarque, D. Lee, B. Mendoza, T. Nakajima, A. Robock, G. Stephens, T. Takemura and H. Zhang, 2013: Anthropogenic and Natural Radiative Forcing. In: Climate Change 2013: The Physical Science Basis. Contribution of Working Group I to the Fifth Assessment Report of the Intergovernmental Panel on Climate Change [Stocker, T.F., D. Qin, G.-K. Plattner, M. Tignor, S.K. Allen, J. Boschung, A. Nauels, Y. Xia, V. Bex and P.M. Midgley (eds.)]. Cambridge University Press, Cambridge, United Kingdom and New York, NY, USA.

National Research Council (NRC) (1998): Decade-to-Century Scale Climate Variability and Change: A Science Strategy. National Academy Press, Washington, D.C., 141 pp. (http://www.nap.edu).

Nerem, R. S., D. P. Chambers, C. Choe, and G. T. Mitchum (2010), Estimating Mean Sea Level Change from the TOPEX and Jason Altimeter Missions, *Mar. Geod.*, *33*, 435–446, doi:10.1080/01490419.2010.491031.

Ngo-Duc, T., K. Laval, J. Polcher, A. Lombard, and A. Cazenave (2005), Effects of land water storage on global mean sea level over the past half century, *Geophys. Res. Lett.*, *32*(9), L09704, doi:10.1029/2005GL022719.

Nicholls, R. (2011), Planning for the Impacts of Sea Level Rise, *Oceanography*, *24*(2), 144–157, doi:10.5670/oceanog.2011.34.

Nicholls, R. J. (2010), Impacts of and responses to Sea-Level rise, in *Understanding Sea-Level Rise and Variability*, edited by J. A. Church, P. L. Woodworth, T. Aarup, and W. S. Wilson, pp. 17–51, Wiley-Blackwell.

Nicholls, R. J., and A. Cazenave (2010), Sea-Level Rise and Its Impact on Coastal Zones, *Science*, *328*(5985), 1517–1520, doi:10.1126/science.1185782.

Nicholls, R. J., N. Marinova, J. A. Lowe, S. Brown, P. Vellinga, D. de Gusmão, J. Hinkel, and R. S. J. Tol (2011), Sea-level rise and its possible impacts given a "beyond 4°C world" in the twenty-first century, *Philos. Trans. R. Soc. Lond. Math. Phys. Eng. Sci.*, *369*(1934), 161–181, doi:10.1098/rsta.2010.0291.

Nicholls, R. J., S. Hanson, C. Herweijer, N. Patmore, S. Hallegatte, J. Corfee-Morlot, J. Château, and R. Muir-Wood (2008), *Ranking Port Cities with High Exposure and Vulnerability to Climate Extremes*, OECD Environment Working Papers, Organisation for Economic Co-operation and Development, Paris.

Nicholls, R.J., P.P. Wong, V.R. Burkett, J.O. Codignotto, J.E. Hay, R.F. McLean, S. Ragoonaden and C.D. Woodroffe, 2007: Coastal systems and low-lying areas. Climate Change 2007: Impacts, Adaptation and Vulnerability. Contribution of Working Group II to the Fourth Assessment Report of the Intergovernmental Panel on Climate Change, M.L. Parry, O.F. Canziani, J.P. Palutikof, P.J. van der Linden and C.E. Hanson, Eds., Cambridge University Press, Cambridge, UK, 315-356.

Nidheesh, A. G., M. Lengaigne, J. Vialard, A. S. Unnikrishnan, and H. Dayan (2013), Decadal and long-term sea level variability in the tropical Indo-Pacific Ocean, *Clim. Dyn.*, *41*(2), 381–402, doi:10.1007/s00382-012-1463-4.

Okumura, Y. M., C. Deser, A. Hu, A. Timmermann, and S.-P. Xie (2009), North Pacific Climate Response to Freshwater Forcing in the Subarctic North Atlantic: Oceanic and Atmospheric Pathways, *J. Clim.*, *22*(6), 1424–1445, doi:10.1175/2008JCLI2511.1.

Palanisamy, H., A. Cazenave, B. Meyssignac, L. Soudarin, G. Wöppelmann, and M. Becker (2014), Regional sea level variability, total relative sea level rise and its impacts on islands and coastal zones of Indian Ocean over the last sixty years, *Glob. Planet. Change*, *116*, 54–67, doi:10.1016/j.gloplacha.2014.02.001.

Palanisamy, H., A. Cazenave, O. Henry, P. Prandi, and B. Meyssignac (2015a), Sea Level Variations Measured by the New Altimetry Mission SARAL-AltiKa and its Validation Based on Spatial Patterns and Temporal Curves Using Jason-2, Tide Gauge Data and an Overview of the Annual Sea Level Budget, *Mar. Geod.*, *0*(ja), 00–00, doi:10.1080/01490419.2014.1000469.

Palanisamy, H., A. Cazenave, T. Delcroix, and B. Meyssignac (2015b), Spatial trend patterns in the Pacific Ocean sea level during the altimetry era: the contribution of thermocline depth change and internal climate variability, *Ocean Dyn.*, 1–16, doi:10.1007/s10236-014-0805-7.

Palanisamy, H., B. Meyssignac, A. Cazenave, and T. Delcroix (2015c), Is anthropogenic sea level fingerprint already detectable in the Pacific Ocean?, *Environ. Res. Lett.*, *10*(8), 084024, doi:10.1088/1748-9326/10/8/084024.

Palanisamy, H., M. Becker, B. Meyssignac, O. Henry, and A. Cazenave (2012), Regional sea level change and variability in the Caribbean sea since 1950, *J. Geod. Sci.*, *2*(2), 125–133.

Pardaens, A. K., J. A. Lowe, S. Brown, R. J. Nicholls, and D. de Gusmão (2011), Sea-level rise and impacts projections under a future scenario with large greenhouse gas emission reductions, *Geophys. Res. Lett.*, *38*(12), L12604, doi:10.1029/2011GL047678.

Peltier, W. R. (2004), Global glacial isostasy and the surface of the ice-age earth: the ice-5g (vm2) model and grace, *Annu. Rev. Earth Planet. Sci.*, *32*(1), 111–149, doi:10.1146/annurev.earth.32.082503.144359.

Peltier, W. R. (2009), Closure of the budget of global sea level rise over the GRACE era: the importance and magnitudes of the required corrections for global glacial isostatic adjustment, *Quat. Sci. Rev.*, *28*(17–18), 1658–1674, doi:10.1016/j.quascirev.2009.04.004.

Penduff, T., M. Juza, L. Brodeau, G. C. Smith, B. Barnier, J.-M. Molines, A.-M. Treguier, and G. Madec (2010), Impact of global ocean model resolution on sea-level variability with emphasis on interannual time scales, *Ocean Sci.*, *6*(1), 269–284, doi:10.5194/os-6-269-2010.

Peng, D., H. Palanisamy, A. Cazenave, and B. Meyssignac (2013), Interannual Sea Level Variations in the South China Sea Over 1950–2009, *Mar. Geod.*, *36*(2), 164–182, doi:10.1080/01490419.2013.771595.

Peters, G. P., G. Marland, C. Le Quéré, T. Boden, J. G. Canadell, and M. R. Raupach (2012), Rapid growth in CO2 emissions after the 2008-2009 global financial crisis, *Nat. Clim. Change*, *2*(1), 2–4, doi:10.1038/nclimate1332.

Philander, S.G. (2012), Encyclopedia of Global Warming and Climate Change, Second Edition, Sage Publications.

Pielke A.J., Rubiera J., Landsea C., Fernandez M.L. and Klein R., 2003, Hurricane Vulnerability in Latin America and the Caribbean: Normalized Damage and Loss Potentials. Nat. Haz. Rev., 4, 3, DOI: 10.1061/(ASCE)1527- 6988(2003)4:3(101).

Pierce, D. W. (2001), Distinguishing coupled ocean-atmosphere interactions from background noise in the North Pacific, *Prog. Oceanogr.*, *49*(1), 331–352, doi:10.1016/S0079-6611(01)00029-5.

Pierce, D. W., P. J. Gleckler, T. P. Barnett, B. D. Santer, and P. J. Durack (2012), The fingerprint of human-induced changes in the ocean's salinity and temperature fields, *Geophys. Res. Lett.*, *39*(21), L21704, doi:10.1029/2012GL053389.

Pokhrel, Y. N., N. Hanasaki, P. J.-F. Yeh, T. J. Yamada, S. Kanae, and T. Oki (2012), Model estimates of sea-level change due to anthropogenic impacts on terrestrial water storage, *Nat. Geosci.*, *5*(6), 389–392, doi:10.1038/ngeo1476.

Ponte, R. M., and P. Gaspar (1999), Regional analysis of the inverted barometer effect over the global ocean using TOPEX/POSEIDON data and model results, *J. Geophys. Res. Oceans*, *104*(C7), 15587–15601, doi:10.1029/1999JC900113.

Power, S., F. Delage, C. Chung, G. Kociuba, and K. Keay (2013), Robust twenty-first-century projections of El Nino and related precipitation variability, *Nature*, *502*(7472), 541–545, doi:10.1038/nature12580.

Power, S., M. Haylock, R. Colman, and X. Wang (2006), The Predictability of Interdecadal Changes in ENSO Activity and ENSO Teleconnections, *J. Clim.*, *19*(19), 4755–4771, doi:10.1175/JCLI3868.1.

Preisendorfer, R.W., 1988. Principal component analysis in meteorology and oceanography. Developments in Atmospheric Science, vol. 17. Elsevier (425 pp.).

Purkey, S. G., and G. C. Johnson (2010), Warming of Global Abyssal and Deep Southern Ocean Waters between the 1990s and 2000s: Contributions to Global Heat and Sea Level Rise Budgets*, *J. Clim.*, *23*(23), 6336–6351, doi:10.1175/2010JCLI3682.1.

Purkey, S. G., G. C. Johnson, and D. P. Chambers (2014), Relative contributions of ocean mass and deep steric changes to sea level rise between 1993 and 2013, *J. Geophys. Res. Oceans*, *119*(11), 7509–7522, doi:10.1002/2014JC010180.

Ray, R. D. (1999), A Global Ocean Tide Model From TOPEX/POSEIDON Altimetry: GOT99.2,

Ray, R. D., and B. C. Douglas (2011), Experiments in reconstructing twentieth-century sea levels, *Prog. Oceanogr.*, *91*(4), 496–515, doi:10.1016/j.pocean.2011.07.021.

Reason, C. J. C., R. J. Allan, J. A. Lindesay, and T. J. Ansell (2000), ENSO and climatic signals across the Indian Ocean Basin in the global context: part I, interannual composite patterns, *Int. J. Climatol.*, *20*(11), 1285–1327, doi:10.1002/1097-0088(200009)20:11<1285::AID-JOC536>3.0.CO;2-R.

Ribes, A., J.-M. Azaïs, and S. Planton (2009), A method for regional climate change detection using smooth temporal patterns, *Clim. Dyn.*, *35*(2-3), 391–406, doi:10.1007/s00382-009-0670-0.

Richter, K., and B. Marzeion (2014), Earliest local emergence of forced dynamic and steric sea-level trends in climate models, *Environ. Res. Lett.*, *9*(11), 114009, doi:10.1088/1748-9326/9/11/114009.

Rignot, E., J. E. Box, E. Burgess, and E. Hanna (2008), Mass balance of the Greenland ice sheet from 1958 to 2007, *Geophys. Res. Lett.*, *35*(20), L20502, doi:10.1029/2008GL035417.

Ripesi, P., F. Ciciulla, F. Maimone, and V. Pelino (2012), The February 2010 Arctic Oscillation Index and its stratospheric connection, *Q. J. R. Meteorol. Soc.*, *138*(669), 1961–1969, doi:10.1002/qj.1935.

Riva, R. E. M., J. L. Bamber, D. A. Lavallée, and B. Wouters (2010), Sea-level fingerprint of continental water and ice mass change from GRACE, *Geophys. Res. Lett.*, *37*(19), L19605, doi:10.1029/2010GL044770.

Rogers, J. C., and H. Van Loon (1979), The Seesaw in Winter Temperatures between Greenland and Northern Europe. Part II: Some Oceanic and Atmospheric Effects in Middle and High Latitudes, *Mon. Weather Rev.*, *107*(5), 509–519, doi:10.1175/1520-0493(1979)107<0509:TSIWTB>2.0.CO;2.

Rohling, E. J., K. Grant, M. Bolshaw, A. P. Roberts, M. Siddall, C. Hemleben, and M. Kucera (2009), Antarctic temperature and global sea level closely coupled over the past five glacial cycles, *Nat. Geosci.*, *2*(7), 500–504, doi:10.1038/ngeo557.

Saji, N. H., B. N. Goswami, P. N. Vinayachandran, and T. Yamagata (1999), A dipole mode in the tropical Indian Ocean, *Nature*, *401*(6751), 360–363, doi:10.1038/43854.

Saji, N., and T. Yamagata (2003), Possible impacts of Indian Ocean Dipole mode events on global climate, *Clim. Res.*, *25*, 151–169, doi:10.3354/cr025151.

Santamaría-Gómez, A., M. Gravelle, X. Collilieux, M. Guichard, B. M. Míguez, P. Tiphaneau, and G. Wöppelmann (2012), Mitigating the effects of vertical land motion in tide gauge records using a state-of-the-art GPS velocity field, *Glob. Planet. Change*, *98–99*, 6–17, doi:10.1016/j.gloplacha.2012.07.007.

Schneider, D. P., C. M. Ammann, B. L. Otto-Bliesner, and D. S. Kaufman (2009), Climate response to large, high-latitude and low-latitude volcanic eruptions in the Community Climate System Model, *J. Geophys. Res. Atmospheres*, *114*(D15), D15101, doi:10.1029/2008JD011222.

Schneider, N., and B. D. Cornuelle (2005), The Forcing of the Pacific Decadal Oscillation*, *J. Clim.*, *18*(21), 4355–4373, doi:10.1175/JCLI3527.1.

Shepherd, A. et al. (2012), A Reconciled Estimate of Ice-Sheet Mass Balance, *Science*, *338*(6111), 1183–1189, doi:10.1126/science.1228102.

Slangen, A. B. A., C. A. Katsman, R. S. W. van de Wal, L. L. A. Vermeersen, and R. E. M. Riva (2011), Towards regional projections of twenty-first century sea-level change based on IPCC SRES scenarios, *Clim. Dyn.*, *38*(5-6), 1191–1209, doi:10.1007/s00382-011-1057-6.

Slangen, A. B. A., J. A. Church, X. Zhang, and D. Monselesan (2014), Detection and attribution of global mean thermosteric sea level change, *Geophys. Res. Lett.*, n/a–n/a, doi:10.1002/2014GL061356.

Smith, D. (2013), Oceanography: Has global warming stalled?, *Nat. Clim. Change*, *3*(7), 618–619, doi:10.1038/nclimate1938.

Solomon, S., D. Qin, M. Manning, Z. Chen, M. Marquis, K. Averyt, M. Tignor, and H. Miller (Eds.), *Contribution of Working Group I to the Fourth Assessment Report of the Intergovernmental Panel on Climate Change, 2007*, Cambridge University Press, Cambridge, United Kingdom and New York, NY, USA, 2007.

Solomon, S., K. H. Rosenlof, R. W. Portmann, J. S. Daniel, S. M. Davis, T. J. Sanford, and G.-K. Plattner (2010), Contributions of Stratospheric Water Vapor to Decadal Changes in the Rate of Global Warming, *Science*, *327*(5970), 1219–1223, doi:10.1126/science.1182488.

Spada, G., J. L. Bamber, and R. T. W. L. Hurkmans (2013), The gravitationally consistent sea-level fingerprint of future terrestrial ice loss, *Geophys. Res. Lett.*, *40*(3), 482–486, doi:10.1029/2012GL053000.

Sreenivas, P., C. Gnanaseelan, and K. V. S. R. Prasad (2012), Influence of El Niño and Indian Ocean Dipole on sea level variability in the Bay of Bengal, *Glob. Planet. Change*, *80–81*, 215–225, doi:10.1016/j.gloplacha.2011.11.001.

Stammer, D. (2008), Response of the global ocean to Greenland and Antarctic ice melting, *J. Geophys. Res. Oceans*, *113*(C6), C06022, doi:10.1029/2006JC004079.

Stammer, D., A. Cazenave, R. M. Ponte, and M. E. Tamisiea (2013), Causes for contemporary regional sea level changes., *Annu. Rev. Mar. Sci.*, *5*, doi:10.1146/annurev-marine-121211-172406.

Stammer, D., A. Cazenave, R. M. Ponte, and M. E. Tamisiea (2013), Causes for contemporary regional sea level changes., *Annu. Rev. Mar. Sci.*, *5*, doi:10.1146/annurev-marine-121211-172406.

Stammer, D., N. Agarwal, P. Herrmann, A. Köhl, and C. R. Mechoso (2011), Response of a Coupled Ocean–Atmosphere Model to Greenland Ice Melting, *Surv. Geophys.*, *32*(4-5), 621–642, doi:10.1007/s10712-011-9142-2.

Swenson, M. S., and D. V. Hansen (1999), Tropical Pacific Ocean Mixed Layer Heat Budget: The Pacific Cold Tongue, *J. Phys. Oceanogr.*, *29*(1), 69–81, doi:10.1175/1520-0485(1999)029<0069:TPOMLH>2.0.CO;2.

Tamisiea, M. E., E. M. Hill, R. M. Ponte, J. L. Davis, I. Velicogna, and N. T. Vinogradova (2010), Impact of self-attraction and loading on the annual cycle in sea level, *J. Geophys. Res. Oceans*, *115*(C7), C07004, doi:10.1029/2009JC005687.

Tamisiea, M.E., and J.X. Mitrovica. 2011. The moving boundaries of sea level change: Understanding the origins of geographic variability. *Oceanography* 24(2):24–39, http://dx.doi.org/10.5670/oceanog.2011.25.

Tamisiea, M.E., and J.X. Mitrovica. 2011. The moving boundaries of sea level change: Understanding the origins of geographic variability. *Oceanography* 24(2):24–39, http://dx.doi.org/10.5670/oceanog.2011.25.

Terray, L., L. Corre, S. Cravatte, T. Delcroix, G. Reverdin, and A. Ribes (2012), Near-Surface Salinity as Nature's Rain Gauge to Detect Human Influence on the Tropical Water Cycle, *J. Clim.*, *25*(3), 958–977, doi:10.1175/JCLI-D-10-05025.1.

Thompson, D. W. J., and J. M. Wallace (1998), The Arctic oscillation signature in the wintertime geopotential height and temperature fields, *Geophys. Res. Lett.*, *25*(9), 1297–1300, doi:10.1029/98GL00950.

Timmermann, A., S. McGregor, and F.-F. Jin (2010), Wind Effects on Past and Future Regional Sea Level Trends in the Southern Indo-Pacific*, *J. Clim.*, *23*(16), 4429–4437, doi:10.1175/2010JCLI3519.1.

Törnqvist, T. E., D. J. Wallace, J. E. A. Storms, J. Wallinga, R. L. van Dam, M. Blaauw, M. S. Derksen, C. J. W. Klerks, C. Meijneken, and E. M. A. Snijders (2008), Mississippi Delta subsidence primarily caused by compaction of Holocene strata, *Nat. Geosci.*, *1*(3), 173–176, doi:10.1038/ngeo129.

Torres, R. R., and M. N. Tsimplis (2013), Sea-level trends and interannual variability in the Caribbean Sea, *J. Geophys. Res. Oceans*, *118*(6), 2934–2947, doi:10.1002/jgrc.20229.

Toumazou, V., Cretaux, J.F., 2001. Using a Lanczos eigensolver in the computation of empirical orthogonal functions. Mon. Weather Rev. 129, 1243–1250.

Tran, N., D. Vandemark, B. Chapron, S. Labroue, H. Feng, B. Beckley, and P. Vincent (2006), New models for satellite altimeter sea state bias correction developed using global wave model data, *J. Geophys. Res. Oceans*, *111*(C9), C09009, doi:10.1029/2005JC003406.

Trenberth, K. E., and J. T. Fasullo (2013), An apparent hiatus in global warming?, *Earths Future*, *1*(1), 19–32, doi:10.1002/2013EF000165.

Trenberth, K. E., J. T. Fasullo, and M. A. Balmaseda (2014), Earth's Energy Imbalance, *J. Clim.*, *27*(9), 3129–3144, doi:10.1175/JCLI-D-13-00294.1.

Tsimplis, M. N., A. G. P. Shaw, R. A. Flather, and D. K. Woolf (2006), The influence of the North Atlantic Oscillation on the sea-level around the northern European coasts reconsidered: the thermosteric effects, *Philos. Trans. R. Soc. Lond. Math. Phys. Eng. Sci.*, *364*(1841), 845–856, doi:10.1098/rsta.2006.1740.

Tsimplis, M. N., and S. A. Josey (2001), Forcing of the Mediterranean Sea by atmospheric oscillations over the North Atlantic, *Geophys. Res. Lett.*, *28*(5), 803–806, doi:10.1029/2000GL012098.

Unnikrishnan, A. S., and D. Shankar (2007), Are sea-level-rise trends along the coasts of the north Indian Ocean consistent with global estimates?, *Glob. Planet. Change*, *57*(3–4), 301–307, doi:10.1016/j.gloplacha.2006.11.029.

van Loon, H., and J. C. Rogers (1978), The Seesaw in Winter Temperatures between Greenland and Northern Europe. Part I: General Description, *Mon. Weather Rev.*, *106*(3), 296–310, doi:10.1175/1520-0493(1978)106<0296:TSIWTB>2.0.CO;2.

Vaughan, D.G., J.C. Comiso, I. Allison, J. Carrasco, G. Kaser, R. Kwok, P. Mote, T. Murray, F. Paul, J. Ren, E. Rignot, O. Solomina, K. Steffen and T. Zhang, 2013: Observations: Cryosphere. In: Climate Change 2013: The Physical Science Basis. Contribution of Working Group I to the Fifth Assessment Report of the Intergovernmental Panel on Climate Change [Stocker, T.F., D. Qin, G.-K. Plattner, M. Tignor, S.K. Allen, J. Boschung, A. Nauels, Y. Xia, V. Bex and P.M. Midgley (eds.)]. Cambridge University Press, Cambridge, United Kingdom and New York, NY, USA.

Velicogna, I. (2009), Increasing rates of ice mass loss from the Greenland and Antarctic ice sheets revealed by GRACE, *Geophys. Res. Lett.*, *36*(19), L19503, doi:10.1029/2009GL040222.

Venegas, S. A. (2003), The Antarctic Circumpolar Wave: A Combination of Two Signals?, *J. Clim.*, *16*(15), 2509–2525, doi:10.1175/1520-0442(2003)016<2509:TACWAC>2.0.CO;2.

Verdon, D. C., and S. W. Franks (2006), Long-term behaviour of ENSO: Interactions with the PDO over the past 400 years inferred from paleoclimate records, *Geophys. Res. Lett.*, *33*(6), L06712, doi:10.1029/2005GL025052.

Verron, J. et al. (2015), The SARAL/AltiKa Altimetry Satellite Mission, *Mar. Geod.*, *0*(ja), 00–00, doi:10.1080/01490419.2014.1000471.

von Schuckmann, K., and P.-Y. Le Traon (2011), How well can we derive Global Ocean Indicators from Argo data?, *Ocean Sci*, *7*(6), 783–791, doi:10.5194/os-7-783-2011.

von Schuckmann, K., F. Gaillard, and P.-Y. Le Traon (2009), Global hydrographic variability patterns during 2003–2008, *J. Geophys. Res. Oceans*, *114*(C9), C09007, doi:10.1029/2008JC005237.

von Schuckmann, K., J.-B. Sallée, D. Chambers, P. Y. Le Traon, C. Cabanes, F. Gaillard, S. Speich, and M. Hamon (2014), Consistency of the current global ocean observing systems from an Argo perspective, *Ocean Sci.*, *10*(3), 547–557, doi:10.5194/os-10-547-2014.

Wada, Y., L. P. H. van Beek, F. C. Sperna Weiland, B. F. Chao, Y.-H. Wu, and M. F. P. Bierkens (2012), Past and future contribution of global groundwater depletion to sea-level rise, *Geophys. Res. Lett.*, *39*(9), L09402, doi:10.1029/2012GL051230.

Wahr, J. M. (1985), Deformation induced by polar motion, , doi:10.1029/JB090iB11p09363.

Wakelin, S. L., P. L. Woodworth, R. A. Flather, and J. A. Williams (2003), Sea-level dependence on the NAO over the NW European Continental Shelf, *Geophys. Res. Lett.*, *30*(7), 1403, doi:10.1029/2003GL017041.

Walker, G. T. (1928). World weather, III, *Memoirs of India Meteorological Department*, 2, 97-106.

Walker, G. T., and Bliss, E. W. (1930). World weather, IV, *Memoirs of Royal Meteorological Society*, **3**, 81-95.

Walker, G.T. and Bliss, E.W., (1932). World Weather V**,***Memoirs of the Royal Meteorological Society,*4, (36)**,**53-84.

Watanabe, M., Y. Kamae, M. Yoshimori, A. Oka, M. Sato, M. Ishii, T. Mochizuki, and M. Kimoto (2013), Strengthening of ocean heat uptake efficiency associated with the recent climate hiatus, *Geophys. Res. Lett.*, *40*(12), 3175–3179, doi:10.1002/grl.50541.

White, W. B., S.-C. Chen, and R. G. Peterson (1998), The Antarctic Circumpolar Wave: A Beta Effect in Ocean–Atmosphere Coupling over the Southern Ocean, *J. Phys. Oceanogr.*, *28*(12), 2345–2361, doi:10.1175/1520-0485(1998)028<2345:TACWAB>2.0.CO;2.

Wigley, T. M. L. (2005), The Climate Change Commitment, *Science*, *307*(5716), 1766–1769, doi:10.1126/science.1103934.

Willis, P., C. Boucher, H. Fagard, B. Garayt, and M.-L. Gobinddass (2010), Contributions of the French Institut Géographique National (IGN) to the International DORIS Service, *Adv. Space Res.*, *45*(12), 1470–1480, doi:10.1016/j.asr.2009.09.019.

Woodroffe, C. D. (2005), Late Quaternary sea-level highstands in the central and eastern Indian Ocean: A review, *Glob. Planet. Change*, *49*(1–2), 121–138, doi:10.1016/j.gloplacha.2005.06.002.

Woodworth, P. L. (2005), Have there been large recent sea level changes in the Maldive Islands?, *Glob. Planet. Change*, *49*(1-2), 1–18, doi:10.1016/j.gloplacha.2005.04.001.

Woodworth, P. L., M. Menéndez, and W. R. Gehrels (2011), Evidence for Century-Timescale Acceleration in Mean Sea Levels and for Recent Changes in Extreme Sea Levels, *Surv. Geophys.*, *32*(4-5), 603–618, doi:10.1007/s10712-011-9112-8.

Woolf, D. K., A. G. P. Shaw, and M. N. Tsimplis (2003), The influence of the North Atlantic Oscillation on sea-level variability in the North Atlantic region, *J. Atmospheric Ocean Sci.*, *9*(4), 145–167, doi:10.1080/10236730310001633803.

Wöppelmann, G., and M. Marcos (2012), Coastal sea level rise in southern Europe and the nonclimate contribution of vertical land motion, *J. Geophys. Res. Oceans*, *117*(C1), C01007, doi:10.1029/2011JC007469.

Wöppelmann, G., B. Martin Miguez, M.-N. Bouin, and Z. Altamimi (2007), Geocentric sea-level trend estimates from GPS analyses at relevant tide gauges world-wide, *Glob. Planet. Change*, *57*(3–4), 396–406, doi:10.1016/j.gloplacha.2007.02.002.

Wöppelmann, G., C. Letetrel, A. Santamaria, M.-N. Bouin, X. Collilieux, Z. Altamimi, S. D. P. Williams, and B. M. Miguez (2009), Rates of sea-level change over the past century in a geocentric reference frame, *Geophys. Res. Lett.*, *36*(12), L12607, doi:10.1029/2009GL038720.

Wunsch, C., and D. Stammer (1997), Atmospheric loading and the oceanic "inverted barometer" effect, *Rev. Geophys.*, *35*(1), 79–107, doi:10.1029/96RG03037.

Wunsch, C., R. M. Ponte, and P. Heimbach (2007), Decadal Trends in Sea Level Patterns: 1993–2004, *J. Clim.*, *20*(24), 5889–5911, doi:10.1175/2007JCLI1840.1.

Wyrtki K, Kendall R (1967) Transports of the Pacific equatorial countercurrent. J Geophys Res 72(8):2073–2076

Yasunaka, S., and K. Hanawa (2003), Regime Shifts in the Northern Hemisphere SST Field: Revisited in Relation to Tropical Variations, *J. Meteorol. Soc. Jpn. Ser II*, *81*(2), 415–424, doi:10.2151/jmsj.81.415.

Yeh, S.-W., J.-S. Kug, B. Dewitte, M.-H. Kwon, B. P. Kirtman, and F.-F. Jin (2009), El Niño in a changing climate, *Nature*, *461*(7263), 511–514, doi:10.1038/nature08316.

Yin, J., S. M. Griffies, and R. J. Stouffer (2010), Spatial Variability of Sea Level Rise in Twenty-First Century Projections, *J. Clim.*, *23*(17), 4585–4607, doi:10.1175/2010JCLI3533.1.

Yip, S., C. A. T. Ferro, D. B. Stephenson, and E. Hawkins (2011), A Simple, Coherent Framework for Partitioning Uncertainty in Climate Predictions, *J. Clim.*, *24*(17), 4634–4643, doi:10.1175/2011JCLI4085.1.

Zhang, X., and J. A. Church (2012), Sea level trends, interannual and decadal variability in the Pacific Ocean, *Geophys. Res. Lett.*, *39*, doi:10.1029/2012GL053240.

Zhang, Y., J. M. Wallace, and D. S. Battisti (1997), ENSO-like Interdecadal Variability: 1900–93, *J. Clim.*, *10*(5), 1004–1020, doi:10.1175/1520-0442(1997)010<1004:ELIV>2.0.CO;2.

Appendix A: List of publications

Palanisamy, H., M. Becker, B. Meyssignac, O. Henry, and A. Cazenave (2012), Regional sea level change and variability in the Caribbean sea since 1950, *J. Geod. Sci.*, *2*(2), 125–133.

Munier, S., **H. Palanisamy**, P. Maisongrande, A. Cazenave, and E. F. Wood (2012), Global runoff anomalies over 1993–2009 estimated from coupled Land–Ocean–Atmosphere water budgets and its relation with climate variability, *Hydrol Earth Syst Sci*, *16*(10), 3647–3658, doi:10.5194/hess-16-3647-2012.

Cazenave, A., O. Henry, S. Munier, T. Delcroix, A. L. Gordon, B. Meyssignac, W. Llovel, **H. Palanisamy**, and M. Becker (2012), Estimating ENSO Influence on the Global Mean Sea Level, 1993–2010, *Mar. Geod.*, *35*(sup1), 82–97, doi:10.1080/01490419.2012.718209.

Cazenave A., Dieng H.B., Munier S., Henry O., Meyssignac B., **Palanisamy H.**, Llovel W, 2012, L'influence d'El Niño et de La Niña sur le niveau de la mer. La Météorologie - n° 79.

Peng, D., **H. Palanisamy**, A. Cazenave, and B. Meyssignac (2013), Interannual Sea Level Variations in the South China Sea Over 1950–2009, *Mar. Geod.*, *36*(2), 164–182, doi:10.1080/01490419.2013.771595.

Palanisamy, H., A. Cazenave, B. Meyssignac, L. Soudarin, G. Wöppelmann, and M. Becker (2014), Regional sea level variability, total relative sea level rise and its impacts on islands and coastal zones of Indian Ocean over the last sixty years, *Glob. Planet. Change*, *116*, 54–67, doi:10.1016/j.gloplacha.2014.02.001.

Dieng, H. B., A. Cazenave, B. Meyssignac, O. Henry, K. von Schuckmann, **H. Palanisamy**, and J. M. Lemoine (2014), Effect of La Niña on The Global Mean Sea Level And North Pacifc Ocean Mass Over 2005-2011, *J. Geod. Sci.*, *4*(1).

Bulteau, T., A. Baills, L. Petitjean, M. Garcin, **H. Palanisamy**, and G. Le Cozannet (2015), Gaining insight into regional coastal changes on La Réunion island through a Bayesian data mining approach, *Geomorphology*, *228*, 134–146, doi:10.1016/j.geomorph.2014.09.002.

Palanisamy, H., A. Cazenave, O. Henry, P. Prandi, and B. Meyssignac (2015a), Sea Level Variations Measured by the New Altimetry Mission SARAL-AltiKa and its Validation Based on Spatial Patterns and Temporal Curves Using Jason-2, Tide Gauge Data and an

Overview of the Annual Sea Level Budget, *Mar. Geod.*, *0*(ja), 00–00, doi:10.1080/01490419.2014.1000469.

Palanisamy, H., A. Cazenave, T. Delcroix, and B. Meyssignac (2015b), Spatial trend patterns in the Pacific Ocean sea level during the altimetry era: the contribution of thermocline depth change and internal climate variability, *Ocean Dyn.*, 1–16, doi:10.1007/s10236-014-0805-7.

Palanisamy, H., B. Meyssignac, A. Cazenave, and T. Delcroix (2015c), Is anthropogenic sea level fingerprint already detectable in the Pacific Ocean?, *Environ. Res. Lett.*, *10*(8), 084024, doi:10.1088/1748-9326/10/8/084024.

Dieng, H. B., **H. Palanisamy**, A. Cazenave, B. Meyssignac, and K. von Schuckmann (2015), The Sea Level Budget Since 2003: Inference on the Deep Ocean Heat Content, *Surv. Geophys.*, *36*(2), 209–229, doi:10.1007/s10712-015-9314-6.

Appendix B: List of publications not included in the context of the manuscript

In this appendix, we have attached five co-authored publications worked on during the course of the Ph.D. but have not been a part of the Ph.D. framework.

Hydrol. Earth Syst. Sci., 16, 3647–3658, 2012
www.hydrol-earth-syst-sci.net/16/3647/2012/
doi:10.5194/hess-16-3647-2012

Hydrology and Earth System Sciences

Global runoff anomalies over 1993–2009 estimated from coupled Land–Ocean–Atmosphere water budgets and its relation with climate variability

S. Munier[1], **H. Palanisamy**[1], **P. Maisongrande**[1], **A. Cazenave**[1], **and E. F. Wood**[2]

[1]Laboratoire d'études en géophysique et océanographie spatiales, UMR5566, LEGOS/CNES/CNRS/IRD/UPS, Toulouse, France
[2]Department of Civil and Environmental Engineering, Princeton University, Princeton, NJ, USA

Correspondence to: S. Munier (simon.munier@gmail.com)

Received: 14 March 2012 – Published in Hydrol. Earth Syst. Sci. Discuss.: 11 April 2012
Revised: 3 August 2012 – Accepted: 13 September 2012 – Published: 16 October 2012

Abstract. Whether the global runoff (or freshwater discharge from land to the ocean) is currently increasing and the global water cycle is intensifying is still a controversial issue. Here we compute land–atmosphere and ocean–atmosphere water budgets and derive two independent estimates of the global runoff over the period 1993–2009. Water storage variations in the land, ocean and atmosphere reservoirs are estimated from different types of data sets: atmospheric reanalyses, land surface models, satellite altimetry and in situ ocean temperature data (the difference between altimetry based global mean sea level and ocean thermal expansion providing an estimate of the ocean mass component). These data sets are first validated using independent data, and then the global runoff is computed from the two methods. Results for the global runoff show a very good correlation between both estimates. More importantly, no significant trend is observed over the whole period. Besides, the global runoff appears to be clearly impacted by large-scale climate phenomena such as major ENSO events. To infer this, we compute the zonal runoff over four latitudinal bands and set up for each band a new index (combined runoff index) obtained by optimization of linear combinations of various climate indices. Results show that, in particular, the intertropical and northern mid-latitude runoffs are mainly driven by ENSO and the Atlantic multidecadal oscillation (AMO) with opposite behavior. Indeed, the zonal runoff in the intertropical zone decreases during major El Niño events, whereas it increases in the northern mid-latitudes, suggesting that water masses over land are shifted northward/southward during El Niño/La Niña. In addition to this study, we propose an innovative method to estimate the global ocean thermal expansion. The method is based on the assumption that the difference between both runoff estimates is mainly due to the thermal expansion term not accounted for in the estimation of the ocean mass. We find that our reconstructed thermal expansion time series compares well with two existing data sets in terms of year-to-year fluctuations but somewhat differs on longer (multi-year) time scales. Possible explanations include non negligible steric variations from the deep ocean.

1 Introduction

Continental waters are continuously exchanged with atmosphere and oceans through vertical and horizontal mass fluxes (precipitation, evaporation, transpiration of the vegetation, surface runoff and underground flow). Freshwater discharge from land to ocean (or global runoff) is a key component of the global water cycle. Its variability reflects the continental hydrological dynamics and is then impacted by climate change (e.g. intensification of precipitation over land) and anthropogenic activities (reservoirs, land use changes, irrigation, groundwater pumping). As noted by many authors (e.g. Labat, 2004; Huntington, 2006; Gerten et al., 2008; Dai et al., 2009), global runoff may be seen as an indicator of the intensification of the hydrological cycle. Besides, since global runoff represents an integrated response to continental hydrological dynamics, it has also been used to detect the

impact of anthropogenic activities (e.g. Gleick, 2003; Nilsson et al., 2005; Milliman et al., 2008).

Numerous studies have focused on the characteristics of global runoff, in terms of long term mean, trends, spatial distribution and interannual variability. The most basic way to estimate global runoff is the use of gauged based measurements of river discharge at the outlets of the world's major basins. Databases such as the Global Runoff Data Centre (GRDC) provide such data for a large number of gauge stations worldwide. Although this approach gives the most direct estimation of global runoff, it remains limited by some important drawbacks (see e.g. Legates et al., 2005; Peel and McMahon, 2006 or Syed et al., 2009 for detailed discussions), among which are the following:

- Many regions remain unmonitored. For instance, Fekete et al. (2002) provided global runoff estimates from the 663 major river basins, which represent 71 % of the global runoff. Milliman et al. (2008) used data from 131 river basins, representing 51 % of the global runoff.
- The time periods covered by gauge stations are very irregular in terms of start and end time and gaps in observations.
- Alternative pathways (direct groundwater flows, floodplain inundation, deltaic regions, etc.) are not accounted for.
- Data sharing remains often difficult because of economic and geopolitical constraints and the density of gauge network is decreasing (Shiklomanov et al., 2002).

To counterpart these drawbacks, some authors proposed to use hydrological models (with associated errors and uncertainties) rather than or in combination with in situ data (Trenberth et al., 2007; Dai et al., 2009; Alkama et al., 2011; Haddeland et al., 2011).

An alternative method consists in solving the water budget at the global scale, while distinguishing three main compartments: land, ocean and atmosphere. The latter may be separated into the region over land (land atmosphere) and its complementary part (ocean atmosphere). Figure 1 schematizes water stocks and fluxes involved in the global water cycle. The following equations describe the land (1), ocean (2) and atmosphere (3) global water budgets, respectively (Peixoto and Oort, 1992).

$$\frac{\partial S_{\mathrm{l}}}{\partial t} = P_{\mathrm{l}} - E_{\mathrm{l}} - R \tag{1}$$

$$\frac{\partial S_{\mathrm{o}}}{\partial t} = P_{\mathrm{o}} - E_{\mathrm{o}} + R \tag{2}$$

$$\frac{\partial W_{\mathrm{l/o}}}{\partial t} = E_{\mathrm{l/o}} - P_{\mathrm{l/o}} - \mathrm{div}\,(Q_{\mathrm{l/o}}) \tag{3}$$

where S_{l} represents the terrestrial water storage, S_{o} the ocean mass, R the global runoff, P the precipitation, E the evapo(transpi)ration, W the total column water vapor and div(Q) the divergence of the vertically integrated water vapor flux. Subscripts l and o designate the spatial average over land and ocean, respectively.

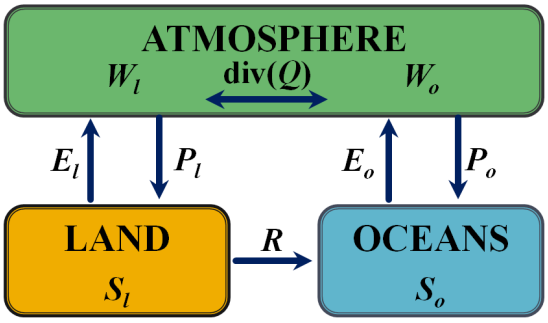

Fig. 1. Stocks and fluxes in the global water cycle. Refer to the text for a detailed description of the variables. S_{l} represents the terrestrial water storage, S_{o} the ocean mass, R the global runoff, P the precipitation, E the evapo(transpi)ration, W the total column water vapor and div(Q) the divergence of the vertically integrated water vapor flux. Subscripts l and o designate the spatial average over land and ocean, respectively.

The global runoff may be estimated directly from the land or ocean water budgets (Eqs. 1–2) (see e.g. Seo et al., 2009 or Syed et al., 2010), then involving estimations of P and E. Even though precipitation data benefit from dense observation networks (ground based and remotely sensed), it may suffer from large uncertainties in some sparsely monitored regions. Moreover, very few direct measurements of evapotranspiration exist (flux towers) and modeling E at the global scale is subject to large uncertainties (Vinukollu et al., 2011). The atmospheric water budget has been introduced by some authors (e.g. Oki et al., 1995; Oki, 1999; Syed et al., 2009) to overcome difficulties in estimating P and E. Dai and Trenberth (2002) showed that the use of the atmospheric water budget improved model based estimates of global runoff.

For the past decade, the ocean mass and the terrestrial water storage can be provided by the Gravity Recovery and Climate Experiment (GRACE) (Tapley et al., 2004; Wahr et al., 2004) space gravimetry mission, as done for instance by Syed et al. (2009) for S_{l}. Before its launch in 2002, no direct measurements of S_{l} and S_{o} were available and since it was difficult to validate estimates from models, variations in water storage were usually neglected (e.g. Oki, 1999; Dai and Trenberth, 2002) then leading to an estimation of the global runoff directly from the net precipitation (P–E). Nevertheless, Syed et al. (2009) showed the importance of taking this term into account by using GRACE estimates of S_{l}.

GRACE products are available since 2002, which may limit the time span of the study to the last decade. Alternatively, Land Surface Models (LSMs) provide monthly estimations of S_{l} with a satisfactory accuracy at basin to global scales, as shown in the various studies comparing GRACE

and LSMs (see Ramillien et al., 2008 for a review of studies prior to 2008). The covered period of LSMs depends on the model, but simulations generally run at least over the last two decades. Besides, the ocean mass S_o may be derived from satellite radar altimetry observations, which provide estimations of the global mean sea level (GMSL), and from in situ hydrographic data. To derive the ocean mass variations, GMSL has to be corrected from the steric component (effect of temperature and salinity), as done by, for example, Syed et al. (2010).

In this study, we use the coupled land–ocean–atmosphere water budgets to estimate the interannual variability of global runoff. Two estimates are computed: one from the land/atmosphere coupling (Eq. 4) and the other from the ocean/atmosphere coupling (Eq. 5).

$$R_l = -\frac{\partial W_l}{\partial t} - \mathrm{div}\,(Q_l) - \frac{dS_l}{\mathrm{d}t} \quad (4)$$

$$R_o = \frac{\partial W_o}{\partial t} + \mathrm{div}\,(Q_o) + \frac{dS_o}{\mathrm{d}t}. \quad (5)$$

S_l is estimated from three LSMs, S_o from altimetry based GMSL and the net precipitation term (time derivative of W and $\mathrm{div}(Q)$) from atmospheric reanalyses. Considering the level of uncertainties on each term appearing in the above equations, each data set used to compute the global runoff is cross-validated with independent data. Besides, since altimetry observations are used, our global runoff estimates cover the altimetry time span (1993–2009). This study expands the previous ones by providing for the first time a comparison of global runoff estimates from land and ocean water budgets, in terms of interannual variability, over the last two decades.

Section 2 presents the data sets used in this study, whereas results are presented in Sects. 3, 4 and 5. In Sect. 3, each data set is compared with independent data to ensure its reliability and to give an idea of its uncertainties. The comparison between both global runoff estimates, in terms of interannual variability, is given in Sect. 4. Our global runoff estimate is also compared with global climate indices (ENSO related SOI, AMO). A discussion on the ocean thermal expansion used in the estimation of the ocean mass and an innovative method to estimate it are provided in Sect. 5.

2 Data and models used in this study

In this section, we present the data and models used to compute global runoff by the two methods (R_l and R_o from Eqs. 4–5). Data used for validation purposes are also presented.

2.1 Altimetry-based sea level data

For the altimetry-based sea level data, we use the DT-MSLA "Ref" series provided by Collecte Localisation Satellite (CLS; http://www.aviso.oceanobs.com/en/data/products/sea-surface-height-products/global/msla/index.html). This data set is used over the time span from January 1993 to December 2009. It is available as $0.25° \times 0.25°$ Mercator projection grids at weekly interval from a combination of several altimetry missions (Topex/Poseidon, Jason-1 and 2, Envisat and ERS 1 and 2). Most recently improved geophysical corrections are applied to the sea level data (see Ablain et al., 2009, for details). The weekly sea level grids are geographically averaged between 65° S and 65° N to obtain a GMSL time series. The data are further averaged on a monthly basis.

2.2 Steric data

Steric sea level is estimated using the updated in situ ocean temperature and salinity data from Ishii and Kimoto (2009), v6.12 (called hereafter IK09). The IK09 temperature data are corrected for the XBT depth bias. The temperature and salinity data are available at monthly intervals over 16 depth levels ranging from the ocean surface down to 700 m depth, on a global $1° \times 1°$ grid from 1955 to 2009. Steric sea level anomalies are computed over the 0–700 m depth range for the period January 1993 to December 2009. The deep ocean contribution cannot be accounted for since hydrographical data below 700 m are too sparse. Recent studies have shown that in terms of trend, the deep ocean contributes by $\sim 10\,\%$ to the total steric effect (Church et al., 2011). Besides, almost all interannual variability in steric sea level is confined in the upper 300–500 m of the ocean (e.g. Llovel et al., 2011). At global scale, salinity does not contribute to the GMSL and is therefore neglected in the following.

2.3 Land Surface Models

To estimate the terrestrial water storage component (S_l), we use monthly gridded outputs of three different LSMs: (1) the WaterGAP Global Hydrology Model (WGHM) (Döll et al., 2003); (2) the Interactions between Soil, Biosphere and Atmosphere – Total Runoff Integrating Pathways (ISBA-TRIP) model (Alkama et al., 2011; Decharme et al., 2010); and (3) the Land Dynamics (LaD) model (Milly and Shmakin, 2002). WGHM outputs are available through December 2009, whereas ISBA ends in December 2008 and LaD in July 2007. Discrepancies among S_l derived from the different LSMs may come from differences in the numerical schemes and meteorological forcing. As noted by Syed et al. (2009), discrepancies among models outputs provide an estimation of the model uncertainties.

Independently, the evapotranspiration modeled by the three LSMs is used for the validation of net precipitation over land (P_l–E_l) computed from the atmospheric water budget (Eq. 3).

2.4 GRACE data

To validate LSMs derived S_l and altimetry-based S_o, a comparison with GRACE data is proposed in Sect. 3. Here we use GRACE products (release 2) for the period 2003–2009 (with missing data for June 2003), computed by the Groupe de Recherche de Géodesie Spatiale (GRGS) (Bruinsma et al., 2010). It consists of monthly $1° \times 1°$ gridded time series of water volume (S_l or S_o), expressed in terms of equivalent water height (EWH). At each grid mesh, the volume anomalies are obtained by removing the temporal mean. The GRGS data are stabilized during the generation process so that no smoothing or filtering is necessary. When GRACE data is used at basin scales, it has to be corrected from leakage effects due to its low resolution (Longuevergne et al., 2010). Nevertheless, such effects have minor impact at the global scale and GRACE data is not corrected here.

As said previously, GRACE provides reliable estimations of spatiotemporal water volume variations since 2002 and it would have been possible to complete GRACE data with LSMs outputs and altimetry based ocean mass for the period 1993–2002. In order to keep consistency in our computations over 1993–2009, we prefer not to use GRACE products to estimate terrestrial water storage and ocean mass variations. Nevertheless, in both cases, comparison with GRACE observations is performed to increase confidence in data.

2.5 Meteorological data

Data used in this study to compute P-E from the atmospheric water budget (W and $\mathrm{div}(Q)$) are based on reanalysis products from the European Centre for Medium-Range Weather Forecast (ECMWF) ERA-Interim data set (Dee et al., 2011). These are daily global data provided on $1.5° \times 1.5°$ grids in units of $\mathrm{mm\,day^{-1}}$. All gridded data are further expressed in terms of monthly averages over the period 1993–2009.

For validation purposes, we also consider six global precipitation data sets: Global Precipitation Climatology Centre (GPCC, Schneider et al., 2008), Climatic Research Unit (CRU, available online at http://badc.nerc.ac.uk/data/cru/), the Willmott-Matsuura product (WM, Willmott and Matsuura, 2010), Global Precipitation Climatology Project (GPCP, Adler et al., 2003), Climate Prediction Center (CPC) Merged Analysis of Precipitation (CMAP, Xie and Arkin, 1997), the Princeton Global Forcing (PGF, Sheffield et al., 2006). These data sets are obtained either from ground based observations (GPCC, CRU, WM) or from merged ground based and satellite observations (GPCP, CMAP, PGF).

3 Processing and evaluation of the data and models

3.1 Data processing

As the focus of this study is the interannual variability of the global runoff, the seasonal component of each signal presented in the following is removed. This component is obtained by fitting two sinusoidal signals periods of 6 and 12 months. Moreover, although the mean value of the global runoff is still subject to discussions (see e.g. Syed et al., 2009, and references therein), it is not in the scope of this paper. Hence, the temporal mean is also removed from the global runoff estimates. In Eqs. (5)–(6), S_l and S_o are derivated with respect to time and any trend in S_l and S_o would lead to constants in the runoff. Consequently, S_l and S_o are detrended in the following. Note that detrending S_l and S_o does not impact the runoff trend since change in storage (i.e. first order differencing) filters out linear trends.

As a spherical harmonics (SH) truncation at degree 50 (resolution of 400 km) is applied on GRACE data to obtain water mass variations, we applied the same SH truncation to LSM outputs for a more relevant comparison between GRACE and LSMs derived S_l (as suggested by many authors, e.g. Longuevergne et al., 2010). SH truncation is applied only for the model validation, not for the runoff computation.

Finally, all graphs showing temporal evolution of the spatial mean of any variable have been smoothed using a 3-months moving average.

3.2 Land/Ocean masks: estimate of the high latitudes contribution

As indicated above, altimetry products used here are available only in the 65° S–65° N domain. Moreover, ice sheets (Greenland and Antarctica) are generally not modeled in LSMs because of their very specific hydrological behavior, all the more so as very few in situ data are available in these regions and the models' validation is then quite difficult. Hence ice sheets and high latitude oceans are excluded from the present study. Figure 2a shows the land and ocean regions considered here.

The exclusion of ice sheets and high latitude oceans has no major consequences in the following since these regions only play a minor role in the interannual variability of global runoff. To assess this, Fig. 2b and c presents S_l and S_o variations derived from GRACE over the four regions shown in Fig. 2a. Despite significant trends in water mass variations – not shown in the graphs – in ice sheets ($-160\,\mathrm{km^3\,yr^{-1}}$) and high latitude oceans ($-66\,\mathrm{km^3\,yr^{-1}}$), these regions are scarcely involved in the global water cycle in terms of interannual variability.

3.3 Comparison of terrestrial water storage from GRACE and LSMs

Figure 3a shows the total water storage derived from the LSMs; the blue shading represents the root mean square (RMS) deviation of each model with respect to the average. The RMS between LSMs is 1.26 mm, which is quite low compared to the amplitude of the interannual variations of S_l.

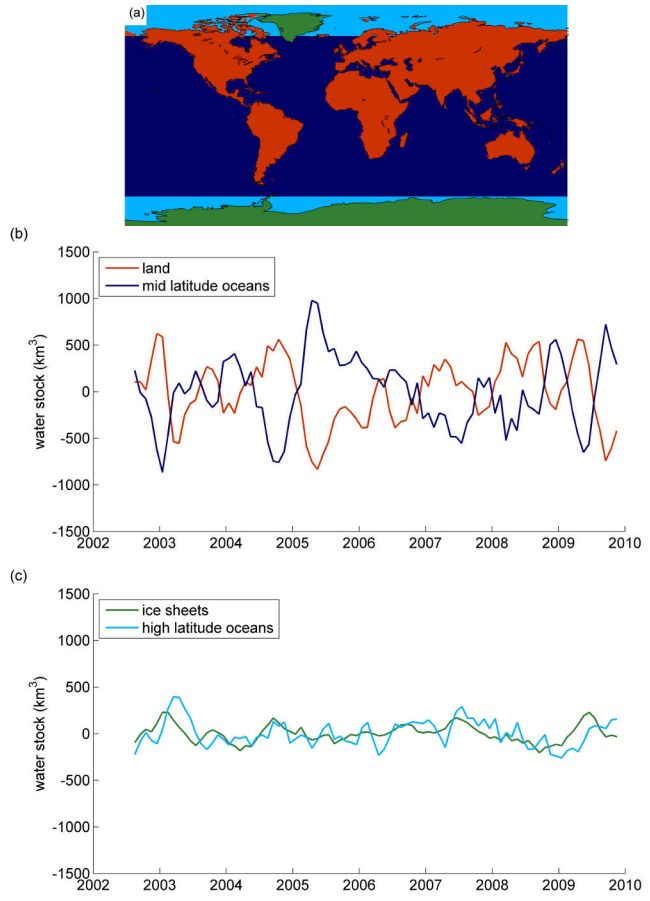

Fig. 2. (a) Land and ocean masks (high latitude Arctic and Antarctic oceans in light blue and ice sheets in green). **(b)** Detrended interannual variations of GRACE derived water stocks in land (except ice sheets) and oceans (except high latitudes). **(c)** Detrended interannual variations of GRACE derived water stocks in ice sheets and high latitude oceans.

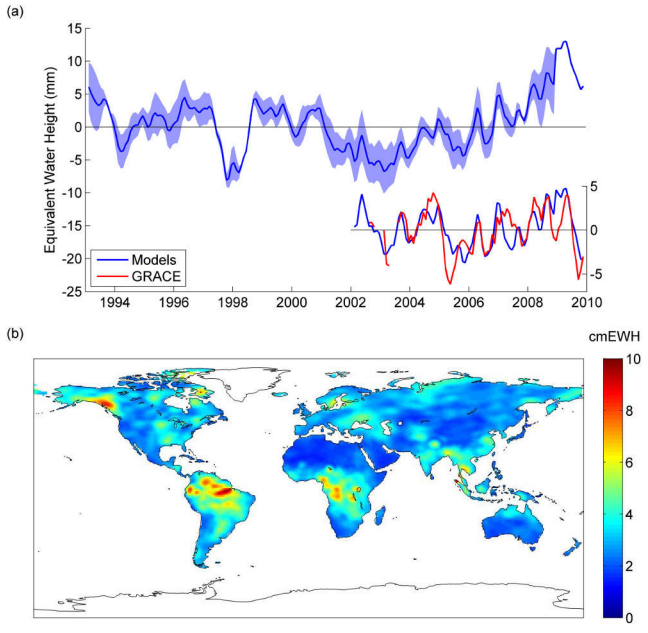

Fig. 3. (a) Terrestrial water storage interannual variations from models and GRACE. Blue shading represents discrepancies between models. **(b)** Mean RMS over 2002–2009 between GRACE and LSMs terrestrial water storage.

The comparison with GRACE over 2002–2009 is shown in the lower right corner (the trend of LSMs S_l over the GRACE period has been removed for the purpose of this comparison). The good agreement between the independent LSMs and GRACE derived S_l (correlation coefficient of 0.66) reinforces the reliability of both estimates. Figure 3b presents the spatial distribution of the RMS differences between both estimates. Main differences are localized in the intertropical zone and more specifically in the Amazon and Congo basins. Two main reasons may explain this: (1) the hydrological cycle has greater amplitude in these basins than in others leading to higher RMS and (2) GRACE errors are larger near the equator than in high latitudes (Swenson and Wahr, 2006). High RMS between GRACE and LSMs are also found in glacier regions (Alaska, Scandinavia, Himalaya) which may come from the fact that, contrarily to GRACE, LSMs generally do not account for glaciers. These discrepancies are of less importance in terms of volume since pixel area tends to 0 in high latitudes.

3.4 Ocean mass estimate

Global mean sea level (GMSL) variations are the result of variations in the ocean mass (S_o) and in the steric component. Salinity has little effect at the global scale so that the remaining steric component corresponds to the ocean thermal expansion (TE). Ocean mass variations are then derived from GMSL variations corrected from TE according to Eq. (6).

$$S_o = \mathrm{GMSL} - \mathrm{TE} \quad (6)$$

Figure 4 presents the ocean mass variations S_o derived from GRACE and computed from GMSL, corrected or not from the thermal expansion TE. The thermal expansion correction over 2002–2005 clearly deteriorates the correlation with GRACE derived S_o (correlation coefficient of 0.17 and 0.45, respectively with and without correction, for the common period 2002–2009). In particular, the TE correction leads to a great negative peak in 2003–2004 that is not shown in GRACE S_o. Considering the mitigated efficiency of the TE correction, we prefer not to apply it for the runoff computation done in Sect. 4. Nevertheless, we will come back to this issue in Sect. 5.

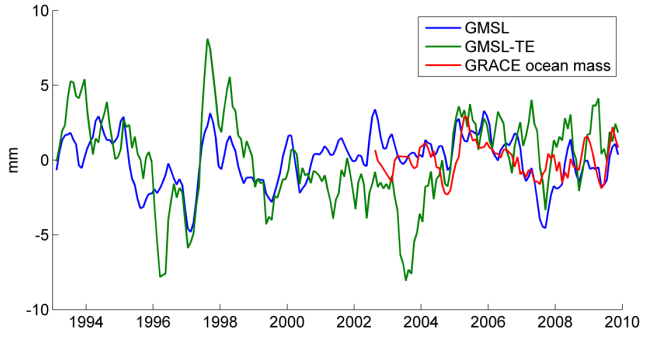

Fig. 4. Comparison of global mean sea level (GMSL) computed from altimetry, GMSL corrected from the thermal expansion TE and GRACE ocean mass.

3.5 P–E over land and atmospheric water budget

Figure 5a shows net precipitation over land (P_l–E_l) computed from the atmospheric water budget (Eq. 3) and ERA-Interim data. This graph shows a sudden increase in P_l–E_l in 2003. The difference between the temporal mean over 1993–2002 and the one over 2003–2009 equals 3 mm month^{-1}, which is of the same order of magnitude as the interannual variability. We are currently investigating the causes of this important shift, but we suspect a change in input data in the ERA-Interim procedure. Namely radiance measurements from AIRS have been assimilated since July 2003, which may have an impact on the global water cycle (P. Poli, personal communication, 2011). To assess the artificial origin of the discontinuity, we compare P_l–E_l from ERA-Interim with independent precipitation and evapotranspiration data sets (see Sect. 2). We use the outputs of the three LSMs presented previously (ISBA, WGHM and LaD) to estimate evapotranspiration. The blue curve and blue shading in Fig. 5b show the mean and standard deviation of the 18 computed time series of P_l–E_l. The observed P_l minus modeled E_l is very similar to the ERA-Interim estimate before 2003 but it has not present any shift since 2003, which reinforces the assumption of an artificial origin of the discontinuity. We then decided to correct ERA-Interim P_l–E_l by adding a constant offset over the period 2003–2009. The value of the offset is obtained by minimizing the difference between ERA-Interim P_l–E_l and observed P_l minus modeled E_l. The optimum offset value (-2.78 mm month^{-1}) leads to a very good correlation between the two estimates.

The same analysis may have been done over oceans but very few evaporation data over ocean exist and comparison between two of the main existing data sets (OA-Flux, Yu and Weller, 2007 and HOAPS, Andersson et al., 2007) shows large discrepancies in terms of interannual variability (Fig. 6). Besides, Fig. 7 represents the interannual variations of div(Q) and dW/dt over oceans and land. Note that the discontinuity correction (offset of -2.78 mm month^{-1})

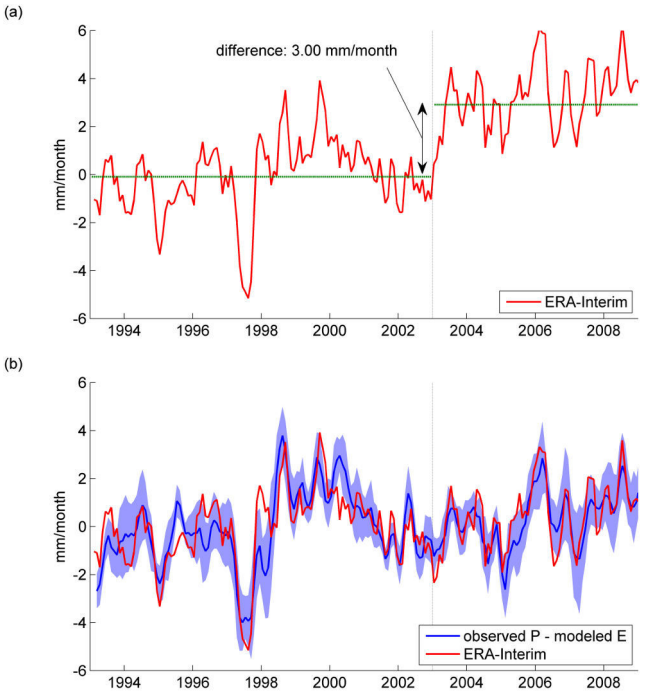

Fig. 5. (a) Interannual variability of precipitation minus evapotranspiration over land (P_l–E_l) computed from the atmospheric water budget and ERA-Interim data. **(b)** Corrected P_l–E_l with a uniform offset of -2.78 mm month^{-1} over 2003–2009, and observed P_l minus modeled E_l used to find the optimum offset (blue shading represents discrepancies between P_l–E_l obtained from the different the data sets).

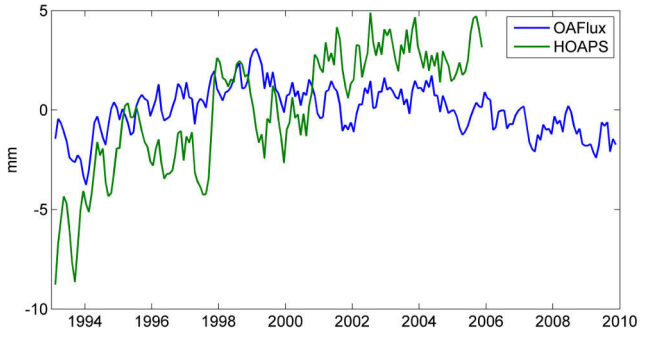

Fig. 6. Interannual variability of evaporation over ocean from OAFlux and HOAPS.

has been applied in div(Q) over land and oceans. First, it is shown that dW/dt plays a minor role in the interannual variability of the global water cycle. Second, div(Q_l) is very similar to $-$div(Q_o) which means that very little water is horizontally exchanged between high- and mid-latitude regions of the atmosphere (separated by the 65° S and 65° N parallels). These considerations lead to P_l–$E_l = -(P_o$–$E_o)$. In that sense, the same offset is applied in the estimation of P_o–E_o.

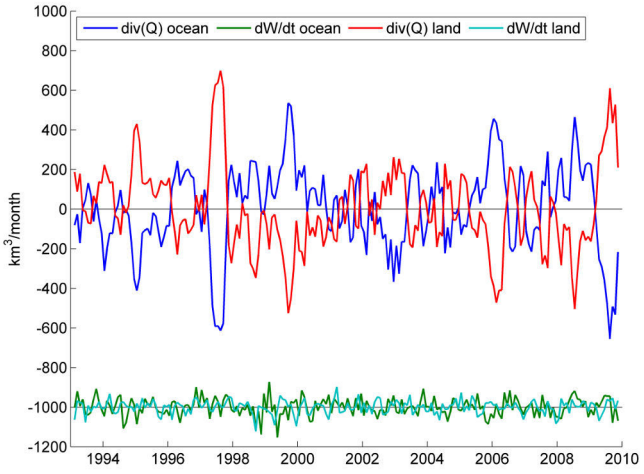

Fig. 7. Components of the atmospheric water budget. Spatial mean over ocean and land. The dW/dt time series are shifted vertically for clarity.

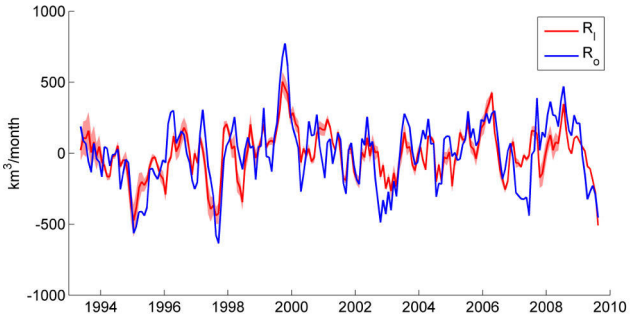

Fig. 8. Comparison of runoff computed from land–atmosphere (R_l) and ocean–atmosphere (R_o) water budgets. The red shading represents discrepancies relative to the different considered LSMs.

4 Global runoff and climate variability

4.1 Comparison of the two global runoff estimates

The comparison between estimates of the global runoff from the land–atmosphere and the ocean–atmosphere water budgets is shown in Fig. 8. Both estimates are very well correlated (correlation coefficient of 0.73, mean standard deviation of 63 $km^3\ month^{-1}$). Interannual variations of global runoff ranges from about -200 to 200 $km^3\ month^{-1}$, with higher peaks during major ENSO events. In particular, negative peaks in 1994–1995, 1997–1998 and 2009–2010 are related to lower than normal precipitation over land during El Niño events, whereas the positive peak in 1999–2000 is related to higher than normal land precipitation during La Niña event. One can notice that the 1997–1998 El Niño event is clearly visible on Fig. 3a, which shows a great negative peak in S_l during this period, a result of lower/higher precipitation intensity over land/ocean (Gu et al., 2007). The ENSO effects on precipitation over land and oceans is also shown on Fig. 7.

Besides, no significant trend is observed over the whole period. Indeed, the trend equals 48 $km^3\ month^{-1}$ per decade for R_l and 72 $km^3\ month^{-1}$ per decade for R_o, which is negligible compared to the mean standard deviation of R_l and R_o (169 and 228 $km^3\ month^{-1}$, respectively). These values are quite lower than the one found by Syed et al. (2010) (540 $km^3\ yr^{-2}$ or 450 $km^3\ month^{-1}$ per decade) but are in agreement with results of some other previous studies (Dai et al., 2009; Milliman et al., 2008) which found insignificant trends. The difference with Syed et al. (2010) may be partly explained by the fact that the authors computed the trend over 1995–2006 and that the global runoff presents higher values before 1995 and lower values after 2006, leading to a reduction of the global trend. Indeed, with the methodology developed in this study, the global runoff trend over the period 1995–2006 equals 128 $km^3\ month^{-1}$ per decade for R_l and 143 $km^3\ month^{-1}$ per decade for R_o. While these values are higher than for the period 1993–2009, they are still lower than the value obtained by Syed et al. (2010). The difference likely comes from the different data sets used to compute $P-E$ over oceans. Namely, Syed et al. (2010) considered two estimates of E_o (OA-Flux and HOAPS) which are quite different in terms of interannual variability (Fig. 6).

Other authors (Dai et al., 2009; Alkama et al., 2011) found non negligible trends over some of the major river basins for the last decades, but these trends seem to compensate against each other at the global scale.

The differences between R_l and R_o may be explained by two main factors: modeling errors and TE not accounted for in the ocean mass estimation. Concerning the former, considering three different LSMs help us to quantify modeling errors. We find a mean standard deviation of 43 $km^3\ month^{-1}$ due to LSMs discrepancies (represented by the red shading in Fig. 8), which is very low compared to the interannual variability of R. This suggests that the differences between R_l and R_o are mainly explained by the fact that the ocean mass is not corrected from TE. Nevertheless, the good correlation between R_o and R_l shows that TE plays a minor role in the interannual variability of global runoff. In Sect. 5, we investigate a new method to estimate the ocean thermal expansion component by using the difference R_o–R_l.

4.2 Zonal runoff and correlation with climate indices

As said previously, the global runoff seems to be highly impacted by major ENSO events. Many studies, including Dai et al. (2009), Syed et al. (2010) and Labat (2010), also showed this particular link. In addition, Gu et al. (2007) reported high correlations between ENSO and land precipitation in the intertropical zone and lower but not null correlations in mid- and high latitudes. In this section, we propose

to investigate the correlation between the zonal runoff and different global scale climate phenomena.

First, the zonal runoff is computed over four latitudinal bands separated by the 60° N, 20° N and 20° S parallels (solid lines in Fig. 9). As expected, while the intertropical zone contributes for the most part to the interannual variability of the global runoff, northern high latitude and southern mid latitude zonal runoffs are quite negligible.

For each zone, the zonal runoff is then compared with different linear combinations of several climate indices. The indices considered here are the following: the Multivariate ENSO Index (MEI), the Atlantic multidecadal oscillation (AMO), the Pacific Decadal Oscillation (PDO), the Pacific–North America teleconnection (PNA) and the Arctic Oscillation index (AO). The reader may refer to Rossi et al. (2011) for a detailed presentation of these indices. For each subset of one or two indices, the linear combination is optimized by maximizing the correlation between the zonal runoff and the combined index. Subsets that give the best results are used to compute a new index called combined runoff index (CRI). Optimization results are given, for each zonal band, by Eq. (7) (climate indices have been normalized before the optimization).

$$\begin{aligned} \mathrm{CRI}(-60/-20) &= 0.53 \times \mathrm{PDO} + 0.47 \times \mathrm{AMO} \\ \mathrm{CRI}(-20/+20) &= -0.62 \times \mathrm{MEI} - 0.38 \times \mathrm{AMO} \\ \mathrm{CRI}(+20/+60) &= 0.54 \times \mathrm{MEI} + 0.46 \times \mathrm{AMO} \\ \mathrm{CRI}(+60/+90) &= 0.73 \times \mathrm{PNA} + 0.27 \times \mathrm{AO} \end{aligned} \quad (7)$$

Since LSMs and ERA-Interim outputs are available since 1980 or earlier (apart from WGHM which is only available since 1992), we also compared CRI and zonal R_l over the period 1980–1992, period not used in the calibration of CRI. Figure 9 shows (dashed lines) results of calibration (period 1993–2009) and validation (period 1980–1992); CRI has been normalized to match the range of zonal runoffs variability. The two numbers in the brackets in the legend represent the correlation between zonal R_l and CRI for the calibration period and for the overall period, respectively. Figure 9 clearly shows a very good correlation for the intertropical zone (namely during the validation period) and more contrasted correlations in mid- and high latitudes.

Not surprisingly, MEI contributes for the most part in the intertropical and northern mid-latitude zonal runoffs. For these two zonal runoffs, AMO also plays an important role. Figure 9 and Eq. (7) show that these two zonal runoffs are highly anti-correlated, namely with higher/lower runoffs than normal in mid-latitude/intertropical zones during major El-Niño events (e.g. in 1983 or in 1998). The reciprocal is true for La-Niña events (e.g. in 1989 or in 2000). This suggests that during El-Niño events, while water mass is shifted westward from the South American continent to the tropical Pacific Ocean (Gu et al., 2007), it is also shifted northward to mid-latitude continents. Besides, ENSO seems to play a less important role in northern high latitudes and southern

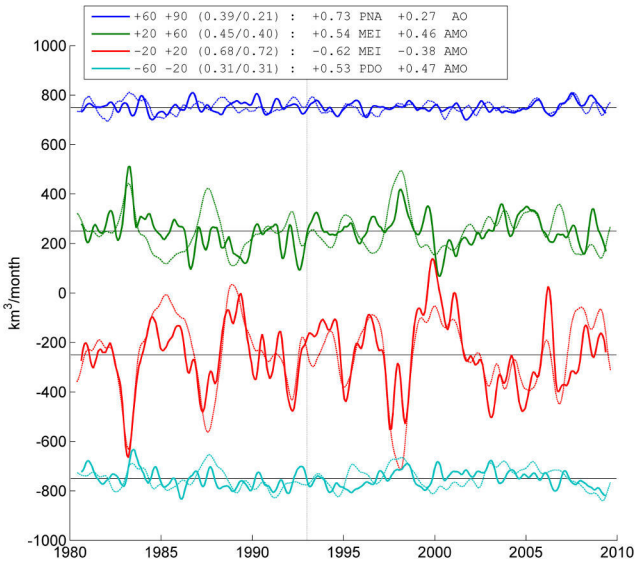

Fig. 9. Comparison of zonal runoff computed from land–atmosphere–water budgets (R_l, solid lines) and combined runoff index (CRI, dashed lines) over northern high latitudes (60° N–90° N), northern mid-latitudes (20° N–60° N), intertropical zone (20° S–20° N) and southern mid-latitudes (60° S–20° S). For each zone, time series are shifted vertically for clarity. CRI has been normalized to match the range of global runoff variability. The two numbers in the brackets represent the correlation between R_l and CRI for the calibration period (1993–2009) and the whole period, respectively. Results of calibration (climate indices and related coefficients) are given in the legend box.

mid-latitudes. Northern high latitude zonal runoff is logically governed by northern mid- to high latitude climate phenomena (Pacific–North America teleconnection and Arctic Oscillation). For each of the three other zones, CRI is a combination of a climate index related to the Pacific Ocean and another related to the Atlantic Ocean.

Further investigations are suggested to complete these preliminary results, namely about the relationship between the zonal runoff and climate indices characteristics in the frequency domain (Rossi et al., 2011).

5 Reconstruction of the ocean thermal expansion

In this subsidiary section, we come back to the aforementioned problem of the ocean thermal expansion (TE) correction and propose an innovative method to reconstruct this component of the global mean sea level. Indeed, as said previously, the observed difference between R_l and R_o may be mainly attributed to TE. Assuming that $P_l - E_l = -(P_o - E_o)$ (see Sect. 3.5) and combining Eqs. (1)–(2) leads to $S_l + S_o = \text{constant}$. Then combining this last equation with Eq. (6) leads to the following estimate of TE (after removing the constant):

$$TE = GMSL + S_l. \quad (8)$$

We further compare our TE reconstruction with TE data from two different databases: the IK09 (presented in Sect. 2.2) and the WOD09 (Levitus et al., 2009). The WOD09 and IK09 databases account for depth-bias corrections on XBT temperature data (e.g. Wijffels et al., 2008). The TE data from the two databases are publicly available at: http://www.noaa.gov/ for WOD09 and http://atm-phys.nies.go.jp/~ism/pub/ProjD/v6.9/ for IK09. For each database, we computed the thermosteric sea level on a $1° \times 1°$ grid at monthly interval since 1993, integrating temperature anomalies from the surface down to 700 m. For that purpose, we first computed density anomalies at each standard level down to 700 m by considering temperature anomalies and using the classical equation of state of the ocean. Then, we integrated density anomalies at each grid point and each time step to obtain the thermosteric sea level (Gill, 1982).

Figure 10 compares TE obtained from our reconstruction and from IK09 (a) and WOD09 (b). Noting a 3 months lag between our reconstruction and the two other curves – which cause is still under investigation – we have accounted for this delay in Fig. 10. The comparison shows that our TE reconstruction has similar high frequency (i.e. year-to-year) behavior as IK09 and WOD09 time series, but significantly differs at lower frequency (multi-year variability). In addition to the uncertainties of each time series, the difference with our TE estimate may arise from that deep ocean contribution (below 700 m) that is inherently accounted for in our TE is not accounted for in IK09 and WOD09 data. Even though we expect deep ocean contribution to be small (see Sect. 2.2), it may have a low frequency behavior that could explain the differences with our reconstruction.

Anyway, one may note that the differences between our reconstruction and each data set are of the same order as the difference between IK09 and WOD09. Concerning the period 2003–2004, this comparison seems to confirm an overestimation of TE derived from IK09 and WOD09 already noted in Sect. 3.4 and Fig. 4. To corroborate or invalidate this overestimation, we are presently performing a specific study about the origin of such discrepancies over this period (comparison with TE derived from global circulation models).

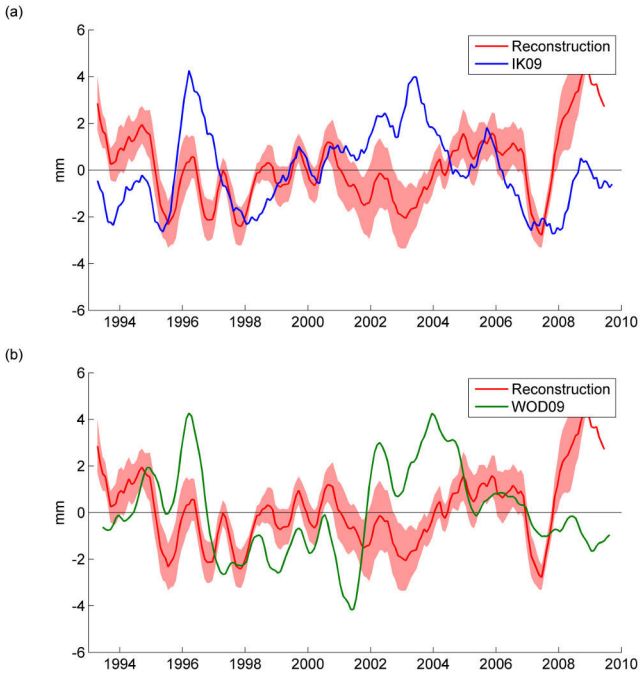

Fig. 10. Comparison of the interannual variations of the thermal expansion obtained from this study and from **(a)** Ishii and Kimoto (2009) v6.12 (IK09) and **(b)** Levitus et al. (2009) (WOD09). Red shading represents discrepancies due to LSMs. Note that the reconstructed time series have been shifted by 3 months forward.

6 Conclusions

The impacts of climate change and anthropogenic factors on the global water cycle represent a critical and timely issue. Namely, the question about an intensification of the global water cycle is highly debated and the answers are still controversial. Evidence of such intensification may be derived by looking at different parameters of the water cycle, e.g. an increase in global runoff (R), with potential implications on basin scale water management. Here we investigated two methods to estimate R over the period 1993–2009. Both methods are derived from the coupling of the land–atmosphere and ocean–atmosphere water budgets, respectively. Independent data sets are used to estimate water storage variations in each compartment: atmospheric reanalyses, land surface models, satellite altimetry and in situ ocean temperature data. Each component of the water budget is first cross-validated using other independent data sets, such as GRACE for ocean mass and terrestrial water storage. Concerning the global runoff estimated from the two coupled water budgets, the two main results are

- both estimates correlate very well over the study time span (correlation coefficient of 0.73), giving confidence in the method;
- no significant trend is observed over the whole period (the trend ranges from 48 to 72 $km^3\,month^{-1}$ per decade, which is insignificant compared to the mean standard deviation of R ranging from 169 to 228 $km^3\,month^{-1}$).

Results also show that major ENSO events largely impact the global runoff (decrease/increase during El Niño/La Niña). To infer the link between global runoff and climate variability, we computed the zonal runoff over 4 latitudinal

bands (intertropical zone, northern and southern mid-latitudes and northern high latitudes) and compared it with different climate indices. We then set up a combined runoff index (CRI) obtained for each zone by optimization of climate indices linear combinations. We showed that CRI well correlates with the zonal runoff even over a validation period not used for the optimization, especially for the intertropical zone, which contributes for the most part in the global runoff. Besides, linear coefficients resulting from the optimization provide information about which large-scale climate phenomena are the main drivers for each zonal runoff. Namely, the intertropical and northern mid-latitude zonal runoffs are mainly driven by ENSO and AMO. Moreover, the zonal runoffs in these two zones are anti-correlated, particularly during ENSO events. This suggests that water masses are shifted northward/southward during major El Niño/La Niña events.

Lastly, the difference between the two runoff estimates may be mainly explained by the ocean thermal expansion (TE) term which has not been accounted for in the ocean mass estimate. Consequently, we used our runoff reconstruction to propose an innovative method for providing a new estimate of TE. The comparison with two existing data sets shows a quite good agreement in terms of interannual variability, showing the relevance of the method, but points out a period (2003–2004) during which ocean thermal expansion data may be in error.

More generally, these results have implications for studies on the global water cycle, with the underlying issues of global warming and water resources availability. Namely, we show that an intensification of the global water cycle due to the global warming is not obvious over the last two decades. Besides, as large scale climate phenomena may be seen as drivers of the zonal (or regional) runoffs, analyzing their evolution with climate change should provide indicators of potential evolutions of the global runoff. The mechanisms relating such phenomena and runoff need to be addressed in further studies.

Acknowledgements. We would like to acknowledge Andreas Güntner (GFZ German Research Centre for Geosciences) and Bertrand Decharme (CNRM, MeteoFrance) for sharing WGHM and ISBA outputs, respectively. S. Munier and H. Palanisamy received a grant from the Centre National d'Etudes Spatiales (CNES, France) and from ANR Cecile, respectively. We are also grateful to the two anonymous reviewers who helped us to improve the paper.

Edited by: H. Cloke

The publication of this article is financed by CNRS-INSU.

References

Ablain, M., Cazenave, A., Valladeau, G., and Guinehut, S.: A new assessment of the error budget of global mean sea level rate estimated by satellite altimetry over 1993–2008, Ocean Sci., 5, 193–201, doi:10.5194/os-5-193-2009, 2009.

Adler, R. F., Huffman, G. J., Chang, A., Ferraro, R., Xie, P. P., Janowiak, J., Rudolf, B., Schneider, U., Curtis, S., Bolvin, D., Gruber, A., Susskind, J., Arkin, P., and Nelkin, E: The version-2 global precipitation climatology project (GPCP) monthly precipitation analysis (1979–present), J. Hydrometeorol., 4, 1147–1167, 2003.

Alkama, R., Decharme, B., Douville, H., and Ribes, A.: Trends in Global and Basin-Scale Runoff over the Late Twentieth Century: Methodological Issues and Sources of Uncertainty, J. Climate, 24, 3000–3014, doi:10.1175/2010JCLI3921.1, 2011.

Andersson, A., Bakan, S., Fennig, K., Grassl, H., Klepp, C., and Schulz, J.: Hamburg Ocean Atmosphere Parameters and Fluxes from Satellite Data – HOAPS-3 – monthly mean, World Data Center for Climate, electronic publication, 2007.

Bruinsma, S., Lemoine, J. M., Biancale, R., and Vales, N.: CNES/GRGS 10-day gravity field models (release 2) and their evaluation, Adv. Space Res., 45, 587–601, doi:10.1016/j.asr.2009.10.012, 2010.

Church, J. A., White, N. J., Konikow, L. F., Domingues, C. M., Cogley, J. G., Rignot, E., Gregory, J. M., van den Broeke, M. R., Monaghan, A. J., and Velicogna, I.: Revisiting the Earth's sea-level and energy budgets from 1961 to 2008, Geophys. Res. Lett., 38, L18601, doi:10.1029/2011GL048794, 2011.

Dai, A. and Trenberth, K. E.: Estimates of Freshwater Discharge from Continents: Latitudinal and Seasonal Variations, J. Hydrometeorol., 3, 660–687, 2002.

Dai, A., Qian, T. T., Trenberth, K. E., and Milliman, J. D.: Changes in Continental Freshwater Discharge from 1948 to 2004, J. Climate, 22, 2773–2792, doi:10.1175/2008JCLI2592.1, 2009.

Decharme, B., Alkama, R., Douville, H., Becker, M., and Cazenave, A.: Global Evaluation of the ISBA-TRIP Continental Hydrological System, Part II: Uncertainties in River Routing Simulation Related to Flow Velocity and Groundwater Storage, J. Hydrometeorol., 11, 601–617, doi:10.1175/2010JHM1212.1, 2010.

Dee, D. P., Uppala, S. M., Simmons, A. J., Berrisford, P., Poli, P., Kobayashi, S., Andrae, U., Balmaseda, M. A., Balsamo, G., Bauer, P., Bechtold, P., Beljaars, A. C. M., van de Berg, L., Bidlot, J., Bormann, N., Delsol, C., Dragani, R., Fuentes, M., Geer, A. J., Haimberger, L., Healy, S. B., Hersbach, H., Holm, E. V., Isaksen, L., Kallberg, P., Koehler, M., Matricardi, M., McNally, A. P., Monge-Sanz, B. M., Morcrette, J. J., Park, B. K., Peubey, C., de Rosnay, P., Tavolato, C., Thepaut, J. N., and Vitart, F.: The ERA-Interim reanalysis: configuration and performance of the

data assimilation system, Q. J. Roy. Meteor. Soc., 137, 553–597, doi:10.1002/qj.828, 2011.

Doll, P., Kaspar, F., and Lehner, B.: A global hydrological model for deriving water availability indicators: model tuning and validation, J. Hydrol., 270, 105–134, 2003.

Fekete, B. M., Vorosmarty, C. J., and Grabs, W.: High-resolution fields of global runoff combining observed river discharge and simulated water balances, Global Biogeochem. Cy., 16, 1042, doi:10.1029/1999GB001254, 2002.

Gerten, D., Rost, S., von Bloh, W., and Lucht, W.: Causes of change in 20th century global river discharge, Geophys. Res. Lett., 35, L20405, doi:10.1029/2008GL035258, 2008.

Gill, A. E.: Atmosphere-Ocean Dynamics, Academic Press, San Diego, 1982.

Gleick, P.: Global freshwater resources: Soft-path solutions for the 21st century, Science, 302, 1524–1528, doi:10.1126/science.1089967, 2003.

Gu, G., Adler, R. F., Huffman, G. J., and Curtis, S.: Tropical rainfall variability on interannual-to-interdecadal and longer time scales derived from the GPCP monthly product, J. Climate, 20, 4033–4046, doi:10.1175/JCLI4227.1, 2007.

Haddeland, I., Clark, D. B., Franssen, W., Ludwig, F., Voß, F., Arnell, N. W., Bertrand, N., Best, M., Folwell, S., Gerten, D., Gomes, S., Gosling, S. N., Hagemann, S., Hanasaki, N., Harding, R., Heinke, J., Kabat, P., Koirala, S., Oki, T., Polcher, J., Stacke, T., Viterbo, P., Weedon, G. P., and Yeh, P.: Multi-Model Estimate of the Global Terrestrial Water Balance: Setup and First Results, J. Hydrometeorol., 12, 869–884, doi:10.1175/2011JHM1324.1, 2011.

Huntington, T. G.: Evidence for intensification of the global water cycle: Review and synthesis, J. Hydrol., 319, 83–95, 2006.

Ishii, M. and Kimoto, M.: Reevaluation of historical ocean heat content variations with time-varying XBT and MBT depth bias corrections, J. Oceanogr., 65, 287–299, doi:10.1007/s10872-009-0027-7, 2009.

Labat, D.: Evidence for global runoff increase related to climate warming, Adv. Water Resour., 27, 631–642, doi:10.1016/j.advwatres.2004.02.020, 2004.

Labat, D.: Cross wavelet analyses of annual continental freshwater discharge and selected climate indices, J. Hydrol., 385, 269–278, doi:16/j.jhydrol.2010.02.029, 2010.

Legates, D., Lins, H., and Mccabe, G.: Comments on "Evidence for global runoff increase related to climate warming" by Labat et al., Adv. Water Resour., 28, 1310–1315, doi:10.1016/j.advwatres.2005.04.006, 2005.

Levitus, S., Antonov, J. I., Boyer, T. P., Locarnini, R. A., Garcia, H. E. and Mishonov, A. V.: Global ocean heat content 1955-2008 in light of recently revealed instrumentation problems, Geophys. Res. Lett., 36, L07608, doi:10.1029/2008GL037155, 2009.

Llovel, W., Meyssignac, B., and Cazenave, A.: Steric sea level variations over 2004–2010 as a function of region and depth: Inference on the mass component variability in the North Atlantic Ocean, Geophys. Res. Lett., 38, L15608, doi:201110.1029/2011GL047411, 2011.

Longuevergne, L., Scanlon, B. R., and Wilson, C. R.: GRACE Hydrological estimates for small basins: Evaluating processing approaches on the High Plains Aquifer, USA, Water Resour. Res., 46, W11517, doi:10.1029/2009WR008564, 2010.

Milliman, J. D., Farnsworth, K. L., Jones, P. D., Xu, K. H., and Smith, L. C.: Climatic and anthropogenic factors affecting river discharge to the global ocean, 1951–2000, Global Planet. Change, 62, 187–194, doi:10.1016/j.gloplacha.2008.03.001, 2008.

Milly, P. C. D. and Shmakin, A. B.: Global modeling of land water and energy balances. Part I: the land dynamics (LaD) model, J. Hydrometeorol., 3, 283–299, 2002.

Nilsson, C., Reidy, C., Dynesius, M., and Revenga, C.: Fragmentation and flow regulation of the world's large river systems, Science, 308, 405–408, doi:10.1126/science.1107887, 2005.

Oki, T.: The global water cycle, Global Energy and Water Cycles, edited by: Browning, K. A. and Gurney, R. J., Cambridge University Press, 10–29, 1999.

Oki, T., Musiake, K., Matsuyama, H., and Masuda, K.: Global atmospheric water balance and runoff from large river basins, Hydrol. Process., 9, 655–678, doi:10.1002/hyp.3360090513, 1995.

Peel, M. C. and McMahon, T. A.: Continental Runoff: A quality-controlled global runoff data set, Nature, 444, E14–E14, doi:10.1038/nature05480, 2006.

Peixoto, J. P. and Oort, A. H.: Physics of climate, Springer, 1992.

Ramillien, G., Famiglietti, J., and Wahr, J.: Detection of Continental Hydrology and Glaciology Signals from GRACE: A Review, Surv. Geophys., 29, 361–374, 2008.

Rossi, A., Massei, N., and Laignel, B.: A synthesis of the time-scale variability of commonly used climate indices using continuous wavelet transform, Global Planet. Change, 78, 1–13, doi:10.1016/j.gloplacha.2011.04.008, 2011.

Schneider, U., Fuchs, T., Meyer-Christoffer, A., and Rudolf, B.: Global Precipitation Analysis Products of the GPCC, Global Precipitation Climatology Centre (GPCC), DWD, Internet Publication, available at: http://www.dwd.de, 1–12, 2008.

Seo, K. W., Waliser, D. E., Tian, B. J., Famiglietti, J. S., and Syed, T. H.: Evaluation of global land-to-ocean fresh water discharge and evapotranspiration using space-based observations, J. Hydrol., 373, 508–515, doi:10.1016/j.jhydrol.2009.05.014, 2009.

Sheffield, J., Goteti, G., and Wood, E. F.: Development of a 50-year high-resolution global dataset of meteorological forcings for land surface modeling, J. Climate, 19, 3088–3111, 2006.

Shiklomanov, A. I., Lammers, R. B., and Vörösmarty, C. J.: Widespread decline in hydrological monitoring threatens Pan-Arctic Research, Eos, Transactions American Geophysical Union, 83, 13, doi:10.1029/2002EO000007, 2002.

Swenson, S. and Wahr, J.: Post-processing removal of correlated errors in GRACE data, Geophys. Res. Lett., 33, L08402, doi:10.1029/2005GL025285, 2006.

Syed, T. H., Famiglietti, J. S., and Chambers, D. P.: GRACE-Based Estimates of Terrestrial Freshwater Discharge from Basin to Continental Scales, J. Hydrometeorol., 10, 22–40, doi:10.1175/2008JHM993.1, 2009.

Syed, T. H., Famiglietti, J. S., Chambers, D. P., Willis, J. K., and Hilburn, K.: Satellite-based global-ocean mass balance estimates of interannual variability and emerging trends in continental freshwater discharge, Proc. Natl. Ac. Sci. USA, 107, 17916–17921, doi:10.1073/pnas.1003292107, 2010.

Tapley, B. D., Bettadpur, S., Watkins, M. M., and Reigber, C.: The gravity recovery and climate experiment; mission overview and early results, Geophys. Res. Lett., 31, L09607, doi:10.1029/2004GL019920, 2004.

Trenberth, K. E., Smith, L., Qian, T. T., Dai, A., and Fasullo, J.: Estimates of the global water budget and its annual cycle using observational and model data, J. Hydrometeorol., 8, 758–769, doi:10.1175/JHM600.1, 2007.

Vinukollu, R. K., Sheffield, J., Wood, E. F., Bosilovich, M. G., and Mocko, D.: Multi-model analysis of Energy and Water Fluxes: Intercomparisons between Operational Analyses, Land Surface Model and Remote Sensing, J. Hydrometeorol., 13, 3–26, doi:10.1175/2011JHM1372.1, 2011.

Wahr, J., Swenson, S., Zlotnicki, V., and Velicogna, I.: Time-variable gravity from GRACE: First results, Geophys. Res. Lett., 31, L11501, doi:10.1029/2004GL019779, 2004.

Wijffels, S. E., Willis, J., Domingues, C. M., Barker, P., White, N. J., Gronell, A., Ridgway, K., and Church, J. A.: Changing Expendable Bathythermograph Fall Rates and Their Impact on Estimates of Thermosteric Sea Level Rise, J. Climate, 21, 5657–5672, doi:10.1175/2008JCLI2290.1, 2008.

Willmott, C. J. and Matsuura, K.: Terrestrial air temperature and precipitation: monthly and annual time series (1900–2008), V2.01, Center of Climatic Research, University of Delaware, 2010.

Xie, P. P. and Arkin, P. A.: Global precipitation: A 17-year monthly analysis based on gauge observations, satellite estimates, and numerical model outputs, B. Am. Meteorol. Soc., 78, 2539–2558, 1997.

Yu, L. and Weller, R. A.: Objectively analyzed air-sea heat fluxes for the global ice-free oceans (1981–2005), B. Am. Meteorol. Soc., 88, 527–539, doi:10.1175/BAMS-88-4-527, 2007.

Marine Geodesy, 35(S1):82–97, 2012

ISSN: 0149-0419 print / 1521-060X online
DOI: 10.1080/01490419.2012.718209

Taylor & Francis
Taylor & Francis Group

Estimating ENSO Influence on the Global Mean Sea Level, 1993–2010

A. CAZENAVE,[1] O. HENRY,[1] S. MUNIER,[1] T. DELCROIX,[1]
A. L. GORDON,[3] B. MEYSSIGNAC,[1] W. LLOVEL,[2]
H. PALANISAMY,[1] AND M. BECKER[4]

[1]LEGOS, OMP, Toulouse, France
[2]JPL, Pasadena, California, USA
[3]LDEO, Columbia University, New York, New York, USA
[4]UMR Espace-DEV/UAG, Cayenne, French Guiana

Interannual global mean sea level (GMSL) variations and El Nino-Southern Oscillation (ENSO) are highly correlated, with positive/negative GMSL anomalies during El Nino/La Nina events. In a previous study, we showed that interannual GMSL and total land water storage variations are inversely correlated, with lower-than-average total water storage on land and higher-than-average GMSL during El Nino. This result is in agreement with the observed rainfall deficit/excess over land/oceans during El Nino (and vice versa during La Nina). It suggests that the positive GMSL anomaly observed during El Nino is likely due to an ocean mass rather than thermal expansion increase. Here, we analyze the respective contribution of the Atlantic, Indian, and Pacific oceans to the interannual (ENSO-related) GMSL anomalies observed during the altimetry era (i.e., since 1993) with an emphasis on the 1997/1998 El Nino event. For each oceanic region, we compute the steric contribution, and remove it from the altimetry-based mean sea level to estimate the ocean mass component. We find that mass changes of the tropical Pacific Ocean, mainly in the region within 0–25°N, are mostly responsible for the observed 1997/1998 ENSO-related GMSL anomaly. The ocean mass excess of this region almost perfectly compensates the total land water deficit during the 1997/1998 El Nino. An estimate of the ocean-atmosphere water balance of this region shows that the time derivative of the ocean mass component is well correlated with net P-E (precipitation minus evaporation) over most of the study period, except during the 1997/1998 ENSO event, where there is a temporary ocean mass increase, not compensated by the net P-E. We thus propose that the 1997/1998 ocean mass increase of this north tropical Pacific area be linked to an imbalance between the inflow/outflow entering/leaving the north tropical Pacific. A preliminary qualitative analysis indicates that a significant reduction of the Makassar Strait transport, (about 80% of the total Indonesian throughflow), as previously reported in the literature during the strong 1997/1998 El Nino event, could explain the north tropical Pacific Ocean mass excess reported in this study, hence the observed positive GMSL anomaly.

Keywords Sea level, ENSO, land waters, steric sea level, ocean mass

Received 13 January 2012; accepted 27 April 2012.
Address correspondence to Anny Cazenave, LEGOS, 18 Avenue Edouard Belin, 31401 Toulouse Cedex 9, France. E-mail: anny.cazenave@legos.obs-mip.fr

1. Introduction

On interannual to multidecadal time scales, global mean sea level (GMSL) variations can be explained by ocean thermal expansion and water mass variations (due to land ice melt and land water storage changes) (e.g., Bindoff et al. 2007). Over the altimetry era (1993–2010), the rate of GMSL rise amounts to 3.2 +/− 0.4 mm/yr (e.g., Ablain et al. 2009; Nerem et al. 2010) and is rather well explained by ocean thermal expansion (by ∼30%) and land ice loss (∼60%) (e.g., Cazenave and Llovel 2010; Church et al. 2011). So far, however, little attention has been given to explain the origin of the GMSL interannual variability. For the altimetry era, Nerem et al. (2010) noticed that detrended GMSL changes are correlated to El Nino-Southern Oscillation (ENSO) occurrences, with positive/negative sea level anomalies observed during El Nino/La Nina. This is illustrated in Figure 1a showing detrended altimetry-based GMSL over 1993–2010 and the Multivariate ENSO Index (MEI; Wolter and Timlin 1998). The correlation between the two monthly data sets is rather modest (equal to 0.4) for the whole time span but reaches 0.7 when the calculation is performed over the 1997–98 period including the very strong record-breaking 1997/1998 El Nino event. This suggests that ENSO influences either ocean thermal expansion or ocean mass (or both). Interestingly, Llovel et al. (2011a) reported that the interannual GMSL variations are inversely correlated to interannual variations in global land water storage, with a tendency for a deficit in land water storage during El Nino events (and vice versa during La Nina). This was shown through a global water mass conservation approach using Gravity Recovery and Climate Experiment (GRACE) space gravimetry data and the Interactions between Soil, Biosphere and Atmosphere–Total Runoff Integrating Pathways (ISBA-TRIP) global hydrological model developed at MeteoFrance (Alkama et al. 2010) to estimate land water storage changes over the altimetry era.

Continental waters are continuously exchanged between atmosphere, land and oceans through vertical and horizontal mass fluxes (precipitation, evaporation, transpiration of the vegetation, surface runoff, and underground flow). Conservation of total water mass in the climate system at interannual time scale (neglecting to a first approximation, the atmospheric reservoir as in Llovel et al. 2011a) leads to:

$$\Delta M_{ocean} \approx -\Delta M_{LW} \tag{1}$$

where ΔM_{ocean} and ΔM_{LW} represent changes with time of ocean mass and total land water storage due to total fresh water input/output from precipitation, evaporation-transpiration, and runoff. Total land water storage change can be further expressed in terms of equivalent sea level change by simply dividing the total continental water volume change by the mean surface of the oceans and changing its sign (i.e., multiplying by -1 to reflect that less water on land corresponds to more water in the oceans, and inversely). Figure 1b shows the total land water storage change over 1993–2008 (an update of Llovel et al. 2011a; see Section 2.3), expressed in equivalent sea level, superimposed to the detrended GMSL. We can note the good quantitative agreement between the two curves, in particular during the 1997/1998 El Nino event. This result is not surprising as it is known that during an El Nino, there is more rain over the oceans and less rain on land as reported by several studies (e.g., Dai and Wigley 2000; Gu et al. 2007; Gu and Adler 2011). The fact that the positive 1997/1998 GMSL anomaly is quantitatively explained by the negative total land water storage anomaly suggests that there is almost perfect water mass compensation between ocean and land during that period and that other processes (e.g., ocean heat storage change) are negligible.

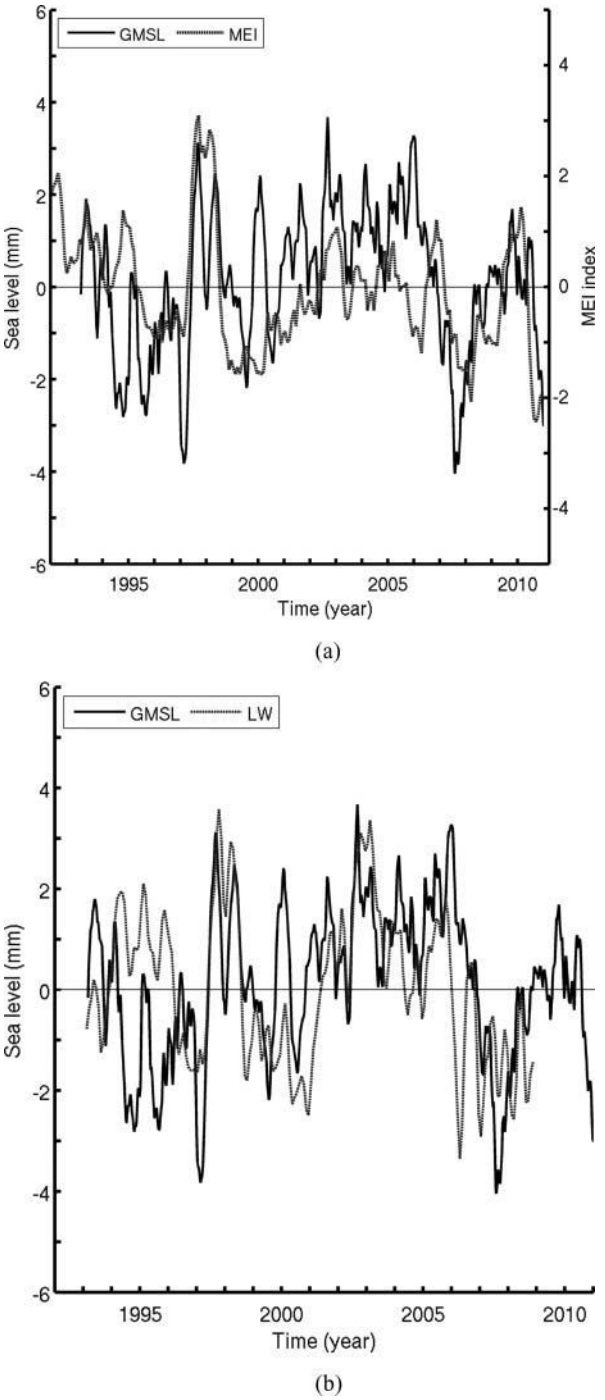

Figure 1. (a) Detrended altimetry-based global mean sea level (GMSL, black curve) and multivariate ENSO Index (MEI, black dotted curve). Positive MEI values denote El Nino periods, and negative values La Nina periods (b) Detrended altimetry-based global mean sea level (GMSL, black curve) and reversed (i.e., multiplied by -1) total land water storage from the ISBA-TRIP model expressed in equivalent sea level (LW, black dotted curve).

In the present study, we investigate this issue further and intend to determine whether the total ocean water mass excess noticed during El Nino is uniformly distributed over the oceans. If not, we want to know which ocean basin and/or region are mainly responsible for the ENSO-related GMSL anomalies. For that purpose, we consider the altimetry time span (since 1993) but mostly focus the discussion on the 1997/1998 ENSO event. We compute the detrended mean sea level in different oceanic regions, estimate the steric component (thermal expansion plus salinity effects) using in situ ocean temperature and salinity data, and deduce the ocean mass component for each region (from the difference between altimetry-based mean sea level and steric sea level). We find that it is the north tropical Pacific region that mostly contributes to the observed (anti) correlation between interannual GMSL and global land water storage during ENSO. We further estimate the water budget of the ocean-atmosphere system over the north Pacific region, considering the time derivative of ocean mass, precipitation P, evaporation E, and transport of water in and out the considered region. Finally we discuss potential processes causing the north tropical Pacific mass anomaly during ENSO.

2. Datasets

2.1. Sea Level Data

For the altimetry-based sea level data, we use the DT-MSLA "Ref" series provided by Collecte Localisation Satellite (CLS; http://www.aviso.oceanobs.com/en/data/products/sea-surface-height-products/global/msla/index.html). This dataset is used over the timespan from January 1993 to December 2010. It is available as 1/4° × 1/4° Mercator projection grids at weekly interval from a combination of several altimetry missions (Topex/Poseidon, Jason-1 and 2, Envisat, and ERS 1 and 2). Improved geophysical corrections are applied to the sea level data (see Ablain et al. 2009 for details).

2.2. Steric Data

Steric sea level is estimated using an updated version (v6.12) of in situ ocean temperature and salinity data from Ishii and Kimoto (2009) (called hereafter IK09). The IK09 temperature data are corrected for the XBT depth bias. The temperature and salinity data are available at monthly interval over 16 depth levels ranging from the ocean surface down to 700 m depth, on a global 1° × 1° grid from 1955 to 2009. Steric sea level anomalies are computed over the 0–700 m depth range for the period January 1993 to December 2009. The deep ocean contribution cannot be accounted for since hydrographic data below 700 m are too sparse, noting that recent studies showed that almost all interannual variability in steric sea level in confined in the upper 300–500 m of the ocean (e.g., Llovel et al. 2011b). At global scale, salinity does not contribute to the GMSL, but this is not true at regional scale. This is why here we account for salinity in this study.

2.3. ISBA-TRIP Global Hydrological Model

To estimate global land water storage, we use the ISBA-TRIP global hydrological model developed at MeteoFrance. The ISBA land surface scheme calculates time variations of surface energy and water budgets. Soil hydrology is represented by three layers: a thin surface layer (1 cm) included in the rooting layer and a third layer to distinguish between the

rooting depth and the total soil depth. The soil water content varies with surface infiltration, soil evaporation, plant transpiration, and deep drainage. ISBA uses a comprehensive parameterization of subgrid hydrology to account for heterogeneity of precipitation, topography, and vegetation within each grid cell. It is coupled with the Total Runoff Integrating Pathways (TRIP) module (Oki and Sud 1998). TRIP is a simple river routing model converting daily runoff simulated by ISBA into river discharge on a global river channel network here defined at 1° by 1° resolution. Details on the ISBA-TRIP model can be found in Decharme et al. (2006) and Alkama et al. (2010). The outputs of the ISBA-TRIP model cover the period January 1950 to December 2008, with values given at monthly interval on a 1°x1° grid. They are based on a forced mode run, with global meteorological forcing provided by the Princeton University on a 3-hourly time step and 1° resolution. We updated by two additional years (up to December 2008) the total land water storage computation done by Llovel et al. (2011a) using the ISBA-TRIP model. The whole land surface has been considered. The reversed total (i.e., whole land area-averaged) land water storage curve shown in Figure 1b (estimated from ISBA-TRIP model and expressed in sea level equivalent) has not been detrended (unlike the GMSL curve) because the land water storage trend is negligible. The correlation between the two curves is 0.4 over the whole period. It increases to 0.70 when considering the 1997–98 timespan (El Nino event).

2.4. Precipitation, Evaporation and Wind Stress Data

Precipitation P and evaporation E data used in this study are based on different datasets. For precipitation, we used products from the Global Precipitation Climatology Project (GPCP; Adler et al. 2003) and Climate Prediction Center Merged Analysis of Precipitation (CMAP; Xie and Arkin 1997). For evaporation, we used the Objectively Analyzed air-sea Fluxes product (OAFlux; Yu and Weller 2007) and the Hamburg Ocean Atmosphere Parameters and Fluxes from Satellite Data (HOAPS; Anderson et al. 2007). We also used reanalysis products from the European Centre for Medium-Range Forecast (ECMWF) ERA-Interim data (Simmons et al. 2007), which provides both precipitation and evaporation data. To give more confidence in the inferred net precipitation (P-E), we also estimated (P-E) using other parameters of the atmospheric moisture budget, namely precipitable water P_{water} and moisture flux divergence divQ (as done in several global- and regional-scale studies; e.g., Syed et al. 2009; Sahoo et al. in press). This was performed through the relationship:

$$P - E = -(dP_{water}/dt + divQ) \quad (2)$$

The P_{water} and divQ data were provided by the ECMWF ERA-Interim and the National Centers for Environmental Prediction/National Center for Atmospheric Research (NCEP/NCAR; Kalnay et al. 1996) databases.

These datasets provide monthly global data on regular grids (resolution from 0.5° to 2.5° depending on the dataset) in units of mm/month. All gridded data are further expressed in terms of monthly averages over the period January 1993 to December 2009.

2.5. Filtering, Averaging, Weighting, Smoothing and Data Uncertainties

As we focus here on the interannual variability, for all datasets we remove the seasonal signal at each mesh of all gridded fields (i.e., before area-averaging) through a least-squares adjustment of 6-month and 12-month period sinusoids. Mean time series are obtained by geographical averaging applying a cosine (latitude) weighting. To each spatially averaged

time series, we also remove a linear trend over the 1993–2009 timespan. A 3-month running filter is further applied.

Estimate of data uncertainties depends on the dataset. For altimetry-based sea level data, uncertainty of 3-month area-averaged sea level data is estimated to ∼1 mm (assuming a 4 mm error for 10-day mean values; see Ablain et al. 2009). The steric sea level error is estimated from the difference between the IK09 and Levitus et al. (2009) steric datasets. We find a mean error of ∼1.5 mm for the 3-month globally area-averaged steric sea level data. A similar approach is conducted to infer the P-E error using the differences between direct P and E estimates as well as indirect estimates from the atmospheric water balance equation (see Section 4.1).

3. Results: Contributions of Steric Sea Level and Mass Component to the Mean Sea Level in the Atlantic, Indian and Pacific Oceans, 1993–2010

We computed the spatially averaged, altimetry-based, and steric sea level, as well as mass component (i.e., the difference between altimetry-based mean sea level and steric component, assuming that the deep ocean contribution is negligible) over the: (1) Atlantic Ocean (70°W to 20°E; 60°S to 60°N latitude), (2) Indian Ocean (20°E to 120°E, 60°S to 30°N), and (3) Pacific Ocean (120°E to north and south America coasts, 60°S to 60°N). Figures 2a–c show the relative contributions of the Atlantic, Indian, and Pacific oceans to the interannual GMSL, as well as corresponding steric and ocean mass components. The term "relative contributions" means that each curve is weighted by the ratio between the surface of the considered area and the whole ocean surface (hereafter called "area weighting").

The contributions of the Atlantic, Indian, and Pacific sea level to the GMSL display significant interannual variability, with mean standard deviations of 1.1, 1.4, and 1.2 mm, respectively. Atlantic and Indian oceans show positive sea level anomalies peaking in 1998/early 1999, likely related to the La Nina phase that followed the 1997/1998 El Nino. These sea level anomalies are likely of thermal origin as the steric component closely follows the observed sea level. The correlation between mean sea level and steric sea level over 1997–98 is 0.75 and 0.67 for the Atlantic and Indian oceans, respectively, reinforcing the fact that during this El Nino period the sea level anomaly in these two basins has mostly a steric origin.

In late 1997/early 1998, the Pacific steric sea level is negative while the observed sea level is slightly positive. The correlation between the mean sea level and steric sea level is only 0.2 over 1997–98, contrasting with the higher correlation values discussed above for the Atlantic and Indian oceans.

The Pacific mass component presents a large negative anomaly in 1997 followed by a steep rise and a positive anomaly in early 1998. This result suggests that the 1997/1998 GMSL anomaly could be located in the Pacific Ocean.

To further infer the exact location of this mass anomaly, we computed the zonally averaged (from 120°E to the American coasts) time-latitude diagram of the Pacific Ocean mass anomalies (considering 1° wide latitudinal bands). The diagram is shown in Figure 3. It displays a positive anomaly in the ∼10°S–20°N latitude band during the 1994/1995 El Nino, followed by another positive anomaly during the 1997/1998 El Nino, located in the 5°S–30°N latitude band, and with an amplitude of ∼20 mm. The mass anomalies of this tropical band are then weaker or even slightly negative during the remaining time period that includes both El Nino and La Nina events.

From the diagram presented in Figure 3, we may conclude that the main 1997/1998 ENSO-related Pacific Ocean mass anomaly seen in Figure 2c is located in the 5°S–30°N

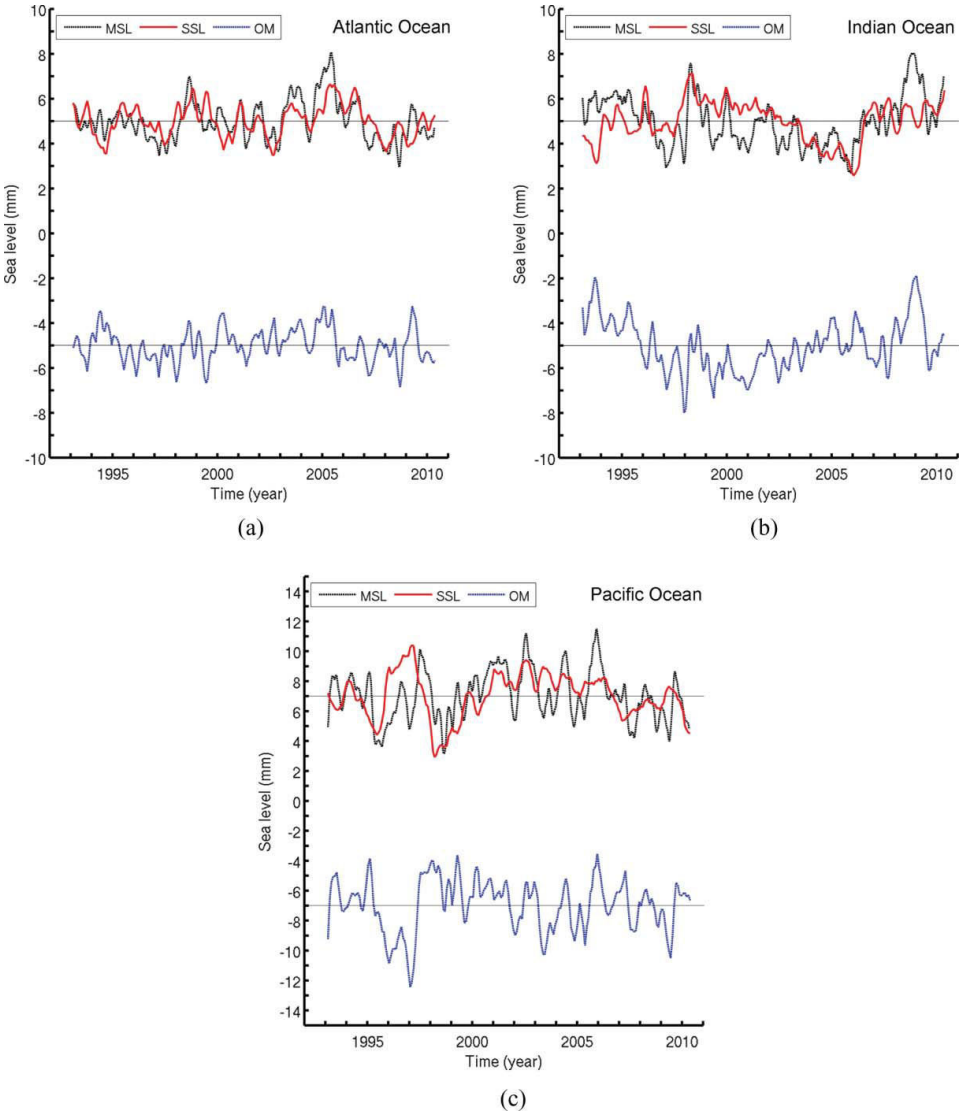

Figure 2. Contribution of the (a) Atlantic, (b) Indian, and (c) Pacific basins to the global mean sea level: area-averaged mean sea level (MSL, black curve), area-averaged mean steric sea level (SSL, red curve) and ocean mass component (difference between the former two) (OM, blue curve). See text for basin boundaries. Units are mm (sea level equivalent). The MSL/SSL and OM time series are shifted vertically for clarity. Note that the time series are area-weighted (i.e., multiplied by the ratio between the surface of considered region and the whole ocean surface). (Color figure available online.)

latitudinal band. To further detail the importance of such an anomaly, the top inset in Figure 3 represents the (reverse) total land water storage time series expressed in equivalent sea level (as in Figure 1b), and the right-hand side inset shows the correlations (computed over the 1993–2008 and 1996–2000 timespans; respectively, black and red curves) between the land water time series and the Pacific mass anomalies within successive 1° latitudinal bands. The right-hand side curves shows that positive correlations are obtained in the north tropical domain, with correlation maxima (reaching 0.8) around the equator, 10°N and 20°N. In the following, we consider the 0°–25°N latitudinal band for the tropical Pacific mass anomaly.

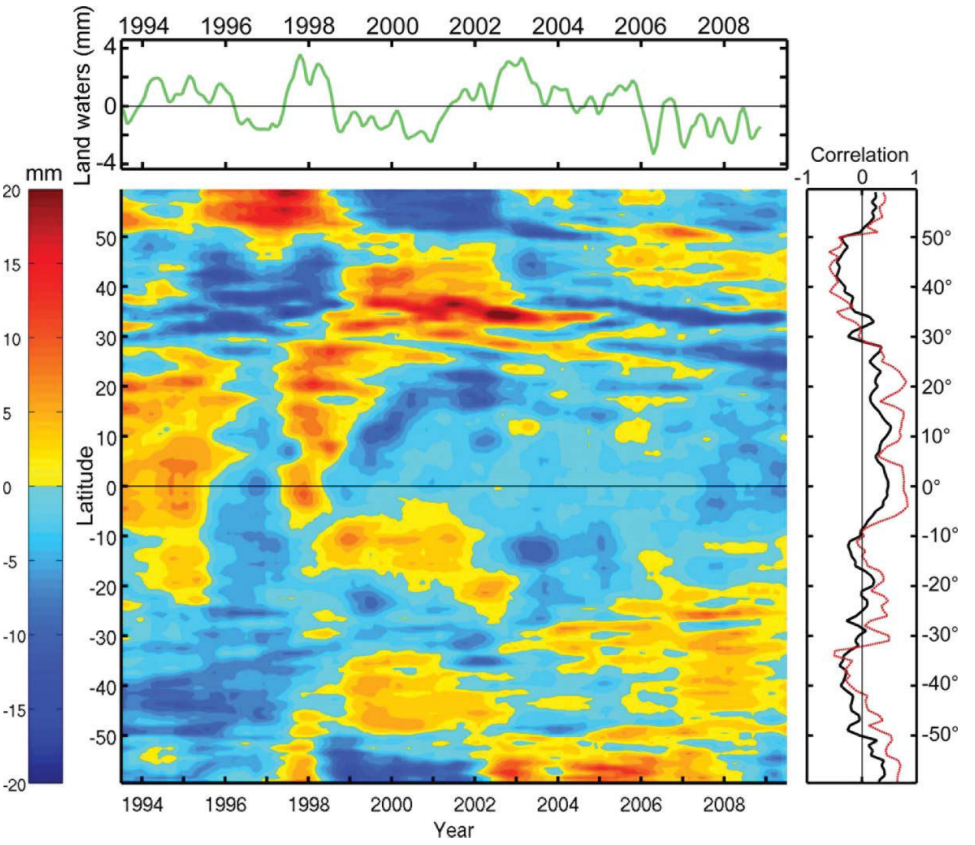

Figure 3. Time-latitude diagram of the zonally averaged (from 120°E to the American coasts) Pacific ocean mass component. Values have been smoothed with a 6-month running mean for clarity. Units: mm (sea level equivalent). The top curve represents the reversed total land water storage time series expressed in equivalent sea level, as in Figure 1b. The right-hand side black and red curves are the correlations as a function of latitude between the land water storage curve (in equivalent sea level) and Pacific ocean mass in successive 1° wide latitudinal bands over the whole timespan and over 1996–2000, respectively. (Color figure available online.)

But tests have shown that considering slightly different bands (e.g., 5°S–25°N or 0°–30°N) leads to essentially similar results. Note also that considering a longitude area as of 100°E instead of 120°E (i.e., including the South China Sea) does not change these results.

To determine the zonal extension of the 0°–25°N mass anomaly, we computed a longitude-time diagram of the mass anomalies shown in Figure 4. In Figure 4 we observe a band of positive mass anomalies during the 1997/1998 El Nino extending from about 120°E–140°E to the coast of America. In contrast, we note a band of negative anomalies located in the central tropical Pacific during the 1999/2000 La Nina.

To check whether the north tropical Pacific mass anomaly quantitatively correlates with (i.e., is compensated by) the total land water storage change, we restricted the analysis done for Figure 2c to the 0°–25°N tropical Pacific. The corresponding altimetry-based sea level, steric sea level, and ocean mass time series are shown in Figure 5 (with area-weighting). On the ocean mass curve we have superimposed the (reversed) total land water

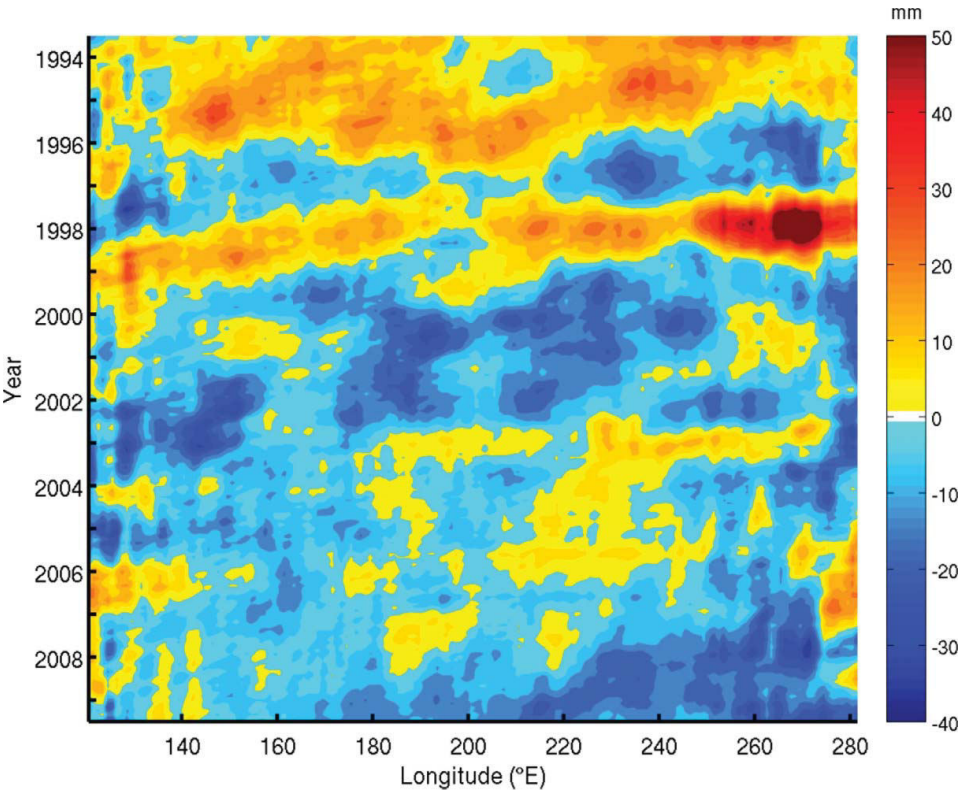

Figure 4. Longitude-time diagram of meridionally averaged Pacific ocean mass component (data averaged in latitude between 0° and 25°N). Values have been smoothed with a 6-month running mean for clarity. Units: mm (sea level equivalent). (Color figure available online.)

curve (expressed in equivalent sea level). We note an overall good agreement and a quasi perfect quantitative agreement during the 1997/1998 El Nino, indicating that total land water deficit during that El Nino was almost totally compensated by an increase of the north tropical Pacific Ocean mass. The correlation between north tropical Pacific Ocean (0°–25°N) mass and land water storage (expressed in equivalent sea level) amounts to 0.91 over 1997–98 (considering slightly different latitudinal bands for the ocean mass averaging, e.g., 0°–30°N, has negligible influence on the shape of the curve shown in Figure 5, as well as on the correlation).

4. Discussion

In Section 3, we showed that the 1997/1998 positive anomaly of the (detrended) GMSL is largely due to an excess of mass located in a zonal band of the north tropical Pacific Ocean between ∼0° and 25°N latitude. We also showed that this north tropical Pacific mass excess quantitatively compensates the total land water storage deficit observed during that El Nino event. The question now is: Which process causes the 1997/1998 El Nino-related north tropical Pacific positive mass anomaly?

A budget analysis of all terms involved in the mass conservation equation would be necessary to solve that question. While this is not possible with the observation data we

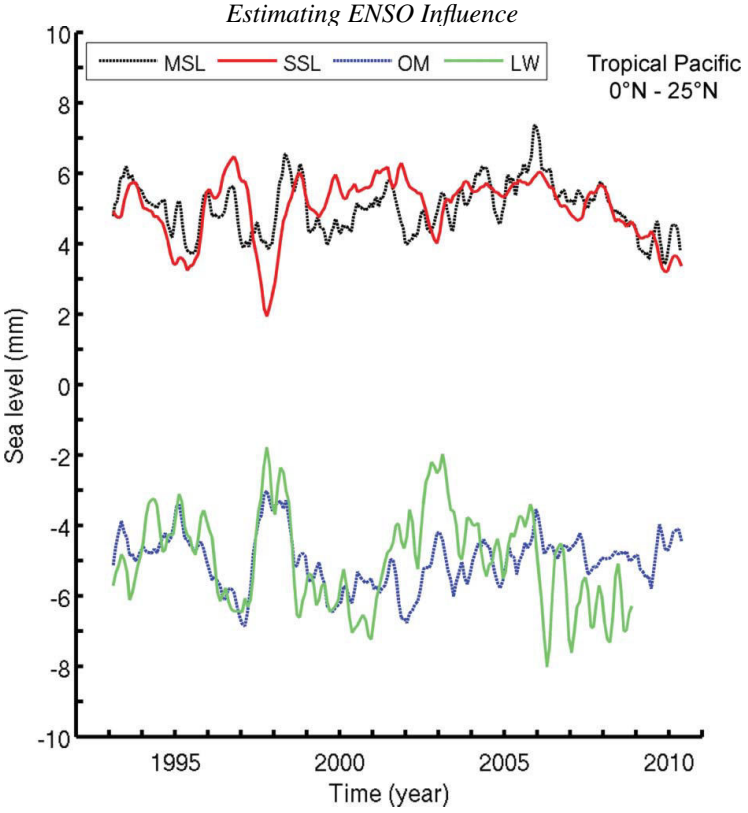

Figure 5. Contribution of the tropical north Pacific (0–25°N) to the GMSL: mean sea level, MSL (black curve), steric sea level, SSL (red curve) and ocean mass component (difference between the former two), OM (blue curve). The reversed total land water time series (expressed in equivalent sea level) LW (green curve) is superimposed. The MSL/SSL, OM/LW time series are shifted vertically for clarity. Units: mm (sea level equivalent). (Color figure available online.)

have in hand, we do believe instructive to present tentative explanations that may stimulate ocean modellers and/or new ideas. In the following, we examine successively different terms of the mass budget equation over the north tropical Pacific Ocean (0°–25°N).

Given our definition of the north tropical Pacific in terms of area (i.e., between 0° and 25°N latitude and ~120°E to the American coasts) its mass changes can be due to variations of surface P-E, river runoff (R), and water mass transports across the open boundaries. The mass balance equation can then be written as:

$$\mathrm{dOM/dt} = \mathrm{P} - \mathrm{E} + R + \mathrm{Inflow/Outflow} \tag{3}$$

In Eq. (3), dOM/dt is the time derivative of the north tropical Pacific ocean mass (area defined above). The term called Inflow/Outflow (denoted I/O in the following) represents transport of water in and out the considered domain (counted positive when entering the domain). The I/O term results from: (1) flow across the equator via the interior pathway and the western boundary current, (2) flow across the 25°N parallel, and (3) flow at the western boundary (i.e., the Indonesian throughflow-ITF; Gordon 2005). Note that R in Eq. (3) can be neglected as no major river flows into the considered region.

In the following two subsections, we estimate the two dominant terms of the right-hand side of the water budget equation (Eq. (3)), that is, net precipitation (P-E) (subsection 4.1)

and Inflow/Outflow (I/O; subsection 4.2). Corresponding analysis is performed over the 0–25°N tropical Pacific.

4.1. (P-E) Changes over the North Tropical Pacific Ocean (0–25°N)

ENSO events produce large scale anomalies of the atmospheric circulation in the tropics, with direct effects on precipitation (e.g., Dai and Wigley 2000; Trenberth et al. 2002; Neelin et al. 2003; Smith et al. 2006). Warm ENSO events (El Nino) give rise to more rainfall over the oceans and less rainfall over land, with opposite variations during cold events (La Nina) (Gu et al. 2007). Gu et al. (2007) and Gu and Adler (2011) showed that strong positive/negative precipitation anomalies affect tropical ocean/land during ENSO warm phases, with ocean/land responses being always opposite in sign. They also showed that the ENSO-related total precipitation signal in the tropics (ocean plus land) is weak. Dai and Wigley (2000) and Curtis and Adler (2003) showed how precipitation patterns evolve in the tropical Pacific during the ENSO development. For example, El Nino produces positive precipitation anomalies in the central equatorial Pacific that move eastward and southward as the event matures.

We computed P-E time series using the different meteorological datasets described in Section 2.4. Figure 6a shows the P-E time series over the 0–25°N tropical Pacific from the different datasets between 1993 and 2009. This graph clearly shows a high correlation between the different computations (mean standard deviation of 0.44 mm/month over the whole period) and particularly during the 1997/1998 El Nino event. Figure 6b compares the net precipitation mean (averaging all individual time series) and associated standard deviation (red curve and shading) with the dOM/dt time series (blue curve). Their difference is shown in Figure 6c. Figure 6b indicates a reasonably good correlation between mean net precipitation and dOM/dt (correlation of 0.58) during the whole timespan. However, during the 1997/1998 El Nino peak, dOM/dt is less negative than P-E. The difference curve (Figure 6c) indeed shows a large positive residual peaking in early 1998, indicating that there is no compensation between dOM/dt and P-E; thus, the I/O term appearing in Eq. (3) may not be neglected. The result shown in Figure 6c corroborates the fact that changes in net precipitation cannot to be directly responsible for the north tropical Pacific mass anomaly because of fast water spreading at the surface by the ocean currents (see Huang et al. 2005).

4.2. Mass Transport into and out from the North Tropical Pacific Ocean (0–25°N)

In the following, we examine the inflow/outflow term of the north tropical Pacific water budget.

Figure 7 shows the I/O term (difference between dOM/dt and P-E) over the north tropical Pacific (0–25°N) (same as Figure 6c but over 1996–2000 only to enhance the 1997/1998 ENSO period) on which is superimposed the negative I/O (i.e., -I/O) term computed as the difference between dOM/dt and P-E over the whole Indian Ocean and whole south Pacific domain (0–60°S). Looking at Figure 7, we clearly see a high anti-correlation (−0.95) between the inflow/outflow terms of these two regions. Figure 7 also shows the I/O term over the northern part of the Pacific Ocean (25°N–60°N) (green curve). The corresponding curve is rather flat, with very small interannual variations compared with the two other curves, indicating that water transfers in/out the 25°N parallel are almost balanced.

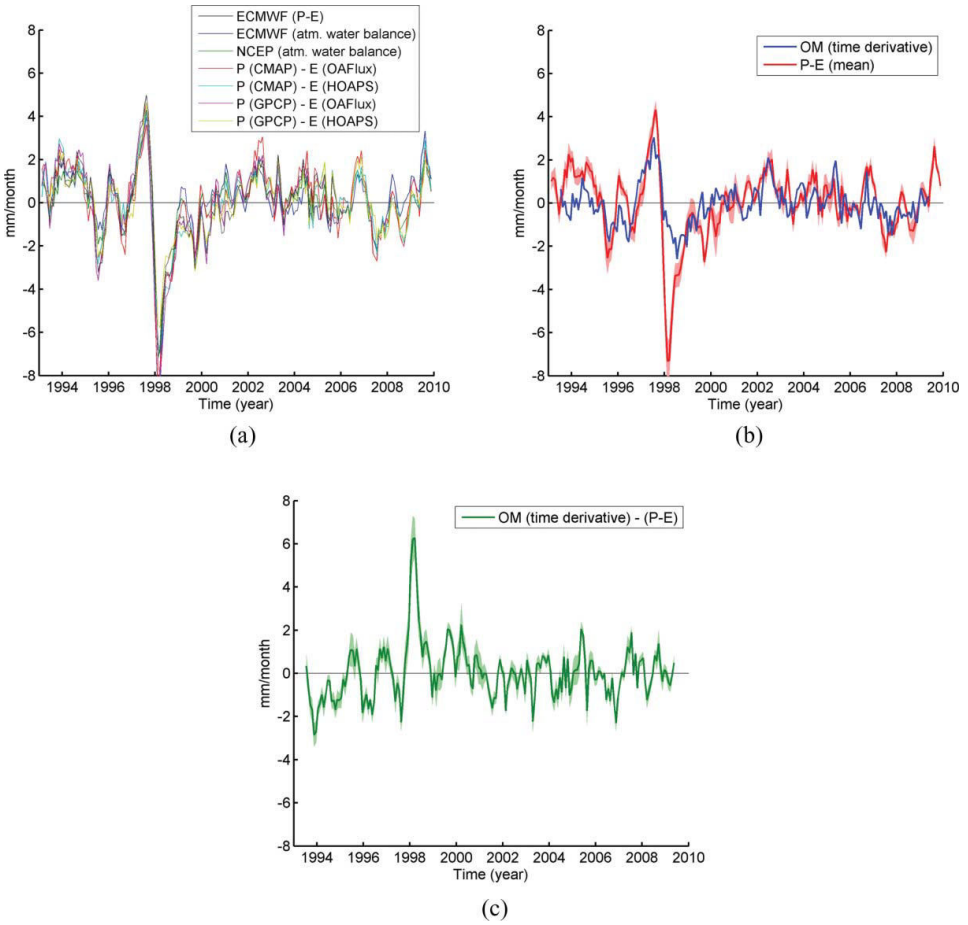

Figure 6. (a) Direct and indirect (from atmospheric water balance) estimates of net P-E over the north Pacific Ocean (0–25°N) from different meteorological data sets. (b) Time derivative of the mass component (blue curve) and mean P-E (red curve) values averaged over the North Pacific Ocean (0–25°N). (c) Difference time series between the time derivative of the North Pacific Ocean mass component and mean (P-E). Red and green shadings in Figures 6a and 6b represent spreading the P-E estimates. Unit: mm/month. (Color figure available online.)

The reported anti-correlation between the inflow/outflow terms of the north tropical Pacific (0–25°N) and the combined Indian oceans plus south Pacific domain suggests that the water exchanges with the Atlantic Ocean at the eastern and western boundaries are also compensated.

The above two results suggests that the positive mass anomaly in the north tropical Pacific is linked to flow variations across the equator via the interior pathway and the western boundary current and/or variations of the Indonesian throughflow (ITF). We briefly discuss the latter possibility.

The Makassar Strait located between Borneo and Sulawesi is the main channel for the ITF, carrying about 80% of the total ITF, which amounts to 15 Sv (Sv = 10^6 m^3/s) (Gordon et al. 2010). On average, the depth-integrated transport at the Makassar Strait is on the order of 8–12 Sv (Gordon 2005; Gordon et al. 2008), but interannual variability of

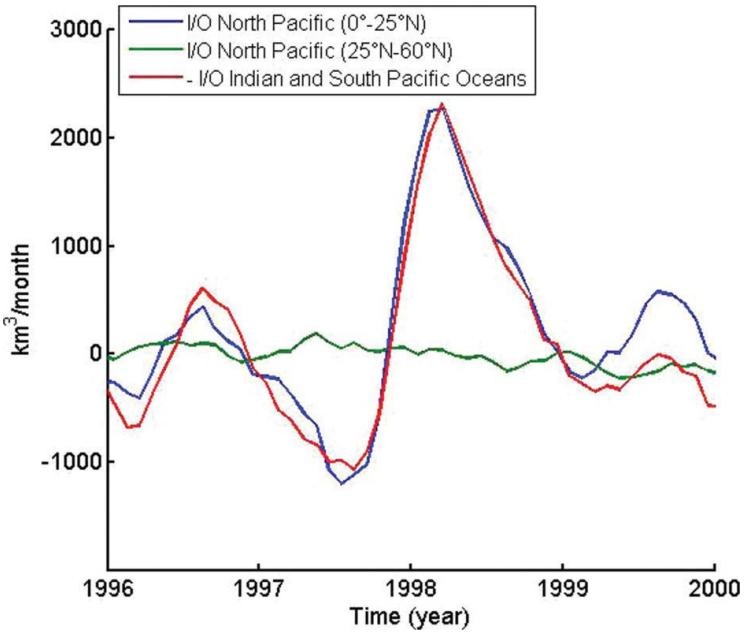

Figure 7. Time series of the difference (term I/O in Eq. (3)) between the time derivative of the ocean mass component and (P-E) for (blue curve) the north tropical Pacific Ocean (0–25°N) and (red curve) the Indian ocean plus south Pacific domain. Note that the sign of the red curve has been reversed to ease the comparison. The green curve represents the I/O term across the 25°N parallel in the north Pacific. Units are in km^3/month (i.e., data are multiplied by the areas of the considered domains). (Color figure available online.)

the ITF associated with ENSO has been reported (e.g., England and Huang 2005; Vranes and Gordon 2005). From in situ measurements, Susanto and Gordon (2005) showed that during the calendar year 1997, the Makassar transport was 7.9 Sv, falling to less than 5 Sv during the peak of the 1997/1998 El Nino. During 2004–06, the ENSO phase was generally that of El Niño (with a brief La Niña phase in early 2006), though substantially subdued relative to the 1997/1998 event. The 2004–06 Makassar Strait transport averaged 11.6 Sv (Gordon et al. 2008; Gordon et al. 2010). During 2007–10, when the ENSO phase shifted toward La Niña, a single current measuring mooring in Makassar Strait observed elevated southward velocity, with an estimated transport of 13–14 Sv (Gordon et al. 2012). Surface water from the tropical Pacific is lost as the Mindanao Current leaks into the ITF; that is, not all of the Mindanao Current turns eastward to feed into the Pacific's North Equatorial Counter Current. In this way, the ITF does act to redistribute the mass input from rainfall. Gordon et al. (2012) showed that the leakage of surface water from the Mindanao Current into the ITF is reduced during El Niño when the surface layer is drawn more from the 19°N Luzon Strait throughflow to enter Makassar Strait from the South China Sea. During La Nina, the Luzon Strait throughflow goes to near zero allowing greater surface layer inflow from the Mindanao. Such water transport changes are related to large-scale wind field changes over the Pacific and Indian oceans during ENSO (e.g., Godfrey 1996).

Reduced ITF of a few Sv, if not compensated by flow variations across the equator, is of the right order of magnitude to explain the north tropical Pacific mass excess observed during the 1997/1998 El Nino peak. In effect, a crude calculation shows that

1 Sv reduction over 1 month corresponds to a water volume of 2600 km^3 remaining in the north tropical Pacific while the observed mass excess in this region corresponds to $\sim$1500 km^3.

The above results may suggest that the 1997/1998 El Nino event could be related to an important variation of the water mass transfer between the north tropical Pacific Ocean (0–25°N) and Indian and South Pacific oceans. In particular, a reduction of the ITF possibly combined with an intensification of water transfers from the south Pacific could have led to an important water mass increase in the north tropical Pacific region. Even though this study does not allow us to discriminate between the relative importance of these contributions, we cannot exclude that an important part of the water transport variations may have occurred at the Makassar Strait. Further quantitative analyses are required to confirm this, for example, using ocean general circulation model outputs.

5. Conclusion

The results presented in this study confirm that interannual variability of the GMSL has essentially a water mass origin, as the interannual GMSL is highly inversely correlated with total land water storage change, in particular during ENSO events. Focusing on the large positive GMSL anomaly observed during the 1997/1998 El Nino, we show that this anomaly is largely due to a mass excess of the north tropical Pacific (located between 0° and 25°N in latitude and $\sim$120°E to the American coasts in longitude). We also show that the ocean-atmosphere water budget computed over the north tropical Pacific (0–25°N) is not closed during the 1997/1998 El Nino peak if the inflow/outflow terms are not accounted for. The north tropical Pacific mass excess associated with this El Nino event is consistent with the reduced depth-integrated water transport at the Makassar Strait (the Indonesian throughflow) previously reported during the 1997/1998 El Nino, although we cannot exclude that flow across the equator via the interior pathway and the western boundary current also play some role. Further analyses are required to quantitatively confirm or infirm this conclusion.

A similar investigation should be performed for La Nina events, during which important drops of the GMSL are observed. This was the case, for example, in 2007–08 and 2010–11. It will be interesting to determine whether the transport at the Makassar Strait is also a good candidate to explain the GMSL variability, as well as to assess the potential role of meridional mass transports across the equator. In line with our observation-based results, a precise quantification of all processes responsible for the GMSL at the ENSO time scale will be conducted with the help of ocean general circulation model outputs.

Acknowledgements

O. Henry, S. Munier, W. Llovel, and H. Palanisamy are supported, respectively, by a European grant in the context of the Monarch Project, a postdoctoral grant from CNES, a postdoctoral grant from JPL/NASA, and the French ANR CECILE project. A. L. Gordon research is supported by the National Science Foundation grant OCE-0725935. This is Lamont-Doherty contribution number 7545.

We thank H. Douville, B. Decharme, and R. Alkama for providing us with the ISBA-TRIP model outputs.

References

Ablain, M., A. Cazenave, S. Guinehut, and G. Valladeau. 2009. A new assessment of global mean sea level from altimeters highlights a reduction of global slope from 2005 to 2008 in agreement with in-situ measurements. *Ocean Sci.* 5(2):193–201.

Adler, R. F., G. J. Huffman, A. Chang, R. Ferraro, P. P. Xie, J. Janowiak, B. Rudolf, U. Schneider, S. Curtis, D. Bolvin, A. Gruber, J. Susskind, P. Arkin, and E. Nelkin. 2003. The version-2 global precipitation climatology project (GPCP) monthly precipitation analysis (1979–present). *Journal of Hydrometeorology* 4:1147–1167.

Alkama, R., B. Decharme, H. Douville, A. Voldoire, S. Tyteca, P. Le Moigne, M. Becker, A. Cazenave, and J. Sheffield. 2010. Global evaluation of the ISBA-TRIP continental hydrological system Part 1: Comparison to GRACE terrestrial water storage estimates and in-situ river discharges. *Journal of Hydrometeorology* 11:583–600. doi: 10.1175/2010JHM1211

Andersson, A., S. Bakan, K. Fennig, H. Grassl, C. Klepp, and J. Schulz. 2007. Hamburg ocean atmosphere parameters and fluxes from satellite data – HOAPS-3 – monthly mean. *World Data Center for Climate electronic publication*.

Bindoff, N., J. Willebrand, V. Artale, A. Cazenave, J. Gregory, S. Gulev, K. Hanawa, C. Le Quéré, S. Levitus, Y. Nojiri, C. K. Shum, L. Talley, and A. Unnikrishnan. 2007. Observations: Oceanic climate and sea level. In ed. S. Solomon, D. Qin, M. Manning, Z. Chen, M. Marquis, K. B. Averyt, M. Tignor, and H. L. Miller, *Climate Change 2007: The Physical Science Basis. Contribution of Working Group I to the Fourth Assessment Report of the Intergouvernmental Panel on Climate Change*. Cambridge: Cambridge University Press.

Cazenave, A., and W. Llovel. 2010. Contemporary sea level rise. *Annual Review in Marine Science* 2:145–173.

Church, J. A., N. J. White, L. F. Konikow, C. M. Domingues, J. G. Cogley, E. Rignot, J. M. Gregory, M. R. van den Broeke, A. J. Monaghan, and I. Velicogna. 2011. Revisiting the Earth's sea level and energy budgets from 1961 to 2008. *Geophys. Res. Lett.* 38:L18601. doi: 10.1029/2011GL048794

Curtis, S., and R. F. Adler. 2003. Evolution of El Nino-precipitation relationships from satellites and gauges. *J. Geophys. Res.* 108:4153. doi: 10.1029/2002JD002690

Dai, A., and T. M. L. Wigley. 2000. Global patterns of ENSO-induced precipitation. *Geophys. Res. Lett.* 27(9):1283–1286.

Decharme, B., and H. Douville. 2006. Introduction of a sub-grid hydrology in the ISBA land surface model. *Climate Dyn.* 26:65–78.

England, M., and F. Huang. 2005. On the interannual variability of the Indonesian throughflow and its linkage with ENSO. *J. Clim.* 18:1435–1444.

Godfrey, J. S. 1996. The effect of the Indonesian throughflow on ocean circulation and heat exchange with the atmosphere: A review. *J. Geophys. Res.* 101(C5):12217–12237.

Gordon, A. L. 2005. Oceanography of the Indonesian seas and their throughflow. *Oceanography* 18(4):14–27.

Gordon, A. L., R. D. Susanto, A. Ffield, B. A. Huber, W. Pranowo, and S. Wirasantosa. 2008. Makassar Strait throughflow, 2004 to 2006. *Geophys. Res. Letters* 35:L24605. doi: 10.1029/2008GL036372

Gordon, A. L., J. Sprintall, H. M. Van Aken, D. Susanto, S. Wijffels, R. Molcard, A. Ffield, W. Pranowo, and S. Wirasantosa. 2010. The Indonesian throughflow during 2004–2006 as observed by the INSTANT program. Modeling and observing the Indonesian throughflow. In Ed. A. L. Gordon and V. M. Kamenkovich, *Dynamics of Atmosphere and Oceans* 50:115–128.

Gordon, A. L., B. A. Huber, E. J. Metzger, R. D. Susanto, H. E. Hurlburt, and T. R. Adi. 2012. South China Sea throughflow impact on the Indonesian throughflow. *Geophys. Res. Lett.* (in revision).

Gu, G., R. F. Adler, G. J. Huffman, and S. Curtis. 2007. Tropical rainfall variability on interannual to interdecadal and longer time scales derived from the GPCP monthly products. *J. Climate* 20:4033–4046.

Gu, G., and R. F. Adler. 2011. Precipitation and temperature variations on the interannual time scale: Assessing the impact of ENSO and volcanic eruptions. *J. Climate* 24:2258–2270.

Huang, B. Y., V. M. Mehta, and N. Schneider. 2005. Oceanic response to idealized net atmospheric freshwater in the Pacific at the decadal time scale. *J. Phys. Oceanography* 35(12):2467–2486. doi: 10.1175/JPO2820.1

Ishii, M., and M. Kimoto. 2009. Reevaluation of historical ocean heat content variations with varying XBT and MBT depth bias corrections. *Journal of Oceanography* 65:287–299.

Kalnay, E., M. Kanamitsu, R. Kistler, W. Collins, D. Deaven, L. Gandin, M. Iredell, S. Saha, G. White, J. Woollen, Y. Zhu, M. Chelliah, W. Ebisuzaki, W. Higgins, J. Janowiak, K. C. Mo, C. Ropelewski, J. Wang, A. Leetmaa, R. Reynolds, R. Jenne, and D. Joseph. 1996. The NCEP/NCAR 40-year reanalysis project. *Bulletin of the American Meteorological Society* 77:437–471.

Levitus, S., J. I. Antonov, T. P. Boyer, R. A. Locarnini, H. E. Garcia, and A. V. Mishonov. 2009. Global ocean heat content 1955–2008 in light of recently revealed instrumentation problems. *Geophys. Res. Lett.* 36:L07608. doi: 10.1029/2008GL037155

Llovel, W., M. Becker, A. Cazenave, S. Jevrejeva, R. Alkama, B. Decharme, H. Douville, M. Ablain, and B. Beckley. 2011a. Terrestrial waters and sea level variations on interannual time scale. *Global Planet Change* 75:76–82. doi: 10.1016/j.gloplacha.2010.10.008

Llovel, W., B. Meyssignac, and A. Cazenave. 2011b. Steric sea level variations over 2004–2010 as a function of region and depth: Inference on the mass component variability of the North Atlantic. *Geophys. Res. Lett.* 38:L15608. doi: 101029/2011GL047411

Neelin, J. D., C. Chou, and H. Su. 2003. Tropical drought regions in global warming and El Nino teleconnections. *Geophys. Res. Lett.* 30:2275. doi: 10.1029/2003GL018625

Nerem, R. S., D. P. Chambers, C. Choe, and G. T. Mitchum. 2010. Estimating mean sea level change from the TOPEX and Jason altimeter missions. *Marine Geodesy* 33(1):435–446.

Oki, T., and Y. C. Sud. 1998. Design of total runoff integrating pathways (TRIP)—a global river channel network. *Earth Interactions* 2(1):1–37.

Sahoo, A. K., M. Pan, T. J. Troy, R. K. Vinukollu, J. Sheffield, and E. F. Wood. in press. Reconciling the global terrestrial water budget using satellite remote sensing. *Remote Sensing of Environment*.

Simmons, A., S. Uppala, D. Dee, and S. Kobayashi. 2007. Era-interim: New ECMWF reanalysis products from 1989 onwards. *ECMWF Newsletter* 110.

Smith, T. M., X. Yin, and A. Gruber. 2006. Variations in annual global precipitation (1979–2004), based on the global precipitation climatology project 2.5° analysis. *Geophys. Res. Lett.* 33:L06705. doi: 10.1029/2005GL025393

Susanto, R. D., and A. L. Gordon. 2005. Velocity and transport of the Makassar Strait throughflow. *J. Geophys. Res.* 110:C01005. doi: 10.1029/2004JC002425

Syed, T. H., J. S. Famiglietti, and D. P. Chambers. 2009. GRACE-based estimates of terrestrial freshwater discharge from basin to continental scales. *Journal of Hydrometeorology* 10:22–40.

Trenberth, K. E., J. M. Caron, D. P. Stepaniak, and S. Worley. 2002. Evolution of El Nino-southern oscillation and global atmospheric surface temperatures. *J. Geophys. Res.* 107:4065. doi: 10.1029/2000JD000298

Vranes, K., and A. L. Gordon. 2005. Comparison if Indonesian troughflow transport observations, Makassar Strait to eastern Indian Ocean. *Geophys. Res. Lett.* 32:L10606. doi: 10.1029/2004GL022158

Wolter, K., and M. S. Timlin. 1998. Measuring the strength of ENSO—how does 1997/98 rank? *Weather* 53:315–324.

Xie, P. P., and P. A. Arkin. 1997. Global precipitation: A 17-year monthly analysis based on gauge observations, satellite estimates, and numerical model outputs. *Bulletin of the American Meteorological Society* 78:2539–2558.

Yu, L., and R. A. Weller. 2007. Objectively analyzed air-sea heat fluxes for the global ice-free oceans (1981–2005). *Bull. Amer. Meteorol. Soc.* 88(4):527–539.

L'influence d'El Niño et de La Niña sur le niveau de la mer

Anny Cazenave[1], **Habib Boubacar Dieng**[1], **Simon Munier**[1], **Olivier Henry**[1], **Benoit Meyssignac**[1], **Hindumathi Palanisamy**[1] et **William Llovel**[2]

(1) Laboratoire d'études en géophysique et océanographie spatiales (LEGOS) Observatoire Midi-Pyrénées
18 avenue Édouard Belin - 31401 Toulouse Cedex 9, France
(2) Jet Propulsion Laboratory, Pasadena, États-Unis

Résumé

Outre une hausse moyenne de l'ordre de 3 mm par an, le niveau moyen global de la mer présente des fluctuations de quelques millimètres durant les événements El Niño et La Niña. Lors de El Niño, on observe une anomalie positive alors qu'à La Niña correspond une anomalie négative du niveau de la mer. Ces fluctuations du niveau moyen global de la mer sont inversement corrélées aux variations du stock d'eau total sur les continents. Cette observation est en accord avec le fait que, durant El Niño, il pleut davantage sur l'océan que sur les continents, et inversement durant La Niña. Cela suggère que les fluctuations du niveau moyen global de la mer associées aux événements El Niño/La Niña sont plutôt dues à des variations de masse de l'océan qu'à des variations d'origine thermique. Dans cet article, on montre qu'au cours de l'événement El Niño de 1997-1998, l'anomalie positive de masse de l'océan est localisée dans l'océan Pacifique tropical nord. L'excès de masse de cette région compense de manière quasi parfaite le déficit du stock d'eau total des continents à cette période.

...

L'altimétrie spatiale de haute précision a révélé que le niveau moyen global de la mer a monté assez régulièrement depuis début 1993, à la vitesse moyenne de 3,2 ± 0,4 mm par an (Meyssignac et Cazenave, 2012). Cependant, si l'on y regarde de près, on remarque de petites oscillations interannuelles autour de la tendance linéaire (après retrait du cycle saisonnier), dont l'amplitude est de l'ordre de quelques millimètres. Il est assez frappant que le niveau moyen global de la mer présente une anomalie positive assez marquée lors du grand El Niño de 1997-1998. Cela est illustré sur la figure 1 qui présente les fluctuations du niveau moyen global de la mer entre 1993 et 2011 (après retrait d'une tendance linéaire moyenne sur la période). La figure 1 montre aussi des anomalies négatives du niveau moyen global de la mer lors des événements La Niña de 2007-2008 et de 2010-2011. Quelle est la cause de ces anomalies et quel est le lien entre le niveau moyen de la mer et les événements ENSO (El Niño-Southern Oscillation) ?

Aux échelles de temps interannuelles à multi-décennales, les principaux phénomènes à l'origine des variations du niveau moyen global de la mer sont :
- l'expansion (ou la contraction) thermique des océans, causée par des variations de la température de la mer (lorsque la température augmente, l'eau de mer se dilate et le niveau de la mer s'élève, et inversement) ;
- l'augmentation (ou la diminution) du contenu en eau des

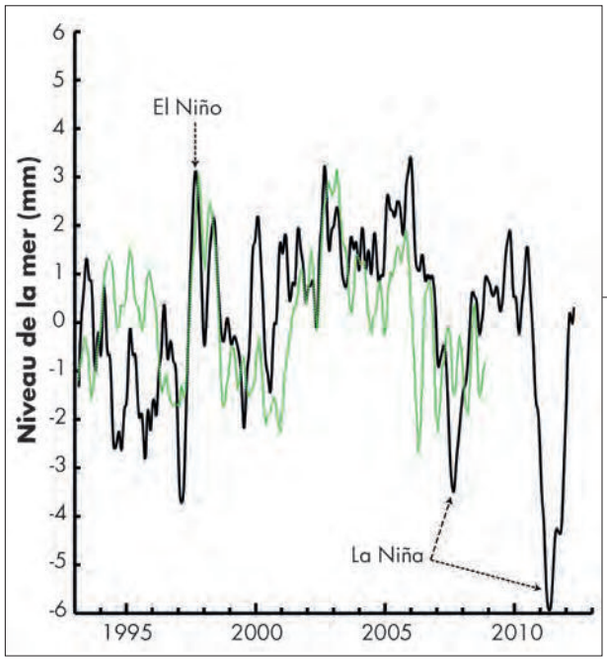

Figure 1 - En noir : niveau moyen global de la mer mesuré par altimétrie spatiale entre janvier 1993 et décembre 2011 (données du site AVISO : www.aviso.oceanobs.com). La tendance linéaire de 3,1 mm/an a été retirée. Les données entre 60° S et 60° N sont considérées.
En vert : stock d'eau continental total, estimé à partir du modèle hydrologique ISBA-TRIP de Météo-France, exprimé en équivalent « niveau de la mer ».

Abstract

The influence of El Nino and La Nina on sea level

The detrended global mean sea level displays positive/negative anomalies of a few millimetres amplitude during El Nino/La Nina events that are inversely correlated to total terrestrial water storage variations. This result is in agreement with the observed rainfall deficit/excess over land/oceans during El Nino (and vice versa during La Nina). It suggests that the positive anomaly observed during El Nino in the global mean sea level is likely due to the ocean mass rather than thermal expansion. A detailed analysis over each oceanic region shows that the global mean sea level anomaly observed during the strong 1997-1998 El Nino resulted from an excess of mass of the north tropical Pacific Ocean with almost perfect compensation with the total terrestrial water deficit during this El Nino.

océans, causée par les apports d'eau douce issus de la fonte des glaces continentales ou associés à des modifications du stock des eaux continentales.

Même si les glaces continentales présentent de petites variations interannuelles, on n'a pas observé de lien net entre leur bilan de masse et ENSO, pour le moment. Il reste donc deux « candidats » pour expliquer les anomalies positives et négatives du niveau moyen global de la mer lors des épisodes ENSO : l'expansion thermique de l'océan et la variation du stock d'eau sur les continents.

Expansion thermique et masse de l'océan durant El Niño

Au cours des cinq dernières décennies, des mesures de température de la mer ont été collectées par les bateaux, par les bouées océanographiques et, depuis quelques années, par les flotteurs profilants du projet international Argo. Grâce à ces données, les océanographes peuvent estimer la contribution de l'expansion thermique de l'océan au niveau de la mer en intégrant, jusqu'à 700-1000 m de profondeur, les anomalies de densité de l'eau induites par les variations de température. La figure 2 (courbes du haut) montre l'expansion thermique moyennée sur l'ensemble du domaine océanique, sur la période 1993-2010 (une tendance linéaire moyenne sur la période a été retirée). Le niveau moyen global de la mer (tendance linéaire retirée) y est superposé. On n'observe pas d'anomalie significative de l'expansion thermique lors de l'épisode El Niño de 1997-1998. On peut donc écarter l'expansion thermique de l'océan comme cause de l'anomalie positive du niveau de la mer observée à cette date.

La figure 2 (courbes du bas) présente les variations du niveau moyen global de la mer (tendance linéaire retirée) et de la masse de l'océan global (calculée par différence entre le niveau moyen global de la mer et l'expansion thermique, après retrait d'une tendance linéaire sur chacune des deux séries temporelles). On note une excellente correspondance entre les deux quantités à l'échelle de temps interannuelle, en particulier lors de l'événement El Niño de 1997-1998. Cela suggère que ce sont plutôt les variations de masse de l'océan, et non celles de l'expansion thermique, qui expliquent les fluctuations observées du niveau moyen global de la mer.

Eaux continentales et niveau de la mer durant El Niño

Dans une étude récente (Llovel et al., 2011), une équipe du Laboratoire d'études en géophysique et océanographie spatiales (LEGOS) a observé une forte corrélation quantitative entre la variabilité interannuelle du niveau moyen global de la mer (tendance linéaire retirée) et le stock total d'eau dans les bassins fluviaux, en particulier lors de l'événement El Niño de 1997-1998. Il y a donc

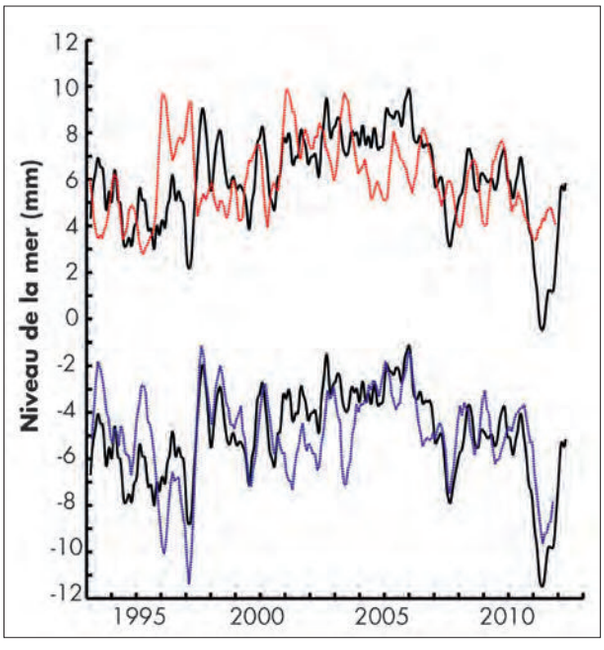

Figure 2 - En haut : en noir, niveau moyen global de la mer mesuré par altimétrie spatiale entre janvier 1993 et décembre 2011, après le retrait de la tendance linéaire (même courbe que sur la figure 1) ; en rouge, expansion thermique moyenne globale, après le retrait de la tendance linéaire (données moyennées entre 60° S et 60° N d'après la version 6.12 des données de Ishii et Kimoto, 2009).
En bas : en noir, niveau moyen global de la mer (même courbe que ci-dessus et sur la figure 1) ; en bleu, composante de masse de l'océan estimée par différence entre niveau moyen global de la mer et expansion thermique (les tendances linéaires ont été retirées).

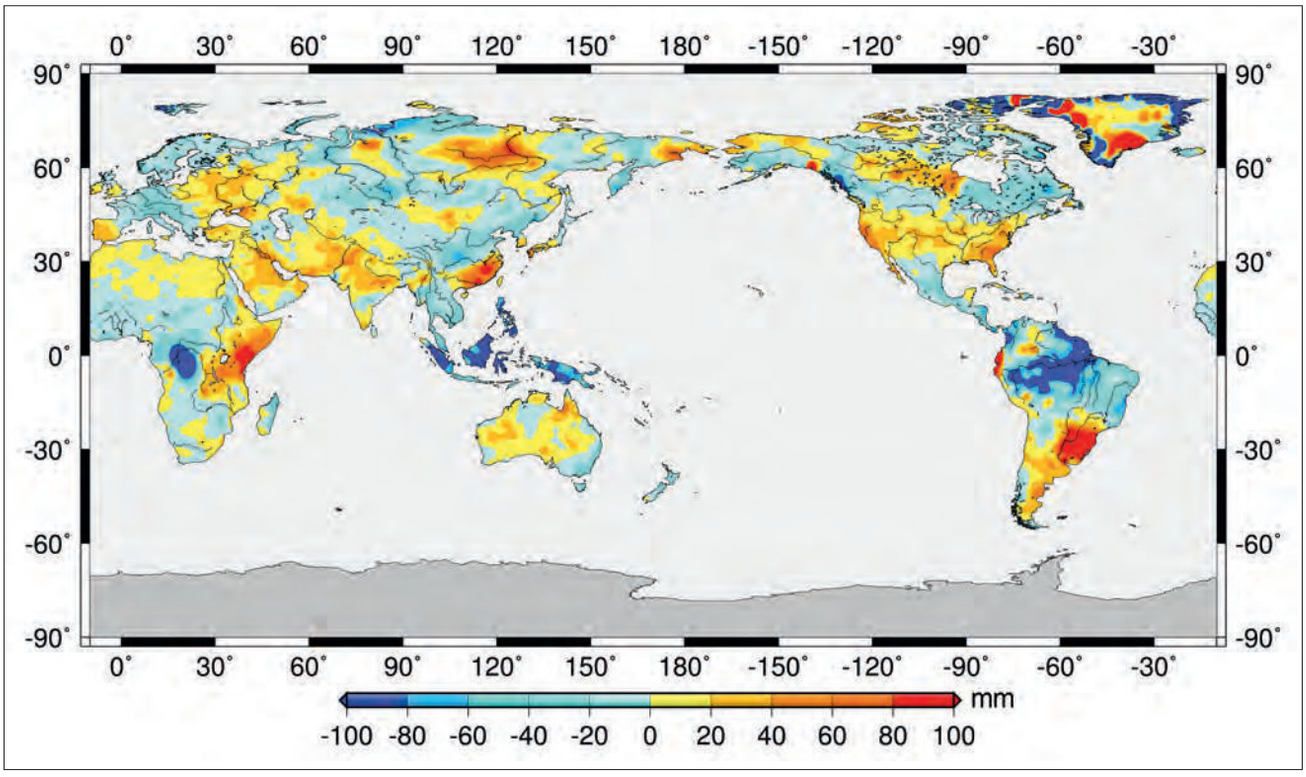

Figure 3 - Carte des anomalies de hauteur d'eau (en mm) sur les terres émergées (d'après le modèle hydrologique ISBA-TRIP de Météo-France). Ces anomalies sont calculées sur une période d'une année (juillet 1997 à juillet 1998) qui coïncide avec l'événement El Niño de 1997-1998.

là une piste pour comprendre le lien entre niveau de la mer et ENSO.

Avec la mission de gravimétrie spatiale *GRACE* lancée en 2002, il est aujourd'hui possible de mesurer, pour la première fois, les variations spatio-temporelles de la gravité de la terre (Cazenave et Chen, 2010). Aux échelles de temps allant de quelques mois à plusieurs années, ces variations temporelles de gravité résultent principalement des variations de la masse de glace des calottes polaires et des glaciers, ainsi que de la masse d'eau sur les continents en réponse à la variabilité climatique ou aux activités humaines (construction de barrages, irrigation, déforestation, urbanisation, etc.). La résolution spatiale de *GRACE* (environ 300 km) permet de cartographier ces différentes sources et les signaux associés, en particulier les variations des stocks d'eau dans les grands bassins fluviaux (Ramillien et al., 2008). Cependant, pour estimer les variations du stock total d'eau sur les continents avant 2002, il faut faire appel à des modèles hydrologiques. C'est ce qu'ont fait Llovel et al. (2011). Ils ont utilisé les sorties du modèle hydrologique global ISBA-TRIP, développé à Météo-France, dans une version utilisant le forçage météorologique de l'université Princeton entre 1950 et 2008, avec un pas de temps d'un mois et une résolution au sol de 1°×1° (voir Alkama et al., 2010). Pour chaque pas de temps, la masse d'eau des différentes couches du sol considérées par le modèle a été moyennée géographiquement sur l'ensemble des terres émergées (à l'exclusion des calottes polaires). Cette masse d'eau a été exprimée en équivalent « niveau de la mer », en pondérant par le rapport des surfaces entre continents et océans, et en multipliant par -1 (pour exprimer le fait qu'un excès d'eau sur les continents correspond à un déficit dans l'océan, et inversement). Sur la figure 1, la série temporelle correspondante est superposée à celle du niveau moyen global de la mer (tendance linéaire retirée). On remarque une correspondance relativement bonne entre les deux quantités lors de l'épisode El Niño de 1997-1998. La corrélation positive entre les deux courbes indique que, pendant cet événement, il y a un excès d'eau dans l'océan et un déficit d'eau sur les continents.

Cela n'est pas vraiment surprenant puisque plusieurs études ont montré que, durant El Niño, il y a davantage de précipitations sur l'océan et moins de pluie sur les continents, en particulier dans les tropiques (Dai et Wigley, 2000 ; Gu et al, 2007 ; Gu et Adler, 2011). L'étude de Llovel et al. (2011) a par ailleurs montré que la contribution dominante au déficit d'eau continental est celle du bassin de l'Amazone, lors de l'événement El Niño de 1997-1998. Cela est illustré par la figure 3 qui montre les anomalies de stock d'eau dans le sol moyennées sur la période juillet 1997-juillet 1998, d'après le modèle ISBA-TRIP de Météo-France (les données sont exprimées en mm d'eau, dans un pixel de 1°×1°). Durant cette période qui correspond au El Niño de 1997-1998, on voit très bien qu'il y a un fort déficit d'eau dans le bassin de l'Amazone.

Augmentation de la masse de l'océan Pacifique tropical nord durant le El Niño de 1997-1998

Ce que traduit la figure 1 est essentiellement la conservation de la masse d'eau dans le système Terre à l'échelle de temps interannuelle (en négligeant le réservoir atmosphérique, ce qui est justifié, en première approximation, compte tenu du court temps de résidence de l'eau dans l'atmosphère). Le déficit d'eau dans les bassins fluviaux lors de l'événement El Niño de 1997-1998 suggère que l'excès d'eau dans l'océan n'est pas causé par le ruissellement des fleuves vers l'océan. Cela est

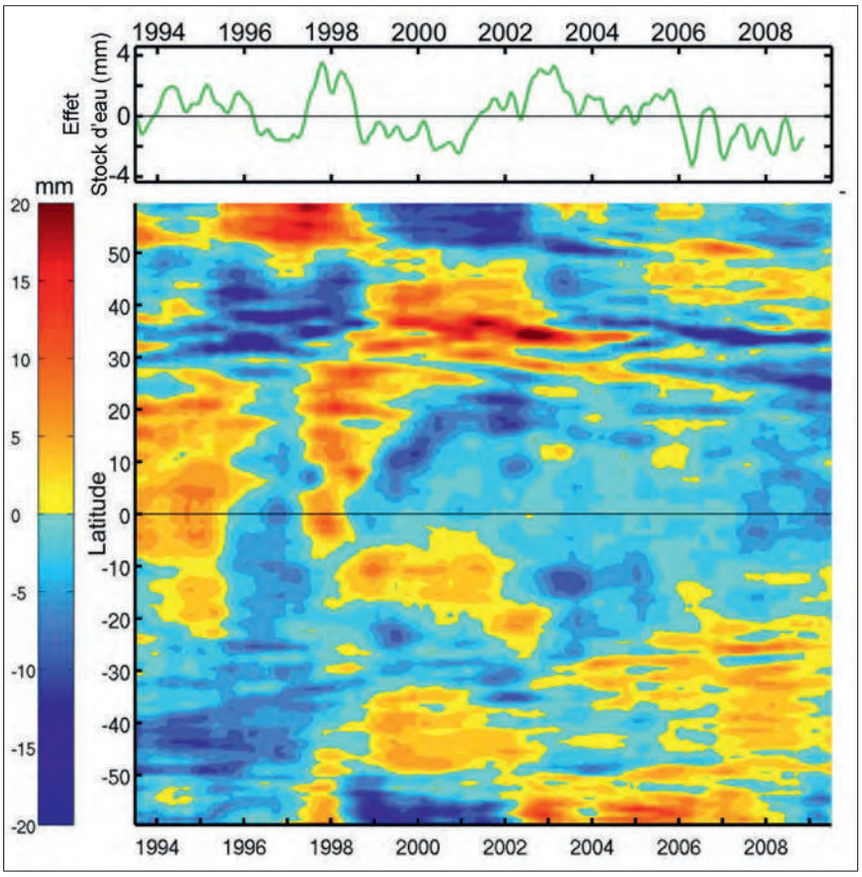

Figure 4 - Diagramme latitude-temps qui représente les variations spatio-temporelles de la masse de l'océan Pacifique moyennée en longitude (entre 120° E et les côtes d'Amérique), en fonction de la latitude et du temps. La courbe du haut (en vert) montre l'évolution, en fonction du temps, du stock d'eau continental exprimé en équivalent « niveau de la mer ».

en accord avec les observations qui indiquent un excès de précipitations sur les océans tropicaux. Mais, l'excès de pluie tombée sur l'océan se répartit uniformément sur le domaine océanique en seulement quelques jours. On pourrait donc s'attendre à ce que l'excès de masse de l'océan qui lui est associé soit uniforme géographiquement. C'est que qu'a cherché à vérifier l'équipe du LEGOS dans une autre étude récemment publiée (Cazenave et al., 2012). L'analyse a consisté à estimer, pour chaque océan, la composante « masse de l'océan » par différence entre le niveau moyen de la mer de cet océan, estimé à partir des données d'altimétrie spatiale, et la composante stérique (après retrait des tendances linéaires). La composante stérique représente la somme de l'expansion thermique et des effets de salinité de l'océan. Cette composante a été calculée en utilisant la base japonaise (mise à jour de Ishii et Kimoto, 2009) de données d'anomalies de température et de salinité de l'océan (alors qu'en moyenne globale, la salinité a une influence négligeable sur le niveau de la mer, ce n'est plus vrai à l'échelle régionale et il faut tenir compte des anomalies de salinité). Pour l'océan Atlantique, l'analyse montre que l'essentiel des variations interannuelles du niveau de la mer est d'origine stérique. La masse de l'océan ne présente aucune anomalie remarquable en 1997-1998. La même observation est faite pour l'océan Indien. En revanche, on voit se dessiner une anomalie positive de la masse de l'océan Pacifique lors de l'événement El Niño de 1997-1998.

Pour cerner plus précisément l'origine géographique de cette anomalie de masse, on a refait la même analyse sur des bandes de latitude de 10° sur tout l'océan Pacifique. On a aussi réalisé un diagramme qui représente les variations spatio-temporelles de la masse de l'océan Pacifique moyennée en longitude (entre 120° E et les côtes d'Amérique) en fonction de la latitude et du temps. Ce diagramme est reproduit sur la figure 4. Il représente également l'évolution, en fonction du temps, du stock d'eau continental exprimé en équivalent « niveau de la mer » (courbe du haut). L'examen de ce diagramme montre bien un excès de masse du Pacifique tropical nord fin 1997-début 1998.

Les deux exercices décrits ci-dessus ont permis de conclure que, durant l'événement El Niño de 1997-1998, l'océan Pacifique présente un excès de masse localisé dans la bande tropicale délimitée par l'équateur et le parallèle 25° N. La figure 5 (courbes du haut) présente le niveau moyen de la mer dans le

▼Figure 5 - En haut : la courbe noire continue représente le niveau moyen de la mer mesuré par altimétrie spatiale sur le Pacifique tropical nord (0-25°N en latitude ; 120° E aux côtes américaines, en longitude) ; la courbe noire en tireté représente la hauteur de la mer stérique moyennée sur la même zone.
En bas : en noir, composante de masse du Pacifique tropical nord (même zone que ci-dessus) ; en vert, stock d'eau continental total, estimé à partir du modèle hydrologique ISBA-TRIP, exprimé en équivalent « niveau de la mer ».

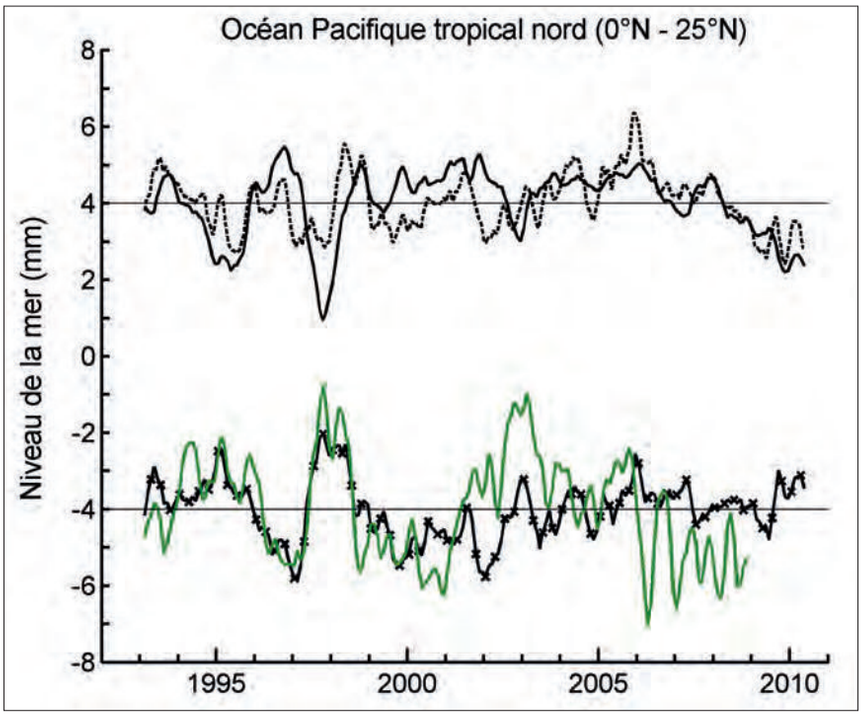

Pacifique tropical nord (0-25° N), superposé à la composante stérique (tendances retirées pour chaque courbe). Les courbes du bas de la figure 5 correspondent à la composante de masse de l'océan Pacifique tropical nord (estimée par la différence entre les deux précédentes quantités) et à la contribution totale des eaux continentales (exprimée en équivalent « niveau de la mer », comme sur la figure 1). On remarque l'excellente correspondance entre la masse du Pacifique tropical nord et la contribution totale des eaux continentales. Cela traduit une compensation quasi parfaite entre l'excès de masse du Pacifique tropical nord et le déficit d'eau sur les continents lors de l'événement El Niño de 1997-1998. Comment expliquer cette observation ?

Bilan d'eau du Pacifique tropical durant El Niño

Une estimation du bilan d'eau sur le Pacifique tropical nord pourrait permettre d'y voir un peu plus clair. Le calcul du bilan d'eau sur la région considérée exprime le fait que la dérivée temporelle de la masse d'eau doit être égale à la somme du terme P-E (précipitation P moins évaporation E) et du terme représentant tous les flux d'eau horizontaux. Ce dernier terme comporte lui-même plusieurs composantes : le ruissellement des fleuves (négligé ici car aucun grand fleuve ne se jette dans l'océan dans la zone considérée) et les transports d'eau horizontaux qui entrent et sortent de la zone. Dans un premier temps, on néglige les transports horizontaux. On observe que, si l'on soustrait le terme (P-E) à la dérivée de la masse d'eau du Pacifique tropical nord, il reste un pic très positif fin 1997-début 1998, comme cela est illustré par la figure 6 (les détails sur les données de précipitation et d'évaporation, utilisées pour ce calcul, se trouvent dans Cazenave et al., 2012). Ce résultat indique que, d'une part, il est nécessaire de faire appel aux transports d'eau horizontaux pour fermer le bilan et que, d'autre part, le flux horizontal net doit être négatif au paroxysme de l'événement El Niño de 1997-1998 (il sort moins d'eau qu'il n'en rentre dans la zone).

Plusieurs études ont montré qu'en période El Niño, le transfert d'eau du Pacifique tropical vers l'océan Indien, via les détroits indonésiens, est réduit

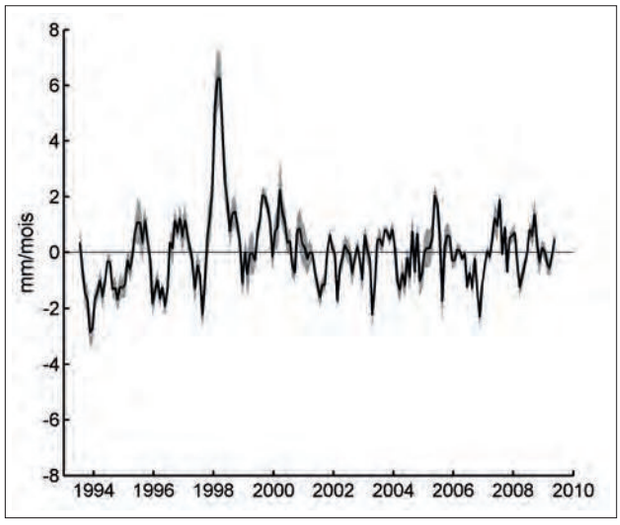

Figure 6 - Différence entre la dérivée de la composante de masse du Pacifique tropical nord et le terme P-E sur la même zone.

d'un facteur 2. Par exemple, Gordon (2005) a montré que, durant le pic de l'événement El Niño de 1997-1998, le transport d'eau au détroit de Makassar (situé entre Bornéo et Sulawasi) est tombé en dessous de 5 Sv, alors que la moyenne est de 8-12 Sv (voir la figure 7 qui montre les échanges d'eau superficiels entre le Pacifique et l'océan Indien, par les détroits indonésiens). L'écoulement de l'eau du Pacifique tropical nord vers l'océan Indien s'est donc ralenti, conduisant à un excès d'eau temporaire dans le Pacifique. Un bref calcul montre que la réduction du transport d'eau aux détroits indonésiens est du bon ordre de grandeur pour expliquer l'excès de masse du Pacifique tropical nord. Cependant, on ne peut exclure qu'une diminution des transports méridiens y contribue également, notamment au niveau de l'équateur. Une analyse plus approfondie s'impose donc.

Figure 7 - Carte représentant les principaux transports océaniques au niveau des détroits indonésiens. (Source : Gordon, 2005.)

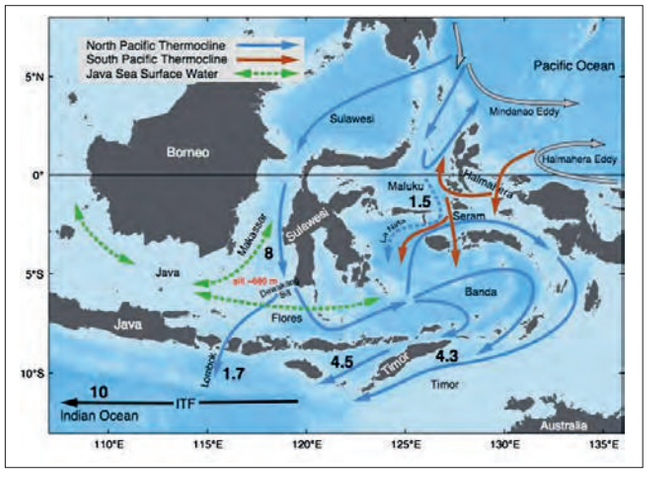

Baisse du niveau de la mer pendant La Niña

Fin 2007-début 2008, ainsi que fin 2010-début 2011, le niveau moyen global de la mer a baissé temporairement de plusieurs millimètres. Ces anomalies négatives coïncident avec deux épisodes La Niña très intenses (voir figure 1). Durant La Niña de 2010-2011, la baisse du niveau de la mer a atteint 5 mm, ce qui représente une perte d'eau (temporaire) de l'océan de 9 000 km^3. Comme durant El Niño, le régime des précipitations dans les tropiques pendant La Niña est considérablement modifié. Mais, à l'inverse de ce qui se passe pendant El Niño, il pleut plus sur les continents et moins sur l'océan durant La Niña, ce qui se traduit pas un déficit d'eau dans l'océan. Dans une étude récente basée sur les données de gravimétrie spatiale *GRACE*, Boeming et al. (2012) ont montré que, lors de l'épisode La Niña de 2010-2011, l'excès d'eau sur les continents est dominé par le bassin de l'Amazone et de l'Orénoque, avec une contribution non négligeable des bassins hydrologiques australiens. Des analyses préliminaires menées au LEGOS semblent indiquer que le déficit d'eau de l'océan se situe principalement dans les océans Pacifique et Indien tropicaux, l'Atlantique ne jouant pratiquement aucun rôle. Mais cela reste à confirmer.

Comme le montre la figure 2 (bas), il faut noter que, durant La Niña de 2010-2011, le déficit de masse de l'océan n'explique que partiellement l'anomalie négative du niveau moyen global de la mer. Il faut donc faire appel à une contribution d'origine thermique lors des phases La Niña. Cela suggère que l'impact de La Niña sur l'océan, sur le niveau de la mer et sur le cycle de

l'eau n'est pas l'exact symétrique de celui d'El Niño, comme suggéré par Okumura et Deser (2010). Des études devront être menées pour clarifier cette question.

Conclusion

Jusqu'à présent, les études sur le niveau de la mer ont principalement concerné les causes de la hausse moyenne globale observée depuis quelques décennies, en lien avec le réchauffement climatique. En revanche, les fluctuations interannuelles ont très peu été analysées. Les résultats récents, mentionnés dans cet article, montrent le rôle majeur des événements ENSO sur le niveau moyen global de la mer, via des modifications importantes du cycle hydrologique global. Plus généralement, ces résultats révèlent que les fluctuations interannuelles du niveau de la mer, associées aux événements El Niño, sont essentiellement causées par des changements de la masse des océans. La composante thermique de l'océan joue un rôle mineur.

Les données globales de niveau de la mer par altimétrie spatiale, ainsi que les données de masse de l'océan par gravimétrie spatiale *GRACE* disponibles depuis 2002, apportent des informations nouvelles et indépendantes des données hydrologiques classiques sur le cycle global de l'eau, en particulier à l'échelle de temps interannuelle.

Bibliographie

Alkama R., B. Decharme, H. Douville, A. Voldoire, S. Tyteca, P. Le Moigne, M. Becker, A. Cazenave et **J. Sheffield**, 2010 : Global evaluation of the ISBA-TRIP continental hydrological system. Part 1: Comparison to GRACE Terrestrial Water Storage estimates and in-situ river discharges. *J. Hydrometeor.*, 11, 583-600, doi:10.1175/2010JHM1211.

Boeming C., J. K. Willis, F. Landerer, S. Nerem et **J. Fasullo**, 2012 : The 2011 La Nina: so strong, the oceans fell. *Geophys. Res. Lett.*, sous presse.

Cazenave A., O. Henry, S. Munier, B. Meyssignac, T. Delcroix, W. Llovel et **H. Palanisamy**, 2012 : ENSO influence on the global mean sea level over 1993-2010. *Marine Geodesy*, doi: 10.1080/01490419.2012.718209, accepté.

Cazenave A. et **J. Chen**, 2010 : Time-variable gravity from space and present-day mass redistribution in the Earth system. *Earth Planet. Sci. Lett.*, 298, 263-274.

Dai A. et **T. M. L. Wigley**, 2000 : Global patterns of ENSO-induced precipitation. *Geophys. Res. Lett.*, 27, 9, 1283-1286.

Gordon A. L., 2005 : Oceanography of the Indonesian seas and their throughflow. *Oceanography*, 18 (4), 14-27.

Gu G. et **R. F. Adler**, 2011 : Precipitation and temperature variations on the interannual time scale: assessing the impact of ENSO and volcanic eruptions. *J. Climate*, 24, 2258-2270.

Gu G., R. F. Adler, G. J.Huffman et **S. Curtis**, 2007 : Tropical rainfall variability on interannual to interdecadal and longer time scales derived from the GPCP monthly products. *J. Climate*, 20, 4033-4046.

Ishii M. et **M. Kimoto**, 2009 : Reevaluation of historical ocean heat content variations with varying XBT and MBT depth bias corrections. *Journal of Oceanography*, 65, 287-299.

Llovel W., M. Becker, A. Cazenave, S. Jevrejeva, R. Alkama, B. Decharme, H. Douville, M. Ablain et **B. Beckley**, 2011 : Terrestrial waters and sea level variations on interannual time scale. *Global and Planetary Change*, 75, 76-82, doi: 10.1016/j.gloplacha.2010.10.008.

Meyssignac B. et **A. Cazenave**, 2012 : Sea level: a review of present-day and recent-past sea level change and variability. *J. Geodyn.*, 58, 96-109.

Okumura Y. et **C. Deser**, 2010 : Asymmetry in the duration of El Nino and La Nina. *J. Climate*, 23, 5826-5843.

Ramillien G., S. Bouhours, A. Lombard, A. Cazenave, F. Flechtner et **R. Schmidt**, 2008 : Land water contributions from GRACE to sea level rise over 2002-2006. *Global and Planetary Change*, 60, 381-392.

Research Article **Open Access**

Habib B. Dieng, Anny Cazenave, Benoit Meyssignac, Olivier Henry, Karina von Schuckmann, Hindumathi Palanisamy, and Jean Michel Lemoine

Effect of La Niña on the global mean sea level and north Pacific ocean mass over 2005-2011

Abstract: Interannual fluctuations of the global mean sea level are highly correlated with El Niño-Southern Oscillation (ENSO) events, with positive/negative anomalies during El Niño/La Niña. In a previous study we showed that during the 1997 – 1998 El Niño, a positive anomaly observed in the global mean sea level was mostly caused by an increase of the ocean mass component rather than by steric (thermal) effects. This result was related to an increase of precipitation over the tropical ocean and a deficit in land water storage. In the present study, we investigate the effect of the recent 2008 and 2011 La Niña events on the satellite altimetry-based global mean sea level. We find that the large global mean sea level drop associated with the 2011 La Niña results from the combined decrease of the steric and ocean mass components, with a slightly dominant contribution from the latter. We show that the ocean mass contribution to the global mean sea level drop is spatially confined over the north eastern tropical Pacific (just as was found previously for the 1997 – 1998 El Niño, but with opposite sign). Corresponding ocean mass spatial pattern is closely correlated to observed sea level and steric spatial patterns over the duration of the La Niña event. This is also observed for previous El Niño and La Niña events. Such a drop in ocean mass during ENSO in the eastern part of the tropical Pacific has not been reported before. It is possibly related to a temporary decrease in the net precipitation over the north eastern Pacific (opposite situation was found during the 1997 – 1998 El Niño).

Habib B. Dieng: LEGOS, OMP, 18 avenue Edouard Belin, 31401 Toulouse Cedex 9
Anny Cazenave: LEGOS, OMP, 18 avenue Edouard Belin, 31401 Toulouse Cedex 9, E-mail: anny.cazenave@legos.obs-mip.fr
Benoit Meyssignac, Olivier Henry: LEGOS, OMP, 18 avenue Edouard Belin, 31401 Toulouse Cedex 9
Karina von Schuckmann: University of Toulon
Hindumathi Palanisamy: LEGOS, OMP, 18 avenue Edouard Belin, 31401 Toulouse Cedex 9
Jean Michel Lemoine: GRGS

1 Introduction

On interannual to decadal time scales, global mean sea level (GMSL) variations mostly result from thermal expansion and mass variations of the oceans. The ocean mass variations themselves result from land ice mass changes (from glaciers and ice sheets), land water storage changes plus a small contribution from atmospheric water vapor. Over the satellite altimetry era (1993-2012), GMSL rise (amounting to 3.1 +/- 0.4 mm/yr) is due to the ocean thermal expansion (by ~30%) and land ice loss (~55%) contributions (e.g., Church et al., 2011, Hansen et al., 2011, Meyssignac and Cazenave, 2012, Hannna et al., 2013, Church et al., 2013). While thermal expansion and land ice dominate the GMSL trend, this is not the case at interannual time scale, as shown by a few recent studies (Llovel et al., 2010, 2011, Cazenave et al., 2012, Boening et al., 2012). These interannual variations appear closely related to ENSO (El Niño-Southern Oscillation) events, with positive/negative sea level anomalies observed during El Niño/La Niña (Nerem et al., 2010). Focusing on the 1997 – 1998 El Niño, Llovel et al. (2010, 2011) showed that GMSL anomalies are inversely related to interannual variations in global land water storage, with a tendency for water deficit on land during El Niño events. This was investigated in more details by Cazenave et al. (2012) who showed that during the 1997 – 1998 El Niño, the GMSL anomaly was largely due to an increase in ocean mass almost fully compensated by water storage deficit on land (with a dominant contribution from tropical river basins –mostly the Amazon-). This is related to the fact that during an El Niño, there is rainfall deficit on land and rainfall excess over tropical oceans (mostly the Pacific Ocean, e.g., Dai and Wigley, 2000, Gu and Adler, 2011). Another result from the Cazenave et al. (2012)' study concerned the location of the ocean mass increase. Counter intuitively, the ocean mass increase was not uniformly distributed over the oceans but concentrated over the northeast tropical Pacific. To explain this ocean mass excess during the 1997 – 1998 El Niño, several hypotheses were investigated (for example, a possible reduced water flow between the Pacific and In-

dian oceans at the Indonesian straits, Gordon et al., 2010) but no definite conclusion has been drawn.

In the present study, we study the interannual variations of the GMSL over 2005-2011, a period with prevailing La Niña events. Over this time span, the interannual GMSL displays negative anomalies of several mm amplitude, coinciding with the 2008 and 2011 La Niña events. As shown by Boening et al. (2012), the GMSL drop during the 2011 La Niña in part results from a temporary decrease in ocean mass (and associated increase in land water storage, Fasullo et al., 2013), as estimated from GRACE space gravimetry data. Here we also compare the interannual GMSL with the sum of the contributions (i.e., the steric and mass components, estimated using different data sets) and explore whether, as for the 1997 – 1998 El Niño, the La Niña-related ocean mass decrease has a particular spatial pattern or not.

2 Method

Interannual variations in GMSL are computed in two ways:

1. Directly from satellite altimetry data after removing, over the study period, the longer-term signal in the GMSL time series,
2. By estimating separately the steric (i.e., due to ocean temperature and salinity) and ocean mass (ΔM_{ocean}) contributions.

The ΔM_{ocean} component can itself be estimated in two ways:

1. By averaging the GRACE space gravimetry data over the oceans to recover the ocean mass variations,
2. By summing up the land water, atmospheric water vapor and land ice components.

In effect, conservation of total water mass in the climate system at interannual time scale leads to:

$$\Delta M_{ocean} = -\Delta M_{LW} - \Delta M_{WV} - \Delta M_{LI} \quad (1)$$

where ΔM_{ocean}, ΔM_{LW} and ΔM_{WV} represent interannual changes of the ocean mass, total land water storage and atmospheric water vapor, respectively. ΔM_{LI} refers to interannual fluctuations in land ice mass.

For regional comparisons with the 1997 – 1998 El Niño (i.e., prior to the GRACE era), we also estimate the ocean mass component by computing the difference between the altimetry-based sea level and steric sea level.

All components are expressed in equivalent sea level (ESL) (see below).

3 Data

3.1 Sea level data

For the altimetry-based sea level data, we use two different products : (1) the GMSL time series from AVISO (Archiving, Validation and Interpretation of Satellite Oceanographic Data,www.aviso.oceanobs.com/en/data/products/sea-surface-height-products/global/msla/, AVISO hereafter) and (2) the Colorado University GMSL (http://sealevel.colorado.edu/, CU hereinafter). Both data sets are based on Topex/Poseidon, Jason-1 and Jason-2 data.

The two GMSL time series (AVISO and Colorado University) are based on different processing approaches, in particular the geographical averaging process. Moreover some of the geophysical corrections applied to the data are slightly different as well as the editing procedure (see Masters et al., 2012 and Henry et al., 2014, for a discussion on these differences). The two GMSL time series cover the period 1993-2013. But for the purpose of the present study that focuses on GRACE and Argo periods, we limit the study time span to January 2005 to December 2011. In the following, we average the two data sets to produce a single GMSL time series, as no preferred product has been identified so far. The corresponding curve and associated uncertainty (based on the dispersion around the mean) is shown in Fig. 1 for the 2005-2011 time span. For the regional analysis presented in section 6, we also use the gridded AVISO data over 1993-2012 (www.aviso.oceanobs.com). The gridded data are based on a larger set of altimetry missions merged together: in addition to the Topex/Poseidon and Jason-1&2- data, ERS-1&2, Envisat and Geosat follow-on data are also used. The gridded data are provided on a 1/4 degree grid at weekly interval.

Both, global mean and gridded sea level data are corrected for the inverted barometer correction. For detailed description of the geophysical corrections, the reader is referred to the AVISO and Colorado University web sites.

3.2 Steric data

Two steric data sets have been considered:

1. Argo data processed as explained in von Schuckmann and Le Traon (2011). The global mean steric time series (data averaged over the 60°N/60°S domain) is based on a weighted box averaging scheme of Argo data. A reference depth of 1500 m is chosen as the number of profiles in the 1500 m-2000 m depth layer is significantly less than within 0-1500 m before year

2009 (Cabanes et al., 2013, their Figure 7). The Argo profiles undergo re-qualified data validation methods using a tool developed by Gaillard et al. (2009) (see also von Schuckmann et al., 2009). Black-listed profiles and platforms are excluded from the data set. Every profile on alert has been checked visually which allows excluding spurious data (e.g. data drift). This procedure minimizes systematic biases in the global Argo data set as discussed by Barker et al. (2011). Error bars represent one standard error, accounting for reduced degrees of freedom in the mapping and uncertainty in the reference climatology as described in von Schuckmann and Le Traon (2011). The Argo based steric sea level time series covers the period 2005-2011. In the following, we consider both the thermosteric and halosteric components.

2. For comparisons between the recent La Niña events and former El Niño events (in particular the 1997 – 1998 El Niño), we also consider the recent update (V6.12) of the Ishii and Kimoto (2009) ocean temperature data (covering the 0-700 m depth range). These data are vertically integrated to estimate the thermosteric sea level from 1993 onwards at monthly interval. This thermosteric product is called IK12.

3.3 GRACE-based space gravimetry data

To estimate the ocean mass variation, we use the GRACE Release 2 products from the Groupe de Recherche en Geodesie Spatiale (GRGS) (http://www.grgs.obs-mip.fr/grace/variable-models-grace-lageos/grace-solutions-release-02). The degree 2 coefficients –poorly determined by GRACE- are those derived from satellite laser ranging to Lageos 1 and 2. These data are provided at 10-day interval on 1°x1° grids. However the real spatial resolution of this data set is coarser, on the order of 400 km (see below). No Gaussian filtering nor destripping are applied to the GRGS data. Such post-processing is developed by other groups for removing the various errors affecting the GRACE data, in particular the north-south noise (stripes) due to systematic correlated errors of GRACE data within a particular spectral order or the leakage of nearby signals onto the study area due to the coarse GRACE resolution (see Velicogna and Wahr, 2013 for a discussion on errors impacting the GRACE data). Such post processing procedure is usually applied to the GRACE products available from the TELLUS website (http://grace.jpl.nasa.gov) that provides gridded ocean data after strong smoothing (due to the application of a destripping filter, a 500 km half-width Gaussian filter and a spherical harmonic cutoff at degree 40). As indicated on this web site, such a data set should not be used for global ocean mass studies due to strong attenuation of the signal (see also Chambers and Schröter, 2011).

A gain factor is sometimes applied to the data in order to compensate for signal attenuation due to the coarse GRACE resolution (the truncation of the GRACE spherical harmonics series at a given degree implies that short-wavelength signal associated with the missing spherical harmonic coefficients, cannot be recovered). In the case of the GRGS data, this truncation is at degree 50, which corresponds to a spatial resolution of 400 km. No gain factor is applied. When computing the ocean mass, we use a mask that ignores data within 400 km of the continents to avoid leakage from continental hydrology and ice sheet mass loss. Finally, as we only consider the interannual variability, we do not correct the GRACE data for Glacial Isostatic Adjustment (i.e., the visco-elastic response of the solid Earth to last deglaciation) because this effect is a purely linear trend.

3.4 Atmospheric water vapor

To estimate change in atmospheric water vapor mass, we used three different products : (1) atmospheric surface pressure grids from the European Centre for Medium-Range Forecast (ECMWF) ERA-Interim data (//data-portal.ecmwf.int/data/d/interim_moda/), (2) the vertically integrated water vapor grids, also from ERA Interim, and (3) vertically integrated water vapor based on AMSRE remote sensing data (kindly provided to us by R. Allan). As shown by Trenberth and Smith (2005), seasonal and interannual variations in atmospheric surface pressure essentially result from changes in atmospheric water vapor content because of dry air mass conservation. Thus atmospheric surface pressure data can be used to estimate change in water mass of the atmosphere. Data from ERA Interim are provided as 1.5°x1.5° grids, at monthly interval. Data from (3) are given as globally averaged water vapor time series at monthly interval.

The atmospheric water vapor contribution is further expressed in ESL by weighting by the ratio of the total Earth's area to the ocean area and multiplied by -1 (to express the fact that more water in the atmosphere leads to lower sea level, and inversely).

3.5 Land water component

To estimate the global land water storage, we use the ISBA-TRIP global hydrological model developed at MétéoFrance. The ISBA (Interaction Soil Biosphere Atmosphere) land surface scheme calculates time variations of surface energy and water budgets. Soil hydrology is represented by three layers: a thin surface layer (1 cm) included in the rooting layer and a third layer to distinguish between the rooting depth and the total soil depth. The soil water content varies with surface infiltration, soil evaporation, plant transpiration and deep drainage. ISBA uses a comprehensive parameterization of sub-grid hydrology to account for heterogeneity of precipitation, topography and vegetation within each grid cell. It is coupled with the TRIP (Total Runoff Integrating Pathways) module (Oki and Sud, 1998). TRIP is a simple river routing model converting daily runoff simulated by ISBA into river discharge on a global river channel network here defined at 1°x 1° resolution. Details on ISBA-TRIP model can be found in Alkama et al. (2010) and Decharme et al. (2010). The outputs of the ISBA-TRIP model cover the period January 1980 to December 2012, with values given at monthly interval on a 0.5°x0.5° grid. They are based on a run in forced mode (global meteorological forcing based on ERA-Interim at 3-hourly time step and 0.25° resolution). The whole land surface has been considered. The land water storage component is further expressed in ESL (after weighting by the land to ocean areas ratio). In the following the land water term refers to the use of the ISBA-TRIP hydrological model.

4 Comparison between the different products

Data between 66°N and 66°S are considered for all products except the Argo-based steric sea level (60°N to 60°S). All time series are re sampled at monthly interval. The seasonal cycle is removed by least-square fitting of a sine function to the data. As we focus here on the interannual variability, we applied a high-pass filter (<7 years) to all data sets over the 2005-2011 time span. Just removing a linear trend over the study time span gives essentially the same result. Finally a 3-month running filter is applied to each time series.

4.1 Differences between the water vapor time series

Fig. 2a shows the water vapor contributions to sea level for the three products as discussed in section 3.4. The integrated water vapor from ERA Interim and AMSRE agree well while the ERA Interim surface pressure curve departs much from the previous two. Differences of 0.5-1 mm ESL are noticed at some periods, in particular in 2007 and 2009/2010.

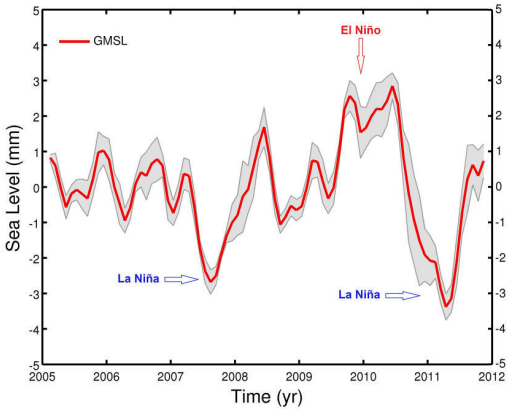

Fig. 1. Interannual GMSL over 2005-2011 based on the mean of the AVISO and Colorado University time series. The gray zone around the red curve represents the uncertainty based on the dispersion of each time series around the mean.

We do not know the source of such differences but it is suspected that the surface pressure curve is less reliable (R. Allan, personal communication). Moreover, global mean water vapor is highly correlated with global mean sea surface temperature (SST). We found a much better correlation between SST and the vertically integrated water vapor than when using the surface pressure data. This is illustrated in Fig. 2b. For that reason, in the following, we use the vertically integrated water vapor time series (from ERA interim).

4.2 Comparison between interannual GMSL and GRACE-based ocean mass & sum of other mass components

In this section we compare the interannual GMSL with the interannual ocean mass component estimated from the GRACE GRGS data as well as with the sum of other mass components (as described by eq. 1): land waters plus water vapor plus land ice. We neglect the interannual variability

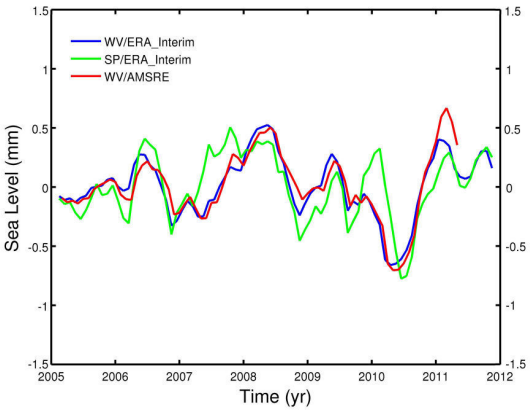

(a)

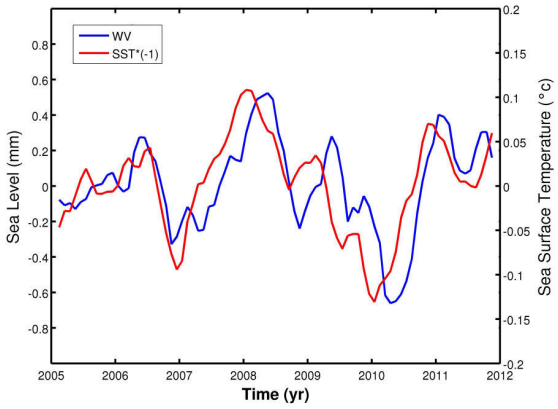

(b)

Fig. 2. a) Interannual global mean water vapor component (expressed in equivalent sea level) from ERA Interim surface pressure (green curve), integrated water vapor from ERA Interim (blue curve) and from AMSRE (red curve); b) Interannual global mean water vapor contribution from ERA Interim (expressed in equivalent sea level, blue curve) and global mean SST (multiplied by -1) (red curve).

of the glaciers as no data are available to estimate it, but account for that of the ice sheets. The latter has been estimated from the GRGS GRACE data averaged over Greenland and Antarctica. It is generally very small, of at most 0.3 – 0.4 mm ESL on interannual time scale (see below).

Fig. 3a compares the interannual GMSL with the GRACE-based ocean mass and the sum of 'land water storage + water vapor + interannual ice sheet component'. Error bars are not shown on this plot. The GRACE GRGS data are not provided with error bars. However from discussions with the GRGS processing group, it comes out that the uncertainty of a single global mean monthly value is on the order of 0.6 mm (1-sigma) (see also Wahr *et. al.*, 2006). Uncertainty of the sum 'land water storage + water vapor + interannual ice sheet component' is also not known. We assume that it is of the same order of magnitude as for the GRACE-based ocean mass. Fig. 3a indicates that the mass component (either from GRACE or from the sum 'land water storage + water vapor + interannual ice sheet component') has a significant contribution to the interannual GMSL, especially during the 2011 La Niña. But clearly not all interannual GMSL signal is of mass origin. In Fig. 3b, we have superimposed the Argo-based steric sea level to the interannual GMSL. The steric signal obviously plays some role at interannual time scale. On Fig. 3b, is also shown the interannual variability of the ice sheets. As mentioned above, this contribution is small, of the same order of magnitude as the water vapor component.

5 Sea level budget at interannual time scale

Fig. 4a,b show the interannual GMSL together with the sum of the steric and mass components (GRACE-based ocean mass for Fig. 4a and sum 'land water storage + water vapor + interannual ice sheet component' for Fig. 4b). From these figures, we clearly see that the negative sea level anomalies coinciding with the 2011 La Niña is almost equally due to a decrease of the ocean mass and steric components. The agreement between the GMSL and the sum of components is less good during the 2008 La Niña, although the use of the sum 'land water storage + water vapor + interannual ice sheet component' (Fig. 4b) gives better result than the use of GRACE (Fig. 4a).

Overall, over the 2005 – 2011 time span, the correlation between interannual GMSL and sum of the contributions amounts to 0.78 in both cases (Fig. 4a and Fig. 4b). We conclude, as previously shown by Boening et al. (2012), that the GMSL drop during the 2011 La Niña event is reasonably well reproduced by the sum of the steric and ocean mass contributions. As indicated above, lesser agreement is noticed for the 2008 La Niña. This calls for further investigation to identify which data set is in error.

6 Spatial patterns of sea level and ocean mass during 2011 La Niña

In this section, we investigate the geographical patterns of the GMSL, steric sea level and ocean mass component during the 2011 La Niña. In particular, we would like to check whether the ocean mass component associated with the 2011 La Niña presents a spatial pattern similar (but with

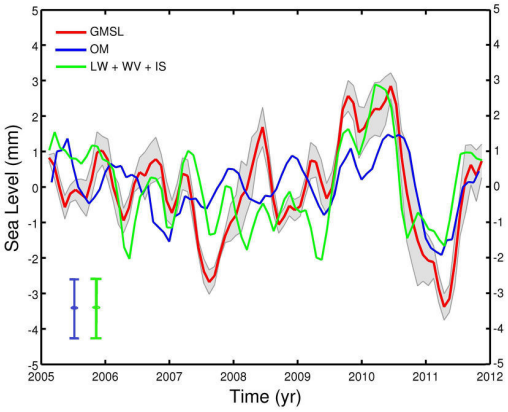

(a)

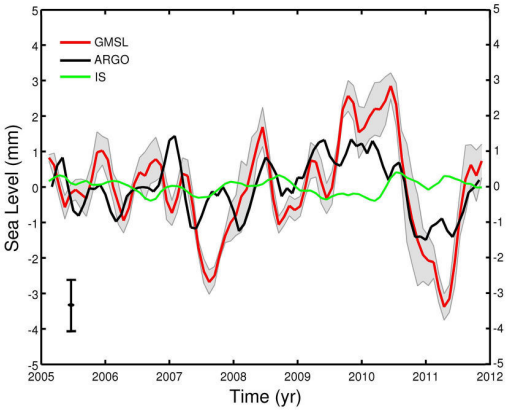

(b)

Fig. 3. a) Interannual GMSL (red curve) on which are superimposed the global mean ocean mass from GRACE (blue curve) and the sum 'land water storage + water vapor + interannual ice sheet, IS, component' (green curve). Vertical bars represent errors on monthly values of GRACE-based ocean mass and sum of mass components; b) Interannual GMSL (red curve) on which are superimposed the steric contribution from Argo (black curve). The interannual ice sheet component is also shown (green curve). The vertical bar represents the error on monthly values of the Argo-based steric sea level.

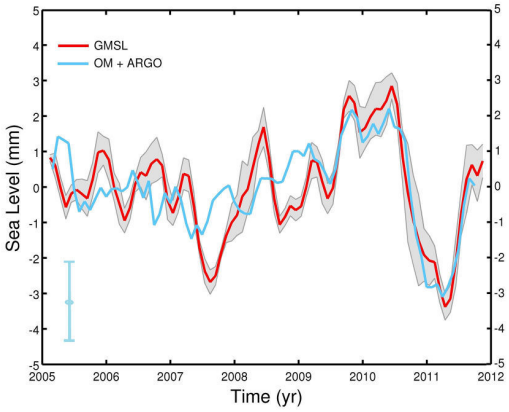

(a)

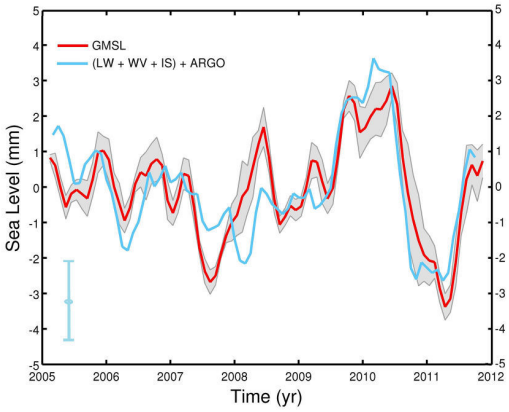

(b)

Fig. 4. a) Interannual GMSL (red curve) on which is superimposed the sum of the mass (from GRACE) and steric contribution from Argo (light blue curve). The vertical bar represents the error on monthly values of the sum of mass and steric contributions; Interannual GMSL (red curve) on which is superimposed the sum of the mass (sum 'land water storage + water vapor + interannual ice sheet component') and steric contribution from Argo. The vertical bar represents the error on monthly values of the sum of mass and steric contributions.

opposite sign) than that observed during the 1997 – 1998 El Niño (Cazenave et al., 2012). As done in Cazenave et al (2012) for El Niño, we first determine the geographical origin of the 2011 ocean mass drop. As for the 1997 – 1998 El Niño, we find that the main contribution comes from the northern tropical Pacific. This is illustrated in Fig. 5 showing the global mean ocean mass from GRACE and north Pacific ocean mass (also estimated from GRACE). The north Pacific area considered here is from 120°E to the coast of America and from the equator to 60°N. While the two curves do not exactly coincide, we find nevertheless good agreement, suggesting that as for El Niño, the La Niña ocean mass anomaly originates in the north Pacific. To investigate in more detail the spatio-temporal variation of the negative ocean mass anomaly during the 2011 La Niña, we constructed a longitude-time diagram of the ocean mass averaging the data in latitude over the north Pacific (same area as indicated above). The diagram is shown in Fig. 6 for the 1996 – 2012 time span (we extended back in time the analysis in order to include the effect of the 1997 – 1998 El Niño). To do this, we computed the ocean mass from the difference between the mean sea level data and IK12 steric data. In effect, for this longer period, neither Argo nor GRACE data can be used (note that

IK12 data cover the 0-700 m depth range only, instead of 0 – 1500 m for Argo). Fig. 6 shows a succession of positive and negative nearly zonal anomalies in the eastern part of the Pacific (west of 180°E). In particular, a strong negative anomaly, amounting –20 to –30 mm and extending east-west, is noticed in 2011. In Fig. 6, we also see the strong positive ocean mass anomaly associated with the 1997 – 1998 El Niño (previously discussed in Cazenave et al., 2012), with the same east-west zonal pattern as the 2011 La Niña anomaly. The results of the present study suggest similar response of the ocean mass during La Niña (but with opposite sign compared to El Niño), likely related to precipitation minus evaporation patterns over the north eastern Pacific characterizing ENSO events (Dai and Wigley, 2000, Gu and Adler, 2011).

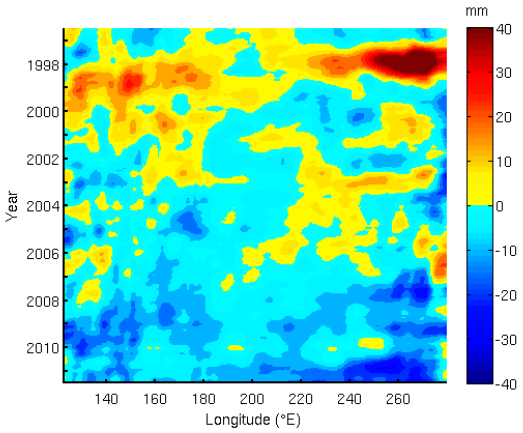

Fig. 6. Longitude/time diagram of the north Pacific (0-60°N) ocean mass from 1996 to 2011 based on the difference between altimetry-based sea level data and IK12 steric data. Units: mm.

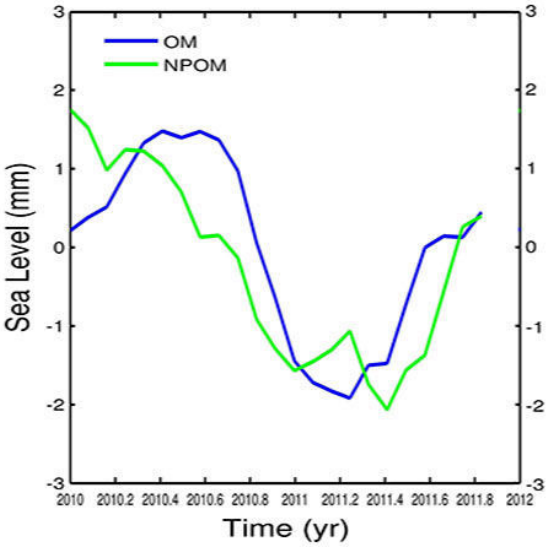

Fig. 5. Interannual global mean ocean mass from GRACE (dark blue curve) and north Pacific ocean mass (also estimated from GRACE) (green curve) during the 2011 La Niña.

We also compared the spatial patterns of the observed, altimetry-based sea level and steric sea level over the north Pacific. A similar treatment was performed on these two data sets (latitude averaging between the equator and 60°N and computation of a longitude/time diagram). These are shown in Fig. 7a and 7b. As expected, the two maps are highly correlated and display clear west-east anomalies during ENSO events. Amplitude of the ENSO-related sea level anomalies is in the range +/–80 mm. Associated ocean mass anomalies shown in Fig. 6 are smaller in amplitude (in the range +/–30-40 mm only) but still significant (local errors in satellite altimetry measurements reach 15 mm –e.g., AVISO website-; they reach 18 mm for IK12 steric data, Llovel et al 2013, which gives a level of local error of 23.4 mm for the mass signal). To confirm that what we interpret as mass anomalies (as shown in Fig. 6) is not a steric contribution not accounted by the IK12 data (i.e., a steric contribution from below 700 m), we computed an ocean mass longitude/time diagram (same procedure as above) by subtracting to the sea level data the Argo data down to 1500 m (but as of 2005 only). Corresponding Argo-based ocean mass diagram is shown in Fig. 8. We note that over their overlapping time span, Fig. 6 and Fig. 8 are very similar. In particular, the west-east negative mass anomalies related to the 2008 and 2011 La Niña events are well reproduced and is still significant when using Argo data down to 1500 instead of IK12 data down to 700 m (local errors in the Argo dataset for the North Pacific reach 15 mm which gives a level of local error of 15 mm for the mass signal). While we cannot exclude that the resulting map contains some steric signal from the deep ocean (below 1500 m), more likely, this results suggests that an ocean mass component is also involved during La Niña, with a very similar geographical pattern as the thermal and sea level anomalies.

7 Conclusions

In this study, we show that the GMSL drop observed during the 2011 La Niña is almost equally due to a decrease in the mass of the ocean and of the steric sea level. This is unlike the positive GMSL anomaly associated with the 1997 – 1998 El Niño that was essentially explained by an increase of the ocean mass due to more rainfall over the tropical Pacific (and associated decrease of water on land)

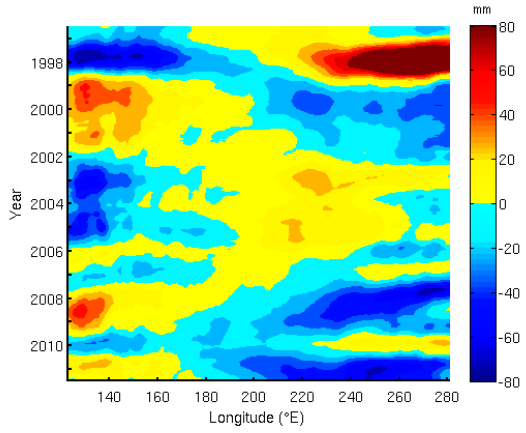

(a)

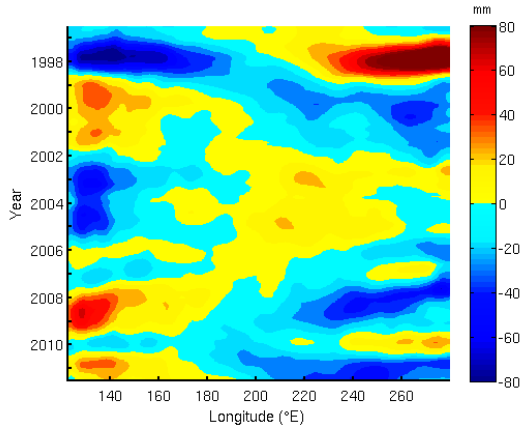

(b)

Fig. 7. Longitude/time diagram of the north Pacific (0-60°N) altimetry-based sea level data from 1996 to 2011. Units: mm; Longitude/time diagram of the north Pacific (0-60°N) steric sea level data from IK12 from 1996 to 2011. Units: mm.

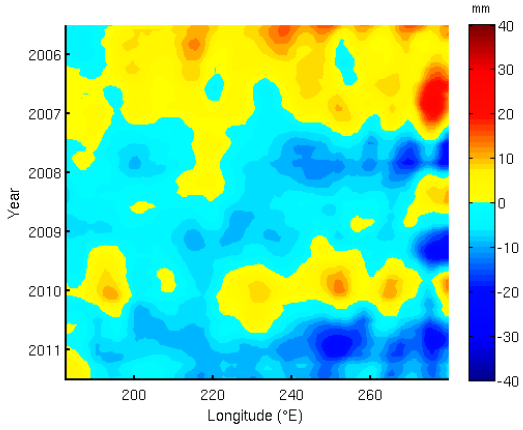

Fig. 8. Longitude/time diagram of the north Pacific ocean (0-60°N) mass sea level data based on the difference between altimetry-based sea level data and Argo steric data (down to 1500 m) over 2005-2011. Units: mm.

(Cazenave et al., 2012). This suggests that the effect of La Niña on the GMSL does not just mirror that of El Niño, as suggested by Okumura and Deser (2010) for other characteristics of these events. This is unlike the spatial patterns in ocean mass anomalies: we find that during the 2011 La Niña, the ocean mass decrease is temporarily confined in the northeastern Pacific, as for 1997 – 1998 El Niño (but with opposite sign).

The origin of this ocean mass decrease during La Niña events is possibly related to the net precipitation over the area, but the exact origin of the observed pattern remains to be investigated. This will be the object of a forthcoming study that should also analyze the relationship between ocean mass anomaly and surface salinity, in particular using data from the SMOS and Aquarius satellite missions. It will be also of interest to investigate whether numerical ocean models are able to reproduce the observed ocean mass decrease and its spatial pattern. This should help better understanding the physical cause of the observed pattern.

Acknowledgement: We thank R. Allan for kindly providing us with water vapor data. H. Palanisamy was supported by a CNES-CLS PhD Grant. K. von Schuckmann was partly supported by the French Lefe/GMMC research programme.

References

Alkama R., Decharme B., Douville H., Becker M., Cazenave A., Sheffield J., Voldoire A., Tyteca S., Le Moigne P. (2010). Global evaluation of the ISBA-TRIP continental hydrologic system; Part 1 : a two-fold constraint using GRACE terrestrial water storage estimates and in situ river discharges J. Hydrometeorology, 11, 583-600, doi:10.1175/2010JHM1211.

Barker P. M., Dunn J. R., Domingues C. M., and Wijffels S. E., (2011) Pressure Sensor Drifts in Argo and Their Impacts, J. Atmos. Ocean. Tech., 28, 1036–1049.

Boening C., Willis J.K., Landerer F.W. and Nerem R.S. (2012). The 2011 La Niña: so strong, the oceans fell, Geophys. Res. Lett., 39, L19602, doi:10.1029/2012GL053055.

Cabanes, C., A. Gourazel, K. von Schuckmann, M. Hamon, V. Turpin, C. Coatanoan, S. Guinehut, C. Boone, N. Ferry, G. Reverdin, S. Pouliquen and P.Y. Le Traon (2013): The CORA dataset: validation and diagnostics of ocean temperature and salinity in situ measurements, Ocean Sci., 9, 1–18, www.ocean-sci.net/9/1/2013/, doi:10.5194/os-9-1-2013.

Cazenave A., O. Henry, S. Munier, B. Meyssignac, T. Delcroix, W. Llovel, H. Palanisamy and M. Becker, (2012). ENSO influence on the global mean sea level over 1993-2010, Marine Geodesy, 35(S1), 82–97.

Chambers D. and J. Schröter (2011). Measuring ocean mass variability from satellite gravimetry, Journal of Geodynamics, 52, 333–

343, doi:10.1016/j.jog.2011.04.004.

Church J.A., N.J. White, L.F. Konikow, C.M. Domingues, J.G. Cogley, E. Rignot, J.M. Gregory, M.R. van den Broeke, A.J. Monaghan, and I. Velicogna (2011). Revisiting the Earth's sea level and energy budgets from 1961 to 2008, Geophys. Res. Lett., 38, L18601, doi:10.1029/2011GL048794.

Church J. A., P. U. Clark, A. Cazenave, J. M. Gregory, S. Jevrejeva, A. Levermann, M. A. Merrifield, G. A. Milne, R. S. Nerem, P. D. Nunn, A. J. Payne, W. T. Pfeffer, D. Stammer and A. S. Unnikrishnan (2013). Sea Level Change. In: Climate Change 2013: The Physical Science Basis. Contribution of Working Group I to the Fifth Assessment Report of the Intergovernmental Panel on Climate Change [Stocker, T. F., D. Qin, G.-K. Plattner, M. Tignor, S. K. Allen, J. Boschung, A. Nauels, Y. Xia, V. Bex and P. M. Midgley (eds.)]. Cambridge University Press, Cambridge, United Kingdom and New York, NY, USA, in press.

Dai A. and Wigley T.M.L (2000), Global patterns of ENSO-induced precipitation, Geophys. Res. Lett., 27, 9, 1283-1286.

Decharme B., Alkama R., Douville H., Becker M., Cazenave A., Sheffield J., Voldoire A., Tyteca S., Le Moigne P. (2010). Global evaluation of the ISBA-TRIP continental hydrologic system using GRACE; Part 2 : results, J. Hydrometeorology, 11, 601- 617.

Fasullo J.T., Boening C. , Landerer F.W. and Nerem R.S. (2013). Australia's unique influence on global mean sea level in 2010-2011, Geophys. Res. Lett., in press.

Gaillard F., Autret E., Thierry V., Galaup P., Coatanoan C., and Loubrieu T. (2009), Quality control of large Argo data sets, J. Atmos. Oceanic Technol., 26, 337–351.

Gordon A.L., Sprintall J., Van Aken H.M., Susanto D., Wijffels S., Molcard R., Ffield A., Pranowo W., Wirasantosa S. (2010) "The Indonesian Throughflow during 2004-2006 as observed by the INSTANT program." "Modeling and Observing the Indonesian Throughflow", Guest Editors: A. L. Gordon and V.M. Kamenkovich, Dynamics of Atmosphere and Oceans, vol(50) 115-128.

Gu G. and Adler R.F. (2011), Precipitation and temperature variations on the interannual time scale : assessing the impact of ENSO and volcanic eruptions, J. Climate, 24, 2258-2270.

Ishii M. and Kimoto M. (2009), Reevaluation of historical ocean heat content variations with varying XBT and MBT depth bias corrections, Journal of Oceanography, 65, 287-299.

Hanna et al. (2013). Ice-sheet mass balance and climate change, Nature, 498, 51-59, doi:10.1038/nature12238.

Henry O., Ablain M., Meyssignac B., Cazenave A., Masters D., Nerem S. and G. Garric (2014). Effect of the processing methodology on satellite altimetry-based global mean sea level rise over the JASON-1 operating period, Journal of Geodesy, in press.

Llovel W., Becker M., Cazenave A. and Crétaux J.F. (2010). Contribution of land water storage change to global mean sea level from GRACE and satellite altimetry, C.R. Geosciences, 342, 179-188.

Llovel W., Becker M., Cazenave A., Jevrejeva S., Alkama R., Decharme B., Douville H., Ablain M. and Beckley B. (2011). Terrestrial waters and sea level variations on interannual time scale, Global Planet. Change, 75, 76-82. doi:10.1016/j.gloplacha.2010.10.008.

Llovel W., Fukumori I. and Meyssignac B. (2013). Depth-dependent temperature change contributions to global mean thermosteric sea level rise from 1960 to 2010, Global Planet. Change, 101, 113-118.

Meyssignac B. and Cazenave A. (2012). Sea level : a review of present-day and recent-past sea level change and variability, J. Geodyn., 58, 96-109.

Nerem R. S., Chambers D. P., Choe C., and Mitchum G. T. (2010), Estimating Mean Sea Level Change from the TOPEX and Jason Altimeter Missions, Marine Geodesy, 33 (1), 435-446.

Oki T. and Sud Y.C. (1998). Design of Total Runoff Integrating Pathways (TRIP), A Global River Channel Network. Earth Inter., Vol. 2., Paper 1.

Okumura Y. and C. Deser (2010). Asymmetry in the duration of El Nino and La Nina. J. Climate, 23, 5826-5843.

Trenberth K. and Smith L. (2005).The Mass of the Atmosphere: A Constraint on Global Analyses, J. Climate, 18, 864-875.

Velicogna I. and Wahr J. (2013), Time variable gravity observations of ice sheet mass balance:precision and limitations of the GRACE satellite data, Geophys. Res. Lett., 40, 1-9, doi:10.1002/grl.50527.

Von Schuckmann K., Gaillard F., and Le Traon P. Y. (2009). Global hydrographic variability patterns during 2003–2008, J. Geophys. Res., 114, C09007, doi:10.1029/2008JC005237.

Von Schuckmann K. and Le Traon P.-Y (2011). How well can we derive Global Ocean Indicators from Argo data?, Ocean Sci., 7, 783–791, doi:10.5194/os-7-783-2011.

Wahr J., Swenson S. and Velicogna I. (2006). Accuracy of GRACE mass estimates, Geophys. Res. Lett., 33, L06401, doi:10.1029/2005GL025305.

Received December 18, 2013 ; accepted February 11, 2013.

Geomorphology 228 (2015) 134–146

Contents lists available at ScienceDirect

Geomorphology

journal homepage: www.elsevier.com/locate/geomorph

Gaining insight into regional coastal changes on La Réunion island through a Bayesian data mining approach

T. Bulteau [a,*], A. Bailles [a], L. Petitjean [a,b], M. Garcin [a], H. Palanisamy [c], G. Le Cozannet [a]

[a] BRGM, 3 avenue Claude Guillemin, 45000 Orléans, France
[b] Laboratoire de Météorologie Dynamique, Paris, France
[c] LEGOS, Toulouse, France

ARTICLE INFO

Article history:
Received 12 February 2014
Received in revised form 28 August 2014
Accepted 1 September 2014
Available online 16 September 2014

Keywords:
Shoreline changes
Bayesian networks
Sea-level rise
Vertical ground motions
Coastal databases
La Réunion island

ABSTRACT

Recent works have highlighted the interest in coastal geographical databases – collected for coastal management purposes – for obtaining insight into current shoreline changes. On La Réunion, a tropical volcanic high island located in the Southern Indian Ocean, a dataset is available which describes shoreline changes, the coastal geomorphology and the presence of anthropic structures. This database is first supplemented with information on the exposure of each coastal segment to energetic waves and to estuarine sediment inputs. To incorporate relative sea-level changes along the coast in the database, levelling data are analysed in combination with GPS, satellite altimetry and sea-level reconstructions. Finally, a method based on Bayesian networks is used to assess the probabilistic relationships between the variables in the database. The results highlight the high degree of dependency between variables: a retrospective model is able to reproduce 81% of the observations of shoreline mobility. Importantly, we report coastal ground motions for La Réunion island of the order of 1 to 2 mm/year along the coast. However, the resulting differing rates of relative sea-level rise do not significantly impact on shoreline changes. Instead, the results suggest a major control of geological processes and local coastal geomorphic settings on shoreline evolution. While any exploration of a coastal database needs to be complemented with human reasoning to interpret the results in terms of physical processes, this study highlights the significance of revisiting other datasets to gain insight into coastal processes and factors causing shoreline changes, including sea-level changes.

1. Introduction

Individual processes that cause shoreline mobility are well known and result from the impacts of hydrometeorological factors, anthropogenic actions and biological processes on sediment stocks inherited from previous states of the coastal system. These processes and their interactions at various spatial and temporal scales are highly complex, so that understanding the respective roles of each factor in controlling shoreline mobility remains a real challenge. In the last two decades, local coastal observations have been increasingly gathered into large coastal datasets (Quelennec et al., 1998; Thieler and Hammar-Klose, 1999; Eurosion, 2004; Yin et al., 2012) in order to inform regional coastal management and to anticipate future changes. Incidentally, such databases have also been used to improve our understanding of recent coastal evolution and the associated causes (Hapke and Plant, 2010; Gutierrez et al., 2011; Yates and Le Cozannet, 2012). Large coastal databases contain – at least partially – information on shoreline mobility, coastal geomorphological settings and forcing factors. By exploring these coastal databases through data mining approaches, it becomes possible to examine the statistical relationships relating these variables.

Among existing data mining approaches, Bayesian networks (BNs) have become a very popular tool since the early '90s (Heckerman, 1997; Aguilera et al., 2011). A BN is a graphical model that encodes probabilistic relationships between variables of interest. They have been used in a variety of different applications, ranging from artificial intelligence to environmental modelling or as decision-support tools (Berger, 2000; Uusitalo, 2007; Catenacci and Giupponi, 2013).

Along with other systemic approaches such as Boolean models (Karunarathna and Reeve, 2007, 2008), the BN approach has been used to model physical coastal processes (Hapke and Plant, 2010; Gutierrez et al., 2011; Plant and Holland, 2011a,b; Plant and Stockdon, 2012; Yates and Le Cozannet, 2012; Loureiro et al., 2013). In these studies, the relationships between shoreline mobility and other coastal geomorphological settings and forcing factors are modelled as Bayesian networks. Applied to coastal databases on the eastern coast of the USA (Gutierrez et al., 2011) this approach suggested that relatively moderate differences in the rates of sea-level rise along this coast (a few mm/year) are an important cause for the different rates of shoreline erosion in this area (a result already suggested by Zhang et al., 2004). However, it

* Corresponding author. Tel.: +33 238643945.
E-mail address: t.bulteau@brgm.fr (T. Bulteau).

http://dx.doi.org/10.1016/j.geomorph.2014.09.002

remains unclear whether this conclusion can be generalized to other coastal sites (Cazenave and Le Cozannet, 2014). To confirm such results, it is necessary to explore other coastal datasets in order to check whether these relationships between sea-level rise and shoreline erosion are fortuitous, related to local conditions or if they apply to many coasts around the world.

The coastal dataset for La Réunion island (Southern Indian Ocean; De La Torre, 2004) was initially compiled for coastal management purposes, in order to characterize and map the coastal morphology and morphodynamics of the island and anticipate future trends (Le Cozannet et al., 2013). For each coastal segment, this dataset describes the observed multidecadal shoreline mobility, geomorphic settings and the presence of anthropic structures in the vicinity of the segment. In this study, we first complete this coastal dataset by constructing three other variables, namely the exposure to energetic waves, the presence of an estuary and the rate of relative sea-level rise, then, we use the method proposed by Gutierrez et al. (2011) to quantify the strength of known relationships between the variables. This enables one to identify the main factors driving decadal shoreline mobility in La Réunion while revealing the particular role of the rate of relative sea-level rise in coastal evolution.

The paper is organized as follows: in part 2, the theory of the BN approach and the tools used to evaluate the BN performance are briefly presented; in part 3, the study site and the dataset used are described; part 4 presents the results (relative sea-level changes at the coast and assessment of the BN performance); and part 5 examines to which extent the results can be interpreted in terms of physical processes.

2. Bayesian networks and their application for exploring coastal databases

A BN is a tool to graphically represent knowledge about a given system and to compute dependencies between parts of that system in terms of probabilities (Pearl, 1986). Formally, a BN $\mathscr{B} = (\mathcal{G}, \theta)$ is defined by:

- A directed acyclic graph $\mathcal{G} = (X,\mathrm{E})$, E being the set of directed edges representing causal relationships between the nodes of the graph that represent a set of random variables $X = \{X_1, \ldots, X_n\}$,
- Parameters $\theta = \{P(X_i|Pa(X_i))\}_{i = 1..\ n}$ that depict the conditional probability of each node X_i given its parents $Pa(X_i)$ within $\mathcal{G}$.

While $\mathcal{G}$ describes qualitatively the dependence (or independence) between variables, θ provides a more quantitative insight. In addition, the conditional independencies expressed by $\mathcal{G}$ allow simplification of the joint probability distribution of X into a product of local conditional probabilities which depend only on the considered node and its parents (see e.g. Pearl, 1986):

$$P(X_1, \ldots, X_n) = \prod_{i=1}^{n} P(X_i|Pa(X_i)) = \prod_{i=1}^{n} \theta_i. \quad (1)$$

This formula is a fundamental property of BNs. It is used for inference that is to compute the probability of any random variable X_i from observations of the others.

Hapke and Plant (2010) and Gutierrez et al. (2011) proposed a BN-based approach to explore coastal databases. The first step in their approach consists of defining a network structure $\mathcal{G}$, formalizing a qualitative understanding of coastal systems. Therefore, $\mathcal{G}$ displays the relationships between a few important parameters of a coastal database such as, for example: geomorphology, wave climate, tidal range, decadal sea-level changes and shoreline evolution. Importantly, in order to be used in a BN, the coastal variables must have states that are mutually exclusive and collectively exhaustive (Heckerman, 1997), which implies simplifying and harmonizing the raw coastal observations, like, for example, considering only a limited number of coastal geomorphology classes (cliffs, wetlands, beaches…) out of the numerous existing ones (Finkl, 2004).

In a second step, the parameters θ are computed from the database (learning phase). When a complete dataset (i.e. no missing data) is considered, the learning phase is straightforward: the parameters θ are determined using the maximum likelihood approach, which consists in estimating the probability of an event with its frequency of appearance in the dataset (Naïm et al., 2007).

The next step of the approach consists of creating a predictive model for shoreline mobility. The conditional probability distribution of shoreline mobility is written as:

$$P\left(SM^i \middle| \widetilde{X}_j\right), \forall i \quad (2)$$

where SM^i is the ith discretized state of the shoreline mobility variable and $\widetilde{X}_j$ represents a combination of all the other variables. For a given combination $\widetilde{X}_j$, the predicted shoreline mobility is the mode of the conditional probability distribution (2). This is written as:

$$SM_{pred} = \arg\max_i \left(P\left(SM^i \middle| \widetilde{X}_j\right)\right) \quad (3)$$

The probability value gives an indication of the prediction uncertainty. Assessing to which extent the observed shoreline mobility can be correctly predicted helps us evaluate the relevance and efficiency of our BN to represent the coastal system. As the same data were used for inference and learning, we are in a case of 'overfitting' (Aguilera et al., 2011) and the resulting predictions might be biased. However, the Bayesian model here is not used to predict future states of coastal geomorphology but as a data mining technique to analyse the relationships between the variables in the database.

The last step consists of analysing what are the most discriminating variables with respect to shoreline changes. This is done by evaluating the BN performance through statistical tools, such as the log-likelihood ratio (LR) which evaluates how much the knowledge of shoreline mobility has been improved owing to the other observations. For a given coastal segment (k) the LR is defined as follows:

$$LR_{(k)} = \log\left(P\left(SM_{(k)} \middle| O_{(k)}\right)\right) - \log\left(P\left(SM_{(k)}\right)\right) \quad (4)$$

where $SM_{(k)}$ is the observed shoreline mobility of segment (k) and $O_{(k)}$ represents the set of all the other variable states corresponding to segment (k).

The $LR_{(k)}$ can be summed over all coastal segments to give a global score of the model performance. By comparing how the global LR evolves with the number and type of variables, Gutierrez et al. (2011) evaluate the relative importance of each variable of the model with respect to shoreline changes.

In this paper, the same method is applied to another dataset for La Réunion island. However, in this application, because each coastal segment has a different length, the learning phase of the network is modified in a way that the importance of each segment is evaluated according to its length. In other words, each coastal segment does not count for one observation during the learning phase; its own length is used instead to weight it in the computation of the maximum likelihood estimators of parameters θ. Subsequently, the global score of LR is also computed accounting for the respective lengths of the segments:

$$LR = \frac{1}{total\ \ length} \sum_k LR_{(k)} length_{(k)}. \quad (5)$$

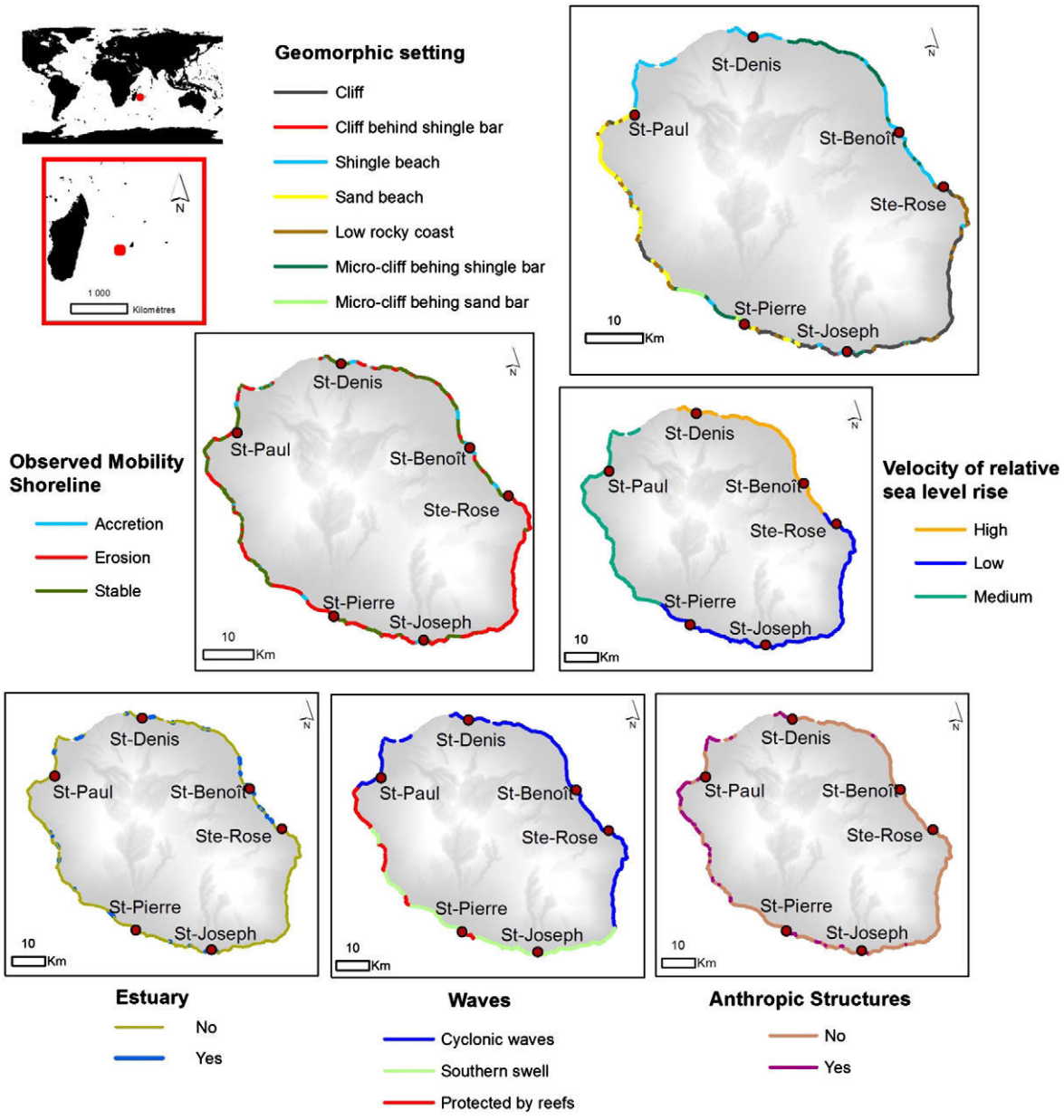

Fig. 1. Location of La Réunion island in the southwest Indian Ocean and spatial representation of the 6 variables of our coastal dataset. Some coastal sectors are completely artificial (e.g. coastal road located west from St-Denis) and cannot be described by the geomorphic settings represented in the top right image. These sectors are not considered in this study. Conversely, coastal segments to which a geomorphic setting can be assigned and where some anthropic structures exist (e.g. walls, etc.) are shown in the bottom right map.

3. Study site and data

3.1. Geographical and geological context

La Réunion is a French volcanic island located in the Western Indian ocean in the Mascarene archipelago (55°30′ E, 21° S), about 700 km east of Madagascar (Fig. 1). The island is made of two volcanoes, products of a hotspot activity. The oldest volcano (Piton des Neiges) caused the formation of the island 3 million years ago and has been inactive for the last 12,000 years (Rocher, 1988). It is located north-west of the island and culminates at 3070 m. The second volcano, the Piton de la Fournaise, is more recent (500,000 years old, Gillot and Nativel, 1989) and is currently one of the most active volcanoes on Earth. It reaches an altitude of 2621 m and is located south-east of the island. The emerged part of the island (about 2512 km^2) represents only 3% of the whole geological formation, which rises from the ocean floor at 4000 m depth. Soil erosion processes have shaped this volcanic formation, creating contrasting reliefs.

The shoreline is 250 km long and is made of a locally scoriaceous basaltic rocky coast. It is sometimes covered by surficial formations after weathering of the substratum and remodelling of slopes (e.g. mudslides, debris avalanches). The island has also a dense hydrographical network which supplies pebble and sand to the shores. In the west of the island, coral reefs have developed protecting beaches from direct wave impacts and supplying them with detrital organic materials. The reefs are relatively narrow (maximum extent from the shore 520 m) and form a discontinuous belt (Fig. 1). Cliffs and low rocky coasts represent about 42% of the whole shoreline whereas almost 45% is made up of beaches. The remaining 13% are completely artificial parts of the coast (De La Torre, 2004).

Table 1
Description of the initial (De La Torre, 2004) and final states of the variables.

Variable	Initial	Final
Morphotype (initial)/Geomorphic setting (GS) (final)	Coherent cliff Low rocky coast Loose or mixed cliff Loose or mixed micro-cliff Riverine shingle bar Marine shingle bar Basaltic sand beach Basaltic sand dune Unevolved coral mixed sand beach Unevolved coral biodetrital sand beach Evolved coral biodetrital sand beach	1-Cliff 2-Cliff behind shingle bar 3-Low rocky coast 4-Micro-cliff behind shingle bar 5-Micro-cliff behind sand bar 6-Shingle beach 7-Sand beach
Anthropic structure (AS)	Completely artificialized Partially artificialized No	1-Yes (corresponding to Partially artificialized state) 2-No
Shoreline mobility (SM)	Stability In transition Moderate erosion Severe erosion Accretion	1-Stability (combining Stability and In transition states) 2-Erosion (combining Moderate erosion and Severe erosion states) 3-Accretion
Estuary	N/A	1-Yes 2-No
Exposure to energetic waves (Waves)	N/A	1-Mainly exposed to cyclonic waves 2-Mainly exposed to southern swells 3-Protected by reefs
Velocity of relative sea level rise (RSLR)	N/A	1-High 2-Low 3-Medium

3.2. Description of the coastal database

3.2.1. Database as a whole

The coastal database for La Réunion island is based on a GIS (Geographical Information System) dataset compiled by the French Geological Survey (BRGM) from field campaigns undertaken between March and June 2004 (De La Torre, 2004), which were updated using more recent information on coastal processes and harmonized to make it suitable for use within a BN approach.

The initial database comprised three variables (Table 1): morphotype (11 states), the presence of anthropic structures (3 states) and shoreline mobility (5 states), that divided the coastline into segments with homogeneous characteristics. This dataset cannot be readily explored using a Bayesian network: for example, the geomorphic setting of a given coastal segment could be described with a combination of 2 morphotypes (e.g. coherent cliff plus marine shingle bar). This counters to the rule of mutually exclusive and collectively exhaustive states for BN variables (Heckerman, 1997). Hence, new classes were defined that both comply with this rule and adequately represent the coastal geomorphology in the island. Another point to consider when preparing the database is as follows: the more states per variable and the more complicated the model structure, the more data is needed to efficiently capture complex empirical distributions (Myllymäki et al., 2002; Uusitalo, 2007). Here, observations are limited by the island shoreline length. Thus, the number of states was reduced to a minimum while maintaining a satisfying representation of the coastal system: from the initial numbers of states of morphotype, anthropic structures and shoreline mobility, we settled on only 7 geomorphic settings, 2 states for the presence of anthropic structures and 3 states of shoreline mobility.

The states of the simplified variables are presented in Table 1. This table also shows that to complete the description of the coastal system, three new variables were added — exposure to energetic waves (3 states) (adapted from Lecacheux et al., 2012), presence of an estuary (2 states) (created within the present study), and the rate of relative sea-level rise (3 states) (created within the present study). Detailed information on the different variables is given in the following subsections. Fig. 1 presents the final coastal data used in the next steps of the approach. The final database divides the island's coastline into 384 segments with different lengths.

3.2.2. Shoreline evolution

The shoreline evolution dataset is based on extensive field observations of shoreline change indicators, such as micro-cliff, apparent tree roots at the upper beach, beach slopes, traces of fallen rocks at the top of the cliff, the presence of an upper beach berm, a small delta, a shingle bar at the foot of the cliff, vegetation of backshore or dunes. De La Torre (2004) positively compared his interpretation from field observations with aerial photographs from IGN campaigns of 1966, 1978 and orthophotographs of 1997. Although this period covers the intense economic and demographic development of the island, several significant climatic events (cyclones Hyacinthe (1980), Florine (1981), Clotilda (1987), Firinga (1989), Colina (1993), Hollanda (1994), Dina (2002)…) as well as volcanic events (eruptions of the Piton de la Fournaise reaching the sea in 1977 and 1986), the good agreement between the two approaches suggests that the coastal dataset can be interpreted as an indication of the main trends of coastal mobility over the last three decades.

3.2.3. Coastal geomorphology, human actions, inputs from river sediments to the coast

In addition to the shoreline evolution, the coastal dataset collected by De La Torre (2004) includes a description of the geomorphic setting for each coastal segment, as well as information about potential anthropic structures in the vicinity of the segment (a wall at the upper beach, a ramp for boats on a shingle beach, homes on top of micro-cliffs or directly on the beach, tourism facilities such as coastal promenades or artificial saltwater swimming pools, jetties, etc.) (Fig. 1). All these anthropic structures can potentially affect shoreline mobility (Eurosion, 2004) by disrupting the alongshore sedimentary transport (e.g. jetty at Saint-Benoît), the sediment transfer from rivers (e.g. river d'Abord at Saint-Pierre) or between sand dunes and beaches (e.g. Etang-Salé les bains), or by modifying the local wave regime (e.g. homes at Saint-Pierre located on the seafront). Thus, they can favour erosion but they can also locally protect the shoreline from it (e.g. a jetty can favour accretion upstream of the alongshore drift, an artificial swimming pool can protect a beach from the erosive action of waves, as has been observed at the Grande Anse beach.). Coastal segments that are completely artificial are discarded from the dataset. In addition, we added information, through a Boolean variable 'presence of an estuary', about the potential for each coastal segment to be significantly nourished by river sediments. This information is derived from the hydrographical network (source BD Carthage, French Geographical Institute (IGN)) considering that the main rivers are those that bring a significant amount of sediments to the coast. In practice, every coastal segment co-located with a river mouth was considered as significantly nourished by river sediments. This does not take into account alongshore sedimentary transport, that is, the capacity of a segment to be supplied with sediments from adjacent segments.

3.2.4. Cyclonic and seasonal waves and swells

The exposure to energetic waves is based on the modelling of the different types of waves affecting La Reunion (Lecacheux et al., 2012): the island is exposed to three main wave regimes — trade waves, southern swells and cyclonic waves. Trade waves are generated by trade winds (persistent planetary-scale surface winds). They come from the east-south-east in the Southern hemisphere and cause alongshore

sedimentary transport from the south-east to the north-west of the island. Southern swells and cyclonic waves are highly energetic and capable of triggering erosion, the first affecting primarily the south-western part of the island and the second the north-eastern part. Considering that this last process is the most important for shoreline changes, we split the island coasts in three categories: "mainly exposed to cyclonic waves", "mainly exposed to southern swells" and "protected by coral reefs" (Fig. 1). This is acknowledged as an oversimplification of reality, for example, coral reef hydrodynamics are particularly complex (see e.g. Storlazzi et al., 2011). The resulting map can be viewed as a first order approximation, which meets the requirements for use in BN, that is the mutual exclusivity and collective exhaustivity of the variables' states (Heckerman, 1997).

3.2.5. Tides

In La Réunion, the tidal regime is semi-diurnal and asymmetrical. It is microtidal since the tidal range varies between 0.1 m (neaps) and 0.9 m (springs) (Bourmaud et al., 2005). The tidal range is uniform all around the island and it cannot explain the heterogeneity of the observed shoreline evolution. Consequently, this factor is not included in our Bayesian model which is focused on shoreline mobility.

3.2.6. Relative sea-level rise at the coast

Relative sea-level rise at the coast can be viewed as the sum of two components: the climatic-component of sea-level rise (global mean sea-level rise plus the regional variability) and regional to local coastal ground motions. Although no tide gauge with a sufficiently long timeseries is available for the island, the multidecadal rates of sea-level rise can be assessed by evaluating each of these components separately.

The climatic component of sea-level rise can be assessed from satellite altimetry available for the two recent decades and for longer time periods (1950–2010) from a reconstruction of past sea-level changes (Fig. 2). In the southern zone of La Réunion, satellite altimetry indicates a rise of 7.5 ± 1.5 mm/yr from 1993 to 2010, whereas a sea-level reconstruction based on Meyssignac et al. (2012) indicates that the rise from 1950 to 2010 has been 1.2 ± 0.65 mm/yr (Palanisamy et al., 2014). In addition, since the size of La Réunion island does not exceed a width of 80 km, the climatic component of sea-level change is not expected to be significantly different around the island. To summarize, these results indicate that La Réunion island has been affected by a uniform climatic rise in sea-level, which has probably not been linear in time (Fig. 2).

To investigate whether the local vertical ground motions in La Réunion are significant and could induce variable relative sea-level rise rates along the coast, data from levelling measurements were used. The precision of this geodetic technique enables one to highlight relative ground motions up to a few millimetres. Using data obtained from surveys undertaken on the island by the French Geographical Institute (IGN) in 1958 and 1989 along the main roads of La Réunion, we compared the cumulative observed differences in height along the coast between these two operations spaced in time and on the same landmarks. The resulting data provide an estimate of the differential vertical ground motions along the coast between 1958 and 1989, up to an additive constant. In other words, additional information on ground deformations between 1958 and 1989 is needed in at least one location to estimate vertical ground motions along the entire levelling path. Here, the reference point for the calculation of the cumulative observed differences in height is chosen at a permanent GPS established by IGN near the point AM-64 (church of St-Leu,) and located close to the levelling path. This enables one to evaluate this constant. The data indicate daily vertical displacement oscillating around 0 cm (http://rgp.ign.fr/STATIONS/#SLEU). Although this time series is short (4 years), it suggests that this area is relatively stable. Therefore, we make the hypothesis that the landmark AM-64 is stable between the two dates.

The data presented above enable one to provide a first estimate of relative sea-level rise rates along the coasts of La Réunion island. These results are presented in detail in Section 4.1, and this information is integrated into the coastal dataset (Fig. 1). Importantly, it is hypothesized that the rates of vertical ground motions are linear, and that no more local ground motions are affecting coastal areas.

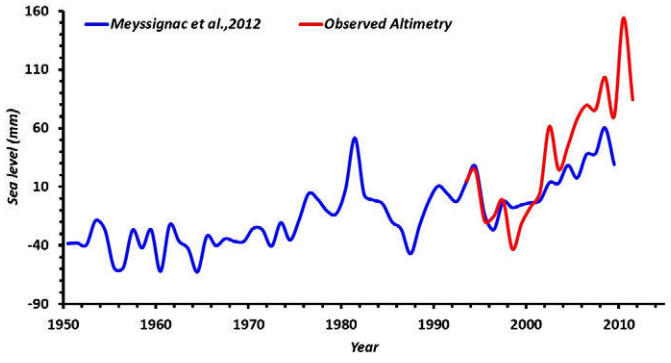

Fig. 2. Sea-level changes around La Réunion island in a geocentric framework (i.e. not taking into account ground motions). Red: observations from satellite altimetry. Blue: reconstruction of past sea-level changes due to climate change and variability (Meyssignac et al., 2012; Palanisamy et al., 2014).

3.3. The Bayesian network for La Réunion

The structure of the Bayesian network applied to the coastal database of La Réunion is represented in Fig. 3. This graph has been elaborated by starting from the one of Gutierrez et al. (2011) and considering the necessary adaptations to the particular case of La Réunion. The final graph therefore reflects a simplified understanding of the functioning of the coastal systems, where 5 explanatory variables are considered: geomorphic setting, presence of an estuary, presence of anthropic structures, exposure to energetic waves and the rate of relative sea-level rise. The influence of one variable on another is represented by an arrow. For example, human works can disrupt the natural sedimentary transfer processes and therefore influence shoreline evolution. Also, since coral reefs are usually non-existent in front of river mouths, there is a direct influence of the variable "presence of an estuary" on the "exposure to energetic waves" variable. It should be mentioned that BNs can work with qualitative or quantitative variables. In the last case, it is possible either to discretize the data in bins or to keep the variables continuous using appropriate methods to compute the parameters (Aguilera et al., 2011). Here, all the variables in the database are originally discrete and each is resolved in several qualitative states or bins. The number of bins and their descriptions for the 5 variables are summarized in Table 1.

The BNT toolbox for Matlab (Murphy, 2001; https://code.google.com/p/bnt/) is used to construct the BN. Some routines have been modified to account for the different length of each coastal segment (see Section 2).

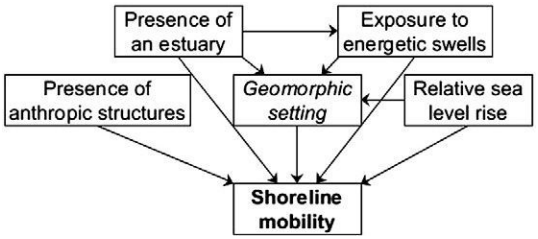

Fig. 3. Structure of the Bayesian network set up for the coastal database at La Réunion. Three types of variable are distinguished. Shoreline mobility is the response variable (in bold). Geomorphic setting is the inherent characteristic of the coastal segment (in italics) while the 4 remaining variables are driving forces of shoreline mobility.

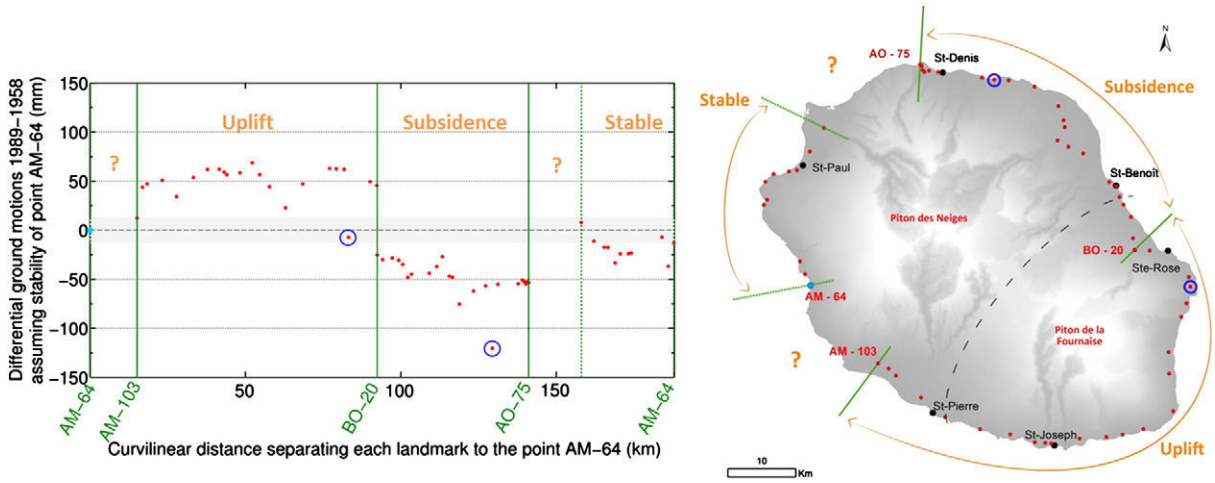

Fig. 4. Differential ground motions between 1989 and 1958 estimated from the analysis of two campaigns of levelling measurements. Ground motions are known up to a constant assumed to be equal to zero at point AM-64. The curvilinear distance from point AM-64 (abscissa axis) goes counter-clockwise around the island. Two points are circled in blue, pointing out probable displacements of landmarks between the two dates. The green lines indicate the boundaries between areas affected by different vertical ground motions. The question marks indicate where these boundaries cannot be placed accurately because no common landmarks are available in these areas between the two levelling surveys. The grey area on the left part of the figure represents the measurement uncertainty (maximum closure difference of 13 mm approximately, obtained for the 1958 series) and the range of non-significant results. Raw levelling data and the computation of raw height differences were produced by IGN (Lavoué, 2013).

4. Results

4.1. Relative sea-level rise along the coasts of La Réunion island

Fig. 4 shows the vertical ground motions along the coast, as obtained by comparing the differential vertical ground motions for the 57 common landmarks of the 1989 and 1958 levelling surveys. Despite some abrupt differences, probably due to the displacement of landmarks (circled in blue in Fig. 4), it appears clearly that the vertical ground motions are not homogeneous across the island between these two dates. Three areas can be distinguished, one with an uplift trend (south and southeast of the island), one which tends to subside (north and northeast of the island) and a "stable" or slightly subsiding area (western part of the island).

These results are rather consistent with intuition since it highlights uplift of the active volcanic system of the island. For the following, an assumption is made that these observed vertical ground motions are representative of a long-term general tendency. The rates of the vertical ground motions are therefore in the range of ± 1 to 2 mm/year. These rates are in the same order of magnitude as global present-day sea-level rise. Combining local-scale ground motions with the climatic component of the total relative sea-level rise signal, we conclude that the relative sea-level rise is significantly affected by vertical ground motions along the coast. Hence the description of the "relative sea-level rise velocity" variable in three states: "high" (corresponding to the subsiding area), "medium" (stable area) and "low" (uplifting area) (Fig. 1 and Table 1).

4.2. Evaluating the BN performance

This section examines the performance of the BN network of Fig. 3, whose parameters are calculated from the observations (Fig. 1). It corresponds to the last two steps of the method described in part 2.

Using all 5 variables, a predictive model based on our BN correctly reproduces the observed mobility for about 83% of the shoreline length (compared to 58% in the random case, see Appendix A). More precisely,

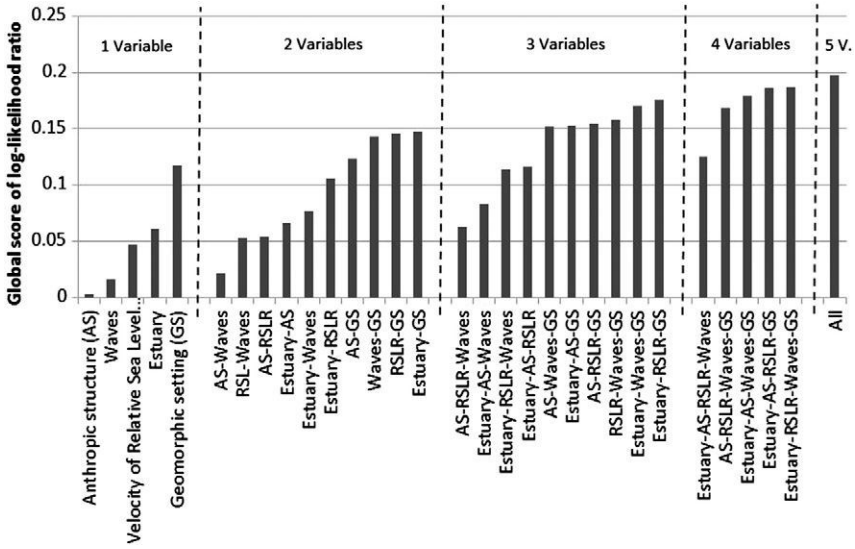

Fig. 5. Global log-likelihood ratio scores obtained for different BNs using 1 to 5 explanatory variables. (Theoretical boundaries: $LR_{min} = 0$; $LR_{max} = 0.38$, see Appendix B).

87% of stable shoreline, 82% of eroding shoreline and 73% of accreting shoreline are correctly predicted. The global log-likelihood ratio *LR* reaches almost 0.2 (Fig. 5).

In order to quantify the strength of the relationships between each explanatory variable and shoreline mobility and to evaluate the relative importance of each variable with respect to shoreline mobility, the global *LR* of the complete model is compared with simpler models using 1 to 5 variables (Fig. 5). For a BN with two variables (shoreline mobility and one explanatory variable), the highest score is obtained when considering the geomorphic setting (GS). For a BN with more variables, any combination of variables including GS systematically leads to the highest values of *LR*. The second most important variable is the presence of estuaries in the vicinity of coastal segments, followed by the rate of relative sea-level rise (RSLR). The last 2 variables, namely the presence of anthropic structures (AS) and the exposure to energetic waves (Waves), have a minor role in the overall performance of the BN, whatever the combination of variables.

To go deeper into the analysis of BN performance, we then identify the states of the variables that are related to successful predictions of accretion, stability or erosion. Fig. 6 shows the characteristics of successful retrospective predictions of the complete model: they correspond to cases where the black squares (correct predictions) take relatively high values while the corresponding diamonds (incorrect predictions) take significantly lower values. Accretion (third row) is found to be successfully predicted for a large proportion of the shoreline located near estuaries. Stability (second row) is correctly predicted for a significant proportion of the shoreline where anthropic structures are present, it is protected by reefs, the geomorphic setting is 'cliff behind shingle bar', 'micro-cliff behind shingle bar', 'shingle beach', 'sand beach' or 'low rocky coast', or the rate of relative sea-level rise is medium to high. Last, erosion (first row) is successfully predicted for a large proportion of the shoreline where it is exposed to southern swell, the geomorphic setting is 'cliff', 'low rocky coast' or the rate of relative sea-level rise is the lowest. The high percentage of shoreline being 'micro-cliff behind sand bar' (bin 5)

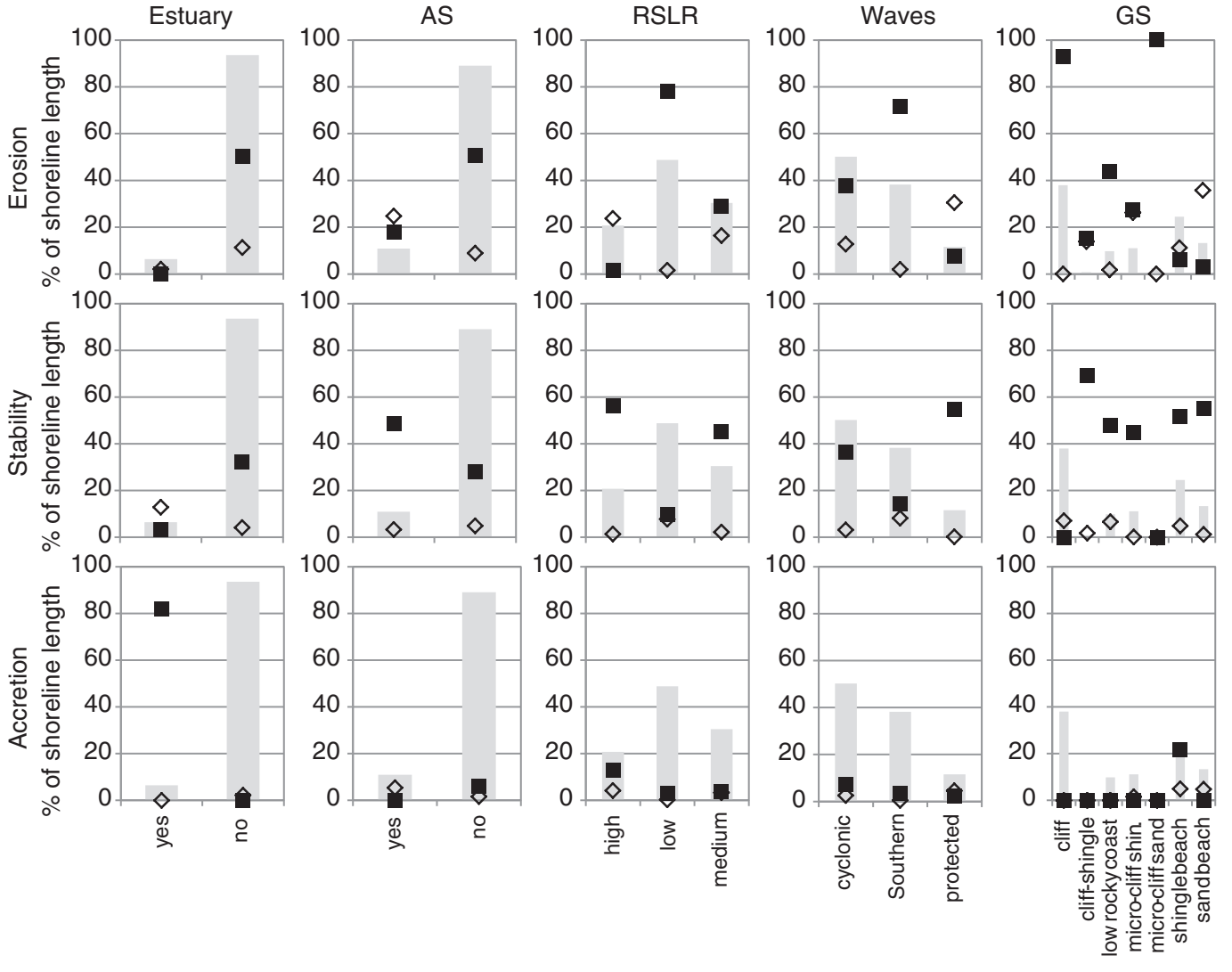

Fig. 6. Characteristics of successful predictions: black squares (resp. diamonds) represent the percentage of shoreline length falling in a given variable state, observed in erosion (first row), stability (second row) or accretion (third row), and correctly (resp. incorrectly) predicted. For black squares, that percentage is obtained as the shoreline length in erosion, stability or accretion correctly predicted where a given variable (column) is in a specific state divided by the total length with that variable state in the dataset and multiplied by 100. For diamonds, it is obtained as the shoreline length in erosion, stability or accretion incorrectly predicted where a given variable (column) is in a specific state divided by the total length with that variable state in the dataset and multiplied by 100. Therefore, the sum of the three black squares and the three diamonds for each variable state equals 100. For example, in the bottom left graph, the highest black square specifies the cumulative length of coastal segments correctly predicted in accretion divided by the cumulative length of coastal segments having an estuary in their neighbourhood in the entire database (then multiplied by 100). Similarly, the corresponding diamond is the cumulative length of coastal segments observed in accretion but wrongly predicted, divided by the cumulative length of coastal segments having an estuary in their neighbourhood in the entire dataset (then multiplied by 100). The grey bars in each graph show the percentage of shoreline length for each variable state in the initial dataset (prior probability distributions).

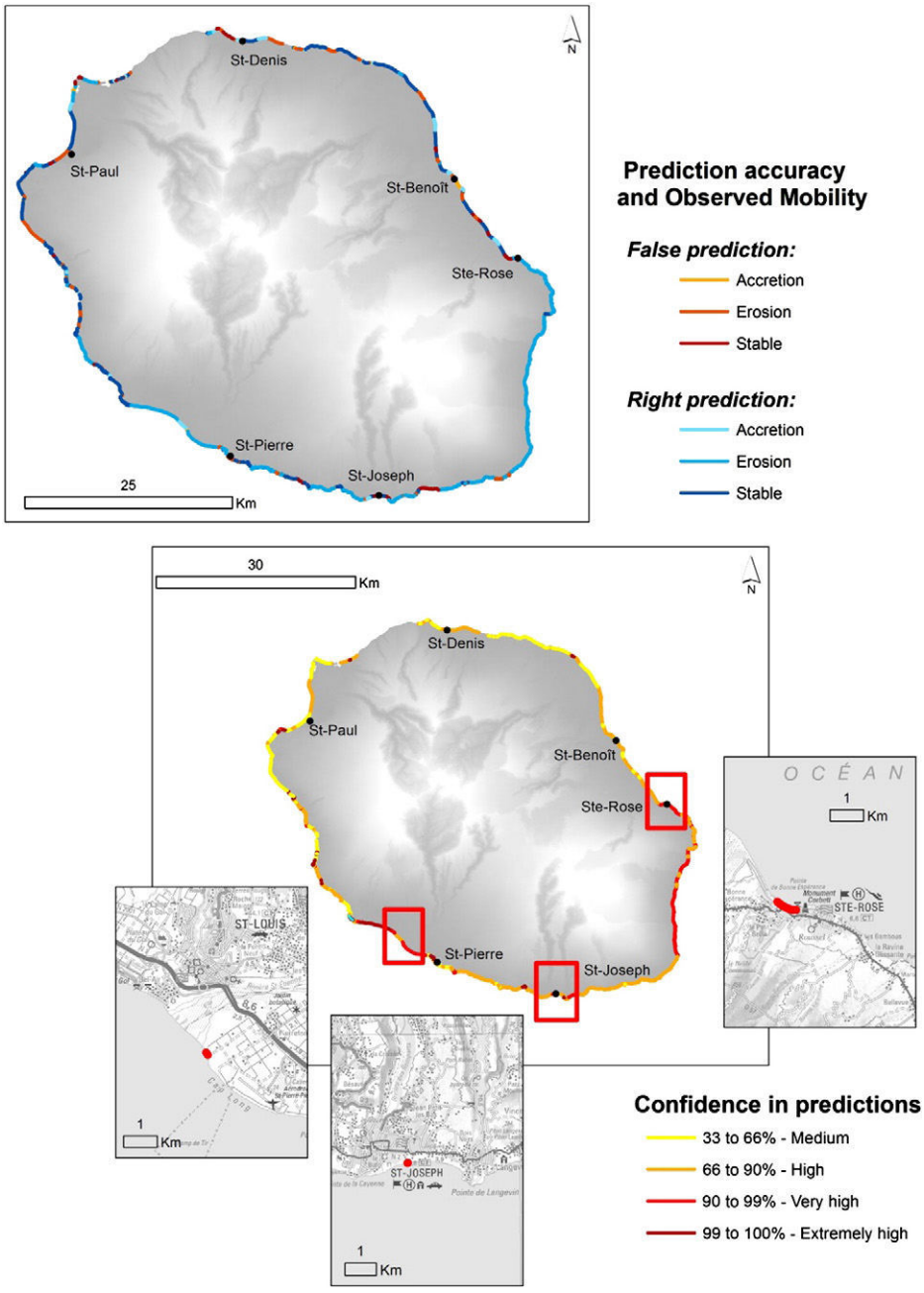

Fig. 7. Spatial variability of the predictive model outcome. Top: false and correct predictions and observed shoreline mobility for each coastal segment. Bottom: map of the confidence in the predictions, i.e. the probability of the predicted outcome. The red rectangles identify 3 segments that are incorrectly predicted with 'very high' confidence. Predictions in the northern part of the island are more uncertain than in the southern part. This indicates characteristics of coastal segments in the north with relatively wider probability distributions of shoreline mobility than in the south.

correctly predicted in erosion comes from the low representation of that variable category in the dataset (2.5% of the whole shoreline). The presence of anthropic structures does not inform much about erosion (black square and diamond taking similar values) but seems to be related to shoreline stability.

All the strong links found between each explanatory variable and shoreline mobility, as shown in Fig. 6, are consistent with an intuitive analysis, except for the rate of relative sea-level rise: for more than 55% of the shoreline where RSLR velocity is the highest, shoreline mobility is correctly predicted as stable, whereas for about 80% of the shoreline whose RSLR velocity is the lowest, shoreline mobility is correctly predicted in erosion. In other words, erosion is more frequent when the RSLR velocity is the lowest. This paradoxical behaviour of RSLR in the model is discussed in detail in Section 5.2.

Because of the counter-intuitive behaviour of the variable RSLR velocity, the next results are obtained using only the four other variables.

4.3. Performance with 4 variables

The global *LR* score of the BN using 4 variables (geomorphic setting, presence of estuary, presence of anthropic structures and exposure to energetic waves) is 0.18 (Fig. 5) and the proportion of the shoreline whose observed mobility is correctly predicted is 81%. More precisely, 85% of stable shoreline, 79% of eroding shoreline and 73% of accreting shoreline are correctly predicted. Fig. 7 (top) shows the locations where the retrospective predictions are correct or not.

Fig. 7 (bottom) maps the probability of the most likely outcome, an indicator which can be interpreted as the confidence in the

retrospective prediction. This map can be used to identify areas where there is a high level of uncertainties or great confidence in the outcome prediction (Gutierrez et al., 2011) which is useful to target where the BN needs improvements. Globally, more than 67% of the shoreline is correctly predicted with a 'high' confidence level or above (probability of the most likely outcome greater than 0.66) and almost 23% of the shoreline is correctly predicted with a 'very high' confidence level or above (probability of the most likely outcome greater than 0.9). By comparing Fig. 7 (top) and (bottom), we can also identify areas where there is great confidence in the outcome while the prediction is wrong. Only 3 of these particular sites are found falling within the 'very high' category, they are identified by red rectangles in Fig. 7 (bottom).

5. Discussion

5.1. Interpretation of BN results in terms of physical processes

Section 4.2 showed that geomorphic setting is the most important variable for understanding shoreline mobility on La Réunion. This is due to the fact that in the dataset, some well represented categories of GS are strongly linked to specific shoreline mobility. For example, 93% of cliffs in La Réunion are observed in erosion and cliffs are the main geomorphic settings around the island (38% of the shoreline). The presence of an estuary in the vicinity of a segment is the second most important variable for understanding shoreline mobility. In particular, it is the only characteristic identified to successfully predict accretion (see Section 4.2 and Fig. 6). This can be easily interpreted as accreting segments around the island are often subjected to the influence of river sediment supply: 73% of accreting shoreline has an estuary in its neighbourhood.

Stable and eroding coasts are better predicted by the BN than accreting shorelines, but the result for the latter category is still satisfying (73%, see Section 4.3). In fact, 100% of correctly predicted accreting shoreline has an estuary nearby which indicates that the remaining 27% of accreting shoreline has no estuary and is systematically mispredicted. That might be the result of a combination of factors including the relative scarcity of data for the accretion category (only 7% of the coast is accreting), which may prevent the BN from accurately identifying combinations of variables leading to accretion, and the incompleteness of the BN structure which does not take into account processes of sedimentary transport along the coast.

Alongshore sedimentary transport processes are generated by currents induced mainly by trade waves (see Section 3.2.4). They redistribute fine and coarse materials of marine or terrestrial origin (cliff and riverine sediments) along the coast from the south-east to the north-west. Although it is difficult to quantify the effect of these processes on shoreline mobility, there is evidence of their influence on local coastal evolution. For example, a natural rocky outcrop at La Pointe du Bourbier acts as a wall, stopping the coastal drift and accumulating sediments upstream. As a result, the coastal segment located immediately upstream of the outcrop is accreting (Fig. 8). Anthropic structures implanted directly on the shoreline, such as harbours, marinas or jetties, also highlight the importance of alongshore sedimentary transport when they disrupt it. A case in point is the jetty of Le Butor at Saint-Benoît where sediments accumulate updrift of the structure whereas erosion is observed downdrift (Fig. 8). These examples attest to the significant role played by alongshore transport in local sedimentary budgets and coastal evolution. As our BN model fails to take it into account, we might expect some mispredictions in the evaluation of BN performance in these cases.

It was noted in Section 4.2 and Fig. 5 that the presence of anthropic structures is the variable which has the weakest explanatory power with respect to shoreline mobility. However, stability seems to be successfully predicted when such structures are present (Fig. 6). This feature is then probably due to spatial correlation with other variables having higher explanatory power. Indeed, anthropic structures are mostly located on the west coast, where sandy beaches can be found as well as protecting reefs. These two variables' states are related to successful stability predictions and the corresponding variables (Geomorphic Setting and Waves) have stronger links with respect to shoreline mobility. Therefore, even if locally there is evidence of the direct influence of human interventions on shoreline mobility, other variables seem to dominate and control shoreline mobility at the scale of the island. It is worth noting that the influence of a human works located on a given coastal segment on an adjacent segment is not taken into account in our model. That might also explain the relatively weak link between the variables Anthropic Structures and Shoreline

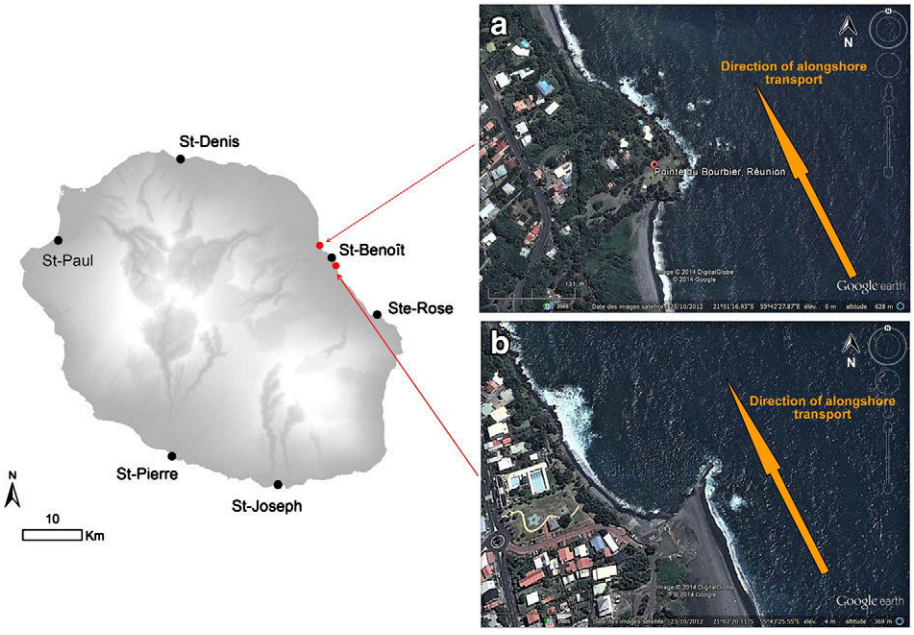

Fig. 8. Satellite views and localisation of a) the natural rocky outcrop at La Pointe du Bourbier, and b) the jetty of Le Butor at Saint-Benoît. The direction of the alongshore sedimentary transport is indicated by an orange arrow.

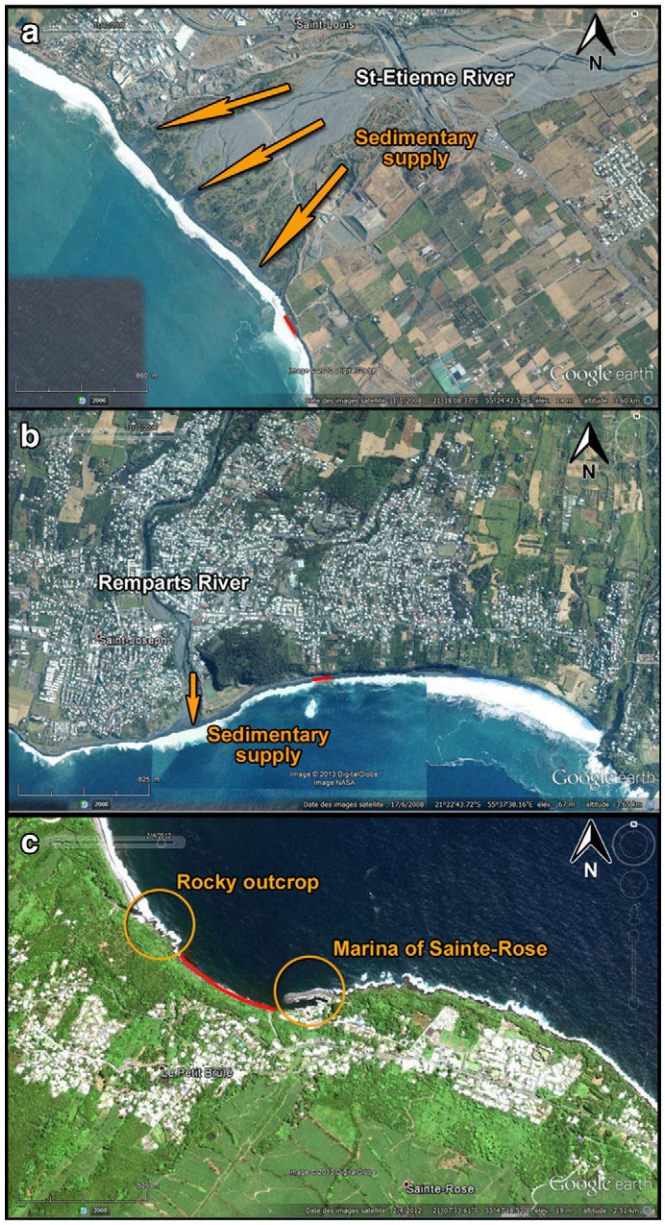

Fig. 9. Satellite views of the 3 zones identified in Fig. 6 (bottom). The coastal segments represented in red are wrongly predicted with great confidence. They are very specific and their mobility differs from the most common behaviour of similar segments. a) Segment located near Saint-Louis. b) Segment located near Saint-Joseph. c) Segment located near Sainte-Rose.

Mobility if the main impact of a structure is not felt in its immediate vicinity (i.e. the same segment) but relatively far from it (i.e. other segments).

Mispredicted areas with a high confidence level in the predicted outcome (Fig. 7) correspond to particular sites that differ from the common behaviour. Indeed, our predictive model constructed from the BN only reproduces the most common or probable shoreline mobility for a given set of characteristics. For example, Fig. 9 shows a satellite view of each of the 3 segments identified in Section 4.2, which are incorrectly predicted with great confidence. Looking more closely at these sites aids understanding as to why they are specific:

- the coastal segment near Saint-Louis (Fig. 9a) is predicted as being in erosion but is observed in accretion. The satellite picture indicates this segment is very close to the mouth of the Saint-Etienne River but not directly in front of it so that the 'Estuary' variable is set to 'No'. However, the influence of the river as a sediment supplier to the coast is likely to be felt by segments away from the mouth due to alongshore sedimentary transport. This might be the cause of the misprediction and it underscores a weakness of the BN, already mentioned above, which fails to take into account alongshore sedimentary transport processes.
- the coastal segment near Saint-Joseph (Fig. 9b) is predicted in erosion but is observed as stable. Its location is in a cove near the mouth of the Remparts River so that, similar to the previous segment, sediment supply by the Remparts river (Garcin et al., 2005) might compensate the erosive trend of that segment type and account for the observed stability of the segment.
- the coastal segment near Sainte-Rose (Fig. 9c) is predicted in erosion while observed as stable. It is located in a cove between a rocky outcrop and the marina of Sainte-Rose. This particular configuration may retain sediments in the cove and protects the shoreline from the impact of waves coming from south to south-east. This could explain the observed relative stability.

These examples show that the retrospective predictions of the BN, whether successful or not, can often be interpreted in terms of physical processes. They also demonstrate that BN results must be interpreted with care to get insight into the role of each variable. This point is discussed more on the particular case of the RSLR velocity variable in the next section.

This analysis at regional scale suggests priorities for future studies focusing on the most significant factors driving shoreline changes in La Réunion, in particular the role of sediment inputs by rivers and their remobilization through coastal alongshore processes, and of different coastal geomorphic features (e.g. stratigraphy, lithology, etc.…), particularly for coastal systems with the most uncertain predictions (e.g. beaches, see Fig. 7). While the last is acknowledged important by many studies (Trenhaile, 1987; Sunamura, 1992; Finkl, 2004; Hampton and Griggs, 2004; Idier et al., 2013; Loureiro et al., 2013), the first often remains difficult to quantify (e.g. Dearing et al., 2006).

5.2. Role of differing rates of sea-level rise in the model and physical sense

In this section, we discuss the counter-intuitive behaviour of the RSLR velocity variable as related to shoreline mobility and described in Section 4.2.

The RSLR velocity is the third most important variable in the 5 variables BN (Fig. 5) but it behaves in a paradoxical way (Fig. 6). This is confirmed in a more general manner looking at the marginal probability distribution of shoreline mobility given RSLR velocity, all the other variables being unknown (Table 2): coastal segments affected by faster rise of sea-level have only 29% chance to be in erosion, whereas those facing a slow rising sea-level have 79% chance to be in erosion. If we just consider beaches, which are considered more sensitive to sea-level rise, we again find no consistency between RSLR and shoreline mobility (Tables 3 and 4): the probability of stability dominates whatever the RSLR velocity for shingle beaches and the probability of erosion is even lower than the probability of accretion; for sand beaches, the probability of erosion is very high (87%) when they face a slow rising level. Should the RSLR velocity variable play a significant role in the shoreline

Table 2
Probability distribution of shoreline mobility given RSLR (5 variables BN). Values are obtained using the junction tree algorithm (Murphy, 2001).

	Shoreline mobility		
RSLR	Stability	Erosion	Accretion
High	0.59	0.29	0.12
Low	0.17	0.79	0.04
Medium	0.51	0.41	0.08

Table 3
Probability distribution of shingle beaches mobility given RSLR (5 variables BN). Values are obtained using the junction tree algorithm (Murphy, 2001).

	Shoreline mobility of shingle beaches		
RSLR	Stability	Erosion	Accretion
High	0.63	0.17	0.20
Low	0.68	0.04	0.28
Medium	0.63	0.15	0.22

mobility, cases where erosion is observed should be correlated with a faster rate of sea-level rise rather than a slow rising level (Zhang et al., 2004; Gutierrez et al., 2011; Romine et al., 2013; Shearman et al., 2013). In the case of La Réunion island, differing rates of relative sea-level rise have therefore no consistent perceivable impacts on shoreline mobility, suggesting that other processes dominate (see e.g. Stive, 2004; Webb and Kench, 2010; Ford, 2013; Yates et al., 2013). Noteworthy is the fact that RSLR is unlikely to impact the coastal geomorphology (recall arrows in Fig. 3) significantly here. Its role is indeed counter-intuitive. For example, Fig. 1 shows that cliffs are more frequent where the RSLR velocity is the lowest. This suggests there is no causal link between RSLR and cliffs. Instead, RLSR seems to serve as proxy for the uplift rate since uplift is the mechanism which creates elevated landforms such as cliffs.

The part of the island with an uplift trend is localised south and south-east and corresponds well with the influence zone of the active volcano Piton de la Fournaise (indicated with a black dashed line in Fig. 3). In fact, all the coastal landforms in this area are remnants, more or less recent, of the volcanic activity of the Piton de la Fournaise. In our BN, the volcanic activity is partially embedded in the GS variable, as cliffs and low rocky coasts are mainly made of more or less consolidated volcanic materials, and in the RSLR variable, integrating the uplift rate. Notwithstanding the limitations of the data used for assessing relative sea-level rise at the coast (see Section 3.2.6), we can interpret the obtained results if we consider that the dominant mode of coastal changes remains inseparable from the volcanic origin of the island: schematically, the volcanic products first reach the sea directly or after remobilization by rainfall and then are permanently undergoing coastal erosion. Our results suggest that the different rates of RSLR have a minor role compared to these processes. The high value of P(SM = erosion| RSLR = low) could just be due to spatial correlation between eroded landforms and uplifting coasts, both features being a consequence of the internal and external geodynamic mechanisms (volcanism (eruptions and uplift), erosion) that dominate the coastal geomorphic changes of the island. This illustrates once more that an in-depth analysis of BN results is required to avoid drawing wrong conclusions.

While this interpretation seems consistent, it would be important to test if coastal ground motions are linear in time or not. A third levelling campaign undertaken in 2007 by IGN is available but cannot be interpreted in terms of coastal ground motions because of data gaps. Delacourt et al. (2009) used InSAR data to provide information on vertical ground motions due to volcanic activity and landslides in La Réunion, but lack of coherence in the interferograms prevents the usage of this technique in the coastal zones. Finally, the recently installed permanent GPS could provide insight to this issue, but only at specific locations. This case study of La Réunion illustrates the fact that the spatial and temporal variability of relative sea-level changes along the coasts are often unknown and difficult to monitor, but they deserve specific attention since they are often not negligible compared to multidecadal sea-level rise.

Table 4
Probability distribution of sand beaches mobility given RSLR (5 variables BN). It should be considered that most of sand beaches are located on the western side of the island. Values are obtained using the junction tree algorithm (Murphy, 2001).

	Shoreline mobility of sand beaches		
RSLR	Stability	Erosion	Accretion
High	–	–	–
Low	0.12	0.87	0.01
Medium	0.60	0.35	0.05

6. Conclusions

While the BN method used in this study is not new, its application to La Réunion island provides different insight into coastal processes than previous applications. First, it is shown that, when building the database, rates of relative sea-level rise are not homogeneous at the scale of the island: the south-eastern part of the island uplifted from 1958 to 1989, the western part remained stable and the north-western part subsided. However, our results show that these differing rates of relative sea-level change did not significantly affect shoreline mobility. Instead, the results suggest that decadal coastal evolution in the island remains largely controlled by three major geomorphic processes ((i) coastal and (ii) inland sediment transport; (iii) volcanism, which provides erodible materials and generates ground motions) and by local geomorphic settings. This finding thus suggests that relative sea-level rise being an important cause for observed different rates of shoreline erosion (Zhang et al., 2004; Gutierrez et al., 2011) is not generally applicable to every other coastal site.

This study confirms the considerable potential for Bayesian networks to explore coastal databases and gain insight into coastal processes and factors causing shoreline changes, including sea-level changes. However, this work also identifies several difficulties in using BNs for exploring coastal datasets:

- First, an initial coastal dataset of high quality is a necessary prerequisite to perform any interpretation of shoreline change causes. To undertake this study, it was necessary to reprocess and complete the initial dataset. Our first tests enabled us to detect and correct small inconsistencies in the initial database, which would have been difficult to notice otherwise due to the large amount of coastal data (e.g. inaccurate location of fringing reefs, etc.).
- Secondly, it is necessary to pay attention to the representativeness of the dataset: a BN can operate even with very few data but at the cost of a lower accuracy in the outcomes, as it has been illustrated with the category 'micro-cliff behind sand bar' in Fig. 6. It is tempting to add other variables to the network or to consider more categories in each variable in order to reduce the uncertainties in the model outcome (Fig. 7). However, such an approach is likely to result in too few data available for each combination of variables, leading to an artificially deterministic BN. Therefore, it is important to find a compromise between improving the description of the network structure and keeping sufficient samples of data for each case considered during the learning phase.
- A third limitation concerns the physical meaning of the network structure: unlike many applications of Bayesian networks, the graph used here (Fig. 3) is not an accurate representation of the reality. On the contrary, it remains simplified scheme of coastal systems evolution. In any application of this approach, it is important to highlight that the graph will significantly impact results as it acts as previous knowledge but also that it inherits the initial dataset ontology, at least partly.
- Finally, the BN approach is useful to highlight particularly strong relationships between variables, but it does not provide us with the nature of those relationships. This last point is illustrated by the role of differing rates of relative sea-level rise in our study and the fact that this variable serves as a proxy for another causal factor (the uplift rate).

Any application of this approach therefore requires systematic completion of BN results with an in-depth analysis of the data and of the processes taking place in these coastal sites.

The complexity of coastal system behaviours currently prevents their modelling purely based on physical concepts. In addition, there is a crucial need for public authorities to understand and manage coastal environments. Bayesian networks contribute to answering this need by improving our understanding of coastal evolution at decadal timescales. They could ultimately allow moving towards long-term predictions of future coastal environment evolution.

Acknowledgements

This work has been completed within the CECILE project (Coastal Environmental Changes: Impact of sea LEvel rise) supported by the French National Agency for Research (ANR) within its Planetary Environmental Changes (CEP) framework: convention n°ANR-09-CEP-001. We thank the regional office of BRGM at La Réunion island (S. Bès de Berc, E. Chateauminois, Y. de la Torre) for providing coastal data initially collected for the Region and DIREN and for their comments. We also thank IGN (S. Lavoué, A. Coulomb) for providing raw levelling data and A. Cazenave, B. Meyssignac, D. Raucoules and C. Mirgon for useful discussions. Last, we thank two anonymous reviewers as well as A.J. Plater for their comments which contributed to improve this paper.

Appendix A. Calculation of the percentage of shoreline length correctly reproduced in the random case

In order to evaluate the significance level of the model, it is necessary to compare the percentage of shoreline length correctly predicted to the one obtained with a completely randomized dataset (while respecting the prior probability distributions of all variables, i.e. the probability distributions of the variables calculated from their frequencies of appearance in the database), thus removing any dependency between variables. In that case, Eq. (2) becomes:

$$SM_{pred} = arg\,\max_i \left(P\left(SM^i \middle| \tilde{X}_j\right)\right) = arg\,\max_i \left(P\left(SM^i\right)\right) \quad (A.1)$$

As a result, whatever the coastal segment, the shoreline mobility state having the maximum prior probability is systematically predicted. We then deduce the percentage of shoreline length correctly predicted in the case of a completely randomized dataset as follows:

$$\%\ correct\ \ predictions = \max_i \left(P\left(SM^i\right)\right) \times 100 \quad (A.2)$$

In our dataset, the prior probability distribution of shoreline mobility is: P(erosion) = 0.58, P(accretion) = 0.07, P(stability) = 0.35. Therefore, the percentage of shoreline length correctly reproduced in the random case is 58%.

Appendix B. Calculation of the possible maximum and minimum theoretical values of the global log-likelihood ratio

The possible maximum theoretical *LR* can be computed directly from Eq. (4) by replacing $LR_{(k)}$ by its maximum theoretical value:

$$LR_{(k)} = \log\left(P\left(SM_{(k)} \middle| O_{(k)}\right)\right) - \log\left(P\left(SM_{(k)}\right)\right) = -\log\left(P\left(SM_{(k)}\right)\right) \quad (B.1)$$

From our dataset, we obtain $LR_{max} = 0.38$.

The minimum *LR* is computed when the entire dataset is randomized (but still following the prior probability distributions) thus removing any dependency between variables and is equal to 0.

References

Aguilera, P.A., Fernandez, A., Fernandez, R., Rumi, R., Salmeron, A., 2011. Bayesian networks in environmental modelling. Environ. Model Softw. 26 (12), 1376–1388.
Berger, J.O., 2000. Bayesian analysis: a look at today and thoughts of tomorrow. J. Am. Stat. Assoc. 95, 1269–1276.
Bourmaud, C.A.F., Abouïdane, A., Boissier, P., Leclère, L., Mirault, E., Pennober, G., 2005. Coastal and marine biodiversity of La Réunion. Indian J. Mar. Sci. 34 (1), 98–103.
Catenacci, M., Giupponi, C., 2013. Integrated assessment of sea-level rise adaptation strategies using a Bayesian decision network approach. Environ. Model Softw. 44, 87–100.
Cazenave, A., Le Cozannet, G., 2014. Sea level rise and its coastal impacts. Earths Futur. 2 (2), 15–34.
De La Torre, Y., 2004. Synthèse morphodynamique des littoraux de La Réunion, état des lieux et tendances d'évolution à l'échelle de l'île. Open file report BRGM/RP-53307-FR.
Dearing, J.A., Richmond, N., Plater, A.J., Wolf, J., Prandle, D., Coulthard, T.J., 2006. Modelling approaches for coastal simulation based on cellular automata: the need and potential. Philos. Trans. R. Soc. A Math. Phys. Eng. Sci. 364 (1841), 1051–1071.
Delacourt, C., Raucoules, D., Le Mouelic, S., Carnec, C., Feurer, D., Allemand, P., Cruchet, M., 2009. Observation of a large landslide on La Reunion Island using differential Sar Interferometry (JERS and Radarsat) and correlation of optical (Spot5 and aerial) images. Sensors 9 (1), 616–630.
Eurosion, 2004. Living with coastal erosion in Europe: sediment and space for sustainability. Part I: Major findings and policy recommendations of the EUROSION project.
Finkl, C.W., 2004. Coastal classification: systematic approaches to consider in the development of a comprehensive scheme. J. Coast. Res. 20 (1), 166–213.
Ford, M., 2013. Shoreline changes interpreted from multi-temporal aerial photographs and high resolution satellite images: Wotje Atoll, Marshall Islands. Remote Sens. Environ. 135, 130–140.
Garcin, M., Poisson, B., Pouget, R., 2005. High rate of geomorphological processes in a tropical area: the Remparts river case study (Réunion Island, Indian Ocean). Geomorphology 67 (3–4), 335–550.
Gillot, P.Y., Nativel, P., 1989. Eruptive history of the Piton de la Fournaise volcano, Réunion island, Indian Ocean. J. Volcanol. Geotherm. Res. 36, 53–65.
Gutierrez, B.T., Plant, N.G., Thieler, E.R., 2011. A Bayesian network to predict coastal vulnerability to sea level rise. J. Geophys. Res. Earth Surf. 116, 15.
Hampton, M.A., Griggs, G.B., 2004. Formation, evolution and stability of coastal cliffs — status and trends. USGS Professional Paper. 1683 (123 pp.).
Hapke, C., Plant, N., 2010. Predicting coastal cliff erosion using a Bayesian probabilistic model. Mar. Geol. 278 (1–4), 140–149.
Heckerman, D., 1997. Bayesian networks for data mining. Data Min. Knowl. Disc. 1, 79–119.
Idier, D., et al., 2013. Vulnerability of sandy coasts to climate variability. Clim. Res. 57 (1), 19–44.
Karunarathna, H., Reeve, D., 2007. Predicting morphodynamic response of a coastal plain estuary using a Boolean model. Proceedings of the 5th IAHR Symposium on River, Coastal and Estuarine Morphodynamics, Enschede, NL, 17–21 September 2007, pp. 1109–1115.
Karunarathna, H., Reeve, D., 2008. A Boolean approach to prediction of long-term evolution of estuary morphology. J. Coast. Res. 24 (2B), 51–61.
Lavoué, S., 2013. Comparaisons de nivellement sur le littoral réunionnais. CR/G 276, IGN, Servive de Géodésie et de Nivellement.
Le Cozannet, G., Garcin, M., Bulteau, T., Mirgon, C., Yates, M.L., Mendez, M., Baills, A., Idier, D., Oliveros, C., 2013. An AHP-derived method for mapping the physical vulnerability of coastal areas at regional scales. Nat. Hazards Earth Syst. Sci. 13 (5), 1209–1227.
Lecacheux, S., Pedreros, R., Le Cozannet, G., Thiebot, J., De La Torre, Y., Bulteau, T., 2012. A method to characterize the different extreme waves for islands exposed to various wave regimes: a case study devoted to Reunion Island. Nat. Hazards Earth Syst. Sci. 12 (7).
Loureiro, C., Ferreira, O., Cooper, J.A.G., 2013. Applicability of parametric beach morphodynamic state classification on embayed beaches. Mar. Geol. 346, 153–164.
Meyssignac, B., Becker, M., Llovel, W., Cazenave, A., 2012. An assessment of two-dimensional past sea level reconstructions over 1950–2009 based on tide-gauge data and different input sea level grids. Surv. Geophys. 33 (5), 945–972.
Murphy, K.P., 2001. The Bayes net toolbox for Matlab. Comput. Sci. Stat. 33 (2), 1024–1034.
Myllymäki, P., Silander, T., Tirri, H., Uronen, P., 2002. B-Course, a web-based tool for Bayesian and causal data analysis. Int. J. Artif. Intell. Tools 11 (3), 369–387.
Naïm, P., Wuillemin, P.-H., Leray, P., Pourret, O., Becker, A., 2007. Réseaux bayésiens. Eyrolles, Paris.
Palanisamy, H., Cazenave, A., Meyssignac, B., Soudarin, L., Woppelmann, G., Becker, M., 2014. Regional sea level variability, total relative sea level rise and its impacts on islands and coastal zones of Indian Ocean over the last sixty years. Glob. Planet. Chang. http://dx.doi.org/10.1016/j.gloplacha.2014.02.001.
Pearl, J., 1986. Fusion, propagation and structuring in belief networks. Artif. Intell. 29, 241–288.
Plant, N.G., Holland, K.T., 2011a. Prediction and assimilation of surf-zone processes using a Bayesian network part I: forward models. Coast. Eng. 58 (1), 119–130.
Plant, N.G., Holland, K.T., 2011b. Prediction and assimilation of surf-zone processes using a Bayesian network part II: inverse models. Coast. Eng. 58 (3), 256–266.
Plant, N.G., Stockdon, H.F., 2012. Probabilistic prediction of barrier-island response to hurricanes. J. Geophys. Res. Earth Surf. 117.
Quelennec, R.-E., Oliveros, C., Uhel, R., Devos, W., 1998. Corine: érosion côtière. Environmental and quality of life series. Office for Official Publications of the European Communities, Luxembourg (170 pp.).
Rocher, P., 1988. Contexte volcanique et structural de l'hydrothermalisme récent dans le massif du Piton des Neiges, île de La Réunion(PhD Thesis) Etude détaillée du Cirque de Salazie. Université de Paris Orsay.

Romine, B.M., Fletcher, C.H., Barbee, M.M., Anderson, T.R., Frazer, L.N., 2013. Are beach erosion rates and sea-level rise related in Hawaii? Glob. Planet. Chang. 108, 149–157.
Shearman, P., Bryan, J., Walsh, J.P., 2013. Trends in deltaic change over three decades in the Asia-Pacific Region. J. Coast. Res. 29 (5), 1169–1183.
Stive, M.J.F., 2004. How important is global warming for coastal erosion? An editorial comment. Clim. Chang. 64 (1–2).
Storlazzi, C.D., Elias, E., Field, M.E., Presto, M.K., 2011. Numerical modeling of the impact of sea-level rise on fringing coral reef hydrodynamics and sediment transport. Coral Reefs 30.
Sunamura, T., 1992. Geomorphology of Rocky Coasts. John Wiley and Sons, New York.
Thieler, E.R., Hammar-Klose, E.S., 1999. National assessment of coastal vulnerability to future sea-level rise: preliminary results for U.S. Atlantic Coast. U.S. Geol. Surv. Open File Report, Woods Hole, Massachusetts, 99-593.
Trenhaile, A.S., 1987. The Geomorphology of Rock Coasts. Oxford University Press, New York.
Uusitalo, L., 2007. Advantages and challenges of Bayesian networks in environmental modelling. Ecol. Model. 203, 312–318.
Webb, A.P., Kench, P.S., 2010. The dynamic response of reef islands to sea-level rise: evidence from multi-decadal analysis of island change in the Central Pacific. Glob. Planet. Chang. 72 (3), 234–246.
Yates, M.L., Le Cozannet, G., 2012. Brief communication 'Evaluating European Coastal Evolution using Bayesian Networks'. Nat. Hazards Earth Syst. Sci. 12 (4), 1173–1177.
Yates, M.L., Le Cozannet, G., Garcin, M., Salaï, E., Walker, P., 2013. Multidecadal atoll shoreline change on Manihi and Manuae, French Polynesia. J. Coast. Res. 29 (4), 870–882.
Yin, J., Yin, Z., Wang, J., Xu, S., 2012. National assessment of coastal vulnerability to sea-level rise for the Chinese coast. J. Coast. Conserv. 16 (1), 123–133.
Zhang, K.Q., Douglas, B.C., Leatherman, S.P., 2004. Global warming and coastal erosion. Clim. Chang. 64 (1–2).